
A PHENOMENOLOGICAL STUDY OF
STAR FORMATION AND CHEMICAL EVOLUTION
IN NEARBY GALAXIES

Thomas M. Hughes

A THESIS SUBMITTED TO
CARDIFF UNIVERSITY
FOR THE DEGREE OF
DOCTOR OF PHILOSOPHY

OCTOBER 2010

UMI Number: U516819

All rights reserved

INFORMATION TO ALL USERS

The quality of this reproduction is dependent upon the quality of the copy submitted.

In the unlikely event that the author did not send a complete manuscript and there are missing pages, these will be noted. Also, if material had to be removed, a note will indicate the deletion.



UMI U516819

Published by ProQuest LLC 2013. Copyright in the Dissertation held by the Author.
Microform Edition © ProQuest LLC.

All rights reserved. This work is protected against
unauthorized copying under Title 17, United States Code.



ProQuest LLC
789 East Eisenhower Parkway
P.O. Box 1346
Ann Arbor, MI 48106-1346

Author: Thomas M. Hughes

Title: A Phenomenological Study of Star Formation and Chemical Evolution in Nearby Galaxies

Date of submission: October 2010

Permission is granted to Cardiff University to circulate and to have copied for non-commercial purposes, at its discretion, the above title upon the request of individuals or institutions. The author reserves other publication rights, and neither the thesis nor extensive extracts from it may be printed or otherwise reproduced without the author's written permission.

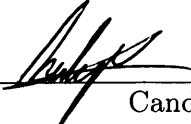
Copyright © 2010 by Thomas M. Hughes

896554

Declaration

This work has not previously been accepted in substance for any degree and is not being concurrently submitted in candidature for any degree.

Signed:


Candidate

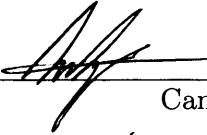
Date:

13/10/2010

Statement 1

This thesis is being submitted in the partial fulfillment of the requirements for the degree of PhD.

Signed:


Candidate

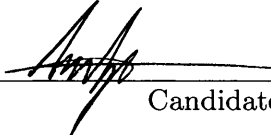
Date:

13/10/2010

Statement 2

This thesis is the result of my own investigations, except where otherwise stated. Other sources are acknowledged giving explicit references. A bibliography is appended.

Signed:


Candidate

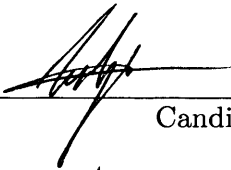
Date:

13/10/2010

Statement 3

I hereby give consent for my thesis, if accepted, to be available for photocopying and for inter-library loan, and for the title and summary to be available to outside organisations.

Signed:


Candidate

Date:

13/10/2010



To my parents,
who always doubted
the bubble may burst.

ABSTRACT

The processes influencing galaxy evolution in the local universe are investigated using a dataset of multiwavelength observations for a new sample of galaxies. The sample is volume and mass limited, and includes galaxies of all morphological types inhabiting a range of different environments, from galaxies in the dense core of the Virgo cluster to relatively isolated systems. As such, the sample is ideal for disentangling the internal and environmental processes driving evolution. The combination of ultraviolet, optical, near- and far-infrared imaging, nuclear and integrated optical spectroscopy, and atomic hydrogen emission line data, traces the key galaxy components, such as the stellar populations, gas content, star formation, metallicity and nuclear activity. The main aims of this thesis are: (a) an investigation into the evolutionary histories of nearby galaxies to determine the dominant mechanism quenching star formation; (b) the determination of the impact of feedback from active galactic nuclei on star formation; and (c) a study of the evolution of the chemical composition of star-forming galaxies in different environments. The analysis performed in this thesis confirms recent observations of a population of late-type galaxies with reduced levels of star formation. I demonstrate that feedback from active nuclei is unlikely to be the dominant mechanism quenching star formation and driving the evolution of these late-type galaxies. In fact, galaxies with quenched star formation are typically gas deficient systems residing in the cluster environment, suggesting that environmental effects are responsible for removing the gas required to fuel star formation in these objects. A fraction of quenched late-type galaxies are, however, not gas deficient, and form a more heterogeneous class of objects with probably more complex evolutionary histories. In contrast to the case of star formation, the chemical evolution of star-forming galaxies, as traced by the stellar mass-metallicity relation, is shown to be invariant across different environments, suggesting that chemical evolution may be driven by internal processes, thus placing an upper limit on the effect of the environment. The clear observational evidence presented here indicates that, in the concordance model of galaxy formation and evolution, environmental effects must be taken into account in order to gain a better understanding of galaxy evolution in the local universe.

ACKNOWLEDGEMENTS

This thesis marks the final steps of my formal education, since first starting primary school 20 years ago. Many people - family, friends and colleagues - have supported me on this incredible journey and I would like to take this opportunity to show my appreciation.

First, I wish to thank my supervisor, Luca Cortese. Without his excellent guidance, advice and constructive criticism, this thesis would not have been possible. I am very much indebted to him for all his time and energy spent on my supervision. I also wish to thank Jonathan Davies, for giving me the fantastic opportunity to research extragalactic astronomy at Cardiff University and for all of his support and advice over the last three years. This thesis is based on data provided by Alessandro Boselli and Giuseppe Gavazzi, for which I am extremely grateful.

Also, I thank the members of the Galaxies research group, for all their useful discussion and stimulating talks, and, in particular, the 'Galaxy Boys': Rory Smith, Rhys Taylor, Matthew Smith and Elizabeth Pearson for all the interesting chats, scientific advice and office banter.

I consider myself fortunate to have made some good friends in the department - Sarah, Ian, Gwen, Sara, Fraser, Vanessa, Olly, Lucy, Laura, Olly, Ciara, and many others - who all played a major role in giving me a lot of happy memories of my time as a postgraduate. I will fondly miss the coffee breaks, cake days and pub trips we shared over the years. In addition, although I only met up with Boris and Julia a few times, I was always glad of our online interaction. I would also like to mention the friendly support from Nick, Chris, Jon, Pad, Sam, Claire, Andrews, Seb, Stuart, Patti, Rob, my fellow Redhawks and, most of all, Rachael, who gave me so much strength and encouragement during the writing of this thesis. And Jack, stop wasting your time with biology, we both know physics provides *all* the answers!

Last, but by no means the least, I wish to thank my family - Mum, Dad, David and Nan - for their unwavering love and support throughout my life, which made all my adventures in astrophysics possible.

Thank you, all.

CONTENTS

Abstract	vii
Acknowledgements	ix
List of Tables	xiv
List of Figures	xvii
1 Introduction	1
1.1 A brief historical introduction	1
1.2 The concordance model	3
1.3 Galaxy evolution	5
1.3.1 Feedback from active nuclei	6
1.3.2 Environmental effects	11
1.4 Nature versus nurture?	14
1.5 Thesis outline	16
2 The HRS+ Sample	19
2.1 The Herschel Reference Survey	19
2.2 Selection criteria	20
2.3 Mutliwavelength observations	23
2.3.1 Summary of observations	25
2.4 Derived physical properties	28
2.4.1 Stellar mass	28
2.4.2 HI mass and deficiency	29
2.4.3 Classification of nuclear activity	31
2.5 Conclusions	33
3 Ultraviolet Photometry	35
3.1 Introduction	35
3.2 The Galaxy Evolution Explorer	36
3.3 UV observations	37
3.4 Aperture photometry	38
3.5 Dust attenuation corrections	39
3.6 Star formation rates	41
3.7 Conclusions	42

4	Optical Spectroscopy	45
4.1	Introduction	45
4.2	The B08 observations	47
4.3	Data Reduction	48
4.3.1	Noise subtraction	48
4.3.2	Wavelength calibration	51
4.3.3	Background subtraction	54
4.3.4	Extraction of 1D spectra	54
4.3.5	Flux calibration	55
4.3.6	Redshift correction	57
4.4	Emission line flux measurements	58
4.5	Conclusions	62
5	Evolutionary Paths of Nearby Galaxies	63
5.1	Introduction	63
5.2	The colour-mass diagram	64
5.3	The link between HI content and colour	68
5.4	Defining the transition region	70
5.5	The properties of transition galaxies	75
5.5.1	HI-deficient systems	75
5.5.2	HI-normal galaxies	81
5.6	Discussion & conclusions	87
5.6.1	The migration of HI-deficient galaxies	89
5.6.2	The HI-normal transition galaxies	91
6	Colour Profiles In Virgo	95
6.1	Introduction	95
6.2	Sample caveat	97
6.3	Surface photometry	98
6.4	Ultraviolet-infrared colour profiles	105
6.5	Variation in isophotal radii	107
6.6	Conclusions	108
7	The Importance Of AGN Feedback	111
7.1	Introduction	111
7.2	Modelling nuclear activity	113
7.2.1	Formation & gas cooling	113
7.2.2	Disk sizes	116
7.2.3	Star formation	116
7.2.4	AGN feedback	117
7.3	Estimating nuclear activity	121
7.3.1	The [OIII] luminosity indicator	121
7.4	Comparison of theory with observations	124
7.4.1	Star formation rates	124
7.4.2	The SFR- M_{acc} relationship	124
7.5	Conclusions	129

8	Measuring Metallicity	133
8.1	Introduction	133
8.2	Determining the metallicity	134
8.3	Calibration methods	137
8.3.1	The R_{23} ratio	138
8.3.2	The $[\text{NII}]/\text{H}\alpha$ ratio	141
8.3.3	The $[\text{OIII}]/[\text{NII}]$ ratio	142
8.4	Discrepancies between calibrations	142
8.5	Metallicity estimates	144
8.6	Base conversion	148
8.7	Conclusions	151
9	The Mass-Metallicity Relation	161
9.1	Introduction	161
9.2	Defining the M-Z relation	162
9.3	Scatter in the M-Z relation	169
9.3.1	Environmental effects	169
9.3.2	HI deficiency	173
9.3.3	Gas content	177
9.4	The closed-box model	180
9.5	Conclusions	190
10	Discussion & Conclusions	193
10.1	Overview	193
10.2	Key results	194
10.3	Constraints on galaxy evolution	195
10.3.1	Star formation on the blue cloud	195
10.3.2	Migration from the blue cloud	197
10.3.3	Evolution from the red sequence	199
10.4	Final conclusion	199
10.5	Future work	201
A	The HRS+ Members	207
B	Optical Spectroscopy	243
C	Emission Line Fluxes	253
D	Radial Profiles	257
E	Metallicity Estimates	267
E.1	Measured oxygen abundances	268
E.2	Final oxygen abundances	274

LIST OF TABLES

2.1	The completeness of the UV data, integrated and nuclear spectroscopy, B and V photometry and HI observations for the total sample and for the different subsamples, as available at the start of this thesis	28
2.2	Mean B-V values from galaxies binned by morphological type	30
3.1	Locations of clusters for which GALEX observations were obtained .	37
4.1	The reddening function $f(\lambda)$ of Lequeux et al. (1979), which is based on the extinction law of Whitford (1958), adopted for the extinction corrections relative to $H\beta$	60
5.1	The properties of HI-normal transition and red-sequence galaxies in the HRS+ sample	80
7.1	The values assumed for various parameters used in the toy analytic model of AGN feedback	120
8.1	A summary of the different calibrations used to estimate the gas-phase metallicity	138
8.2	The number of measured metallicity estimates for the 421 observed galaxies obtained from each (unconverted) calibration and by then converting the estimates using each method as a base calibration.	149
8.3	The validity ranges and coefficients for converting abundances derived from each initial calibration into abundances based on a base calibration	159
9.1	Properties of the 23 galaxies with D02-based metallicities $12+\log(O/H) > 8.9$, all of which display nuclear activity	167
9.2	The coefficients and χ^2_ν values given by linear and polynomial least-squares fits to the total sample in the mass-metallicity plots	168
9.3	The coefficients and χ^2_ν values given by linear and polynomial least-squares fits to the observations of galaxies in different environments in the mass-metallicity plots	172
A.1	The general properties of galaxies comprising the HRS+ sample. . . .	208
C.1	Measured C_1 values and corrected emission line intensities, normalised to the $H\alpha$ intensity	254

E.1	Oxygen abundances in units of $12 + \log (O/H)$ based on different line ratio calibration methods	268
E.2	Oxygen abundances derived from different calibrations and converted into the D02 base metallicity, then averaged to give the final metallicity measurement for each galaxy	274
E.3	Oxygen abundances derived from different calibrations and converted into the PP04 O3N2 base metallicity, then averaged to give the final metallicity measurement for each galaxy	280

LIST OF FIGURES

1.1	The morphological classification scheme of galaxies	2
1.2	The unified model of active galactic nuclei	7
1.3	The observed K-band luminosity function of galaxies in the local Universe compared to theoretical predictions, with and without AGN feedback	9
2.1	The sky distribution of the HRS+ galaxies, with a magnified view of the Virgo cluster region	21
2.2	A comparison of the morphological type and K band luminosity distributions for the HRS and HRS+ samples	22
2.3	The completeness of observations of HRS+ galaxies in the FUV, NUV and B bands	26
2.3	The completeness of HRS+ galaxies imaged in the V band, and with optical spectroscopy and H α line measurements	27
2.4	The BPT diagnostic diagram used to classify the spectra of galaxies in this work	32
3.1	A GALEX NUV band image of VCC1043	38
3.2	A comparison between FUV and NUV magnitudes measured via aperture photometry, for which multiple observations are available	40
3.3	A comparison between the FUV and NUV magnitudes measured in this work to measurements made in previous studies	40
3.4	The completeness of HRS+ galaxies observed in the ultraviolet bands	43
4.1	The spectroscopic coverage of the late-type galaxies in the HRS+ sample	46
4.2	Various CCD images obtained during the reduction of optical spectroscopy	50
4.3	An example exposure of an argon calibration lamp used to calibrate the wavelength scale of the science images	52
4.4	The residual wavelengths from measurements of five prominent sky emission lines and the reduced dispersion of the distribution following corrections	53
4.5	Normalised sensitivity functions across the detector, with a magnified view of the 3300-4300 Å wavelength range	56
4.6	Residual sensitivity functions from standard star observations from each observing night	57
4.7	The optical spectrum of NGC 4561 before and after the flux calibration	58

4.8	Spectroscopic redshifts compared to values reported in NED	59
4.9	A comparison of the emission line fluxes as determined from two independent sets of measurements	61
4.10	The improved spectroscopic coverage of late-type galaxies in the HRS+ sample	62
5.1	The ultraviolet-infrared colour-mass diagrams for galaxies comprising the total sample, the Virgo cluster and the field environment. AGN-hosts and gas deficient galaxies are highlighted	65
5.2	SDSS images arranged from the bluest to the reddest spiral	67
5.3	The relationship between HI content and ultraviolet-infrared colour	69
5.4	The ultraviolet-infrared colour-mass diagram showing the defined boundaries of the transition region	71
5.5	The morphological type distribution of HRS+ galaxies divided according to their location on the colour-mass diagram	72
5.6	The $FUV - H$, $NUV - B$, $B - H$ and $FUV - NUV$ colour-mass diagrams, highlighting the locations of transition region galaxies	73
5.7	Stellar mass distribution of the transition region galaxies, divided by morphological type and by HI content	74
5.8	The cluster-centric projected-distance and line-of-sight velocity distribution of galaxies in the Virgo cluster region	74
5.9	The ultraviolet-infrared colour-mass diagram highlighting galaxies for which a stripping timescale estimate is available	78
5.10	SDSS and GALEX images of HI-normal transition galaxies	82
5.11	SDSS and GALEX images of HI-normal red-sequence galaxies	83
5.12	The Masters et al. (2010) $g - r$ colour-magnitude diagram compared with a $NUV - r$ diagram for the same sample of galaxies	87
5.13	The distribution of the concentration index in H-band for Virgo cluster galaxies	89
5.14	The distribution of the H-band concentration index for Virgo HI-deficient and HI-normal transition galaxies	92
6.1	The completeness of the massive late-type galaxies with colour profiles compared to the VCC and HRS+ samples, and their positions on ultraviolet-infrared colour-mass diagrams	99
6.2	NGC 4548 as imaged in ultraviolet, optical and infrared bands	101
6.3	Aligned and scaled multiwavelength observations of VCC1615 and radial surface brightness profiles obtained for three different bands	104
6.4	Radial NUV-H colour profiles divided according to the integrated NUV-H colour, for the blue cloud, red sequence and the transition region. Profiles are further divided by nuclear activity and HI content	106
6.5	The average radial NUV-H colour profiles of the total sample, HI deficient galaxies and AGN-host galaxies	107
6.6	The $R_{26,NUV}/R_{20,H}$ ratio plotted against the HI deficiency and nuclear activity	109

7.1	Colour-magnitude diagrams for the disk galaxy model of Okamoto et al. (2008) with and without AGN feedback	112
7.2	The dependency of the cooling rate on the temperature and metallicity of gas in the dark matter halo	115
7.3	The M_{halo} - M_{bh} relationship reported by four examples in the literature	118
7.4	A comparison of the $\dot{m}_{heat}/\dot{m}_{cool}$ ratio to the r_{cool}/r_{vir} ratio as a function of halo mass	119
7.5	The spectroscopic coverage of late-type, AGN-host galaxies in the SDSS	123
7.6	A comparison of the predicted relationship between the specific star formation rate (SFR/ M_*) and the stellar mass and the observed relationship in star-forming late-types	125
7.7	The estimated mass accretion and star formation rates	126
7.8	The estimated mass accretion and star formation rates from this work, compared to those from the study of Satyapal et al. (2005)	128
7.9	The estimated mass accretion and star formation rates from this work, compared to the predictions the star formation rate as a function of the mass accretion rate from the toy model	129
7.10	The estimated mass accretion and star formation rates from this work and Satyapal et al. (2005), compared to the predictions the star formation rate as a function of the mass accretion rate from the toy model	130
8.1	Prominent emission line features in the optical spectrum of NGC 4747, including the HI recombination lines and forbidden lines arising from O, N and S	137
8.2	The observed and theoretical relationships between the R_{23} ratio and the NII/OII and NII/ $H\alpha$ ratios	140
8.3	The large discrepancies in the overall shape of M-Z relations derived from different metallicity calibrations	143
8.4	The relationships between the metallicities obtained from the six calibration methods	147
8.5	Z-Z relationships with M91 as the base metallicity	152
8.6	Z-Z relationships with Z94 as the base metallicity	153
8.7	Z-Z relationships with D02 as the base metallicity	154
8.8	Z-Z relationships with PP04 O3N2 as the base metallicity	155
8.9	Z-Z relationships with PP04 N2 as the base metallicity	156
8.10	The distribution of the errors in the final metallicity values, presented for both the D02 and the PP04 base calibrations	158
9.1	The mass-metallicity relationship for the HRS+ sample of galaxies, using D02 and PP04 base calibrations	162
9.2	The mass-metallicity relationship for the HRS+ sample, highlighting estimates derived from single measurements	164
9.3	Oxygen abundance versus the NII/ $H\alpha$ ratio and the D02 metallicity calibration	165
9.4	The BPT diagnostic diagram used to classify the spectra of galaxies in this work	166

9.5	The residual metallicities for the D02 and PP04 estimates	168
9.6	The M-Z relations observed from galaxies residing in the Virgo cluster region and outside the cluster environment	171
9.7	The residual M-Z relations observed for galaxies in the Virgo cluster and outside the cluster environment	173
9.8	The M-Z diagrams, divided according to their HI gas content. The apparent shift in mean metallicity when integrating along abundance gradients based on different metallicity calibrators is demonstrated . .	176
9.9	The relationships between metallicity and gas fraction in different environments	179
9.10	A schematic diagram of metallicity versus the logarithm of the inverse of the gas fraction μ in the simple chemical evolution model	184
9.11	The effective yield versus the logarithm of the stellar mass using metallicities derived from the D02 and PP04 base calibrations, and the observed mean effective yield	185
9.12	The observed relationship between the metallicity and the logarithm of the inverse of the gas fraction μ , fitted by the prediction of the closed-box chemical evolution model	186
9.13	The oxygen abundance versus the logarithm of the gas fraction, fitted with the prediction of the closed-box model	187
9.14	The specific star formation rate versus stellar mass for the HRS+ galaxies	189
10.1	The relationship between metallicity and the dust-to-gas ratio	204
A.1	SDSS composite images of all the HRS+ galaxies.	219
B.1	The reduced and calibrated spectra of the 95 galaxies comprising the B08 observations	244
D.1	The surface brightness profiles and ultraviolet-infrared colour gradients obtained using NUV, FUV and H band photometry	258

CHAPTER 1

INTRODUCTION

1.1 A BRIEF HISTORICAL INTRODUCTION

Extragalactic astronomy is a fascinating, yet surprisingly young subject. In fact, it was approximately ninety years ago that some of the objects observed in the night sky were recognised as existing far beyond the realms of our own Galaxy. These objects appeared as luminous smudges, clearly contrasting with the point-like light distributions of individual stars and more akin to the dim band of light called the Milky Way.

These fuzzy objects were first catalogued by Messier (1781), who called the objects *nebulae*. Larger catalogues of nebulae were later compiled by Herschel, his sister and son, in the General Catalogue (Herschel, 1864), and updated in the New General Catalogue (NGC; Dreyer, 1888). Although the nebulae were found to exhibit a range of morphologies, from spiral and elliptical structures to more irregular shapes, their exact nature was unknown. Spiral nebulae, discovered via drawings of the Whirlpool Galaxy by Lord Rosse, were interpreted by some astronomers as small proto-planetary disks inhabiting the Galaxy, whereas others advocated they were distant objects similar to our own Galaxy. In fact, speculation that the nebulae were ‘island universes’ external to our Galaxy dates back to the 1750s, in the works of Thomas Wright and Immanuel Kant. The so-called ‘Great Debate’ between Shapely and Curtis, arguing the cases for both interpretations, highlights how the controversy surrounding the nature of the nebulae existed as late as 1920. Evidence to conclusively prove the nebulae are not small, nearby objects but are instead vast systems at large distances was only obtained during the 1920s. Using the characteristic variation in the brightness of Cepheid variable stars and their discovery in the nearby Andromeda Nebula, Hubble was able to show that Andromeda must reside approximately 285 kpc

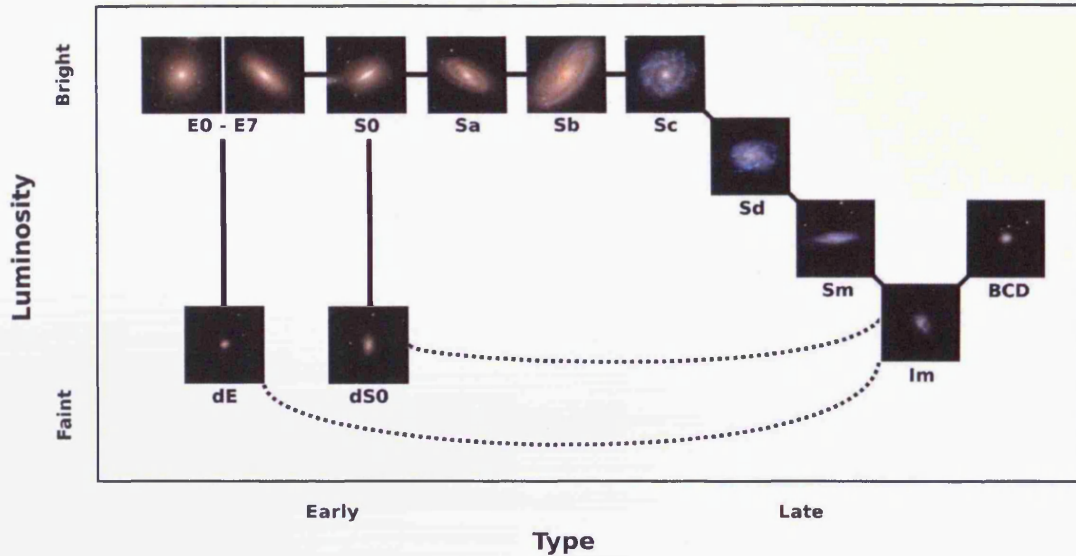


Figure 1.1: The Hubble morphological classification scheme of bright galaxies (E through to Sd), later adapted to include fainter dwarf systems (dE/dS0 to BCD). The dotted lines show the possible connection between early-type and late-type dwarfs. This figure is adapted from Sandage & Binggeli (1984).

away, a distance well outside our own Galaxy (Hubble, 1925). Thus, with the ability to measure the distances to nebulae and discriminate between planetary nebulae and external galaxies, extragalactic astronomy was born.

Hubble went on to make a number of important contributions to the study of galaxies. In 1926, he proposed a classification scheme for galaxies based on their morphology as observed on photographic plates. Galaxies are broadly classified into ellipticals (E), lenticulars (S0) and spirals (S) in the Hubble scheme. This was later updated by Sandage & Binggeli (1984) to include the fainter dwarf elliptical (dE) and lenticular (dS0) galaxies, blue compact dwarfs (BCD) and irregular late-types (Sm and Im). This classification is summarised in Figure 1.1.

Thanks to technological advancements in telescopes and instrumentation during the 20th Century, we now have a much clearer picture of the nature of galaxies, in which the morphology is just the tip of an iceberg of properties inherent to a galaxy. Galaxies are in fact massive, gravitationally bound systems composed of stars, interstellar material, such as gas and dust, and an unobserved but inferred component called dark matter. Studies into the stellar populations, kinematics and structural properties yield important differences in galaxies of varying morphology type. Early-type (elliptical and lenticular) galaxies contain old (> 10 Gyr) stellar populations

with virialized velocities in a spheroidal distribution, with very little interstellar material, suggesting that they have formed the bulk of their stars at high redshift and have evolved passively since. In contrast, late-type galaxies (spirals and irregulars) have younger (0-10 Gyr) stellar populations, with active star formation mainly occurring in a rotating disk of gas and dust. There is a relationship between colour and morphology, due to the different ages in the underlying stellar populations, whereby early-types predominantly display redder colours than late-types (Holmberg, 1958; Roberts & Haynes, 1994).

Thus, there is an apparent bimodality in the properties of the population of galaxies (see e.g. Baldry et al., 2004). Understanding how the varying types and properties of galaxies arise in the Universe is a major goal of modern astrophysics. Since galaxies form the building blocks linking small scale structure, such as planetary systems, to large scale structure, the theory of the formation and evolution of these systems provides an important constraint for cosmological models. The wealth of observational evidence gathered in the last Century has enabled us to develop such a formation theory of galaxies within the currently accepted cosmological framework. Yet, as I shall discuss shortly, there are many pieces of observational evidence we still have to fit into the grand picture.

1.2 THE CONCORDANCE MODEL

The most widely accepted theory for the formation and evolution of galaxies is the concordance Λ CDM model (Peebles, 1982; Blumenthal et al., 1984; Davis et al., 1985). It consists of a cosmology in which the Universe is dominated by a dark energy component, described by the cosmological constant Λ , which drives the present day acceleration in the expansion of the Universe (Carroll, 2004). The dark energy component makes up for 74% of the energy density in the Universe, with the remaining fraction being composed of baryonic matter and non-baryonic dark matter. The nature of the dark matter is unknown, but there is much observational evidence for its existence, based on the gravitational influence exerted on the observable baryonic matter (see e.g. Freeman, 1970; Rubin et al., 1980) and on light itself, via gravitational lensing (e.g. Kochanek, 1995; Keeton, 2001; Koopmans & Treu, 2003).

The early Universe was highly homogeneous, with only slight fluctuations in the density of the cosmic gas. The degree of homogeneity and these fluctuations are evident from observations of the cosmic microwave background (Jarosik et al., 2010). The temperature anisotropies in the radiation can be related to density fluctuations present in the Universe, about 300,000 years after the Big Bang, when photons and

baryons stopped interacting with one another at the epoch of recombination. These anisotropies on large angular scales were first detected by the COBE satellite (Smoot et al., 1992). The gas density declined as the expansion of the Universe proceeded, but localised regions of above average density could form where the enhancements in density attracted surrounding matter. Despite the expansion, volumes of gas were able to collapse where the density became sufficiently high, via gravitational instability. These overly dense regions are thought to be the seeds from which galaxies and clusters of galaxies would eventually form.

Because the amount of dark matter dominates over baryonic matter, the gravitational influence of the dark matter on the baryonic matter is important to consider. Although the nature of the particles that comprise dark matter is currently unknown (see Baugh, 2006), hypothetical dark matter particles are described as ‘cold’ if their velocities are much less than the speed of light and ‘hot’ if their velocities are comparable to the speed of light. Hot dark matter (HDM) models have become less favourable because they predict a greater amount of large scale structure than actually observed, as models tend to form galaxies with masses much greater than observed. This means that present-day galaxies would have to have formed via fragmentation in a ‘top-down’ formation scenario, but the idea of large scale structure forming first seems unlikely.

The cold dark matter (CDM) models predict a ‘bottom-up’ formation scenario; smaller dark matter halos form first, with the merging of these initial objects combined with ongoing gravitational collapse leading to the development of larger structures. The growing dark matter halos generate a gravitational potential, into which the baryonic matter falls. As gas falls into these potential wells, star formation converts gas into stars, which subsequently leads to the production of the heavy elements and dust, and gives rise to the first galaxies. It is the luminous baryonic matter, embedded in the gravitational potential of a dark matter halo, upon which observations are based. The amalgamation of smaller haloes through hierarchical merging eventually creates the galaxies and the clusters of galaxies seen today. Thus, observations of the large scale structure and the power spectrum of galaxy clusters, obtained from the Two-degree Field Galaxy Redshift Survey (2dFGRS; Colless et al., 2001) and the Sloan Digital Sky Survey (SDSS; York et al., 2000), provide important constraints.

Although the concordance Λ CDM model enjoys much success at using the available observations of the cosmic microwave background and large scale structure to describe the formation of non-baryonic dark matter haloes, transforming the baryonic matter at the center of these haloes into a population of galaxies with properties matching those in the Universe has yet to be accurately achieved. This is a complex

problem, since it requires an understanding of all the processes which drive galaxy evolution. We still need to fully understand the processes that affect the baryons, converting the gas which falls into the dark matter halo into stars, and the subsequent production of the heavy elements. To accomplish this requires a great amount of knowledge about star formation, feedback from supernovae and active galactic nuclei, radiative transfer mechanisms in the interstellar medium, and stellar nucleosynthesis. In addition, we also have the effect of the environment to consider. The effects of these various processes are difficult to constrain with observations. Thus, we must first understand the processes that shape the baryons into the galaxies we observe today.

1.3 GALAXY EVOLUTION

Whilst Λ CDM is a successful model for describing the formation of galaxies and the growth of large scale structure from the initial fluctuations in the cosmic microwave background, the theory still does not match all the observational evidence. One of the most concerning discrepancies between theory and observation is in the galaxy luminosity function, the number of galaxies per unit volume per unit luminosity interval. This fundamental observational tool provides a census of the different luminosities of galaxies in the Universe. Observations have demonstrated to high accuracy an abundance of dwarf galaxies at faint luminosities and far fewer massive galaxies at the brighter end of the luminosity function (e.g. Cole et al., 2001; Huang et al., 2003), which is generally well fitted using a Schechter (1976) function. However, the Λ CDM model fails to reproduce the exact shape of the luminosity function, drastically overpredicting both the number of dwarf galaxies and the number of massive galaxies which should be observed at different epochs (Bower et al., 2006; Croton et al., 2006).

As well as overpredicting the number of the most massive galaxies, the hierarchical merging theory also wrongly predicts that the most massive objects were the last to form. Observations indicate that a significant number of massive galaxies had already formed at redshifts $z > 1$ (Drory et al., 2005). This, in conjunction with the bulk of star formation occurring in intermediate mass systems and not massive galaxies since $z \sim 1$ (Kodama et al., 2004), suggests that massive early-type galaxies are the oldest systems. In fact, evidence that the youngest galaxies to form are spirals is apparent in the Hubble Space Telescope Deep Fields, in which the number density of large spirals rapidly decreases with increasing redshift.

The difference between theoretical results and observational evidence may be

removed if consideration is given to the effect of the environment on galaxy formation. If the collapse of the dark matter halos occur at an earlier epoch in dense, cluster regions compared to similar mass halos in the field environment, then star formation is accelerated in the progenitors of cluster galaxies. Gas-poor mergers in the clusters might then create the massive elliptical systems composed of old stellar populations, whilst the spiral galaxies in the field are still forming. As the clusters grow, surrounding spirals can become attracted to the gravitational potential and fall into the cluster. Observational support for this notion lies in the morphology-density relation (Dressler, 1980). This, however, returns to the previous problem with the Λ CDM model: the infall of gas from the halo fuels continuous star formation in the model, yielding elliptical galaxies with younger stellar populations than actually observed.

Thus, in order to understand why the current models overpredict the numbers of luminous galaxies and underpredict the ages of their stellar populations, it appears that we need to better understand when and where star formation occurs in the Universe. The Λ CDM model has been shown by Baugh et al. (1998) to match the observed star formation history of the Universe (Madau et al., 1996; Lilly et al., 1996), and Somerville et al. (2008) demonstrate a similar agreement. However, recent observations have shown that since $z \sim 1$, the total stellar mass contained in quiescent galaxies has increased by at least a factor ~ 2 , while the total stellar mass in star forming galaxies has remained constant, despite continued star formation over several Gyr (see Figure 2 in Bell et al., 2007; also Faber et al., 2007). This suggests that some process is required to quench star formation, turning a once active, star-forming galaxy into a quiescent galaxy, thus increasing the total stellar mass locked in quiescent systems, *but it is still unclear what physical mechanism(s) may be responsible for this quenching.*

It therefore appears that a mechanism is required for quenching star formation in the galaxy population, which may help reconcile the predictions of Λ CDM with the observational evidences discussed above. One such mechanism that has been recently proposed is the feedback from active galactic nuclei.

1.3.1 FEEDBACK FROM ACTIVE NUCLEI

Since the discovery that some galaxies exhibit central luminosities in excess of $L_{bol} \geq 10^{42}$ erg s⁻¹, capable of outshining the total emission from the stellar population, it is now evident that this excess luminosity may occur across the range of the electromagnetic spectrum. Initially observed at radio wavelengths, the central nucleus may also emit strongly in the optical, infrared, ultra-violet, X-ray and gamma

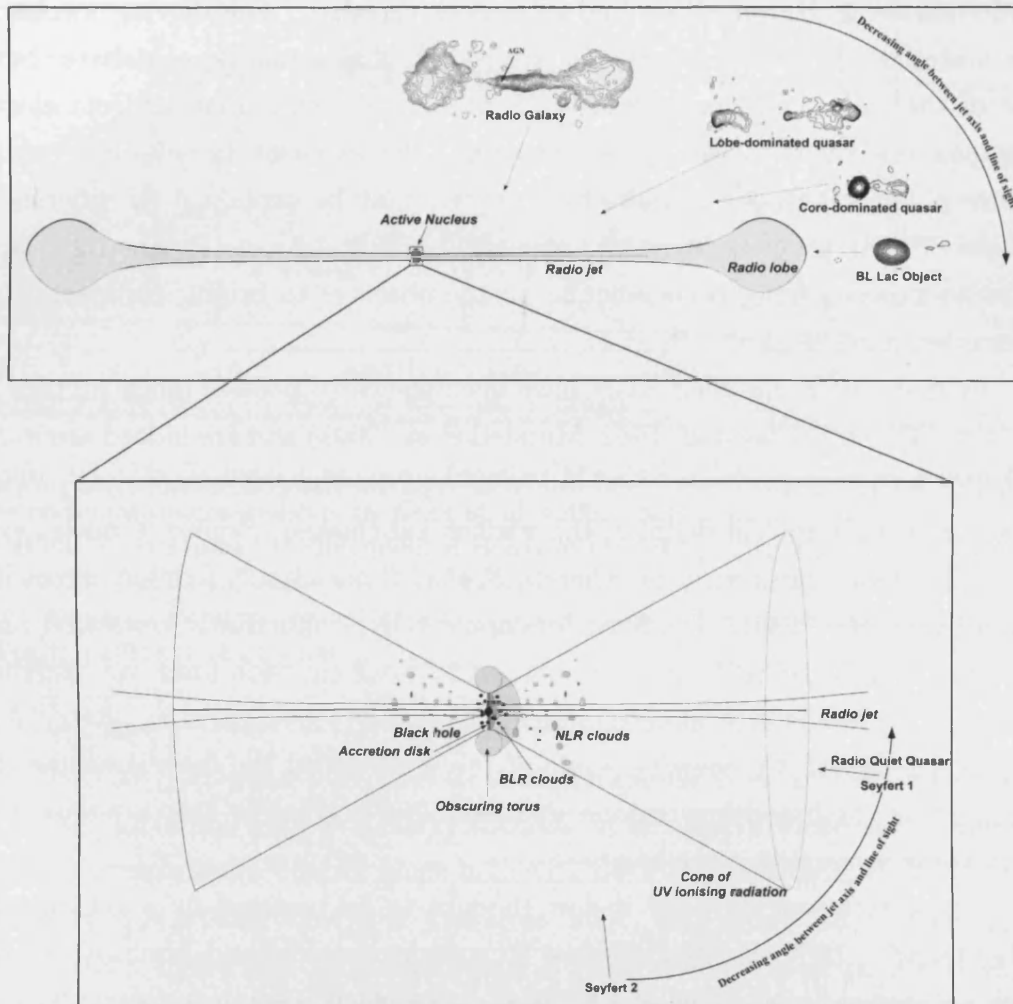


Figure 1.2: The unification scheme of the various multiwavelength observations, showing how the AGN type depends on the observer's viewing angle to the ejection axis of the radio jet. This scheme elegantly explains the various classifications based on radio observations (*top panel*) and the presence of broad or narrow emission lines in galaxy spectra (*bottom panel*). This figure is taken from Mundell (2002).

ray wavebands, and systems demonstrating such behaviour are called *active galactic nuclei* (AGN). The classification scheme of these galaxies is fairly confusing, since the distinctions between various sources mainly reflect historical differences in how they were discovered, as technological advances opened up new wavebands.

Radio-loud AGN, such as quasars, blazars and BL Lac objects, demonstrate strong radio emission. Whilst not present in BL Lac objects, interferometry reveals

jets of plasma originating from the central nucleus of some systems (e.g. Bridle et al., 1994), reaching lobes at distances up to and beyond 1 Mpc from the AGN (see McNamara & Nulsen, 2007 and references therein). The driving mechanisms of the material, ejected at relativistic speeds, are still a matter of debate, but the source of the radio emission is known to be synchrotron radiation from electrons in the magnetic fields in the ejected plasma. The variation in the observed radio structure of the subclasses of radio-loud objects may be explained by differences in the angle of inclination between the observer and the jet (see Figure 1.2), ranging from radio galaxies lying perpendicular to the observer to bright, compact BL Lac objects orientated head-on.

In contrast, *radio-quiet* AGN have been shown to possess much smaller radio lobes (e.g. Wilson & Ulvestad, 1982; Mundell et al., 2001) and are indeed around 100-1000 times weaker than their radio-loud counterparts. Instead, the optical properties play an important role in defining the various subclasses. *Seyfert 1* nuclei exhibit broad and narrow emission lines, whereas *Seyfert 2* nuclei only exhibit narrow emission lines (Seyfert, 1943). The least luminous AGN, dubbed *low ionisation nuclear emitting regions* (LINERS), are characterised by weak emission lines, yet also display a flat-spectrum radio nuclei akin to radio loud quasars (see Nagar et al., 2002). Again, as Figure 1.2 shows, the viewing angle of the observer to the central engine determines whether the broad-line regions are observable or whether they are obscured by a dusty torus surrounding the engine.

The central engine itself is now thought to be powered by a central super-massive ($\sim 10^6 - 10^{10} M_{\odot}$) black hole. To sustain the observed luminosities, AGN require an energy source that is 100 times more efficient than nuclear fusion, and the release of gravitational potential energy from the accretion of material onto the black hole is the only mechanism able to achieve such high efficiency and explain the observations (Lynden-Bell, 1969). Matter falling onto the black hole that possesses angular momentum may become accreted onto a disk, which radiates energy from both frictional heating of layers of the accretion disk, or from the release of gravitational potential energy. Some of the material may become accelerated to relativistic speeds and ejected perpendicular to the accretion disk, forming the jets of radio-loud AGN. The exact mechanisms underlying this scenario are still open to debate.

Having such powerful energy sources residing in the hearts of galaxies naturally raises the question of whether or not the AGN may affect the properties of their hosts. Hence, the transfer of the energy emitted from the accretion disk into the interstellar medium of the galaxy, i.e. *AGN feedback*, has become an important area of research for a number of reasons. Firstly, evidence suggests that most, if not all, massive

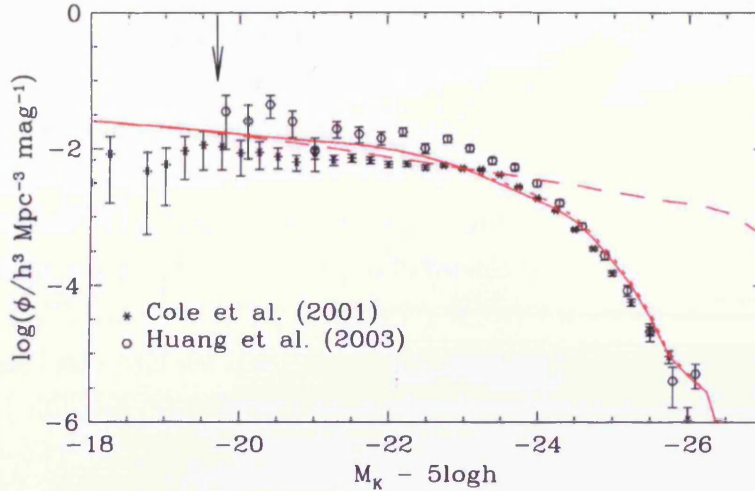


Figure 1.3: The K-band luminosity function of galaxies in the local Universe from observational determinations by Cole et al. (2001) and Huang et al. (2003). These functions are compared to the model of Bower et al. (2006), with and without feedback from AGN (solid and dashed lines, respectively). The arrow indicates the magnitude limit available from the model galaxies in the Millenium Simulation. This figure is taken from Bower et al. (2006).

($M_* > 10^{10} M_\odot$) galaxies play host to AGN (Kauffmann et al., 2003; Ferrarese & Ford, 2005), including our own Galaxy (Schödel et al., 2003). Moreover, a connection between the mass of the central black hole with both the spheroidal mass of a galaxy (Magorrian et al., 1998; Merritt & Ferrarese, 2001; Marconi & Hunt, 2003) and the stellar velocity dispersion in bulges (see e.g. Ferrarese & Merritt, 2000) suggests that the properties of AGN are fundamentally linked to the formation and evolution of the host galaxy. The more recent observation of a connection between the X-ray emission from an AGN and the HI distribution of the host galaxy, NGC 4151, provides additional support of a link between the AGN and the host (Wang et al., 2010).

Secondly, AGN feedback has been invoked to solve some of the problems with the predictions of Λ CDM (Bower et al., 2006; Croton et al., 2006). The accretion of matter onto the central supermassive black hole limits star formation and prevents the formation of very massive, luminous galaxies. Incorporating AGN feedback into semi-analytic models therefore reconciles the mismatch between the predicted and observed galaxy luminosity functions (see Figure 1.3). It should also be noted that the addition of supernova feedback in dwarf galaxies, combined with the suppression of gas cooling in less massive haloes (Benson et al., 2002), reconciles the faint end of the luminosity function as it reduces the formation of dwarf galaxies in the model.

Similarly, the problem of ‘downsizing’ may also be solved with the incorporation of AGN feedback in the Λ CDM model. In the Λ CDM model, gas falling into the halo would continue to fuel star formation in the most massive systems and the observed bimodality of quiescent and star-forming systems would not exist. The infall of gas can be prevented with the inclusion of AGN feedback into the models, where the energy output from the central engine heats the gas and limits continual star formation. AGN feedback stops the infall of gas in massive haloes and thus prevents the formation of ellipticals with young stellar populations. Moreover, this feedback has the potential to explain the evolution of the total stellar mass contained in star-forming and quiescent systems, providing a mechanism for quenching star formation and creating quiescent systems from once star-forming galaxies. This hypothesis has gained recent support from studies showing that, in colour-magnitude diagrams, there is a population of galaxies with colours between those displayed by blue star-forming and red quiescent systems, and that these intermediary galaxies are in fact AGN-hosts (Martin et al., 2007; Schawinski et al., 2007). A correlation between nuclear activity and colour is suggestive of a physical link between AGN feedback and the quenching of the star formation.

Thus, AGN feedback appears to be a successful addition to the physical processes affecting the baryons within the Λ CDM framework (Baugh, 2006; Bower et al., 2006; Croton et al., 2006). The fact that the inclusion of feedback from AGN and supernova provide a better match between theory and observation suggests that developing a better understanding of the physical processes affecting baryonic matter will improve our current theory of galaxy formation and evolution. However, the reliance on AGN feedback to solve the problems in the predictions of the Λ CDM theory should be carefully reconsidered, given that there are still many unanswered questions regarding this process.

The coupling of feedback from the supermassive black hole to the surrounding material in the galaxy is still not properly understood. In models, this coupling is invoked by modifying the rate at which gas cools in the dark matter halo via gas heating from the black hole accretion disk, which consequently reduces the fuel available for star formation (Bower et al., 2006; Croton et al., 2006; Somerville et al., 2008). The method is simple, but the reality is likely to be much more complex. For example, this idea does not account for whether gas heated by the AGN is able to later cool and contribute to the formation of stars, such that star formation is just delayed rather than quenched outright. Although it appears that every galaxy may harbour an AGN, fuelling an ongoing debate over which came first, the central black hole or the host galaxy (see e.g. Volonteri, 2010), we still do not know whether the

AGN feedback mechanism is a universal effect for all Hubble types across the range of galaxy mass, since AGN are mainly observed in massive elliptical galaxies. Evidence for dwarfs playing host to AGN is lacking (see Barth et al., 2004, for one study of a Seyfert dwarf galaxy).

Finally, it is crucial to keep in mind that whilst the incorporation of AGN feedback into simulations may better reproduce the observations, the models are not likely to be a true reflection of the underlying physical processes that drive galaxy evolution. Current simulations do not include all the mechanisms capable of perturbing galaxy evolution. One of the most important perturbing factors, supported by observation yet still not considered in the models, is the effect of the environment on galaxy evolution.

1.3.2 ENVIRONMENTAL EFFECTS

There is mounting evidence suggesting that the evolution of galaxies is greatly influenced by the environment they inhabit. The density of galaxies in the local Universe is not homogeneous; it spans from $\sim 0.2\rho_0$ in voids to $\sim 5\rho_0$ in superclusters and filaments, $\sim 100\rho_0$ in rich cluster cores and $\sim 1000\rho_0$ in compact groups (where ρ_0 is the average field density; Geller & Huchra, 1989). The strongest observational signature that environmental effects may play a role in forging the bimodality in the galaxy population comes from the morphological segregation of galaxies. Dressler (1980) showed that the fraction of early-type galaxies increases with galaxy density, from sparse groups to rich clusters (Postman & Geller, 1984), and with clustercentric radius (Whitmore et al., 1993). Dressler et al. (1997) measured the morphology-density relation via a sample of rich clusters at $z = 0.5$, using high resolution imaging on the Hubble Space Telescope to observe the cluster cores. They found that the fraction of lenticular galaxies in clusters decreases by a factor of 2-3 between $z = 0$ and $z = 0.5$, with a corresponding increase in the fraction of star-forming, late-type galaxies, suggesting a possible evolutionary link between the two morphologies.

Moreover, there is a more general relationship between star formation and density. Kennicutt (1983) compared the star formation activity of 26 Virgo cluster galaxies to similar isolated objects, and demonstrated that those objects in the higher density environment typically display lower levels of star formation and redder colours. Extending this analysis to 545 cluster members, Gavazzi et al. (2002) have confirmed this star formation-density relation. Similarly, the gas content of galaxies significantly varies with environment. In addition to the star formation-density relation, Kennicutt (1983) also found a lower content of atomic hydrogen present in cluster

galaxies compared to isolated objects. By comparing the atomic hydrogen content of cluster galaxies with field galaxies of similar size and morphological type, Haynes & Giovanelli (1984) quantified the gas deficiency displayed by cluster galaxies.

These results suggest that environmental processes are capable of modifying the gas content and thus suppressing (or quenching) star formation. These processes may be broadly classed as gravitational or hydrodynamical interactions.

Gravitational interactions

Galaxies may experience gravitational interactions both with other galaxies and with the potential wells of groups and clusters. *Tidal interactions* between two galaxies may be efficient at removing material from galaxies, depending on the ratio of the galaxy radii to the distance separating the two systems. Gaseous material from the periphery, such as extraplanar HI gas, has been shown by numerical simulations to be most efficiently removed. Interacting pairs typically show an increase in nuclear star formation (Keel et al., 1985; Kennicutt et al., 1987; Hummel et al., 1990), with individual interactions expected to be most effective in groups because the velocity of such encounters is too high for such mergers to be frequent in the cluster (Ghigna et al., 1998; Okamoto & Habe, 1999).

It has also been proposed that the cumulative effect of multiple, high speed galaxy-galaxy encounters combined with the effect of the cluster potential as a whole, may be sufficient to govern the evolution of cluster galaxies (Moore et al., 1996; Moore et al., 1998; Moore et al., 1999). This process, called *galaxy harassment*, mainly depends on the frequency of close (~ 50 kpc) encounters, the strength of each encounter and the distribution of the galaxy potential wells. It is likely to be most effective in lower luminosity systems (Boselli & Gavazzi, 2006).

The gravitational interaction of a galaxy with the whole cluster potential can lead to a tidal compression of the gas, inducing gas inflows, the formation of bar structure and an enhancement of nuclear star formation (Merritt, 1984; Miller, 1986; Byrd & Valtonen, 1990).

Hydrodynamical interactions

Galaxies that find themselves residing in the cluster environment may experience the harsh effects of the intracluster medium (ICM), which is able to modify their gas content, and hence the star formation activity, via a number of different processes.

A galaxy moving through a cluster will encounter ram pressure from the ICM (Gunn & Gott, 1972). If the ram pressure is greater than the binding force of the

galaxy potential, gas will be stripped from the outskirts of the galaxy up to a characteristic stripping radius (Quilis et al., 2000; Vollmer et al., 2001). *Ram pressure stripping* is probably most effective in the cluster core where the ICM density is highest. Although the removal of gas may ultimately quench star formation in the outskirts, gas at the leading edge of the galaxy may be significantly compressed by the ram pressure, triggering a temporary increase in star formation (Bekki & Couch, 2003). In fact, simulations have also predicted that star formation may occur in the stripped gas up to 100 kpc behind a galaxy (Kronberger et al., 2008). However, it is well established that this process leads to a decrease of the global star formation activity.

Another mechanism proposed for removing gas from galaxies in clusters is *viscous stripping* (Nulsen, 1982). The cold, dense ISM in the outskirts of a galaxy travelling through the hot, tenuous ICM may encounter a sufficiently large transfer of momentum that can strip the gas from the galaxy. A turbulent flow results in a drag force similar to the case of ram pressure stripping and, as noted in Boselli & Gavazzi (2006), the signatures of viscous stripping on the gas content, star formation activity and kinematic properties are likely to resemble those of ram pressure stripping.

Thermal evaporation has been shown to remove gas in cluster galaxies (Cowie & Songaila, 1977). A ICM temperature which is much higher than the galaxy velocity dispersion may cause the temperature of the ISM to rapidly increase at the interface between the two mediums, meaning it becomes possible for the gas to escape the galaxy gravitational potential and evaporate away from the galaxy. However, a quantification of the impact on gas content and star formation activity is difficult to obtain and the effects are still unclear.

Finally, Larson et al. (1980) proposed that galaxies may be transformed from spirals into lenticulars via galaxy *starvation/strangulation*, whereby the infall of gas onto the disk from an extended gas reservoir is prevented. This leads to an exhaustion of the remaining gas supply and a quenching of star formation. Simulations by Bekki et al. (2002) showed how this process reduces the presence of spiral arm structure and leads to anemic, disk-dominated lenticular galaxies.

Thus, there are a wide variety of processes that are thought to modify the properties of galaxies. The environment therefore appears to be an important factor in their evolution. However, there is still uncertainty whether chemical evolution in star-forming galaxies is influenced by the environment. The observed relationship between mass

and metallicity is a useful tool for studying chemical evolution in different environments, but various studies find little or no variation with environment (Mouhcine et al., 2007; Ellison et al., 2009). This appears in contradiction with observational evidence that cluster galaxies are typically more metal rich than galaxies in sparse environments (e.g. Shields et al., 1991; Vilchez, 1995; Skillman et al., 1996). Therefore, whilst we still need to determine the relative importance between internal processes and environmental effects in shaping the evolution of galaxies, we additionally have to determine exactly which components of a galaxy are affected by the environment.

1.4 NATURE VERSUS NURTURE?

One of the main questions in modern astrophysics concerns the determination of the forces driving galaxy evolution; do galaxies evolve according to their internal, physical properties or does the influence of the environment play the dominant role? In other words, *is it nature or nurture that governs galaxy evolution?* This thesis investigates the properties of galaxies in the nearby universe, with the goal of disentangling the effects of the environment from internal processes such as AGN feedback, in order to answer some of the open problems concerning the relative importance of various processes in driving galaxy evolution.

Specifically, I shall begin by studying the relationship between AGN feedback and star formation. Recent observational evidence using colour-magnitude diagrams have shown that galaxies with quenched star formation, lying between blue star-forming galaxies and red quiescent systems, are preferentially AGN-hosts (Martin et al., 2007; Schawinski et al., 2007). This correlation between nuclear activity and colour has been interpreted as a physical link between AGN feedback and the quenching of the star formation. It is important to properly test this conclusion, given that the AGN feedback hypothesis is not fully understood and there remains a possibility that the preponderance of AGN residing in quenched systems is coincidental, especially given that most galaxies are thought to host an AGN. As previously discussed, there are a plethora of environmental mechanisms capable of modifying the gas content of galaxies and preventing star formation as a result (Boselli & Gavazzi, 2006). *Are active nuclei responsible for quenching star formation in nearby galaxies? Or does the environment play a role in the quenching?*

I hope to answer these questions by constructing colour-magnitude or colour-mass diagrams and studying the distribution of the properties of a sample of nearby galaxies. By using an ultraviolet-infrared colour, I can separate out star-forming galaxies from quiescent objects and investigate the nuclear activity of systems with

intermediate colours. The effects of the environment may be disentangled in a number of ways. Since AGN feedback is an internal process, one might expect to see similar distributions in the colour-magnitude parameter space of galaxies in different environments if AGN are the dominant quenching mechanism. Alternatively, I could also investigate whether quenching is due to an environmental effect by looking at measurements of their gas content, such as HI deficiency (Haynes & Giovanelli, 1984), which may indicate systems perturbed by the environment.

In addition to using integrated quantities in a colour-magnitude diagram, another test would be to analyse the colour gradients of nearby galaxies. Depending on whether the quenching occurs internally due to AGN feedback or externally via environmental effects, such as ram pressure stripping, one might observe differences in the colour gradients of AGN-hosts compared to gas deficient objects. Hence, the colour gradients may contain the signatures of the quenching mechanism. Whilst this idea has many potential complications, a simple pilot study using ultraviolet-infrared colour gradients may shed some light on the feasibility of this hypothesis.

Confirming a correlation between nuclear activity and colour and establishing whether it forms reliable observational evidence linking AGN feedback and star formation quenching, or whether other environmental mechanisms may play a role, is an important first step in this work. However, we do not fully understand the AGN feedback mechanism itself or whether the mechanism can be applied universally to galaxies regardless of size or morphological type. *Are AGN capable of quenching star formation in late-type galaxies?* Therefore, another goal of this thesis is to determine the impact of AGN feedback on star formation. A quantification of effect of the feedback on star-forming, late-type galaxies may uncover if AGN in low mass halos are capable of quenching star formation. The relationship between AGN feedback and star formation as predicted by current semi-analytic models will help determine if it is theoretically possible, and these predictions may be tested using observational estimates of the star formation rate and nuclear activity in nearby late-types.

Following an investigation into the effect of AGN feedback on star formation, I will focus the remainder of this thesis on studying the effect of the environment on chemical evolution. The contradicting results on the environmental dependence of the mass-metallicity relation are important to understand, as some studies clearly show that galaxies in the cluster environment display enhanced metallicities compared to the field environment (e.g. Skillman et al., 1996), whereas others show little or no environmental variation (e.g. Ellison et al., 2009). *Does the mass-metallicity relation vary with environment or do internal processes dominate the chemical evolution of a galaxy?* To answer this question, I will use integrated, drift scan optical spectroscopy

of galaxies in different environments with a new method for estimating oxygen abundances from spectral emission line data. By comparing the mass-metallicity relations derived from observations of cluster and field galaxies, I hope to measure any influence on the relation by the environment. If cluster galaxies are in fact more metal-rich than field galaxies, I would expect to find some shift in the cluster mass-metallicity relation compared to the field relation, along with a possible deviation of the metallicities of cluster galaxies away from the predictions of a closed-box model of chemical evolution.

The answers to these questions are crucial for better understanding whether AGN feedback really shapes the properties of galaxies, or whether environmental effects must be considered. The studies conducted in this thesis will hopefully indicate which physical processes are the most important in driving galaxy evolution and should therefore be incorporated into future models.

For this investigation, I focus on the galaxies inhabiting a range of environments in the nearby Universe, with the goal of disentangling the effect of internal processes and environmental effects by exploiting the higher resolution, multiwavelength observations afforded at lower redshifts. A multiwavelength dataset is crucial for such a study, since only with ultraviolet to infrared imaging, nuclear and integrated optical spectroscopy, and atomic hydrogen emission line data, can the key components of galaxies be accurately traced, thus providing a complete picture of star formation and chemical evolution in these systems.

1.5 THESIS OUTLINE

In summary, the aim of this thesis is to study the properties of late-type galaxies inhabiting a range of environments in the local universe, in order to extend our knowledge of the different processes important in the evolution of nearby galaxies. I outline the thesis chapters and content as follows:

Chapter 2 describes the selection criteria of the sample, the available multiwavelength data necessary for probing the different components of nearby galaxies and the physical properties derived from observational quantities.

Chapters 3 and **4** explain the data reduction methods for obtaining additional ultraviolet photometry and optical spectroscopy, required to increase the completeness of observations available for galaxies residing in low density environments.

Chapter 5 presents the first analysis of the sample, using colour-mass diagrams to disentangle the effects of internal processes from environmental effects. The properties of galaxies residing in the so-called transition region are examined.

Chapter 6 discusses a pilot study designed to probe the origin of the quenching of star formation by using ultraviolet-infrared radial colour profiles.

Chapter 7 presents a simple semi-analytic model to test the impact of AGN feedback on star formation in late-type galaxies, and a comparison between the model predictions and observations.

Chapter 8 describes the problems of determining the gas-phase metallicity from optical emission lines and introduces a new method of metallicity estimation.

Chapter 9 examines whether the environment affects the galaxy metal content by using the stellar mass-metallicity relation, and a simple closed-box model for chemical evolution is developed to demonstrate the origin of the scatter in the relation.

Finally, **Chapter 10** summarises the main results of this work, and discusses how they provide additional constraint on the evolution of galaxies in the nearby universe.

Part of the work presented in this thesis has been published in astronomical refereed journals, see Hughes & Cortese (2009), Cortese & Hughes (2009) and Boselli et al. (2009).

CHAPTER 2

THE HRS+ SAMPLE

2.1 THE HERSCHEL REFERENCE SURVEY

In order to tackle the problems raised in the Introduction, it is first necessary to construct a sample of galaxies which is both representative of the local galaxy population and consists of objects residing in different environments. These requirements are particularly important for avoiding bias when addressing the question of whether nature or nurture drives galaxy evolution in the local universe.

There are many datasets available covering nearby galaxies in a variety of wavebands, from the ultraviolet observations from the Galaxy Evolution Explorer (Martin et al., 2005), the optical Sloan Digital Sky Survey (York et al., 2000) and the Two Micron All Sky Survey (Jarrett et al., 2003), for example. However, this study requires a multiwavelength dataset, with ultraviolet to infrared imaging, nuclear and integrated optical spectroscopy, and atomic hydrogen emission line data. These data are crucial for tracing the key components of a galaxy, yet few (if any) galaxy samples enjoy such a wide wavelength coverage.

Fortunately, there is one such sample that meets these criteria and is ideal for the aims of this thesis. The Herschel Reference Survey (Boselli et al., 2010; hereafter HRS) is a guaranteed time key project to study dust in the nearby universe using the Herschel Space Telescope (Pilbratt et al., 2010) and the SPIRE instrument (Griffin et al., 2010). The sample is volume-limited and flux-limited in order to include nearby, bright galaxies of morphological types across the Hubble sequence and residing in a wide range of environments. The defined sample was designed to meet a number of scientific objectives in order to study the distribution of the cold dust component of galaxies in the local universe, and to better understand the role of dust in the physics of the ISM, star formation, and the intergalactic dust cycle, amongst other key

objectives. To tackle these objectives, a large dataset has been collected that provides a wide coverage of the electromagnetic spectrum, probing the atomic and molecular gas components, different stellar populations, warm dust, metallicity, star formation and nuclear activity - in short, most of the components of a galaxy. This ancillary data, even without the forthcoming Herschel/SPIRE observations, is extremely useful for studying galaxy evolution.

I chose to investigate the processes driving nearby galaxy evolution using a sample similar to that of the HRS. The HRS selection criteria define a sample which, when combined with the rich dataset of multiwavelength observations, is ideal for disentangling the effects of internal and environmental effects on galaxy evolution at the present epoch. Thus, I initially use the HRS selection criteria as a basis for constructing a sample for this thesis.

2.2 SELECTION CRITERIA

I adopt a sample based on the selection criteria similar to the criteria of the HRS. As described in Boselli et al. (2010), the HRS selection criteria are:

1. Galaxies are selected according to a K band limit, dependent on morphological type. A limit of a 2MASS K band total magnitude $K_{Stot} \leq 12$ mag is imposed for spiral galaxies (Sa-Sd-Im-BCD), whereas the more stringent limit of $K_{Stot} \leq 8.7$ mag is adopted for early-type galaxies (E, S0 and S0a).
2. A volume limit is also imposed. An upper distance limit reduces distance uncertainties and ensures the presence of low luminosity dwarf systems not observable at higher redshifts, whereas a lower distance limit excludes very extended objects that would consume too much observing time with Herschel. Thus, galaxies are selected with an optical recessional velocity between 1050 km s^{-1} and 1750 km s^{-1} . Assuming $H_0 = 70 \text{ km s}^{-1} \text{ Mpc}^{-1}$ and in the absence of peculiar motions, this corresponds to a distance range of $15 \leq D \leq 25 \text{ Mpc}$. The recessional velocities are taken from NED. However, it is noted that in the Virgo cluster ($12\text{h} < \text{R.A.}(2000) < 13\text{h}$; $0^\circ < \text{Dec.} < 18^\circ$) peculiar motions do dominate and so I include all galaxies with recessional velocities $< 3000 \text{ km s}^{-1}$ and belonging to the cluster subgroups defined in Gavazzi et al. (1999). The cluster subgroups included are the Virgo A, North (N) and East (E) clouds, the southern extensions (S) and Virgo B, which lie at distances between 17 and 23 Mpc, but I exclude the W and M clouds lying at 32 Mpc, following the HRS criteria.

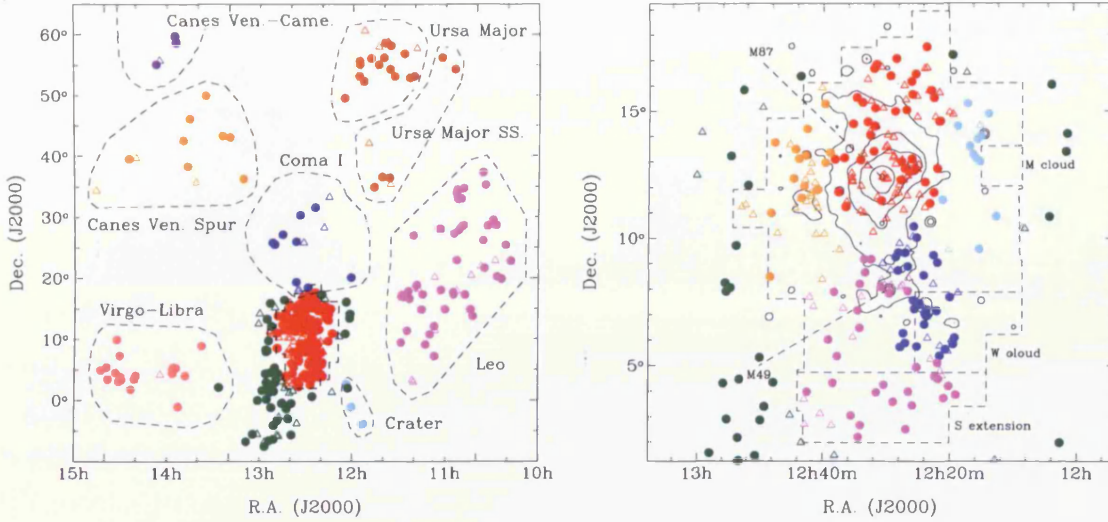


Figure 2.1: The sky distribution of the HRS+ for early-type (E-S0-S0a; open triangles) and late-type (Sa-Sd-Im-BCD; solid circles) galaxies (*left panel*). Dashed contours delimit the different clouds. The big concentration of galaxies in the centre of the figure is the Virgo cluster (red colour) with its outskirts (dark green). Blue symbols are for Coma I Cloud, magenta for Leo Cloud, brown for Ursa Major Southern Spur and Cloud, cyan for Crater Cloud, purple for Canes Venatici Spur and Camelopardalis and orange for Virgo-Libra Cloud galaxies. The Virgo cluster region is magnified for clarity (*right panel*). Black contours show the diffuse X-ray emission of the cluster (from Böhringer et al., 1994). Red symbols are for galaxies belonging to the Virgo A cloud, blue to Virgo B, orange to Virgo E, magenta to Virgo S, cyan to Virgo N and dark green to the Virgo outskirts, as defined by Gavazzi et al. (1999). This figure was adapted from Boselli et al. (2010) to include the HRS+ members.

3. Finally, to minimize galactic cirrus contamination, galaxies residing at high galactic latitude ($b > +55^\circ$) and in regions suffering from low galactic extinction ($A_B < 0.2$; Schlegel et al., 1998) are selected.

The HRS imposes different K band limits depending on the morphology, because quiescent galaxies have lower expected dust content than late-types (Sa-Sd-Im-BCD), so that the integration times necessary to detect dust in early-types would be unreasonable for the Herschel observations. Since this is not an issue for the current work using ancillary data, I use the same K_{Stot} limit for all types. Relaxing the limit to select all galaxies with a 2MASS K band total magnitude of $K_{Stot} \leq 12$, regardless of morphological type, means that the sample is not biased against early-type galaxies. Because the modification to the K_{Stot} limit results in a slightly larger sample than from the HRS criteria, since more early-types are selected, I refer hereafter to

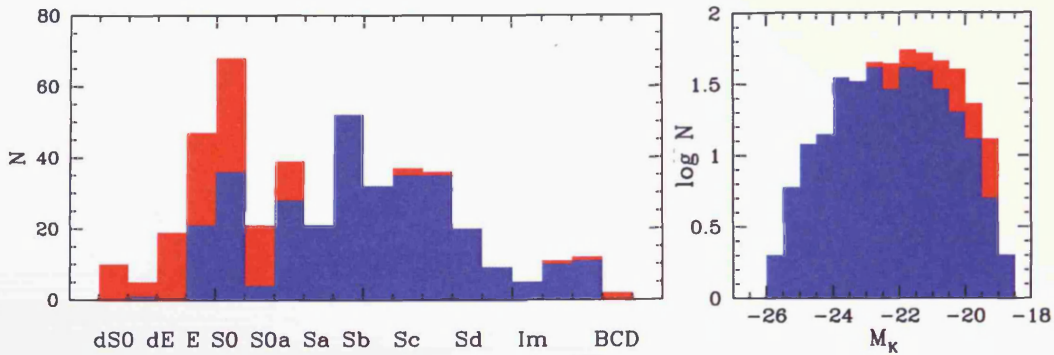


Figure 2.2: The distribution in morphological type (*left panel*) and K_S band luminosity (*right panel*) of the HRS (blue histogram) and the HRS+ (red histogram). The additional early-type galaxies due to the lower K_S band magnitude limit of the HRS+ are evident.

the sample used in this thesis as the *HRS+ sample*. As such, these criteria produce a sample of 454 galaxies residing within the area of sky between $10^{\text{h}} 17^{\text{m}} < \text{R.A.}(2000) < 14^{\text{h}} 43^{\text{m}}$ and $-6^\circ < \text{Dec.} < 60^\circ$, shown in Figure 2.1. This sample consists of 171 early-type and 283 late-type galaxies inhabiting a range of different environments, from members in the dense center of the Virgo cluster to isolated systems. Figure 2.2 demonstrates the difference between the distribution of the additional galaxies in both morphological type and K band luminosity distribution. It is clear that the modified magnitude limit has included a greater number of ellipticals, lenticulars and dwarves, and the inclusion of these galaxies in the sample increase the luminosity distribution at fainter K band magnitudes. A complete list of the galaxies comprising the HRS+ sample, together with some of their key properties and SDSS composite images, may be found in Appendix A.

For the following analysis, two subsamples are created based on the environment inhabited by each object in the sample. All galaxies with membership of the Virgo cluster, as defined by Gavazzi et al. (1999), comprise the ‘cluster’ subsample and galaxies outside Virgo, which range from isolated systems to galaxies in groups, are selected for the ‘non-Virgo’ or ‘field’ subsample (and I refer to this sample of galaxies in low density environments using both terms interchangeably). Finally, it should be noted that although the HRS+ sample is magnitude- and volume-limited, it might be biased towards high-density environments; nearly half of the galaxies in the sample reside within the Virgo cluster, which might not be a fair representation of the local Universe.

2.3 MUTLIWAVELENGTH OBSERVATIONS

The Herschel Space Telescope with the SPIRE instrument will deliver high sensitivity, high resolution images at 250, 350 and 500 μm , which will greatly improve current knowledge of the cold dust properties of nearby galaxies. To fully exploit the data delivered by Herschel, the observations will be combined with ancillary multi-wavelength observations tracing the key components of galaxies. For this reason, a large multiwavelength dataset for the HRS galaxies has been assembled from observations available across the range of the electromagnetic spectrum, from X-ray to radio data (see Table 4 in Boselli et al., 2010). There is a wealth of science that can be accomplished using just this ancillary dataset alone.

I exploit this multiwavelength dataset to trace the key components of galaxies. Ultraviolet to near-infrared imaging is necessary for tracing the different stellar populations and any recent star formation activity. Optical spectroscopy is important for determining the internal dust extinction, measuring the stellar and gas-phase metallicities, quantifying nuclear activity and also measuring star formation activity. The gas content of galaxies can be traced via HI line observations. Finally, mid-infrared observations are used for estimating the warm dust component. In short, the dataset traces all of the components of the stars and the ISM.

Whilst the data used in this work is described below, a full description of all the data available for the HRS may be found in Boselli et al. (2010). The exact number of observations available in each band is summarised in Table 2.1.

Optical & NIR imaging

All the galaxies in the HRS+ sample have been observed by the Two Micron All Sky Survey (2MASS; Jarrett et al., 2003) in the J (1.25 μm), H (1.65 μm) and K_S (2.15 μm) bands. In addition, deep images of the B (442 nm), V (540 nm), H and K_S bands were taken during surveys of the Virgo cluster conducted by Boselli et al. (1997, 2000, 2003) and Gavazzi et al. (2000), and made available in the GOLDMine database (Gavazzi et al., 2003a). Finally, SDSS Data Release 7 (Abazajian et al., 2009) provides images taken with the 2.5 m telescope at Apache Point Observatory for the vast majority of the HRS+ galaxies, covering the u , g , r , i , and z bands with effective wavelengths of 3550Å, 4670Å, 6160Å, 7470Å and 8920Å respectively.

Nuclear spectroscopy

Nuclear spectroscopy sampling the central regions of galaxies are available via the SDSS. The SDSS use 3" diameter fibers that obtain spectra covering from 3800 to

9200Å at a resolution of $1800 < R < 2200$. Nuclear spectra are available for 245 of the 283 late-type galaxies in the HRS+ sample, with emission line properties accessible from the SDSS website¹.

HI line data

Single-dish HI 21 cm line emission data is taken from the digital archive of Springob et al. (2005), which contains observations for ~ 9000 nearby galaxies. The observations were taken at several radio telescopes: the 305 m Arecibo telescope of the National Astronomy and Ionosphere Center, the late 91 m and 42 m Green Bank telescopes of the National Radio Astronomy Observatory, the Nancay radio telescope of the Observatory of Paris, and the Effelsberg 100 m telescope of the Max Planck Institut für Radioastronomie. Although the data was obtained in a heterogeneous manner over the course of 20 years, Springob et al. (2005) have re-analysed the global HI line profiles using a single set of processing and parameter estimation algorithms to deliver a homogeneous catalogue of derived properties. They correct the HI line flux, $S_{obs} = \int S(\nu) d\nu$, for the effects of beam attenuation, pointing offsets and HI self-absorption and the line widths are corrected for instrumental broadening. In addition, some HI line measurements have been taken from Gavazzi et al. (2003a) and from the NASA Extragalactic Database (NED). Thanks to this large dataset, the HRS+ sample is statistically complete in HI line data.

UV imaging & integrated spectroscopy

Unfortunately, despite the completeness in imaging, nuclear spectroscopy and HI line data, the HRS+ sample is incomplete in both UV photometry and optical, integrated spectroscopy. Both types of data are highly important for addressing the aims of this thesis. The UV emission traces recent star formation and allows the estimation of the star formation rate, whereas optical integrated spectroscopy provides a measure of the metallicity. The combination of star formation rates and metallicities provide the key ingredients required for studying the star formation and chemical evolution.

Ultraviolet observations are available from the Galaxy Evolution Explorer (GALEX; see Chapter 3) in the FUV (1528Å: 1344-1786Å) and NUV (2271Å: 1771-2831Å) bands. These were taken as part of several observing campaigns: the Nearby Galaxy Survey (Gil de Paz et al., 2007), the Virgo cluster survey (Boselli et al., 2005) and the All-sky Imaging Survey. A few galaxies are covered by pointed observations in open time proposals. At the start of this thesis, less than a third (146/454) of

¹SDSS imaging and spectroscopy available from www.sdss.org.

the HRS+ galaxies had been observed in the two UV bands, therefore additional observations are required. In addition, it may be beneficial to retrieve the more recent observations from the GR2 and GR3 data releases, which use an updated reduction pipeline. The GALEX data is described in greater detail in Chapter 3.

The nuclear spectroscopy discussed above is not adequate for the purpose of obtaining global metallicity estimates, since the 3" diameter fibers cover a small fraction of the surface area of nearby galaxies. At the distance of the Virgo cluster, the fiber aperture covers ~ 0.5 kpc compared to the typical diameter of a massive spiral being ~ 10 kpc, hence a global galaxy spectrum is not observable. Instead, integrated spectroscopy obtained using the drift scan technique is required. By uniformly drifting the spectrograph slit across the entire extent of the galaxy during exposure of the CCD, a global spectrum is obtained. Integrated spectra have been acquired as part of an observing campaign with the 1.93 m telescope at Observatoire de Haute Provence, the 3.6 m ESO telescope, the 1.52 m Loiano telescope and the 2.1 m San Pedro Martir telescope. The observations taken from 1998 to 2003 cover 225 objects in the Virgo cluster across a typical wavelength range of 3400-7000Å at a resolution of $R \sim 1000$. The fluxes and equivalent widths of the optical emission lines covered by this wavelength range are made available in Gavazzi et al. (2004). Whilst the HRS+ cluster sample may be considered complete, none of the HRS+ field galaxies have reduced optical spectra. The spectral data is discussed in greater detail in Chapter 4.

2.3.1 SUMMARY OF OBSERVATIONS

A large multiwavelength dataset is available for the HRS+ sample. The completeness of the observations in the FUV, NUV, B and V bands, the optical drift-scan and nuclear spectroscopy and the HI line measurements are demonstrated in Figure 2.3, with the exact numbers given in Table 2.1. It is evident that, in order to study the properties of galaxies in different environments, additional FUV and NUV imaging and optical spectroscopy are necessary for galaxies outside the Virgo cluster.

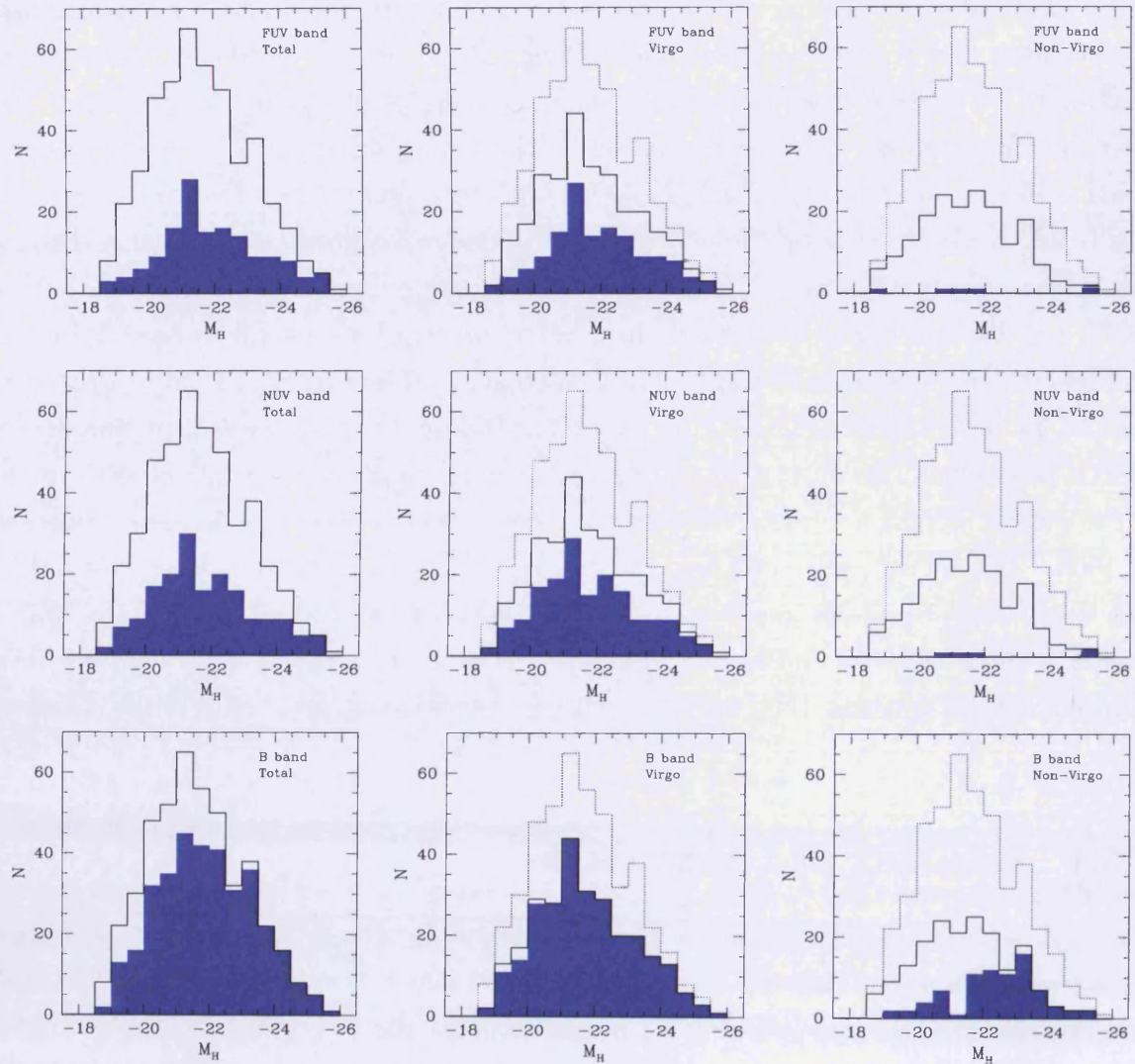


Figure 2.3: The completeness of observations of HRS+ galaxies (blue histogram) in the FUV (*top row*), NUV (*middle row*) and B bands (*bottom row*), compared to total distribution (solid black line) for the entire sample and for galaxies residing inside and outside the Virgo cluster (*left, middle and right columns* respectively). In the diagrams of the latter two columns, the total distribution is plotted for ease of comparison (dotted black line).

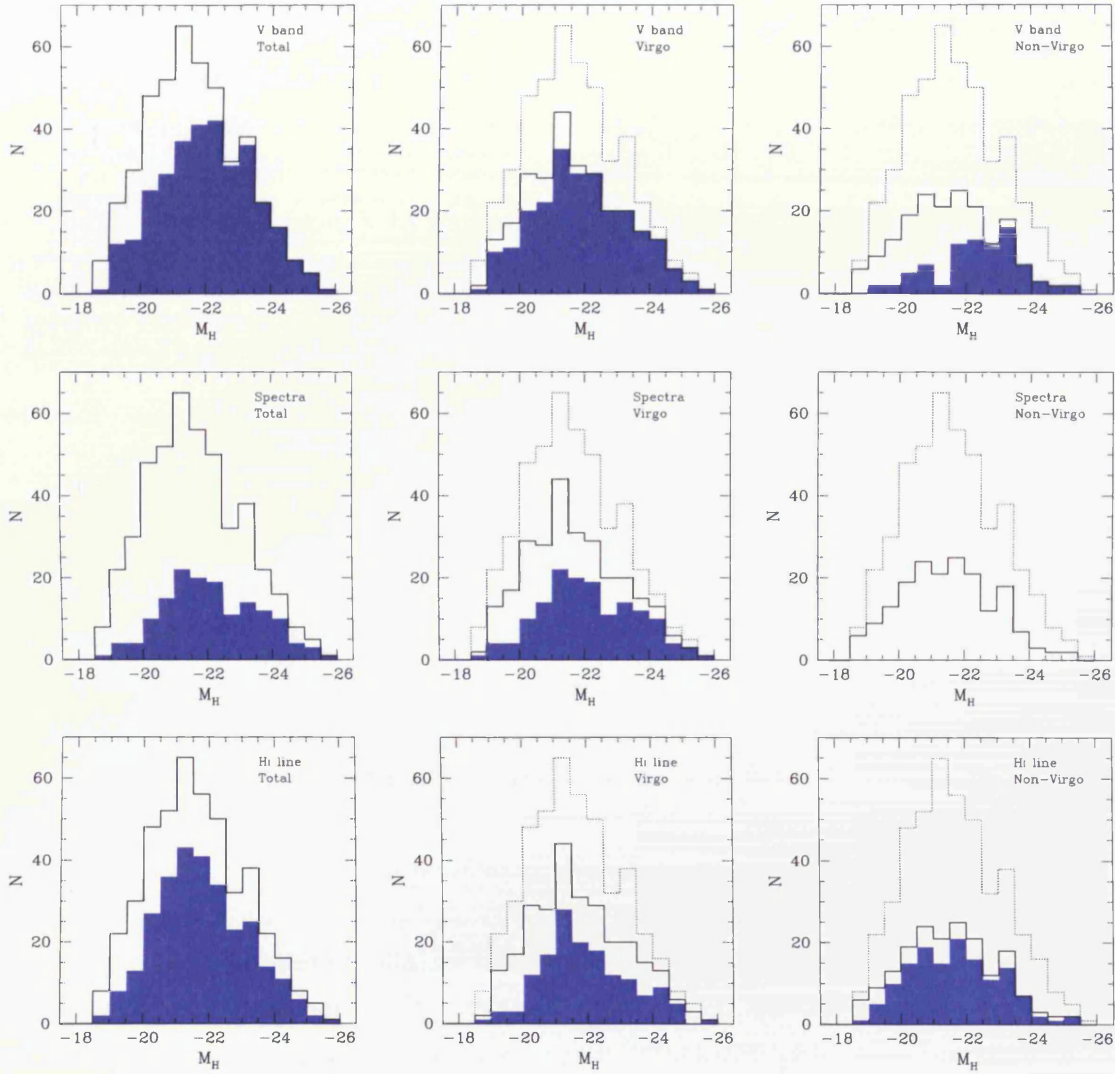


Figure 2.3: Continued from previous page. The completeness of HRS+ galaxies (blue histogram) observed in the V band (*top row*), with optical spectroscopy (*middle row*) and with HI line measurements (*bottom row*). The observations are compared to total distribution (solid black line) for the entire sample and for galaxies residing inside and outside the Virgo cluster (*left, middle and right columns* respectively). In the diagrams of the latter two columns, the total distribution is plotted for ease of comparison (dotted black line).

Sample	FUV	NUV	Spec(Int)	Spec(Nuc)	B	V	HI
Total	32.2%	38.5%	33.0%	76.4%	76.0%	70.2%	86.6%
	(146/454)	(175/454)	(150/454)	(347/454)	(345/454)	(319/454)	(393/454)
Early-type	33.9%	46.1%	-	-	82.4%	71.9%	-
	(58/171)	(79/171)			(141/171)	(123/171)	
Late-type	31.1%	33.9%	36.7%	86.6%	72.1%	69.2%	96.8%
	(88/283)	(96/283)	(104/283)	(245/283)	(204/283)	(196/283)	(274/283)
Late-type (Cluster)	56.9%	62.5%	72.2%	97.9%	100.0%	91.7%	100.0%
	(82/144)	(90/144)	(104/144)	(143/144)	(144/144)	(132/144)	(144/144)
Late-type (Field)	4.3%	4.3%	0%	73.4%	43.2%	46.0%	93.5%
	(6/139)	(6/139)	(0/139)	(102/139)	(60/139)	(64/139)	(130/139)

Table 2.1: The completeness of the UV data, integrated and nuclear spectroscopy, B and V photometry and HI observations for the total sample and for the different subsamples, as available at the start of this thesis.

2.4 DERIVED PHYSICAL PROPERTIES

The multiwavelength observations described in the previous section are all important for tracing the different components of a galaxy, such as the young and old stellar populations, the atomic hydrogen gas, the metal content and any nuclear activity, amongst others. Below, I introduce the methods I adopt for converting the various observational quantities into the physical properties.

2.4.1 STELLAR MASS

Estimating the stellar mass is important for many reasons; the stellar mass assembly of galaxies through cosmic time may shed light on the formation and evolution of structure in the universe. There is an observed bimodality in the galaxy population, with massive systems having formed the bulk of the stellar population in the early universe and less massive systems possessing younger stellar populations. Understanding when galaxies were assembled will provide clues to the origin of this bimodality (e.g. Baldry et al., 2004). Since nearby galaxies represent the end point of an evolutionary process, it is important to have accurate measurements of the distribution of stellar mass with varying morphological types at low redshift, in order to constrain theories derived from high redshift observations. In addition, the stellar mass-to-light ratio is also important for converting between photometry and dynamics (e.g. for measuring the decomposed rotation curves of spiral galaxies to probe dark matter; de Blok & McGaugh, 1998).

Optical luminosity, originally used as an indicator of the stellar mass, may not be reliable because optical luminosities are sensitive to the level of current star formation and are extinguished by dust. Also, near-infrared luminosities can be influenced by the age of the stellar population of a galaxy. Thus, the influence from the stellar populations in the different bands must be accurately determined. Fortunately, reliable stellar mass estimates are now possible with improved stellar evolutionary synthesis models (e.g., Leitherer et al., 1999; Fioc & Rocca-Volmerange, 1997; Bruzual & Charlot, 2003; Maraston, 2005). Bell & de Jong (2001) use stellar population synthesis models to determine prescriptions for converting optical colors and photometry into stellar masses assuming a Salpeter (1955) initial mass function. These prescriptions were updated by Bell et al. (2003), who construct stellar mass-to-light estimates using fits to SDSS *ugriz* and 2MASS K band fluxes and provide a range of conversions using optical colours and infrared luminosities.

I adopt the $B - V$ colour-dependent stellar mass-to-light ratio relation based on the H band luminosity

$$\log(M_*/M_\odot) = -0.359 + 0.21(B - V) + \log(L_H/L_\odot) \quad (2.1)$$

from Bell et al. (2003), which assumes a Kroupa et al. (1993) initial mass function. This relation is most suitable for determining the stellar masses for the HRS+ galaxies because of the completeness of the available observations in the B, V and H bands. B and V band observations are available for 312 of the 454 galaxies and morphologically averaged $B - V$ colours are used when optical observations are unavailable (presented in Table 2.2). Since the sample is complete in the H band, stellar masses are thus available for all the galaxies in the HRS+ sample. Bell et al. (2003) report the errors in the mass-to-light ratio increase with $B - V$ colour, typically being 0.1 dex at the red end and 0.2 dex at the blue end. Some additional uncertainty arises from the assumed IMF. However, since M_* just provides an indication of the stellar mass for a comparison with models, the uncertainties in the assumed IMF and the choice of calibration does not affect the conclusions of this work.

2.4.2 HI MASS AND DEFICIENCY

Neutral hydrogen acts as the fuel for potential star formation and, combined with the stellar mass, the mass of neutral hydrogen gas may also be used as an observational indicator of the state of chemical evolution of a galaxy (see Chapter 9). The HI mass, M_{HI} , is calculated from the line fluxes available from Springob et al.

Type	N	$B - V$
dS0-dE	21	0.754
E-E/S0	38	0.887
S0-S0/S0a	63	0.856
Sa-Sd	167	0.517
Sm-dIrr-BCD	24	0.406

Table 2.2: Mean B-V values from galaxies binned by morphological type, which are applied as the colour correction in Equation 2.1 where B and V band observations are unavailable.

(2005) and Gavazzi et al. (2003b), according to

$$\left(\frac{M_{HI}}{M_{\odot}}\right) = 2.36 \times 10^5 \left(\frac{D}{\text{Mpc}}\right)^2 \int \left[\frac{S(\nu)}{\text{Jy}}\right] \left(\frac{\nu}{\text{km s}^{-1}}\right) \quad (2.2)$$

where the expression within the integral represents the HI flux density integrated over the profile width, in units of Jy km s^{-1} (i.e. S_{obs}).

This quantity can provide a useful probe of the physical conditions of a galaxy environment. This is because the HI distribution in normal, isolated galaxies is radially flat, often extending beyond the optical disk and with a thickness comparable to the optical thickness (Cayatte et al., 1994; Salpeter & Hoffman, 1996; Lee & Irwin, 1997), meaning that the HI gas is only weakly bound by the gravitational potential of a galaxy. Therefore, HI gas can easily be removed from a galaxy and the resultant variation between cluster members and isolated galaxies has been observed. Many studies have observed the gas content of the Virgo cluster, and have all found that cluster galaxies have a lower HI gas content compared to field galaxies. Indeed, mapping of the HI distribution in Virgo and Coma cluster galaxies using high resolution interferometry (Warmels, 1988; Cayatte et al., 1990; Bravo-Alfaro et al., 2000) has shown that cluster galaxies are not only deficient of HI gas, but also have a less extended HI distribution compared to relatively isolated systems (see Gavazzi (1989); Boselli et al., 2002). The HI deficiency parameter, introduced by Haynes & Giovanelli (1984), provides a quantitative measure of the difference between the observed gas content of a galaxy and the expected gas content of an isolated galaxy of the same optical size, D_{opt}^{obs} , and morphological type, T^{obs} . Thus, I estimate the HI deficiency parameter, $DEF(HI)$, according to

$$DEF(HI) = \log M_{HI}(T^{obs}, D_{opt}^{obs}) - \log M_{HI}^{obs} \quad (2.3)$$

as defined by Haynes & Giovanelli (1984), with the morphologically-dependent coefficients presented in Table 2 of Solanes et al. (1996). The regression line coefficients are almost identical from Sa to Sbc types, whereas they significantly vary going to E/S0 or to Sc and later types (Solanes et al., 1996). The typical uncertainty in the estimate of $DEF(\text{HI})$ is ~ 0.3 (e.g. Haynes & Giovanelli, 1984; Fumagalli et al., 2009), but it may increase slightly for dwarf and early-type galaxies. Galaxies are classified as ‘HI deficient’ if $DEF(\text{HI}) > 0.5$ i.e. they have lost $\geq 70\%$ of their original atomic hydrogen when compared to similar isolated galaxies, and ‘HI normal’ otherwise.

2.4.3 CLASSIFICATION OF NUCLEAR ACTIVITY

Understanding the role of AGN in the evolution of galaxies remains an area of active research. With the HRS+ sample, it may be possible to constrain the relative impact of active nuclei on the host galaxy compared to environmental effects, therefore an accurate classification of the nuclear activity is important.

AGN are broadly classified by luminosity, ranging from high luminosity quasars, less luminous Seyferts, and to low luminosity, low-ionization nuclear emission regions (LINERs). There are various observational tools used to discriminate AGN-hosts from normal galaxies, and further classify the different types of AGN. These are based on X-ray observations (e.g. Anderson et al., 2003), mid-infrared spectroscopy (see e.g. Laurent et al., 2000; Hernán-Caballero et al., 2009 and references therein), infrared colours (Cutri et al., 2002) and also optical spectroscopy (e.g. Baldwin et al., 1981).

Nuclear activity may be classified from optical spectroscopy by using different suites of emission lines present in nuclear spectra. The emission lines in the spectra of normal star-forming galaxies originate from various elements, ionized by young stars in HII regions, whereas the emission lines from AGN arise from ionization due to a harder radiation field. Because emission lines in normal galaxies are powered by massive stars, there is a well-defined upper limit on the intensities of collisionally excited lines relative to recombination lines (such as $\text{H}\alpha$ and $\text{H}\beta$). On the other hand, AGNs are a source of more energetic photons so that collisionally excited lines are typically more intense and surpass the upper limits in emission lines from HII regions of star-forming galaxies. Thus, the ratios of the intensities of collisionally excited lines relative to recombination lines can indicate the underlying nature of the ionising field and measure the level of nuclear activity in a galaxy. Diagnostic diagrams introduced by Baldwin et al. (1981, hereafter BPT diagrams) typically rely on such ratios, like the $[\text{OIII}] \lambda 5007/\text{H}\beta$, $[\text{NII}] \lambda 6584/\text{H}\alpha$, $[\text{OI}] \lambda 6300/\text{H}\alpha$ and $([\text{SII}] \lambda 6717 + [\text{SII}] \lambda 6731)/\text{H}\alpha$

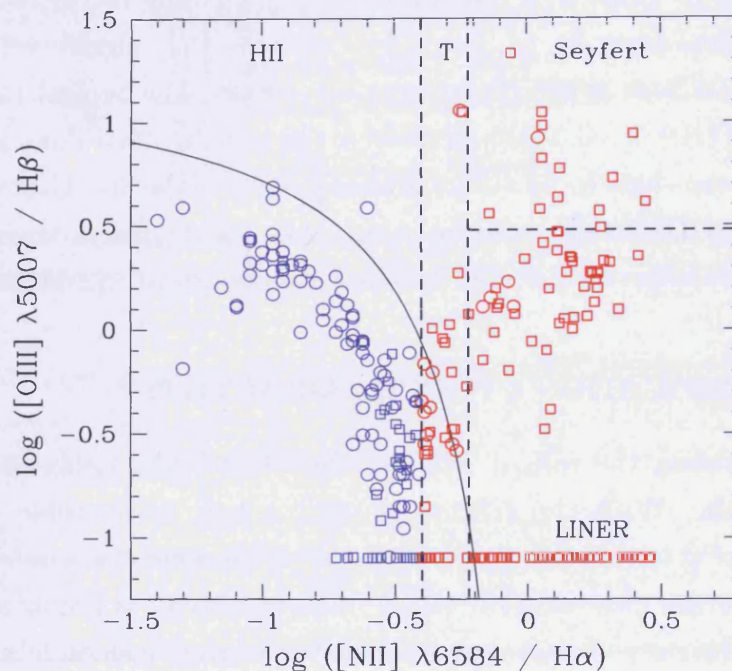


Figure 2.4: The BPT (Baldwin, Phillips & Terlevich, 1981) diagnostic diagram used to classify the spectra of galaxies in this work, based on the $[\text{NII}]/\text{H}\alpha$ and $[\text{OII}]/\text{H}\beta$ line ratios. Objects for which a measurement of $[\text{OII}]/\text{H}\beta$ is not available are plotted at $\log([\text{OII}]/\text{H}\beta) = -1.1$. The Decarli et al. (2007) scheme (straight dashed lines) marks the classification boundaries between star-forming (blue symbols), LINER, Seyfert and composite galaxies (red symbols), as described in the text. Line ratios are taken from either Decarli et al. (2007, circles) or Ho et al. (1997, squares). In addition, the demarcation lines between star-forming and AGN-host galaxies from Kauffmann et al. (2003, solid black line) is shown.

line ratios (see also e.g. Veilleux & Osterbrock, 1987; Kewley et al., 2001; Kauffmann et al., 2003; Lamareille et al., 2004).

In a recent study by Stasińska et al. (2006), these different indicators are compared using a large (~ 20000) sample of SDSS galaxies and photoionization models. They find $[\text{OIII}]\lambda 5007/\text{H}\beta$ versus $[\text{NII}]\lambda 6584/\text{H}\alpha$ diagrams are the most efficient indicators of nuclear activity, since the dichotomy of the galaxy population is not so clear in the diagrams using other combinations of the aforementioned line ratios and because photoionization models tend to underpredict the $[\text{SII}]/\text{H}\alpha$ and $[\text{OI}]/\text{H}\alpha$ ratios. They proposed a classification scheme based on the $[\text{NII}]/\text{H}\alpha$ ratio for discriminating between AGN-hosts, normal star-forming galaxies and hybrid or ‘composite’ galaxies, which demonstrate line ratios characteristic of both star formation and nuclear

activity. Galaxies may thus be divided into these three classes according to

1. $[\text{NII}]/\text{H}\alpha < 0.4$ for HII -like nuclei of normal star-forming galaxies;
2. $[\text{NII}]/\text{H}\alpha > 0.6$ for AGNs;
3. $0.4 < [\text{NII}]/\text{H}\alpha < 0.6$ for HII /AGN composite objects.

In addition, Decarli et al. (2007) adopted the $[\text{OIII}] \lambda 5007/\text{H}\beta$ to further divide the AGN-hosts according to lower luminosity LINERs ($[\text{OIII}]/\text{H}\beta < 3$) and the more power Seyfert nuclei ($[\text{OIII}]/\text{H}\beta \geq 3$) where observations are available, otherwise AGN are classified as Seyfert/LINER. This classification scheme is also adopted for the HRS+ sample (see Figure 2.4), although it should be noted that I refer to any galaxies with $[\text{NII}]/\text{H}\alpha > 0.6$ as AGN-hosts regardless of the AGN type.

It should also be kept in mind that there may be some bias in the classification of edge-on galaxies, where difficulty is experienced in obtaining accurate spectra from the central region for measurement of the nuclear activity. Possible contamination of the spectra from any star formation along the line-of-sight through the outskirts to the centre may lead to an incorrect measure of nuclear activity and result in a classification as a composite or, in cases of intense star formation, a purely star-forming galaxy. At present, this effect has not been thoroughly examined and remains a topic of future investigation.

2.5 CONCLUSIONS

Although a large multiwavelength dataset was available for the HRS+ sample at the beginning of this thesis, additional FUV and NUV imaging and optical spectroscopy are necessary for galaxies outside the Virgo cluster. This data is crucial for any study comparing the properties of galaxies in different environments and, therefore, I must first acquire the data necessary for this work. Therefore, the following two chapters focus on increasing the availability of ultraviolet photometry and optical spectroscopy.

CHAPTER 3

ULTRAVIOLET PHOTOMETRY

3.1 INTRODUCTION

Observations of the ultraviolet (UV) properties of nearby galaxies are essential for understanding galaxy evolution in the local universe. Massive, young stars emit most of their energy as UV radiation and this emission can dominate the spectral energy distribution of star-forming galaxies (e.g. Bruzual & Charlot, 2003). For late-type spiral and irregular galaxies, the UV emission is a reliable indicator of recent ($t < 10^8$ yr) star formation (Kennicutt, 1998). The emission of UV is also important for studies of quiescent early-type galaxies, following the discovery of an unexpected excess of UV flux in these systems (the ‘UV upturn’; Code, 1969; Bertola et al., 1982). Understanding this phenomenon may shed light on the evolution of low mass stars on the horizontal branch (Burstein et al., 1988; O’Connell, 1999). UV observations have also revealed residual star formation in a fraction of nearby elliptical galaxies (Yi et al., 2005). In addition, UV light can be very efficiently absorbed by dust and then re-emitted at far-infrared wavelengths, and so a comparison of the infrared and UV emission is a useful tool to determine the dust attenuation (see e.g. Cortese et al., 2008). Therefore, there is much that can be learnt from ultraviolet observations.

The studies presented in this thesis use the UV properties of nearby galaxies in a number of different ways. By using integrated UV magnitudes in ultraviolet-infrared colour-magnitude diagrams (Chapter 5), radial surface brightness profiles (Chapter 6), and estimates of the star formation rates in late-type systems (Chapters 7 and 9), I hope to constrain current theories of galaxy evolution. Fortunately, many UV observations of local galaxies are now available from the Galaxy Evolution Explorer satellite (Martin et al., 2005; hereafter GALEX), which observes in the far-UV (FUV) and near-UV (NUV) band observations. The following sections describe the GALEX

observations, the available data and the measurements of UV magnitudes.

3.2 THE GALAXY EVOLUTION EXPLORER

The Galaxy Evolution Explorer (GALEX) is a NASA Small Explorer ultraviolet space telescope, launched into orbit on the 28th April 2003. The satellite consists of a 50 cm-diameter, modified Ritchey-Chretien telescope with a 1.2 deg circular field of view and instruments capable of taking both imaging and spectroscopic observations. Two detectors image two UV bands: the FUV band (1528Å: 1344-1786Å) and the NUV band (2271Å: 1771-2831Å). The FUV detector has a peak quantum efficiency of 12% and the NUV detector has an efficiency of 8%. The instrumental configuration can be used to image both bands simultaneously using a dichroic beam splitter. The resolution of the system is typically 4.5(6.0)" in the FUV(NUV). Full details about the mission are given in Martin et al. (2005) and Morrissey et al. (2005).

The GALEX mission includes a number of spectroscopic and imaging surveys with varying sky coverage and depth. Here, I focus on describing the main imaging missions:

- All-sky Imaging Survey (AIS): The AIS aims to observe the entire sky down to a sensitivity of $m_{AB} \simeq 19.9$ mag (20.8 mag) in the FUV(NUV) band. The large sky coverage is achieved by observing up to twelve 100-second pointed exposures per eclipse at positions chosen to avoid gaps between the observed fields. Approximately 75-95% of the observable sky will be imaged (subject to the strict brightness limits imposed to protect the sensitive detectors). In the latest data release (GR4), over 28000 deg² of the sky have been observed.
- Medium Imaging Survey (MIS): The MIS images are single eclipse exposures, typically 1500 seconds, with sensitivity $m_{AB} \simeq 23$ mag, which aims to cover 1000 deg². The MIS pointings cover positions matching the Sloan Digital Sky Survey (SDSS; York et al., 2000), the Two Degree Field Galaxy Redshift Survey (2dFGRS; Colless et al., 2001) and the AA-Omega (WiggleZ) project (Glazebrook et al., 2007).
- Deep Imaging Survey (DIS): The DIS consists of 30000 second exposures taken over 20 eclipses, reaching sensitivity limits of $m_{AB} \simeq 25$ mag. Over 80 deg² of sky has been observed, with significant overlap with other surveys (e.g. COSMOS).
- Nearby Galaxies Survey (NGS): The NGS targets well-resolved nearby galaxies, imaging with 1000-1500 second exposures and reaching surface brightness limits

of $m_{AB} \simeq 27.5$ mag arcsec². The GR4 release contains 433 pointings.

Cluster name	Coordinate range (J2000)
Abell 262	26.6 < R.A. < 31.0 ; 34.5 < Dec. < 38.5
Cancer cluster	123.5 < R.A. < 127.0 ; 20.5 < Dec. < 22.0
Coma supercluster	174.0 < R.A. < 202.0 ; 17.5 < Dec. < 31.5
Virgo cluster	182.0 < R.A. < 192.5 ; 2.0 < Dec. < 17.5
Abell 2199	239.0 < R.A. < 242.0 ; 14.5 < Dec. < 19.5
Abell 2147	245.0 < R.A. < 249.0 ; 38.5 < Dec. < 41.5

Table 3.1: The locations of clusters for which GALEX observations were retrieved, where available.

Images taken as part of these observing campaigns are used in this work to derive the UV magnitudes used throughout this thesis. In the following sections, I describe the selection of the GALEX pointings and the method employed for measuring the UV properties of galaxies.

3.3 UV OBSERVATIONS

GALEX observations covering the Virgo cluster, thus including the Virgo galaxies present in the HRS+ sample, were selected together with observations of five other nearby clusters (see Table 3.1). The extra clusters were obtained in order to either update or expand the number of UV magnitudes available as part of the multiwavelength dataset contained in the GOLDMine database (see Gavazzi et al., 2003a). The GALEX observations were obtained from the GR2/GR3 data release for the FUV (1528Å: 1344-1786Å) and NUV (2271Å: 1771-2831Å) bands, where available. In total, there are 357 NUV and 162 FUV fields of view covering these regions. The lower number of FUV observations was due to a technical problem with the GALEX FUV detector.

Galaxies selected from two catalogues were then extracted from the GALEX observations. The Catalogue of Galaxies and Clusters of Galaxies (CGCG; Zwicky et al., 1961) and, in particular for Virgo, the Virgo Cluster Catalogue (VCC; Binggeli et al., 1985) contained the coordinates to locate the galaxies within the GALEX observations for extraction. In all clusters, galaxies brighter than $m_{ph} = 15.7$ mag were selected from the CGCG, except for Virgo where objects brighter than $m_{ph} = 20.0$ mag were selected from the VCC. From the images of the complete GALEX

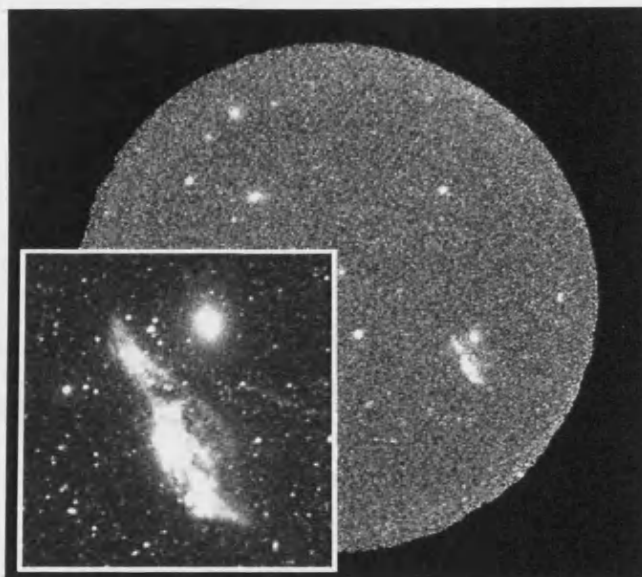


Figure 3.1: The GALEX NUV band field of view containing VCC 1043, as an example, with the finding chart of the object presented as the inset.

field of view, cropped images (finding charts) containing each individual galaxy were obtained and then used for the remainder of this work. An example of the GALEX field of view and generated finding chart for a galaxy is presented in Figure 3.1. This process generated 2883 NUV and 1676 FUV find charts covering observations of 2181 galaxy members of the six clusters.

3.4 APERTURE PHOTOMETRY

To obtain magnitudes from these UV observations, aperture photometry is performed utilising the *funtools* software for *ds9*. This software counts the number of photons in a defined source aperture and subtracts the background number of counts, determined from the mean flux from several background count measurements after normalisation by the area. As the GALEX images are normalised by the exposure time, each photon count is actually a count rate. The location, size and position angle of the source apertures to measure the count rate are initially set using the $\mu(B) = 25$ mag arcsec² isophote and based on the NUV band finding charts. For cases where the NUV emission extends beyond this isophote, the contour is manually edited by eye, such that the apertures contained the entire NUV flux from the object. The source

flux, in counts per second, is then converted into an AB magnitude using

$$\begin{aligned} m_{AB}(FUV) &= -2.5 \log f_{FUV} + 18.82 \\ m_{AB}(NUV) &= -2.5 \log f_{NUV} + 20.08 \end{aligned} \quad (3.1)$$

This conversion is accurate to $\pm 10\%$ (Martin et al., 2005). Possessing multiple observations of individual galaxies from the different GALEX imaging missions meant that the reproducibility of a measured magnitude can be tested; a comparison of 981 galaxies with more than one measured magnitude demonstrates good agreement between the different measurements (see Figure 3.2). The standard deviation of the residual magnitudes, $\sigma_{\delta m}$, where

$$\delta m = m_{x,1} - m_{y,2} \quad (3.2)$$

gives the error in the magnitudes. The calculated values of $\sigma_{\delta m}$ are 0.11 mag for the m_{NUV} and 0.12 mag for the m_{FUV} residual magnitudes. A significant fraction of the sample in both GALEX bands has been published in previous works (Cortese et al., 2005; Cortese et al., 2006; Boselli et al., 2008), allowing for a comparison between the results presented here and in the literature. Magnitudes for 428 and 168 galaxies in the NUV and FUV, respectively, are available from these works. The calculated values of $\sigma_{\delta m}$ for the comparison (presented in Figure 3.3) are 0.16 mag for the m_{NUV} and 0.14 mag for the m_{FUV} residual magnitudes. These values are slightly larger than those from the previous comparison of multiple measurements in this work, but this is unsurprising because the values from past studies are based on an earlier GALEX data release (GR1), for which the photometric calibration was less precise than the current data release. The typical uncertainty in the magnitudes and the colours used in the following work is therefore ≤ 0.2 mag and this error is reduced further by using the average magnitude from all the observations available for each galaxy.

3.5 DUST ATTENUATION CORRECTIONS

The presence of dust in galaxies must be taken into account when attempting any quantification of properties derived from UV emission. The UV light is predominantly emitted by young stars, typically surrounded by dust clouds. Dust grains preferentially absorb the UV photons, which consequently reddens the spectral energy distribution of a galaxy at short wavelengths. This can lead to incomplete or biased conclusions about the star formation activity in a galaxy, if the UV emission is

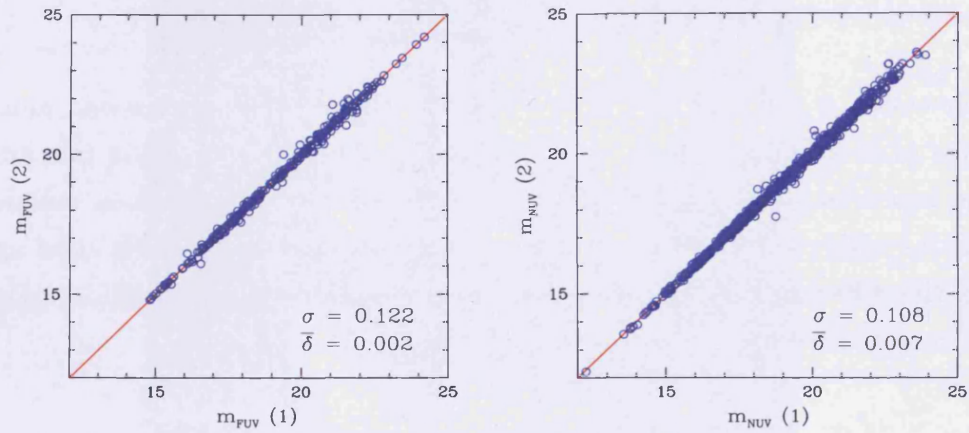


Figure 3.2: A comparison between resulting m_{FUV} (left panel) and m_{NUV} (right panel) magnitudes obtained for all galaxies for which multiple observations are available. The scatter σ and the offset of the residual magnitudes δm are also presented.

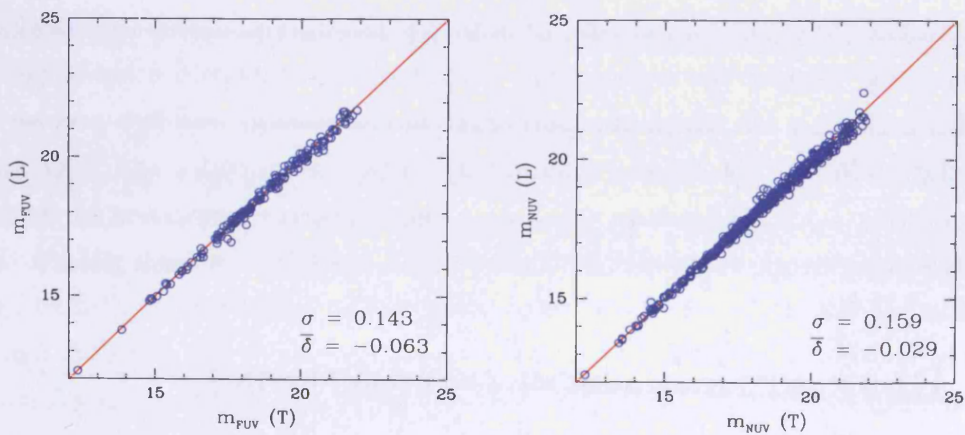


Figure 3.3: The m_{FUV} (left panel) and m_{NUV} (right panel) magnitudes obtained from this work (denoted by T) are compared with those obtained from previous work (denoted by L). The scatter σ and the offset of the residual magnitudes δm are also presented.

not properly corrected for the attenuation due to dust. Since this work relies on accurate measurements of the UV emission for studying the properties of galaxies using various approaches (i.e. colour-magnitude diagrams, surface brightness profiles, star formation rates), it is especially important to derive accurate extinction corrections.

There are a number of indicators available to estimate the dust attenuation. The ultraviolet spectral slope (β), the Balmer decrement and the ratio of the total infrared to UV emission (L_{TIR}/L_{FUV}) have all been studied as possible measures of the amount of attenuation (e.g. Buat, 1992; Xu & Buat, 1995; Meurer et al., 1995; Meurer et al., 1999). The latter method is based on the assumption that a fraction of the photons emitted by stars and gas are absorbed by the dust. The dust then heats up and re-emits the energy at infrared wavelengths. Since the method is nearly independent of the dust geometry or the assumed extinction law (e.g. Buat & Xu, 1996), the L_{TIR}/L_{FUV} method is considered the most reliable. However, the ratio does depend on the age of the underlying stellar populations, as dust heating by old stars is more important in systems with low specific star formation rates and so the IR emission does not fully correspond to the absorption of UV photons.

Past studies on samples of star-forming galaxies could rightly consider this age effect negligible (Gordon et al., 2000), but age-dependent attenuation corrections have become necessary since GALEX UV observations of galaxies cover the entire zoo of morphologies (see e.g. Martin et al., 2007; Schawinski et al., 2007). Cortese et al. (2008) demonstrate that applying age-independent corrections could systematically overestimate the attenuation (> 1 mag) even in late-type galaxies, which can lead to a significant bias in the interpretation of the UV observations. They provide empirical relations for estimating the UV attenuation that take into account the dependence of the age of the stellar populations.

Thus, I use the L_{TIR}/L_{UV} method and the age-dependent relations of Cortese et al. (2008) to correct the UV magnitudes for internal dust attenuation. The TIR luminosity is obtained from IRAS 60 and 100 μm fluxes or, in the few cases when IRAS observations are not available, using the empirical recipes described in Cortese et al. (2006). The typical uncertainty in the NUV dust attenuation is ~ 0.5 mag.

3.6 STAR FORMATION RATES

The recent star formation rate (SFR) of a galaxy may be measured from the light emitted from the young stellar population since their luminosity is directly proportional to the rate at which they are currently forming. Because most of the UV photons are originally emitted by stars younger than $\sim 10^8$ yr, the UV emission

of star-forming galaxies is closely related to recent star formation and therefore is a useful indicator of the current SFR. Since a fraction of the UV photons emitted by the young stars are scattered or absorbed by dust enshrouding the young stars or present along the line of sight to the galaxy, it is important to first correct the observed UV emission for dust attenuation in order to derive accurate star formation rates.

Iglesias-Páramo et al. (2006) investigate the use of the GALEX bands to estimate star formation rates. They find that the conversion relations of

$$\log SFR_{NUV} (M_{\odot} \text{ yr}^{-1}) = \log L_{NUV} (L_{\odot}) - 9.33 \quad (3.3)$$

$$\log SFR_{FUV} (M_{\odot} \text{ yr}^{-1}) = \log L_{FUV} (L_{\odot}) - 9.51 \quad (3.4)$$

provide rates that are accurate to $<20\%$. Hence, I adopt these relations throughout this work.

3.7 CONCLUSIONS

GALEX observations covering six clusters (including Virgo and Coma) were obtained from the GR2/GR3 data release. Using aperture photometry, source fluxes were measured and converted into AB magnitudes. The reproducibility of the magnitudes was tested using multiple observations of the same target from the different GALEX observing missions and the scatter in the AB magnitudes was found to be slightly larger than ~ 0.1 mag. These magnitudes were compared to observations taken from the previous GR1 data release. The two sets of results were found to be consistent with a slightly higher scatter (< 0.2 mag). The AB magnitudes were corrected for internal dust attenuation following the L_{TIR}/L_{UV} method (e.g. Xu & Buat, 1995) and the new age-dependent relations of Cortese et al. (2008). The result of this work was the measurement of over 1600(2800) FUV(NUV) magnitudes for over 2100 galaxies, with approximately 900 magnitudes added/updated in the GOLDMine database (Gavazzi et al., 2003a). As such, the HRS+ sample is now almost complete in both UV bands (see Figure 3.4) for both the cluster and field subsamples.

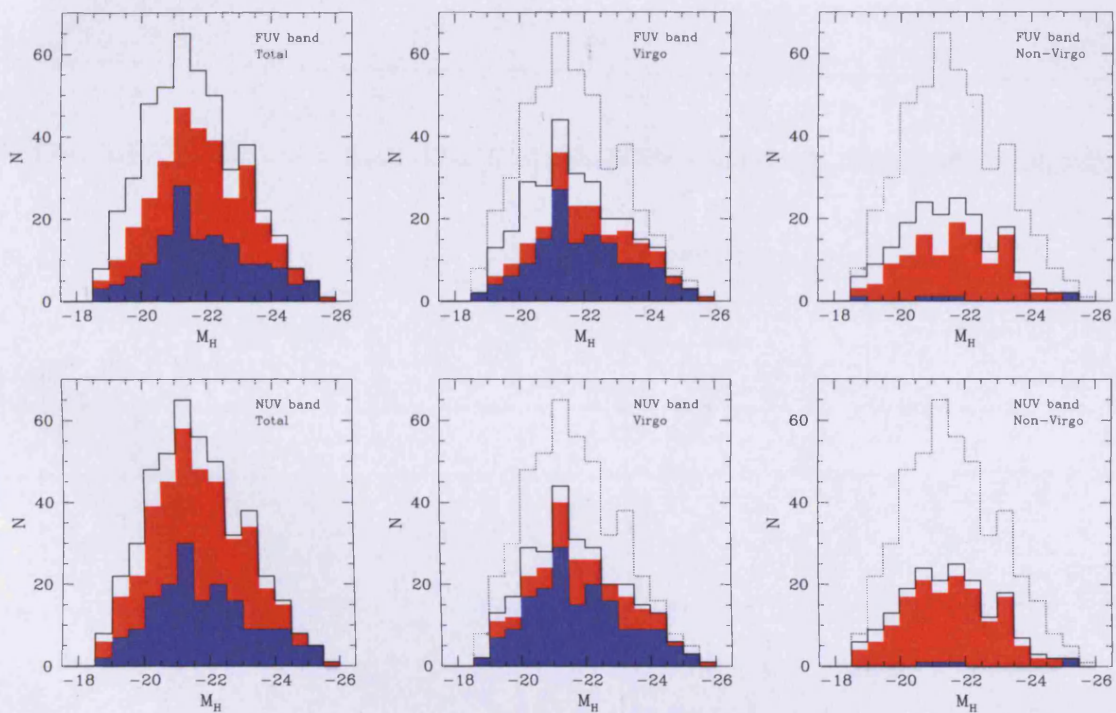


Figure 3.4: The completeness of HRS+ galaxies observed in the FUV (*upper row*) and NUV band (*lower row*). The coverage before (blue histogram) and after this work (red histogram) are compared to total distribution (solid black line) for the entire sample and for galaxies residing inside and outside the Virgo cluster (*left, middle and right panels* respectively). In the diagrams of the latter two columns, the total distribution is plotted for ease of comparison (dotted black line).

CHAPTER 4

OPTICAL SPECTROSCOPY

4.1 INTRODUCTION

There is a wealth of information contained within the spectrum of light emitted by a galaxy. For example, emission lines originating from gaseous nebulae and observed in galaxy spectra reveal conditions of the gas, such as the temperature, density and the abundances of the heavier elements or ‘metals’. The combination of optical spectroscopy with the ultraviolet and infrared photometry grants knowledge of the metal content of the interstellar medium, the star formation rate and the stellar mass, and thus provides information necessary to study the chemical evolution of galaxies (see Chapter 9). Spectroscopic observations of galaxies in different environments are therefore important for investigating whether chemical evolution is driven by environmental effects or internal processes. The range of environments inhabited by galaxies in the HRS+ sample makes it an ideal sample of galaxies for investigating the role of the environment in galaxy evolution.

There are few extensive spectroscopic surveys of galaxies focussed on galaxies in different environments. The pioneering survey of 90 galaxies by Kennicutt (1992), was primarily focussed on the characterisation of the spectroscopic properties of nearby galaxies along the Hubble sequence, with the aim of forming a comprehensive dataset that could be used to interpret the spectra of high redshift systems. Aiming to expand this work to include a larger number of galaxies in different environments, a spectroscopic survey of nearby galaxies in different environments was carried out by Jansen & Kannappan (2001). Whilst the SDSS (York et al., 2000) provides medium resolution optical spectroscopy for a large number of galaxies (currently >78000), the spatial coverage of the 3" aperture fibers is incomplete for nearby galaxies, meaning the spectra are not representative of the overall optical emission

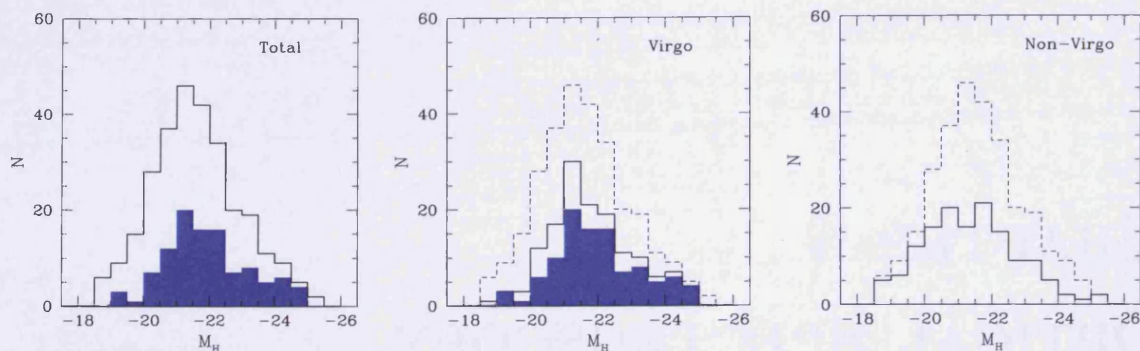


Figure 4.1: The coverage of spectroscopic observations of late-type galaxies by G04 (blue histogram) compared to the total number of late-type galaxies (black solid line) present in the entire HRS+ sample (*left*), in the Virgo cluster members (*middle*) and outside the Virgo cluster (*right*). The total sample is displayed in the latter two plots for ease of comparison (black dashed line).

from the galaxy. Integrated spectra obtained using the drift scan technique, whereby the entire extent of the galaxy is observed, are required for deriving global properties to study chemical evolution. For this reason, integrated optical spectrophotometry for a sample of 417 nearby galaxies was obtained by Moustakas & Kennicutt (2006), which is currently one of the few spectroscopic surveys with integrated spectra.

Recognising the lack of spectroscopic surveys of nearby clusters and inspired by previous studies, Gavazzi et al. (2004, hereafter G04) initiated a project to spectroscopically characterise galaxies within the Virgo cluster using integrated spectra. They observed 225 Virgo cluster members over a wavelength range of 3600 - 6800Å, which includes the main emission lines at optical wavelengths, via drift-scan spectroscopy. From these observations, intensities and equivalent widths of prominent optical emission lines are available. As Figure 2.3 shows, most of the Virgo galaxies in the HRS+ sample have been observed spectroscopically as part of the G04 observations and so the sample representing the cluster environment can be considered complete.

However, by using the G04 observations alone, a study of how spectroscopically-derived properties vary in different environments is still not possible, since the G04 sample does not provide spectral data for galaxies residing outside of the Virgo cluster and which are included in the HRS+ sample. In order to form a complete field sample and increase the overall completeness of the HRS+ sample, drift scan spectra of HRS+ field galaxies were obtained as part of an observing campaign lead by A. Boselli during 2007 and 2008. By adopting the methods of G04, the Boselli data

(hereafter referred to as B08) can be used to measure the emission line intensities so that the two datasets may be combined to increase the spectral coverage of the HRS+ sample.

This Chapter is structured as follows. In the next section, I introduce the B08 observations. I describe my reduction of these observations into calibrated, one-dimensional spectra in Section 4.3. The method for measuring the emission line fluxes and the results of these measurements are treated in Section 4.4. Finally, Section 4.5 presents the conclusions of this work.

4.2 THE B08 OBSERVATIONS

Observations of 99 galaxies were taken using the 1.93m telescope at the Observatoire de Haute Provence (OHP) over 12 nights between 11th and 22nd April 2007 and over 6 nights between the 3rd and 8th March 2008. The observing campaign was led by A. Boselli with some of the observations completed in service mode.

The CARELEC spectrograph (Lemaitre et al., 1990) was used during both observing runs. This instrument is a spectrograph, with a slit length of 50 mm that is fully covered by the 5.5 arcmin field of view of the telescope. A thin, back-illuminated EEV CCD chip operates as the detector, consisting of 2048 x 1024 pixels with dimensions of 13.5 μm . Using the 300 lines/mm grating provides a resolving power, R , of 900 and a dispersion of 133 $\text{\AA}/\text{mm}$, a wavelength range of 3400-7000 \AA was incident across the CCD in 2007 and a range of 3600-7200 \AA was covered in 2008.

The observations were taken in drift-scan mode, whereby the slit is placed parallel to the major axis and drifts across the galaxy along the semi-major axis. Due to the drift-scan method, the observations are marginally affected by the seeing, which was typically 1.5'' - 3.5''. Whilst some observations were made through cirrus, most were taken in transparent or photometric conditions. Six nights were recorded as photometric in 2007 and two in 2008.

Calibration frames were typically taken at the beginning and end of each observing night. These consisted of around five bias frames, captured as zero second exposures, calibration lamp frames of either argon or helium with ~ 12 second exposures, approximately five flat field frames each with 3 second exposures. Finally, the standard star frames were obtained from observations of either Hz 44 or Feige 34 using 300 second and 480 second exposures respectively, and either of these were imaged before and after the main science observations. The observations of galaxies were typically made with 1200 - 1800 second exposures.

The galaxies targeted in the observing campaign were all selected from those

objects in the HRS+ sample which had not been observed as part of the G04 sample. The sample consisted predominantly of ‘field’ late-types together with a handful (6) of Virgo cluster members, thus satisfying the aim of increasing the level of completeness for the field and cluster environments. In total, 99 galaxies were successfully observed.

4.3 DATA REDUCTION

In order to combine the G04 and B08 observations into a homogeneous dataset, the B08 observations are reduced and calibrated with the same method as presented in G04. The reduction of the observations from the raw, two-dimensional images into calibrated, one-dimensional spectra is performed using standard tasks within the IRAF package. The method follows six steps: correcting the science images for bias, flat field and cosmic rays, calibration of the wavelength scale across the CCD, the subtraction of the background, the extraction of one dimensional spectra, calibration of the integrated flux of these one-dimensional spectra and finally blueshifting the spectra to their rest frame wavelengths.

4.3.1 NOISE SUBTRACTION

When an image or spectra is obtained, such observations are susceptible to noise introduced by the instruments used to obtain the data. Noise is present in the CCD electronics, variations of the sensitivity across the CCD, and nonuniform illumination of the CCD due to the optical setup. Such instrumental effects have to be removed to obtain a clean science image and a number of steps are completed before this noise in the data can be reduced.

Bias frames

Bias current applied through the CCD has the effect that a non-zero count is recorded in the pixels. The effect of the current is measured using bias frames, zero second exposures of the CCD, which were taken during each night of observing. The removal of bias noise is achieved by combining the median of several bias frames into a single frame, called a master bias frame (see the top panel of Figure 4.2), and then subtracting this frame from all the science images and the calibration images. The IMCOMBINE and IMARIT tasks in IRAF are used for this step. Noise from the dark current present in CCDs, due to thermal electrons, can be treated exactly as the bias frames.

Flat frames

The pixel array of the CCD is not illuminated uniformly. Also, the dependence of quantum efficiency with wavelength causes a variation in sensitivity across the CCD when obtaining spectra. Exposures of homogeneously illuminated areas, such as the interior of the telescope dome or the twilight sky, can be used to correct for such variations across the CCD. A master flat frame is produced using the median from a combination of exposures of standard calibration lamps. The bias current is present in the flat fields and is removed according to:

$$Flat_{master} = (Flat - Bias) / \langle Flat - Bias \rangle \quad (4.1)$$

by once again using the IMARIT task to perform arithmetic operations on the images. The second panel of Figure 4.2 shows an example master flat frame obtained from an observing night in 2007.

Cosmic rays

Whilst cosmic rays in bias frames can be removed during the averaging process of combining multiple exposures using a median filter, it is not always possible (mainly due to observing time constraints) to take multiple (>3) exposures of science images. I dealt with cosmic rays in two ways to ensure a clean image. The science frames are cleaned of cosmic rays by first running the COSMICRAY package in IRAF to remove point sources, then visually inspected to ensure that emission line features, important for the work in Chapters 8 and 9, had not been affected by the package. Remaining extended features are then manually removed by replacing the value of an affected pixel with an average derived from an annulus around the pixel, using the IMEDIT package. Visual inspection of the raw images can identify any bad pixels on the CCD, which are masked from the science frames by replacing them with an annuli-based average.

Following the creation of the master bias and master flat frames, and the cleaning of cosmic rays from the science images, the final reduced image is created according to

$$Science = (Science - Bias_{master}) / Flat_{master} \quad (4.2)$$

In Figure 4.2, the third and fourth panels depict a raw (uncorrected) observation of a galaxy spectrum and the same spectrum corrected for bias, flat field effects and cosmic rays, respectively. The next step is the wavelength calibration.

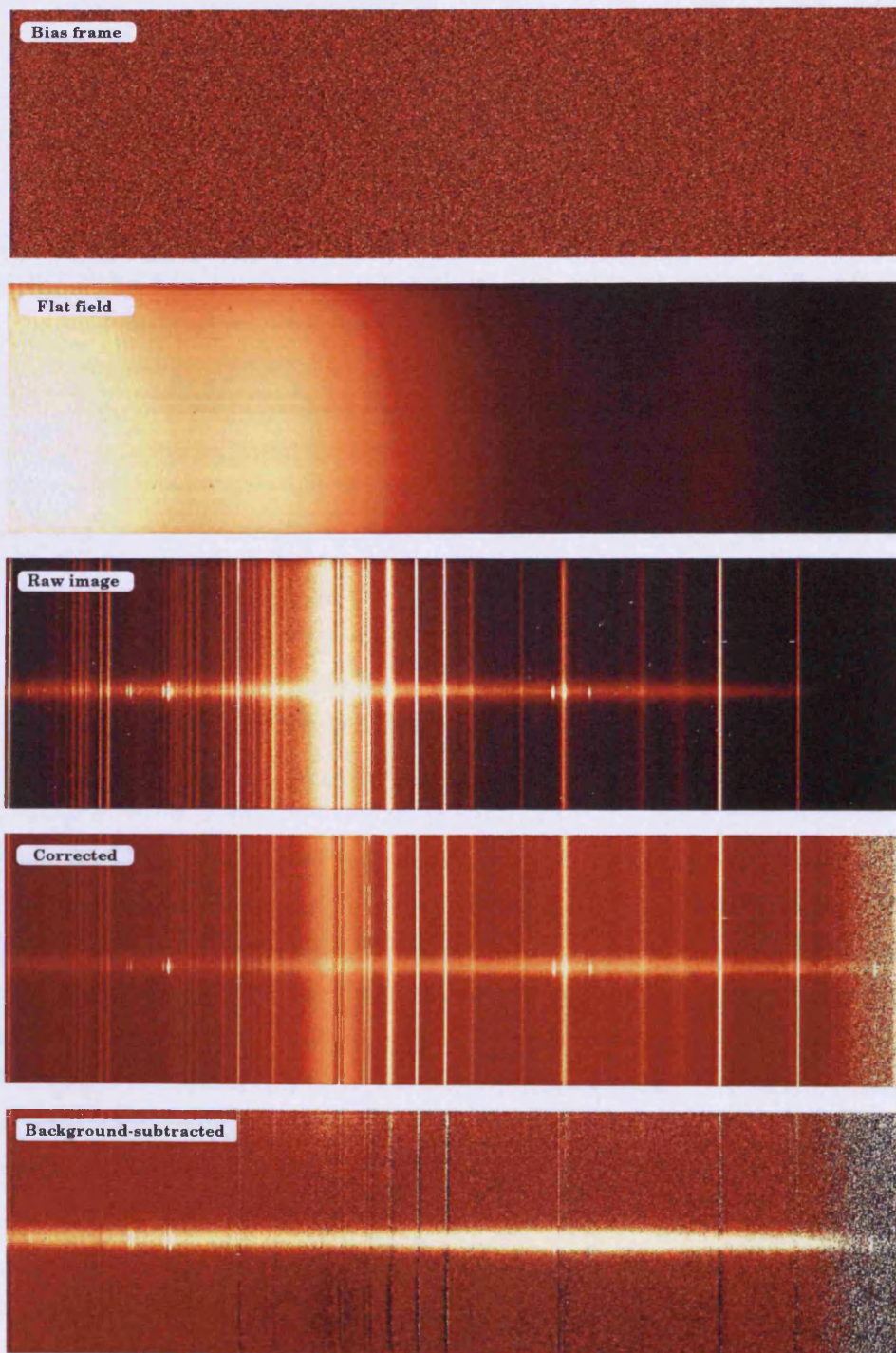


Figure 4.2: Each panel displays different observations used at different stages of the data reduction. *First panel:* The master bias frame. *Second panel:* The master flat obtained by combining the bias-subtracted flat fields. Note the variation in the sensitivity across the CCD, which should ideally be uniform. *Third panel:* Raw observation of a spectrum of a galaxy. *Fourth panel:* Previous galaxy spectrum corrected for bias, flat field effects and cosmic rays. *Fifth panel:* Previous panel following the subtraction of the background sky emission to leave the flux from the galaxy.

4.3.2 WAVELENGTH CALIBRATION

Wavelength calibration involves assigning a wavelength scale to the pixels along the axis of diffraction. To determine the wavelength scale, exposures of argon and helium calibration lamps, obtained during each night of the observing run, are used. An example image of a calibration lamp is displayed in Figure 4.3. The emission lines in the diffracted light of the calibration lamp occur at known wavelengths. Therefore, identifying the spectral lines on the lamp image with the corresponding known emission line features yielded the wavelengths of photons incident at each pixel on the CCD. The wavelength scale determined from the lamp exposures is then applied to the science images and the accuracy of the calibration is tested using emission features from the atmosphere, i.e. skylines, which occur in the science data at known wavelengths. This process is described in detail below.

To start, exposures of different calibration lamps (argon and helium) taken consecutively during the observing run can be combined into one calibration frame using IMCOMBINE. Then, the known emission line features of the lamps are identified and a calibration solution was found using the IDENTIFY, REIDENTIFY and FITCOOR tasks.

The IDENTIFY task is run to identify spectral features on one column of pixels on the lamp image. The strongest emission features of the calibration lamp on the CCD are identified and marked from a comparison with reference spectra¹. As many of the features as possible are identified with the corresponding reference features across the entire image to assure a calibration solution applicable to the full spatial extent of the images. Once the main features are marked, a solution for the wavelength scale is fitted to the spectrum and any remaining features contained in the reference file are then identified by the task. Ambiguous features, which may be identified by the software but are actually of an uncertain nature, are excluded from the calibration. Approximately 15-20 spectral features with an assigned wavelength are required to produce the wavelength calibration solution. The results of the solution are visually inspected by comparing how the solution wavelengths match the marked wavelength values. I reject any major outliers (with residuals greater than 1 Å). Once the wavelength scale for one column has been accurately determined, the REIDENTIFY task is used to apply this solution to the rest of the pixel columns across the image.

¹Reference calibration lamp images are available from <http://www.obs-hp.fr/guide/carelec/carelec-eng.shtml>



Figure 4.3: An example exposure of an argon calibration lamp used to calibrate the wavelength scale of the science images.

This procedure generates the calibration between the pixel scale and the wavelength scale. The FITCOORD routine then transforms the wavelength solutions across the image into a coordinate matrix that can be applied to the science images. If the first and last wavelength values applied to the pixels along the spatial axis are found to disagree, this indicates that a distortion in the coordinate matrix is present. These distortions are difficult to correct for and rely entirely on the accuracy of the previous steps. When the distortions are significant (over several Å) then the IDENTIFY task is rerun to attempt a better fit.

I then apply the calibration to the science frames with TRANSFORM. On initial inspection, it is found that sometimes systematic offsets are introduced into the final calibration. These offsets arise due to small variations in the optical setup occurring as the telescope moves into different pointing positions during the course of the night, which means light of a particular wavelength may be incident on the CCD at a slightly offset position compared to that from the calibration lamp image taken at the start of the night. These offsets are expected and are easily corrected. The accuracy of the calibration is tested by measuring the wavelengths of sky emission lines present in the data, since the emission lines from the atmosphere occur at known restframe wavelengths. The prominent sky emission line features in the observations arise from mercury in streetlights emitting the lines HgI $\lambda\lambda 4046, 4358, 5461$, and from oxygen airglow in the atmosphere producing the [OI] $\lambda\lambda 5577, 6300$ lines. These known wavelengths were compared to the (calibrated) wavelengths of the emission lines in the science images.

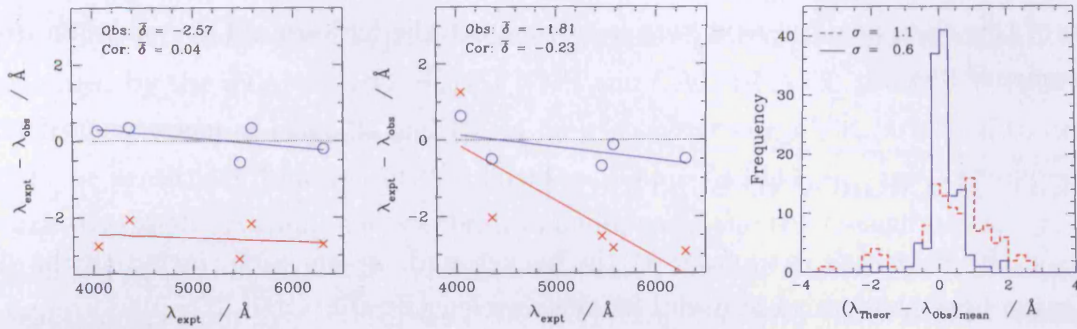


Figure 4.4: Plotting the residual wavelength from a comparison of the expected wavelength with the observed wavelength, $\lambda_{\text{expt}} - \lambda_{\text{obs}}$, of five prominent sky emission lines demonstrates the corrections necessary to remove both systematic offsets (*left panel*) as well as wavelength-dependent offsets (*middle panel*). In each of these panels, the observations and wavelength are shown before (red crosses and line) and after (blue circles and line) the wavelength solution is manually corrected. The dispersion in the distribution of the mean residual wavelengths per galaxy (*right panel*) after the manual corrections are applied (solid blue line) is smaller compared to the original dispersion (dashed red line).

The observed wavelengths of the sky emission lines are measured within the SPLOT task and compared with the expected values. I confirm the systematic offsets in the wavelength calibrations, which are typically between 0.5 and 2.5 Å, and also find that some calibrations introduce an offset that vary across the image. The wavelength scale applied to the science images follows a linear $y = mx + c$ relationship, where c is the wavelength of the first pixel and m is the wavelength increment size. Thus, I correct any offset in the relationship between the observed and the expected values by manually adjusting the m and c values, to produce a more accurate wavelength scale. The effects of these adjustments on the applied wavelength scale, for two individual galaxies and the total sample of galaxies, are presented in Figure 4.4. The plots of the residual wavelengths, i.e. a comparison of the expected wavelength with the observed wavelength, $\lambda_{\text{expt}} - \lambda_{\text{obs}}$, for each of the five prominent sky emission lines, demonstrate the necessity of the corrections to remove both systematic offsets as well as wavelength-dependent offsets. The removal of these offsets, where possible, reduces the dispersion, σ , in the distribution of the mean residual wavelengths for each galaxy, δ , which is clearly evident in the comparison between the corrected and uncorrected mean residual wavelength distributions, as presented in the right panel of Figure 4.4. The dispersions are hence reduced from $\sigma = 1.1$ Å to $\sigma = 0.6$ Å.

To summarise the last point, the calibration of the wavelength scale is sufficiently accurate for the production of reliable galaxy spectra and the subsequent

identification and measurement of the emission line properties, which forms the main aim of this chapter. The next step is to subtract the background sky emission from the science images.

4.3.3 BACKGROUND SUBTRACTION

The next task is to subtract the background sky emission, including the sky emission lines that prove so useful for the wavelength calibration. The background is subtracted using the `BACKGROUND` task. The task first displays the cross-sectional profile of the emission at a specified wavelength, corresponding to a particular column of the image. The background apertures are selected from this cross-sectional profile. For standard stars, any column can be used, as the flux along the spectra is usually strong and continuous. However, for galaxies, where the emission is extended and may be fainter in some places along the spatial and wavelength axes, a column is used which contains a strong emission feature across the extent of the galaxy. In the case of this sample of galaxies, $H\alpha$ $\lambda 6563$ is most often chosen for determining the extent of the source and indicate the regions of background emission. For each column in the image, a cubic spline function is fitted to the lines specified as the background region. This function is then subtracted across the image. The bottom panel of Figure 4.2 shows the effect of subtracting the background sky emission from the images, and comparing the middle and bottom panels clearly demonstrates that the task removes most of the sky emission lines across the image. However, as in the case of the example in Figure 4.2, some residual features of the sky emission lines remain in a large fraction of the images. These are noted and manually removed.

4.3.4 EXTRACTION OF 1D SPECTRA

The subtraction of the background is the last step to be performed on the two dimensional images, as the next step is the integration of the flux at each wavelength across each image to form one dimensional spectra. The integration is carried out with the `APSUM` task. The source aperture is selected in a similar manner to the background, as described previously, and the flux within the source aperture of each column is then integrated at each wavelength, producing spectra of counts versus wavelength.

4.3.5 FLUX CALIBRATION

The flux calibration to transform the measured intensities into flux densities is performed by the STANDARD, SENSFUNC and CALIBRATE tasks. The standard star frames, taken of Feige 34 and Hz 44 on each observing night, are used to determine the sensitivity function of the detector. The STANDARD task integrates the standard star observations over calibration bandpasses and the measurements are corrected for extinction using the reference extinction data in IRAF. The observational measurements from these bandpasses are then compared with the standard reference observations to determine the system sensitivity as a function of wavelength. The calibration factor used to convert from the measured intensities into flux densities at each wavelength is determined with SENSFUNC according to

$$C(\delta\lambda) = 2.5 \log \frac{f_{obs}}{t_{exp} \delta\lambda f_{star}} + aE \quad (4.3)$$

where f_{obs} is the observed counts in a bandpass, $\delta\lambda$, of an observation, t_{exp} is the exposure time of the observation, f_{star} is the flux per Ångstrom at the bandpass for the standard star, a is the airmass of the observation, and E is the extinction at the bandpass. Therefore, the calibration factor is in magnitude units derived from the ratio of two fluxes: the observed flux measured in counts $s^{-1} \text{Å}^{-1}$ and the reference standard star flux given in units of $\text{ergs cm}^{-2} s^{-1} \text{Å}^{-1}$. Cubic spline functions are fitted to the calibration points. The polynomial fits typically produce the best results using orders between the 15th and 25th order, although the orders are kept as small as possible to avoid introducing spurious features in the data.

The sensitivity functions produced by SENSFUNC, based on observations of the Feige 34 or Hz44 standard stars during each observing night, are presented in Figure 4.5. At wavelengths longer than 4000 Å, it is clear that the overall shape of the sensitivity function remains consistent between each observing night. Although the sensitivity curves do vary slightly across the entire wavelength range, these variations are caused by periods of variable transparency and are the results of taking observations through thin clouds. However, not all of the sensitivity functions are in agreement at wavelengths shorter than 3700 Å. The majority of the functions see a drop in sensitivity approaching the edge of the images, which is to be expected from a quick visual inspection of the CCD images in Figure 4.2, where noise levels increase significantly at one edge of the observations. However, four of the functions possess a strong ‘bump’ in the system sensitivity centered around 3500 Å. This bump is present due to the presence of a filter, probably mistakenly included in the optical setup during observations taken during service mode. The inset panel of Figure 4.5

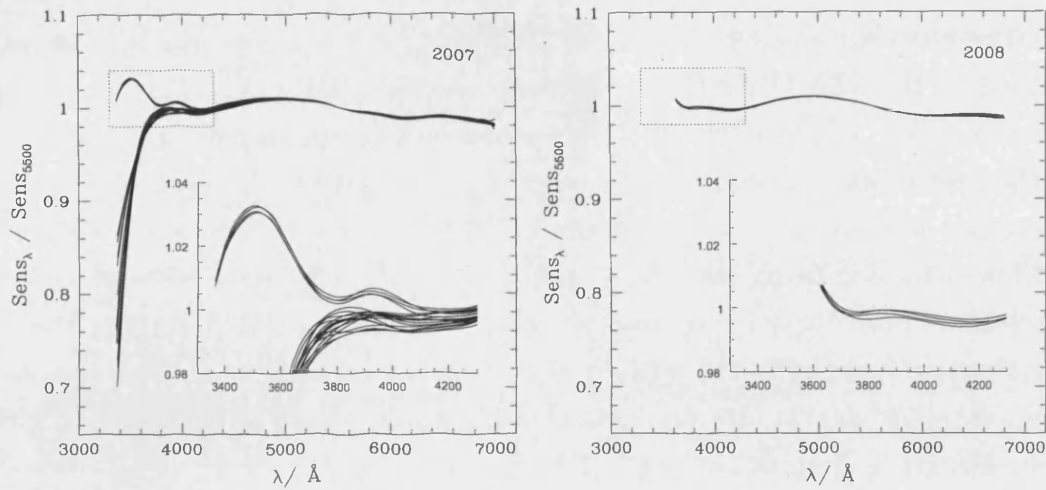


Figure 4.5: The 2007 and 2008 sensitivity functions are shown in the left and right diagrams respectively. *Main panels:* Sensitivity normalised at $\lambda 5500$ as a function of wavelength across the detector on each observing night (black lines). *Inset panels:* Magnified view of the 3300-4300 Å wavelength range, highlighting the anomalous functions occurring during the 2007 observations.

magnifies this wavelength region to examine the shape of the sensitivity functions in greater detail. The four functions that display this ‘bump’ occur in observations from two nights during the 2007 observations. The ultimate goal of all this work on spectroscopic data reduction is the measurement of emission line intensities to study the metal content and chemical evolution of galaxies, which, as I describe in Chapter 8, requires accurate measurements of the [OII] $\lambda 3727$ emission line. The intensity of this emission line may be significantly affected by a calibration based on a sensitivity function containing the ‘bump’ feature. Thus, to avoid the contamination of the dataset, observations taken during the affected nights of the 2007 observations (consisting of four galaxies) are excluded from further data reduction.

Figure 4.6 shows a comparison between the sensitivity functions from the two standard star images taken at the start and end of each observing night, except for the two nights where the filter was present. The typical variations of the sensitivity are always ~ 0.01 mag, corresponding to an error in the calibrated flux of 1%.

The CALIBRATE task uses these sensitivity functions to convert the observed intensities at each wavelength in each spectra into flux densities, i.e. with units of $\text{erg s}^{-1} \text{cm}^{-2} \text{\AA}^{-1}$, corrected for atmospheric extinction. When applying a flux calibration, CALIBRATE divides the spectra by the sensitivity function produced by the SENSFUNC task. At each wavelength, the measured intensities are converted

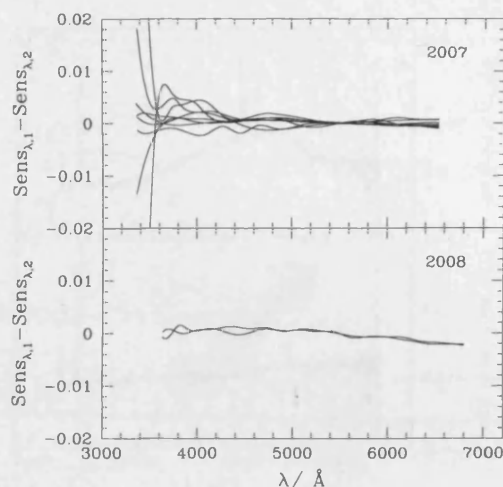


Figure 4.6: The residual sensitivities obtained by subtracting the two standard star observations made during each observing night (black lines) for the 2007 (*upper panel*) and 2008 (*lower panel*) observing runs.

according to

$$f_{cal} = f_{obs} 10^{-0.4 C(\delta\lambda)} \quad (4.4)$$

where f_{cal} is the new calibrated flux, f_{obs} is the observed flux and $C(\delta\lambda)$ is the value from the sensitivity spectrum at a particular wavelength. This marks the final step in calibrating the flux scale of the observations. Figure 4.7 shows an example spectrum before and after the flux calibration.

4.3.6 REDSHIFT CORRECTION

Finally, each spectra is shifted to the rest frame wavelength. Two template spectra are chosen to represent absorption-line objects or emission-line objects, and these templates are shifted to their rest frame wavelength. The FXCOR task cross-correlates the template spectrum to the remaining spectra of each object type, thus determining the relative shift for each spectra. This shift is then applied with DOPCOR. Figure 4.8 compares the redshifts obtained from the B08 observations with the redshift values presented in NED and, with the exception of a few obvious outliers, there is strong agreement between the two values. The offset of the results ($\bar{\delta} = 17 \text{ km s}^{-1}$) is much smaller than the average scatter ($\sigma = 67 \text{ km s}^{-1}$).

The final spectra, normalised to their mean intensity between 5400-5600 \AA ,

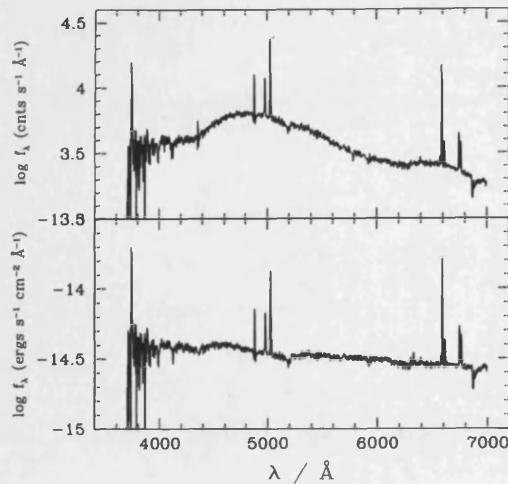


Figure 4.7: The spectrum of NGC 4561 before (*upper panel*) and after (*lower panel*) the flux calibration. The underlying shape of the sensitivity function across the CCD is removed.

are presented in Appendix B.

4.4 EMISSION LINE FLUX MEASUREMENTS

I measure the emission lines of each spectra by visually inspecting them using SPLOT, and obtain a measurement of the relative flux for the detected emission lines. The emission lines which are necessary for the analysis in Chapter 8, by order of wavelength, are [OII] λ 3727, H β λ 4861, [OIII] $\lambda\lambda$ 4958,5007, [NII] $\lambda\lambda$ 6548,6584, and H α λ 6563, but the H δ λ 4101, H γ λ 4340 and [SII] $\lambda\lambda$ 6717,6731 are also measured if detected.

The H β line often displays underlying stellar absorption which must be corrected for, otherwise the measured flux of the emission line is underestimated. The H β absorption feature is deblended from the emission line using SPLOT. To be conservative, no mean additive correction is applied to those lines where underlying absorption is not detected. The measurement of the H α plus [NII] lines also required slightly more attention, since the lines tend to overlap at the continuum. Hence, the H α plus [NII] lines are all measured by simultaneously fitting gaussian profiles to each line in the triplet using the same baseline fit to the continuum.

The intensities I measured were verified by being independently measured. The scatter between the two sets of independent results are minimal (<10%) with no significant systematic offsets, as evident in Figure 4.9. The largest scatter is in

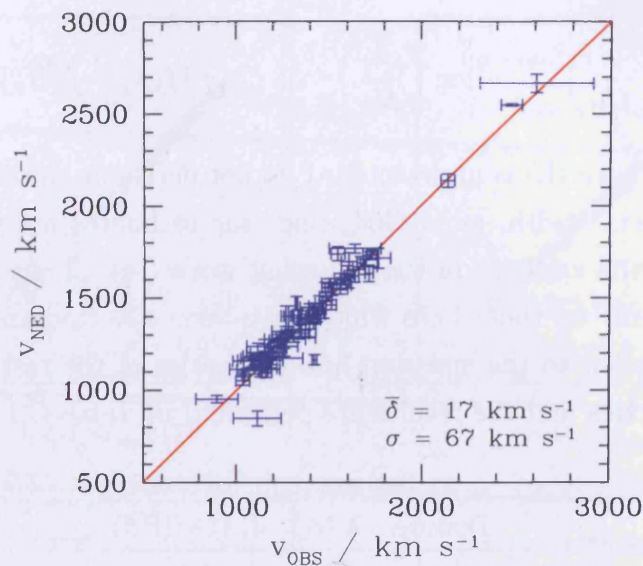


Figure 4.8: A comparison of redshifts determined from the Fourier cross-correlation between two spectra using FXCOR and redshift values taken from NED. The 1:1 line (red line) denotes where the redshifts would lie if the measurements agree. The scatter, σ , is the standard deviation of the residuals between the two plotted calibrations, $\delta = V_{NED} - V_{obs}$.

the measurement of the $H\beta$ lines. These lines are more difficult to measure because estimating the baseline continuum is made non-trivial due to underlying stellar absorption.

The emission line intensities are corrected for internal extinction using the Balmer decrement. With the $H\beta$ line corrected for underlying absorption, the Balmer decrement is given by

$$C_1 = \left[\log \left(\frac{H_\alpha}{H_\beta} \right)_{theor} - \log \left(\frac{H_\alpha}{H_\beta} \right)_{obs} \right] / [f(H_\alpha) - f(H_\beta)] \quad (4.5)$$

where $\log (H_\alpha/H_\beta)_{theor}$ is the theoretically expected ratio between $H\alpha$ and $H\beta$, $\log (H_\alpha/H_\beta)_{obs}$ is the observed value and $[f(H_\alpha) - f(H_\beta)]$ is the reddening function relative to $H\beta$. The theoretical ratio depends on the electron density and the gas temperature. Assuming that $T = 10000$ K and $n = 100$ e/cm³ (case B from Osterbrock 1989), which are values typical of HII regions, then $(H_\alpha/H_\beta)_{theor} = 2.86$. Combining this result with the reddening function $f(\lambda)$ of Lequeux et al. (1979), which is based on the extinction law of Whitford (1958) and is presented in Table 4.1, the measured

line fluxes are corrected for internal extinction according to

$$\log \left(\frac{\lambda}{H\beta} \right)_{corr} = \log \left(\frac{\lambda}{H\beta} \right)_{obs} + C_1 \times [f(\lambda) - f(H\beta)] \quad (4.6)$$

In those galaxies where $H\beta$ is undetected, I do not derive an upper limit to C_1 based on the $H\alpha$ equivalent width, as in G04, since the estimates are very uncertain and are not useful for the analysis in the following work (see Chapter 8). As such, my results are based only on those lines which have been detected and measured. These corrections are applied to the emission line intensities of the rest frame, normalized spectra for 95 galaxies and the results are presented in Table C.1.

Feature	λ (\AA)	$f(\lambda) - f(H\beta)$
[OII]	3727	0.31
H δ	4101	0.20
H γ	4340	0.13
H β	4861	0
[OIII]	4958	-0.02
[OIII]	5007	-0.03
[NII]	6548	-0.33
H α	6563	-0.33
[NII]	6584	-0.34
[SII]	6717	-0.37
[SII]	6731	-0.37

Table 4.1: The reddening function $f(\lambda)$ of Lequeux et al. (1979), which is based on the extinction law of Whitford (1958), adopted for the extinction corrections relative to $H\beta$.

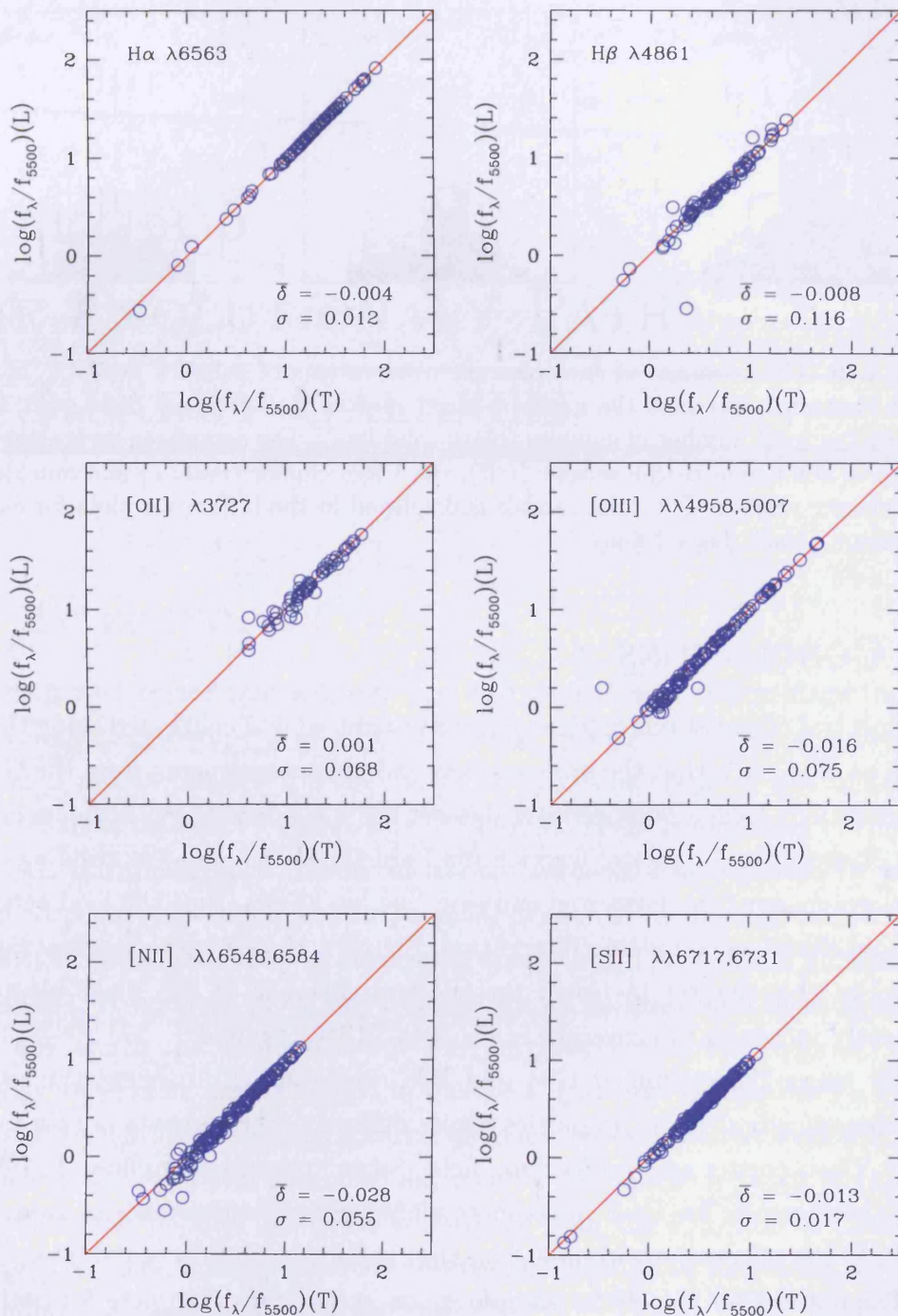


Figure 4.9: A comparison of the emission line fluxes as determined from two independent sets of measurements (where T denotes the measurements of the author and L denotes the measurements of L. Cortese). The 1:1 line (red line) denotes where the flux values would lie if the measurements agree, emphasizing that overall the measurements are consistent. The scatter, σ , is the standard deviation of the residuals between the two plotted calibrations, $\delta = L - T$.

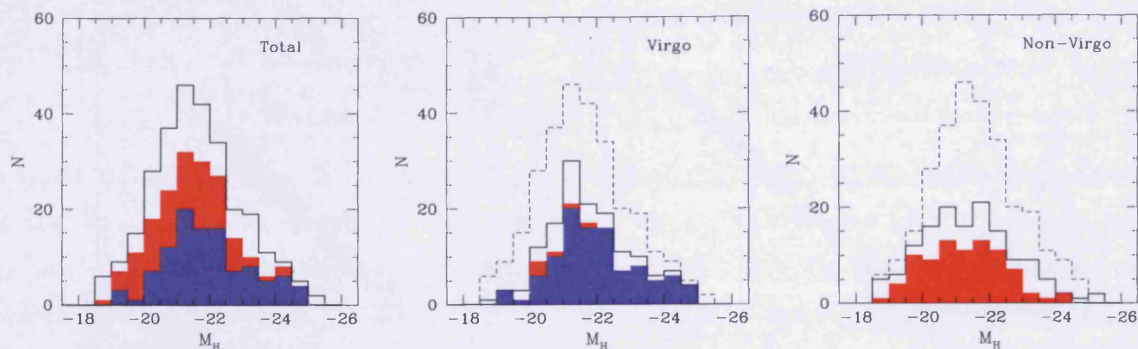


Figure 4.10: The coverage of spectroscopic observations of galaxies available in G04 (blue histogram) and with the newly reduced spectra included (red histogram) compared to the total number of galaxies (black solid line). The completeness is shown for galaxies in the whole HRS+ sample (*left*), the Virgo cluster (*middle*) and outside the Virgo cluster (*right*). The total sample is displayed in the latter two plots for ease of comparison (black dashed line).

4.5 CONCLUSIONS

Spectral observations of 95 objects were reduced and calibrated using the same methods as G04, such that the optical emission line measurements from the G04 and B08 observations form a homogeneous dataset when combined. With the inclusion of the B08 observations, a greater fraction (64%) of the HRS+ galaxies residing outside of the Virgo cluster have measured emission line intensities, thus the field subsample can be considered as complete. In addition, Figure 4.10 demonstrates how the work presented in this chapter increases the spectral coverage of the Virgo cluster and consequently increases the coverage of the total HRS+ sample.

By using the combined G04 and B08 observations, studying the variation of spectroscopically-derived properties across different environments is now possible, since the Virgo cluster and non-Virgo, ‘field’ subsamples are complete. In Chapters 8 and 9, these results are used to estimate global oxygen abundances of galaxies and hence study the effect of environment on the chemical evolution of galaxies.

The dataset for the HRS+ sample is now statistically complete for both ultraviolet imaging and optical spectroscopy, meaning that the aims of this thesis may now be addressed. I shall proceed by focussing on the first aim, and attempt to uncover the mechanism quenching star formation in the nearby galaxy population.

CHAPTER 5

THE EVOLUTIONARY PATHS OF NEARBY GALAXIES

5.1 INTRODUCTION

It is well known that galaxies form two sequences in colour-magnitude space: star-forming disks occupy a blue cloud whereas quiescent, bulge-dominated objects reside on a red sequence (e.g. Tully et al., 1982). The origin of this bimodality in the colour distribution of galaxies is still a puzzle. There is mounting evidence that, since $z \sim 1$, the stellar mass density of the red sequence has increased by at least a factor ~ 2 , while surprisingly the stellar mass density of the blue cloud has remained constant, despite continued star formation over several Gyr (Bell et al., 2007; Faber et al., 2007). A possible explanation of this is that galaxies form most of their stars while they are in the blue cloud but then migrate to the red sequence, gradually increasing the stellar mass retained in quiescent systems. In this case, a quenching of the star formation is required to drive galaxies towards the red sequence, but it is still unclear what physical mechanism(s) may be responsible for such migration.

The most popular candidate is feedback from the accretion of material onto supermassive black holes (i.e., AGN feedback). The AGN may heat or expel the surrounding gas, thus preventing star formation (e.g., Croton et al., 2006). Theoretical studies have shown that models including AGN feedback provide a better match between theory and observations (e.g. the bright end of the luminosity function), making this quenching mechanism very promising (Baugh, 2006). Recently, this hypothesis has gained additional support from observations showing that the AGN-host fraction peaks in the region between the blue and red sequence (i.e., the transition region or *green valley*, Martin et al., 2007; Schawinski et al., 2007). However, it is

still a matter of debate whether these results imply a physical connection between AGN activity and suppression of the star formation in galaxies (e.g. Westoby et al., 2007; Georgakakis et al., 2008). In addition, though AGN feedback has been directly observed in the giant ellipticals in the centre of clusters (e.g. Forman et al., 2007), it is unclear whether this mechanism works in spirals (Okamoto et al., 2008), which typify the transition galaxies today.

In contrast to the above internal mechanism, environmental effects may be responsible for quenching the star formation activity, driving the migration of spiral galaxies out of the blue cloud. Gravitational interactions (Merritt, 1984; Moore et al., 1996), ram pressure stripping (Gunn & Gott, 1972), and hybrid processes combining multiple mechanisms such as preprocessing (Fujita, 2004; Cortese et al., 2006), can in fact quench star formation in galaxies in high density environments (see Boselli & Gavazzi, 2006 for a detailed review of these processes). This is clearly reflected in the morphology-density (Dressler, 1980; Whitmore et al., 1993), star formation-density (e.g. Kennicutt, 1983) and gas-density relations (Haynes & Giovanelli, 1984) observed in the local universe. In addition, it has recently been shown that the environment may be responsible for the formation of the red sequence at low luminosities (Boselli et al., 2008). Contrary to these findings, Masters et al. (2010) argue that the environment is not responsible for the quenching of star formation, since they see no environmental variation in the properties of red passive spirals selected from the Galaxy Zoo project (Lintott et al., 2008). Thus, there is still some debate over the impact of the environment. Discriminating between the effects of AGN feedback and environment on star formation is therefore necessary to unravel the evolutionary history of transition galaxies.

In this chapter, I attempt to assess whether the mechanism suppressing the star formation in nearby spirals is an internal or environmental process.

5.2 THE COLOUR-MASS DIAGRAM

The $NUV-H$ vs. M_* colour-mass diagrams for the total sample are presented in Figure 5.1 (top row). The bimodality in the galaxy population is clearly evident, with early-type galaxies mainly segregated in the red sequence and late-types occupying the blue cloud. As already shown by van den Bergh (2007) in optical and Wyder et al. (2007) in UV, the two sequences are not well separated, since a significant number of disk galaxies lie in the region between the two clouds (i.e., the transition region) and even in the red sequence. This supports the common idea that galaxies start their journey towards the red sequence as disks. Figure 5.2 presents the SDSS images

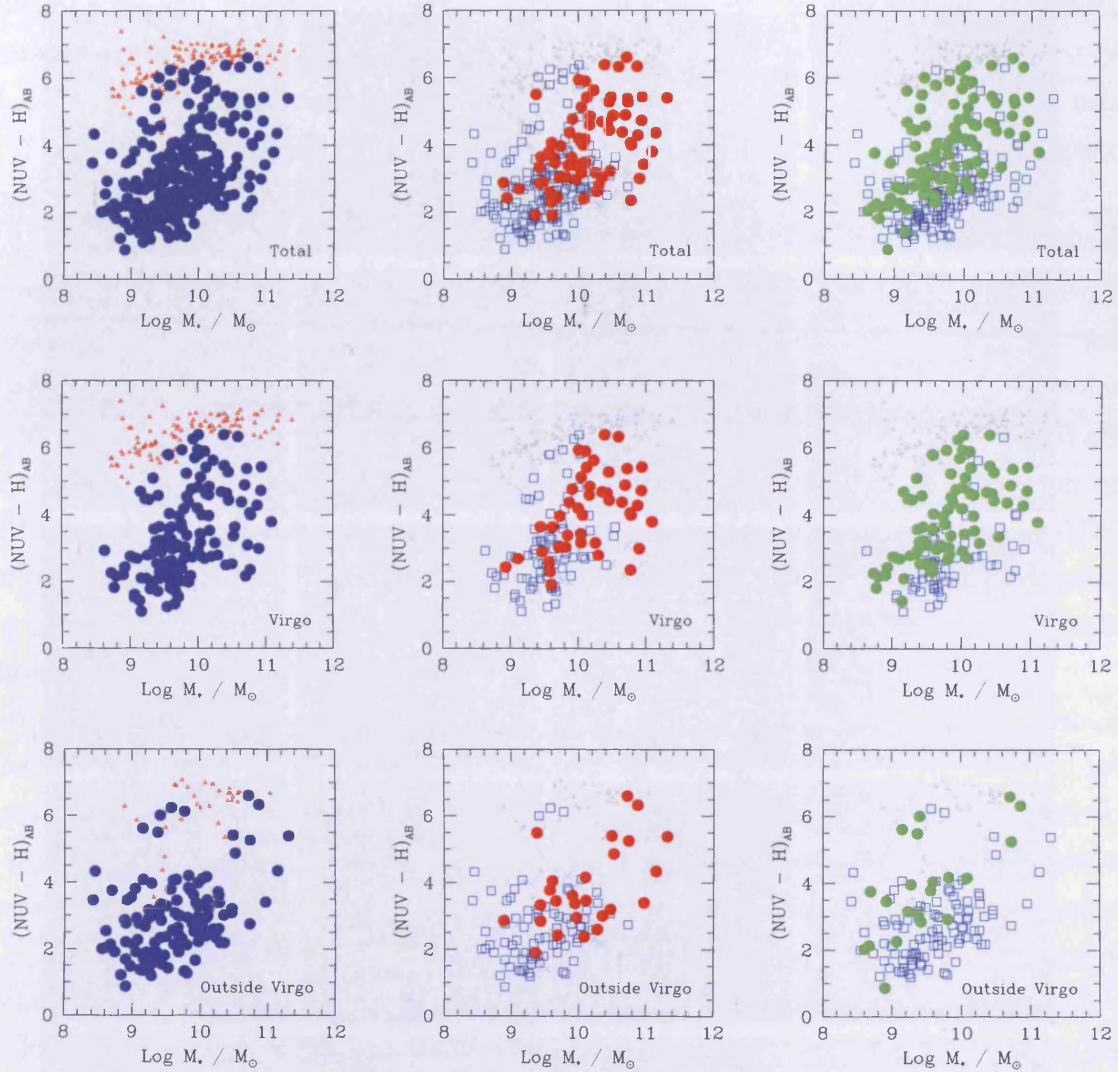


Figure 5.1: The $NUV-H$ vs. M_* colour-mass diagrams for galaxies comprising the total sample (*top row*), the Virgo cluster (*middle row*) and ‘field’ environment (*bottom row*). *Left column*: Early-types (open red triangles) form a red sequence and late-types (filled blue circles) form a blue cloud. *Center column*: Objects displaying AGN-like behavior (filled red circles), HII star-forming regions (open blue squares) or composites of the two (cyan crosses) are highlighted. *Right column*: Galaxies are classified as HI-deficient (filled green circles) and HI-normal (open blue squares). In the latter two columns, galaxies without nuclear classification or HI observations are considered normal disks (blue open squares), and early-type galaxies (grey triangles) are retained only as a visual aid.

of a small random sample of the massive late-types residing across the blue cloud and transition region, demonstrating the visible reddening at optical wavelengths. Therefore, in the rest of this section I focus on the properties of late-type galaxies to try to understand the mechanisms behind the quenching of the star formation. I also note that a few early-type galaxies lie well outside the red sequence. These are misclassified or peculiar objects and their properties will be investigated later.

To investigate whether the quenching is due to AGN feedback or environmental effects, I divide the sample according to nuclear activity and HI content (Figure 5.1, top row, central and right panel, respectively), as described in Chapter 2. For $M_* \gtrsim 10^{10} M_\odot$, AGN-host spirals are uniformly distributed across the range of colour (consistent with Martin et al., 2007 and Schawinski et al., 2007), whereas for lower stellar masses they are segregated in the blue sequence. In other words, AGNs are not preferentially found in the transition region. In addition, at fixed stellar mass, AGNs do not tend to be redder (i.e., have a lower specific star formation rate) than galaxies with HII star-forming nuclei or composite systems. Thus, I do not find any clear evidence of a suppression of the star formation in AGNs.

On the contrary, quenched spirals are generally characterized by a low atomic hydrogen content. Unlike the AGN-hosts, which occupy the transition region only for masses $M_* \gtrsim 10^{10} M_\odot$, the HI deficient galaxies tend to lie at the red edge of the blue sequence and in the transition region, independent of the stellar mass. More importantly, at fixed stellar mass, HI deficient systems have a typical colour at least 1 mag redder than gas-rich systems, suggesting that the gas depletion is really accompanied by a suppression of the star formation.

If this is the case, transition galaxies should be more frequent in high density environments, since the HI deficiency is usually associated with a truncation of the gas disk via environmental effects (Cayatte et al., 1994). In order to test this scenario, I split the sample depending upon whether the galaxies inhabit the Virgo cluster or not (see Figure 5.1 middle and bottom rows).

A comparison of the cluster and ‘field’ colour-mass diagrams clearly shows that very few disk galaxies have their star formation suppressed outside the cluster environment. The vast majority of transition spirals are in fact composed of HI deficient cluster galaxies. In addition, almost 50% of transition disks outside Virgo reside in groups or pairs, supporting the idea that the loss of gas and quenching of the star formation is related to the environment. I note that some galaxies between the blue cloud and red sequence are not HI deficient. These appear to be peculiar objects and their properties will be investigated in the following sections.

The significant difference found in the colour-mass distribution of galaxies in



Figure 5.2: SDSS composite images of a small selection of massive late-type galaxies residing across the blue cloud and transition region. The images are organised based on the colour-mass diagram in Figure 5.1, from the bluest (*bottom left panel*) to the reddest spiral (*top right panel*).

and outside Virgo is consistent with van den Bergh (2007), who showed that objects in small groups differ from cluster galaxies and are more similar to isolated systems. However, it is evident that in the ‘field’ sample, the separation between the blue and the red sequence is more clear-cut than in optical colour-magnitude relations. For example, a K-S test shows that there is $<0.01\%$ probability that the $NUV - H$ colour distribution of the HRS+ field sample has the same shape as the $U - B$ colour distribution in the van den Bergh (2007) ‘field+groups’ sample. The use of UV to near-infrared colours is in fact crucial to clearly show the environmental dependence of the transition population in the local universe.

This interpretation is additionally supported by the fact that (1) the fraction of AGN-host galaxies does not vary strongly with the environment (e.g., Miller et al., 2003; Kauffmann et al., 2004), and (2) also in the field, at fixed stellar mass, AGN-host spirals do not show a lower specific star formation rate than HII galaxies. Both observational lines of evidence do in fact contrast with what is expected if quenching was via AGN feedback, favouring the environment as the main mechanism responsible for the suppression of the star formation in the sample.

Thus, from the analysis presented here, the colour-mass diagrams suggest that AGN feedback is not important in the role of migrating galaxies and in fact the environment appears to play the greater role in driving evolution. However, to strengthen this result, especially in the light that not all galaxies in the transition region are gas deficient objects in the Virgo cluster, the statistical and individual properties of transition galaxies must be investigated in detail. By reconstructing the evolutionary history of galaxies in the transition region, I hope to uncover further evidence to determine the underlying nature of the mechanism(s) quenching star formation.

5.3 THE LINK BETWEEN HI CONTENT AND COLOUR

The suggestion that a loss of gas quenches the star formation leads to a prediction of a general relationship between the gas content and colour, which is shown in Figure 5.3. The left panel shows the correlation between colour and HI deficiency: galaxies outside the blue cloud have not only lost a significant fraction of their atomic hydrogen content, but there also exists a correlation between HI deficiency and $NUV - H$ colour, although with large scatter. At least part of the scatter is due to the large uncertainty in the estimate of HI deficiency (~ 0.3 dex). The same relation can be expressed in terms of gas fraction (defined as the ratio of the HI to the stellar mass), as discussed by Kannappan (2004) and shown in the central and right panels of Figure 5.3. Lower gas fractions correspond to redder colours. The

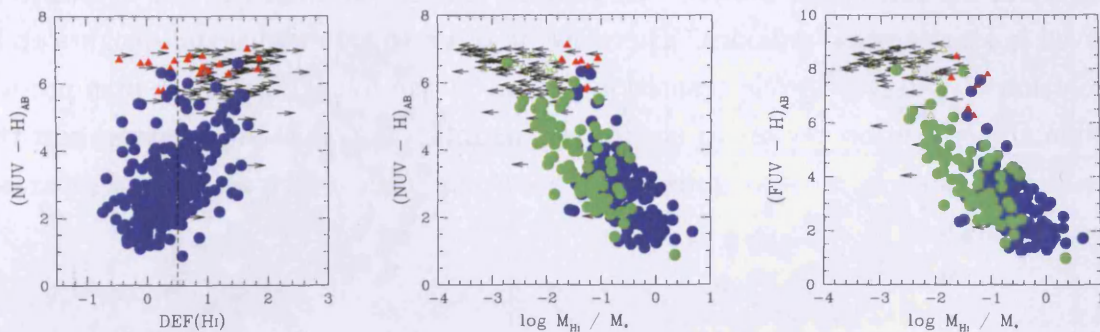


Figure 5.3: The link between HI-content and colour. *Left*: $NUV - H$ colour vs. HI deficiency. The vertical dotted line separates galaxies with ‘normal’ gas content from HI-deficient systems. *Center*: $NUV - H$ colour vs. gas-fraction. *Right*: $FUV - H$ vs. gas-fraction. Late- and early- type galaxies are indicated with circles and triangles respectively. Green symbols highlight detected HI-deficient galaxies, while arrows show upper limits.

best linear fit to the relation (excluding upper-limits) is

$$\log(M_{HI}/M_*) = -0.35 \times (NUV - H) + 0.19, \quad (5.1)$$

with a dispersion of ~ 0.43 dex. However, from the three panels in Figure 5.3 it clearly emerges that not all transition region and red-sequence galaxies are HI-deficient, but a number of systems have an amount of hydrogen typically observed in objects lying in the blue cloud. This is particularly interesting when the colour-gas-fraction relations are examined (central and right panels). Outside the blue cloud, galaxies lie mainly at the two edges of the relation depending on whether they are HI-deficient (green circles) or not (blue circles), and the colour-gas-fraction relation appears more scattered¹. This suggests that at redder colours (i.e. $NUV - H > \sim 4.5$ mag), the gas-fraction is not a good proxy of the UV-optical colour anymore and vice-versa. The dispersion in the colour-gas-fraction relation increases from ~ 0.35 dex (consistent with Kannappan, 2004 and Zhang et al., 2009) to ~ 0.54 dex when moving from HI-normal blue-cloud galaxies to transition and red-sequence objects. This is in reality a lower-limit on the real scatter increase since I have not included upper-limits in the calculation.

The results shown in Figure 5.3 are strongly suggestive of a) a different evolutionary path followed by HI-deficient and HI-normal galaxies outside the blue cloud

¹The fact that, for the same colour, HI-deficient objects have a lower gas fraction is expected, since both quantities trace the specific amount of atomic hydrogen in a galaxy.

and b) of a weaker link between HI content and colour than the one typically observed in star-forming galaxies. Therefore, in order to gain additional insights on the evolution of galaxies in the transition region, in the following I must first properly define the transition region to accurately identify the transition galaxies, and then divide these objects into two subsamples according to their gas content and separately investigate their properties.

5.4 DEFINING THE TRANSITION REGION

In order to properly select a sample of transition region galaxies, I must define quantitative bounds of the transition region in the colour-mass diagrams. However, it is difficult to accurately quantify where the blue cloud ends, where the red sequence begins and thus determine the range of colours that characterise galaxies residing between the two sequences.

Since the transition region appears to be populated preferentially by HI-deficient galaxies in high density environments, I decide to define the blue cloud by using the population of HI-normal galaxies, representing unperturbed systems. Figure 5.4 shows that, when selecting only HI-normal late-type galaxies, the blue cloud and red sequence are clearly separated at all masses in the colour-mass diagram. Galaxies with suppressed star formation therefore typically reside at colours $NUV - H > 4.5$ mag, and I adopt this value as the lower limit of the transition region. This colour cut corresponds to the 90th percentile of the colour of HI-normal spirals with $M_{\star} > 10^{10} M_{\odot}$. Under this convention, M31 is defined as a HI-normal galaxy belonging to the blue cloud ($NUV - H \sim 4.1$ mag).

I now define an upper limit on the transition region or, in other words, I determine the lower limit of the red sequence. UV-to-near-infrared colours typical of the red sequence ($NUV - H \gtrsim 6$ mag) can either indicate low residual star formation activity or old, evolved stellar populations (e.g. Boselli et al., 2005). The phenomenon of the UV-upturn (O’Connell, 1999) makes colours redder than $NUV - H \sim 6$ mag difficult to interpret so that the $NUV - H$ colour cannot be considered as a good proxy for the specific star formation rate (SSFR). Following Kaviraj et al. (2007), I use observations of well known strong UV-upturn galaxies to derive a lower limit on the $NUV - H$ colour typical of evolved stellar populations. In detail, given the typical colour observed in M87 ($NUV - H \sim 6.1$ mag) and NGC 4552 ($NUV - H \sim 6.4$ mag), $NUV - H = 6$ mag is assumed as a conservative lower limit to discriminate between residual star formation and UV-upturn. The validity of this colour-cut is confirmed by a visual inspection of GALEX colour images, which indicates that only

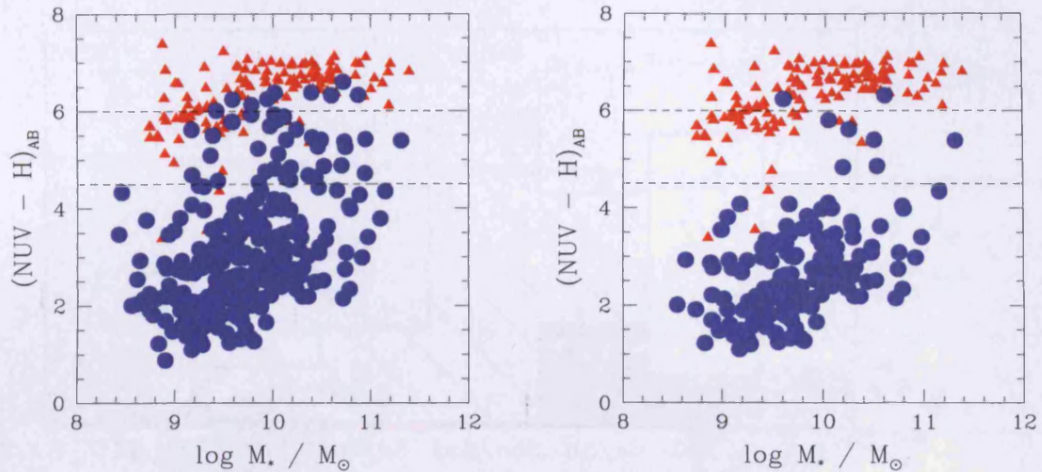


Figure 5.4: The $NUV - H$ colour-stellar-mass relations for the HRS+ sample. Late and early-types are indicated with circles and triangles respectively. The separation between blue and red sequence is clearly evident when only HI-normal late-type galaxies are shown (*right panel*). The dotted lines in both panels show the boundaries of the transition region as defined in Section 5.4.

6% (i.e. 6 objects) of galaxies redder than $NUV - H = 6$ mag show clear evidence of residual star formation (e.g., blue star-forming knots).

The morphological type distributions for galaxies belonging to the three groups, based on their position on the colour-mass diagram (i.e., blue cloud, red sequence and transition region), are shown in Figure 5.5. It clearly emerges that red and blue galaxies are two disjoint families not only in colour, but also in morphology.

Of course, the criteria described above are arbitrary and vary according to the colour adopted and to the stellar mass range investigated. This can be clearly seen in Figure 5.6, where the positions of ‘transition galaxies’ in different UV and optical colour-stellar-mass diagrams are highlighted. Although it is indisputable that not all transition galaxies are outside the red sequence in a $FUV - H$ and $NUV - B$ colour diagram (in particular at low stellar-masses), it emerges that the definition adopted here is able to select a statistically representative sample of galaxies with suppressed star formation. Moreover, the comparison between the top and bottom row in Figure 5.6 highlights the necessity of UV colours to select fair samples of transition galaxies: e.g., a simple $B - H$ colour-cut would significantly contaminate our sample with star-forming blue-sequence and quiescent red-sequence systems. Finally, it is interesting to note the wide range in $FUV - NUV$ colour spanned by the transition galaxies, suggesting different current star formation rates.

As shown in the following sections, the sample of transition galaxies selected

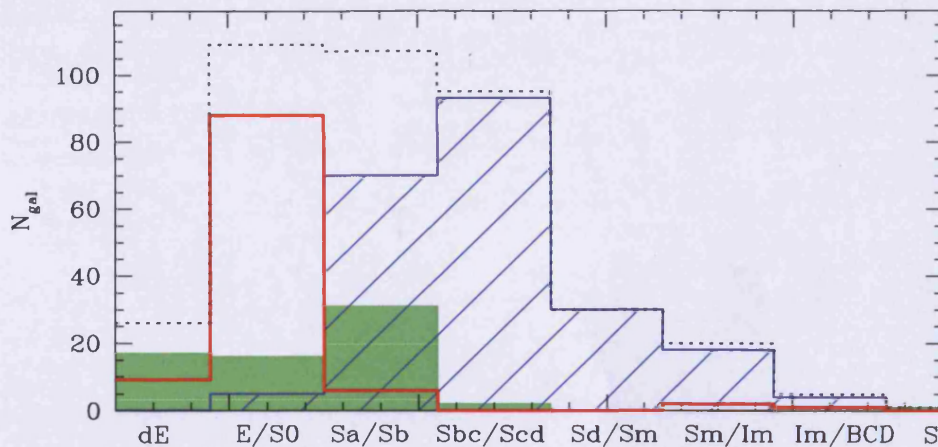


Figure 5.5: The morphological type distribution of galaxies in the HRS+ sample (dotted histogram). The filled histogram represents galaxies in the transition region, while red and blue sequence galaxies are shown with the empty and dashed histogram, respectively.

using these criteria is not significantly contaminated either by active star-forming or quiescent galaxies erroneously classified as transition systems. Thus I refer to the colour interval $4.5 < NUV - H < 6$ mag as the ‘transition region’ for the remainder of this thesis.

Before investigating the detailed properties of transition galaxies, it is worth adding a few notes about the validity of the classification for HI-normal transition systems. The low number of objects in this category and the large uncertainties in the estimate of gas fractions and UV dust attenuation might suggest that these are just random outliers, not different from the bulk of the HI-deficient population. Although I cannot exclude the presence of a few misclassified galaxies in both the HI-deficient and HI-normal population, it is very unlikely that all (and only) the HI-normal galaxies outside the blue sequence are affected by a large (>0.5 dex) systematic underestimate of dust attenuation, and/or gas fraction. More importantly, the analysis presented in the next sections will clearly show that these two families have reached the transition region following different evolutionary paths.

Finally, it is noted that, in all the figures presented in this work, the UV-near-infrared colour is directly related to the SSFR only outside the red sequence. For colours redder than $NUV - H \sim 6$ mag, UV magnitudes cannot be blindly used to quantify current SFRs and the presence of a sequence does not imply that all red galaxies have the same SSFR, as shown in the following sections.

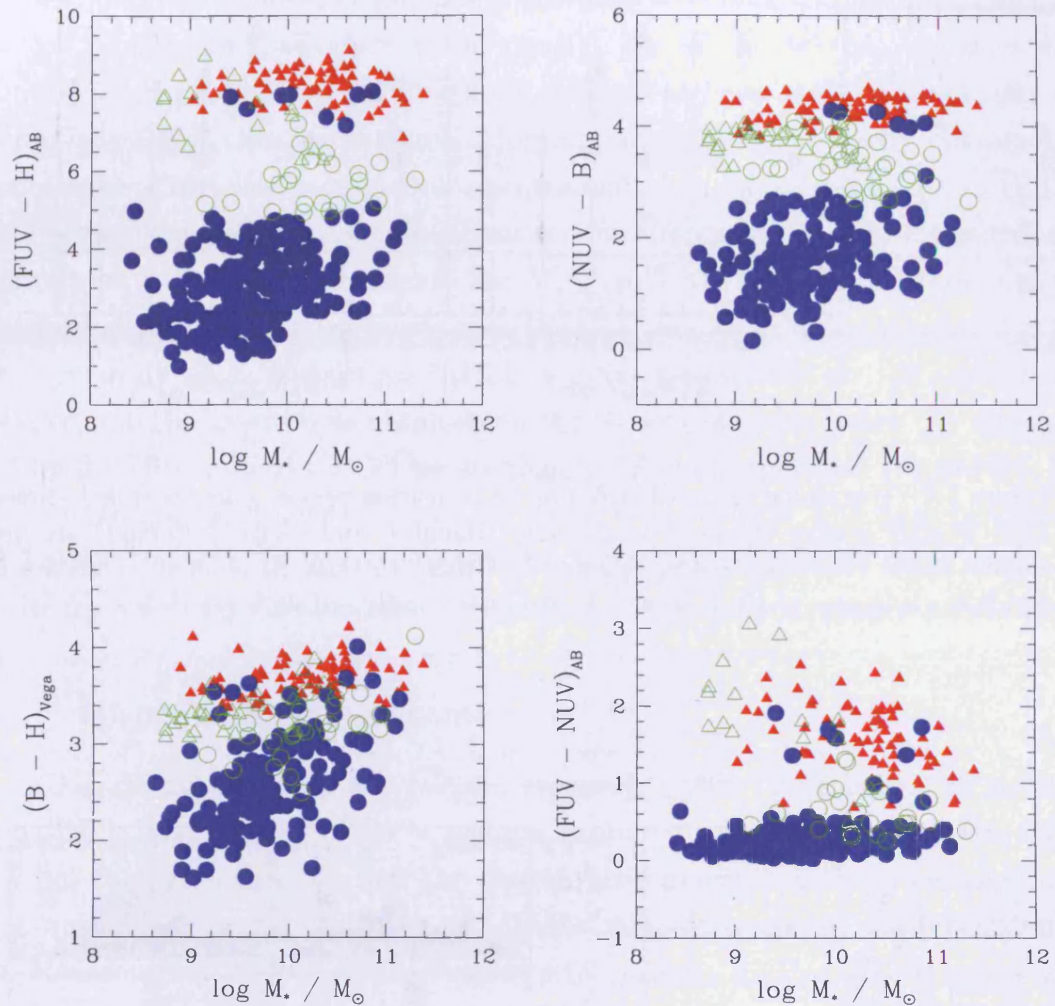


Figure 5.6: The $FUV - H$ (upper left), $NUV - B$ (upper right), $B - H$ (lower left) and $FUV - NUV$ (lower right) colour-stellar-mass relations for our sample. Symbols are as in Figure 5.4. Green empty symbols show transition galaxies as defined in Section 5.4. I note that, given the incomplete UV and optical coverage available for our sample, each graph includes a different number of galaxies. These plots must thus be considered just as an indication of the typical colour range occupied by transition galaxies.

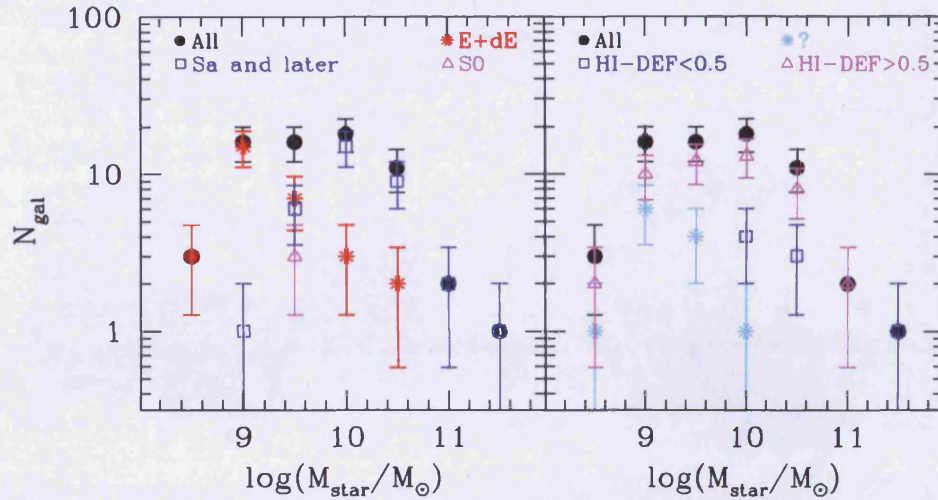


Figure 5.7: The stellar mass distribution of transition region galaxies (filled circles). *Left*: Spirals (empty squares), lenticulars (triangles) and E+dE (asterisks) are indicated. *Right*: Galaxies are highlighted according to their HI content. Galaxies for which the estimate of HI deficiency is unsure are indicated with asterisks.

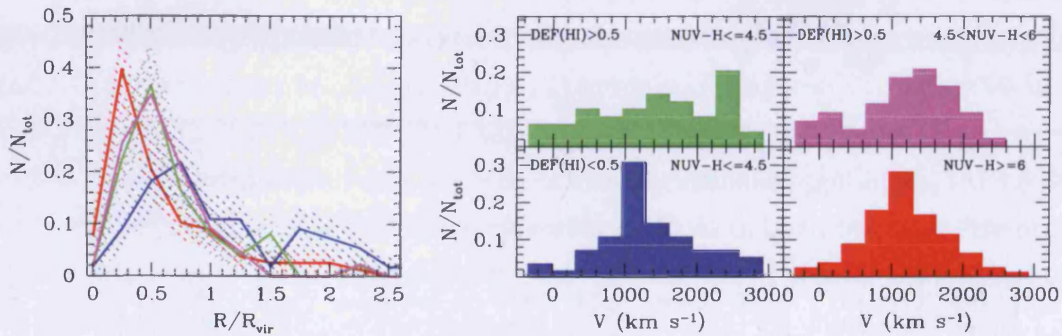


Figure 5.8: The cluster-centric projected-distance (*left*) and line-of-sight velocity distribution (*right*) of galaxies in the Virgo cluster region. Galaxies are divided into four sub-samples according to their colour and HI-content: blue-cloud HI-normal ($NUV - H \leq 4.5$ and $DEF(HI) < 0.5$; blue), blue-cloud HI-deficient ($NUV - H \leq 4.5$ and $DEF(HI) > 0.5$; green), transition HI-deficient ($4.5 < NUV - H < 6$ and $DEF(HI) > 0.5$; magenta) and red-sequence ($NUV - H \geq 6$; red) galaxies. The shaded areas in the left panel show the uncertainty in the radial distributions.

5.5 THE PROPERTIES OF TRANSITION GALAXIES

In total, 67 galaxies lie in the transition region as defined in Section 5.4, corresponding to $\sim 17\%$ in both number and total stellar-mass. In Figure 5.7, the stellar-mass distribution of transition galaxies are divided according to their morphological type (left panel) and gas content (right panel). For $M_* \gtrsim 10^{10} M_\odot$, galaxies with $4.5 < NUV - H < 6$ mag are mainly spirals, whereas at lower stellar masses they are preferentially dwarf elliptical systems. More importantly, the majority of transition galaxies have $\gtrsim 70\%$ less atomic hydrogen content than isolated galaxies of similar optical size and morphological type. However, as already noted, not all galaxies in the transition region are HI-deficient. For $M_* \gtrsim 10^{10} M_\odot$, $\sim 30\%$ (8 galaxies) of the transition galaxies have HI deficiency lower than 0.5. For lower stellar masses, it is difficult to quantify the number of gas-rich objects. HI observations are not available for 9 galaxies, and the lower limits obtained for the HI deficiency are below the threshold of 0.5 for 3 additional objects. These are mainly dE cluster galaxies (Figure 5.7, left panel), suggesting that their evolution is related to the cluster environment (Boselli et al., 2008). However, to be conservative, in the following analysis I focus on the 55 galaxies for which the classification as HI-deficient or HI-normal galaxy is reliable.

5.5.1 HI-DEFICIENT SYSTEMS

Overall, sure HI-deficient galaxies represent $\sim 70\%$ (47 galaxies) in number and $\sim 63\%$ in stellar mass of the transition region. All except four galaxies lie in the Virgo cluster, suggesting that the cluster environment is playing an important role in quenching the star formation. Additional support to this scenario is obtained when consideration is given to the properties of galaxies divided according to their gas content and their position in the colour-mass diagram. I now compare the median projected distance from the cluster center of the different populations. Given the large asymmetry of Virgo and the presence of two main sub-clusters (Virgo A and Virgo B, at ~ 1 virial radii projected-distance), the projected-distance from the center of both clouds for each galaxy was determined and I adopt the smallest of the two values. The results do not qualitatively change if just the distance from M87 is adopted. The median cluster-centric distance decreases from ~ 0.83 virial radii (R_{vir}), in case of HI-normal blue-cloud galaxies, to 0.51, 0.52 and 0.42 R_{vir} for HI-deficient blue-cloud, HI-deficient transition and red-sequence objects, respectively (see Figure 5.8, left panel). Similarly, the difference between the 25th and 75th percentiles of the line-of-sight velocity distribution (i.e. a good estimate of the velocity dispersion in case of non gaussian distributions) increases in the blue cloud from ~ 760 km s $^{-1}$ to ~ 1400

km s⁻¹ when we consider HI-normal and HI-deficient galaxies respectively. Then, the typical velocity dispersion gradually decreases to ~ 915 km s⁻¹ and ~ 610 km s⁻¹ when considering the transition region and the red sequence respectively (see Figure 5.8, right panel). The gradual variation in projected distance and velocity distribution when moving in the colour magnitude diagram from blue, HI normal systems to red, quiescent objects supports the idea that HI-deficient galaxies represent a population of galaxies which have recently fallen into the cluster and not yet virialized. For example, a free-falling population is expected to have a velocity dispersion $\sqrt{2}$ times larger than the virialized population. Moreover, the velocity dispersion profile for HI-deficient galaxies decreases with cluster-centric distance consistent with isotropic velocities in the center and radial velocities in the external regions, as expected in the case of galaxy infall onto the cluster (Girardi et al., 1998). The opposite trend (i.e., increasing with cluster-centric distance) is observed for red-sequence galaxies, as expected in a relaxed cluster undergoing two-body relaxation in the dense central region, with circular orbits in the center and more isotropic velocities in the external regions. Finally, a visual investigation of UV images reveals that in at least 50% of star-forming Virgo galaxies in the transition region the star formation is only present well within the optical radius, further supporting environmental effects being responsible for the quenching of star formation in HI-deficient Virgo galaxies.

However, there is some uncertainty as to the nature of the mechanism quenching star formation in the 4 HI deficient galaxies residing outside of the Virgo cluster. These are NGC 4684, UGC 8756, UGC 8032 and NGC 5566. NGC 5566 is the brightest member of a galaxy triplet while UGC 8032 lies just ~ 1.1 virial radii from the center of Virgo. Therefore, there remains a possibility that environmental effects are playing a role in stripping the gas in these two objects. The fact that UGC 8032 is not included in our Virgo sample despite its small distance from M87 is due to the fact that it just lies outside the Virgo boundaries defined by Gavazzi et al. (2003b). The origin of the HI deficiency in NGC 4684 and UGC 8756 remains a puzzle. UGC 8756 has in fact no nearby companions or any clear sign of interaction. NGC 4684 is a lenticular galaxy with very strong UV nuclear emission, probably related to the extended H α outflow discovered by Bettoni et al. (1993). The outflow has been interpreted as related to bar instability and it is not clear whether such a process can be responsible for the HI deficiency observed in this object. Thus, the origin of the HI deficiency in these two objects still remains unclear.

Time-scales for the migration

Combining the observational evidence presented above with previous works on the Virgo cluster (e.g. Boselli & Gavazzi, 2006 and references therein), it appears that a hydrodynamical interaction like ram pressure stripping is the cause of the gas deficiency. However, I note that gravitational interactions cannot be excluded in at least one case (NGC 4438, e.g., Boselli et al., 2005; Vollmer et al., 2005; Kenney et al., 2008).

Only recently, has it become possible to accurately quantify the time-scale for the quenching of the star formation after the stripping event (Boselli et al., 2006; Crowl & Kenney, 2008). Conveniently, almost all the objects for which a stripping timescale has been computed are included in the sample. In Figure 5.9, the position of these six objects in the colour-mass diagram according to the age of the stripping event are highlighted: hexagons and squares indicate galaxies in which the star formation in the outer regions has been suppressed less or more than ~ 300 Myr, respectively. Interestingly, there is a difference in the average colour between very recent quenching ($t < 300$ Myr) and older events, so that only galaxies with quenching timescales ~ 400 -500 Myr are at the edge or have already reached the transition region. This is consistent with the fact that the Virgo transition galaxy population is not virialized, implying a recent (≤ 1.7 Gyr, i.e., the Virgo crossing time; Boselli & Gavazzi, 2006) infall into the cluster center. Thus, I conclude that once the HI has been stripped from the disk, a galaxy moves from the blue cloud to the transition region in a time-scale roughly ~ 0.5 -1 Gyr.

How long will these systems remain in the transition region? As already pointed out by Crowl & Kenney (2008) and Boselli et al. (2008), one cluster-crossing is not sufficient to completely halt the star formation in massive ($M_* \gtrsim 10^{10} M_\odot$) galaxies. In fact, while the outer disk is completely deprived of its gas content and star formation is quickly stopped, in the central regions the restoring force is too strong, keeping the atomic hydrogen reservoir necessary to sustain continuous star formation. Moreover, Boselli et al. (2008) showed that two cluster crossings (~ 2 -3 Gyr) are already necessary to move the brightest dwarf elliptical galaxy from the blue to the red sequence, suggesting that the transition galaxies described here will take at least the same amount of time to have their star formation completely quenched. Assuming that the Gunn & Gott (1972) formalism for ram-pressure is still valid after the first passage and that the galaxy's orbit does not change significantly, it can be expected that very little additional gas will be stripped during the second passage by ram-pressure. Significant stripping would occur only if the galaxy's restoring force is

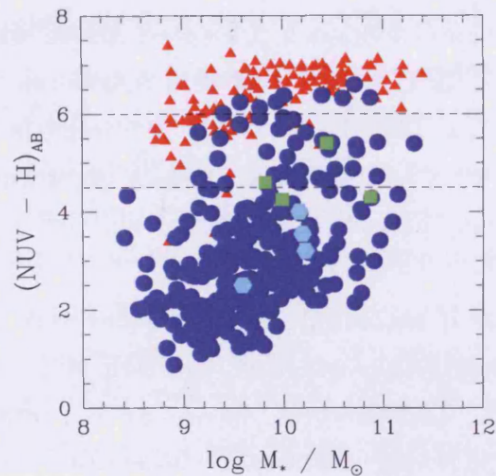


Figure 5.9: Same as the left panel of Figure 5.4. Highlighted symbols indicate galaxies in the Crowl & Kenney (2008) sample for which a stripping timescale estimate is available. Stripping timescales shorter than 300 Myr and between 300-500 Myr are shown with hexagons and squares respectively.

lowered by gravitational interactions with other members and the cluster potential well. Other environmental effects related to the intracluster medium, like viscous stripping (Nulsen, 1982) and thermal evaporation (Cowie & Songaila, 1977), may thus play an important role in the complete suppression of the star formation.

An upper limit to the time spent by HI-deficient galaxies in the transition region can be obtained under the assumption all the remaining gas will be consumed by star formation. It is in fact plausible that the intra-cluster medium will prevent additional infall of cold gas. In this case, the ‘Roberts’ time’ (Roberts, 1963, defined as the ratio of the gas mass to the current star formation rate: i.e., $M(\text{gas})/\text{SFR}$) can be used to obtain a rough estimate of the gas consumption time. Assuming that 15% of the total gas is in the molecular state (Boselli et al., 2002) and $\sim 30\%$ is composed by helium and heavy elements (Boselli et al., 2001), the ‘Roberts’ time’ is already $\sim 2.2 \text{ Gyr}^2$. This is in reality a lower limit to the real value since it does not take into account gas recycling. As shown by Kennicutt et al. (1994), the real gas consumption time is 1.5-4 times longer than the time scale calculated above. Thus, although they have lost a significant amount of their original gas content, HI-deficient transition galaxies still have enough fuel to sustain star formation at the current rate for at least a couple of Gyr.

²This value decreases by a factor ~ 1.5 if a Salpeter IMF is adopted

Detailed simulations focused on the effect of the cluster environment after the first passage will thus be extremely interesting to understand the future evolution of these systems. At this stage, the main conclusion I can draw from this analysis is that at least ~ 3 Gyr seem to be necessary for the complete migration of a galaxy from the blue to the red sequence when gas stripping via the intracluster medium is involved.

HI-normal transition galaxies														
NAME	TYPE	D	AGN	B-V	FUV	NUV	H	F _{60μm}	F _{100μm}	M(HI)	M(HI)	C ₃₁ (H)	Merging	Ref.
		Mpc			m _{AB}	m _{AB}	m _{AB}	Jy	Jy	10 ⁸ M _⊙	/M _{star}		/accretion?	
NGC 3619	S0	20.7	-	0.86	16.86	16.14	7.40	0.43	1.61	7.08	0.04	6.2	Yes	1,2
NGC 3898	Sa	15.7	Lin	0.79	-	15.03	6.25	0.42	2.02	26.9	0.09	3.1	Maybe	3
NGC 4324	Sa	17.0	Lin/Sey	0.87	16.62	15.99	7.29	0.45	1.96	6.76	0.05	3.5	-	-
NGC 4370	Sa	23.0	NoL	0.70	-	18.26	8.28	0.94	3.27	4.0	0.04	3.8	Yes	4,5
NGC 4378	Sa	17.0	Sey	0.81	16.00	15.50	7.23	0.36	1.45	10.0	0.07	4.9	-	-
NGC 4772	Sa	17.0	Lin	0.87	17.07	16.16	7.12	0.38	1.32	6.17	0.04	5.1	Yes	6
NGC 5701	Sa	20.1	Lin	0.84	15.48	15.11	6.74	0.27	1.36	61.7	0.20	4.0	-	-
HI-normal red-sequence galaxies														
NAME	TYPE	D	AGN	B-V	FUV	NUV	H	F _{60μm}	F _{100μm}	M(HI)	M(HI)	C ₃₁ (H)	Merging	Ref.
		Mpc			m _{AB}	m _{AB}	m _{AB}	Jy	Jy	10 ⁸ M _⊙	/M _{star}		/accretion?	
NGC 4203	S0	17.0	Lin.	0.99	16.94	15.87	6.26	0.59	2.16	33.1	0.09	6.8	Yes	7
NGC 4262 ^a	S0	17.0	NoL	0.83	-	16.9	7.20	-	0.50	5.13	0.04	6.0	Yes	8
NGC 4698 ^a	Sa	17.0	Sey	0.83	16.64	15.71	6.16	0.63	1.89	17.0	0.04	4.2	Yes	9
NGC 4866	S0	17.0	Lin	0.96	17.26	16.27	6.76	-	-	13.5	0.06	3.7	-	-
NGC 5103	Sab	17.0	-	-	19.49	17.76	8.29	-	-	2.40	0.05	6.3	-	-

Table 5.1: The properties of HI-normal transition and red-sequence galaxies in the HRS+ sample. ^a UV fluxes increase significantly if the UV rings outside the optical radius are included. References are (1) van Driel et al. (1989); (2) Howell (2006); (3) Noordermeer et al 2005; (4) Bertola et al. (1988); (5) Patil et al. (2009); (6) Haynes et al. (2000); (7) van Driel et al. (1988); (8) Krumm et al. (1985); (9) Bertola et al. (1999)

5.5.2 HI-NORMAL GALAXIES

In contrast to HI-deficient objects, HI-normal transition galaxies are equally distributed between the field and cluster environments. They are $\sim 12\%$ in number (8 objects in total), but if all galaxies without HI measurements are HI-normal galaxies then this fraction might increase up to $\sim 30\%$. I note that NGC 4565 is the only example of perfectly edge-on transition object, thus it cannot be excluded that the corrections adopted still underestimate the real UV extinction (Panuzzo et al., 2003) making this galaxy possibly an erroneous transition object. Therefore, NGC 4565 is excluded from the following analysis.

The properties of the remaining 7 objects are listed in Table 5.1 as follows: Col. 1: Name. Col. 2: Morphological type. Col. 3: Distance in Mpc. Col. 4 AGN classification (following the criteria described in Decarli et al., 2007): Lin=LINER, Sey=Seyfert, NoL= No emission lines. Col. 5: $B - V$ colour corrected for dust extinction. Col. 6-8: FUV, NUV and H AB magnitudes. Col. 9-10: IRAS fluxes at 60 and 100 μm . Col. 11: HI mass. Col. 12: HI- to stellar-mass ratio. Col. 13: concentration index in H band taken from 2MASS ($C_{31}(H)$ defined as the ratio between the radii containing 75% and 25% of the total H-band light). Col. 14-15: Note regarding any evidence (and relative reference) supporting an external origin for the HI. In Figure 5.10, I show SDSS optical and GALEX UV colour images for each galaxy.

From this analysis, it emerges that HI-normal transition galaxies are a heterogeneous class of objects ranging from merger remnants (e.g. NGC 3619) with star-formation activity limited to the center, to satellites of big ellipticals (NGC 4370), with no evident signs of recent star formation. Contrary to the HI-deficient galaxies, there is no indication that ram pressure stripping has played a role in the recent evolution of the HI-normal galaxies. As expected in the case of massive ($M_* \geq 10^{10} M_\odot$) galaxies, the majority of these objects host an ‘optical’ AGN. More surprisingly, our analysis shows that, although they have likely followed different evolutionary paths, a significant fraction of these galaxies (at least 4 out of 7) has recent star formation mainly in the form of one or more UV rings. As shown in Figure 5.10, the UV rings have different morphologies going from inner rings (NGC 3898, NGC 4324, NGC 4772) to Hoag-like objects (NGC 5701). Resolved HI maps, available for two of our objects (NGC 3898, NGC 4772), reveal that the HI is distributed in extended low surface density disks, significantly exceeding the typical column density of $1\text{-}2 M_\odot \text{pc}^{-2}$ only in the star forming rings. Thus, in these cases, star formation is reduced not because the HI has been stripped but just because the gas is not able to collapse

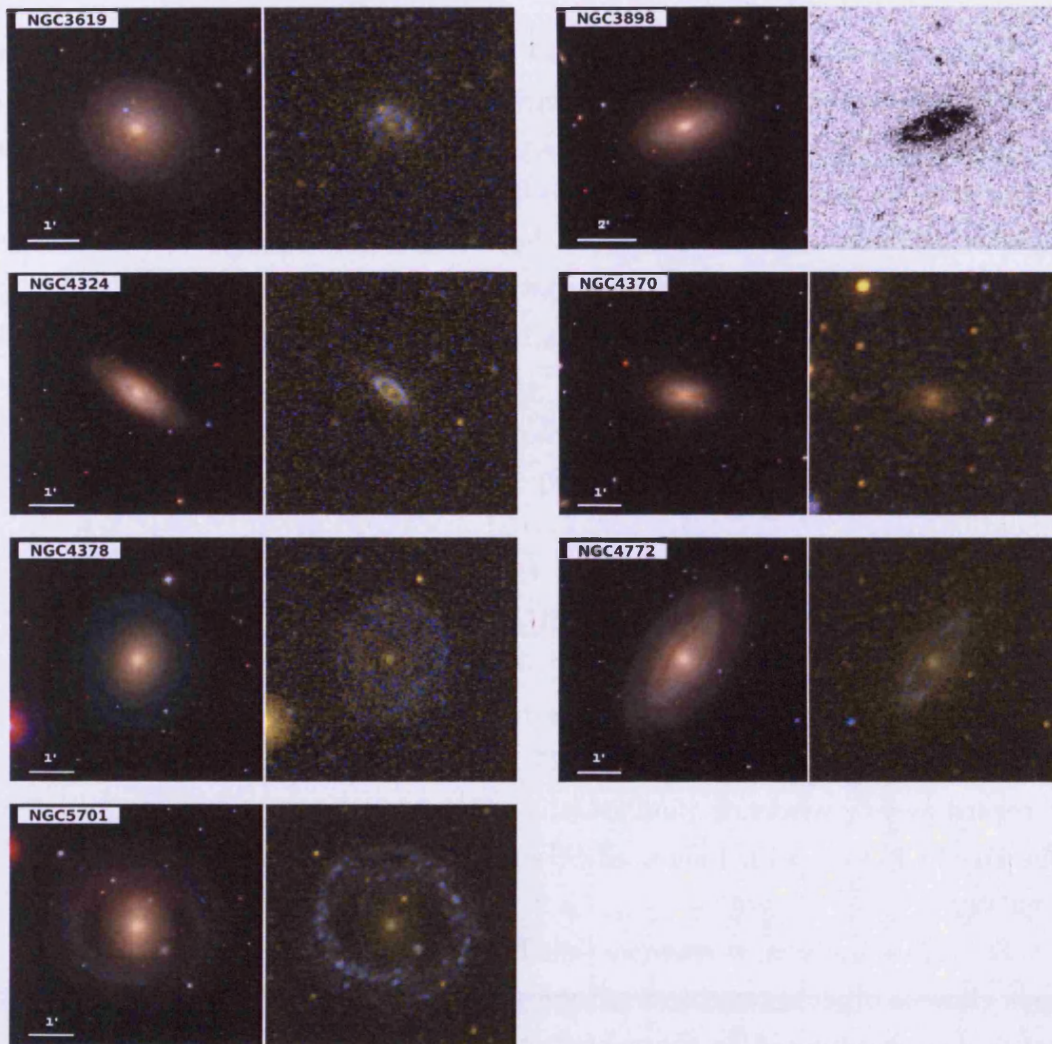


Figure 5.10: HI-normal transition galaxies. For each galaxy, the SDSS RGB and GALEX FUV-NUV colour images are shown. In case GALEX FUV observations are not available the NUV image is shown in black and white.

into stars efficiently. This is likely due to the fact that the gas reservoir has a typical column density well below the critical density necessary to convert the atomic hydrogen into molecular hydrogen and commence star formation (Krumholz et al., 2009).

The presence of UV rings becomes more intriguing when HI-normal galaxies in the ‘NUV red sequence’ are also taken into account (5 galaxies in total, see Table 5.1 and Figure 5.11). The four galaxies with clear star formation activity (NGC 4203, NGC 4262, NGC 4698, NGC 4866) have star-forming regions mainly arranged in

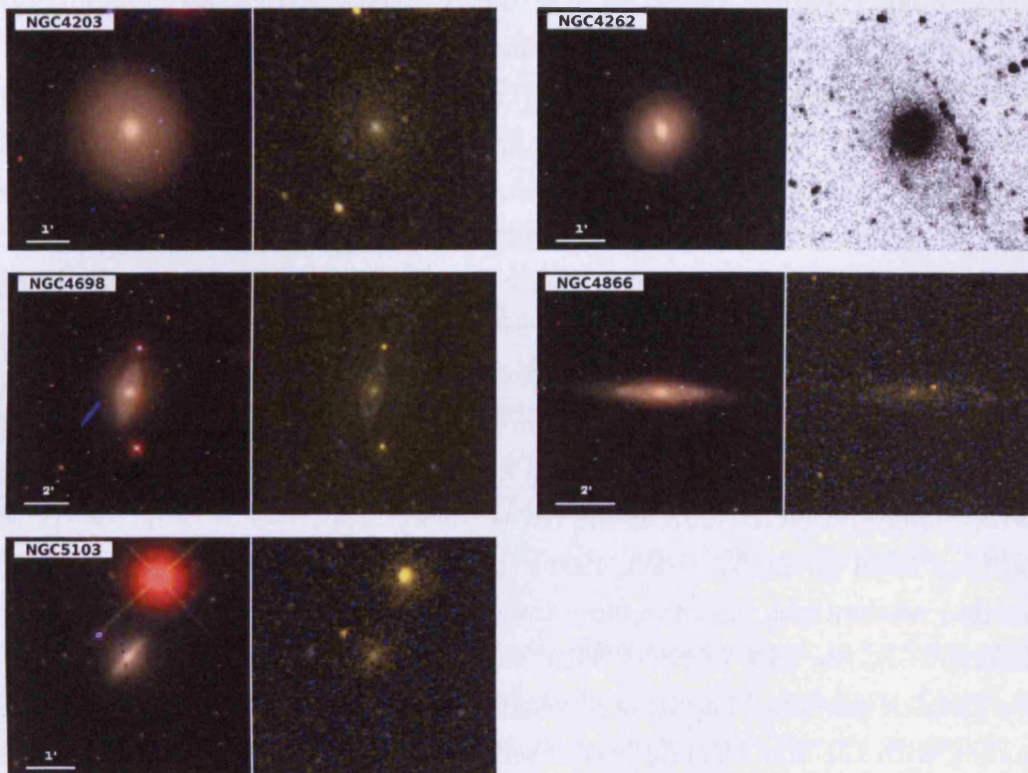


Figure 5.11: Same as Figure 5.10 for HI-normal red-sequence galaxies. NGC 4262 and NGC 4698 return to the transition region if the outer UV rings are included in the estimate of the UV flux.

structures which are suggestive of one or multiple rings (see Figure 5.11). In the case of NGC 4203 and NGC 4698, HI maps reveal a morphology similar to the one observed in HI-normal transition objects with extended low surface density HI disks and peaks of column density in correspondence of UV star-forming regions. The only known exception is represented by NGC 4262, where the HI is mainly segregated in the UV star forming ring. Interestingly, NGC 4262 and NGC 4698 could be immediately reclassified as transition region galaxies if the outer UV rings are included in the estimate of the UV flux. All this observational evidence strongly suggests that the evolutionary paths leading these objects to the transition region have been significantly different from the path followed by HI-deficient galaxies.

Past and future evolution in the colour-mass diagram

To understand the recent evolutionary history of these unusual ‘gas-rich’ systems, the origin of their gas reservoir must be determined. Has the gas an external origin (e.g,

accretion, infall, merging, shells, etc.) or was it always part of the galactic halo but has not been efficiently converted into stars? The origin of the gas not only provides clues on the past history of these objects (i.e., whether they are really migrating from the blue to the red sequence) but also may help in predicting their future evolution in the colour-mass diagram. In the following, I combine the information available for HI-normal transition and red sequence galaxies to determine whether these systems have recently left the blue sequence after a quenching episode or are migrating back from the red sequence to the transition region thanks to a recent accretion event.

Many galaxies in this sample show direct or indirect evidence of past gas accretion/infall events (e.g, warps, counter-rotating or decoupled components, stellar shells). Among the best candidates for an external origin of all the HI observed, there are NGC 4262 and NGC 4203 in the red sequence and NGC 3619 in the transition region (van Driel & van Woerden, 1991). However, it is interesting to note that the acquisition mechanisms (and therefore the evolution) of the three systems is likely to be different. In the case of NGC 3619, the most likely scenario is a minor merger with a gas-rich satellite. The HI is segregated well within the optical radius, roughly coinciding with the star forming disk observed in UV, suggesting that a satellite has sunk into the center, triggering an episode of star formation. Given that the stellar populations have ages and metallicities typical of unperturbed ellipticals (Howell, 2006), the most plausible scenario is that NGC 3619 has left the red sequence after the merging event. Interestingly, at the current SFR ($\sim 0.1 M_{\odot} \text{ yr}^{-1}$), the amount of atomic hydrogen present within the optical disk ($\sim 7 \times 10^8 M_{\odot}$) is sufficient to sustain the star formation for several billion years. Thus, NGC 3619 will either remain in the transition region for a long time or, in case of a significant increase of the SFR, may be able to temporarily rejoin the blue cloud in a UV-near-infrared colour magnitude diagram. A similar evolutionary path could also have been followed by the dust-lane early-type NGC 4370. However, the lack of detailed HI maps prevent us from drawing any conclusion.

On the contrary, the infall of HI into NGC 4203 and NGC 4262 has likely followed less ‘violent’ paths. In NGC 4262, the presence of a ring composed only of HI and newly formed stars is strongly suggestive of recent accretion, apparently ruling out that the ring has been formed from galactic material through bar instability. An interesting possibility is that the bar could still be responsible for the peculiar configuration of the HI, preventing the newly accreted gas to collapse into the center. What remains unclear is whether the gas in the ring has been accreted from the intergalactic medium (as proposed in the case of polar ring galaxies; e.g., Macciò et al., 2006) or during an interaction with another galaxy (Vollmer et al., 2005). As

for NGC 3619, the gas reservoir in the ring is sufficient to keep the galaxy in the transition region for several Gyr or to move it back to the blue cloud, building-up a new stellar disk/ring. To this regard, it is tempting to consider NGC 4262 the ancestor of Hoag-type objects like NGC 5701, thus implying that these two systems may be on their way back to the UV blue cloud. However, at this stage it is impossible to determine whether these two systems are at different stages of the same evolutionary path.

A migration back to the transition region appears instead very unlikely in the case of NGC 4203. Despite its huge HI reservoir, this galaxy shows only weak traces of recent star formation activity and at this rate the integrated colour will not be significantly affected, leaving this object in the red sequence. A similar scenario could also be valid for NGC 5107 and NGC 4886 which already are in the red sequence. However, additional observations are required to unveil the evolutionary history of these systems.

In summary, for at least a few cases, observations seem to suggest that HI-normal red galaxies have recently acquired atomic hydrogen and have started a new cycle of star formation activity leaving, at least temporarily, the red sequence.

For other transition galaxies, this scenario appears extremely unlikely. This is particularly the case for NGC 3898, NGC 4772 and NGC 4698. These three systems have very similar properties: i.e., Sa/Sab type with a significant bulge component (bulge-to-total ratio $\sim 0.2-0.4$; Drory & Fisher, 2007), HI mainly distributed in two rings, one inside and one outside the optical radius, corresponding to the sites of recent star formation activity. HST images reveal that all three galaxies possess a classical bulge (Drory & Fisher, 2007), consistent with a ‘violent’ and quick bulge formation in the past through mergers or clump coalescence in primordial disks (e.g., Noguchi, 1999; Kormendy & Kennicutt, 2004; Elmegreen et al., 2008). In addition, the presence of a decoupled core (NGC 4698) or a counter-rotating gas disk (NGC 4772) is suggestive of a more recent accretion event (e.g., minor merger) supporting an external origin for at least part of the HI in these objects. The preferred explanation for the properties of NGC 4698 is in fact a later formation of the disk through the acquisition of material by a completely formed spheroid. Thus, it would be natural to argue this is observational evidence for the build-up of the disk and that these galaxies are gradually moving from the red to the blue cloud, following a path consistent with what expected by hierarchical models (Baugh et al., 1996; Kauffmann, 1996). However, a rough time-scale argument rules out this hypothesis. All three galaxies harbor massive stellar disks ($M_{disk} \sim 1-3 \times 10^{10} M_{\odot}$ depending on the mass-to-light ratio difference between bulge and disk) and a SFR of $\sim 0.7-2 M_{\odot} \text{ yr}^{-1}$ during the

last Hubble time is thus necessary to form the observed disks. These SFRs are more typical of blue-cloud galaxies and a factor ~ 10 larger than the SFR observed in these systems ($SFR \sim 0.07-0.2 M_{\odot} \text{ yr}^{-1}$). While minor mergers have probably affected these systems, I can exclude that a great part of the stellar disk is composed of ‘accreted stars’, since the whole stellar component of the satellite is supposed to collapse into the center, contributing to the growth of the bulge (Hopkins et al., 2009). Although the uncertainties in the estimate of stellar masses and SFR are still quite significant, the large discrepancy between the observed and expected SFR suggests that the existing stellar disks are too massive to have been formed at the current SFR. Of course, I cannot exclude multiple transitions from the blue to the red sequence and vice-versa (Birnboim et al., 2007), but this scenario is not considered in the analysis given the low amount of observational constraints available. I propose that the SFR in the disks was higher in the past or, in other words, that these galaxies have probably migrated from the blue cloud. A reduction in the SFR is likely due to the low HI column density in these systems: on average below the threshold for the onset of star formation. What caused this reduction is still unclear and only more detailed theoretical models and simulations will help us to solve this mystery. The same mechanism is probably behind the ring-like structures observed in both HI and UV. Both internal (e.g. bar instability) or external (e.g. accretion, merging) processes can be responsible for such features. However the absence of strong bars, the presence of decoupled/counter rotating components and the size-ratio of the inner and outer rings ($\sim 3.3-3.6$, i.e. different from the typical value expected for Lindblad resonances ~ 2.2 , although not completely inconsistent; Athanassoula et al., 1982; Buta, 1995), favour an external mechanism behind the unusual properties of these systems. Since all these galaxies harbour an AGN, it is natural to think about AGN feedback. However, these are generally low-energetic AGNs and no direct evidence (e.g., jets) supporting this scenario has been found so far. Moreover, it is not clear how star-forming rings and low surface density HI disks can be formed via AGN-feedback.

Finally, it is important to note that, whatever the past evolutionary history of these systems, the hydrogen reservoir available can sustain the current star formation activity in these galaxies for at least 2-5 Gyrs (ignoring molecular hydrogen, helium and recycling). Thus, if star formation will remain as efficient as it is now, it will take a long time for these galaxies to reach the red sequence in a UV-optical/near-infrared colour-mass diagram.

Unfortunately, no speculation can be made about the past evolutionary history of NGC 4324 and NGC 4378 given the lack of multiwavelength observations.

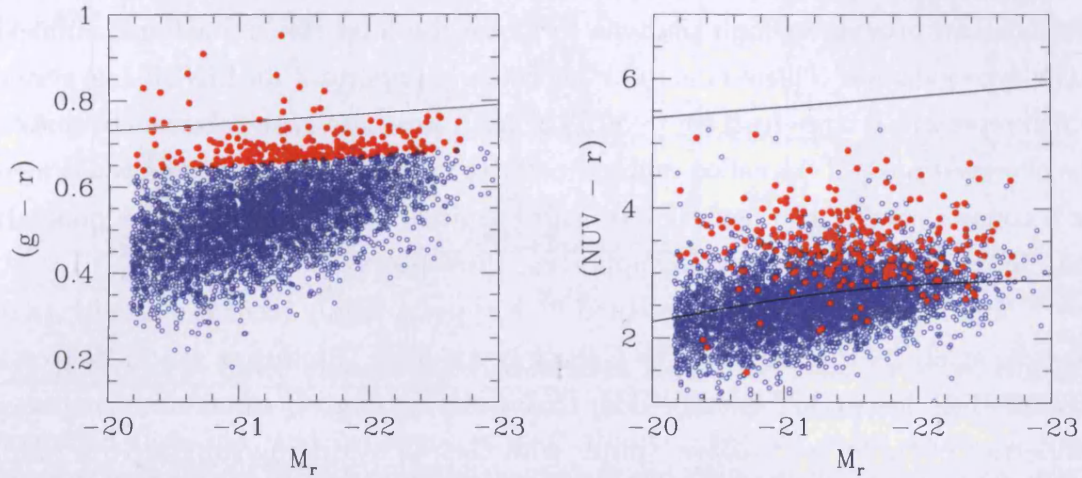


Figure 5.12: *Left*: The $g - r$ versus M_r colour magnitude diagram from Masters et al. (2010), highlighting the best fit to the red sequence of the SDSS galaxies in the Galaxy Zoo sample (solid black line), the face-on, disk-dominated objects identified as ‘red passive’ spirals (solid red circles), and the face-on, blue star-forming spirals forming the blue cloud (open blue circles). *Right*: The $NUV - r$ versus M_r colour magnitude diagram, showing the best fit to the red sequence and blue cloud in Wyder et al. (2007). The majority of the red ‘passive’ spirals actually display $NUV - r$ colours similar to the blue star-forming spirals.

5.6 DISCUSSION & CONCLUSIONS

I have shown for the first time that, at all stellar masses, transition spirals tend to be HI deficient galaxies, preferentially found in high-density environments. Although I confirm that the fraction of AGN-host spirals peaks in the transition region (see also Martin et al., 2007; Schawinski et al., 2007), it is demonstrated that, at fixed stellar mass, AGNs are not associated with a systematic decrease in the star formation activity whereas HI deficient galaxies are redder than gas-rich systems. Thus, environmental effects could explain the suppression of the star formation over the whole range of stellar masses investigated in this work, and no direct connection between AGN activity and quenching of the star formation is observed in the HRS+ sample.

However, biases in the classification of nuclear activity could be introduced by using optical emission lines. On one hand, AGN activity in blue sequence galaxies could be totally obscured or outshone by star formation. This would imply an underestimate of the AGN fraction in the blue sequence, thus reinforcing the results.

On the other hand, Stasińska et al. (2008) have recently shown that old stellar populations can provide enough photons to ionize the inter-stellar medium, mimicking AGN-type galaxies. This seems to be particularly important for LINER-like systems, which represent a large fraction ($\sim 56\%$) of AGN-host late-type galaxies. In this case, the observed peak of ‘so-called’ nuclear activity in the transition region would merely be a consequence of the fact that transition spirals have an older stellar population than blue sequence disks, again supporting these results.

I note that the result presented here appears highly inconsistent with that of Masters et al. (2010), who use the Galaxy Zoo sample (Lintott et al., 2008) to select face-on, disk-dominated spirals redder than a stipulated $g-r$ colour and compare the properties of these ‘red passive’ spirals with their star-forming counterparts residing on the blue cloud of the $g-r$ colour-magnitude diagram (see Figure 5.12). They find no significant difference between the properties of ‘passive’ spirals in different environments, in contrast to what I find in the HRS+ sample. They suggest that the ‘passive’ spirals are either satellite galaxies in massive halos with quenched star formation from strangulation, the descendants of bar-dominated, normal spirals with efficient accretion of gas or are merely old spirals which have consumed all of their gas.

However, under closer inspection of their sample, I find that their definition of ‘passive’ spirals does not correspond to the definition used here. I matched the SDSS galaxies from the Galaxy Zoo sample in Masters et al. (2010) with GALEX objects from the GR4/GR5 online archives. Most of the sample (88.1%; 4787/5433) had NUV magnitudes measured by the GALEX pipeline. Thus, I reconstruct the $NUV-r$ versus M_r colour-magnitude diagrams and use the best fit relations to define the blue cloud and red sequence from Wyder et al. (2007). Plotting the $NUV-r$ colours for the Galaxy Zoo sample (see Figure 5.12), I find that the blue star-forming galaxies are scattered around the best fit relation, in agreement with Wyder et al. (2007). Yet, the ‘passive’ spirals actually appear to be more active than first thought, since the majority of them reside inside or on the edge of the $NUV-r$ blue cloud. Few ‘passive’ spirals reside in the transition region, with rapidly decreasing numbers of objects approaching the red sequence. Thus, the sample of ‘passive’ galaxies based on the $g-r$ colour selection would likely be classified as star-forming galaxies on the blue cloud in the $NUV-H$ colour-mass diagrams. From this result, it is easy to see why Masters et al. (2010) might find no environmental difference between the properties of the ‘passive’ spirals, since Figure 5.1 demonstrates that the blue cloud is present in all environments and that truly passive spirals would less likely be present in the field environments. It should be noted that the $NUV-r$ colours in Figure

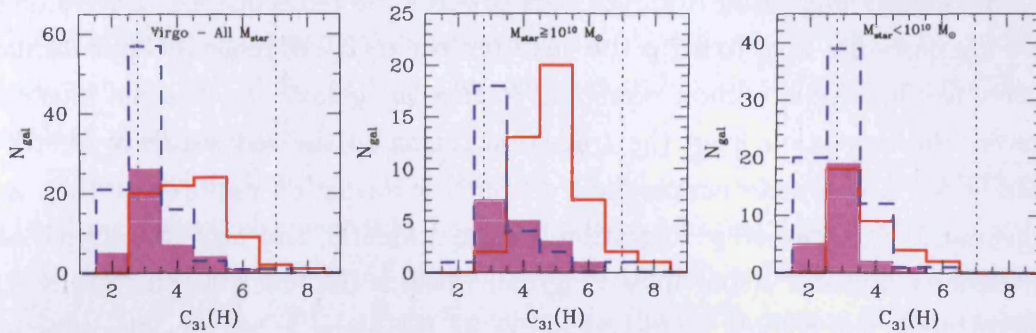


Figure 5.13: The distribution of the concentration index in H-band for Virgo cluster galaxies. Galaxies are divided into blue-cloud (blue, dashed histogram), HI-deficient transition (magenta) and red-sequence (red) objects. The left panel shows all the galaxies in the Virgo sample, while in the central and right panels only high and low stellar mass objects are shown respectively. The dotted lines show the expected values for an exponential and $r^{1/4}$ light profiles.

5.12 have not been properly corrected for internal dust extinction and it is likely that the galaxies actually possess slightly bluer $NUV - r$ colours. This merely strengthens the conclusion of this exercise, which suggests the discrepancy between our results stems from the problem of using optical colours to discriminate between star-forming and quiescent systems, which was previously noted in the B-H colour-mass diagram presented in Figure 5.6.

The fact that the quenching of the star formation in transition galaxies is driven by the environment is not completely surprising, considering the plethora of observations supporting the significant impact of the environment on galaxy evolution (e.g., Dressler, 1980; Boselli & Gavazzi, 2006). However, the use of HI data to discriminate between the effects of AGN feedback and environment on star formation shows not only that a physical link between nuclear activity and position in the colour-mass diagram, but also provides additional insights on the evolutionary history of spiral galaxies outside the blue sequence. In fact, I also discovered a small fraction of transition galaxies which are not HI deficient and/or do not lie in high density regions.

5.6.1 THE MIGRATION OF HI-DEFICIENT GALAXIES

Galaxies in the transition region are typically HI deficient late-type galaxies, predominately found in the Virgo cluster. They form a fairly homogeneous population

which are clearly migrating from the blue towards the red sequence. Environmental effects are certainly able to strip the gas from the disk, reducing the star formation in just a few hundreds million years and forcing the galaxy to leave the blue cloud. However, the migration from the transition region to the red sequence is still uncertain, since a complete suppression of the star formation requires at least a few billion years. This ‘two-step’ migration is more dramatic, and perhaps only visible in an ultraviolet-infrared colour-mass diagram, whereas the first stripping event is sufficient to make the colours almost as red as an early-type galaxy in diagrams based on optical colours.

Given the large uncertainty on the typical migration timescale and uncertainties on the observations, the current migration rate cannot place any meaningful constraint on the growth of the red sequence. It is possible to investigate whether a morphological transformation occurs during the migration to the red sequence. The crucial question here is whether the red sequence is fed with bulge dominated or disk galaxies. The answer is clear from Figure 5.13, where I examine the distribution of the concentration index in H-band for galaxies in the Virgo cluster. In the transition region, only Virgo HI-deficient galaxies are shown. Overall (Figure 5.13, left panel), HI-deficient transition galaxies have a concentration index much more similar to blue than red-sequence systems. However, such a difference is only evident at stellar masses higher than $\sim 10^{10} M_{star}$ (Figure 5.13, central panel) whereas for smaller galaxies (right panel) the distribution of $C_{31}(H)$ does not significantly vary across the whole range of colours, reflecting the fact that dwarf ellipticals have exponential light profiles like dwarf irregulars (e.g., Binggeli & Cameron, 1991). This result implies that, while HI-deficient transition galaxies are likely the progenitors of cluster low-mass red objects (see also Haines et al., 2008; Boselli et al., 2008), this is not completely true at high stellar masses. This is additionally supported by the fact that the vast majority of high-mass transition galaxies are early-type spirals and almost no ellipticals are present (see Figures 5.5 and 5.7). The vast majority of galaxies in the process of reaching the red sequence are thus disk systems, significantly different from ellipticals or bulge-dominated galaxies characterizing high-mass, quiescent objects at low redshift.

Since a significant fraction of HI-deficient transition galaxies appear to have recently fallen into the center of Virgo and will likely spend a few Gyr in the transition region (see Section 5.5.1), it may be possible that a morphological transformation still takes place before reaching the red sequence. Although this scenario cannot be completely excluded, it is considered unlikely. Given the long time required to halt the star formation, galaxies with increased bulge component should be present

in our sample. Moreover, since gas stripping appears not to significantly increase the bulge component in early type galaxies (e.g., Boselli et al., 2006), an additional environmental effect (different from the one responsible for the quenching of the star formation) must be invoked.

Thus, the fact that transition galaxies are not morphologically transformed before reaching the red sequence may have two different implications: either 1) galaxies are morphologically transformed once already in the red sequence, or 2) the mechanism controlling the accretion of stellar mass into the red sequence at $z \sim 0$ is not the one responsible for the creation of the red sequence in the first place. Although it is possible that the bulge component is enhanced in some red galaxies via gravitational interactions, such scenario seems unlikely to explain the growth of the red sequence. Firstly, the mechanism responsible for the morphological transformation should be efficient only on giants and not on dwarf systems, which seems inconsistent with what is known about environmental effects (Boselli & Gavazzi, 2006). Secondly, the major mergers required to significantly increase the bulge component are extremely rare in today's clusters of galaxies. Thirdly, the presence of red-sequence galaxies in isolation implies that star formation has been suppressed also outside clusters of galaxies. Although my sample could be biased against isolated objects, the fact that no field galaxies are clearly migrating from the blue sequence may suggest that in low density environments the red sequence has been mainly populated in the past. Finally, if the morphological transformation takes place in the red sequence, the number of bulge-dominated/elliptical galaxies should decrease at increasing redshift, which does not seem to be the case (Postman et al., 2005; Desai et al., 2007). Thus, the most favourite scenario emerging from the analysis is that the red sequence is currently accreting mass, at all masses, mainly via disk galaxies. No significant structural modification takes place during the journey from the blue cloud to the red sequence. The main process responsible for the suppression of the star formation in nearby galaxies is thus not the same responsible for the formation of the red sequence at high redshift.

5.6.2 THE HI-NORMAL TRANSITION GALAXIES

While in the case of HI-deficient objects it seems plausible to associate transition galaxies with objects that are migrating from the blue to red sequence, this is not always the case for HI-normal transition galaxies. They represent $\sim 12\%$ of the HRS+ transition galaxy population and are only found at high stellar masses ($M_* > 10^{10} M_{star}$). As shown in Figure 5.14, these galaxies are mainly disks with a significant bulge component (they are in fact all Sa or S0 galaxies) and, despite

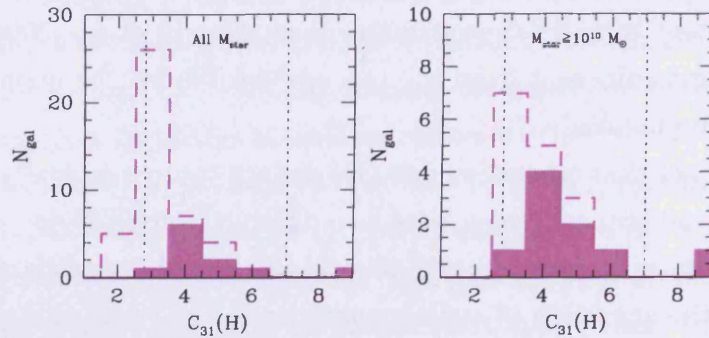


Figure 5.14: . The distribution of the H-band concentration index for Virgo HI-deficient (dashed) and HI-normal transition galaxies. All galaxies and galaxies with $M_{\star} \geq 10^{10} M_{\odot}$ are shown in the left and right panel respectively.

the low number statistics, it seems clear that there are very few ‘disk-only’ galaxies, contrary to the HI-deficient population.

Despite their different properties, a great fraction of these galaxies show active star-forming regions and HI segregated in one or multiple ring-like structures. Red sequence galaxies can acquire a new gas supply and restart their star formation activity, as predicted by cosmological simulations. However, it is unlikely that the red galaxies in our sample will re-build a significant stellar disk (see also Hau et al., 2008). Merging, accretion of gas-rich satellites and exchange of material during close encounters are among the likely scenarios responsible for this rejuvenation. Such processes are more frequent in low density environments, where red-sequence galaxies are rarer, perhaps reducing the chances to observe such phenomenon.

When a suppression of star formation is the most likely scenario to explain HI-normal transition galaxies, the process behind such migration is still unclear. In this case, star formation must be reduced by making the HI stable against fragmentation (e.g., by decreasing the HI column density below the threshold for star formation) and not via HI stripping as observed in HI-deficient objects. Starvation (Larson et al., 1980) by removing any extended gaseous halo surrounding the galaxy, preventing further infall, could be a possibility. This would imply a longer time-scale (several Gyr) for the migration from the blue cloud (Boselli et al., 2006, 2008) than the one observed in the case of HI stripping (a few hundreds million years). However, the evidence for gas accretion in some of these objects may suggest that starvation, if efficient, is not the only mechanism at work.

Martig et al. (2009) have recently proposed a ‘morphological quenching’ to

explain the origin of gas-rich bulge-dominated objects. The idea behind this mechanism is that the presence of a bulge could inhibit the collapse of a gas disk. However, the ‘morphological quenching’ appears only to be effective when the disk stellar component is negligible, which is not the case for the majority of the systems in our sample.

Thus, a picture has emerged in which galaxies not only migrate from the blue cloud to the red sequence, but also migrate into the transition region from the red sequence. Whilst the mechanisms governing the evolutionary paths of HI-normal transition galaxies still need to be unravelled, it is clear that environmental effects are driving the migration of late-type galaxies from the blue cloud to the red sequence. Finally, I remind the reader that although galaxies in the transition region do display active nuclei, I find no evidence in support of AGN feedback suppressing the star formation in the migrating population.

CHAPTER 6

THE COLOUR PROFILES OF VIRGO CLUSTER MEMBERS

6.1 INTRODUCTION

The results of the previous chapter suggest that the migration of galaxies from the blue cloud to the red sequence may be governed more by the effects of the environment and less, as recently proposed (Martin et al., 2007; Schawinski et al., 2007), due to AGN feedback quenching star formation. This result was obtained using integrated UV-H colours to separate quiescent systems from star forming galaxies. An alternative approach may be to look at the differential light from a galaxy, rather than the integrated colours, to test for signatures of internal processes or environmental effects causing a quenching of the star formation.

This is motivated by the results of recent studies, which demonstrate that the cluster environment can affect the extent of the star-forming disks in spirals. Koopmann et al. (2006) conducted a $H\alpha$ imaging survey of 55 Virgo cluster galaxies. They found that star formation activity is quenched in the outer disks, which produces truncated $H\alpha$ profiles compared to that of the stellar disk. This truncation is linked to HI deficiency, whereby gas is removed by external processes that results in a quenching of the star formation activity. The gas stripping process has been demonstrated for individual objects (e.g. NGC 4569; Boselli et al., 2006) and statistically using the relationship between the optical-to- $H\alpha$ ratio and HI deficiency (see Figure 11 of Boselli & Gavazzi, 2006).

Thus, environmental processes such as ram pressure stripping are known to affect the gas content and hence star formation in the outskirts of the galaxy (e.g. Cayatte et al., 1994). Consequently, this quenching of the star formation from the

‘outside-in’ may be evident in the colour profiles of galaxies in the transition region, since these objects were found to be preferentially HI deficient cluster galaxies with quenched star formation. Colour profiles based on the UV and H bands could indicate where star formation has recently been quenched, since a reduction in the star formation on short timescales ($t < 10^8$ yrs) will affect the UV emission but not the H band emission, which traces the older stellar population. The UV-H colour profile would therefore appear redder if star formation was quenched. In fact, it may be possible to observe where the quenching has occurred, and thus discriminate between different possible quenching mechanisms. In the case of a galaxy affected by ram pressure stripping, this would produce the ‘outside-in’ profile discussed above.

On the other hand, AGN feedback is thought to heat or expel the gas at the center of a galaxy, thus quenching star formation in the interior of a galaxy. This mechanism could produce an increased reddening of the colour profile from the nuclear region towards the outskirts of the disk (an ‘inside-out’ profile). It may then be possible that the observed interior UV-H colours will be different in transition objects compared to galaxies on the blue sequence if AGN feedback is playing a role. However, I note that contrary to the case of ram pressure stripping, any clear effects of AGN on the colour profiles have yet to be demonstrated observationally.

Thus, there is a potential for the nature of the quenching mechanism to be imprinted in the colour profiles. Uncovering such signatures of proposed quenching mechanisms is likely to be a difficult task for a number of reasons. Firstly, the effects of the different quenching mechanisms on the colour profiles are still unclear. The impact of AGN feedback on the evolution of late-type galaxies is still not properly understood and whilst ram pressure stripping has been well studied (see e.g. Roediger, 2009; Vollmer, 2009; Tecce et al., 2010), the timescales involved are likely to be very short (< 0.5 -1 Gyr; see Chapter 5), making it difficult to observe the colour variation. It is also likely that the combination of different mechanisms acting on the disks may complicate the colour profiles to the point where it is not possible to disentangle the processes behind the quenching.

Finally, it is important to note that the UV-H colour profiles cannot currently be properly corrected for internal dust attenuation, necessary to accurately interpret the UV emission (as discussed in Section 3.5). This is due to a current lack of far infrared observations with the spatial resolution necessary to determine radial dust attenuation corrections. However, with the capability of the SPIRE instrument to deliver high resolution 250, 350 and 500 μm observations using the Herschel Space Telescope, it will soon be possible to determine the radial distribution of dust in spiral galaxies and thus develop radial corrections for the dust attenuation. Until

then, it will be difficult to discriminate between the reddening due to dust extinction and the reddening due to an ageing stellar population following the quenching of star formation.

Given the myriad of complications surrounding the simple hypothesis, I conducted a pilot study using a small sample of galaxies to (a) assess the ease of analysing colour profiles and (b) test the validity of the hypothesis. I begin by discussing the incompleteness of the sample used in this work and then proceed with the construction of UV-H colour profiles.

6.2 SAMPLE CAVEAT

Whilst the HRS+ sample is used predominately throughout this thesis, the colour profiles obtained here were initially selected based on an early version of a sample of VCC galaxies. This early sample was constructed from NUV-H versus H band colour-magnitude diagrams using Virgo galaxies. In these original colour-magnitude diagrams, the most luminous galaxies were selected based on $M_H > -21$ mag and using only the UV images from the deeper GALEX surveys, i.e. using the NGS/MIS observations and excluding the AIS observations (see Chapter 3). This criteria yielded a sample of 54 late-type galaxies for which NUV-H colour profiles were obtained. However, this initial sample is both incomplete and poorly defined, and so is not statistically useful for drawing conclusions from the profiles.

Using the better defined sample afforded by the VCC, I first determine the completeness of the sample of galaxies with colour profiles. The initial sample was magnitude limited at $M_H > -21$ mag, which corresponds to a stellar mass of approximately $10^{9.5} M_\odot$ using the adopted conversion from the H band luminosity to stellar mass (as described in Section 2.4). Hence, I compare the galaxies with colour profiles to the total sample of massive ($>10^{9.5} M_\odot$) late-type systems. The mass distribution of the total VCC sample is compared to that of the galaxies with profiles in Figure 6.1. A low fraction 53% (49/92) of the massive systems have colour profiles, and this fraction drops below 50% in the range $10^{9.5} < M_* < 10^{10.3} M_\odot$. I note that the difference between the 54 profiles in the initial selection and the 49 profiles available in the VCC arises from the conversion of a magnitude-limited to mass-limited selection criteria, since the colour correction used in Equation 2.1 means the magnitude limit of $M_H > -21$ mag may deviate slightly from the mass limit of $10^{9.5} M_\odot$. In comparison, the situation appears worse when looking at the selected galaxies which overlap with the HRS+ sample. The mass distribution of the late-types in the HRS+ sample is compared to that of the galaxies with profiles in Figure 6.1. Only 37% (36/98) of

galaxies above $10^{9.5} M_{\odot}$ overlap with the VCC sample which also have colour profiles.

It is also important that the galaxies are distributed evenly across the range of NUV-H colours, in order to derive average profiles for galaxies residing on the blue sequence, in the transition region and towards the red sequence. The NUV-H colour-mass diagrams for the VCC and HRS+ galaxies are also shown in Figure 6.1. It is evident that in the VCC sample, the massive galaxies are distributed fairly evenly and it is possible to create different average colour profiles for different bins of NUV-H colour. The HRS+ sample lacks galaxies with integrated colours redder than $\text{NUV-H} > 6$.

I shall proceed by using all the available colour profiles, given that neither the VCC or HRS+ sample of massive galaxies with profiles can be considered complete. It must be kept in mind that since the sample is incomplete, the conclusions may not accurately represent the properties of the late-type galaxy population in the local universe.

6.3 SURFACE PHOTOMETRY

In this section, I describe the procedure I use for first extracting surface brightness (SB) profiles from multiwavelength images, which can subsequently be used for creating UV-H colour profiles. This procedure is outlined below and follows five main steps:

1. assigning a world coordinate system to those images which are lacking sky position information;
2. aligning the multiwavelength images of each galaxy such that each pixel in each band corresponds to the same position on the sky;
3. measuring and subtracting the background sky emission from each image;
4. smoothing the resolution of each image to that of the lowest resolution observation; and
5. extracting the SB profile by measuring the surface brightness of the galaxy within apertures of increasing radii.

The images used in this photometry are GALEX NUV and FUV band images from the GR2/GR3 data release and H band images taken from UKIDSS and GOLDMine, as described in Section 2.3. Detailed descriptions of each step are presented below.

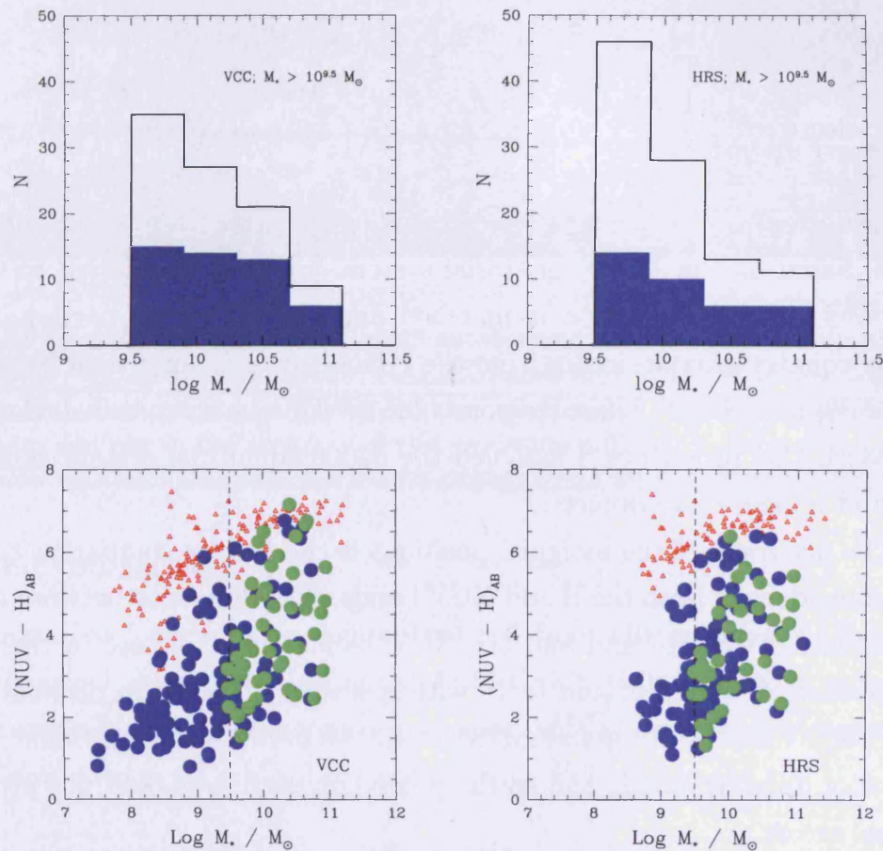


Figure 6.1: *Upper panels:* The completeness of the massive ($M_* > 10^{9.5} M_\odot$) late-type galaxies with colour profiles (blue histogram) compared to the massive late-types in the VCC sample (*left panel*; black line) and the HRS+ sample (*right panel*; black line). *Lower panels:* The NUV-H colour-mass diagrams for the VCC sample (*left*) and the HRS+ sample (*right*), highlighting those galaxies for which profiles are determined (solid green circles) out of the total sample of late-type (solid blue circles) and early-type systems (open red triangles). The dashed line shows the approximate mass selection limit at $M_* \sim 10^{9.5} M_\odot$.

Setting the WCS

Each pixel of each image corresponds to a point on the sky. Information for the position of each image on the sky is required for accurately aligning multiwavelength observations. However, some of the H band observations obtained for this work have corrupted or missing sky position information. Thus, the first step is to check each image and, where necessary, assign a coordinate system (referred to as the world coordinate system; WCS) to the pixel array of the images.

To create a WCS matrix, positions are first identified to act as reference points to calculate the matrix. I obtained SDSS r band images, which all have an assigned WCS, for those galaxies lacking WCS information. Using the Gaia software package, stars are selected which are visible in both the r band and H band observations. These stars are evenly distributed over the whole image. The star positions are determined from the centroid of the peak of the light distribution in the r band images. These positions, based on the J2000 equatorial system, are then transferred to the H band observations and each position is matched and aligned to the corresponding star. Thus, the equatorial coordinates from the r band images could then be saved to the H band images, acting as reference points for a WCS matrix to be calculated for each image. With this procedure, I assigned the J2000 equatorial system as the WCS to the H band images of 15 objects.

The accuracy of the assigned positions is checked by comparing the positions of stars coincident in both the H and NUV bands. The difference between the position measurements of the H band and the NUV bands are < 0.2 sec in right ascension with a scatter of ~ 0.1 sec, and $< 1''$ with a scatter of $\sim 0.6''$ in declination. These errors are equivalent to the standard discrepancies between the positional information of images of different bands and so the procedure used here does not introduce any additional errors.

Image alignment

The next step in the construction of UV-H colour profiles is to align the images, such that the same point in the sky has matching observations in different bands. In this case, the NUV and FUV observations are aligned and scaled to the H band images. This process follows two steps.

Firstly, the spatial transformation function, which maps the coordinate system of the reference image to the coordinate system of the input image, is determined. This is performed with the IRAF software package, using the WCSMAP task. The task determines the function from comparing the coordinates in the reference image, in this case the H band observations, and the UV images. This is the reason why it is necessary to apply a WCS to images lacking sky position information, since WCSMAP requires a coordinate system to determine the transformation function.

Secondly, the transformation is applied with the GEOTRAN task and the images are visually inspected to check that the alignment was successful, by comparing the positions of stars or the positions of the maximum of the galaxy emission in the different aligned images.

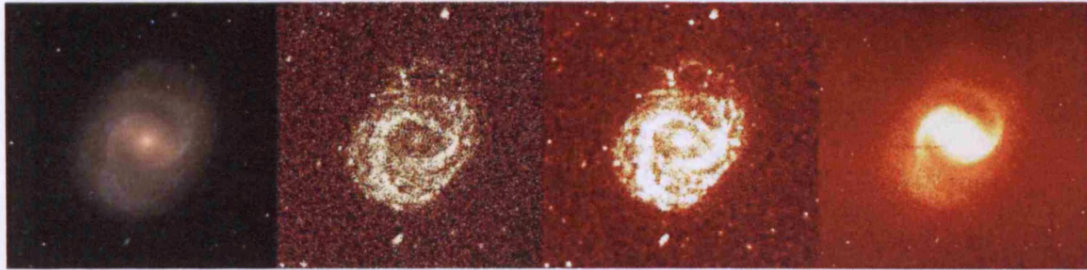


Figure 6.2: *From left to right:* NGC 4548 as observed in the SDSS (composite g , r and i) bands, in the FUV and NUV GALEX bands and in the H band. Note that this figure is to illustrate the galaxy at different wavelengths, as such the alignment is approximate and not to the accuracy of the procedure outlined in Section 6.3.

Background subtraction

The background sky emission is then subtracted from all the images. Rectangular background regions are selected using the MARKSKY task, a custom script for the IRAF environment. Another custom script called SKYFIT then calculates the mean of the background regions and subtracts this value from the image.

Resolution matching

The last step before extracting the surface brightness profiles is to match the resolution of all the images. This is achieved by reducing the image resolution to that of the lowest observed resolution. In this case, the H band images typically had the highest resolution ($\sim 1.5''$) compared to the GALEX UV observations ($4.2(5.3)''$ for the FUV(NUV) bands; Morrissey et al., 2007), so the resolution of the H band images is lowered. The H band images are therefore convolved with a Gaussian profile with a full width half maximum (FWHM) given by

$$FWHM = \sqrt{PSF(UV)^2 - PSF(H)^2} \quad (6.1)$$

to rescale the resolution to match the UV images. The IRAF GAUSS task performs the convolution. The results of the convolution are checked by comparing the PSF of stars coincident in the H and UV band images and found to be consistent within 15%.

Profile extraction

Once the images are aligned, background-subtracted and then rescaled to the resolution of the lowest resolution observation, the surface brightness profiles are extracted for each set of images. The CPHOT task, a custom task written by L. Cortese, fitted ellipses of increasing diameter to the image by utilising the ELLIPSE task in the IRAF package. The center of the ellipses are determined by taking the maximum of the light distribution of the galaxy as the center, and this central position is fixed throughout the fitting procedure. The ellipticity and position angles are also fixed parameters and are initially determined based on the overall shape of the distribution of the NUV band emission. The axial ratios of the ellipses are kept constant. For each set of observations, the fitted ellipse parameters are determined from the H band image and then applied to the FUV and NUV band images to get radially integrated surface brightness profiles for each band. Thus, all the ellipse parameters are fixed during the fitting. The outer ellipse used in this work is either the aperture fixed by visual inspection of the NUV image or when the signal-to-noise ratio approached 1, depending on which boundary condition is reached first.

I briefly tested whether this approach produces surface brightness profiles that accurately represent the surface brightness distribution, compared to if the ellipse parameters are allowed to vary. Using ellipses fitted with varying parameters, I found that the profiles obtained from using fixed and free ellipse parameters show very little difference. Thus, for the purposes of this pilot study, it is sufficient to keep the parameters fixed.

Before fitting the ellipses, stars within the outer ellipse are masked. The CPHOT task then fits the ellipses and computes the surface brightness within each ellipse. Figure 6.3 shows the outer ellipses used for the H, NUV and FUV band observations of VCC1615, together with the extracted surface brightness profiles. The UV surface brightness profiles are compared with the profiles presented in the GALEX Ultraviolet Atlas of Nearby Galaxies (Gil de Paz et al., 2007). The sample includes the vast majority of the massive late-types in the VCC sample and the UV profiles are available online¹. From a visual inspection of the surface brightness profiles and the corresponding apertures, it appeared that both the profiles and apertures of this work are similar to those of Gil de Paz et al. (2007), although no quantitative comparison of the two sets of profiles is possible. The error in the surface brightness measurements are typically $0.1 \text{ mag arcsec}^{-2}$, although the errors for outer measurements show

¹The FUV and NUV surface brightness and colour profiles for the GALEX Ultraviolet Atlas of Nearby Galaxies are available online at http://nedwww.ipac.caltech.edu/level5/GALEX_Atlas/Gildepaz_fig3.html.

increased uncertainty.

To statistically compare the surface brightness profiles of all 54 galaxies, the profiles are normalised to the scale length of the disk, determined from the H band profile. The surface brightness profiles of the disk are well approximated by

$$\Sigma(r) = \Sigma_0 \exp\left(-\frac{r}{r_s}\right) \quad (6.2)$$

where Σ_0 is the central surface brightness of the disk in units of $M_\odot \text{ pc}^{-2}$ and r_s is the scale length (Sersic, 1968). Expressing the surface brightness in terms of logarithmic units, where $\mu_0 = -2.5 \log_{10} \Sigma_0$, then

$$\mu = \mu_0 - 1.086\left(\frac{r}{r_s}\right) \quad (6.3)$$

Thus, performing a linear least squares fit to the extracted profiles yields the scale length, since the gradient of the linear fit $m \equiv 1.086/r_s$. The dashed line in the H band surface brightness profile in Figure 6.3 demonstrates a typical fit to the disk, which avoids the central bulge component and instead fits to the outer exponential disk.

Finally, the surface brightness profiles are used to create NUV-H and, where possible, FUV-H colour profiles by simply subtracting the profiles. The surface brightness profiles and colour profiles for 54 galaxies are presented in Appendix D.

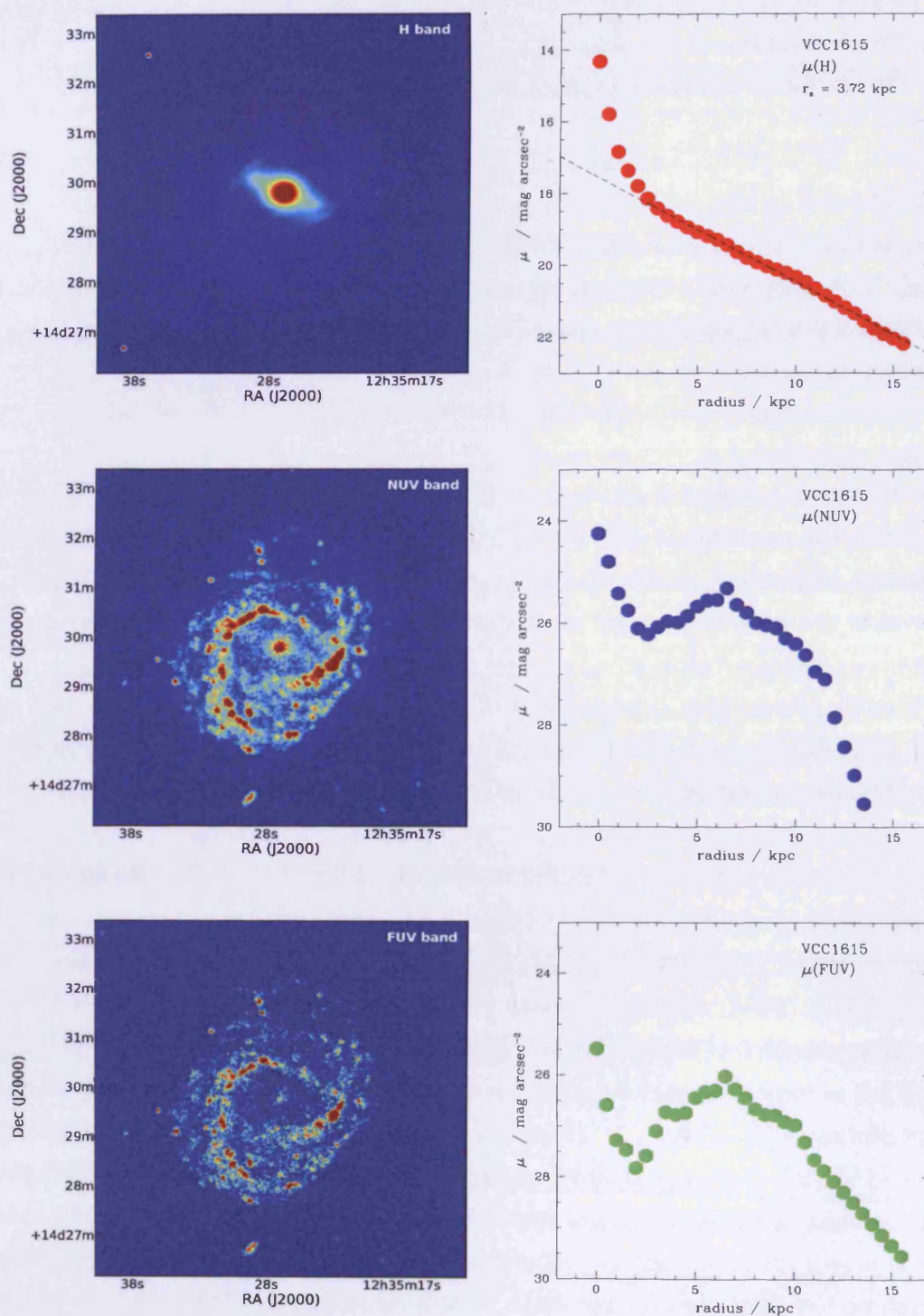


Figure 6.3: Aligned and scaled multiwavelength observations of VCC1615 (*left panels*) illustrating the radial surface brightness profiles (*right panels*). The H, NUV and FUV bands are shown in the top, middle and center panels, respectively.

6.4 ULTRAVIOLET-INFRARED COLOUR PROFILES

I now test the hypothesis that the signatures of environmental effects, such as ram pressure stripping, or AGN feedback may be observed in the UV-H colour profiles obtained in the previous section. I divide the 54 galaxies into three different subsamples based on their integrated NUV-H colours, in a similar fashion to the previous chapter; galaxies with $\text{NUV-H} < 4.5$ are designated as residing on the blue cloud, whilst the red sequence lies at $\text{NUV-H} \geq 6$ and the transition region lies between the two sequences (i.e. $4.5 \leq \text{NUV-H} < 6$). Average profiles were determined based on the galaxies inhabiting these three different colour regions, in an initial attempt to determine any systematic differences in the shapes of the colour profiles. The top row panels of Figure 6.4 present the results of this exercise. It is immediately evident that no significant variations exist in the shapes of the average profiles. Any small differences from the average profiles either arise from a low number of profiles in each radial bin or are much smaller than the typical error bars associated with the points under scrutiny.

The lack of variation in the shapes of the average colour profiles for the total sample may indicate that such an approach may be inconclusive, since such variations may be subtle and the effects of reddening from either the environment or internal processes are removed during the averaging process. However, individual profiles and subsequently the averaged profiles in the three different colour bins do appear to decrease in radial extension with progressively redder NUV-H colours. This indicates that the NUV profile becomes truncated compared to the H band as star formation is quenched, a prediction of the effect by the environment. Since the truncation of star formation activity in the outskirts of a galaxy has been linked with the loss of gas from the disk (e.g. Boselli et al., 2006; Boselli & Gavazzi, 2006), the average profiles for the HI deficient galaxies present in the sample may be different compared to the total sample.

When comparing the profiles of HI deficient galaxies or objects classified as AGN-host galaxies, both sets of results tend to show no significant variation in shape between the average profiles of the different colour bins. However, the profiles show the same decrease in radius of the NUV profile as seen in the average profiles derived from the total sample (if the last points of the average red sequence profile are excluded, since they are derived from one extensive profile). Thus it appears that there may be some evidence supporting the truncation of star formation activity in the outskirts of the disk.

The average profiles from Figure 6.4 are compared in Figure 6.5. From this

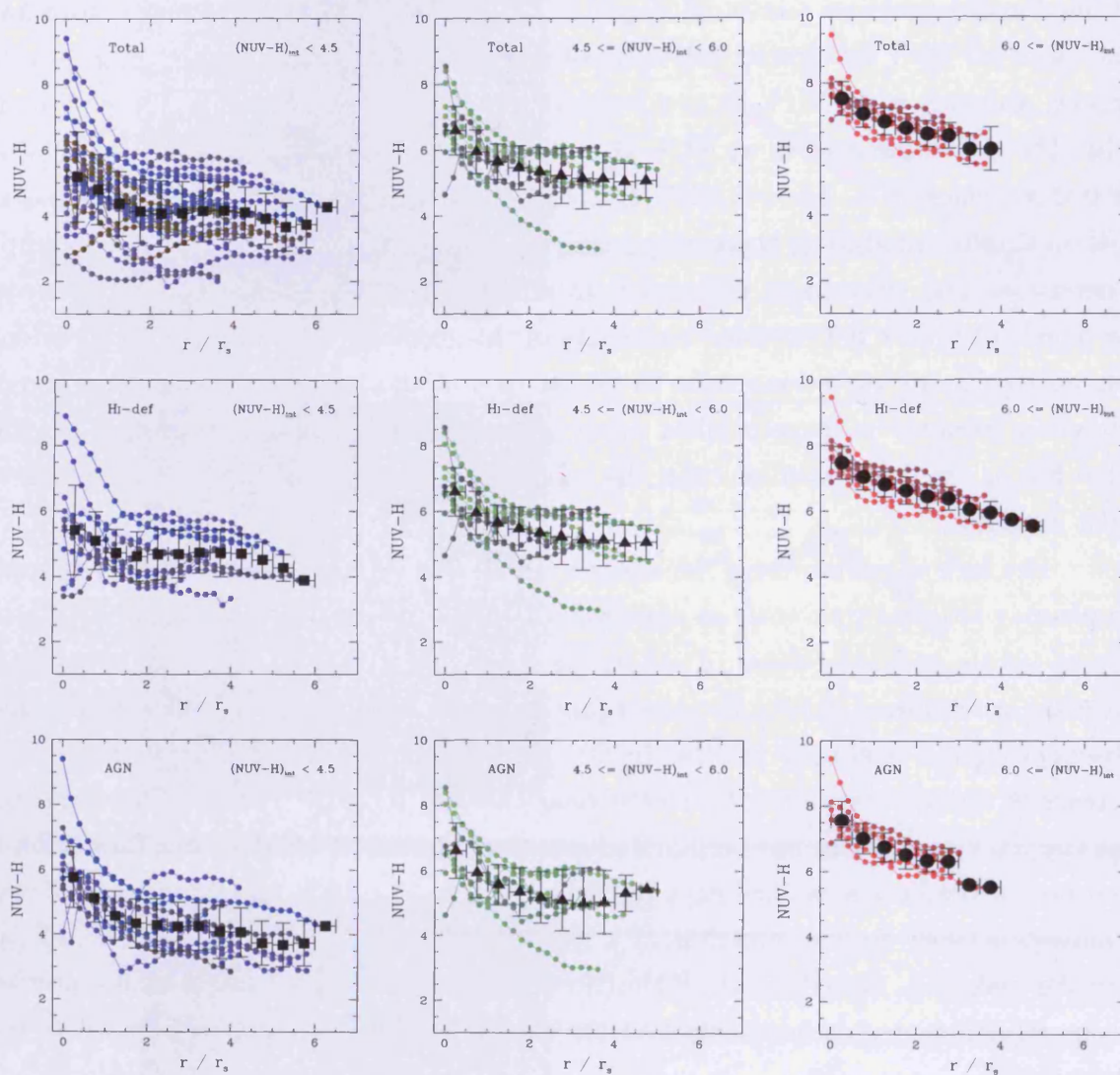


Figure 6.4: Radial NUV-H colour profiles divided according to the integrated NUV-H colour (coloured circles), for the blue cloud ($\text{NUV-H} < 4.5$; *left column*), the transition region ($4.5 \leq \text{NUV-H} < 6$; *middle column*) and the red sequence ($\text{NUV-H} \geq 6$; *right column*). The binned profiles for the total sample of 54 galaxies (*top row*) are compared to the binned profiles for HI deficient galaxies (*middle row*) and galaxies displaying AGN-like behavior (*bottom row*). The average profile for each colour bin is shown in each plot (black symbols).

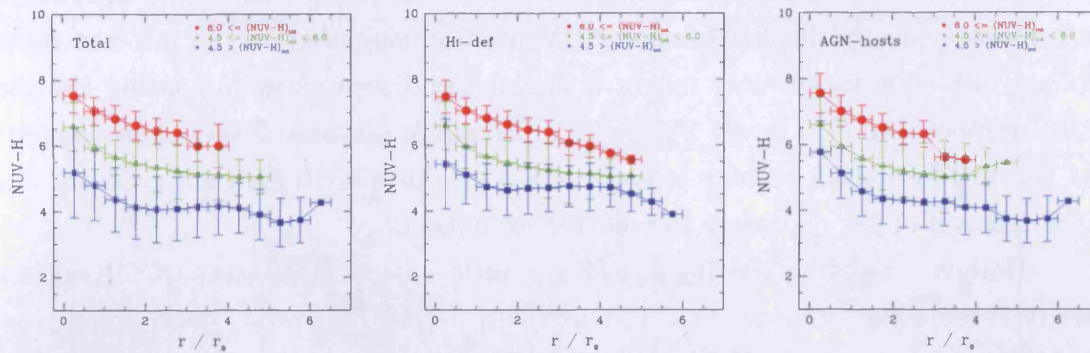


Figure 6.5: The average radial NUV-H colour profiles of the total sample (*left panel*), HI deficient galaxies (*middle panel*) and AGN-host galaxies (*right panel*), divided according to the integrated NUV-H colour (coloured symbols).

figure, it is clearly evident that the average profiles are fairly consistent between the AGN-host galaxies and the HI deficient galaxies and do not yield any significant variation from the average profiles obtained with the total sample of 54 galaxies.

6.5 VARIATION IN ISOPHOTAL RADII

The extent of the average profiles shown in Figure 6.5 appear to decrease with increasing colour for both AGN host galaxies and the HI deficient objects. Since a truncation of the star formation, hence a truncation of the NUV surface brightness profile, may be expected, I adopted an alternative method of comparing the NUV and H band profiles for the AGN-host and HI deficient galaxies.

An alternative approach may be to seek variations in the isophotal radii of the surface brightness profiles, since these may give an indication of the effect of the environment. I define the radius $R_{26,NUV}$ as the NUV band isophote at $\mu = 26$ mag arcsec $^{-2}$ and the radius $R_{20,H}$ as the H band isophote at $\mu = 20$ mag arcsec $^{-2}$. Thus, the ratio $R_{26,NUV}/R_{20,H}$ can be used to compare the extent of star formation compared to the stellar disk and indicate the possible ‘truncation’ in the profiles due to environmental effects, such as ram pressure stripping. In Figure 6.6, the $R_{26,NUV}/R_{20,H}$ is compared to the HI deficiency for the 54 galaxies. A correlation between the two quantities is evident, with a Spearman coefficient of $r_s = -0.63$, relating to a probability $P(r_s) > 99.9\%$. This anticorrelation suggests that galaxies with normal gas content tend to have more extensive NUV band profiles compared to the H band profiles and, conversely, HI deficient galaxies are likely to have ‘truncated’ NUV profiles compared to the H band profiles. This is a new result, since it has not

been previously shown statistically that cluster late-type galaxies with a reduced gas content typically display smaller NUV profiles compared to the infrared radii, although this observation does mirror a similar trend seen when comparing $H\alpha$ and optical isophotal radii (i.e. see Figure 11 in Boselli & Gavazzi, 2006). This suggests that the star formation activity is lower in the outskirts of HI deficient galaxies, due to the removal of gas necessary to fuel star formation.

However, plotting the $R_{26,NUV}/R_{20,H}$ ratio against a measure of the nuclear activity reveals the same result. The $\log([\text{NII}] \lambda 6584/H\alpha)$ ratio, determined from spectroscopic observations (as described in Chapter 4), can be used to classify the nuclear activity of a galaxy. Under the Decarli et al. (2007) scheme for classifying nuclear activity, galaxies with $\log([\text{NII}] \lambda 6584/H\alpha) > -0.4$ are classified as displaying AGN-like behaviour (see Section 2.4.3). Figure 6.6 also presents the $R_{26,NUV}/R_{20,H}$ ratio plotted against the $\log([\text{NII}]/H\alpha)$ ratio. A correlation between the two quantities is evident, with a Spearman coefficient of $r_s = -0.62$, relating to a probability $P(r_s) > 99.0\%$. The plot could be interpreted that AGN-host galaxies tend to have smaller star forming disks than the normal spiral galaxies. However, as it was demonstrated in Chapter 5, most massive galaxies tend to host AGN. Whilst the fraction of AGN-host spirals peaks in the transition region, I showed that at fixed stellar mass, AGNs are not associated with a systematic decrease in the star formation activity whereas HI deficient galaxies are redder than gas-rich systems. Thus, it is likely that the relationship demonstrated in Figure 6.6 is actually driven by the HI deficient objects and that the AGN-hosts are typically found in these massive galaxies (Kauffmann et al., 2003). This is most probable, given that the $\log([\text{NII}]/H\alpha)$ ratio and the HI deficiency are both equivalently correlated with the $R_{26,NUV}/R_{20,H}$ ratio. The relation really suggests that the UV emission, hence star formation, is gradually reduced in truncated disks, which is consistent with star formation truncated by the environment.

6.6 CONCLUSIONS

In this chapter, I present a method for using the differential NUV-H colour profiles, to discriminate between the impact on star formation from the effects of the environment and from internal processes such as AGN feedback. This hypothesis was tested by obtaining surface brightness profiles and colour profiles for 54 galaxies from the VCC sample. Although the sample was incomplete, I attempted to analyse the differences in the shapes of the average profiles for different bins of NUV-H colour, which reflected whether galaxies resided on the blue cloud, red sequence or the transition region, as defined in Chapter 5.

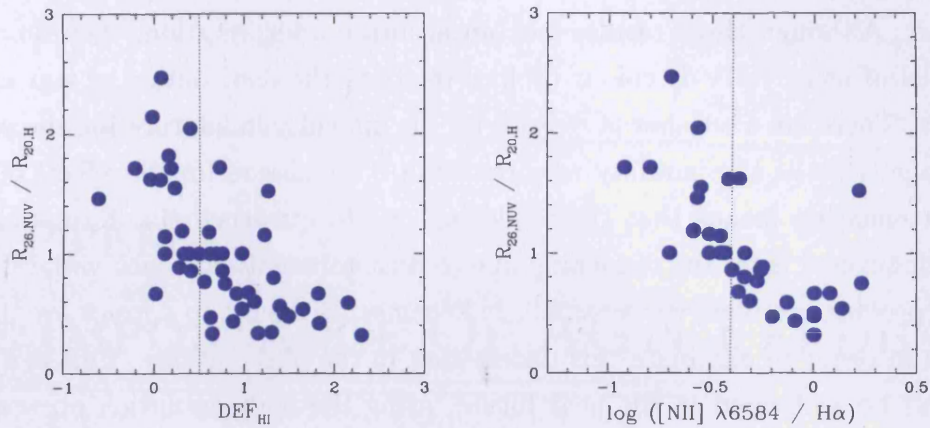


Figure 6.6: *Left panel:* The $R_{26,NUV}/R_{20,H}$ ratio plotted against the HI deficiency. The $DEF_{HI} > 0.5$ limit for dividing HI deficient from HI normal galaxies is shown (dashed line). *Right panel:* The $R_{26,NUV}/R_{20,H}$ ratio plotted against $\log([\text{NII}]/\text{H}\alpha)$, where galaxies with $\log([\text{NII}]/\text{H}\alpha) > -0.4$ are classified as AGN-hosts (dashed line).

I found that the radial extent of the average colour profiles decreased significantly with increasing NUV-H colour, indicating that systems with quenched star formation inhabiting the transition region and red sequence also have smaller star-forming disks than their counterparts still residing on the blue cloud. After defining isophotal radii in the NUV and H bands, an anticorrelation is observed between the gas content and the extent of the NUV band profiles compared to the H band profiles. Galaxies with normal atomic hydrogen content typically display more extensive NUV profiles than galaxies which have had a large fraction of their gas content removed. This is the first time it has been demonstrated statistically that cluster late-type galaxies with a reduced gas content typically display smaller NUV profiles compared to infrared isophotal radii. This result mirrors a similar trend seen when comparing $\text{H}\alpha$ and optical isophotal radii (i.e. see Figure 11 in Boselli & Gavazzi, 2006) and has been shown for individual galaxies (Koopmann et al., 2006). Combining these observations, this suggests that the quenching of star formation is typically due to environmental effects (e.g. ram pressure stripping) modifying the gas content in the outskirts of galaxies, truncating the gas disk and removing the fuel for the star formation process.

Apart from the radial extension of the colour profiles, no significant variations in the shapes of some of the colour profiles were observed. Rather than use the statistical approach to study variations in the colour profiles used here, I conclude

that it would be more constructive to first understand the colour profiles of individual galaxies. Although these results lack an accurate interpretation, they do show the potential of using NUV-H colour profiles to study the distribution of star formation in disks. There are a number of reasons for the difficulty in interpreting the profiles at this stage. Firstly, the inability to correct the UV emission for the effects of internal dust attenuation means that the reddening due to quenched star formation cannot be distinguished from the reddening due to dust attenuation. Since variations in the colour profiles are likely to be small, it becomes necessary to correct for the effects of dust in order to eliminate this uncertainty in the observations. This is a problem that can be addressed in the near future, using the high resolution observations of the Herschel Space Telescope to study the radial dust properties of the galaxies in the HRS sample. Secondly, it was apparent that without modelling the effects of either ram pressure stripping or AGN feedback on the colour profiles, it is not possible to gain a measure of the significance of these results. The individual profiles clearly show differences in the shape of their colour profiles and understanding the underlying nature of these variations can only be properly tested by reproducing the observed profiles using models. This is also necessary due to the possibility that multiple mechanisms are influencing the star formation in the disk at the same time, thus disentangling these mechanisms will pose a problem.

Thus, this pilot study highlights the need to properly correct radial UV profiles for dust attenuation and that theoretical modelling of the effects of ram pressure stripping and AGN feedback on the colour profiles of disks is necessary to obtain any additional insight. However, whilst this pilot study was unsuccessful at thoroughly testing the initial hypothesis and understanding the shapes of the colour profiles, it does raise an interesting question. The overall effect of ram pressure stripping on star-forming disks has been modelled by a number of different studies (see e.g. Kronberger et al., 2008; Kapferer et al., 2009; Vollmer, 2009). On the other hand, the theoretical predictions of the impact of AGN feedback on star formation in disk galaxies is not clear (Okamoto et al., 2008), meaning that the uncertainty of the effects of AGN feedback is not limited to the understanding of the colour profiles, but extends to all the properties of late-type galaxies. Indeed, it is even questionable whether the central engines in the nuclei of late-types are even powerful enough to affect the entire disk. Therefore, in the next chapter I shall investigate the predictions of current theoretical models for the evolution of late-type AGN-host galaxies.

CHAPTER 7

THE IMPORTANCE OF AGN FEEDBACK

7.1 INTRODUCTION

Several recent studies have claimed that a large fraction of galaxies in the transition region between the red and the blue sequence are in fact AGN-hosts. It has been proposed that the correlation between nuclear activity and colour suggests that AGN feedback is responsible for the quenching of star formation (e.g. Nandra et al., 2007; Schawinski et al., 2007). In Chapter 5, however, I demonstrated that the various evolutionary paths likely followed by galaxies residing in the transition region are typically governed in part by the effects of the environment, despite the majority of massive galaxies in the transition region playing host to active nuclei. There is no indication, nor requirement, that AGN feedback should to be invoked in order to explain the observed properties of the transition region galaxies.

This conclusion apparently contradicts previous observations linking the central supermassive black hole to the evolution of the host galaxy. Firstly, the discovery of a connection between the mass of the central black hole with both the spheroidal mass of a galaxy (Magorrian et al., 1998; Merritt & Ferrarese, 2001; Marconi & Hunt, 2003) and the stellar velocity dispersion in bulges (see e.g. Ferrarese & Merritt, 2000) suggests that the properties of AGN are fundamentally linked to the formation and evolution of the host galaxy. The more recent observation of a connection between the X-ray emission from an AGN and the HI distribution of the host galaxy, NGC 4151, provides additional support towards for a scenario in which AGN feedback quenches star formation by modifying the gas properties in individual galaxies (Wang et al., 2010). Moreover, AGN feedback has become ever more important in semi-analytic models of galaxy formation, since the process can decrease the bright end of the galaxy luminosity function in the population (Bower et al., 2006; Croton et al., 2006)

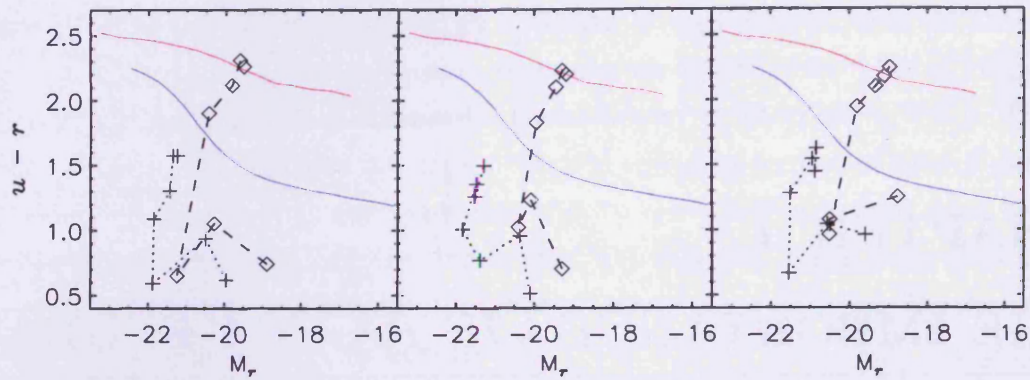


Figure 7.1: Colour-magnitude diagrams for model disk galaxies without feedback from an active nucleus (*left*), with weak feedback (*middle*), and with strong feedback (*right*). The galaxies at $z = 3, 2, 1.5, 1, 0.5, 0.2$ and 0 are indicated by the plus signs connected by the dotted line. The colours of their spheroidal components are also indicated by the diamonds. The upper and lower thin solid lines represent mean colours of the red and blue populations taken from Baldry et al. (2004). This figure is taken from Okamoto et al. (2008), where details of the models may be found.

and even provide sufficient energy to create radio cavities that can limit gas cooling flows in clusters (Dalla Vecchia et al., 2004; Sijacki & Springel, 2006). AGN feedback thus provides an improved match between the observations and the current theory of galaxy evolution.

Despite these advancements in our understanding of AGN feedback, theoretical studies incorporating the feedback are typically based around early-type, bulge-dominated galaxies since they generally host normal, bright AGN and feedback is the most plausible mechanism for stopping star formation in elliptical galaxies. The role of AGN in the evolution of late-type, spiral galaxies has been overlooked, even though most spirals are thought to contain supermassive black holes, typically displaying Seyfert nuclei or LINERs. The recent theoretical study by Okamoto et al. (2008) focusses on the formation of AGN-host disk galaxies and they investigate the resulting co-evolution of the AGN and the host galaxy. Comparing the impact of the active nucleus on the host galaxy, they find that AGN feedback has only minor effects on the observed colours of disk galaxies (see Figure 7.1) and find no significant difference in the evolution of simulated disk galaxies with and without feedback.

Therefore, to understand the apparent contradiction in the results, it is important to understand the relationship between the active nucleus and the host galaxy as predicted from current models. In this chapter, I attempt to clarify the role of AGN in late-type galaxies, from the viewpoint of a simple toy model representing the

currently accepted ideas of AGN feedback in the literature. The aim of this work is to quantify the impact of AGN feedback on star formation and hence determine whether the transition region spirals contain AGN powerful enough to quench star formation. I tackle this problem by first developing the simple model, and then comparing the theoretical relationship between the star formation rate and the power of the AGN with the observed values.

7.2 MODELLING NUCLEAR ACTIVITY

The aim of this model is to predict the impact of AGN on the star formation rate in spiral galaxies. This model is based on different elements from the semi-analytic models of Mo et al. (1998), Croton et al. (2006) and Somerville et al. (2008). The various underlying assumptions are discussed throughout, but the overall philosophy is to keep the model and assumptions as simple as possible, whilst still retaining the accurate predictions. However, one of the main assumptions adopted in this model is that the galaxy evolves according to a closed box with no environmental influences. Whilst the theory involved in this section is deeply rooted in the literature, current state-of-the-art models use N-body simulations to populate a universe with dark matter halos, which grow via mergers with neighbouring halos. This is not possible in this work. Instead, I use an analytical approach to study galaxies embedded in virialized dark matter halos of varying mass. The baryonic component, which is a fraction of the galaxy halo mass, cools to form a gas disk. Energy radiated from gas accretion onto a central supermassive black hole heats the cooling gas and prevents condensation.

7.2.1 FORMATION & GAS COOLING

Galaxy formation is a two stage process; dark matter halos form through dissipationless hierarchical clustering and the cooling of gas occurs in the halo interior. The first step in constructing a model galaxy is to specify the properties of the dark matter halo in which the observable baryons condense. Following the model of Mo et al. (1998) and Croton et al. (2006), a dark matter halo with mass, M_{halo} , and velocity dispersion, v_{vir} , are related to a limiting radius for the halo

$$r_{200} = \frac{v_{vir}}{10H(z)} \quad ; \quad M_{halo} = \frac{v_{vir}^2 r_{200}}{G} = \frac{v_{vir}^3}{10GH(z)} \quad (7.1)$$

where r_{200} is defined as the radius containing a mean mass density of 200 times the critical density, and $H(z) = H_0 = 70 \text{ km s}^{-1} \text{ Mpc}^{-1}$ in the local universe.

The cooling of the gas within the halo is a fundamental process for galaxy formation, as it governs the rate at which gas becomes available to fuel star formation. The gas is assumed to be shock heated during relaxation following the collapse, up to the virial temperature of the halo, T_{vir} , given by:

$$T_{vir} = \frac{1}{2} \frac{\mu m_H}{k_B} v_{vir}^2 = 35.9 [v_{vir} (\text{km s}^{-1})]^2 \text{ K} \quad (7.2)$$

where μ is the mean molecular mass of the gas, m_H is the mass of a hydrogen atom and k_B is the Boltzmann constant.

The gas cooling rate depends upon this temperature, which determines its ionization state, and on the metallicity of the gas. Figure 7.2 shows the relationship between the cooling rate and the temperature for three example metallicities as calculated by Sutherland & Dopita (1993). For this toy model, I assume a fixed temperature and metallicity, and adopt a constant cooling rate of the order 10^{-22} erg $\text{cm}^3 \text{ s}^{-1}$, taken as an estimate from Sutherland & Dopita (1993). As I show later, this rough approximation is able to predict the mean observed relationship between specific star formation rate and stellar mass, and is sufficient for the aims of this model. The cooling time is defined as the thermal energy density divided by the cooling rate per unit volume:

$$t_{cool} = \frac{\frac{3}{2} \mu m_p k_B T_{vir}}{\rho(r) \Lambda(T, Z)} \quad (7.3)$$

where $\Lambda(T, Z)$ is the cooling rate of the gas and $\rho(r)$ is the gas density profile.

The gas density profile, $\rho(r)$, is obtained by considering a singular isothermal sphere (SIS) in hydrostatic equilibrium

$$\frac{\delta}{\delta r} \left(\frac{r^2 \delta \rho}{\rho \delta r} \right) = -4\pi \frac{GM}{k_B T} \rho r^2 \quad (7.4)$$

which has the solution of

$$\rho(r) = \frac{v_{vir}^2}{2\pi G r^2} \quad (7.5)$$

For this model I use the above SIS density solution, but it should be noted that a Navarro, Frenk & White (1996) profile is more commonly used and will be the subject of future study. A cooling radius, r_{cool} , can now be defined as the point where the local cooling time is equal to the dynamical time of the halo. Substituting the SIS profile into Equation 7.3, the radius within which all the gas cools within a given

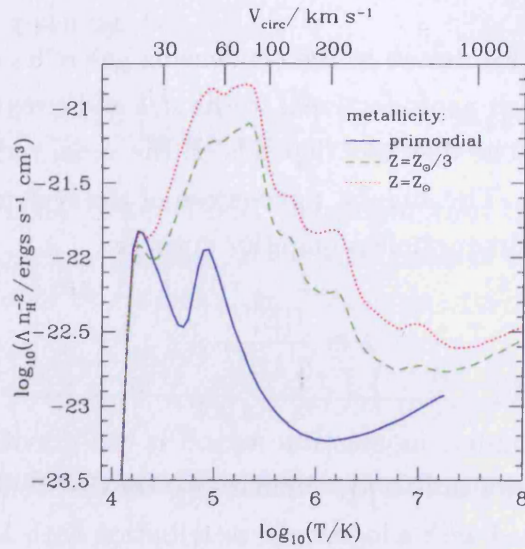


Figure 7.2: The cooling rate $\Lambda(T, Z)$ plotted as a function of the virial temperature of the hot halo gas T_{vir} , with different curves illustrating the dependence upon the metallicity of the gas. The equivalent circular velocity of the halo is indicated on the top axis. This figure, taken from Baugh (2006), uses the results of Sutherland & Dopita (1993).

cooling time becomes

$$r_{cool} = \left[\frac{m_{hot} t_{cool} \Lambda(T, Z)}{6\pi\mu m_p k_B T_{vir}} \right]^{1/2} \quad (7.6)$$

Different models use different values for t_{cool} , either the Hubble time (t_H ; Kauffmann et al., 1993), the time since the last merger (t_{mrg} ; Somerville & Primack, 1999) or the halo dynamical time (t_{dyn} ; Croton et al., 2006). The cooling time is an important assumption, because $t_{dyn} < t_{mrg} < t_H$ and shorter cooling times lead to faster cooling rates, as shown below in Equation 7.8. I adopt the halo dynamical time,

$$t_{dyn} = r_{vir} / v_{vir}. \quad (7.7)$$

The expression for the mass within this cooling radius can be differentiated to give \dot{m}_{cool} , the rate at which gas cools

$$\dot{m}_{cool} = 0.5 m_{hot} \frac{r_{cool}}{r_{vir}} \frac{1}{t_{cool}} \quad (7.8)$$

7.2.2 DISK SIZES

The rate of star formation in the condensing gas relies on the dynamical time of the gaseous disk, which is proportional to the size and circular velocity of the disk, which I now consider. The disk size depends on the virial radius of the halo and on its angular momentum. The angular momentum of the system is often quantified by the spin parameter, a dimensionless quantity given by

$$\lambda \equiv \frac{J|E|^{1/2}}{GM_{halo}^{5/2}}, \quad (7.9)$$

where J is the total angular momentum and E is the gravitational binding energy (Peebles, 1969). As shown in N-body simulations, the distribution of the spin parameter can be approximated with a lognormal distribution with $\bar{\lambda} = 0.05$ and $\sigma(\lambda) = 0.5$ (Cole & Lacey, 1996; Bullock et al., 2001). I adopt the mean value for λ . The disc radius may be related to the spin parameter and virial radius by assuming that the angular momentum of the disc is a fixed fraction of the angular momentum of the halo,

$$r_{disk} = \frac{1}{\sqrt{2}} \left(\frac{j_d}{m_d} \right) \lambda r_{vir} \quad (7.10)$$

where m_d is the ratio between the disk mass and halo mass, and j_d is the ratio between the angular momentum of the disc and the halo. This is valid for halos with an isothermal profile, which is another motivation for using the SIS gas density profile. Mo et al. (1998) make the further assumption that the two ratios m_d and j_d are equivalent, meaning that galaxies are an order of magnitude smaller than their haloes.

Finally, I further assume that the self-gravity of the disk is negligible, hence the circular velocity is equal to the virial velocity. From these assumptions, I can then determine the disk dynamical timescale, $t_{disk} = r_{disk}/v_{vir}$.

7.2.3 STAR FORMATION

I adopt a model for star formation based on the Croton et al. (2006) prescription. I begin with the assumption that the star formation rate is proportional to the mass of cold gas in the disk, which provides the fuel for star formation, and inversely proportional to the time-scale of star formation, the dynamical time of the disk. There is a critical surface density above which star formation can occur, but

below this threshold no stars are allowed to form. The critical surface density at a radial distance of R is given by

$$\Sigma_{crit}(R) = 120 \left(\frac{v_{vir}}{200 \text{ km s}^{-1}} \right) \left(\frac{R}{\text{kpc}} \right) M_{\odot} \text{ pc}^{-2} \quad (7.11)$$

in a study by (Kauffmann, 1996). Under the assumption that this cold gas is uniformly distributed throughout the disk, the critical mass of cold gas required for star formation is

$$m_{crit} = 3.8 \times 10^9 \left(\frac{v_{vir}}{200 \text{ km s}^{-1}} \right) \left(\frac{r_{disk}}{10 \text{ kpc}} \right) M_{\odot} \quad (7.12)$$

The star formation rate is then governed by

$$\dot{m}_{*} = \alpha_{SF} (m_{cold} - m_{crit}) / t_{disk} \quad (7.13)$$

where the star formation efficiency is initially set at $\alpha_{SF} = 10\%$ and the disk dynamical timescale is $t_{disk} = r_{disk} / v_{vir}$.

7.2.4 AGN FEEDBACK

Cooling gas is accreted onto a central supermassive black hole and converted into energy. The energy radiated from the AGN then heats the gas, reducing the rate that the gas can cool and limiting star formation. The energy output couples to the gas and heats it at a rate, \dot{m}_{heat} , given by

$$\dot{m}_{heat} = \frac{L_{bol}}{\frac{3}{2} [v_{vir} (\text{km s}^{-1})]^2} \quad (7.14)$$

so that the net cooling flow becomes

$$\dot{m}_{net} = \dot{m}_{cool} - \dot{m}_{heat}, \quad (7.15)$$

which is the standard method used in the literature for suppressing gas cooling using AGN feedback (see Croton et al., 2006; Bower et al., 2006; Somerville et al., 2008).

Theoretically, the bolometric luminosity of the AGN, L_{bol} , can be calculated by assuming Bondi (1952) accretion onto the black hole and a mass accretion rate. The accretion rate and hence the AGN power is governed by the mass of the black hole, so it is necessary to determine the black hole mass M_{bh} . In the semi-analytic models embedded in N-body simulations, the black hole masses grow during the accretion

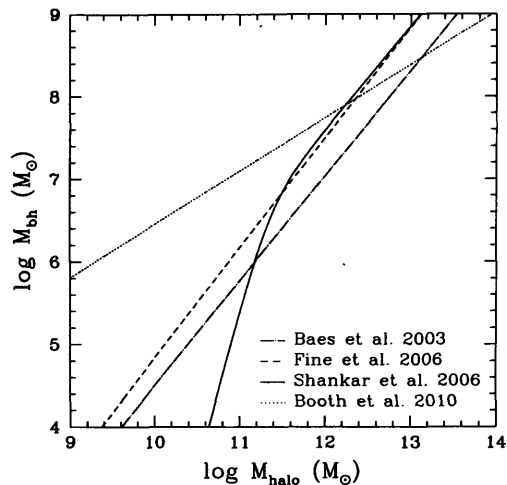


Figure 7.3: The M_{halo} - M_{bh} relationship reported by four examples in the literature, demonstrating the discrepancies between the different studies.

of material and via mergers as the simulated universe evolves. Since I do not have the resources to replicate such simulations, I instead estimate the black hole mass from the halo mass. In the last decade, many studies have attempted to constrain the observed M_{halo} - M_{bh} relation, both observationally (e.g. Baes et al., 2003; Fine et al., 2006; Shankar et al., 2006) and theoretically (e.g. Booth & Schaye, 2010), with varying results (see Figure 7.3). I adopt the observed relationship of Fine et al. (2006), as they report the lowest scatter for their relation. Thus, I assume the relationship between the halo mass and the black hole mass follows

$$\log \frac{M_{bh}}{M_{\odot}} = -8.5 + \frac{4}{3} \log \frac{M_{halo}}{M_{\odot}} \quad (7.16)$$

It then follows from Bondi accretion that the accretion rate, \dot{M}_{acc} , is proportional to the black hole mass via

$$\dot{M}_{acc} = \kappa_{radio} \left(\frac{M_{bh}}{10^8 M_{\odot}} \right) \left(\frac{v_{vir}}{200 \text{ km s}^{-1}} \right)^3 \quad (7.17)$$

where κ_{radio} is a constant with units of an accretion rate, $M_{\odot} \text{ yr}^{-1}$ (Somerville et al., 2008). Finally, the mass accreted onto the black hole is converted into energy such that

$$L_{bol} = \zeta \kappa_{heat} \dot{M}_{acc} c^2 \quad (7.18)$$

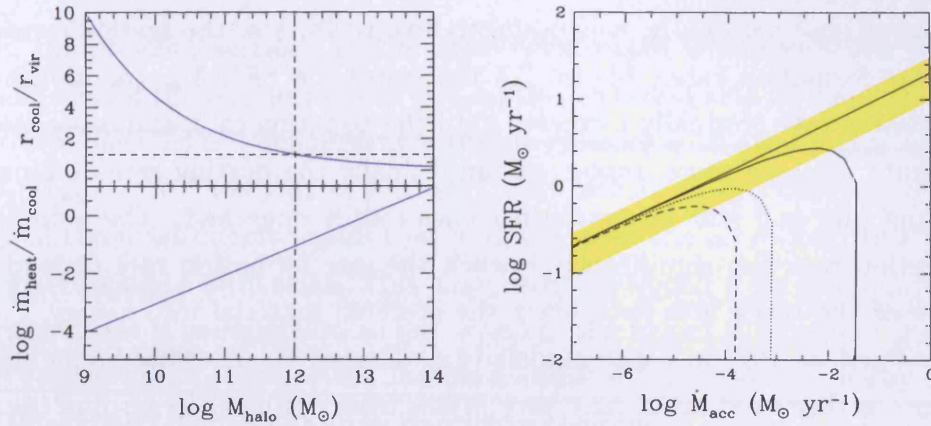


Figure 7.4: *Left*: A comparison of the $\dot{m}_{\text{heat}}/\dot{m}_{\text{cool}}$ ratio (*top panel*) to the $r_{\text{cool}}/r_{\text{vir}}$ ratio (*bottom panel*). The condition of $r_{\text{cool}} < r_{\text{vir}}$ is shown in both panels (dashed line), marking when the heating rate becomes important under the Somerville et al. (2008) prescription. *Right*: The model star formation rate as a function of the mass accretion rate, using accretion efficiencies of 1% (dashed line), 5% (dotted line) and 10% (solid line). The range of efficiency of star formation, $5\% < \alpha_{\text{SF}} < 15\%$ (shaded yellow region) is shown for the model without feedback.

where ζ is the efficiency of the conversion. This is initially adopted as 10% following Somerville et al. (2008) but, as discussed in Section 7.4.2, it is likely that this varies between bright AGN and less luminous, LINER-like systems. As such, I will later test scenarios for $\zeta = 0.01, 0.05$ and 0.1 . Combining Equations 7.16 to 7.18, it is possible to calculate the accretion rate and consequent luminosity of the AGN, which modifies the net amount of cold gas available for star formation according to Equation 7.15. The variable κ_{heat} is the coupling efficiency of the energy to the hot gas that, as an upper limit, is assumed to be 100%, which is standard practice in other models.

Figure 7.4 demonstrates how the importance of the heating rate \dot{m}_{heat} to the cooling rate \dot{m}_{cool} varies with the virial mass of the halo. The heating rate only becomes significant for halo masses $> 10^{12} M_{\odot}$. However, Somerville et al. (2008) define a distinction between gas accretion flows; when $r_{\text{cool}} < r_{\text{vir}}$ the cooling gas becomes shock heated to near T_{vir} and then cools, but when $r_{\text{cool}} > r_{\text{vir}}$ normal cooling flows occur. When $r_{\text{cool}} > r_{\text{vir}}$, it is assumed that gas is not susceptible to AGN heating and cools at the normal rate, setting Equation 7.14 to zero. A comparison of the two radii is shown in Figure 7.4 and it should be noted that (in the model) AGN feedback would only be ‘switched on’ for halos with mass $> 10^{12} M_{\odot}$ if this criteria is followed.

Since the accretion rate is directly proportional to the heating rate and can be estimated observationally, it is useful to investigate how the accretion rate relates to the star formation rate. Figure 7.4 illustrates the $\text{SFR}-\dot{M}_{acc}$ relationship. The star formation rate gradually increases until the accretion rate, and consequently the heating rate, become more important, until finally the heating rate dominates over the cooling rate and star formation becomes totally quenched. The point at which the accretion rate can significantly quench the star formation rate depends on the efficiency of the black hole to convert the accreted material into energy, ζ . This is typically fixed at 10% in other models (e.g. Croton et al., 2006; Somerville et al., 2008) but, as discussed later, may vary in low mass systems. Regarding the scenario when $\zeta = 0.1$, star formation becomes quenched in halos $> 10^{12} M_{\odot}$.

Thus, the results of this model seem to indicate that only in those halos with virial velocities $> 150 \text{ km s}^{-1}$ and massive halos $> 10^{12} M_{\odot}$ does the heating rate become significant compared to the cooling rate. However, the model has several limitations, as a number of different assumptions regarding the physical processes and properties have been adopted. The model should also be adjusted to take into consideration whether the AGN can reheat previously cooled gas, and thus not just prevent gas cooling. Presently, the work suggests that the heating effect from AGN is not enough to significantly modify the cooling rate, and subsequently the star formation rate, of less massive galaxies.

Finally, adopted values of parameters are summarised in Table 7.1.

Parameter	Description	Equation	Value	Plausible range	Ref.
$\Lambda(T,Z)$	Gas cooling function	7.3, 7.6	10^{-22}	$10^{-21}-10^{-24}$	(1)
λ	Halo spin parameter	7.12	0.05	0.0-0.2	(2)
α_{SF}	Star formation efficiency	7.13	0.10	0.05-0.15	(3)
κ_{radio}	Normalization of accretion rate	7.17	6×10^{-6}	-	(4)
ζ	Conversion efficiency of rest mass to energy	7.18	0.1	0.001-0.1	(3,4)
κ_{heat}	Coupling efficiency of energy with hot gas	7.18	1.0	-	(3,4)

Table 7.1: The values assumed for various parameters used in this model and the main equations in which they appear. References are (1) Sutherland & Dopita (1993); (2) Mo et al. (1998); (3) Somerville et al. (2008); and (4) Croton et al. (2006).

7.3 ESTIMATING NUCLEAR ACTIVITY

In the previous section, a model was constructed which was able to predict the dependence of the star formation rate on the accretion rate of material onto the supermassive black hole. I demonstrated that in galaxies with masses typical of spiral galaxies ($M_{halo} < 10^{12} M_{\odot}$, $M_{*} < 10^{10} M_{\odot}$), star formation proceeds as normal and it is only in the most massive halos that feedback from the accretion can sufficiently prevent gas cooling to form stars. This model was developed from existing models in the literature, but it is important to test whether the model successfully predicts an observed relationship between AGN feedback and star formation in nearby spirals.

Developing reliable indicators to observe the central engine has been the subject of much research in the last two decades, due to the importance of understanding the nature of AGN, via the bolometric luminosity. The modern unified model of galactic nuclei envisages an optically thick torus of dusty material that surrounds the central engine, and it is the varying viewing angles between the observer and the nucleus that lead to the multitude of different classifications of nuclear activity (i.e. Seyfert 1 and 2, among others; see Figure 1.2). The viewing angle determines the line of sight through the torus and thus the amount of obscuration of photons emitted from the central engine. For high column densities (typically $N_H > 10^{25} \text{ cm}^{-2}$), even high energy X-rays are Compton-scattered, hence the central engine is fully obscured and it is not possible to directly determine the bolometric luminosity. As such, the luminosity of the [OIII] $\lambda 5007$ line (Heckman et al., 2004; Netzer et al., 2006), the [OIV] $25.89 \mu\text{m}$ line (Meléndez et al., 2008), the infrared continuum (Horst et al., 2006) and the 2-10 keV X-ray flux (Satyapal et al., 2005, hereafter S05) have all been proposed as indirect indicators for estimating the AGN power. In this work, I chose to use the $L_{[\text{OIII}]}$ indicator and describe the method for estimating L_{bol} in the following section.

7.3.1 THE [OIII] LUMINOSITY INDICATOR

I use the [OIII] $\lambda 5007$ emission line as a tracer of AGN activity, by inferring the bolometric luminosity of the AGN from the [OIII] luminosity. The [OIII] emission line arises in the narrow line region of the galactic nucleus, where the gas in this region is photoionised by continuum radiation escaping from the torus. Therefore, the observed emission line flux is not strongly affected by the viewing angle to the torus and so it provides an estimate of the nuclear bolometric luminosity, assuming the bolometric correction factor is reliably known.

This line was chosen for a number of reasons. Firstly, it is usually the strongest emission line in the optical spectra of type 2 AGNs and does not often become blended with neighbouring emission line features. Secondly, it is significantly less contaminated by a contribution from star-forming regions compared to other methods, although there has been some recent debate about whether it is necessary to apply a correction for star formation (e.g. see Lamastra et al., 2009). Finally, optical spectroscopy of the nuclear regions are available for a large fraction of the late types in my sample via the SDSS. I note that the drift-scan spectroscopy reduced in Chapter 4 is not adequate for the purposes here, since the drift-scan method provides the integrated spectral emission from across the entire extent of a galaxy, thus the emission lines will be dominated by emission from HII star-forming regions and gaseous nebulae. The spectroscopic observations of nuclear regions afforded by the SDSS may reliably measure the nuclear emission from the narrow line region, since the 3'' diameter fibers cover a small fraction of the surface area of nearby galaxies. At the distance of the Virgo cluster, the fiber aperture covers ~ 0.5 kpc compared to the typical diameter of a massive spiral being ~ 10 kpc. Thus spectra from fibers placed over the nucleus will be significantly less contaminated by star formation.

Therefore, measurements of the [OIII] emission line flux of the late-type galaxies in the HRS+ sample were obtained from the SDSS Data Release 7, only using spectra from fibers placed over the nuclear regions. For the AGN-host late-type galaxies with available star formation rates, spectra exist for a large fraction, although the observations are slightly biased towards brighter objects (Figure 7.5). The [OIII] luminosities span a range of $\sim 10^5$ to $\sim 10^8 L_{\odot}$, similar to the range reported for the samples of Heckman et al. (2004) and Lamastra et al. (2009).

A correction to the [OIII] luminosity is necessary for converting to the bolometric luminosity. Heckman et al. (2004) determined a bolometric correlation using a two step process based on a sample of type 1 and type 2 AGN. Firstly, they estimated a mean ratio between the continuum luminosity at 5000 Å and the [OIII] luminosity, and then determined the bolometric luminosity and the 5000 Å continuum luminosity from the average intrinsic spectral energy distribution of a type 1 AGN as reported by Marconi et al. (2004). From the results of their analysis, the ratios are $L_{5000}/L_{[OIII]} \approx 320$ and $L_{bol}/L_{5000} = 10.9$, such that the implied bolometric correction is therefore

$$L_{bol} \approx 3500L_{[OIII]} \quad (7.19)$$

and the variance in the correction is ~ 0.4 dex. In a more recent study, Wu (2009)

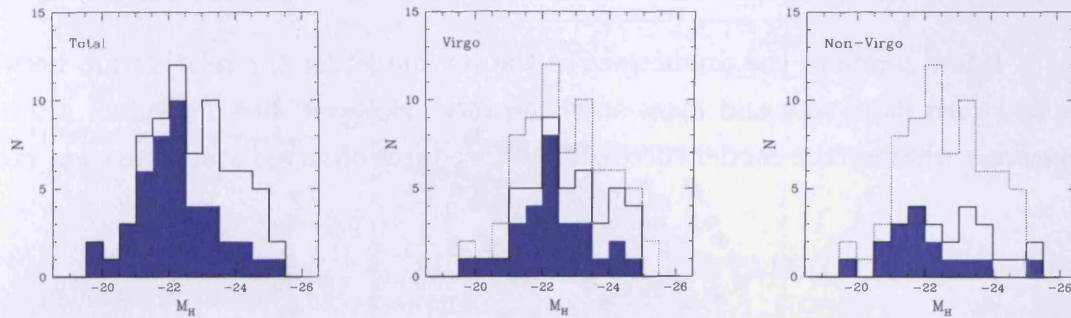


Figure 7.5: The coverage of spectroscopic observations of late-type, AGN-host galaxies in the SDSS (blue histogram) compared to the total number of late-type AGN-hosts (black solid line) present in the entire HRS+ sample (*left*), in the Virgo cluster members (*middle*) and outside the Virgo cluster (*right*). The total sample is displayed in the latter two plots for ease of comparison (black dashed line).

estimated an alternative bolometric correction,

$$\log L_{bol} = (0.95 \pm 0.08) \log L_{[OIII]} + (5.39 \pm 3.17) \quad (7.20)$$

which is also based on a sample of type 1 AGN. These two corrections provide very similar results. Because the Wu (2009) correction is based only on type 1 AGN, whereas Heckman et al. (2004) uses both type 1 and type 2 AGN similar to the HRS+ sample, I proceed using Heckman et al. (2004) correction. Since the Heckman et al. (2004) correction assumes the [OIII] luminosity is uncorrected for internal dust attenuation, I follow the same procedure and do not correct the [OIII] measurements for attenuation. Combining the bolometric correction with Equation 7.18, I estimate the mass accretion rates of the AGN in the sample by assuming a conversion efficiency of rest mass to energy of $\zeta = 0.1$. This is a standard assumption for the conversion efficiency and is based on a geometrically thin yet optically thick accretion disk (Shakura & Sunyaev, 1973; Narayan & Yi, 1995).

Finally, as previously mentioned, I use the NUV emission to estimate current star formation rates (see Section 3.6). In the following section, I present and discuss the results of this exercise.

7.4 COMPARISON OF THEORY WITH OBSERVATIONS

I now compare the predictions of the toy model for the relationship between the star formation rate and mass accretion rate. However, first I conduct a test to determine whether the model successfully reproduces observed star formation rates.

7.4.1 STAR FORMATION RATES

As a test of the model, I compare the relationship between the stellar mass and specific star formation rate (SFR/M_* ; SSFR) as predicted by the model with the observed M_* -SSFR relationship, based on the NUV star formation rates (see Section 3.6) for the late-types in the HRS+ sample. The predictions and observations are compared in Figure 7.6. The model successfully predicts the slope of the observed SSFR- M_* relationship, by using the assumption that the stellar mass is a constant fraction (1%) of the halo mass, but the range of observed SSFRs is not matched by a variability of α_{SF} alone. This may be due to a number of reasons. Firstly, the sample used to construct the figure contains perturbed objects with quenched star formation, as clearly shown in Chapter 5, and a large fraction of the scatter from the mean SSFR is due to these perturbed systems. Because the model assumes that the galaxy evolves according to a closed box model, it does not take into account the quenching of star formation via environmental effects, which, as I have previously shown, play a significant role in suppressing star formation. Secondly, it is likely that some of the fixed values I have assumed for variables does not reproduce the observed range of SSFR. For example, adopting a fixed value for the cooling function is not accurate, since this value actually depends on the temperature and metallicity of the cooling gas and, as shown in Figure 7.2, has a range of values from $\sim 10^{-21}$ - 10^{-24} $\text{erg cm}^3 \text{s}^{-1}$. Whilst the constant value I have adopted fits the mean observed relationship, the range of values may be accounted for if the cooling rate is allowed to vary based on the temperature and metallicity of the halo gas. However, since the model does provide a good match between the predicted relationship and the mean observed relationship, I proceed with using the model to investigate the relationship between star formation and AGN feedback.

7.4.2 THE $\text{SFR}-M_{acc}$ RELATIONSHIP

The relationship between the star formation rate and the mass accretion rate is investigated in Figure 7.7. The observations show no trend; the observations for the

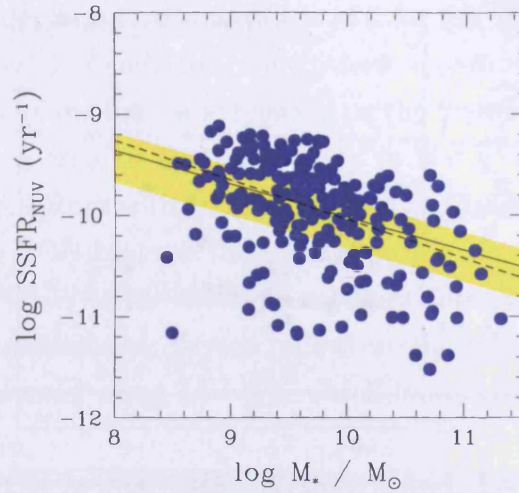


Figure 7.6: A comparison of the predicted relationship between the specific star formation rate (SFR/M_*) and the stellar mass (solid black line) and the relationship observed in star-forming, late-types (solid blue circles). The range of efficiency of star formation, $5\% < \alpha_{SF} < 15\%$ (shaded yellow region), successfully predicts the mean observed relationship (dashed black line).

44 AGN-hosts yield a Spearman correlation coefficient of $r_s = 0.08$ with a probability of $P(r_s) < 99.5\%$, hence there is no significant correlation.

I compare the results found here with those of S05. They published the bolometric luminosities, estimated from the 2-10 keV X-ray luminosity, and FIR luminosities for a large sample of 129 galaxies representing the broad range of AGN classifications, including LINERs, Seyferts, radio-loud and radio-quiet quasars, and narrow-line Seyferts (previously explained in Section 1.3.1). Following the method of S05, I convert the published L_{FIR} into a star formation rate using the relations presented in Bell et al. (2003). The mass accretion rate is calculated from the bolometric luminosity assuming $\zeta = 0.1$.

Although there is a slight overlap between the HRS+ and S05 samples, any comparison of individual results is limited to one galaxy: NGC 4527 / HRS 201. This is due to the S05 sample containing a fraction of early-types, excluded from this analysis, and galaxies outside the distance limits of the HRS+ selection criteria, i.e. $D < 15$ Mpc and $D > 25$ Mpc. For both rates available for NGC 4527, the values obtained in this work are consistent within the errors with the values presented in S05. The HRS+ (S05) values are $\text{SFR} = 0.44(0.31) M_\odot \text{ yr}^{-1}$ and $\log \dot{M}_{acc} = -5.46(-4.54) M_\odot \text{ yr}^{-1}$.

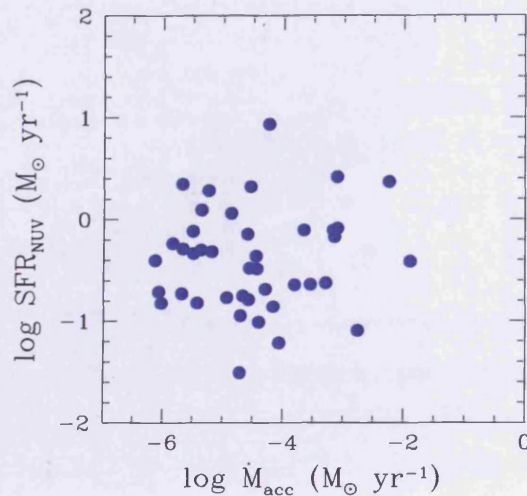


Figure 7.7: The estimated mass accretion and star formation rates from this work (blue circles).

Despite the lack of overlap between the samples, I can compare the distribution of the HRS+ AGN-host subsample in the $\text{SFR}-\dot{M}_{acc}$ parameter space to that of the S05 sample. Figure 7.10 shows the properties of the AGN from the S05 sample. It shows the apparently differing relationships of the LINER and Seyfert galaxies and the linear fits to these AGN subclasses, as reported by S05. The HRS+ AGN-hosts clearly occupy the same parameter space as the LINER systems, showing lower mass accretion rates compared to the Seyferts. This is an expected result, since the HRS+ LINER galaxies typically demonstrate less energetic AGN-like behaviour compared to the Seyfert galaxies predominate in the S05 sample. Thus, the AGN-hosts in the HRS+ sample appear to have accretion and star formation rates typical of the LINER regime, consistent with S05.

However, it should be noted that the apparent difference between the Seyferts and LINERS may be resolved with a varying mass-to-energy conversion efficiency across the different AGN classes, instead of the assumption that all AGN work at an efficiency of $\zeta = 0.1$. It has been shown that the radiative efficiency for systems with low \dot{M}_{acc} is likely to be much smaller than this value, even possibly a decreasing function of \dot{M}_{acc} (Narayan & Yi, 1995). A transition between a radiatively efficient, geometrically thin, optically thick accretion flow and a radiatively inefficient, geometrically thick, optically thin flow is theoretically expected (Narayan & Yi, 1994) and also has observational support (Jester, 2005). Applying a single value for ζ to

a sample of AGNs is therefore likely to be incorrect. Indeed, Wu & Cao (2006) demonstrate this by calculating varying values of ζ for the LINER systems in the S05 sample, based on a model of radiatively inefficient accretion flows, finding that the LINERs are shifted to follow the same relation as the Seyfert galaxies.

Even taking into account the uncertainty in the value of ζ by adopting the lower limit of 0.001 (consistent with RIAF models, e.g. Quataert, 2003), the accretion power of the late-type AGN-hosts in the HRS+ sample are still typically lower than the normal bright AGNs. With the available ancillary data, it is not currently possible to observationally determine the correct radiative efficiencies for each AGN in the sample. As such, I proceed using $\zeta = 0.1$, which is an upper limit of the effect of feedback.

To summarise the results of this section, I find that the HRS+ AGN-hosts residing in late-type galaxies are typically LINER-like galaxies, with low mass accretion rates that only weakly influence the rate of star formation. These results are consistent with previous studies (Okamoto et al., 2008), although it is noted that some uncertainty lies in the assumed conversion between the accreted rest mass and energy output, since not all AGN convert mass to energy with a constant efficiency. By assuming an upper limit for the conversion efficiency, it is still possible to test the predictions of a toy model, discussed in Section 7.2, and determine whether AGN feedback is important for quenching star formation in these AGN-hosts.

The [OIII] emission line luminosity and the NUV luminosity are tracers of the mass accretion and star formation rates, which may now be compared with the predictions from the toy model. Figure 7.9 shows the predicted star formation rate as a function of the mass accretion rate, which is linked to the heating of the gas. Since the mass accretion rate essentially scales according to the mass of the simulated system, the model predicts that for lower mass systems, the star formation rate gradually increases proportional to the accretion rate. As the mass accretion gradually increases, the star formation rate is reduced due to the energy output from the central black hole heating the gas and quenching the star formation. Eventually, feedback from the AGN fully heats the available gas and star formation (in the model) becomes totally quenched. The predicted halo mass at which the gas heating rate dominates over the gas cooling rate is dependent primarily on the conversion efficiency, as indicated by the SFR- \dot{M}_{acc} curves based on varying ζ presented in Figure 7.9.

Comparing these predictions with the observations, the main result is that the LINER galaxies (in both the S05 and HRS+ sample) appear to lie below the threshold where the accretion rate becomes large enough to significantly impact the cooling of gas, thus modifying the amount of cold gas available for star formation. This is

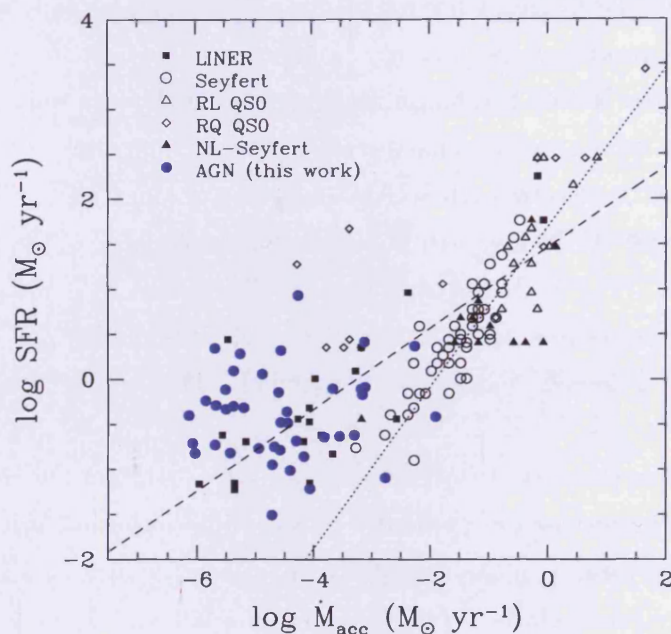


Figure 7.8: The estimated mass accretion and star formation rates from this work (solid blue circles), compared to those from the study of Satyapal et al. (2005, other symbols), assuming $\zeta = 0.1$. The differing relationships found by S05 between the LINERS (dashed line) and the Seyferts (dotted line) are also shown.

true regardless of the efficiency adopted for converting the rest mass of the accreted material into radiative energy from the black hole, as evident from the various $\text{SFR}-\dot{M}_{acc}$ curves. Consider the effect of removing the assumption that the observed $\zeta = 0.1$ and adopting a varying efficiency. In this scenario, the LINER-like systems may be shifted to lie on the same $\text{SFR}-\dot{M}_{acc}$ relationship for the Seyfert-like systems presented in S05, as demonstrated by Wu & Cao (2006), albeit with lower star formation and accretion rates. However, reducing the model ζ accordingly still yields the result that the LINERS lie below the threshold where AGN feedback has a significant impact.

Whilst the distribution of the \dot{M}_{acc} of the observed galaxies shows that the LINERS typically lie below the threshold for significant quenching via AGN feedback, it is obvious from a comparison of the model $\text{SFR}-\dot{M}_{acc}$ relation to the observed relations presented in S05 that they are not consistent. Investigating this issue by exploring the feasible range of the different parameters (e.g. the cooling function $\Lambda(T, Z)$, the star formation efficiency α_{SF}), I found that whilst the slope and intercept of the $\text{SFR}-\dot{M}_{acc}$ relation may vary significantly if the adopted values are changed according to the ranges in Table 7.1, the observation that the LINERS lie below the

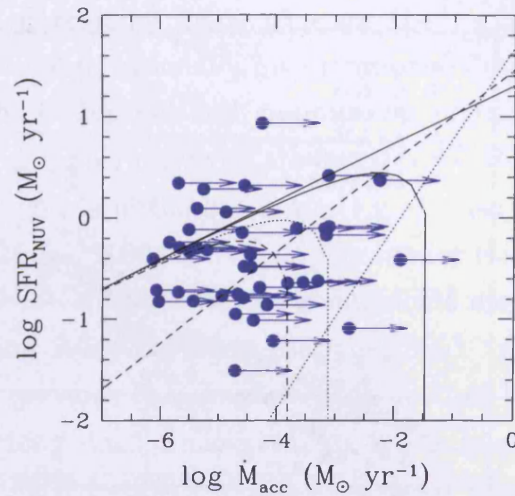


Figure 7.9: The estimated mass accretion and star formation rates from this work (blue circles) compared to the predictions the star formation rate as a function of the mass accretion rate in the toy model, using accretion efficiencies ζ of 10% (dashed curve), 5% (dotted curve) and 1% (solid curve). The blue arrows demonstrate the effect of systematically decreasing ζ to 0.01. For reference, the relationships found by S05 for Seyferts (dashed line) and LINERs (dotted line) are also shown.

threshold of total quenching remains.

Taking these points into account, the model predicts that LINER-like AGN are never powerful enough to fully quench the star formation, suggesting that for my sample, AGN feedback does not significantly affect the star formation rate of their host galaxies.

7.5 CONCLUSIONS

I constructed a simple model to test whether the AGN present in late-type galaxies are powerful enough to significantly quench the star formation in the disks, thus driving the spirals from the blue to the red sequence. Based on current theory, the model indicates that although in large halos, the central black holes are massive enough to rapidly accrete material and efficiently radiate energy capable of quenching star formation, this is not true for smaller halos ($M_{halo} < 10^{12} M_{\odot}$). Thus, the predictions of the model match those of other studies (e.g. Croton et al., 2006; Somerville et al., 2008).

Given the large number of assumptions in this model, the theoretical predictions for how the AGN power affected the star formation rate were tested using the

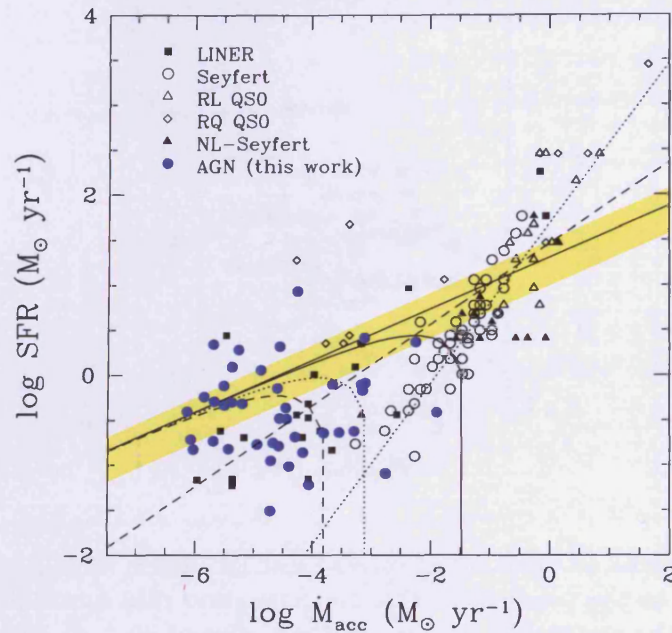


Figure 7.10: The estimated mass accretion and star formation rates from this work (solid blue circles), compared to those from the study of Satyapal et al. (2005, other symbols), assuming $\zeta = 0.1$. The predicted star formation rate as a function of the mass accretion rate in the toy model, with accretion efficiencies ζ of 10% (dashed curve), 5% (dotted curve) and 1% (solid curve) are plotted, together with the relationship where feedback is switched off (yellow shaded region). The differing relationships found by S05 between the LINERS (dashed line) and the Seyferts (dotted line) are also shown.

NUV and [OIII] $\lambda 5007$ emission line luminosities as tracers of the star formation rate and mass accretion rate, respectively. Comparing these observational indicators with the model predictions, I explored the relationship between the AGN and the star forming disk. I found that the AGN in the sample were never powerful enough to reach the predicted threshold where the radiative energy from the black hole accretion became significant enough to impact the star formation rate. The results suggest that the AGN residing in late-type galaxies are typically LINER-like systems, consistent with the current understanding of low luminosity AGN.

It was also found that to properly understand the relationship between the mass accretion rate and the host galaxy SFR, it is necessary to determine the radiative efficiencies and decouple their effects on the derived mass accretion rates for the entire sample. With the current data available, combined with the theoretical uncertainties, I could not reliably expand further the investigation in order to give a more accurate indication on the true value of ζ for all galaxies in our sample. As the $L_{[\text{OIII}]}$ indicator

is a useful proxy for the AGN power to trace the model predictions and future work should be focussed on developing more accurate (i.e. < 0.1 dex, not ~ 0.4 dex) bolometric corrections to observationally investigate the distribution of ζ .

Regardless of the limitations and assumptions of this simple toy model, the results still hold under closer scrutiny and are found to be consistent with the predictions of more complex models in the literature (e.g. Croton et al., 2006; Somerville et al., 2008; Okamoto et al., 2008). I remind the reader that I have not added any new physics into this model and the various components are standard to most semi-analytic models invoking AGN feedback (Baugh, 2006). Combining these results with the analysis from previous two chapters, I do not find any evidence in support of AGN feedback quenching star formation in late-types, in agreement with Okamoto et al., suggesting that AGN feedback is not a universal effect for all morphological types. In fact, observational evidence points towards the environment as the cause of suppressed star formation in the local universe. This concludes the investigation to determine the quenching mechanism.

For the remainder of the analysis, I now focus my attention on the final aim of this thesis, and investigate the effect of the environment on the chemical evolution of galaxies.

CHAPTER 8

MEASURING METALLICITY

8.1 INTRODUCTION

The chemical composition of galaxies provides a crucial insight into the processes governing galaxy evolution. There are still many open questions about the internal processes that drive chemical evolution and the importance of the role of the environment in shaping the evolution of galaxies. As galaxies evolve, star formation converts gas into stars, which in turn produce the heavy elements via nucleosynthesis. These metals are then expelled into the surrounding medium during the later stages of stellar evolution, thus enriching gas that may become fuel for future star formation episodes. Therefore the abundance of heavier elements present in a galaxy, the metallicity, provides an important indicator of the evolutionary history of a galaxy. Accurate metallicity measurements are necessary to reliably constrain the current models of chemical evolution.

There are a number of methods for estimating the metal content of a galaxy. Stellar photospheric absorption lines (e.g. Mehlert et al., 2002) and interstellar absorption features (e.g. Savaglio et al., 2004) have both been used as indicators of the stellar metallicity, whereas the emission lines of gaseous nebulae are used to estimate the abundance of the interstellar gas. In this chapter, I shall focus on obtaining gas phase abundances via the emission lines of gaseous nebulae. Throughout this work, I adopt the *oxygen abundance* as a tracer of the overall gas phase *metallicity* and use the two terms interchangeably.

8.2 DETERMINING THE METALLICITY

Common methods of measuring the metal content of the gas in a galaxy rely on optical emission line ratios. The aim of this section is to provide an introduction to the background physics involved in the production of emission lines and describe how observations of gaseous nebulae can be used to determine the metallicity from these lines.

Gaseous nebulae are optically visible clouds of gas present in our Galaxy and in other galaxies. As gas collapses to form stars, these new stars emit ultraviolet photons capable of ionising surrounding gas left over from the star formation process. This heated gas emits photons that ultimately yield information about the properties of the interstellar medium in galaxies.

The chemical composition of a galaxy may be obtained from the spectrum of emitted photons. The spectra of nebulae are dominated by emission lines across the electromagnetic spectrum; they include the permitted Balmer, Lyman and Paschen lines of hydrogen, e.g. $H\alpha$ $\lambda 6563$, $H\beta$ $\lambda 4861$ and $H\gamma$ $\lambda 4340$, and helium, the optical forbidden lines of ions of common elements, including $[OII]$ $\lambda\lambda 3726, 3729$, $[OIII]$ $\lambda\lambda 4959, 5007$, $[NII]$ $\lambda\lambda 6548, 6584$, $[SII]$ $\lambda\lambda 6717, 6731$ and $[SIII]$ $\lambda\lambda 9069, 9523$, and the strong infrared and ultraviolet lines of $[NeII]$ $\lambda 12.8 \mu m$ and $[MgII]$ $\lambda\lambda 2796, 2803$. Numerous other weaker emission lines are also present. The continuum emission is often weak and consists of an atomic component, arising from the Paschen and Balmer continuum of HI , and a reflective continuum, which is starlight scattered by dust.

The emission from the nebulae is powered by ultraviolet radiation from hot stars ($T_* > 3 \times 10^4$ K). Ultraviolet photons heat the gas predominantly by photoionization of hydrogen. During photoionization, photons with energies greater than the ionization potential of hydrogen are absorbed and any additional energy from the photon becomes kinetic energy of an emitted photoelectron. The photoelectrons quickly become thermalized following collisions with other electrons and ions, with velocities in a Maxwellian distribution and temperatures between 5000 and 20000 K in a typical nebula. These thermal electrons take part in atomic processes which lead to the generation of the emission line spectra.

The permitted lines arise from the recapture of thermal electrons by ions. These recaptures produce excited atoms, which subsequently decay to the ground state by emitting photons. Famous examples of this process are the Balmer and Paschen lines in the HI spectrum, from photons emitted by H^0 following the recombination of H^+ . For heavier elements, the lower energy levels of ions become excited by collisional excitation. Since collisional de-excitation is not probable due to the low

densities of typical nebulae ($n_e < 10^4 \text{ cm}^{-3}$), downward transitions from the excited levels via photon emission become the main mechanism for returning the ion to lower energy levels. Therefore, forbidden lines (or, more appropriately, collisionally excited lines) are also observed in the spectra of nebulae.

The emission lines arise from these different atomic processes within the gas cloud. The intensity of the emission lines are all dependent on the electron temperature, T_e , density, n_e , and chemical composition of the nebula and hence observations of the emission lines yield important information regarding the state of the ionized gas. Knowledge of the temperature and density of the electrons can be gained by measuring the relative intensities of particular pairs of emission lines. This information is crucial for obtaining metallicity estimates.

The electron temperature, T_e , can be determined from the ratio of intensities of lines emitted from a single ion from two levels with different excitation energies. The best example of this is the [OIII] ion, of which the [OIII] $\lambda 4363$ line originates from a different energy level compared to the [OIII] $\lambda\lambda 4959, 5007$ lines, and these different levels have different excitation energies that depend very strongly on T_e . Under the assumptions that the nebulae are optically thin to the forbidden line radiation, for the example of the [OIII] ion it can be shown that

$$\frac{j_{\lambda 4959} + j_{\lambda 5007}}{j_{\lambda 4363}} = \frac{7.9 \exp(3.29 \times 10^4 / T_e)}{1 + 4.5 \times 10^{-4} n_e / T_e^{1/2}} \quad (8.1)$$

where j_λ are the emission coefficients and the numerical factors arise from the ratios of the collision strengths and transition probabilities corresponding to the energy levels responsible for the photon emission (Osterbrock, 1989). If the typical electron density is $\sim 1 \text{ cm}^{-3}$, then it is clear that this intensity ratio is strongly dependent on the temperature. Typical temperatures of HII regions lie in the range of 7000-14000 K and 10000 K is usually adopted as an estimate.

In a similar manner to temperature measurements, the electron density, n_e , can be determined from the ratio of intensities of lines emitted from a single ion from two levels with similar energies but varying radiative transition probabilities. The [OII] $\lambda\lambda 3726, 3729$ or [SII] $\lambda\lambda 6717, 6731$ lines can be used for measuring the electron density, since the two levels involved in each line for each ion have different radiative transition probabilities that mean the relative populations of the levels depend strongly on the density.

Once the temperature and density are known, the abundance ratio between two ions can be determined from the relative intensity between the measured lines,

e.g.

$$\frac{O^{++}}{H^+} = \frac{[OIII]\lambda 5007/H\beta}{j_{[OIII]}(T_e, n)/j_{H\beta}(T_e)} \quad (8.2)$$

where $j_{[OIII]}(T_e, n)$ is the emission coefficient (Stasińska, 2002).

However, this method of measuring abundances, referred to in the literature as the ‘direct’ or ‘ T_e ’ method, is not easy. The [OIII] $\lambda 4363$ line is often either undetected or extremely weak. Successful measurements of the line intensity require long integration times, making large surveys unfeasible and so accurate temperature measurements are unavailable. In addition, the [OII] and [SII] lines are sometimes unresolved, impeding the determination of the density.

Faced with these observational challenges, other methods were developed for determining the metallicity using statistical or ‘strong line’ methods and theoretical models. The strong line methods rely on empirical relationships between different optical emission line ratios and metallicities determined via the T_e method, based on observations of large samples of HII regions. Pagel et al. (1979) first proposed the use of strong nebular lines from O and H to indicate the oxygen abundance for giant extragalactic HII regions, via the ratio $O_{23} = ([OII]\lambda 3727 + [OIII]\lambda 5007)/H\beta$. Since then, many more calibration methods have been introduced to gain reliable estimates of metallicities based on different suites of emission lines (e.g., Pilyugin, 2001, hereafter P01; Pettini & Pagel, 2004, PP04; Pilyugin & Thuan, 2005, P05). For example, P01 and later P05 developed calibrations for similar ratios of $([OII]\lambda 3727 + [OIII]\lambda 4959 + [OIII]\lambda 5007)/H\beta$, the R_{23} method, whereas the Denicoló et al. (2002, hereafter D02) and PP04 calibrations rely on the [NII] $\lambda 6584/H\alpha$ ratio.

The difficulty of observationally determining T_e also lead to the development of theoretical calibrations (e.g., Zaritsky et al., 1994, Z94; Kewley & Dopita, 2002, KD02; Kobulnicky & Kewley, 2004, KK04). Photoionization models of nebula, (e.g. Cloudy; Ferland et al., 1998), are combined with stellar population synthesis models (e.g. Starburst99; Leitherer et al., 1999), to calculate the thermal equilibrium which arises from the ionizing radiation field emitted by a stellar population, allowing for theoretical emission line ratios to be predicted from varying input metallicities, temperatures and densities. Theoretical calibrations between different emission line ratios and the metallicities are then possible, such as the calibration of R_{23} by McGaugh (1991, hereafter M91). Another approach is to simultaneously fit all the strong emission lines and use theoretical models to generate a probability distribution of metallicities and statistically estimate abundances (Tremonti et al., 2004, hereafter T04).

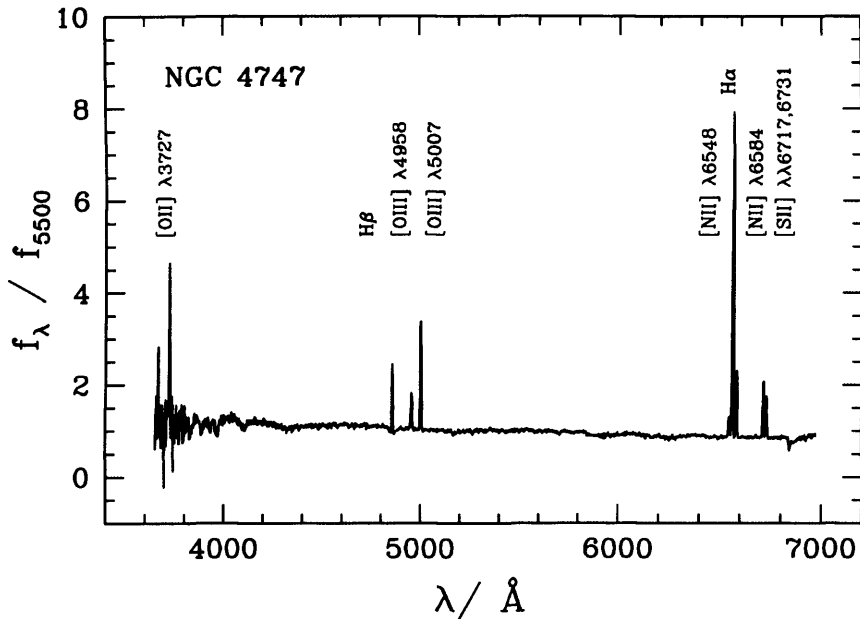


Figure 8.1: Prominent emission line features in the optical spectrum of NGC 4747, including the HI recombination lines and forbidden lines arising from O, N and S.

These calibrations can then be applied to galaxy spectra. The nebulae emission lines from HII star-forming regions throughout a galaxy are observed in the integrated spectrum of the galaxy, as in the example shown in Figure 8.1 (see also the spectra presented in Appendix B). Thus, using the previously discussed methods for determining element abundances from emission line ratios, we can determine the average global abundances for a galaxy and infer the degree of chemical enrichment. Whilst a complete review of the empirical and theoretical calibrations is presented in Stasińska (2002), the following section focusses on the specific calibration methods used for deriving metallicity estimates in this work.

8.3 CALIBRATION METHODS

As previously mentioned, the calibrations between the emission line ratios and the oxygen abundances are either derived empirically, based on theoretical results from photoionization models, or utilise combinations of theory and observation.

In order to compare the metallicity estimates given by the different metallicity indicators and hence determine the best calibration, I use six calibrations derived from empirical observations and theoretical models. The methods of PP04 and P05

Method	Emission Lines	Class	Limits
M91	R_{23} , [OIII]/[OII]	Theoretical	$7.1 < 12+\log(\text{O}/\text{H}) < 9$
Z94	R_{23}	Theoretical	$12+\log(\text{O}/\text{H})_{upper} > 8.4$
D02	[NII]/H α	Combined	$7.2 < 12+\log(\text{O}/\text{H}) < 9.1$
PP04 N2	[NII]/H α	Empirical	$7.17 < 12+\log(\text{O}/\text{H}) < 8.87$
PP04 O3N2	[NII]/H α , [OIII]/H β	Empirical	$8.12 < 12+\log(\text{O}/\text{H}) < 9.05$
P05	R_{23} , [OIII]/[OII]	Empirical	$8.25 < 12+\log(\text{O}/\text{H})_{upper} < 8.8$ $7.2 < 12+\log(\text{O}/\text{H})_{lower} < 8.00$

Table 8.1: A summary of the different calibrations used to estimate the gas-phase metallicity.

are empirical estimates of the oxygen abundances calibrated from observations of HII regions. The calibrations of M91 and Z94 are theoretical methods. Finally, the calibration presented in D02 is based on a combination of empirical and theoretical metallicities.

The following sections describe the underlying emission line ratios used to obtain oxygen abundances and introduce the calibration relations obtained in the various studies. These relations are important since they will be used to estimate the mean oxygen abundances of the HRS+ galaxies. Table 8.1 provides a summary of the different calibrations, the emission lines used for each calibration and the limits of validity of the relations.

8.3.1 THE R_{23} RATIO

The R_{23} intensity ratio was first formulated in the studies of Pagel et al. (1979) and Pagel et al. (1980), but has been used and recalibrated in many other studies (see Kobulnicky et al., 1999 for a review). It is defined as

$$R_{23} \equiv \log \left(\frac{[\text{OII}]\lambda 3727 + [\text{OIII}]\lambda 4959 + [\text{OIII}]\lambda 5007}{H\beta} \right) \equiv X \quad (8.3)$$

However, in addition to being sensitive to metallicity, the R_{23} ratio is also sensitive to the ionization state of the gas or the ‘ionization parameter’, which is defined as the ratio of the ionizing photon flux passing through a unit area and the local number density of hydrogen atoms. The sensitivity to the ionization parameter may

be corrected using the O_{32} ratio, given by

$$O_{32} \equiv \log \left(\frac{[\text{OIII}]\lambda 4959 + [\text{OIII}]\lambda 5007}{[\text{OII}]\lambda 3727} \right) \equiv Y \quad (8.4)$$

One disadvantage of the R_{23} ratio is that it can correspond to two values of oxygen abundance. Most values of R_{23} yield both a low metallicity estimate (referred to as the ‘lower branch’) and a high metallicity estimate (or the ‘upper branch’). This method therefore requires additional emission line measurements in order to break the degeneracy between the upper and lower branches. The $[\text{NII}]\lambda 6584/\text{H}\alpha$ and $[\text{NII}]\lambda 6584/[\text{OII}]\lambda 3727$ ratios may be used to discriminate between the two branches, although it was recently shown by Kewley & Ellison (2008, hereafter KE08) that the latter ratio produces a clearer distinction between the branches of the R_{23} method and so is more reliable for breaking the degeneracy and estimating whether the value is an upper or lower estimate (see Figure 8.2). KE08 report that the break between the upper and lower branches occurs at $\log([\text{NII}]/[\text{OII}]) \sim -1.2$, corresponding to a metallicity of $12 + \log(\text{O}/\text{H}) \sim 8.4$. I adopt this value to divide the two branches.

Three of the six calibrations I use in this study are based on the R_{23} ratio taken from the works of M91, Z94 and P05. The X and Y notation in Equations 8.3 and 8.4 is used to simplify the calibration relations given for these studies.

M91 (McGaugh, 1991)

The M91 calibration of R_{23} is a theoretical method based on HII region models using the photoionization code Cloudy (Ferland et al., 1998). The calibration includes the correction for ionization parameter variations using the O_{32} ratio and the R_{23} degeneracy is broken using the $[\text{NII}]/[\text{OII}]$ line ratio. The oxygen abundances for the upper and lower branches, as presented in Kobulnicky & Zaritsky (1999), are

$$\begin{aligned} 12 + \log(\text{O}/\text{H})_{\text{upper}} &= 9.061 - 0.2X - 0.237X^2 - 0.305X^3 - 0.0283X^4 \\ &\quad - Y(0.0047 - 0.0221X - 0.102X^2 - 0.0817X^3 - 0.00717X^4) \\ 12 + \log(\text{O}/\text{H})_{\text{lower}} &= 7.056 + 0.767X + 0.602X^2 \\ &\quad - Y(0.29 + 0.332X - 0.331X^2) \end{aligned} \quad (8.5)$$

This method is accurate to ~ 0.15 dex.

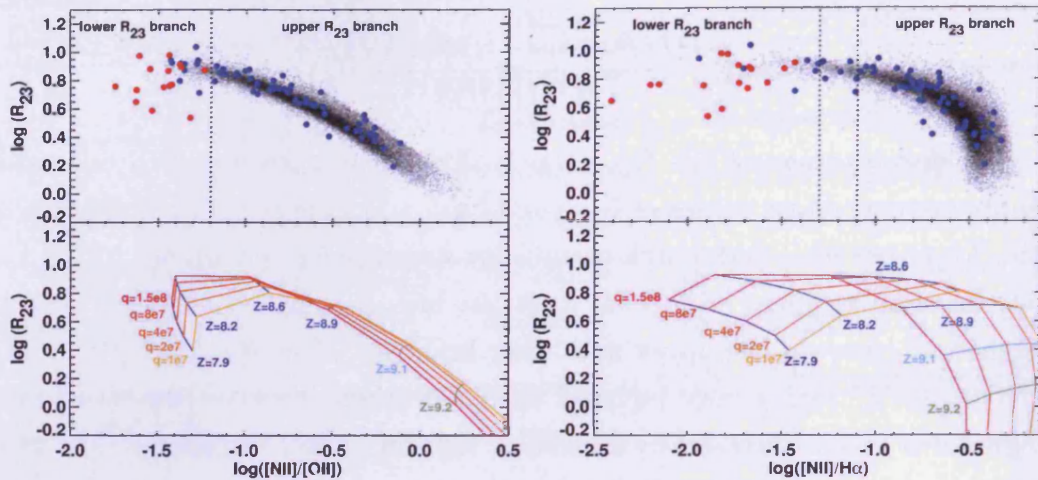


Figure 8.2: The observed and theoretical relationships between the R_{23} ratio and the $[\text{NII}] \lambda 6584 / [\text{OII}] \lambda 3727$ (*left diagram*) and $[\text{NII}] \lambda 6584 / \text{H}\alpha$ (*right diagram*) ratios. *Top panels*: The observed relationships using the samples from KE08 (*black circles*), Kong & Cheng (2002, *blue circles*) and Brown et al. (2006, *red circles*). The division between the upper and lower branches is shown for $\log([\text{NII}]/[\text{OII}]) \sim -1.2$ (*dashed black line*), where the R_{23} reaches a maximum. However, $[\text{NII}]/\text{H}\alpha$ cannot discriminate between the two branches over the range of $-1.3 < \log([\text{NII}]/\text{H}\alpha) < -1.1$ (*dashed black lines*), making the $[\text{NII}]/[\text{OII}]$ the preferred ratio for breaking the R_{23} degeneracy. *Bottom panels*: Theoretical relationships based on the stellar population synthesis and photoionization model grids of KD02, for constant metallicities and ionisation parameters. This figure was taken from Figures 8 and 9 in KE08.

Z94 (Zaritsky et al., 1994)

The Z94 calibration was derived from the average of three calibrations: Edmunds & Pagel (1984), Dopita & Evans (1986) and McCall et al. (1985). The Z94 calibration is only valid for the upper R_{23} branch and does not use the O_{32} ratio to account for the sensitivity to the ionization parameter. The Z94 calibration is

$$12 + \log(O/H)_{\text{upper}} = 9.265 - 0.33X - 0.202X^2 - 0.207X^3 - 0.333X^4 \quad (8.6)$$

and is only valid for the upper R_{23} branch. The uncertainty in this method is 0.1 dex, given by the difference in the metallicity estimates of the three calibrations.

P05 (Pilyugin & Thuan, 2005)

The P05 calibration is based on the relationship between R_{23} and T_e metallicities using spectra of 700 HII regions for which the $[\text{OII}] \lambda 4363$ line is detected. The

upper R_{23} branch calibration is valid for $12+\log(\text{O}/\text{H}) > 8.25$ whilst the lower branch is valid for $12+\log(\text{O}/\text{H}) < 8.0$. I use the $[\text{NII}]/[\text{OII}]$ line ratio to discriminate between the upper and lower branches, which are

$$\begin{aligned} 12 + \log(\text{O}/\text{H})_{\text{upper}} &= \frac{R_{23} + 726.1 + 842.2P + 337.5P^2}{85.96 + 82.76P + 43.98P^2 + 1.793R_{23}} \\ 12 + \log(\text{O}/\text{H})_{\text{lower}} &= \frac{R_{23} + 106.4 + 106.8P - 3.4P^2}{17.72 + 6.6P + 6.95P^2 - 0.302R_{23}} \end{aligned} \quad (8.7)$$

where $P = [([\text{OIII}]\lambda 4959 + [\text{OIII}]\lambda 5007)/\text{H}\beta]/R_{23}$. The uncertainty in the P05 calibration is estimated to be 0.1 dex.

8.3.2 THE $[\text{NII}]/\text{H}\alpha$ RATIO

The $[\text{NII}]\lambda 6584/\text{H}\alpha$ (N2) ratio may not be the best line ratio for breaking the R_{23} degeneracy, but it is a reliable estimator of the oxygen abundance over a wide dynamical range. The ratio was first proposed as a calibrator by Storchi-Bergmann et al. (1994), who showed that the N2 ratio correlates with abundance over the range $8.3 < 12+\log(\text{O}/\text{H}) < 9.2$. Further studies have since recalibrated the ratio and extended the validity range to include lower metallicity systems, e.g. $7.8 < 12+\log(\text{O}/\text{H}) < 8.6$ (Raimann et al., 2000), and I use the more recent N2 calibrations provided by D02 and PP04.

D02 (Denicoló et al., 2002)

The D02 calibration was determined from the relationship between the T_e metallicities and the $[\text{NII}]/\text{H}\alpha$ line ratio for ~ 155 HII regions, of which approximately 100 regions have metallicities derived via the T_e method and 55 regions have metallicities estimated from either the M91 R_{23} method or the empirical method of Díaz & Pérez-Montero (2000). An oxygen abundance of $12+\log(\text{O}/\text{H}) \sim 8.4$ divides T_e -based and the strong-line-based metallicity estimates which were used for calibrate the ratio. The D02 calibration is given by

$$12 + \log(\text{O}/\text{H})_{\text{upper}} = 9.12 + 0.73 \times N2 \quad (8.8)$$

where in this case $N2 = \log([\text{NII}]\lambda 6584/\text{H}\alpha)$. The estimated uncertainty in this calibration is 0.2 dex.

PP04 N2 (Pettini & Pagel, 2004)

The PP04 N2 calibration was determined from T_e -based metallicities for a sample of 137 HII regions. The N2 calibration has a validity range of $7.17 < 12 + \log(O/H) < 8.87$ and is given by

$$12 + \log(O/H)_{N2} = 9.37 + 2.03 \times N2 + 1.26 \times N2^2 + 0.32 \times N2^3 \quad (8.9)$$

where N2 is the logarithm of the ratio. The error on this calibration is estimated to be 0.18 dex.

8.3.3 THE [OIII]/[NII] RATIO

The O3N2 ratio, defined as $O3N2 \equiv \log\left(\frac{[OIII]\lambda 5007/H\beta}{[NII]\lambda 6584/H\alpha}\right)$, was first investigated as a potential metallicity estimator by Alloin et al. (1979), as it was shown that comparing the N2 calibrator with the [OIII]/H β ratio could improve the accuracy of the metallicity estimation. I use the recent recalibration of the O3N2 relation presented in PP04.

PP04 O3N2 (Pettini & Pagel, 2004)

The PP04 [OIII]/[NII] ratio (hereafter PP04 O3N2) was calibrated using T_e -based metallicities for a sample of 137 HII regions. The O3N2 calibration is only valid for values of $-1 < O3N2 < 1.9$, corresponding to a metallicity range of $8.12 < 12 + \log(O/H) < 9.05$. The relation is given by

$$12 + \log(O/H)_{O3N2} = 8.73 - 0.32 \times O3N2 \quad (8.10)$$

PP04 estimate the error on this calibration to be 0.14 dex.

8.4 DISCREPANCIES BETWEEN CALIBRATIONS

Obtaining reliable methods for measuring the metallicity of a galaxy is still a focus of current efforts in research, since large discrepancies exist in the metallicities obtained from different calibrations. Liang et al. (2006) compared the metallicity calibrations from four different methods applied to ~ 40000 galaxies selected from the SDSS (York et al., 2000), and observed discrepancies as large as 0.6 dex between observational estimates and the results from photoionization models. Yin et al. (2007)

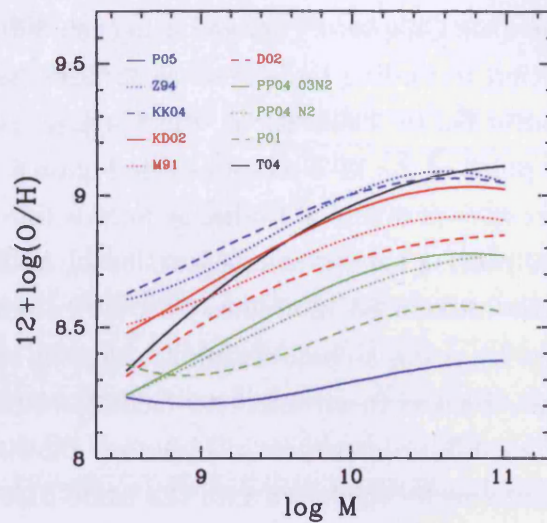


Figure 8.3: The large discrepancies in the overall shape of M-Z relations derived from different metallicity calibrations (adapted from Figure 2 of KE08 and references therein).

also found a discrepancy of 0.6 dex when comparing the empirical calibration of P01 to the theoretical results of T04.

The problem is important for understanding the formation and evolution of galaxies. Hierarchical galaxy formation models within the Λ CDM framework which incorporate chemical evolution models are able to predict the evolution of the stellar mass-metallicity (hereafter M-Z) relation (see e.g. De Lucia et al., 2004; de Rossi et al., 2007; Davé & Oppenheimer, 2007). Reliable observations are required in order to accurately constrain the shape of the M-Z relation, and thus constrain current theories of both the formation of galaxies and their subsequent chemical evolution. For example, many open questions still remain regarding the chemical evolution of a galaxy, and it is still not clear whether internal processes or environmental effects govern the M-Z relation (see Chapter 9 for further discussion). Advancements in the capabilities of telescopes and spectrographs allow for the observation of the M-Z relation out to higher redshifts (e.g. Kobulnicky & Zaritsky, 1999; Erb et al., 2006; Liang et al., 2006; Mouhcine et al., 2006). However, the discrepancies between metallicities from different calibrations mean the M-Z relations derived from observations of galaxies at earlier epochs may not be accurate. The discrepancies between the calibrations need to be first understood, so that the observed M-Z relations at higher redshifts may accurately constrain the models.

Motivated by the need for an in-depth study of these discrepancies, KE08 compared M-Z relations (see Chapter 9) derived using ten different calibrations from the literature. In addition to finding large systematic discrepancies of up to 0.7 dex in the metallicities from different calibrations, there was an evident disparity in the overall shape and zero point of the M-Z relations (see Figure 8.3). Such discrepancies mean that comparing results of different studies is not possible and it is crucial to use the same metallicity calibration for any comparisons of the M-Z relation. False trends in the data may also be introduced in studies that try to maximise the number of available measurements by using a combination of different calibrations (see Figure 3 in Boselli & Gavazzi, 2006). In an effort to facilitate comparisons between the results of various samples, KE08 determined conversions allowing metallicities derived with different calibrations to be converted into the same base calibration. The new conversions removed the 0.7 dex systematic discrepancies.

Using these new metallicity conversions, it is now possible to compare metallicities derived using different calibrations reliant on different sets of emission lines. A better estimate of the relative oxygen abundance of a galaxy may be obtained by converting each metallicity estimate into the same base metallicity and then using the average metallicity from all the available estimates. I shall first test the metallicity calibrations and base conversions presented in KE08 with the HRS+ sample since, at the time of writing, no other study has performed an independent check of the base conversions presented in KE08. These new estimates could then be used to study the M-Z relation and potentially explore the different theories of chemical evolution.

8.5 METALLICITY ESTIMATES

First, oxygen abundances are estimated from measurements of emission line fluxes with the six calibrations described in Section 8.3: M91, Z94, D02, PP04 O3N2 and N2, and P05. There are a number of points to note about the application of the methods to the data. Galaxies with detected $H\beta$ and $H\alpha$ emission, i.e. a positive value of C1 (see Section 4.4), and OII emission are suitable for use with all the calibration methods. However, those systems with an upper limit to the C1, derived from estimating the (undetected) $H\beta$ emission using the $H\alpha$ equivalent width, only have metallicities estimated with the D02 and PP04 N2 calibrations. Unlike the other emission line ratios exploited by the remaining calibrations, the NII and $H\alpha$ lines used in these two calibrations have very close wavelengths and are similarly affected by dust extinction. In fact, the values of the reddening function adopted for extinction corrections (presented in Table 4.1) are similar for the NII and $H\alpha$ lines. Thus, the

ratio does not require a measurement of C1 and can still be used for estimating oxygen abundances. A full table of results are presented in Appendix E and a summary of the number of estimates is given in Table 8.2.

From these results, I examine the relationship between the estimates of the different calibrations. The metallicity-metallicity (Z - Z) plots in Figure 8.4 have each calibration method plotted against the other five methods. The figure is important for a number of reasons. Firstly, it demonstrates significant discrepancies which arise when using different calibration methods: no single pair of calibration methods used in this work follow the 1:1 relationship on the Z - Z plots. The methods in most agreement are the D02 and PP04 N2 calibrations. The mean residual metallicity given by $\bar{\delta}$, where $\delta = x - y$, is 0.1 dex and the standard deviation of the difference between the estimates of the two calibrations is lowest for D02 and PP04 N2 at $\sigma = 0.03$ dex. However, this is not so surprising when considering that this pair of calibrations are the most similar, since both calibrations are based on the same line ratios ($[\text{NII}]/\text{H}\alpha$) with similar derived relations (compare Equations 8.8 and 8.9). The method which agrees the least with any other method is P05. As noted by KE08, this calibration has a very non-linear shape with a large scatter and mean offset when plotted against all the other calibrations ($\sigma \sim 0.4$ dex and $\bar{\delta} \sim 0.5$ dex). Secondly, by comparing the Z - Z plots from my data with those presented in Figure 3 of KE08 and online¹, it is evident that the estimates are consistent to those of KE08. The systematic discrepancies are clearly similar in the size of the deviation from the 1:1 relationship between all the calibration methods. For a more quantitative approach, the Z - Z relations obtained from fitting the data in KE08 are shown for each Z - Z plot in Figure 8.4, excluding the relations for P05 estimates, for which a reliable fit was not possible. It is clear that there is a high level of agreement between all of the KE08 relations and the data. However, whilst a slight offset does exist between the estimates and the fitted relationships of KE08, this offset is within the observed errors (typically 0.1 dex) and is not significant.

It thus emerges that the estimates from this work are consistent with those found in previous studies. Both the discrepancies and the shape of the relations between different calibrations agree with those found in KE08. This is encouraging when one considers that the two datasets were obtained in different ways: KE08 use spectroscopy from SDSS fibers, whereas this work uses integrated, drift-scan spectroscopy.

On closer inspection of the Z - Z plots, it can be seen that outliers from the main

¹ Z - Z plots for all calibrations used in KE08 have been made available online at <http://www.ifa.hawaii.edu/~kewley/Metallicity>.

Z-Z relationships exist in calibrations which rely on using the NII or H α lines. The outlying objects, approximately 8 in total, have oxygen abundances derived from the emission line measurements of low resolution ($R < 1000$) spectra obtained in G04. In these spectra, the NII and H α lines were not resolved and G04 estimate the [NII] $\lambda 6548$, [NII] $\lambda 6584$ and H α lines using a relationship between metallicity and luminosity. However, whilst this method may be more accurate than the alternative method of deblending the lines using SPLOT, for this work it is important to have accurate and reliable emission line flux measurements. Because the data for these 8 objects produce unreliable abundance estimates, these objects are removed from the analysis of the mass-metallicity relation in the following chapter.

Since the abundance estimates appear consistent with results in the literature, I shall now proceed by removing the systematic discrepancies between the different calibrations by converting the results into a ‘base’ metallicity, such that all the abundance estimates from different calibrations are comparable.

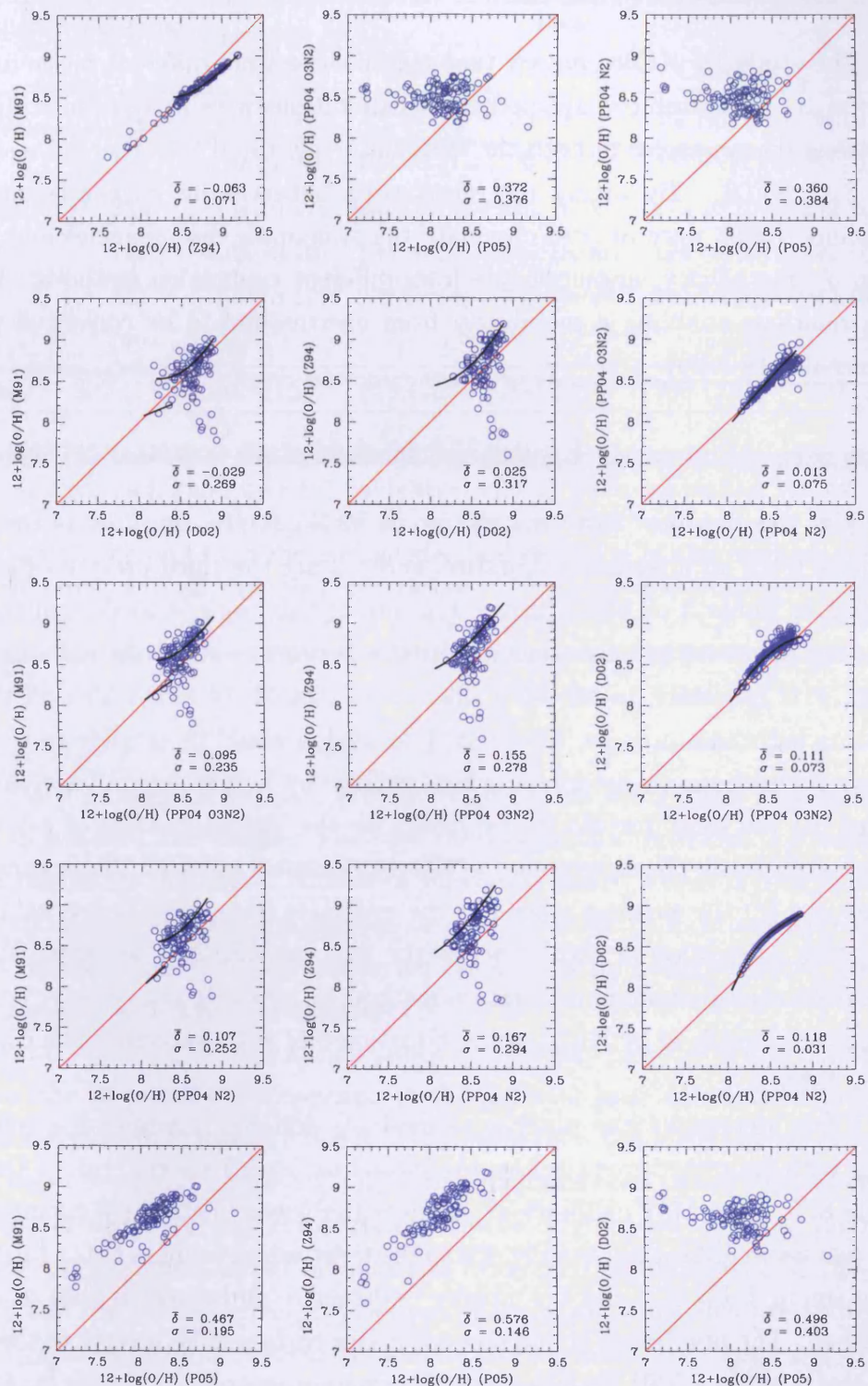


Figure 8.4: The relationships between the metallicities obtained from the six calibration methods (*blue open circles*). The 1:1 line (*red line*) denotes where the metallicities would lie if the calibrations agree, highlighting the large variation and scatter of using different metallicity calibrations. The relationships are well fitted by the Z-Z relations given in KE08 (*black line*). The scatter, σ , is the standard deviation of the residuals between the two plotted calibrations.

8.6 BASE CONVERSION

The study by KE08 showed that metallicities from different methods do not follow the 1:1 relationships expected if the calibrations were in agreement, but often show strong discrepancies in both the systematic offset and the observed scatter (see Figure 3 in KE08). By fitting the relationship between the various results of the calibrations, KE08 were able to eliminate the systematic discrepancies and produce comparable metallicity measurements from different calibration methods. The conversion relations enabling a metallicity from one method to be converted into any other metallicity follow

$$y = a + bx + cx^2 + dx^3 \quad (8.11)$$

where y is the final or ‘base’ metallicity in $12+\log(\text{O}/\text{H})$ units, x is the original metallicity from an alternate calibration and $a-d$ are the third order coefficients, as presented in Table 3 of KE08. Since the aim of this work is to determine reliable and homogeneous oxygen abundance estimates in order to study the mass-metallicity relation, it is necessary to choose a single base metallicity into which all the other metallicity estimates may be converted. I decided it would be sensible to test all the different calibrations to determine which calibration acting as the base calibration provides (a) the most metallicity estimates for the largest number of galaxies, (b) the least systematic offset between metallicity estimates using all the remaining calibrations and (c) the smallest scatter in the estimates from the different calibrations. Taking each calibration in turn to act as the base calibration, I converted the abundances from each remaining calibration method by applying the relevant conversion relations as determined by KE08, using Equation 8.11 with the conversion coefficients ($a-d$) in Table 8.3.

I first determine the number of methods and the corresponding number of galaxies with estimated metallicities available from each base calibration (presented in Table 8.2). The M91 calibration produces the fewest metallicity estimates when acting as a base calibration, mainly due to the tight validity ranges of the M91 conversions (given in Table 8.3) and the number of detected [OII] emission lines required for the method. The number of abundance estimates corresponds directly to the number of galaxies, therefore M91 also produces the smallest sample of galaxies for which the metallicity is estimated. In comparison, the conversion to the Z94, PP04 O3N2 and N2 calibrations all produce similar results when acting as the base calibration, with between 830-890 estimates available for ~ 250 galaxies. This essentially corresponds to a greater number of methods for measuring the metallicity being available per galaxy,

Method	Measured	Base				
		M91	Z94	D02	O3N2	N2
M91	112	112 (0.18)	94 (0.16)	83 (0.09)	83 (0.11)	83 (0.10)
Z94	102	90 (0.10)	102 (0.21)	90 (0.12)	90 (0.12)	90 (0.11)
D02	285	145 (0.11)	242 (0.14)	285 (0.08)	242 (0.10)	242 (0.10)
O3N2	194	132 (0.12)	191 (0.15)	191 (0.09)	194 (0.10)	191 (0.10)
N2	244	140 (0.11)	229 (0.14)	244 (0.08)	229 (0.10)	244 (0.10)
P05	112	-	-	-	-	-
Total	937 (285)	619 (154)	858 (252)	893 (285)	835 (251)	850 (252)

Table 8.2: The number of measured metallicity estimates for the 421 observed galaxies obtained from each (unconverted) calibration and by then converting the estimates using each method as a base calibration. The bracketed number for a calibration is the scatter, derived from the average standard deviation of the residuals between the calibration and all the other calibrations. The bracketed number on the last row denotes the the actual number of galaxies corresponding to the total number of estimates derived from each method using the different base calibrations.

meaning that an average estimate is more reliable when using these base calibrations instead of the M91 calibration. The base calibration that provides the most metallicity estimates for the largest number of galaxies is clearly the D02 base calibration. This method offers the best results compared to the other calibrations, providing the greatest number of methods for measuring the metallicity being available per galaxy (893 estimates derived for 285 galaxies).

With regard to the metallicity values, rather than just the number of estimates available, the effects of the conversion to the different base calibrations are evident from the Z-Z plots in Figures 8.5 to 8.9. The figures show the relationships between the metallicities obtained from the five calibration methods once converted into each base calibration in turn. For easy comparison with the original, unconverted metallicities in Figure 8.4, the unconverted metallicities from each calibrations and the 1:1 line denoting the theoretical agreement between calibration estimates are shown. It is evident from these figures that the systematic discrepancies are significantly reduced, since the overall estimate distributions are now shifted to lie around the 1:1 line. The mean discrepancy between the metallicities $\bar{\delta}$ - a measure of the offset from the 1:1 relationship - is always <0.1 dex regardless of the calibration used and is typically $\lesssim 0.05$ dex, consistent with the offsets presented in KE08. I remind that the previous

offsets for (unconverted) metallicity estimates were typically between 0.1 and 0.3 dex.

I now compare the scatter in set of Z-Z plots for each base calibration. The mean scatter, calculated using the standard deviation of the differences between the estimate of the base metallicity and the remaining four estimates, is 0.16 dex for Z94, and 0.13 dex for M91. The scatter is smaller between estimates converted into the D02, PP04 O3N2 and N2 base calibrations compared to the M91 and Z94 bases. Therefore, the oxygen abundances show better agreement when using the $[\text{NII}]/\text{H}\alpha$ -based or $[\text{OIII}]/[\text{NII}]$ -based conversions than those calibrations based on the R_{23} ratio. In fact, the smallest mean scatter between metallicities is obtained when using the D02 calibration as the base metallicity ($\sigma = 0.09$ dex).

To summarise, the results presented here, i.e. the relationships between the different calibrations, the magnitude of the systematic discrepancies and the observed scatter between the estimated metallicities etc., are all consistent with the results of KE08. I find that the M91 and Z94 calibrations are not the best choice for using as base calibrations, since these calibrations tend to estimate metallicities for the least number of galaxies compared to the other methods. In addition, these R_{23} -based estimates are more scattered compared to the other types of metallicity calibrators. Excluding the M91 and Z94 calibrations as candidates for the base metallicity, it appears that the D02 calibration is the best base calibration to use when attempting to compare the oxygen abundance estimates, as it produces a greater number of less scattered estimates when compared to the other base calibrations used in this work.

The conclusion that the best method to use as a base metallicity is the D02 calibration appears to disagree with the conclusions of KE08, who conclude that the M91, PP04 O3N2 and KD02 (not used in this work) methods are the best base calibrations. I actually conclude that the M91 calibration is possibly the worst choice as a base calibration, given the smaller number of estimates and the higher discrepancies associated with the results from this calibration. The M91 calibration may not be the best estimator of the metallicity for the HRS+ sample because it is reliant on accurate measurements of the $[\text{OII}]$ line for determining the O_{32} ratio and for breaking the R_{23} degeneracy. The $[\text{OII}]$ line is much more affected by the extinction correction from the estimation of the Balmer decrement. Since some of the $\text{H}\beta$ measurements were not corrected for underlying stellar absorption, as discussed in Section 4.4, this could result in inaccurate $[\text{OII}]$ intensities and thus make the M91 calibration seem unreliable. Future work will investigate this issue, possibly by determining a mean additive correction for the $\text{H}\beta$ lines where underlying absorption is not detected, similar to the G04 absorption correction.

The results presented here instead favour the D02, PP04 O3N2 and N2 calibrations. Disregarding M91, for the reasons discussed above, the difference between our conclusions arises out of the necessity to derive reliable metallicities for as many galaxies as possible without introducing additional errors/discrepancies. The consequence of this requirement is that the D02 calibration becomes favourable over the PP04 O3N2 or N2 calibrations as, whilst the offset and scatter associated with using the two calibrations as bases are comparable, the D02 calibration estimates the most metallicities for galaxies in the sample. Rather than restrict the analysis in Chapter 9 to using metallicity estimates converted into one base metallicity, I decided to calculate two sets of final metallicity estimates, one based on the D02 calibration and the other on the PP04 O3N2 calibration. The reason for this is that a comparison of the M-Z relations derived from two sets of metallicities based on different calibrators may provide a key test as to whether the conclusions are dependent on the choice of calibrator.

Thus, the final values adopted for the metallicity of each galaxy were derived from the mean of all the measured oxygen abundances from the different calibration methods applicable to the emission line data of the galaxy, once converted into the D02 base metallicity and, for comparison, into the PP04 O3N2 base metallicity. Both sets of final metallicity estimates with errors are presented in Tables E.2 and E.3, together with the number of calibrations available for each galaxy under each base calibration regime. The distributions of the errors, presented in Figure 8.10, illustrate the similar mean and scatter in the D02 and PP04 O3N2 results, with standard deviations of ~ 0.1 dex. This value should be noted for the following analysis in Chapter 9 as it represents the overall error in the metallicity estimates.

8.7 CONCLUSIONS

The aim of this work was to obtain estimates of the metallicity for the HRS+ sample of galaxies, which could then be used to study the M-Z relation and observe any influence from the environment.

Six different calibrations were studied: M91, Z94, D02, PP04 N2 and O3N2, and P05. These calibrations were applied to the emission line data combined from Chapter 4 and G04. The resulting oxygen abundance estimates displayed large discrepancies (upto 0.3-0.4 dex in scatter) and systematic offsets, as observed by previous studies comparing the use of different calibrations (e.g. Liang et al., 2006). The relationships between the results of the calibrations, presented in KE08, were also in agreement with the results of this work.

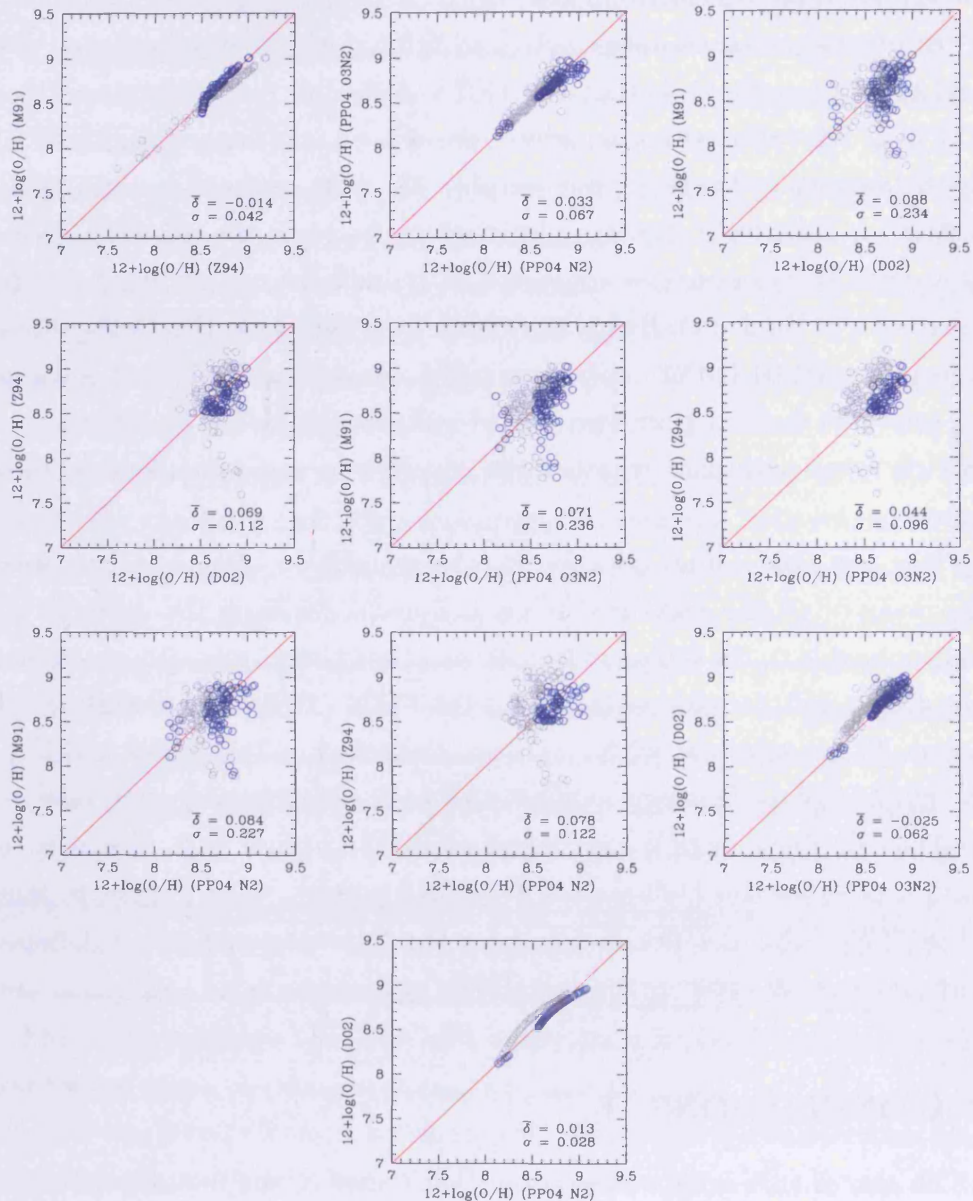


Figure 8.5: The relationships between the metallicities obtained from the six calibration methods once converted into the M91 base metallicity (*blue open circles*). The 1:1 line (*red line*) denotes where the metallicities would lie if the calibrations agree and the unconverted metallicities from each calibration, as presented in Fig 8.4, are shown for comparison (*grey open circles*). The scatter, σ , is the standard deviation of the residuals, δ , between the two plotted calibrations.

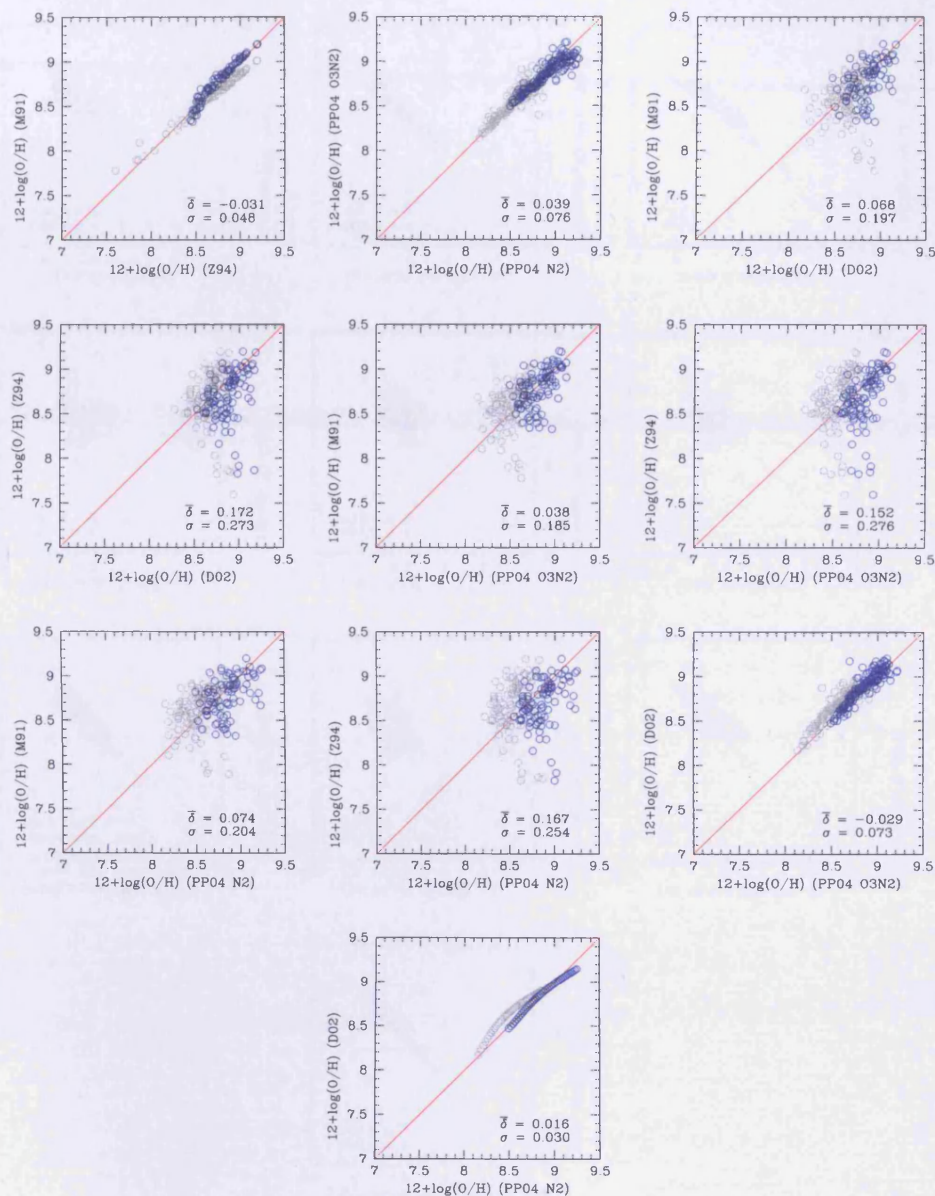


Figure 8.6: The relationships between the metallicities obtained from the six calibration methods once converted into the Z94 base metallicity (*blue open circles*). The 1:1 line (*red line*) denotes where the metallicities would lie if the calibrations agree and the unconverted metallicities from each calibration, as presented in Fig 8.4, are shown for comparison (*grey open circles*). The scatter, σ , is the standard deviation of the residuals, δ , between the two plotted calibrations.

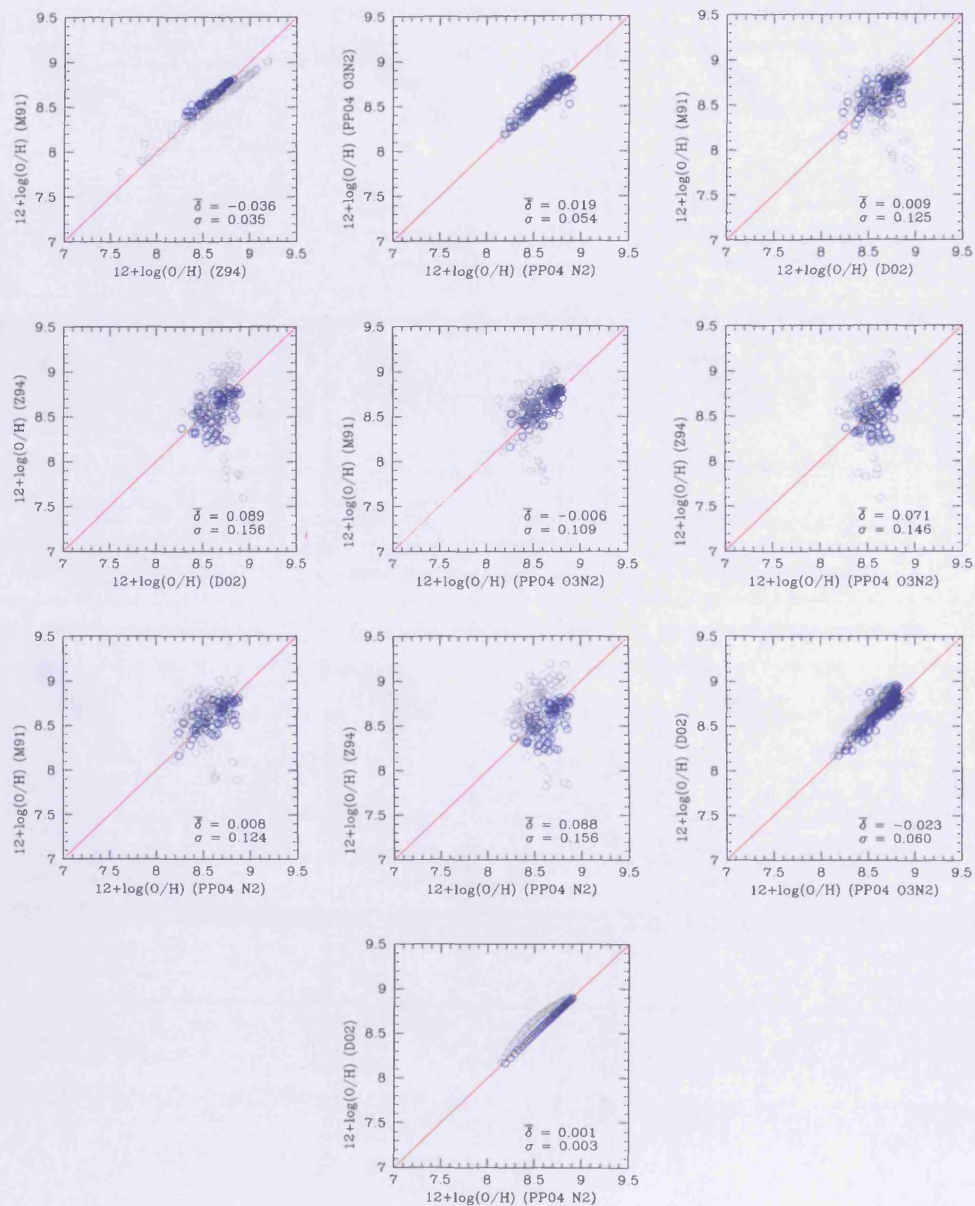


Figure 8.7: The relationships between the metallicities obtained from the six calibration methods once converted into the D02 base metallicity (*blue open circles*). The 1:1 line (*red line*) denotes where the metallicities would lie if the calibrations agree and the unconverted metallicities from each calibration, as presented in Fig 8.4, are shown for comparison (*grey open circles*). The scatter, σ , is the standard deviation of the residuals, δ , between the two plotted calibrations.

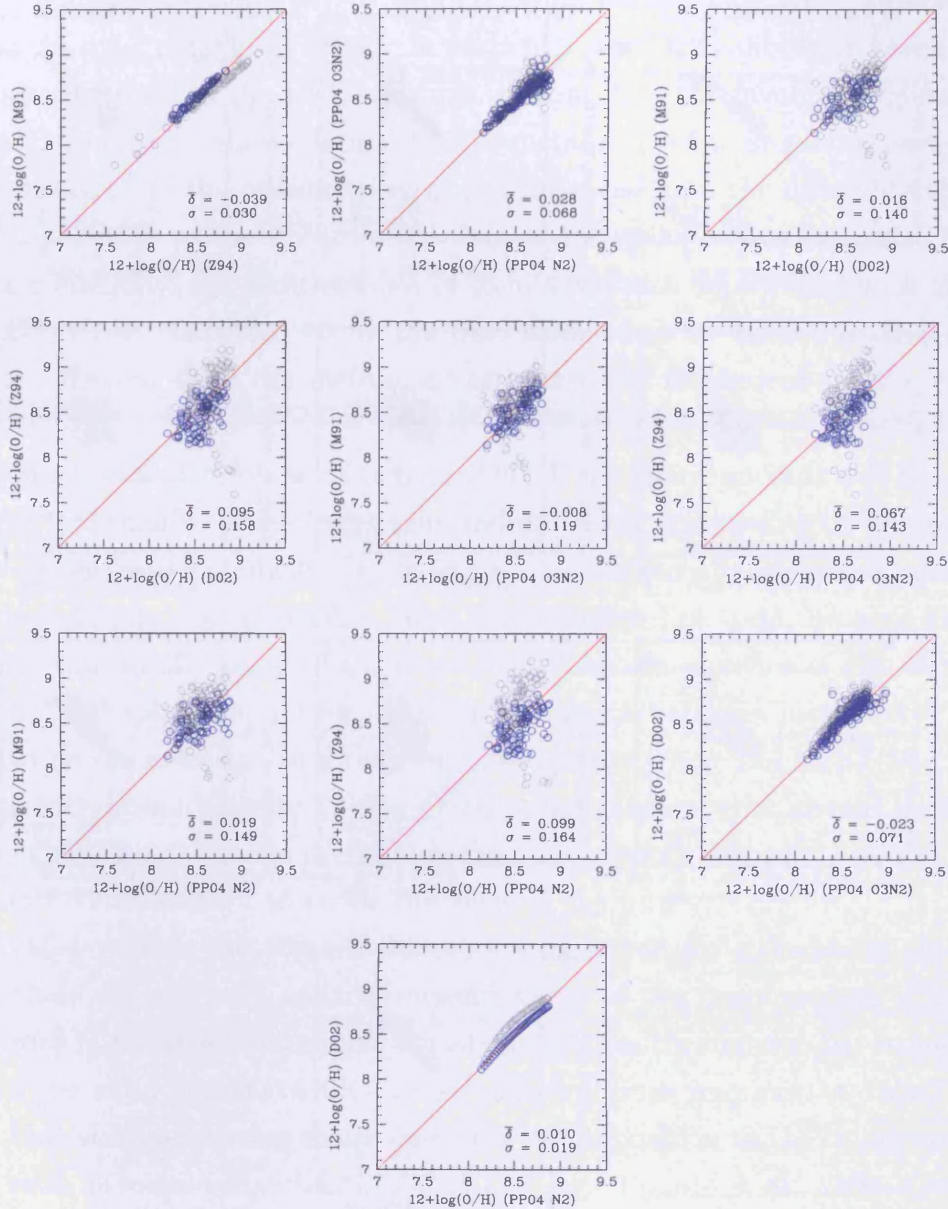


Figure 8.8: The relationships between the metallicities obtained from the six calibration methods once converted into the O3N2 base metallicity (*blue open circles*). The 1:1 line (*red line*) denotes where the metallicities would lie if the calibrations agree and the unconverted metallicities from each calibration, as presented in Fig 8.4, are shown for comparison (*grey open circles*). The scatter, σ , is the standard deviation of the residuals, δ , between the two plotted calibrations.

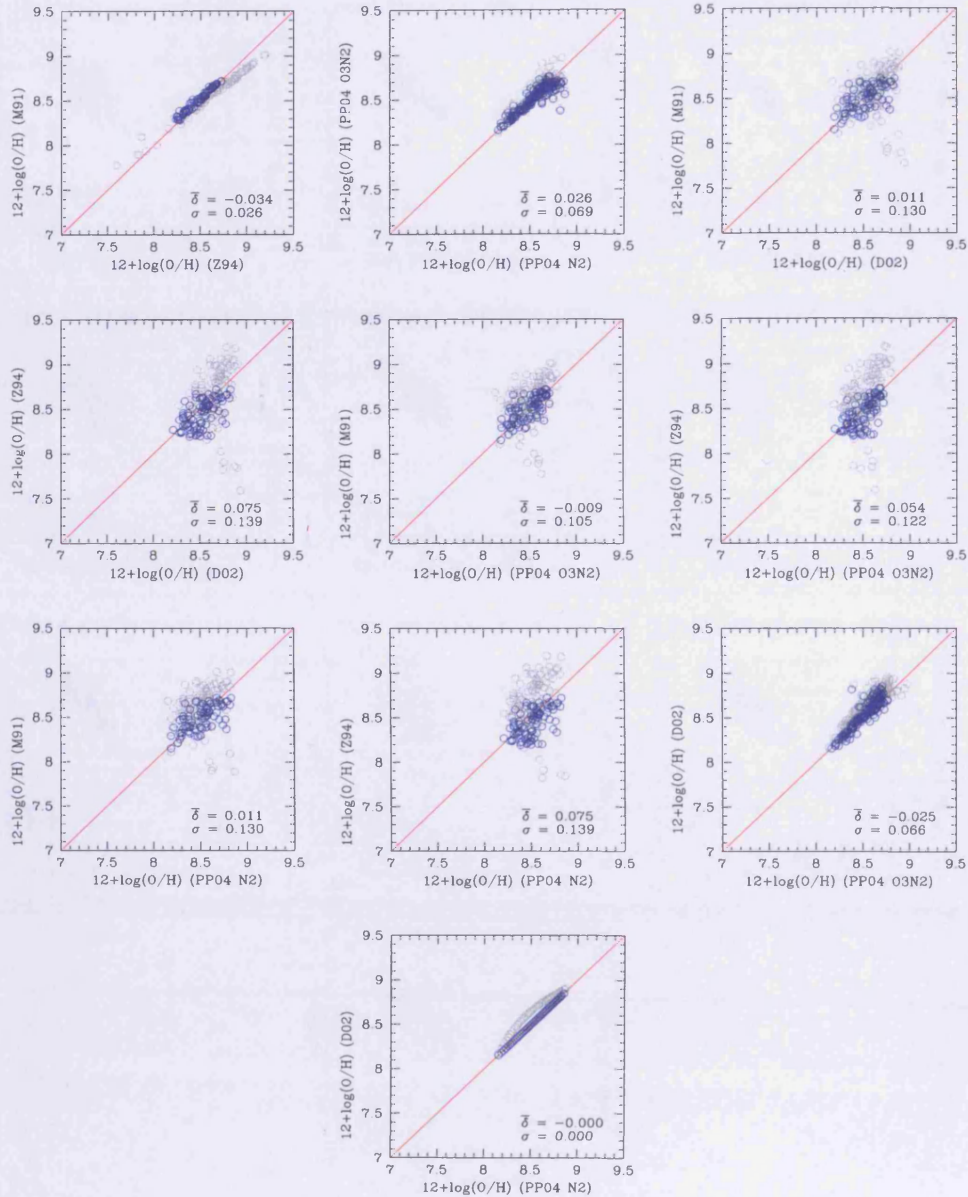


Figure 8.9: The relationships between the metallicities obtained from the six calibration methods once converted into the N2 base metallicity (*blue open circles*). The 1:1 line (*red line*) denotes where the metallicities would lie if the calibrations agree and the unconverted metallicities from each calibration, as presented in Fig 8.4, are shown for comparison (*grey open circles*). The scatter, σ , is the standard deviation of the residuals, δ , between the two plotted calibrations.

Based on the results presented here, I conclude that the [NII]/H α -based calibrations are the better base calibrations to use when attempting to compare the oxygen abundance estimates derived from different calibrations, since these methods produced the most reliable estimates. In particular, the D02 calibration gave the most results when applied to the HRS+ sample, making this the favoured choice of base metallicity. The final values adopted for the metallicity of each galaxy were derived from the mean of all the measured oxygen abundances from the different calibration methods applicable to the emission line data of the galaxy, once converted into the D02 base metallicity. An additional set of results was also determined with the PP04 O3N2 calibration, concluded to be the best calibration by KE08, to test whether conclusions derived from the metallicity estimates are dependent on the choice of calibration.

Some issues with this work remain. One of the main concerns was the number of metallicity estimates which became invalid under the constraints of the conversion into any chosen base metallicity. In some cases, an oxygen abundance estimate could not be used despite having reliable, high S/N emission line data, because the value fell outside the validity range of the conversion. The consequence of this is not only of ‘wasting’ valuable data, but also that the dynamical range in metallicity that can be studied becomes limited to a range of approximately $8 < 12+\log(\text{O}/\text{H}) < 9$, thus excluding metal-poor galaxies $12+\log(\text{O}/\text{H}) < 8.0$. Future work should be focussed towards expanding the range over which these conversions are valid. With the data used here, I could attempt to tackle this issue in the future.

Whilst reliable metallicities have been measured for galaxies in the HRS+ sample, these are still only relative measurements of the mean oxygen abundance. Fluctuations in the temperature and density structures throughout HII regions mean that even the ratio of collisionally-excited emission lines may not be reliable. It is possible that studies into diagnostic lines that are insensitive to the temperature and density, such as metal recombination lines (see e.g. Tsamis et al., 2003; Liu, 2002), or IR fine structure lines (e.g. Hunt et al., 2010), may help resolve the metallicity discrepancy problem in the near future.

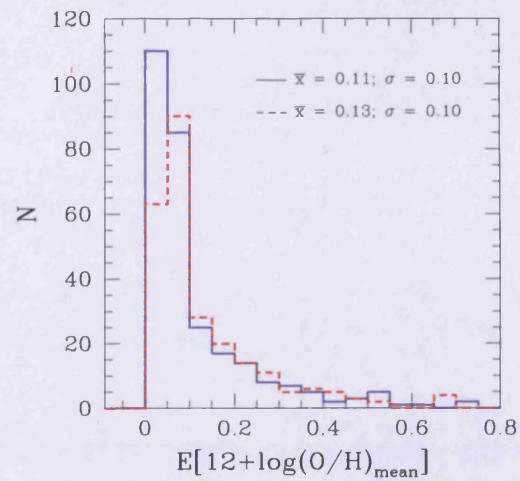


Figure 8.10: The distribution of the errors in the final metallicity values, presented for both the D02 (solid blue line) and the PP04 (dashed red line) base calibrations.

Base	M91(x)	Z94(x)	D02(x)	PP04 O3N2(x)	PP04 N2(x)
M91(y)					
Branch	-	...	upper;lower	upper;lower	upper;lower
Range	-	8.4-9.2	8.2-8.9;8.05-8.4	8.2-8.9;8.05-8.4	8.2-8.8;8.05-8.3
a	-	393.9855	85.2839;4.7927	267.3936;2.4196	87.371;0.7641
b	-	-127.8604	-18.63342;0.40796	-85.20014;0.70167	-19.39959;0.90362
c	-	14.05033	1.130870	9.219665	1.193544
d	-	-0.5109532	...	-0.3267103	...
Z94(y)					
Branch
Range	8.4-9.1	-	8.05-8.9	8.05-8.9	8.05-8.8
a	-868.280	-	63.6386	230.9335	40.5515
b	291.6262	-	-13.87785	-76.73906	-8.67461
c	-32.42779	-	0.872216	8.711059	0.581691
d	1.206416	-	...	-0.3244087	...
D02(y)					
Branch	upper;lower	...	-
Range	8.5-9.1;8.0-8.4	8.4-9.3	-	8.05-8.9	8.05-8.9
a	-121.3958;-1.0361	-114.3143	-	-1.3992	-629.0499
b	28.86410;1.13468	32.79523	-	-5.32702	215.37940
c	-1.599613	-2.782591	-	1.562757	-24.305910
d	...	0.0731175	-	-0.0938063	0.9168766
PP04 O3N2(y)					
Range	8.5-9.1;8.05-8.4	8.4-9.3	8.05-8.9	-	8.05-8.8
Branch	upper;lower	-	...
a	-65.0991;2.1063	52.2389	36.6598	-	-8.0069
b	15.74995;0.74427	-18.67559	-7.64786	-	2.74353
c	-0.837514	2.447698	0.508480	-	-0.09368
d	...	-0.1011578	...	-	...
PP04 N2(y)					
Branch	upper;lower
Range	8.5-9.1;8.05-8.4	8.4-9.3	8.05-8.9	8.05-8.9	-
a	1334.9130;3.1447	656.5128	-444.7831	512.7575	-
b	-464.86390;0.61788	-224.1124	165.426	-180.47540	-
c	54.166750	25.734220	-20.202	21.41588	-
d	-2.0986640	-0.98122624	0.8249386	-0.8427312	-

Table 8.3: The validity ranges and coefficients for converting abundances derived from each initial calibration (x) into abundances based on a base calibration (y) using Equation 8.11.

CHAPTER 9

THE MASS-METALLICITY RELATION

9.1 INTRODUCTION

Since the discovery of a relationship between luminosity and metallicity by Lequeux et al. (1979), numerous studies have confirmed the existence of a luminosity-metallicity or stellar mass-metallicity (hereafter M-Z) relation (see e.g. Rubin et al., 1984; Skillman et al., 1989; Vila-Costas & Edmunds, 1992). As the stellar mass and metallicity respectively measure the amount of gas converted into stars and the amount of gas converted into metals, the evolutionary stage of a galaxy can be inferred from reliable knowledge of these two quantities. Therefore, the M-Z relation provides a valuable tool for studying the chemical evolution of galaxies. However, despite mounting observational evidence for the existence of the M-Z relation, many questions remain regarding the origin, scatter and the possibility of a dependence on the environment.

It is now possible to explore the nature of the M-Z relation in different environments using the HRS+ sample of galaxies combined with the new estimates of the gas-phase metallicities presented in Chapter 8. Whilst the new method produces reliable metallicity estimates, it is important to ascertain that any observed trends are real and not dependent on the choice of base calibration. For this reason, I will use two sets of abundance measurements: one set of measurements use the calibration of Denicoló et al. (2002, D02) to act as the base metallicity and the other uses the Pettini & Pagel (2004, PP04) O3N2 calibration as the base metallicity¹. I refer to the two sets as either the D02-based or PP04-based results. Throughout the following analysis, these results will be compared to demonstrate that any trends in the observations are real and occur irrespective of the choice of base calibration.

¹The decision to use these two particular calibrations is discussed in Section 8.6.

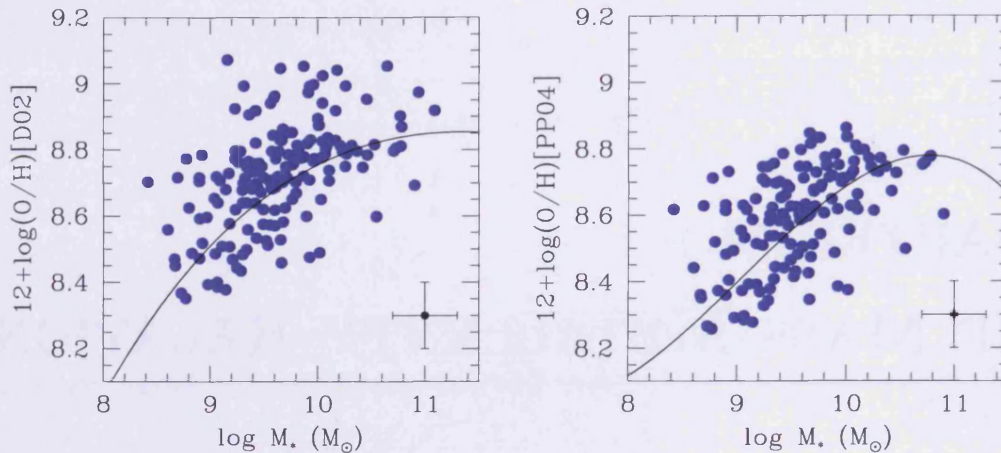


Figure 9.1: The relationship between stellar mass and oxygen abundance for the total sample of galaxies (blue circles), using metallicity estimates based on the D02 (*left panel*) and the PP04 (*right panel*) base calibrations. In each panel, the best fit M-Z relations presented in KE08 (solid black line) for the two calibrations are presented.

9.2 DEFINING THE M-Z RELATION

First, I shall investigate the relationship between stellar mass and gas-phase oxygen abundance. Figure 9.1 presents the M-Z relationships from gas-phase oxygen abundances derived using both the D02 and PP04 O3N2 calibrations. For both calibrations, it is evident that a positive correlation exists between the two quantities. Indeed, each calibration yields a correlation with a Spearman coefficient of rank correlation of $\rho = 0.56$, corresponding to a probability $P(\rho) > 99.9\%$ that the two variables are correlated.

Although the correlation coefficients are equal, the M-Z relations are not the same since both the dynamical range and the dispersion of the metallicity estimates are different. The range of metallicity estimates of the D02- and PP04-based results are approximately $8.3 < 12+\log(\text{O}/\text{H}) < 9.1$ and $8.2 < 12+\log(\text{O}/\text{H}) < 8.9$, respectively. As well as the offset in the metallicity ranges, there is also an offset in the mean metallicities; the D02-based mean metallicity is $12+\log(\text{O}/\text{H}) \sim 8.7$ whereas the PP04-based mean metallicity is ~ 8.6 . This suggests a systematic offset of approximately 0.1 dex between the two sets of results, which is as large as the error associated with the abundance estimates. The dispersion in the metallicities is much greater for the D02-based results ($\sigma = 0.18$) compared to the PP04-based results ($\sigma = 0.14$).

Also displayed in Figure 9.1 are the respective fits to the D02 and PP04-based M-Z relations presented in KE08 (see also Figure 8.3). The PP04-based fit is fairly consistent with the observations, but the fit to the D02-based observations is less consistent since the population of galaxies is much more scattered. The figure suggests that the increase in the scatter for the D02-based results is due to the galaxies with metallicities $12+\log(\text{O}/\text{H}) > 8.9$, since these objects do not appear to follow the KE08 M-Z relation. In addition, a direct comparison between the two panels in Figure 9.1 supports the idea that the increased scatter in the D02-based results arises from the presence of galaxies with metallicities $12+\log(\text{O}/\text{H}) > 8.9$ that are not present in the PP04-based results.

I concluded in the previous chapter that the D02 calibration acts as the best base calibration, due to 23 more metallicity estimates being available with this calibration than the PP04 O3N2 or N2 calibrations (see Section 8.6 for the discussion of this point). This means that some galaxies in the D02 calibration are based on a single measurement of the $[\text{NII}] \lambda 6584/\text{H}\alpha$ emission line ratio and not from the error-weighted average of different calibration estimates based on different suites of emission lines, i.e. the new approach to estimating the oxygen abundance that I introduced in the previous chapter. Thus, I identify the additional galaxies in the M-Z diagram by highlighting those galaxies which have metallicities derived using a single measurement. Figure 9.2 shows the same M-Z relationships as presented in Figure 9.1 with the KE08 best fit lines plotted, but galaxies with only one metallicity estimate are now highlighted as red circles. It is clear that all of the galaxies with D02 estimates > 8.9 arise from single measurements of the $[\text{NII}] \lambda 6584/\text{H}\alpha$ emission line ratio and not from the error-weighted average of different estimates. These additional metallicity estimates for 23 galaxies, are only deemed valid by this method because of the broader validity range ascribed to the D02 calibration than to other calibrations: $7.2 < 12+\log(\text{O}/\text{H}) < 9.1$. However, since the $[\text{NII}] \lambda 6584/\text{H}\alpha$ emission line ratio is susceptible to contamination due to AGN emission and may lead to an overestimate of the oxygen abundance, this raises an important issue about the use of the D02 calibration as the base metallicity when only single measurements are available.

Whilst the $[\text{NII}] \lambda 6584/\text{H}\alpha$ emission line ratio used for the D02 calibration does correlate with the oxygen abundance over a wide validity range, an inspection of Figure 9.3, taken from Denicoló et al. (2002), shows that the calibration may not be reliable at higher metallicities (e.g. $12+\log(\text{O}/\text{H}) \sim 9.1$). At high metallicities, it appears that the mean oxygen abundance from the observational data deviates from the linear fit that defines the calibration. Although a galaxy may possess an oxygen abundance of 9.1 and a corresponding $\log([\text{NII}] \lambda 6584/\text{H}\alpha)$ of -0.5, the D02

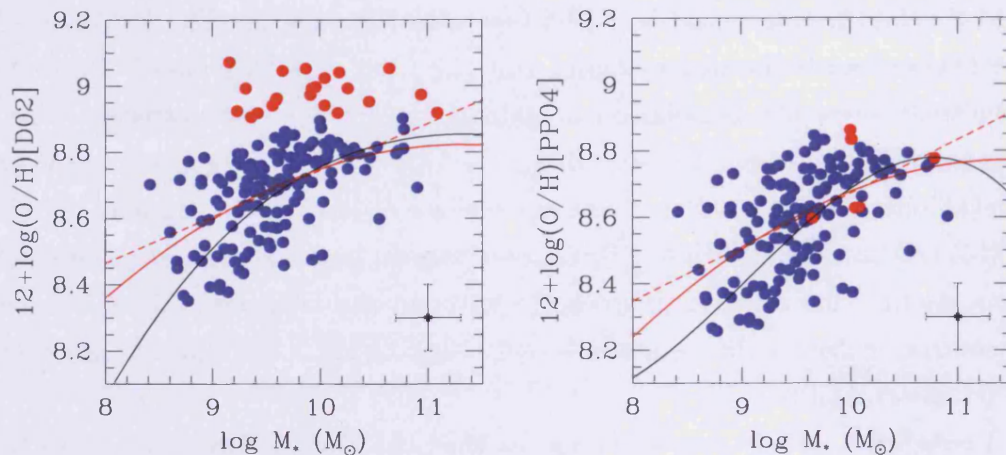


Figure 9.2: The relationship between stellar mass and metallicity for the total sample of galaxies (blue circles), using metallicity estimates based on the D02 (*left panel*) and the PP04 (*right panel*) base calibrations. In each panel, linear and polynomial fits to this data (dashed and solid red lines, respectively) and the KE08 data (solid black line) are presented.

calibration actually yields $12+\log(\text{O}/\text{H}) = 9.1$ when $\log([\text{NII}] \lambda 6584/\text{H}\alpha) = 0$. Therefore, this means that larger emission line ratios become valid under the D02 range. Under the Decarli et al. (2007) scheme for classifying nuclear activity, galaxies with $\log([\text{NII}] \lambda 6584/\text{H}\alpha) > -0.4$ are classified as displaying AGN-like behaviour. Hence, AGN-like galaxies may fall within the validity range of the calibration and, since the calibrations assume the emission lines occur due to star formation and not nuclear ionisation, this contamination leads to an incorrect overestimate of the oxygen abundance. Indeed, Figure 9.4 demonstrates that the 23 additional galaxies are classified as either displaying composite (i.e. a mixture of AGN and star forming) activity or AGN-like behaviour, with these classifications presented in Table 9.1. It is clear that most of these galaxies are displaying some degree of AGN-like behavior, with emission line ratios and corresponding oxygen abundances that are deemed valid by the D02 calibration but are otherwise invalid by the other calibrations. Since these galaxies are likely AGN-host galaxies displaying some level of nuclear activity, hence yielding unreliable metallicity estimates, they are excluded from the following analysis. However, the galaxies are retained in the various figures in order to demonstrate how AGN-host galaxies may affect observed trends.

Excluding these galaxies, I then examined the relationship between stellar mass and metallicity by using the IDL polyfit task to perform a least squares fit of

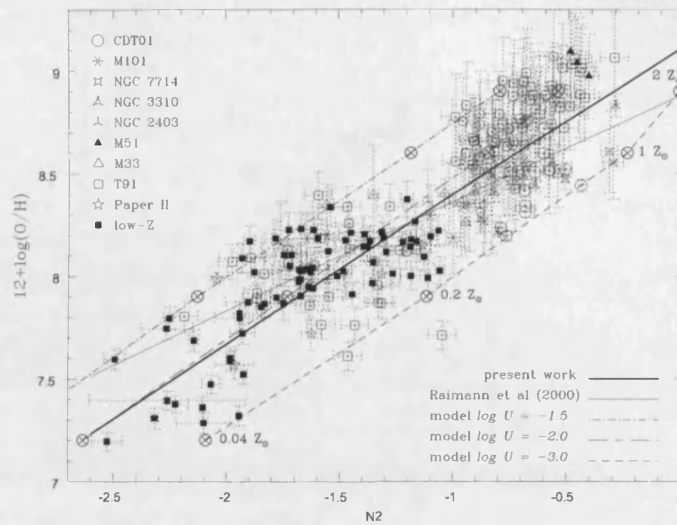


Figure 9.3: The plot shows the oxygen abundance versus the $[\text{NII}] \lambda 6584/\text{H}\alpha$ calibrator. The relation used as the D02 metallicity calibration is given by the solid black line. Taken from Denicoló et al. (2002).

the two datasets. From a visual inspection of Figure 9.1, a linear fit would most likely suffice to describe the M-Z relation. However, recent studies have reported that the M-Z relation flattens with increasing stellar mass and that the relation is best described using a polynomial function (see e.g. KE08 and references therein). The use of a polynomial has a physical as well as observational basis, since simple chemical evolution models predict that as gas is consumed via star formation, with a consequent increase of the stellar mass, the metallicity reaches a maximum upper limit that is determined by the mass of metals freshly produced in stars and ejected into the ISM (see e.g. Edmunds, 1990; Erb, 2008). This is an important point, to which I shall return during a discussion of a simple chemical evolution model in Section 9.4. Hence, I fit both linear and polynomial functions to the data and shall compare the two fits.

The best fit relations between stellar mass and oxygen abundance follow

$$y = a + bx + cx^2 + dx^3 \quad (9.1)$$

where y is the oxygen abundance expressed as $12+\log(\text{O}/\text{H})$, x is the logarithm of the stellar mass and $a-d$ are the coefficients of the best fit line. The coefficients for each sample are displayed in Table 9.2 along with the reduced Chi-squared values, χ^2_ν ,

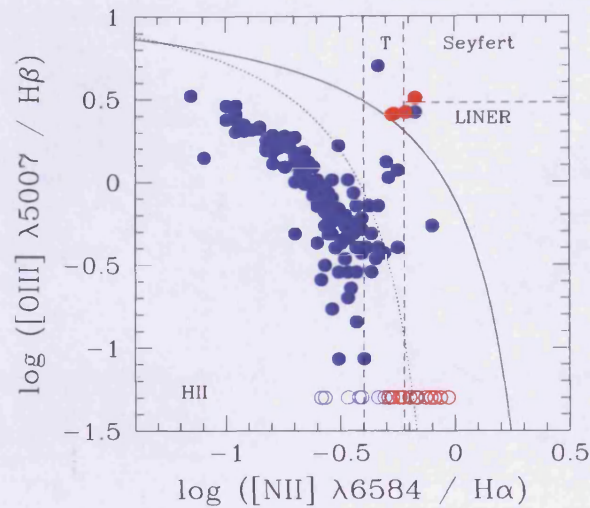


Figure 9.4: The BPT (Baldwin et al., 1981) diagnostic diagram used to classify the spectra of galaxies in this work, based on the $[\text{NII}]/\text{H}\alpha$ and $[\text{OII}]/\text{H}\beta$ line ratios. Objects for which a measurement of $[\text{OII}]/\text{H}\beta$ is not available are plotted at $\log([\text{OII}]/\text{H}\beta) = -1.3$. The Decarli et al. (2007) scheme (straight dashed lines) marks the classification boundaries between star-forming, LINER, Seyfert and composite galaxies, as described in the text. In addition, the demarcation lines between star forming and AGN-host galaxies from Kewley et al. (2001, solid black line) and Kauffmann et al. (2003, dashed black line) are shown. The galaxies with D02-based metallicities $12+\log(\text{O}/\text{H}) > 8.9$ using a single method are highlighted (solid red circles) compared to all other galaxies (blue circles).

produced from each fit. These fits are fairly consistent with the D02-based and PP04-based M-Z relations presented in KE08. The discrepancies between the fits presented here and the KE08 fits are within the errors over most of the range in stellar mass, but are largest at stellar masses lower than $\sim 10^9 M_{\odot}$. These discrepancies arise due to the sample having too few low mass galaxies to accurately constrain the y-intercept of the M-Z relation, compared to the larger range of the sample used in KE08.

The metallicity residuals from the linear and polynomial fits to both the D02- and PP04-based results are presented in Figure 9.5. This figure is important since the residuals represent the scatter in the mass-metallicity relationship, and it is important that the fitted relationship does not introduce any artificial trends across the mass range, in order to accurately study the origin of the scatter. All the residual distributions are remarkably similar, with no trends introduced from the fits. Indeed, the Spearman correlation coefficients for each of the panels are all smaller than 0.05,

Name	R.A.(hms)	Dec.($^{\circ}$ ''')	[NII]/H α	[OIII]/H β	Classification
IC 610	102628.44	201339.8	0.67	2.63	LINER
NGC 3501	110247.26	175921.6	0.53	2.54	Composite
NGC 3756	113648.01	541736.8	0.67	3.20	Seyfert
NGC 4045	120242.26	015836.4	0.57	-	Composite
VCC 167	121554.22	130859.7	0.63	-	AGN
VCC 404	122017.34	041206.0	0.54	2.57	Composite
NGC 4289	122102.30	034320.0	0.60	-	AGN
VCC 517	122201.30	050600.0	0.86	-	AGN
VCC 656	122338.81	065714.5	0.53	-	Composite
VCC 713	122414.10	083203.7	0.68	-	AGN
VCC 792	122522.07	100101.2	0.59	-	Composite
VCC 979	122711.65	092515.1	0.78	-	AGN
VCC 1086	122816.00	092610.6	0.81	-	AGN
VCC 1379	123139.62	165107.5	0.79	0.54	LINER
VCC 1401	123158.91	142509.7	0.53	-	Composite
VCC 1552	123415.77	130429.1	0.74	-	AGN
VCC 1615	123526.33	142948.8	0.81	-	AGN
VCC 1757	123817.79	130635.8	0.51	-	Composite
VCC 1859	124057.47	115441.7	0.63	-	AGN
VCC 2066	124815.05	105906.7	0.67	-	AGN
NGC 4791	125443.96	080310.6	0.57	-	Composite
NGC 5356	135458.45	052001.4	0.61	2.62	LINER

Table 9.1: Properties of the 23 galaxies with D02-based metallicities $12+\log(\text{O}/\text{H}) > 8.9$. Under the classification scheme of Decarli et al. (2007), all these objects display some degree of AGN-like behaviour. I have distinguished between Seyfert and LINER systems where possible.

where a coefficient of zero indicates no observed trend in the data. The PP04 estimates have a slightly higher scatter ($\sigma = 0.13$ dex) compared the scatter of the D02 estimates ($\sigma = 0.11$ dex, excluding the AGN-hosts) and this result holds regardless of whether using the linear or polynomial best fit. The observation that the scatter in the metallicity is around ~ 0.1 dex is in agreement with the scatter reported in T04, which is also comparable to the 0.1 dex error associated with the metallicity estimates (see Chapter 8). Therefore, the choice of linear or polynomial fit does not make a significant difference to the distribution of the residual metallicities.

Finally, since the new D02-based and PP04 based M-Z relations presented in this work are fairly consistent (within the errors) with the D02-based and PP04-based M-Z relations presented in KE08, this suggests the new M-Z relations are reliable to be used in the following analysis.

Base	Fit	a	b	c	d	χ^2_ν
D02	linear	7.339	0.140	-	-	1.21
	polynomial	0.727×10^{-3}	1.979	-0.144	3.360×10^{-3}	1.19
PP04	linear	7.054	0.161	-	-	1.63
	polynomial	0.814×10^{-3}	1.884	-0.129	2.752×10^{-3}	1.60

Table 9.2: The coefficients and χ^2_ν values given by linear and polynomial least-squares fits to the data, where $y = a + bx + cx^2 + dx^3$.

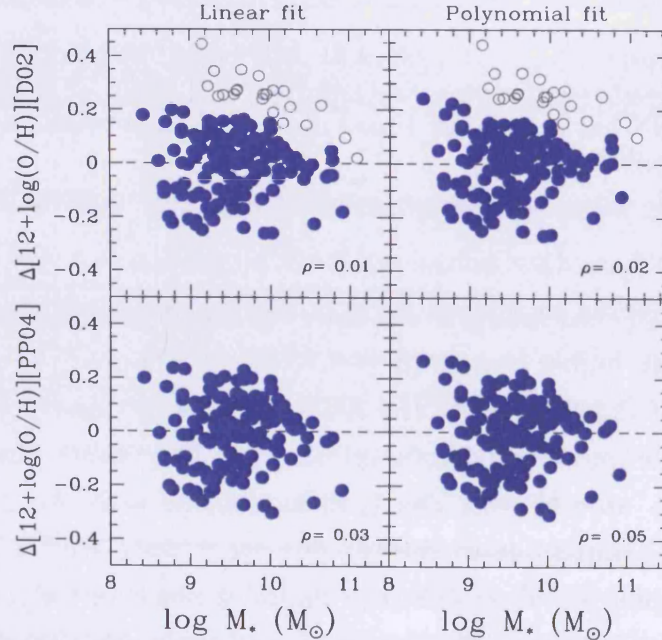


Figure 9.5: The residual metallicities (solid blue circles) for the D02 and PP04 estimates (*top* and *bottom panels*, respectively), obtained when using either the linear or polynomial lines of best fit (*left* and *right panels*, respectively). The open grey circles show the 23 AGN-host galaxies excluded from the analysis.

9.3 SCATTER IN THE M-Z RELATION

In the previous section, a correlation between the stellar mass and gas-phase oxygen abundance is observed, which spans a range of a factor of 10 in metallicity and a factor of 100 in stellar mass. The most interesting observation is the tightness of the correlation, as the scatter from the fitted M-Z relations are only ~ 0.1 dex, which is comparable to the error associated with the metallicity estimates and in agreement with the scatter observed in T04. This observation is quite remarkable when consideration is given to the plethora of processes that potentially affect both quantities. In the following, I attempt to uncover the cause of the scatter in the M-Z relation and determine whether this scatter is due to environmental effects or internal processes.

9.3.1 ENVIRONMENTAL EFFECTS

The stellar mass and metallicity are both regulated by the star formation history of a galaxy, since the formation of stars subsequently leads to the production of metals. However, as discussed in Chapter 5, there is mounting observational evidence which indicates that star formation activity may be significantly altered by environmental effects. Gravitational interactions (Merritt, 1984; Moore et al., 1996), ram pressure stripping (Gunn & Gott, 1972), and hybrid processes combining multiple mechanisms e.g. preprocessing (Fujita, 2004; Cortese et al., 2006), can modulate star formation in galaxies in high density environments. In fact, the observed morphology-density (Dressler, 1980; Whitmore et al., 1993) and star formation-density (e.g. Kennicutt, 1983) relations are thought to partially arise from these external processes.

Since star formation is influenced by internal processes and environmental effects, it is therefore quite surprising that the observed scatter is only 0.1 dex and, naively, I would expect some variation in the M-Z relation in different environments. Seeking to determine any variation in the M-Z relation as a function of environment, Mouhcine et al. (2007) selected a sample of over 37000 galaxies from the SDSS and examined the dependence of the oxygen abundance on the stellar mass and an estimate of the local density, based on the distances to the nearest neighbours of each galaxy. Across a range of environments, from isolated systems to the periphery of clusters, they reported only a weak dependence of the M-Z relations on local density, with changes in metallicity between 0.02 and 0.08 dex occurring over a factor 100 change in local density. They also found that for a fixed stellar mass, galaxies in denser environments displayed a slight metal enhancement compared to galaxies in sparser environments, in agreement with previous results (see e.g. Skillman et al.,

1996 and Dors & Copetti, 2006). It is argued that this suggests that the primary mechanism(s) driving galaxy evolution are dependent on intrinsic properties rather than environmental effects. Moreover, in a recent study performed by Ellison et al. (2009), it is concluded that whilst cluster galaxies are on average more metal rich than field galaxies at a fixed stellar mass, the enhancements are dependent on the local overdensity and not simply cluster membership.

I decided to investigate whether any environmental variation in the M-Z relation or the scatter in the relationship could be present in the HRS+ sample, using the M-Z relations obtained in the previous section and the cluster and field subsamples as defined in Section 2.2. The upper and lower panels of Figure 9.6 present the D02-based and PP04-based results, respectively, for the Virgo cluster members and those galaxies residing outside the cluster. Since the difference between the environment is likely to be small, as suggested by the 0.02 - 0.08 dex metallicity variations reported by Mouhcine et al. (2007) and Ellison et al. (2009), I try a number of different approaches to check for any variations with environment, in order to reach a confident conclusion.

Firstly, I attempt to seek any difference between the scatter of the observations in the two different environments. The M-Z relation displays only minor differences between galaxies in the Virgo cluster and galaxies residing in sparser environments. From a visual inspection of Figure 9.6, it appears that the cluster may have a slightly higher scatter than the field. However, a quantification of the scatter yields no significant difference between the two distributions, as the D02-based(PP04-based) dispersion is 0.13(0.15) dex in the cluster compared to a dispersion of 0.12(0.14) dex in the field galaxies. The correlation in the M-Z diagram of the cluster galaxies is also similar, with Spearman correlation coefficients of 0.53(0.48) in the cluster and 0.58(0.56) in the field. These coefficients relate to probabilities of the two quantities being correlated of $P(\rho) > 99\%$. Thus, the observation that cluster galaxies are distributed at slightly higher metallicities than the field is only a qualitative observation, which I shall return to later in the discussion. The main interesting point to note is that these minor differences are observed in both the D02 and PP04 results, suggesting that they are real differences that occur independently of the choice of calibration.

Secondly, I investigate whether there is a systematic difference between the two environments, by determining the average metallicity for bins at fixed stellar masses. Comparing the binned data for the cluster and field environments (upper right panel of Figure 9.6), it is apparent that whilst the differences in the average metallicity estimates at each fixed stellar mass are of the order of 0.05 dex, there is no systematic metallicity enhancement across the range of mass bins observed for either

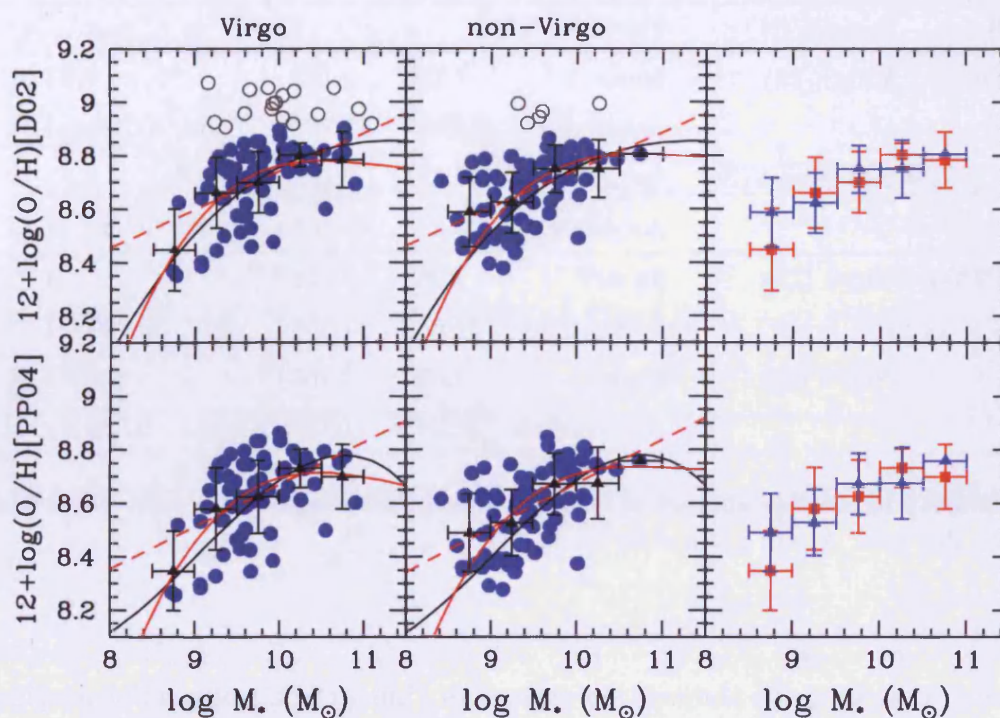


Figure 9.6: The M-Z relations observed from galaxies in the Virgo cluster (*left panels*) and outside the cluster environment (*middle panels*) for both the D02 and PP04 metallicity estimates. The best fit lines given in Table 9.2 are plotted (dashed and solid red lines) together with the KE08 M-Z relations (solid black lines). A comparison of the binned data points from the two different environments (*right panels*) yields minor variations in the M-Z relations of the Virgo (red squares) and non-Virgo (blue triangles) galaxies. The excluded AGN-host galaxies are represented by open grey circles.

environment. Indeed, neither environment shows an enhanced metallicity in any two adjacent mass bins. No real difference is observed between galaxies residing inside or outside the Virgo cluster, especially when taking the error in each average metallicity into account. It should be noted that this same observation holds regardless of the assumed size of the mass bins. Similarly, the lower panels of Figure 9.6 present the PP04-based M-Z relations for the two discrete environments and, concordant with the D02-based results, no systematic metallicity enhancement occurs in the binned data for either environment, despite a qualitative hint that individual galaxies in the cluster have higher oxygen abundances than the field. Thus, no systematic differences in the metallicities of galaxies inhabiting different environments are observed across the range in mass using this approach.

Finally, the metallicity residuals from fitted M-Z relations are investigated for

Base	Sample (N)	Fit	a	b	c	d	χ^2_ν
D02	Virgo (72)	linear	7.320	0.142	-	-	1.29
		polynomial	-34.481	11.760	-1.062	0.031	1.15
	Non-Virgo (74)	linear	7.321	0.142	-	-	1.17
		polynomial	-34.575	11.765	-1.062	0.031	1.17
PP04	Virgo (72)	linear	7.089	0.158	-	-	1.77
		polynomial	-34.080	11.456	-1.017	0.029	1.58
	Non-Virgo (74)	linear	7.021	0.165	-	-	1.56
		polynomial	-34.645	11.765	-1.062	0.031	1.49

Table 9.3: The coefficients and χ^2_ν values given by linear and polynomial least-squares fits to the data, where $y = a + bx + cx^2 + dx^3$.

any differences between the two environments. Linear and polynomial relations are fitted to the data in each environment, using the same method as described in the previous section. The best fit coefficients from the fitted relations and the χ^2_ν values produced by the fit are given in Table 9.3. The M-Z relations demonstrate very little variation between environments (Figure 9.6). In order to uncover any environmental variation in the M-Z relations, the field M-Z relation is used to calculate the residual metallicities for galaxies in both environments. These residuals are plotted against stellar mass in each environment in Figure 9.7.

Overall, the Virgo cluster members do not demonstrate a higher dispersion compared to the non-cluster galaxies and this is independent of the choice of base calibration. No systematic variations between the environments are observed; the individual data points may visually hint at a slight metallicity enhancement in the cluster environment, but a quantification of the data shows no such enhancement. Thus, I find no evidence suggesting an environmental dependence to the scatter of the M-Z relation. However, this may mean that any subtle underlying trend may not be found due to being masked by the observational errors.

In all the results, I do not find any significant variation in the M-Z relation due to the environment inhabited by a galaxy. Although it appears that the M-Z relation is insensitive to the environment a galaxy inhabits, I can not rule out the possibility that an underlying variation is hidden within the observational errors. This may not be such a surprising result. Although Ellison et al. (2009) found that the metallicity enhancement in the cluster M-Z relation was up to 0.05 dex, they also warn that such

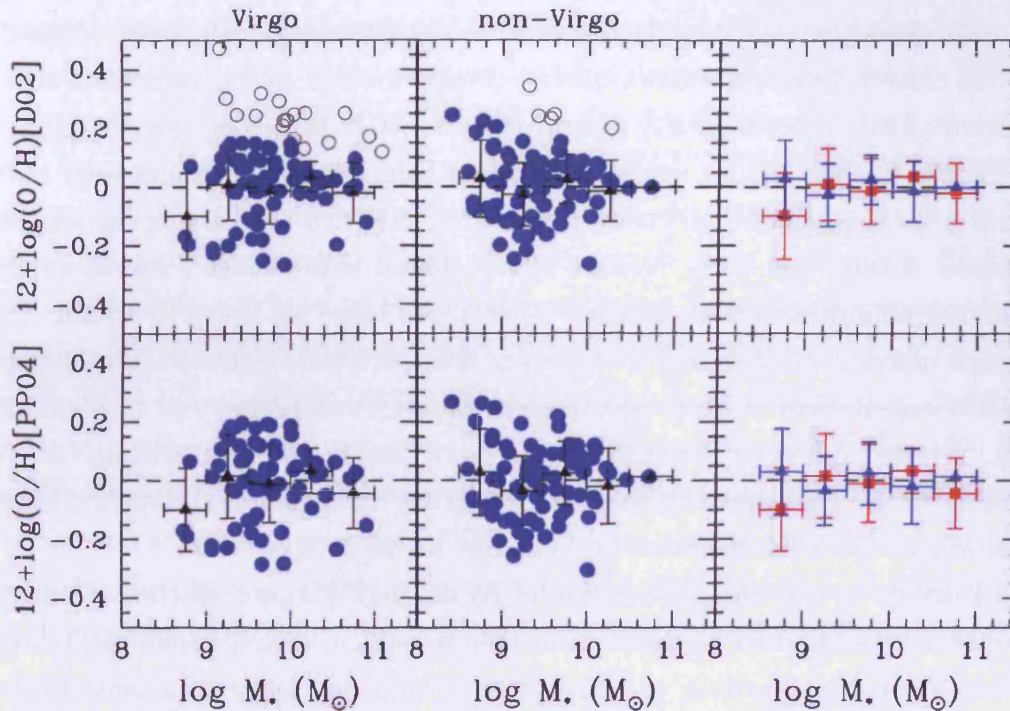


Figure 9.7: The residual M-Z relations observed for galaxies in the Virgo cluster (*left panels*) and outside the cluster environment (*middle panels*) for both the D02 and PP04 residual metallicity estimates calculated from the best fit line to the field M-Z diagram, given in Table 9.2. A comparison of the binned data points from the two different environments (*right panels*) yields minor variations in the M-Z relations of the Virgo (red squares) and non-Virgo (blue triangles) galaxies. The excluded AGN-host galaxies are represented by open grey circles.

environmental differences are subtle and may not be clearly observed in the unbinned data of even large samples (>1300) of galaxies. Whilst the results are not sensitive enough to discriminate whether the small variations I observe are really due to the environment or merely arise from observational errors, I can place an upper limit of 0.1 dex on any environmental variation.

9.3.2 HI DEFICIENCY

Whilst this result is consistent with Ellison et al. (2009) and Mouhcine et al. (2007), it appears to disagree with the study by Skillman et al. (1996). They demonstrate that some individual galaxies within the cluster environment display metallicity enhancements of approximately 0.2 dex, whereas those galaxies on the periphery of the cluster have similar abundances as counterpart systems in sparse environments. In

fact, many initial works based on small samples of well-studied galaxies (e.g. Shields et al., 1991; Henry et al., 1992; Henry et al., 1994; Skillman et al., 1996) suggest that the Virgo cluster members which typically display metallicity enhancements also have a tendency to be environmentally perturbed systems, indicated by a deficiency in their gas content. Recent studies using much larger samples have also indicated that gas deficient objects in the Virgo cluster are more metal rich than field galaxies (Boselli & Gavazzi, 2006). Similarly, Vilchez (1995) found that cluster dwarves appear to have higher abundances than isolated objects. All these studies suggest that the environment plays a greater role in affecting the chemical abundance than compared to the findings presented here, and those of Ellison et al. (2009) and Mouhcine et al. (2007). Whilst I noted earlier that slightly more galaxies are metal rich in the cluster compared to the non-cluster galaxies, such strong environmental dependence is not seen in any of the M-Z diagrams presented in Figures 9.6 or 9.7.

I decide to test the distribution of HI-deficient galaxies on the M-Z diagrams for the D02-based and PP04-based calibrated metallicities (left panels of Figure 9.8). Galaxies are split according to those with a high deficiency of atomic hydrogen, $DEF_{HI} > 0.5$, meaning they have lost $\sim 70\%$ of their gas content compared to similar isolated systems, and those with normal gas content, $DEF_{HI} < 0.5$. It is clearly evident, regardless of the base calibration used, that the HI-deficient galaxies are typically metal rich. The trend is clearer when using the average metallicities for each bin of fixed stellar mass, also shown in Figure 9.8, as this demonstrates that the HI-deficient galaxies do not follow the M-Z relation derived from the overall sample, but typically have enhanced metallicities.

These observations appear consistent with e.g. Skillman et al. (1996). The general interpretation of this observation is that the metals in cluster galaxies are less diluted in the unpolluted gas, due to HI ablation. However, preliminary results from the Herschel Space Telescope have uncovered a correlation between the ratio of the submillimetre-to-optical diameter and with the HI-deficiency, suggesting that the cluster environment is capable of stripping not only gas but also dust and, likely, metals (Cortese et al., 2010). Taking this result into account, the ablation argument becomes hard to imagine, since it implies the enhanced metallicity of HI deficient galaxies is due to the presence of metals that avoid being stripped from a galaxy along with the gas and dust.

An alternative explanation for the observed metallicity enhancements is based on the possibility of a selection effect in the observations. Consider the scenario where gas is stripped from the galaxy via an environmental mechanism, such as ram pressure stripping. In the outskirts of a galaxy, this will lead to a reduction

in the number of observed HII regions, since a reduction of the star formation rate following the removal of gas, combined with the effects of stellar evolution, means that the number of hot young stars emitting ionising photons will decrease. Therefore, only HII regions within the stripping radius will be observed, where gas remains as fuel for new stars to continue to be created, and, in the case of galaxies with strong metallicity gradients, only the most metal rich HII regions will contribute to an integrated measurement of the metallicity. In this scenario, a HI deficient galaxy might appear to have an enhanced metallicity. To test this scenario, I use the radial abundance profiles from two galaxies presented in Skillman et al. (1996). The galaxies, NGC 4254 and NGC 4321, were arbitrarily chosen due to their clear oxygen abundance gradients (when using the Z94 metallicity calibration). The Z94 profiles were first converted into the D02 and PP04 base calibrations, using a polynomial with the conversion coefficients provided in Table 8.3, such that the integrated metallicities from the profile are comparable with the D02 and PP04-based M-Z diagrams. The Z94 and converted D02 and PP04 profiles are presented in the right panels of Figure 9.8.

Firstly, it is evident that the metallicity gradient is dependent on the choice of calibration used for the base metallicity. The Z94 profiles from Skillman et al. (1996) were chosen for displaying the strongest metallicity gradients of the nine galaxies in the Skillman et al. (1996) sample, with the aim of demonstrating the largest possible effect on the observed metallicity due to ram pressure stripping. Yet the metallicity gradient is very weak when the D02 acts as the base calibration. The gradient is still present in the PP04-based profile. The observation that the choice of calibration affects the observed metallicity gradient is an important one and I shall return to this point later in the discussion.

I obtained the integrated metallicities observed in the cases ‘before’ and ‘after’ gas stripping. The integrated metallicity ‘before’ gas stripping was found by weighting the metallicity gradient by an exponentially declining intensity profile $\propto e^{-R/R_E}$, and finding the average intensity-weighted metallicity for the full profile. To calculate the observed metallicity ‘after’ gas stripping, the average intensity-weighted metallicity was found within an assumed stripping radius of $R/R_E = 1.5$. This value is purely an approximation given that the stripping radius found in galaxy models varies depending on the model ingredients and are often around 11-15 kpc in a galaxy with semimajor axis of 25 kpc (Kronberger et al., 2008; Tonnesen & Bryan, 2009). However, this assumption is sufficient for the illustrative purposes of this toy model. From these calculations, it is shown that metallicity enhancements could be produced, dependent on the choice of calibration used and the metallicity gradient within the

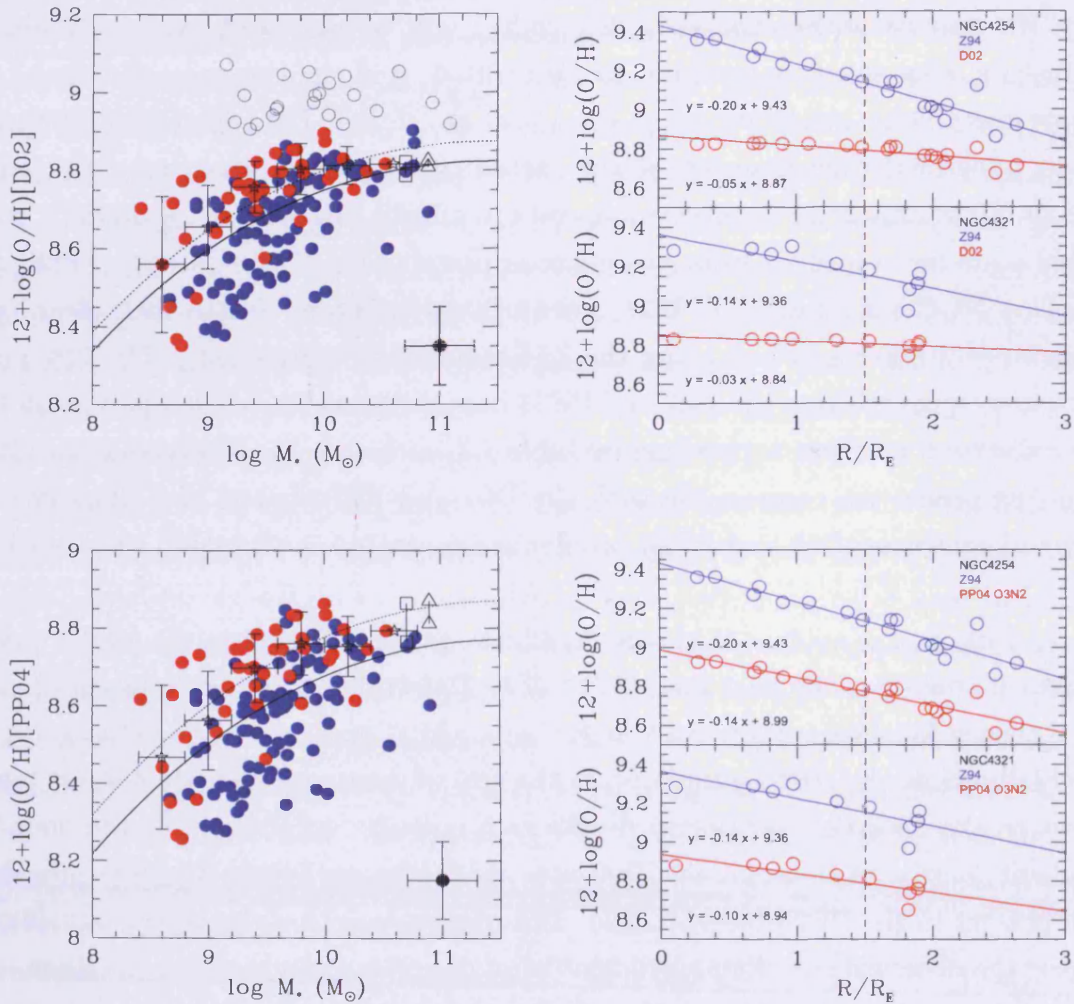


Figure 9.8: The M-Z diagrams for the D02-based and PP04-based calibrated metallicities (*left panels*). Galaxies are split according to those with a high deficiency of atomic hydrogen, $DEF_{HI} > 0.5$ (blue circles), and those with normal gas content, $DEF_{HI} < 0.5$ (red circles). Integrated metallicities are obtained from the radial abundance profiles from Skillman et al. (1996), showing the published Z94-based metallicities and the D02 and PP04-based profiles. The two limits plotted in the left panels for NGC 4254 (black triangle) and NGC 4321 (black square) are based on the integrated metallicities for the total profile and for $R/R_E < 1.5$. Finally, the variation to the M-Z relation (solid black line) when accounting for the increase in the observed (integrated) metallicities due to HI deficient galaxies is shown (dashed black line). The average metallicity for bins of fixed stellar mass (open black stars) typically lie above this line.

galaxy. The D02-based integrated metallicities show small increases in the metallicity for the two galaxies, due to the weak metallicity gradients. However, the variation can be ~ 0.1 dex in the presence of steeper abundance gradients, as demonstrated for the PP04-based metallicity. This is a significant increase to the observed metallicity. Thus, this simple model may partially explain the presence of gas deficient galaxies displaying higher abundances in the cluster environment than in the field, without requiring a M-Z relation which varies in different environments.

9.3.3 GAS CONTENT

Although the metal enhancements observed in HI deficient objects may arise from a selection effect, one might still expect that the gas content of the galaxy will play a role in determining the metallicity of a galaxy, since any variation in the gas content of a galaxy may impact the star formation, which may yield an environmental variation in the chemical abundances. In fact, from a sample of 10^5 SDSS galaxies with estimated HI mass measurements, Zhang et al. (2009) showed that galaxies with a lower gas content often display enhanced metallicities at a fixed stellar mass and found a systematic change in the gas fraction along the M-Z relation. The trend observed in Zhang et al. (2009) was determined from a colour-dependent estimator of the HI-to-stellar-mass ratio, which was calibrated from a sample of 800 galaxies with HI mass measurements from the HyperLeda catalogue and possess a scatter of 0.31 dex. However, they did not investigate this trend in different environments.

With data available for the HRS+ sample, it is possible to investigate the importance of the gas fraction using actual observations and not estimates of the HI mass. It is also possible to examine whether a trend exists between the metallicity and gas fraction in the field and cluster environments. Such a trend should be observed only in the cluster environment, where the environment is known to affect the gas content of the galaxy. Following previous work, I define the gas fraction as the ratio of the HI mass to the sum of the HI and stellar mass,

$$\mu = \frac{M_{HI}}{M_{*} + M_{HI}} \quad (9.2)$$

such that it represents the amount of gas which has not yet been turned into stars. It should be noted that this is a ‘hybrid’ gas fraction, since it does not take into account the contributions of molecular hydrogen or helium gas.

Figure 9.9 shows the relationship between the oxygen abundance and gas fraction, and careful inspection of the figure yields an interesting result. The figure is

divided into two diagrams; the top diagram uses the metallicity estimates based on the D02 calibration and the bottom diagram uses estimates from the PP04 calibration. Both calibrations produce matching results. In the left panels of each diagram, both the M-Z relations and the residual M-Z relations (determined from the best fitting polynomial) show little variation between the Virgo members and the field galaxies, as previously shown in Figures 9.6 and 9.7. These panels emphasize the trends found in the middle and right panels, where the relationship of the metallicity, residual metallicity and gas fraction are investigated in the different environments. The oxygen abundance shows a strong anti-correlation with the gas fraction regardless of environment, although the gas fractions possessed by the Virgo cluster galaxies extend to values lower than the gas fractions of galaxies in the field. Despite the cluster galaxies having lower gas fractions, there is no observed difference in the gas fraction-metallicity trends in the range of μ where the two samples overlap (i.e. $-1.5 < \mu < 0.0$). This confirms that galaxies with high gas-phase metallicities are typically objects with slightly lower gas content. The insensitivity of the metallicity-gas fraction ($Z-\mu$) relation to the environment also lends support to the scenario in which the chemical evolution of galaxies is driven by their intrinsic properties and is not significantly affected by the environment. From this point, the environment shall no longer be considered as a primary mechanism driving the metallicity evolution, since I find no observational support for an environmentally driven M-Z relation.

These results suggest that the gas content of galaxies is typically inversely proportional to the metal content, regardless of the environment they inhabit.

To summarise the main points of this section, I find no significant variation of the M-Z relations interior or exterior to the Virgo cluster, but also cannot conclusively rule out the possibility of a weak sensitivity to the environment. I also demonstrated how a possible selection effect could enhance the observed abundances of HI deficient galaxies without invoking an environmental variation in the M-Z relation. All these findings, consistent with previous studies, suggest that environmental processes play a secondary role in governing the M-Z relation. If this is the case, it raises the question of what internal processes may be responsible for driving the relation. Since there exists a clear relationship between the gas fraction and the metal content of a galaxy, which observations suggest is driven by internal processes rather than environmental effects, I shall now investigate whether this correlation can be modelled using a simple model for galactic chemical evolution.

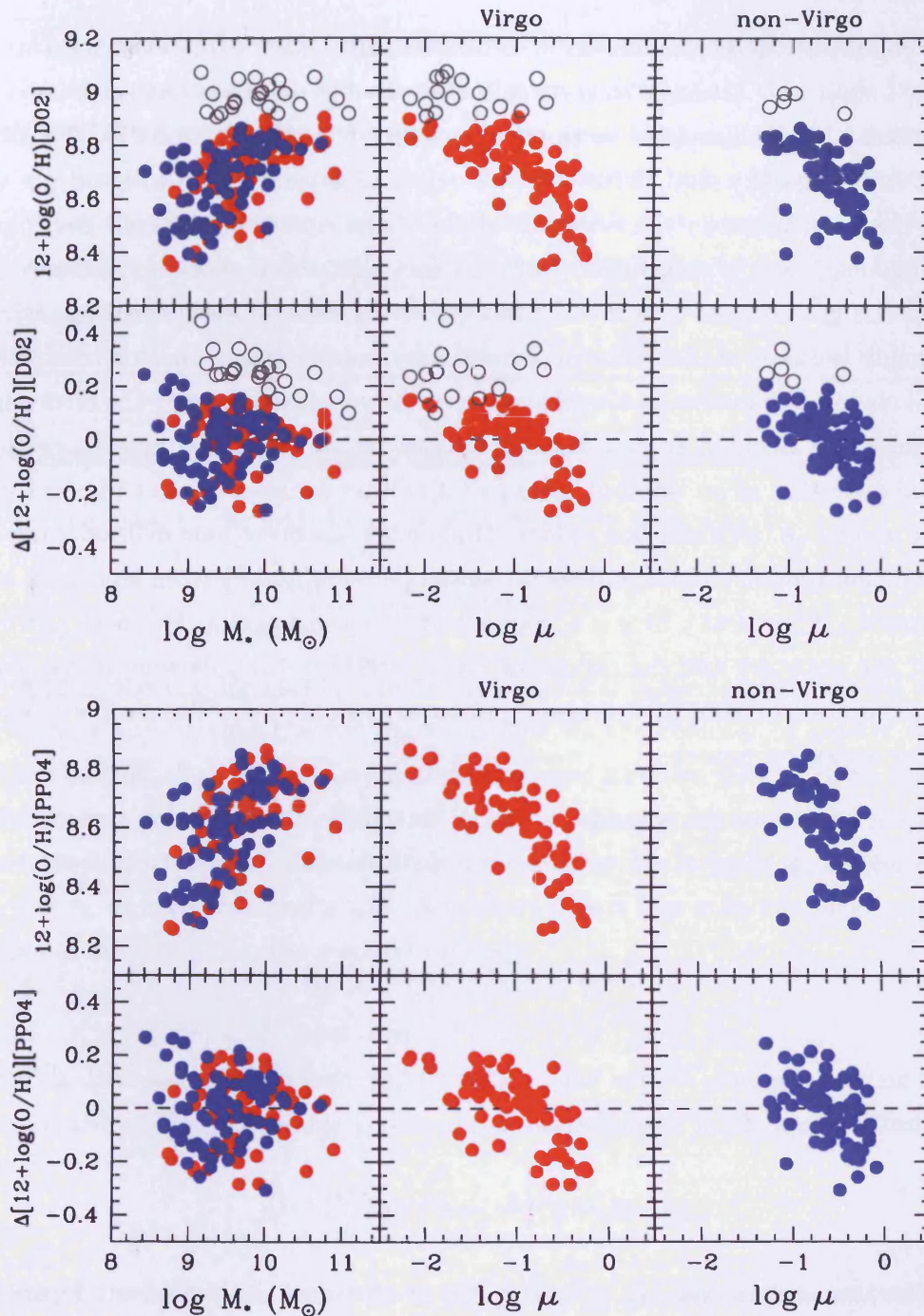


Figure 9.9: The D02-based (*top diagram*) and PP04-based (*bottom diagram*) M-Z relations and residual M-Z relations observed for galaxies in the Virgo cluster (solid red circles) and outside the cluster environment (solid blue circles) are shown in the left panels of each diagram. The oxygen abundance shows a strong anti-correlation with the gas fraction regardless of environment, although Virgo galaxies tend to have a lower gas content than the field (*middle and right panels* of the two diagrams). The excluded AGN-host galaxies are represented by open grey circles.

9.4 THE CLOSED-BOX MODEL

Following the confirmation of a relationship between metal content and gas content, I shall now attempt to constrain the possible scenarios that give rise to this observation. In the previous sections, I concluded that it is probably the intrinsic properties of a galaxy that drive the M-Z relation, since very little significant difference is observed between the relations of the Virgo cluster or the field environment. This conclusion was strengthened from the fact that there exists an anti-correlation between the gas content and metal content, which remains even when removing the relationship between stellar mass and metallicity, supporting the notion that late-type galaxies chemically evolve as closed systems relatively insensitive to the environments they inhabit. I decided to test this conclusion by adopting a simple model for the chemical evolution of an isolated galaxy that neither accretes gas nor removes gas via galactic winds, i.e. a closed-box model. Much work has been done in developing chemical evolution models, and the ideas presented here are mainly from landmark studies by Schmidt (1959, 1963), Searle & Sargent (1972) and Pagel & Patchett (1975), but I adopt the notation and definitions of Pagel (1997) in the following derivation. To start, a number of simplifying assumptions are adopted for the simple closed-box chemical evolution model:

1. The total mass M is made constant to represent an isolated system with no inflow or outflow of material, such that the mass of gas, $g(t)$, and the mass of gas locked in stars and stellar remnants, $s(t)$, are related by

$$M = g(t) + s(t) = \text{const.} \quad (9.3)$$

2. The model galaxy begins with an initial gas mass of pure ‘unenriched’ material that is yet to form stars, hence

$$g(0) = M; S(0) = Z(0) = 0 \quad (9.4)$$

3. The interstellar medium is well mixed at all times and any newly formed stars at a particular time t have the same heavy element abundance as the gas i.e. $Z = Z(t)$.
4. Stellar evolution processes, nucleosynthesis, the ejection of stellar material into the ISM occur on short time scales ($t < 10^7$ yr) compared to the time scales of galactic evolution i.e. the instantaneous recycling approximation introduced by Schmidt (1963).

5. The initial mass function (IMF) $\phi(m) dm$ remains constant.

Using assumptions (4) and (5), three constant parameters can be defined. Here, I adopt α as the proportion of mass in each generation of stars that is retained in long-lived stars and stellar remnants, $\beta \equiv 1 - \alpha$ as the proportion of mass ejected in each generation of stars, and $p \equiv p'/\alpha$ as the mass of heavy elements ejected into the ISM per the unit mass retained in long-lived stars and remnants i.e. the yield of heavy elements (Searle & Sargent, 1972). I can now begin to derive a relationship between the gas content and the gas-phase metallicity. It is obvious from assumption (1) that

$$\frac{dM}{dt} = \frac{dg}{dt} + \frac{ds}{dt} = 0 \quad (9.5)$$

meaning the mass of gas and the mass of stars evolve according to

$$\frac{dg}{dt} = -\frac{ds}{dt} = e(t) - \psi(t) \quad (9.6)$$

where $\psi(t)$ is the star formation rate by mass and $e(t)$ is the ejection rate of material from stars, meaning that the gas mass changes via the removal of gas by astration and the replenishment of gas from material expelled into the ISM by dead stars. The ejection rate is related to the IMF and SFR by applying assumption (5), such that each star ejects material instantaneously upon death. Defining m_{rem} as the remnant mass and τ_m as the lifetime of a star of mass m , then a star is formed at time $(t - \tau_m)$ if it dies at time t . Thus, the ejection rate is

$$e(t) = \int_{m_{\tau=t}}^{m_U} (m - m_{rem}) \psi(t - \tau(m)) \phi(m) dm \quad (9.7)$$

The total abundance of a stable (non-radioactive) element in the gas is

$$\frac{d}{dt}(gZ) = e_z - Z\psi \quad (9.8)$$

i.e. some of the element is lost from the ISM during the star formation process, but may be returned to the ISM via the ejection of material from stars. The term e_z is the total amount of metals ejected from stars. Given that $f_Z(m)$ is the mass fraction of a star which is converted into metals and ejected, the ejection rate of these new metals is

$$e_{new}(t) = \int_{m_{\tau=t}}^{m_U} m f_Z(m) \psi(t - \tau(m)) \phi(m) dm \quad (9.9)$$

However, this equation does not take into account the unprocessed material within a star with a metal abundance of $Z(t - \tau(m))$. The unprocessed material has a mass of $(m - m_{rem} - mf_Z(m))$ then the total ejection rate of both new and old metals is

$$e_Z(t) = \int_{m_\tau=t}^{m_U} [(m - m_{rem} - mf_Z(m)) Z(t - \tau(m)) + mf_Z(m)] \dots \\ \times \psi(t - \tau(m)) \phi(m) dm \quad (9.10)$$

which takes into account recycling of an element without any change in abundance combined with any increase in the abundance due to nuclear processes in stellar evolution.

The mass fraction α which remains locked up in stars with long lifetimes and compact stellar remnants, is given by

$$\alpha = 1 - \int_{m_\tau}^{m_U} (m - m_{rem}) \phi(m) dm \quad (9.11)$$

where the subtracted integral is the return fraction R , the fraction of mass in stars that is returned to the ISM within the lifetime of a star. This is related to the true yield² p_Z which is the mass of newly produced metals ejected from a generation of stars in units of the mass that remains locked up in stars with long lifetimes and compact stellar remnants i.e. $p_Z \propto \alpha^{-1}$. In fact,

$$p_Z = \alpha^{-1} \int_{m_t=\tau}^{m_U} mf_Z(m) \phi(m) dm \quad (9.12)$$

Invoking the instantaneous recycling assumption (4), Equations 9.7 and 9.11 can be assumed to describe stars that die instantly so that $(t - \tau_m)$ becomes t . Thus

$$e(t) = R\psi(t) \\ e_Z(t) = RZ\psi(t) + p_Z\alpha[1 - Z]\psi(t) \quad (9.13)$$

and in the limit of $Z \ll 1$ this equation becomes

$$e_Z(t) = RZ\psi(t) + p_Z\alpha\psi(t) \quad (9.14)$$

²The *true yield* refers to the theoretical value from the simple model whilst the *effective yield*, p_{eff} , introduced later in the text, is the yield derived from observations.

Substituting Equation 9.13 into 9.6 and Equation 9.14 into Equation 9.8 respectively gives

$$\frac{dg}{dt} = -\alpha\psi ; \quad (9.15)$$

and

$$\frac{d}{dt}(gZ) = -\alpha Z\psi + p_Z\alpha\psi \quad (9.16)$$

Now, I solve for the abundance Z of the gas by applying the product rule

$$\frac{d}{dt}(gZ) = g\frac{dZ}{dt} + Z\frac{dg}{dt} \quad (9.17)$$

which gives

$$g\frac{dZ}{dt} = p_Z\alpha\psi \quad (9.18)$$

Eliminating the time dependence by dividing Equation 9.18 by Equation 9.15 provides the relation

$$g\frac{dZ}{dg} = -p_Z \quad (9.19)$$

which can be rearranged to give

$$Z = p_Z \ln \frac{g(0)}{g} = p_Z \ln \frac{M}{g} = p_Z \ln(\mu^{-1}) \quad (9.20)$$

which is the well known relationship between the metallicity and the gas fraction, $\mu = g/M$, first explicitly stated by Searle & Sargent (1972). Finally, it can be seen that for a closed-box model, the ratio $Z_{gas}/\ln(\mu^{-1})$ should be a constant equal to the nucleosynthetic, true yield. The above ratio can actually be defined as the effective yield p_{eff} , such that

$$p_{eff} \equiv \frac{Z_{gas}}{\ln(\mu^{-1})} \quad (9.21)$$

which will be a constant for a galaxy which evolves as a closed-box system i.e. $p_Z = p_{eff}$.

Edmunds (1990) demonstrated in a series of theorems that the ratio will in fact be lower due to pristine inflows and enriched outflows of gas. Figure 9.10, adapted

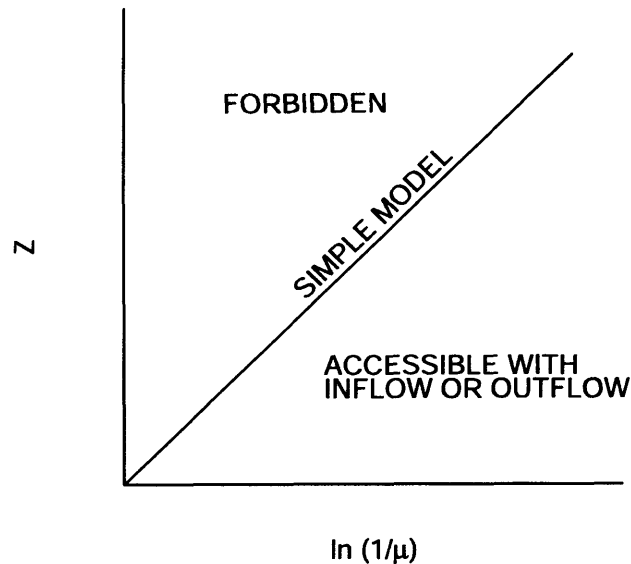


Figure 9.10: A schematic diagram of metallicity versus the logarithm of the inverse of the gas fraction μ in the simple chemical evolution model. The straight line shows the behavior for the closed-box model. The region in the upper left cannot be populated by systems with outflow or unenriched inflows of gas. This figure was taken from Garnett (2002), which is adapted from Edmunds (1990).

from Figure 1 of Edmunds (1990), demonstrates the different populated zones on the Z versus $\ln(\mu^{-1})$ plot. The simple closed box model considered here is a straight line in the diagram with a slope equal to the true yield. There is a region of the diagram where Z is greater than the Z of the simple model, that is forbidden to systems with outflows or unenriched inflows. In these cases the effective yield is always smaller than the true yield. Thus, in the context of the simple chemical evolution model, it may be possible to investigate whether the observed relationship between the metallicities and gas fractions from the previous section is consistent with the closed-box model, or whether inflows and outflows of gas are important. For instance, should the M-Z relation arise due to the variation with the gas fraction (as shown in various panels of Figure 9.9) then I would expect that the effective yields from the sample should be constant. On the other hand, a systematic variation of the effective yield with galaxy mass could indicate that gas flows are important and the closed-box model is not sufficient to explain the origin of the M-Z relation.

In order to test whether the closed-box model is capable of describing the relationship between the oxygen abundance and the gas fraction, I first investigate the effective yield. Figure 9.11 shows the effective yield versus the logarithm of the stellar mass. Firstly, the dynamical ranges of the effective yield is consistent

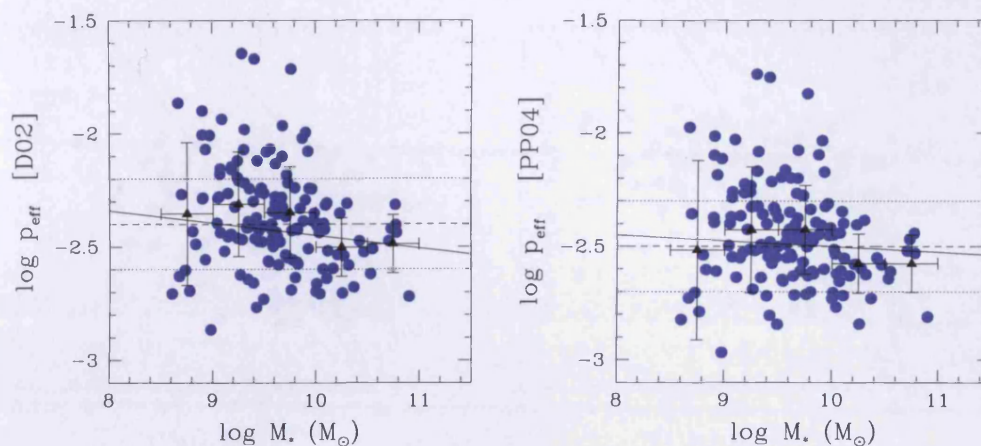


Figure 9.11: The effective yield versus the logarithm of the stellar mass using metallicities derived from the D02 (*left panel*) and PP04 (*right panel*) base calibrations, for all the HRS+ galaxies (blue circles) and the mean yield in stellar mass bins (black triangles). The average yield (dashed black line) and the best fit to the data (solid black line) are plotted together with the 1σ limits (dashed black line). The plot suggests that the mean effective yield of oxygen is fairly constant for all stellar masses.

with yields found for the late-type galaxies in Pilyugin et al. (2004). The D02- and PP04-based yields are similar, with a 0.1 dex systematic offset between the yields, with averages of $p_{eff} = 10^{-2.4}$ and $p_{eff} = 10^{-2.5}$ respectively. Both yields have a standard deviation of 0.2 dex. These are consistent with the yields reported in Pilyugin et al. (2004) and Pilyugin et al. (2007). This average effective yield appears to be fairly constant across the range of stellar mass, although a least squares fit shows a slight trend present when using both calibrations. The Spearman coefficient of rank correlation between the two quantities is $\rho = -0.25$ and $\rho = -0.23$ for the D02 and PP04 results, respectively, indicates there is only a weak anticorrelation between the effective yield and the stellar mass. These values have corresponding probabilities of $P(\rho) > 95\%$. However, p_{eff} is most scattered towards lower mass systems and this is likely due to the tendency of the oxygen abundances also being more scattered on the M-Z relation towards lower stellar masses. Thus, the weak trend observed here is not likely to be significant and I assume that the average effective yield is constant across the range of stellar mass.

The observed average p_{eff} values are adopted as the value of the true nucleosynthetic yield p_Z in Equation 9.20. In Figure 9.12, I construct diagrams of the abundance versus the natural logarithm of the inverse of the gas fraction, similar to

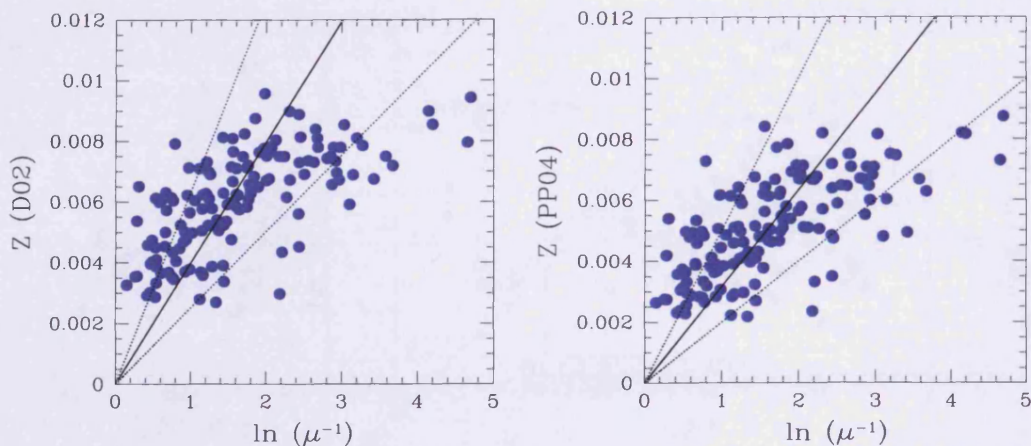


Figure 9.12: The relationship between the metallicity and the logarithm of the inverse of the gas fraction μ in the simple chemical evolution model. The straight line shows the behavior for the closed-box model, which appears to fit the observations (blue circles), and the 1σ limits (dashed black line). The two panels show the D02-based (left) and PP04-based (right) results.

the schematic diagram presented in Figure 9.10. With the adopted values, it is evident that the simple closed-box model relating the abundance and the gas fraction fits the observations reasonably well, considering not only the many assumptions which go into the derivation of Equation 9.20 but also the differences in the theoretical and observational gas fractions. The theoretical gas fraction is the ratio of the total gas mass to the total baryonic mass, whereas the observed gas fraction does not take into account the molecular hydrogen or helium gas. It is possible that if the measurements of the neglected gas components were to be included, the plotted points would shift towards the left, thus reinforcing the fit of the closed-box model. It is important to note that the model does not fit well the galaxies with lower gas fractions (i.e. $\log \mu > \sim 3$) at higher metallicities. Since it was shown in Figure 9.9 that the Virgo cluster members typically have the lowest gas fraction, the poor fit is most likely due to the closed-box model neglecting the removal of gas via environmental mechanisms. Finally, I show the predictions of the simple closed box model in a slightly different way, to demonstrate how the model matches the observed relationship between the oxygen abundance and the gas fraction. In Figure 9.13, I reproduce the $12+\log(\text{O}/\text{H})$ versus $\log \mu$ plot for the whole sample (as previously shown in Figure 9.9) with the predicted results from the closed-box model, again using the adopted values for p_Z . Since I used the oxygen abundances given by number relative to hydrogen (i.e. units

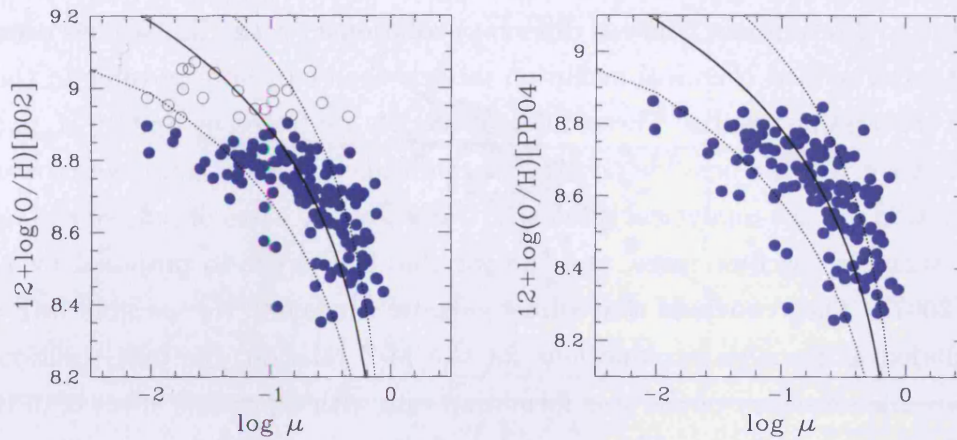


Figure 9.13: The oxygen abundance versus the logarithm of the gas fraction, derived using the D02 (*left panels*) and PP04 (*right panel*) base calibrations. Galaxies (blue circles) are fitted by the prediction of the closed-box model (solid black line), described by Equation 9.20, together with the 1σ limits (dashed black line).

of $12+\log(\text{O}/\text{H})$), whereas the value of Z in the chemical evolution equations is given in units of mass fraction, the conversion from abundance by number to abundance by mass of

$$Z_{\text{O}} = 12(\text{O}/\text{H}) \quad (9.22)$$

was adopted from Garnett et al. (1997) and Garnett (2002). This conversion was used to predict the $12+\log(\text{O}/\text{H})$ versus gas fraction relationship shown in Figure 9.13 from Equation 9.20. The results suggest that the relationship may be explained by a galaxy evolving according to a closed-box system, where inflows or outflows of gas are not so important.

To summarise the main results so far, there is some indication that most of the galaxies in the sample evolve according to a closed-box model of evolution. At this point, I cannot rule out a contribution from the inflows or outflows of gas, particularly when the closed-box model fails to predict the M-Z relation for gas deficient objects in the Virgo cluster. Indeed, galaxies are not closed systems. In addition, Dalcanton (2007) showed that it may not be possible to draw conclusions about the impact of inflows or outflows by using measurements of the effective yields, concluding that any change to the effective yield due to gas flows may quickly be returned to the true yield expected by closed-box evolution. As such, galaxies may be observed to evolve according to a closed-box model despite actually being affected by inflows and

outflows. Yet, despite these results suggesting that the approach employed here is too simplistic to discriminate between different evolutionary scenarios, studies using more accurate and refined chemical evolution models than currently possible in this work present contrasting results. These different models are tested by Spitoni et al. (2010), who study some of the possible physical mechanisms that could contribute towards the M-Z relation via the analytical solutions. They test the cases of inflows and outflows of gas, variable gas flow rates, and the variable IMF scenario proposed by Köppen et al. (2007). They conclude that whilst galactic winds and the variable IMF cannot be excluded as possible explanations for the M-Z relation, the best solution could be a variable efficiency of the star formation rate with a possible effect of outflowing gas in lower mass galaxies. Therefore, their findings are partially consistent with the interpretation seen here.

Thus, as the gas content of a galaxy becomes depleted as stars are formed, the stars then produce a roughly constant yield of heavy elements and progressively enrich the ISM as the galaxy evolves. In this scenario, the M-Z relation arises out of a varying star formation efficiency with galaxy mass, such that low mass galaxies are less efficient at converting gas into metals. The effects of this are observed in Figure 9.9: removing the dependence of the metallicity on the stellar mass shows that the lower mass galaxies have higher gas fractions and lower metallicities, supporting the notion that a mass-dependent star formation efficiency produces the observed M-Z relation. Unfortunately, it is not possible to analytically explore the case of increasing star formation efficiency with increasing mass, since the SFR does not appear in the solution of the closed-box model derived above. However, this scenario has recently been studied by Calura et al. (2009), who find that the M-Z relation can be reproduced using an increasing efficiency of star formation with mass in galaxies of all morphological types, without any need to invoke inflows of pristine gas or outflows of enriched gas that favour the loss of metals in the less massive galaxies. Their findings successfully predict the M-Z relation not just in the local universe, as studied in this work, but also out to the high redshift universe. Thus, their work supports the scenario of a varying star formation efficiency.

The conclusion that less massive galaxies are less evolved compared to larger galaxies, due to the efficiency of star formation being larger in more massive systems, is not a new result. Indeed, the scenario has both observational (e.g. Lequeux et al., 1979; Matteucci, 1994) and theoretical support from N-body simulations (e.g. Mouhcine et al., 2008). Fortunately, I can observationally test for a variation of star formation efficiency with mass by using the GALEX NUV magnitudes obtained in Chapter 3 to estimate the SFR of the HRS+ galaxies. I use the conversion relation

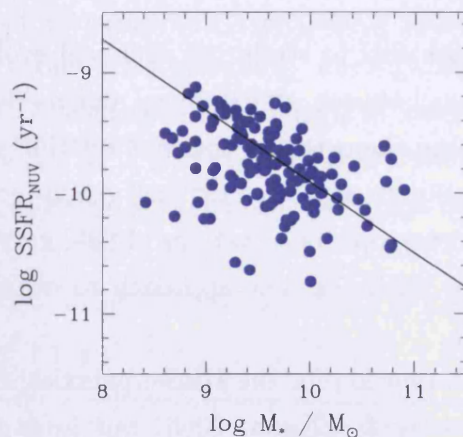


Figure 9.14: The SSFR versus stellar mass for the HRS+ galaxies (*blue circles*). The best fit to the data is shown (*black line*).

of Iglesias-Páramo et al. (2006), given by

$$\log SFR_{NUV}(M_{\odot} \text{ yr}^{-1}) = \log L_{NUV}(L_{\odot}) - 9.33 \quad (9.23)$$

to determine the SFRs. The ratio of the star formation rate to the stellar mass, called the specific SFR (hereafter SSFR), compares the present rate of star formation to the amount of stars made due to the past SF history. Figure 9.14 presents the SSFR plotted against the stellar mass. It is evident that there is a slight trend between the SSFR and M_{\star} , with a Spearman correlation coefficient of $\rho = -0.42$ (with a significance of $P(\rho) > 99.9\%$). Thus, the timescales for the lower mass galaxies to form their stars at the present rate of SF are shorter than the higher mass galaxies. This suggests that the high mass systems formed the bulk of their stellar content at an earlier time. Therefore, these observations support the notion that a variation of the star formation efficiency across the stellar mass produces the observed M-Z relation. Lower mass galaxies are less efficient at converting their gas into stars, leading to a lower metal content compared to systems with higher masses that are able to convert their gas into stars more efficiently, producing a lower gas content and higher metal content.

9.5 CONCLUSIONS

The aim of this work was to study the chemical evolution of galaxies and, in particular, the relationship between stellar mass and metallicity. Constraining the possible explanations behind the origin of the M-Z relation would yield an important understanding of the dominant processes driving galaxy evolution in the local universe. I used the new spectroscopic observations of field galaxies in the HRS+ sample (see Chapter 4) combined with the new approach to obtaining reliable metallicity estimates (see Chapter 8).

I observed the M-Z relation for the HRS+ galaxies, finding it to be consistent with previous works (Kewley & Ellison, 2008) but identifying possible AGN-host galaxies contaminating the sample, which were excluded from further analysis. I used best fit polynomial functions, motivated by previous observations, to determine the M-Z relations.

I investigated whether any environmental variation in the M-Z relation or the scatter in the relationship could be present in the HRS+ sample, by looking at the best fit M-Z relations of galaxies interior and exterior to the Virgo cluster. I found no evidence suggesting an environmental dependence of either the M-Z relation or the scatter of relation. Although I cannot rule out the weak environmental trends reported by some recent studies (e.g. Mouhcine et al., 2007; Ellison et al., 2009), I concluded that contribution to the scatter of the M-Z relation by the environment is probably a secondary effect and that the M-Z relation is most likely driven by internal processes. Indeed, a correlation was found between the metal content and gas content of a galaxy, which could be described by a closed-box model. As the gas content of a galaxy becomes depleted as stars are formed, the stars then produce a roughly constant yield of heavy elements and progressively enriches the ISM as the galaxy evolves. In this scenario, the M-Z relation arises out of a varying star formation efficiency with galaxy mass, such that low mass galaxies are less efficient at converting gas into metals. Whilst I could not exclude other scenarios involving gas flows, my interpretation of the results is consistent with previous studies.

Overall, I conclude that the chemical evolution of a galaxy is most likely driven by internal processes and any environmental effects are of secondary importance.

Finally, using metallicity estimates derived from either the D02 or the PP04 calibration as the base metallicity yield similar results. Often, only a systematic shift was observed between the two sets of results, which is expected due to the relationship between the two calibrations. Since the same conclusions were reached independently of the choice of calibration used, it is likely that these conclusions are real and not

spurious trends introduced via the method of metallicity estimation.

In order to further constrain the conclusions presented here, future studies using the HRS+ sample should involve a more thorough analytical approach to modelling the different possible scenarios of the chemical evolution models, and not just rely on the closed-box model. It is important to constrain the contribution, if any, of galactic winds in low mass galaxies that may also shape the M-Z relation.

CHAPTER 10

DISCUSSION & CONCLUSIONS

10.1 OVERVIEW

The aim of this thesis was to study the properties of late-type galaxies inhabiting a range of environments in the local universe, in order to extend our knowledge of the processes which play a role in the evolution of nearby galaxies and so constrain current theories on evolutionary scenarios. In particular, I was interested in disentangling environmental effects from internal processes, and seek an answer to the question of whether nature or nurture drives galaxy evolution.

The analysis presented in this work was specifically focussed towards answering three current problems in galaxy evolution. Are active nuclei responsible for quenching star formation in late-type galaxies, or do environmental effects play a role? Is the feedback from active nuclei even capable of significantly influencing star formation in late-types? Does the mass-metallicity relation vary with environment, or do internal processes dominate the chemical evolution of a galaxy?

These questions were investigated using a volume-limited sample of 454 galaxies, covering the entire range of morphological type, mass and local density, from galaxies evolving in relative isolation to the heart of the dense Virgo cluster. As defined, the sample was ideal for addressing the aims of this work. Ultraviolet to infrared imaging, optical nuclear and drift-scan spectroscopy, and atomic hydrogen (21 cm) line data were all available for a statistically representative fraction of the total selected sample. The combination of this multiwavelength data enabled the different stellar populations, star formation activity, nuclear activity, gas-phase metallicity and gas content to be traced. Observing these key components allowed the investigation of the processes affecting star formation and chemical evolution in nearby galaxies.

10.2 KEY RESULTS

The main results of this investigation are as follows:

1. The bimodality in the galaxy population is confirmed. Galaxies occupy different regions in the ultraviolet-infrared colour-mass parameter space: star-forming late-types occupy a blue cloud, quiescent early-types reside on a red sequence and a population of galaxies reside in the transition region.
2. The population of the transition region are found to host active nuclei, yet no evidence is found to suggest that the nuclear activity is linked to the redder colours of late-type galaxies with quenched star formation. Transition region systems are predominantly gas deficient, late-type galaxies typically residing in the cluster environment, suggesting that the environment does play a role in quenching star formation. However, not all transition region galaxies are gas deficient, cluster members and some are in fact red sequence galaxies which have rejuvenated their star formation, possibly by a merger with a gas rich companion or via the accretion of additional gas.
3. From the ultraviolet-infrared colour profiles of galaxies, it is shown that the typical extent of their ultraviolet emission decreases with respect to the infrared emission as the integrated colour becomes redder, indicating that the star-forming disks become truncated from the outside-in. The observed correlation between the ratio of the ultraviolet to infrared isophotal radii with the gas deficiency again points to the removal of gas from the outskirts of galaxies by the environment causing the star formation quenching.
4. Although this study also confirms that the bulk of the transition region population display some level of nuclear activity, at no point during these investigations is evidence found for the influence of AGN feedback on the star formation activity of late-type galaxies. The predictions from a simple toy model for the effect of AGN feedback on star formation demonstrate that the accretion power of active nuclei in low mass haloes typical of star-forming late-types are not powerful enough to significantly quench the star formation. A comparison of these predictions with observational estimates of the feedback from AGN support this notion. I conclude that the AGN observed in the transition region galaxies are not powerful enough to influence star formation.
5. Star forming galaxies on the blue cloud convert their gas into metals according to internal processes with an efficiency apparently dependent on the mass of

the system. Lower mass galaxies are less efficient at consuming their gas supply than higher mass galaxies, giving rise to the observed mass-metallicity relation. The relation appears to be invariant to the effects of different environments and, in fact, blue cloud galaxies inhabiting different environments share similar properties.

Therefore, I have obtained new insights into the driving forces of galaxy evolution in the nearby Universe. These results can now be placed into the broader framework of galaxy evolution theory, and the remainder of this chapter focusses on how these new constraints improve our understanding in this field.

10.3 CONSTRAINTS ON GALAXY EVOLUTION

The observation of the bimodal distribution of the ultraviolet-infrared colours of galaxies confirms the results of previous studies (e.g. Baldry et al., 2004); star-forming late types populate a blue cloud, quiescent early-types form a red sequence and, between these two populations, a transition region is populated by galaxies with a variety of properties. Following from the analysis of the properties of these populations presented in this thesis, a more detailed picture of the influences on the evolution of galaxies in the nearby universe emerges.

10.3.1 STAR FORMATION ON THE BLUE CLOUD

Star-forming objects form a blue cloud in both low and high density environments. The relationship between the stellar mass and metallicity is an important observational tool for studying chemical evolution in these objects, yet previous studies have provided contradicting results on whether the environment played any role in either the shape or scatter of the relation. Galaxies in the cluster environment are shown by Skillman et al. (1996), among others, to display enhanced metallicities compared to the field environment, whereas others show little or no environmental variation (Mouhcine et al., 2007; Ellison et al., 2009). At the start of this thesis, I posed the question: *does the mass-metallicity relation vary with environment or do internal processes dominate the chemical evolution of a galaxy?*

To answer this question, I used integrated, drift scan optical spectroscopy of galaxies in different environments, and developed a new method for reliably estimating gas phase oxygen abundances. With this new method, I then compared the mass-metallicity (M-Z) relations derived from observations of cluster and field galaxies. I

found no evidence for an environmental dependence on the M-Z relation. Regardless of the environment they inhabit, star-forming systems are observed to convert their gas into stars and subsequently metals, as seen in relations between the gas content, star formation rate, stellar mass and gas-phase metallicity. Indeed, the latter three properties have recently been shown to form a distinct plane in the three dimensional parameter space, a so-called ‘Fundamental Metallicity Relation’ (Mannucci et al., 2010).

The efficiency with which galaxies are increasing their stellar mass, indicated by their specific star formation rates, is dependent on the mass of the systems, as lower mass systems possess higher specific rates of star formation than higher mass systems. Whilst not a new result (e.g. Lequeux et al., 1979; Boselli et al., 2001), it indicates that more massive galaxies have formed the bulk of their stellar mass at earlier epochs compared to smaller systems. Thus, lower mass galaxies appear to be less efficient at converting their gas into stars and subsequently metals and it appears that the observed mass-metallicity relation of star-forming galaxies on the blue cloud may arise from a mass-dependent variation in the star formation efficiency. In other words, low mass galaxies simply have a lower metal content because they have converted less gas into stars, hence less metals have been produced. As such, the scatter in the M-Z relation may therefore originate from the scatter in the gas content of late-type galaxies. The fact that the M-Z relation is not observed to vary significantly between different environments, and that a relationship exists between metallicity and gas content, which is well fitted by closed-box model for chemical evolution, seems to lend credence to the conclusion that the relation and scatter are mainly driven by internal processes. No clear evidence is presented to suggest that the environment plays a dominant role in shaping the M-Z relation, although it is possible that environmental effects may play a small secondary role.

Whilst the results may imply that, at least in the local universe, the effect of the environment does not need to be taken into account when attempting to replicate the M-Z relation for star-forming objects in theoretical models, I cannot exclude some of the internal effects that may be unobserved yet still important for chemical evolution. As noted by Dalcanton (2007), the analytical method adopted may not be sufficient to differentiate between the effects of the inflow or outflow of gas, due to the possibility of short timescales involved in the replenishment of metals lost via gas outflow. However, the analysis presented in this thesis has indicated that these effects are likely of second order importance.

10.3.2 MIGRATION FROM THE BLUE CLOUD

In addition to studying whether nature or nurture played a dominant role in shaping the stellar mass-metallicity relation and driving the chemical evolution of galaxies, I also studied the processes affecting star formation in late-type galaxies.

Recent observational evidence using colour-magnitude diagrams have shown that galaxies with quenched star formation, lying between blue star-forming galaxies and red quiescent systems, are preferentially AGN-hosts (Martin et al., 2007; Schawinski et al., 2007). This correlation between nuclear activity and colour has been interpreted as a physical link between AGN feedback and the quenching of the star formation. Motivated by the need to properly test this conclusion, in light of the many other mechanisms capable of modifying the gas content of galaxies and quenching star formation as a result (Boselli & Gavazzi, 2006), one of the aims of this thesis was to determine *if active nuclei are responsible for quenching star formation in nearby galaxies*.

The importance of AGN feedback

Although AGN-host galaxies do reside in the transition region, the observations showed that AGNs are not preferentially found in the transition region and also reside on the blue sequence. In addition, at fixed stellar mass, AGNs do not tend to be redder (i.e., have a lower specific star formation rate) than galaxies with HII star-forming nuclei or composite systems. Thus, I do not find any clear evidence of a suppression of the star formation in AGNs.

The evidence suggesting that active nuclei are not responsible for the migration of nearby spirals from the blue to the red sequence is not only contradictory to the interpretation of Schawinski et al. (2007), but also casts doubt on whether AGN feedback is capable of quenching star formation. Indeed, another goal of this thesis was to determine the impact of AGN feedback on star formation. To tackle this problem, I constructed a simple model to test whether the AGN present in late-type galaxies are powerful enough to significantly quench the star formation in the disks, thus driving the spirals from the blue to the red sequence. Based on current theory, the model indicates that although in large halos, the central black holes are massive enough to rapidly accrete material and efficiently radiate energy capable of quenching star formation, this is not true for small halos ($M_{halo} < 10^{12} M_{\odot}$), in agreement with other studies (e.g. Croton et al., 2006; Somerville et al., 2008).

Given the large number of assumptions in the model, the theoretical predictions for how the AGN power affected the star formation rate were tested using the

ultraviolet imaging and optical emission line data as tracers of the star formation rate and mass accretion rate, respectively. Comparing these observational indicators with the model predictions, I explored the relationship between the AGN and the star forming disk. I found that the AGN in the sample are not powerful enough to reach the predicted threshold where the radiative energy from the black hole accretion became significant enough to impact the star formation rate. The results suggest that the AGN residing in late-type galaxies are typically LINER-like systems, consistent with the current understanding of low luminosity AGN. As such, I show that it appears that AGN feedback is not as important to the evolution of star-forming galaxies as the environment they inhabit.

However, I remind the reader that the conclusions presented here may only be valid for the local universe, and as such should not be blindly applied to observations of the high redshift Universe. It is likely that different processes have come to dominate the evolution of galaxies during the evolution of the Universe, and AGN feedback may play a role in driving galaxy evolution at earlier epochs.

The importance of the environment

There already exists mounting observational evidence that strong modifications to the gas content of galaxies, via environmental effects, can drastically alter the current rate of star formation. Although the star-forming galaxies on the blue cloud appear to evolve according to a closed system, with galaxies of a given mass displaying similar chemical abundances, it appears that a removal of the gas eventually leads to a quenching in star formation, which drives the galaxy from the blue cloud towards the red sequence as the existing stellar populations evolve towards redder colours.

This scenario is suggested and supported by the observed population of late-type galaxies occupying the transition region, which typically show a deficiency of their atomic hydrogen content. In addition, these late-types preferentially reside in high density environments, suggesting that the quenching of the star formation may be caused via hydrodynamical interactions with the intercluster medium. Thus, the quenching of star formation and subsequent stellar evolution may drive the galaxy from the blue cloud towards the red sequence and into the transition region, creating a population of late-type, spiral galaxies with redder ultraviolet-infrared colours, lower star formation rates and typically with low gas content. Timescales for migrating across the transition region are estimated at ~ 1 Gyr with an upper limit of 3 Gyr.

This result has implications for current models of galaxy evolution, since it suggests that the red sequence, predominately composed of early-type systems which

have produced their stars a long time ago, is being polluted by disk galaxies in the local universe. The additional flux of galaxies towards the red sequence is not at present predicted by theoretical models, as environmental effects such as ram pressure stripping are not incorporated into the prescriptions for numerical N-body simulations (such as e.g. the Millenium Run simulations). Although the resolution of today's simulations cannot feasibly include such detailed calculations, future efforts must account for the effects of the environment in order to gain an accurate picture of galaxy evolution.

10.3.3 EVOLUTION FROM THE RED SEQUENCE

Not all galaxies in the transition region are gas deficient, late-types or reside exclusively in high density environments like clusters. It may be possible that early-type systems may rejuvenate their star formation via mergers with gas-rich systems or via gas accretion, thus, there are multiple evolutionary paths that can lead into the transition region. The flux of galaxies from the red sequence must be small, however, since the red sequence has been shown to increase with cosmic time. In the local universe, at least, it appears that environmental effects are more important for galaxy evolution.

It is clear that the evolutionary histories of the transition region galaxies are more complicated than previously thought. Because the transition region has been shown to host the peak of the AGN population, it was suggested that feedback from an AGN causes the quenching of the star formation and subsequent migration. However, no evidence for AGN feedback quenching star formation in late-type galaxies with properties that typify the transition region population is seen in this work. The impact of AGN feedback on star formation only appears important in the evolution of massive galaxies and, although this behaviour aids the matching of theoretical luminosity functions to those observed in the universe, it appears that environmental factors need to be incorporated into future models.

10.4 FINAL CONCLUSION

The main aims of this thesis were to uncover the dominant mechanism(s) driving nearby galaxy evolution, determine the impact of feedback from active galactic nuclei on star formation, and study the evolution of the chemical composition of star-forming galaxies in different environments.

From the analysis performed in this thesis, I conclude the following. Star-forming galaxies primarily evolve according to their mass, with star formation being

most efficient in the higher mass galaxies and vice versa. Lower mass galaxies are less efficient at converting their gas into stars, leading to a lower metal content compared to systems with higher masses that are able to convert their gas into stars more efficiently, producing a lower gas content and higher metal content. This gives rise to the observed mass-metallicity relation. The chemical evolution of star-forming galaxies, as traced by this relation, is shown to be invariant across different environments, suggesting that chemical evolution may be driven by internal properties, such as the mass. However, galaxies that find themselves in the cluster environment may be subjected to a number of processes capable of removing the gas that acts as the fuel supply for star formation, since late-type galaxies with quenched star formation are typically gas deficient systems residing in the cluster environment. The quenching of star formation and the subsequent ageing of the existing stellar population drives galaxies from a blue cloud of star-forming objects towards the red sequence of quiescent, passively evolving systems. Whilst this migration is likely driven by the effect of the environment, a fraction of quenched late-type galaxies are not gas deficient. These systems form a more heterogeneous class of objects with probably more complex evolutionary histories which remain uncertain. There remains the possibility that some red sequence galaxies have rejuvenated their gas supply and have evolved from the red sequence following a recent episode of star formation, or that star formation has been suppressed by an alternative mechanism to gas stripping. Thus, the origin of transition galaxies with quenched star formation but a normal gas supply is unclear.

This evolutionary scenario is based purely on observational evidence. Since I find no evidence that feedback from active nuclei is playing a role in quenching star formation in late-types, I do not need to invoke AGN feedback as a dominant mechanism driving nearby galaxy evolution in this theory. I remind the reader that this is likely only valid for the local Universe, since AGN feedback may still play a role in the formation of the red sequence at higher redshifts, but the lack of observational support for AGN feedback in late-types should be considered in galaxy models. Moreover, future models should explore the various environmental processes which are more likely to affect the properties of $z \sim 0$ galaxies.

The clear observational evidence presented here indicates that, in the concordance model of galaxy formation and evolution, environmental effects must be taken into account in order to gain a better understanding of galaxy evolution in the local Universe.

10.5 FUTURE WORK

As demonstrated in this thesis, the extended sample of the Herschel Reference Survey, on which the selection criteria of the HRS+ sample is based, provides an ideal sample for studying the properties of nearby galaxies in different environments. I have been able to gain much additional insight into the relative influences of the environment on star formation and chemical evolution in late-type galaxies using the multiwavelength observations available for the HRS+ galaxies. However, this study has also raised a number of open questions that must be addressed, to move towards building a complete picture of how galaxies evolve.

The growth of the red sequence

The migration of galaxies from the blue cloud to the red sequence suggests that, in the nearby universe, the red sequence is becoming ‘polluted’ by disk galaxies with quenched star formation. Whilst the evidence presented here clearly supports the migration scenario for HI deficient galaxies, the large uncertainties on the typical migration timescale and on the observations meant that I could not determine an accurate ‘migration’ rate. This would be useful to quantify the mass accretion rate onto the red sequence, an important constraint for galaxy evolution models. With the current data, a quenching time of ~ 3 Gyr suggests that the red sequence in the HRS+ sample could have been built by the migration of objects from the blue cloud in a Hubble time, consistent with previous works (e.g. Arnouts et al., 2007; Martin et al., 2007; Schiminovich et al., 2007). However, I cannot reject a scenario in which either the observed rate is able to build-up the red sequence in half a Hubble time, or the observed migration cannot explain the growth of the quiescent galaxy population in the last 13 Gyr. Therefore, I place no additional constraints on the evolution of the colourstellar mass diagram from the estimate of the stellar mass accretion rate observed here. Thus, an open question is *what is the mass accretion rate of the present day red sequence?*

This problem is made non-trivial not only due to the necessity of accurate observations to constrain the stellar mass, but also to determine reliable timescales for migration to the red sequence. Moreover, the analysis here shows that there are likely different evolutionary paths into the transition region, hence making a determination of the *net* rate of growth of the red sequence even more difficult to constrain. The transition region is also populated by HI normal galaxies, of which a fraction may have migrated back into the transition region from the red sequence, following a recent episode of star formation from a rejuvenated gas supply. Unfortunately, in contrast

to the HI deficient objects, I was not able to constrain the mechanism(s) responsible for the presence of HI normal galaxies in the transition region, and this also remains an open problem for future investigation.

The determination of an absolute metallicity scale

The absolute uncertainty in the nebular oxygen abundance scale is one of the most important problems in modern astrophysics. As shown by Kewley & Ellison (2008), large discrepancies exist between the absolute scale of metallicities derived from different calibrations (see Chapter 8). For this thesis, reliable metallicity estimates were important in order to investigate the influence of the environment on chemical evolution. Conveniently, the conversions presented in Kewley & Ellison eliminated these systematic errors and allowed for a new method of estimating metallicities to be developed, based on the average estimate derived from different measurements from the same input emission line ratios. In fact, Moustakas et al. (2010) note that, since empirical calibrations likely underestimate the ‘true’ metallicity by ~ 0.2 - 0.3 dex, whereas theoretical calibrations yield abundances that may be too high by the same amount, the best approach for sidestepping the issue may be to average two results. In this work, I average five results. This meant I could neglect the issue of the absolute scale and use relative abundances to achieve the goals of the analysis. However, the problem of obtaining an accurate absolute abundance scale must be addressed. The question is, *how do we determine the zero-point of the abundance scale?*

One method may be to use metal recombination lines. Current direct and empirical abundance methods based on collisionally-excited lines may systematically underestimate the oxygen abundances of star-forming regions, especially in the metal-rich regime (see Stasińska (2010) for a full discussion). Temperature variations in HII regions could cause the electron temperature inferred from the collisionally excited forbidden lines to be overestimated, thus the abundance is underestimated (Stasińska, 2005; Bresolin, 2006). Observations suggest that empirical strong-line calibrations using abundances measured from metal recombination lines, which are not influenced by temperature fluctuations, may provide a solution (e.g. Peimbert & Peimbert, 2005; Bresolin, 2007). In particular, Peimbert et al. (2007) derive a such a calibration of R_{23} using a small number (~ 20) of metal rich galaxies and HII regions with high excitation emission lines. For a given value of R_{23} , this calibration yields oxygen abundances that are ~ 0.25 dex, or a factor of ~ 1.8 , higher than the abundances implied by direct and empirical methods.

Another approach may be to use the mid- and far-infrared metal cooling lines, e.g., [SIII] $\lambda 19 \mu\text{m}$, [OIII] $\lambda 52 \mu\text{m}$, [OIII] $\lambda 88 \mu\text{m}$, [NIII] $\lambda 57 \mu\text{m}$, [NII] $\lambda 122 \mu\text{m}$, which are all insensitive to electron temperature variations (e.g. Martín-Hernández et al., 2002; Rudolph et al., 2006; Rubin et al., 2008). The Herschel Space Telescope will provide spectroscopy from 60-210 μm using the PACS instrument on board the spacecraft, which will pave the way forward for studies into using these emission lines to develop absolute calibrations.

Both observational approaches - using metal recombination lines and infrared cooling lines - will be crucial towards determining the zero-point of the metallicity calibrations.

Additional constraints from Herschel observations

The Herschel Space Telescope is currently observing the HRS galaxies at submillimetre wavelengths, allowing for the cold dust component to be traced. Studying the variation in the properties of this component, such as the dust mass, temperature and the dust-to-gas ratio for galaxies of all morphological types will provide important constraints on the formation and evolution of dust in galaxies. For instance, combining the metallicity measurements derived in this work (Chapter 8) with dust masses obtained using Herschel observations and atomic hydrogen data, will provide a better constraint on the dust-to-gas ratio as a function of metallicity. Such a constraint would further provide a more robust measurement of the proportionality constant in estimating the mass of molecular hydrogen from the CO 1-0 luminosity, the value of which is currently debated and range from $\sim 1 - 4 \times 10^{20} \text{ cm}^{-2} (\text{K km s}^{-1})^{-1}$ (see e.g. Young & Scoville, 1991; Hunter et al., 1997; and Draine et al., 2007). The accurate calibration of this factor will help to properly determine the H_2 content of galaxies, important for understanding the total hydrogen content of galaxies and hence star formation. In fact, a better constraint of the gas fraction gained by using accurate H_2 masses would reduce some of the uncertainty in the comparison of the chemical evolution model to the observed gas fractions, as presented in Chapter 9.

More importantly, using the observed relationship between the dust-to-gas ratio and metallicity will place a better constraint on models of the interstellar dust cycle. The sources of dust and the dependency of dust production on the ISM metallicity are still not properly understood. Previous studies attempting to model dust production and evolution have often assumed that the mass of dust is a fixed fraction of the mass of metals (Frayer & Brown, 1997; Hirashita, 1999), an assumption supported, albeit due to large uncertainties, in observations of spiral galaxies (Issa et al.,

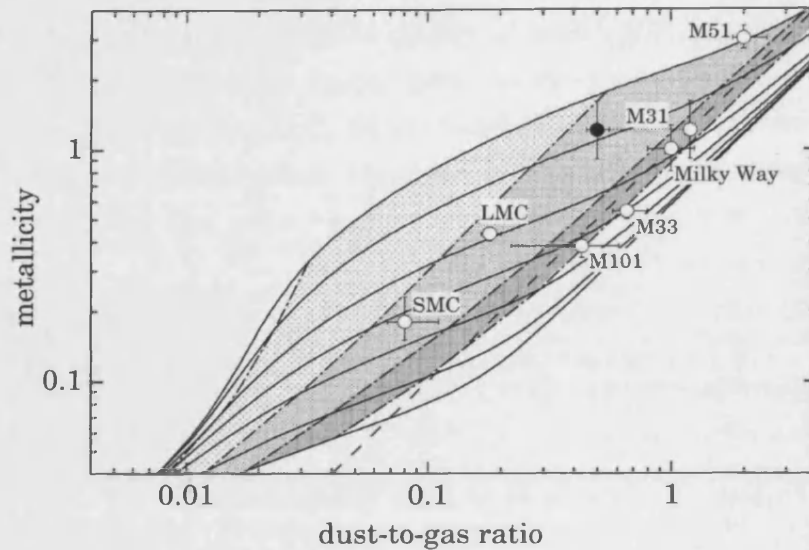


Figure 10.1: The metallicity - dust-to-gas ratio relation. The plotted observations are from Issa et al. (1990), except for M 31 which is from Inoue (2001). The solid curves are theoretical relations with various star formation time-scales ($\tau_{SF} = 1, 2, 5, 10, 20, 50,$ and 100 Gyr from top to bottom). The thin, medium, and thick shaded areas indicate that the galactic age for 15 Gyr, 510 Gyr, and 1015 Gyr, respectively. The dashed straight line represents the sequence of the same dust-to-metal ratio as the Galaxy. This figure is taken from Inoue (2003), where a complete description of the model parameters of this figure may be found.

1990). Edmunds (2001) explored the various scenarios where the ratio of metal mass to dust mass might remain constant, by modelling different sources of dust production - grain core production in both supernovae and giant stars, and mantle growth in the interstellar medium. He demonstrated analytically that the ratio may remain constant under different conditions. However, Inoue (2003) find that the observed linear relation between the dust-to-gas ratio and metallicity for the nearby spiral galaxies is not an evolutionary sequence with a constant dust-to-metal ratio, but is dependent on different ages and star formation histories (see Figure 10.1). Yet, the observational study by Draine et al. (2007), using the SINGS sample Kennicutt et al. (2003), find a dust-to-gas ratio that scales linearly with metallicity, suggesting that uncovering the physical processes that determine the observed relation is a complex problem. *What governs the relationship between the metallicity and the dust-to-gas ratio? Does this relationship vary between galaxies in different environments?*

Thus, there is still uncertainty in the processes underlying the observed relation. This problem may be addressed using the more accurate measurements of the

dust mass provided by the Herschel observations, combined with the reliable metallicity estimates developed in this thesis. Moreover, the HRS sample will not only provide double the number of galaxies as used by Draine et al., but also has the potential to study the relationship between dust and metal content in different environments, which may indicate the effect of the environment on dust evolution and answer the question of what determines the dust-to-metal ratio.

In summary, the results of this thesis have not only highlighted open problems which require future investigation, but have also shed light on the processes shaping star formation and chemical evolution in nearby galaxies, providing us with a better understanding of galaxy evolution in the local Universe.

APPENDIX A: THE HRS+ MEMBERS

Table A.1: The general properties of galaxies comprising the HRS+ sample. Each column contains: (1) the HRS+ identification number; (2) an alternative name taken from either the New General Catalogue (NGC; Dreyer, 1888), the Catalogue of Galaxies and Clusters of Galaxies (CGCG; Zwicky et al., 1961), Uppsala General Catalogue (UGC; Nilson, 1973), the Virgo Cluster Catalogue (VCC; Binggeli et al., 1985), and the Index Catalogue (IC; Dreyer, 1908); (3) J2000 right ascension, from NED; (4) J2000 declination, from NED; (5) distance; (6) the morphological classification from NED; (7) total 2MASS K band magnitude (Skrutskie et al., 2006); (8) the optical isophotal distance D_{25} (25 mag arcsec $^{-2}$); (9) the heliocentric radial velocity from NED; (10) the cluster or cloud membership; and (11) the galactic extinction Schlegel et al., 1998.

HRS+	Alt. Name	R.A.(h m s)	Dec.($^{\circ}$ ' '')	D (Mpc)	Type	K_{Stot}	D_{25} (')	V (km s $^{-1}$)	Member	A_B
(1)	(2)	(3)	(4)	(5)	(6)	(7)	(8)	(9)	(10)	(11)
1	CGCG 123-035	10 17 39.66	+22 48 35.9	15.7	Pec	11.59	1.00	1175	Leo Cl.	0.13
2	UGC 5588	10 20 57.13	+25 21 53.4	17.2	S?	11.03	0.52	1291	Leo Cl.	0.10
3	NGC 3226	10 23 27.01	+19 53 54.7	15.3	E2:pec;LINER;Sy3	8.57	3.16	1169	Leo Cl.	0.10
4	NGC 3227	10 23 30.58	+19 51 54.2	15.4	SAB(s)pec;Sy1.5	7.64	5.37	1148	Leo Cl.	0.10
5	IC 610	10 26 28.37	+20 13 41.5	15.6	Sc	9.94	1.86	1170	Leo Cl.	0.09
6	NGC 3245A	10 27 01.16	+28 38 21.9	17.6	SB(s)b	11.83	3.31	1322	Leo Cl.	0.12
7	NGC 3245	10 27 18.39	+28 30 26.6	17.5	SA(r)0?:HII;LINER	7.86	3.24	1314	Leo Cl.	0.11
8	NGC 3254	10 29 19.92	+29 29 29.2	18.1	SA(s)bc;Sy2	8.80	5.01	1356	Leo Cl.	0.09
9	NGC 3277	10 32 55.45	+28 30 42.2	18.8	SA(r)ab;HII	8.93	1.95	1415	Leo Cl.	0.11
10	UGC 5738	10 34 29.82	+35 15 24.4	20.2	S?	11.31	0.91	1516	Leo Cl.	0.12
11	NGC 3287	10 34 47.31	+21 38 54.0	17.4	SB(s)d	9.78	2.09	1325	Leo Cl.	0.10
12	CGCG 124-041	10 35 42.07	+26 07 33.7	18.6	cl	11.98	0.59	1392	Leo Cl.	0.10
13	NGC 3294	10 36 16.25	+37 19 28.9	21.1	SA(s)c	8.38	3.55	1573	Leo Cl.	0.08
14	NGC 3301	10 36 56.04	+21 52 55.7	17.6	(R')SB(rs)0/a	8.52	3.55	1341	Leo Cl.	0.10
15	NGC 3338	10 42 07.54	+13 44 49.2	17.4	SA(s)c	8.13	5.89	1300	Leo Cl.	0.14
16	NGC 3346	10 43 38.91	+14 52 18.7	16.8	SB(rs)cd	9.59	2.69	1260	Leo Cl.	0.12
17	NGC 3370	10 47 04.05	+17 16 25.3	17.1	SA(s)c	9.43	3.16	1281	Leo Cl.	0.13
18	NGC 3380	10 48 12.17	+28 36 06.5	21.4	(R')SBa?	9.92	1.70	1604	Leo Cl.	0.11
19	NGC 3381	10 48 24.82	+34 42 41.1	21.7	SB pec	10.32	2.04	1630	Leo Cl.	0.09
20	NGC 3395	10 49 50.11	+32 58 58.3	21.7	SAB(rs)cd pec:	9.95	2.09	1617	Leo Cl.	0.11
21	UGC 5958	10 51 15.81	+27 50 54.9	15.8	Sbc	11.56	1.45	1182	Leo Cl.	0.11
22	NGC 3414	10 51 16.23	+27 58 30.0	18.9	S0 pec;LINER	7.98	3.55	1414	Leo Cl.	0.11
23	NGC 3424	10 51 46.33	+32 54 02.7	19.9	SB(s)b?:HII	9.04	2.82	1501	Leo Cl.	0.10
24	NGC 3430	10 52 11.41	+32 57 01.5	21.1	SAB(rs)c	8.90	3.98	1585	Leo Cl.	0.10
25	NGC 3437	10 52 35.75	+22 56 02.9	17.1	SAB(rs)c:	8.88	2.51	1277	Leo Cl.	0.08
26	UGC 5990	10 52 38.34	+34 28 59.3	20.9	Sab	11.71	1.35	1569	Leo Cl.	0.08
27	NGC 3442	10 53 08.11	+33 54 37.3	23.1	Sa?	10.90	0.62	1734	Leo Cl.	0.08
28	NGC 3451	10 54 20.86	+27 14 22.9	17.8	Sd	10.23	1.70	1332	Leo Cl.	0.09
29	NGC 3454	10 54 29.45	+17 20 38.3	14.7	SB(s)c? sp;HII	10.67	2.09	1101	Leo Cl.	0.15
30	NGC 3455	10 54 31.07	+17 17 04.7	14.7	(R')SAB(rs)b	10.39	2.38	1105	Leo Cl.	0.14
31	NGC 3448	10 54 39.24	+54 18 18.8	18.0	I0	9.47	5.62	1374	Ursa Maj. SS	0.05
32	NGC 3457	10 54 48.63	+17 37 16.3	15.4	S?	9.64	0.91	1158	Leo Cl.	0.13

Continued on next page...

Table A.1 – Continued

HRS+ (1)	Alt. Name (2)	R.A.(h m s) (3)	Dec.(^o ' '') (4)	D (Mpc) (5)	Type (6)	K_{Stot} (7)	D_{25} (") (8)	V (km s ⁻¹) (9)	Member (10)	A_B (11)
33	NGC 3485	11 00 02.38	+14 50 29.7	19.1	SB(r)b:	9.46	2.10	1432	Leo Cl.	0.09
34	NGC 3501	11 02 47.32	+17 59 22.2	15.1	Scd	9.41	3.89	1130	Leo Cl.	0.10
35	NGC 3499	11 03 11.03	+56 13 18.2	20.3	I0	10.23	0.81	1522	Ursa Maj. SS	0.04
36	NGC 3504	11 03 11.21	+27 58 21.0	20.5	(R)SAB(s)ab;HII	8.27	2.69	1536	Leo Cl.	0.12
37	NGC 3512	11 04 02.98	+28 02 12.5	18.3	SAB(rs)c	9.65	1.62	1373	Leo Cl.	0.12
38	NGC 3526	11 06 56.63	+07 10 26.1	18.9	SAC pec sp	10.69	1.91	1419	Leo Cl.	0.14
39	UGC 6169	11 07 03.35	+12 03 36.2	20.7	Sb:	11.13	1.86	1557	Leo Cl.	0.07
40	NGC 3547	11 09 55.94	+10 43 15.0	21.1	Sb:	10.44	1.91	1584	Leo Cl.	0.10
41	NGC 3592	11 14 27.25	+17 15 36.5	17.3	Sc? sp	10.78	1.78	1303	Leo Cl.	0.07
42	NGC 3596	11 15 06.21	+14 47 13.5	15.9	SAB(rs)c	8.70	4.06	1193	Leo Cl.	0.10
43	NGC 3608	11 16 58.96	+18 08 54.9	16.7	E2;LINER:	8.10	3.16	1108	Leo Cl.	0.09
44	UGC 6320	11 18 17.24	+18 50 49.0	15.0	S?	10.99	0.89	1121	Leo Cl.	0.10
45	NGC 3619	11 19 21.60	+57 45 27.8	20.7	(R)SA(s)0+:	8.58	2.69	1544	Ursa Major Cl.	0.08
46	NGC 3626	11 20 03.80	+18 21 24.5	19.9	(R)SA(rs)0+	8.16	2.69	1494	Leo Cl.	0.09
47	NGC 3629	11 20 31.82	+26 57 48.2	20.1	SA(s)cd:	10.50	2.29	1507	Leo Cl.	0.08
48	NGC 3631	11 21 02.85	+53 10 11.0	15.4	SA(s)c	7.99	5.01	1155	Ursa Major Cl.	0.07
49	NGC 3640	11 21 06.85	+03 14 05.4	16.7	E3	7.52	3.98	1251	Leo Cl.	0.19
50	NGC 3655	11 22 54.62	+16 35 24.5	19.6	SA(s)c;HII	8.83	1.55	1500	Leo Cl.	0.11
51	NGC 3659	11 23 45.49	+17 49 06.8	17.1	SB(s)m?	10.28	2.09	1299	Leo Cl.	0.08
52	NGC 3657	11 23 55.57	+52 55 15.5	16.2	SAB(rs)c pec	10.29	1.45	1204	Ursa Major Cl.	0.07
53	NGC 3666	11 24 26.07	+11 20 32.0	14.1	SA(rs)c:	9.23	4.37	1060	Leo Cl.	0.14
54	NGC 3681	11 26 29.80	+16 51 47.5	16.5	SAB(r)bc;LINER	9.79	2.25	1244	Leo Cl.	0.11
55	NGC 3684	11 27 11.18	+17 01 49.0	15.5	SA(rs)bc;HII	9.28	2.89	1158	Leo Cl.	0.11
56	NGC 3683	11 27 31.85	+56 52 37.4	22.9	SB(s)c?;HII	8.67	1.86	1708	Ursa Major Cl.	0.07
57	NGC 3686	11 27 43.95	+17 13 26.8	15.4	SB(s)bc	8.49	3.19	1156	Leo Cl.	0.10
58	NGC 3691	11 28 09.41	+16 55 13.7	14.5	SBb?	10.51	1.35	1067	Leo Cl.	0.11
59	NGC 3692	11 28 24.01	+09 24 27.5	23.0	Sb;LINER;HII	9.52	3.16	1717	Leo Cl.	0.14
60	NGC 3729	11 33 49.34	+53 07 31.8	14.1	SB(r)a pec	8.73	2.82	991	Ursa Major Cl.	0.05
61	UGC 6575	11 36 26.47	+58 11 29.0	16.2	Scd;HII	11.40	1.95	1217	Ursa Major Cl.	0.07
62	NGC 3755	11 36 33.37	+36 24 37.2	20.9	SAB(rs)c pec	10.60	3.16	1571	Ursa Maj. SS	0.10
63	NGC 3756	11 36 48.02	+54 17 36.8	17.6	SAB(rs)bc	8.78	4.17	1289	Ursa Major Cl.	0.05
64	NGC 3795	11 40 06.84	+58 36 47.2	16.1	Sc;HII	10.64	2.14	1213	Ursa Major Cl.	0.06
65	NGC 3794	11 40 53.42	+56 12 07.3	18.4	SAB(s)d	11.60	2.24	1383	Ursa Major Cl.	0.06
66	NGC 3813	11 41 18.65	+36 32 48.3	19.5	SA(rs)b:	8.86	2.24	1468	Ursa Maj. SS	0.08
67	UGC 6706	11 44 14.83	+55 02 05.9	19.1	SB(s)m:	11.28	1.91	1436	Ursa Major Cl.	0.06
68	CGCG 186-045	11 46 25.96	+34 51 09.2	18.4	S?	11.44	0.32	1412	Ursa Maj. SS	0.09
69	NGC 3898	11 49 15.37	+56 05 03.7	15.7	SA(s)ab;LINE;HII	7.66	4.37	1171	Ursa Major Cl.	0.09
70	IC 2969	11 52 31.27	-03 52 20.1	21.6	SB(r)bc?;HII	11.15	1.23	1617	Crater Cl.	0.12
71	NGC 3945	11 53 13.73	+60 40 32.0	16.8	SB(rs)0+;LINER	7.53	5.25	1259	Ursa Major Cl.	0.12
72	NGC 3952	11 53 40.63	-03 59 47.5	21.0	IBm: sp;HII	11.01	1.58	1577	Crater Cl.	0.11
73	NGC 3953	11 53 48.92	+52 19 36.4	14.0	SB(r)bc;HII/LINER	7.05	6.92	1050	Ursa Major Cl.	0.13
74	NGC 3982	11 56 28.10	+55 07 30.6	14.8	SAB(r)b;HII;Sy2	8.85	2.34	1108	Ursa Major Cl.	0.06
75	UGC 6919	11 56 37.51	+55 37 59.5	17.1	Sdm:	11.56	1.45	1283	Ursa Major Cl.	0.06
76	UGC 6923	11 56 49.43	+53 09 37.3	14.2	Im:	11.32	2.00	1069	Ursa Major Cl.	0.12

Continued on next page. . .

Table A.1 – Continued

HRS+ (1)	Alt. Name (2)	R.A. (h m s) (3)	Dec. (° ' '') (4)	D (Mpc) (5)	Type (6)	K_{star} (7)	D_{25} (") (8)	V (km s ⁻¹) (9)	Member (10)	A_B (11)
77	NGC 4030	12 00 23.64	-01 06 00.0	19.5	SA(s)bc:HI	7.33	4.17	1458	Crater Cl.	0.11
78	NGC 4032	12 00 32.82	+20 04 26.0	17.0	Im:	10.45	1.86	1269	Crater Cl.	0.15
79	NGC 4019	12 01 10.39	+14 06 16.2	20.3	SB ℓ sp	11.33	2.40	1508	Virgo Out.	0.14
80	NGC 4037	12 01 23.67	+13 24 03.7	12.4	SB(rs)b:	10.11	2.51	932	Virgo Out.	0.12
81	NGC 4045	12 02 42.26	+01 58 36.4	17.0	SAB(r)a:HI	8.75	0.60	2011	Virgo Out.	0.10
82	CGCG 098-037	12 03 35.94	+16 03 20.0	11.8	Sab	11.19	3.00	931	Virgo Out.	0.13
83	UGC 7035	12 03 40.14	+02 38 28.4	16.3	SB(r)a:HI	11.82	1.10	1232	Crater Cl.	0.12
84	NGC 4067	12 04 11.55	+10 51 15.8	17.0	SA(s)b:	9.90	1.20	2424	Virgo Out.	0.11
85	NGC 4100	12 06 08.60	+49 34 56.3	14.3	(R')SA(rs)bc:HI	8.03	5.37	1072	Ursa Major Cl.	0.10
86	NGC 4116	12 07 36.82	+02 41 32.0	17.0	SB(rs)dm	10.27	3.80	1309	Virgo Out.	0.10
87	NGC 4124	12 08 09.64	+10 22 43.4	17.0	SA(r)0+	8.49	4.10	1652	Virgo Out.	0.12
88	NGC 4123	12 08 11.11	+02 52 41.8	17.0	SB(r)c:Strsc:HI	8.79	5.00	1326	Virgo Out.	0.09
89	VCC 66	12 12 46.45	+10 51 57.5	17.0	SB(rs)dm:HI	9.58	5.35	369	Virgo N Cl.	0.12
90	NGC 4179	12 12 52.11	+01 17 58.9	17.0	Sb(f)	7.92	3.80	1279	Virgo Out.	0.14
91	VCC 92	12 13 48.29	+14 54 01.2	17.0	SAB(s)ab:HI:Sy	6.89	9.78	-135	Virgo N Cl.	0.15
92	VCC 131	12 15 04.44	+14 01 44.3	17.0	SB ℓ sp	10.64	2.60	2317	Virgo N Cl.	0.16
93	NGC 4203	12 15 06.06	+33 11 50.4	17.0	SAB0-:LINER:Sy3	7.41	3.39	1091	Coma I Cl.	0.05
94	VCC 145	12 15 16.81	+13 01 26.3	17.0	SA(s)bc:	9.39	5.10	702	Virgo N Cl.	0.14
95	VCC 152	12 15 30.50	+09 35 05.6	17.0	Scd	9.44	1.96	592	Virgo N Cl.	0.07
96	VCC 157	12 15 39.36	+13 54 05.4	17.0	SAC::HI	8.38	3.60	-83	Virgo N Cl.	0.14
97	VCC 167	12 15 54.44	+13 08 57.8	17.0	SAB(s)b:HI/LINER	6.52	9.12	140	Virgo N Cl.	0.14
98	VCC 187	12 16 22.52	+13 18 25.5	17.0	Sc	11.23	3.52	226	Virgo N Cl.	0.14
99	VCC 213	12 16 56.00	+13 37 31.0	17.0	S:BCD	10.35	0.93	-162	Virgo N Cl.	0.15
100	VCC 226	12 17 11.42	+15 19 26.3	17.0	SAB(rs)bc:HI	11.25	2.01	864	Virgo N Cl.	0.13
101	NGC 4251	12 18 08.31	+28 10 31.1	17.0	SB0? sp	7.73	3.63	1014	Coma I Cl.	0.10
102	VCC 307	12 18 49.63	+14 24 59.4	17.0	SA(s)c	6.93	6.15	2405	Virgo N Cl.	0.17
103	VCC 341	12 19 22.24	+06 05 55.2	23.0	SB(s)a	8.54	3.52	1935	Virgo B	0.10
104	UGC 7366	12 19 28.66	+17 13 49.4	12.3	Spiral	11.99	1.20	925	Virgo Out.	0.11
105	VCC 355	12 19 30.58	+14 52 39.8	17.0	SB(s)0-?	8.36	1.87	1369	Virgo A	0.15
106	VCC 393	12 20 07.50	+07 41 31.2	23.0	S(s)c II	10.69	2.10	2617	Virgo B	0.12
107	VCC 404	12 20 17.35	+04 12 05.1	17.0	Sd(f)	11.02	1.89	1733	Virgo S Cl.	0.10
108	VCC 434	12 20 48.49	+05 38 23.5	23.0	Sc(f)	10.74	1.76	2155	Virgo S Cl.	0.08
109	VCC 449	12 21 02.25	+03 43 19.7	17.0	SA(s)ccl: sp	9.89	4.33	2541	Virgo S Cl.	0.09
110	VCC 465	12 21 17.79	+11 30 40.0	17.0	SB(s)cd	9.70	3.95	357	Virgo N Cl.	0.15
111	VCC 483	12 21 32.76	+14 36 22.2	17.0	SA(rs)c	8.47	3.60	1136	Virgo A	0.15
112	VCC 492	12 21 41.47	+05 23 05.4	23.0	Sa	9.53	2.16	2310	Virgo B	0.09
113	VCC 497	12 21 42.48	+14 35 53.9	17.0	Sc: sp	7.83	6.74	1150	Virgo A	0.15
114	VCC 508	12 21 54.90	+04 28 25.1	17.0	SAB(rs)bc:HI:Sy2	6.84	6.59	1568	Virgo S Cl.	0.10
115	VCC 517	12 22 01.30	+05 06 00.2	17.0	SBab(s)	10.79	1.41	1864	Virgo S Cl.	0.08
116	VCC 522	12 22 03.60	+12 44 27.3	17.0	SA(r)a	9.83	2.60	1888	Virgo A	0.18
117	VCC 524	12 22 05.63	+09 02 36.8	23.0	Sb	8.72	3.95	1035	Virgo B	0.10
118	VCC 552	12 22 27.25	+04 33 58.7	17.0	SAB(s)cd	11.20	1.89	1296	Virgo S Cl.	0.10
119	VCC 559	12 22 31.36	+15 32 16.5	17.0	SA(rs)ab: sp	8.79	5.10	153	Virgo A	0.12
120	VCC 570	12 22 38.55	+11 48 03.4	17.0	SA(rs)ab: sp	8.47	5.10	1443	Virgo A	0.16

Continued on next page...

Table A.1 – Continued

HRS+	Alt. Name	R.A. (h m s)	Dec. (° ' ")	D (Mpc)	Type	K_{Stat}	D_{25} (")	V (km s ⁻¹)	Member	A/B
(1)	(2)	(3)	(4)	(5)	(6)	(7)	(8)	(9)	(10)	(11)
121	VCC 576	12 22 42.24	+09 19 56.9	23.0	Sbc	9.25	2.48	1254	Virgo B	0.10
122	VCC 596	12 22 54.90	+15 49 20.6	17.0	SAB(s)bc;LINER;HII	6.59	9.12	1575	Virgo A	0.11
123	VCC 613	12 23 06.18	+05 15 01.5	17.0	SA(r)0+	8.48	3.52	1670	Virgo S Cl.	0.10
124	VCC 630	12 23 17.25	+11 22 04.7	17.0	Scd	9.51	5.86	1564	Virgo A	0.11
125	VCC 648	12 23 34.94	+06 04 54.2	23.0	E0;Sy2	8.54	2.31	1298	Virgo B	0.11
126	VCC 654	12 23 35.31	+16 43 19.9	17.0	SB(r)0+	8.32	3.60	930	Virgo A	0.11
127	VCC 656	12 23 38.70	+06 57 14.7	23.0	SA(rs)bc	8.97	2.48	1014	Virgo B	0.09
128	VCC 667	12 23 48.52	+07 11 12.6	23.0	SAB(s)dm?	11.06	1.89	1420	Virgo B	0.10
129	VCC 685	12 23 57.81	+16 41 36.1	17.0	SA0;LINER	7.82	3.20	1241	Virgo A	0.12
130	VCC 692	12 24 01.56	+12 12 18.1	17.0	SB(rs)ab pec	10.24	2.92	2324	Virgo A	0.13
131	VCC 697	12 24 05.53	+07 02 28.6	23.0	SA(s)cd	10.95	1.55	1231	Virgo B	0.10
132	VCC 699	12 24 07.44	+06 36 26.9	23.0	Sm/Im	11.49	1.95	727	Virgo B	0.11
133	NGC 4359	12 24 11.06	+31 31 17.8	17.0	SB(rs)c? sp	10.81	3.60	1253	Coma I Cl.	0.11
134	VCC 713	12 24 14.53	+08 32 08.9	23.0	Sc	9.69	3.20	1137	Virgo B	0.12
135	VCC 731	12 24 28.23	+07 19 03.1	23.0	E3	6.64	8.73	1240	Virgo B	0.09
136	VCC 758	12 24 54.93	+07 26 40.4	23.0	Sa	9.31	1.76	784	Virgo B	0.10
137	VCC 759	12 24 55.43	+11 42 15.4	17.0	SB(r)0+	7.72	5.10	943	Virgo A	0.16
138	VCC 763	12 25 03.78	+12 53 13.1	17.0	E1;LERC;LINER;Sy2	6.22	10.07	910	Virgo A	0.17
139	VCC 787	12 25 18.06	+05 44 28.3	23.0	Im	11.23	1.84	1186	Virgo B	0.10
140	VCC 785	12 25 18.09	+04 55 30.2	17.0	(R)SA(s)a;Sy2	8.51	3.06	2557	Virgo S Cl.	0.07
141	VCC 792	12 25 22.17	+10 01 00.5	23.0	SA(rs)b?	8.33	3.52	971	Virgo B	0.10
142	VCC 801	12 25 25.50	+16 28 12.0	17.0	Sa? pec;HII	9.49	2.60	1710	Virgo A	0.10
143	VCC 827	12 25 42.63	+07 13 00.1	23.0	SB(s)cd; sp	9.79	3.60	992	Virgo B	0.11
144	VCC 836	12 25 46.82	+12 39 43.5	17.0	SA(s)b; sp;Sy2	8.00	5.10	2515	Virgo A	0.14
145	VCC 849	12 25 50.67	+10 27 32.6	23.0	Sbc(s) II	10.33	2.18	1103	Virgo B	0.13
146	VCC 851	12 25 54.12	+07 33 17.4	23.0	SAB(s)cd; sp	10.47	2.16	1195	Virgo B	0.12
147	VCC 859	12 25 58.30	+03 25 47.3	17.0	Sd(f)	10.18	2.92	1428	Virgo S Cl.	0.10
148	VCC 865	12 25 58.80	+15 40 17.3	17.0	SAcd; sp	10.34	3.36	-124	Virgo A	0.11
149	VCC 873	12 26 07.56	+13 06 46.0	17.0	Sb	8.49	3.95	234	Virgo A	0.12
150	VCC 881	12 26 11.74	+12 56 46.4	17.0	S0(3)/E3	6.10	11.37	-221	Virgo A	0.13
151	VCC 912	12 26 32.25	+12 36 39.5	17.0	(R)SB(rs)ab	9.80	2.92	105	Virgo A	0.14
152	VCC 921	12 26 36.10	+03 57 52.7	17.0	SB(r)b? pec;LINER	9.65	1.89	2289	Virgo S Cl.	0.08
153	VCC 938	12 26 46.72	+07 55 08.4	17.0	SB(rs)cd;Sbrst	10.97	2.18	1395	Virgo S Cl.	0.11
154	VCC 939	12 26 47.23	+08 53 04.6	23.0	SAB(s)cd	10.71	3.45	1271	Virgo B	0.13
155	VCC 944	12 26 50.62	+09 35 03.0	23.0	SB0; s	8.17	3.60	832	Virgo B	0.10
156	VCC 958	12 26 56.43	+15 02 50.7	17.0	SB(s)a;LINER;HII	7.74	3.52	-273	Virgo A	0.14
157	VCC 957	12 26 58.48	+02 29 39.7	17.0	SB(r)bc	9.66	2.01	1695	Virgo S Cl.	0.08
158	VCC 971	12 27 08.97	+05 52 48.6	23.0	Sdm	11.05	3.06	1120	Virgo B	0.09
159	VCC 979	12 27 11.59	+09 25 14.0	23.0	SB(s)a;HII	9.09	4.33	438	Virgo B	0.09
160	VCC 1002	12 27 26.41	+06 15 46.0	23.0	SB(rs)b	9.35	3.02	1450	Virgo B	0.08
161	VCC 1003	12 27 26.56	+11 06 27.1	17.0	SA(r)0+;LINER;HII	6.78	8.12	1130	Virgo A	0.14
162	VCC 1030	12 27 40.49	+13 04 44.2	17.0	SB(s)0;LINER;HII	7.30	2.92	775	Virgo A	0.13
163	VCC 1043	12 27 45.59	+13 00 31.8	17.0	SA(s)0/a pec;LINER	7.27	8.12	70	Virgo A	0.12
164	VCC 1047	12 27 53.57	+12 17 35.6	17.0	SB(rs)a	8.91	2.01	724	Virgo A	0.12

Continued on next page...

Table A.1 – Continued

HRS+	Alt. Name	R.A. (h m s)	Dec. ($^{\circ}$ ' '')	D (Mpc)	Type	K_{Stot}	D_{25} (")	V (km s $^{-1}$)	Member	A_B
(1)	(2)	(3)	(4)	(5)	(6)	(7)	(8)	(9)	(10)	(11)
165	VCC 1048	12 27 55.39	+05 43 16.4	23.0	Sdm:	11.58	1.89	2252	Virgo B	0.09
166	VCC 1062	12 28 03.89	+09 48 13.0	23.0	SB(s)0	7.29	5.05	517	Virgo B	0.10
167	VCC 1086	12 28 15.94	+09 26 10.7	23.0	Sab: sp	9.83	3.20	328	Virgo B	0.11
168	VCC 1091	12 28 18.77	+08 43 46.1	23.0	Sbc	11.77	1.76	1119	Virgo B	0.09
169	UGC 7595	12 28 27.28	+18 24 55.1	17.0	Scd:	10.45	1.10	1701	Coma I Cl.	0.14
170	VCC 1110	12 28 29.63	+17 05 05.8	17.0	SA(s)ab;LINER;Sy3	7.05	6.15	1954	Virgo A	0.12
171	VCC 1118	12 28 40.55	+09 15 32.2	23.0	Sbc:	9.99	1.96	865	Virgo B	0.08
172	VCC 1126	12 28 43.26	+14 59 58.2	17.0	SAB:	9.26	2.92	1687	Virgo A	0.16
173	VCC 1145	12 28 59.01	+03 34 14.2	17.0	(R)SAB(s)0/a;LINER	7.78	2.92	884	Virgo S Cl.	0.09
174	VCC 1154	12 29 00.03	+13 58 42.9	17.0	SA(r)0+;HII;LINER	7.15	3.36	1210	Virgo A	0.20
175	VCC 1158	12 29 03.01	+13 11 01.5	17.0	SB(s)0+:	8.01	3.52	1919	Virgo A	0.10
176	VCC 1190	12 29 28.03	+08 44 59.7	23.0	SB(s)0/a? sp	8.04	4.33	508	Virgo B	0.09
177	VCC 1205	12 29 37.78	+07 49 27.1	17.0	Sa?;HII	10.12	1.84	2339	Virgo S Cl.	0.10
178	VCC 1226	12 29 46.76	+08 00 01.7	17.0	E2/S0;Sy2;LINER	5.40	10.25	868	Virgo S Cl.	0.10
179	VCC 1231	12 29 48.87	+13 25 45.7	17.0	E5	7.16	4.04	2236	Virgo A	0.12
180	VCC 1253	12 30 02.17	+13 38 11.2	17.0	SB(s)0?:Sy2	7.35	3.60	1353	Virgo A	0.14
181	VCC 1279	12 30 17.42	+12 19 42.8	17.0	E2	8.36	1.89	1370	Virgo A	0.11
182	VCC 1290	12 30 26.78	+04 14 47.3	17.0	SAB(s)c	9.75	2.01	2438	Virgo S Cl.	0.10
183	VCC 1316	12 30 49.42	+12 23 28.0	17.0	E+0-1 pec;NLRG;Sy	5.81	11.00	1292	Virgo A	0.10
184	VCC 1326	12 30 57.13	+11 29 00.8	17.0	SB(s)a:	9.88	1.89	497	Virgo A	0.18
185	VCC 1330	12 30 59.74	+08 04 40.6	17.0	SA(s)a?	9.08	1.96	1777	Virgo S Cl.	0.11
186	NGC 4494	12 31 24.03	+25 46 29.9	17.0	E1-2;LINER	7.00	4.79	1310	Coma I Cl.	0.09
187	VCC 1375	12 31 39.21	+03 56 22.1	17.0	SB(rs)m	9.56	4.76	1732	Virgo S Cl.	0.11
188	VCC 1379	12 31 39.57	+16 51 10.1	17.0	SAB(s)d	9.66	2.85	1505	Virgo A	0.13
189	VCC 1393	12 31 54.76	+15 07 26.2	17.0	SB(s)c II.5	10.80	1.69	2100	Virgo A	0.13
190	VCC 1401	12 31 59.22	+14 25 13.5	17.0	SA(rs)b;HII;Sy2	6.27	7.23	2284	Virgo A	0.16
191	VCC 1410	12 32 03.35	+16 41 15.8	17.0	Scd:	11.90	1.48	1629	Virgo A	0.13
192	VCC 1419	12 32 10.53	+13 25 10.6	17.0	Sa pec?	10.26	2.16	737	Virgo A	0.13
193	VCC 1450	12 32 41.88	+14 03 01.8	17.0	IB(s)m:	10.91	2.60	-173	Virgo A	0.15
194	NGC 4517	12 32 45.59	+00 06 54.1	17.0	SA(s)cd: sp	7.33	11.00	1129	Virgo Out.	0.10
195	VCC 1479	12 33 07.56	+14 34 29.8	17.0	SB(rs)ab?	9.99	2.16	958	Virgo A	0.16
196	VCC 1508	12 33 30.25	+08 39 17.1	17.0	SB(rs)d	9.56	3.60	1212	Virgo S Cl.	0.09
197	VCC 1516	12 33 39.66	+09 10 29.5	17.0	SB(s)cd: sp	10.35	4.04	2330	Virgo S Cl.	0.09
198	NGC 4525	12 33 51.19	+30 16 39.1	17.0	Scd:	9.99	3.00	1174	Coma I Cl.	0.10
199	VCC 1532	12 33 56.66	+15 21 17.4	17.0	SB(rs)c pec?	10.58	1.96	2335	Virgo A	0.16
200	VCC 1535	12 34 03.03	+07 41 56.9	17.0	SAB(s)0:	6.47	7.00	448	Virgo S Cl.	0.10
201	VCC 1540	12 34 08.50	+02 39 13.7	17.0	SAB(s)bc;HII;LINER	6.93	5.86	1736	Virgo S Cl.	0.10
202	VCC 1549	12 34 14.79	+11 04 17.7	17.0	S?	11.42	1.10	1357	Virgo A	0.13
203	VCC 1554	12 34 19.33	+06 28 03.7	17.0	IBm;HII	9.48	2.60	2021	Virgo S Cl.	0.09
204	VCC 1555	12 34 20.31	+08 11 51.9	17.0	SAB(s)c;HII	7.38	8.33	1962	Virgo S Cl.	0.08
205	VCC 1562	12 34 27.13	+02 11 16.4	17.0	SAB(rs)bc;HII;Sbrst	7.52	7.23	1807	Virgo S Cl.	0.08
206	VCC 1575	12 34 39.42	+07 09 36.0	17.0	SBm pec;BCD	11.01	2.00	597	Virgo S Cl.	0.10
207	VCC 1588	12 34 50.87	+15 33 05.2	17.0	SAB(rs)cd;LINER;Sy1	9.24	2.60	1288	Virgo A	0.14
208	VCC 1615	12 35 26.43	+14 29 46.8	17.0	SBb(rs);LINER;Sy	7.12	6.00	484	Virgo A	0.16

Continued on next page...

Table A.1 – Continued

HRS+	Alt. Name	R.A. (h m s)	Dec. (° ' ")	D (Mpc)	Type	K_{star}	D_{25} (")	V (km s ⁻¹)	Member	A _B
(1)	(2)	(3)	(4)	(5)	(6)	(7)	(8)	(9)	(10)	(11)
209	NGC 4546	12 35 29.51	-03 47 35.5	14.0	SB(s)0-:	7.39	3.31	1050	Virgo Out.	0.15
210	VCC 1619	12 35 30.61	+12 13 15.4	17.0	SB0: sp;LINER	8.69	3.95	381	Virgo A	0.17
211	VCC 1632	12 35 39.88	+12 33 21.7	17.0	E,LINER;HI;Sy2	6.73	7.23	322	Virgo A	0.18
212	NGC 4561	+19 19 21.4	+19 19 21.4	17.0	SB(rs)dm	10.63	1.51	1410	Coma I Cl.	0.11
213	NGC 4565	12 36 20.78	+25 59 15.6	17.0	SA(s)b? sp;Sy3;Sy1.9	6.06	14.18	1233	Coma I Cl.	0.07
214	VCC 1664	12 36 26.99	+11 26 21.5	17.0	E6	7.94	4.33	1165	Virgo A	0.15
215	VCC 1673	12 36 32.71	+11 15 28.8	17.0	SA(rs)bc	8.30	2.92	2277	Virgo A	0.14
216	VCC 1676	12 36 34.26	+11 14 20.0	17.0	SA(rs)bc	7.52	5.10	2255	Virgo A	0.14
217	VCC 1690	12 36 49.80	+13 09 46.3	17.0	SAB(rs)ab;LINER;Sy	6.58	10.73	-216	Virgo A	0.20
218	VCC 1692	12 36 53.40	+07 14 48.0	17.0	S0(7)/E7	7.69	3.52	1730	Virgo S Cl.	0.10
219	VCC 1720	12 37 30.55	+09 33 18.4	17.0	SA(r)0:	8.40	3.77	2284	Virgo E Cl.	0.09
220	VCC 1727	12 37 43.52	+11 49 05.5	17.0	SAB(rs)b;LINER;Sy1.9	6.49	6.29	1032	Virgo S Cl.	0.18
221	VCC 1730	12 37 48.40	+05 22 06.4	17.0	SAB(rs)a pec	8.77	2.16	1783	Virgo A	0.10
222	VCC 1757	12 38 17.89	+13 06 35.5	17.0	Sdm	10.46	1.96	1788	Virgo S Cl.	0.16
223	VCC 1758	12 38 20.82	+07 53 28.7	17.0	SA(s)a? sp	11.76	1.89	1788	Virgo S Cl.	0.12
224	VCC 1760	12 38 28.44	+04 19 08.8	17.0	SA(s)a? sp	8.47	4.33	792	Virgo S Cl.	0.16
225	VCC 1778	12 38 04.14	+13 21 48.7	17.0	Sb	11.42	1.76	2750	Virgo E Cl.	0.15
226	VCC 1780	12 39 12.44	+06 00 44.3	17.0	SA(s)dm:	10.24	1.96	2424	Virgo S Cl.	0.09
227	NGC 4592	12 39 18.74	-00 31 55.2	14.3	Pec	10.22	5.75	1069	Virgo Out.	0.10
228	-	12 39 22.26	-05 39 53.3	16.0	S?	11.95	0.43	1199	Virgo Out.	0.11
229	VCC 1809	12 39 48.02	+12 58 26.1	17.0	S?	11.11	1.10	2839	Virgo E Cl.	0.17
230	VCC 1811	12 39 51.91	+15 17 52.1	17.0	SAB(rs)b?	10.03	2.16	632	Virgo E Cl.	0.16
231	VCC 1813	12 39 55.94	+10 10 33.9	17.0	SB(r)+;LINER:	7.46	4.76	1834	Virgo E Cl.	0.10
232	VCC 1859	12 40 57.56	+11 54 43.6	17.0	SB(s)a:	9.17	5.10	1645	Virgo E Cl.	0.14
233	VCC 1868	12 41 12.41	+10 09 20.9	17.0	SB(r)0	8.16	4.30	1864	Virgo E Cl.	0.07
234	VCC 1869	12 41 13.29	+07 18 53.2	17.0	(R)SAB0	8.56	2.16	1875	Virgo S Cl.	0.11
235	VCC 1883	12 42 02.32	+11 38 48.9	17.0	E5	6.75	7.67	444	Virgo E Cl.	0.14
236	VCC 1903	12 42 31.15	+03 57 37.3	17.0	IB(s)m?	9.89	2.31	742	Virgo S Cl.	0.13
237	VCC 1923	12 42 32.67	-01 21 02.4	14.9	SAB(s)m pec	11.84	1.38	1116	Virgo S Cl.	0.16
238	NGC 4629	12 42 40.96	+14 17 45.0	17.0	SBcd: sp	9.25	2.92	116	Virgo E Cl.	0.12
239	VCC 1932	12 42 47.43	+11 26 32.9	17.0	S0-	8.21	2.01	1147	Virgo E Cl.	0.11
240	VCC 1938	12 42 49.87	+02 41 16.0	17.0	E/S0/1;LINER;Sy3	6.42	9.63	1094	Virgo S Cl.	0.12
241	VCC 1939	12 42 52.37	+13 15 26.9	17.0	SAB(rs)bc;Sy1.8	8.81	3.20	1048	Virgo E Cl.	0.11
242	VCC 1943	12 43 20.14	+01 58 42.1	17.0	SB(rs)0/a;LINER	7.41	3.00	1346	Virgo Out.	0.13
243	NGC 4643	12 43 32.45	+11 34 57.4	17.0	SAB(rs)c	8.05	2.60	1422	Virgo E Cl.	0.11
244	VCC 1972	12 43 40.01	+11 33 09.4	17.0	E2	5.74	5.10	1095	Virgo E Cl.	0.11
245	VCC 1978	12 43 42.63	+16 23 36.2	17.0	SA(rs)c;LINER	8.03	3.90	797	Virgo Out.	0.12
246	NGC 4651	12 43 56.58	+13 07 36.0	17.0	SAB(rs)cd;HI	7.74	4.99	1039	Virgo E Cl.	0.11
247	VCC 1987	12 44 31.97	+11 11 25.9	17.0	E5	8.21	1.89	1115	Virgo E Cl.	0.14
248	VCC 2000	12 44 45.99	+12 21 05.2	17.0	S	11.91	2.60	844	Virgo E Cl.	0.13
249	VCC 2006	12 45 05.96	+03 03 20.5	17.0	SB(s)0/a	7.43	4.50	785	Virgo Out.	0.11
250	NGC 4665	12 45 08.59	-00 27 42.8	20.4	SAB::HI;LINER	7.06	4.57	1513	Virgo Out.	0.11
251	NGC 4666	12 45 32.14	-00 32 05.0	21.8	SB(s)d::NLGN	10.58	1.38	1619	Virgo Out.	0.11
252	NGC 4668									

Continued on next page...

Table A.1 – Continued

HRS+	Alt. Name	R.A. (h m s)	Dec. (° ' ")	D (Mpc)	Type	K_{Stot}	D_{25} (")	V (km s ⁻¹)	Member	A _B
(1)	(2)	(3)	(4)	(5)	(6)	(7)	(8)	(9)	(10)	(11)
253	NGC 4684	12 47 17.52	-02 43 38.6	20.9	SB(r)0+;HII	8.39	2.88	1490	Virgo Out.	0.12
254	VCC 2058	12 47 45.56	+13 45 46.1	17.0	SA(rs)bc	7.96	5.86	1620	Virgo E Cl.	0.10
255	NGC 4688	12 47 46.46	+04 20 09.9	17.0	SB(s)cd	11.16	4.40	984	Virgo Out.	0.13
256	NGC 4691	12 48 13.63	-03 19 57.8	14.8	(R)SB(s)0/a pec:HII	8.54	2.82	1119	Virgo Out.	0.12
257	VCC 2070	12 48 22.92	+08 29 14.3	17.0	SA(s)ab;Sy2	7.56	5.67	1008	Virgo E Cl.	0.11
258	NGC 4697	12 48 35.91	-05 48 03.1	16.5	E6;AGN	6.37	7.24	1241	Virgo Out.	0.13
259	NGC 4701	12 49 11.56	+03 23 19.4	17.0	SA(s)cd	9.77	3.60	727	Virgo Out.	0.13
260	NGC 4710	12 49 38.96	+15 09 55.8	17.0	SA(r)0+? sp:HII	7.57	4.30	1129	Virgo Out.	0.13
261	UGC 7982	12 49 50.19	+02 51 10.4	15.4	Sd(f)	10.17	3.39	1158	Virgo Out.	0.15
262	NGC 4713	12 49 57.87	+05 18 41.1	17.0	SAB(rs)d;LINER	9.75	3.20	652	Virgo Out.	0.12
263	NGC 4725	12 50 26.61	+25 30 02.7	17.0	SAB(r)ab pec;Sy2	6.17	9.66	1209	Coma I Cl.	0.05
264	UGC 7991	12 50 38.96	+01 27 52.3	17.0	Sd(f)	11.61	1.70	1272	Virgo Out.	0.11
265	NGC 4720	12 50 42.78	-04 09 21.0	20.1	Pec	10.77	0.65	1504	Virgo Out.	0.11
266	NGC 4731	12 51 01.09	-06 23 35.0	19.9	SB(s)cd	9.79	6.61	1491	Virgo Out.	0.14
267	NGC 4747	12 51 45.96	+25 46 38.3	17.0	SBcd? pec sp	10.29	3.95	1179	Coma I Cl.	0.04
268	NGC 4746	12 51 55.37	+12 04 58.9	17.0	Sb: sp	9.50	2.20	1779	Virgo Out.	0.15
269	VCC 2092	12 52 17.56	+11 18 49.2	17.0	SB(r)0-:	7.41	5.03	1377	Virgo E Cl.	0.14
270	NGC 4753	12 52 22.11	-01 11 58.9	16.5	IO	6.72	6.03	1239	Virgo Out.	0.15
271	NGC 4758	12 52 44.04	+15 50 55.9	17.0	Im::HII	10.93	3.00	1240	Virgo Out.	0.11
272	VCC 2095	12 52 56.05	+11 13 50.9	17.0	SB(r)0 sp;LINER	7.30	8.70	985	Virgo E Cl.	0.09
273	NGC 4771	12 53 21.27	+01 16 09.0	17.0	SAd? sp;NLAGN	9.01	4.00	1119	Virgo Out.	0.09
274	NGC 4772	12 53 29.17	+02 10 06.0	17.0	SA(s)a;LINER;Sy3	8.36	2.90	1038	Virgo Out.	0.12
275	NGC 4775	12 53 45.70	-06 37 19.8	20.9	SA(s)d	9.22	2.14	1566	Virgo Out.	0.15
276	NGC 4779	12 53 50.86	+09 42 35.7	17.0	SB(rs)bc;Sbrst	9.87	2.10	2832	Virgo Out.	0.09
277	NGC 4791	12 54 43.97	+08 03 10.7	33.7	cl	11.35	1.20	2529	Virgo Out.	0.14
278	UGC 8032	12 54 44.19	+13 14 14.2	14.8	S	10.39	2.75	1121	Virgo Out.	0.15
279	UGC 8041	12 55 12.68	+00 07 00.0	17.0	SB(s)d	11.98	3.10	1321	Virgo Out.	0.10
280	NGC 4799	12 55 15.53	+02 53 47.9	17.0	S?	9.89	1.60	2802	Virgo Out.	0.15
281	UGC 8045	12 55 23.62	+07 54 34.0	37.3	IBm:	11.82	0.91	2801	Virgo Out.	0.18
282	NGC 4803	12 55 33.67	+08 14 25.8	35.5	Comp	10.71	0.50	2664	Virgo Out.	0.13
283	NGC 4808	12 55 48.94	+04 18 14.7	17.0	SA(s)cd::HII	9.04	2.60	760	Virgo Out.	0.16
284	IC 3908	12 56 40.62	-07 33 46.1	17.3	SB(s)d?;HII	9.10	1.82	1296	Virgo Out.	0.15
285	NGC 4845	12 58 01.19	+01 34 33.0	17.0	SA(s)ab sp;HII	7.79	5.20	1097	Virgo Out.	0.09
286	NGC 4866	12 59 27.14	+14 10 15.8	17.0	SA(r)0+:: sp;LINER	7.92	6.00	1986	Virgo Out.	0.12
287	NGC 4904	13 00 58.67	-00 01 38.8	17.0	SB(s)cd;Sbrst	9.50	2.40	1174	Virgo Out.	0.11
288	NGC 4941	13 04 13.14	-05 33 05.8	14.8	(R)SAB(r)ab::Sy2	8.22	3.63	1114	Virgo Out.	0.16
289	NGC 4981	13 08 48.74	-06 46 39.1	22.4	SAB(r)bc;LINER	8.49	2.75	1678	Virgo Out.	0.18
290	NGC 5014	13 11 31.16	+36 16 54.9	15.0	Sa? sp	10.11	1.70	1136	Canes Ven. Spur	0.03
291	NGC 5103	13 20 30.08	+43 05 02.3	17.0	Sab	9.49	1.45	1297	Canes Ven. Spur	0.08
292	NGC 5145	13 25 13.92	+43 16 02.2	16.3	S?;HII;Sbrst	9.33	2.00	1225	Canes Ven. Spur	0.05
293	NGC 5147	13 26 19.71	+02 06 02.7	14.5	SB(s)/dm	9.73	1.91	1092	Virgo Out.	0.12
294	IC 902	13 36 01.22	+49 57 39.0	21.6	Sb	10.42	2.19	1608	Canes Ven. Spur	0.05
295	NGC 5248	13 37 32.07	+08 53 06.2	15.4	(R)SB(rs)bc;Sy2;HII	7.25	1.79	1152	Virgo-Libra Cl.	0.11
296	NGC 5273	13 42 08.34	+35 39 15.2	14.2	SA(s)0;Sy1.9	8.67	2.75	1064	Canes Ven. Spur	0.04

Continued on next page...

Table A.1 -- Continued

HRS+	Alt. Name	R.A. (h m s)	Dec. (° ' ")	D (Mpc)	Type	K_{Stot}	D_{25} (")	V (km s ⁻¹)	Member	A/B
(1)	(2)	(3)	(4)	(5)	(6)	(7)	(8)	(9)	(10)	(11)
297	NGC 5301	13 46 24.61	+46 06 26.7	20.0	SA(s)bc: sp	9.11	4.17	1508	Canes Ven. Spur	0.07
298	NGC 5302	13 47 44.97	+38 18 16.4	18.9	Pec	10.23	0.91	1419	Canes Ven. Spur	0.06
299	NGC 5300	13 48 16.04	+03 57 03.1	15.6	SAB(r)c	9.50	3.89	1171	Virgo-Libra Cl.	0.10
300	UGC 8756	13 50 35.89	+42 32 29.5	18.1	Sab	10.34	1.70	1354	Canes Ven. Spur	0.06
301	NGC 5334	13 52 54.46	-01 06 52.7	18.5	SB(rs)c:	9.94	4.17	1380	Virgo-Libra Cl.	0.20
302	NGC 5348	13 54 11.27	+05 13 38.8	19.3	SBbc: sp	10.87	3.55	1443	Virgo-Libra Cl.	0.12
303	NGC 5372	13 54 46.01	+58 39 59.4	22.9	S?	10.65	0.65	1717	Canes Ven.-Came. Cl.	0.04
304	NGC 5356	13 54 58.46	+05 20 01.4	18.3	SABbc: sp;HII	9.64	3.09	1370	Virgo-Libra Cl.	0.11
305	NGC 5360	13 55 38.75	+04 59 06.2	15.6	IO	11.15	2.19	1171	Virgo-Libra Cl.	0.13
306	NGC 5363	13 56 07.21	+05 15 17.2	15.2	IO?	6.93	4.07	1136	Virgo-Libra Cl.	0.12
307	NGC 5364	13 56 12.00	+05 00 52.1	16.5	SA(rs)bc pec;HII	7.80	6.76	1242	Virgo-Libra Cl.	0.12
308	UGC 8857	13 56 26.61	+04 23 48.0	14.5	Sb(f)	11.93	0.91	1091	Virgo-Libra Cl.	0.14
309	NGC 5486	14 07 24.97	+55 06 11.1	18.5	SA(s)m:	11.95	1.86	1383	Canes Ven.-Came. Cl.	0.09
310	NGC 5560	14 20 05.42	+03 59 28.4	23.1	SB(s)b pec	9.98	3.72	1718	Virgo-Libra Cl.	0.13
311	NGC 5566	14 20 19.95	+03 56 00.9	20.1	SB(r)ab;LINER	7.39	6.61	1492	Virgo-Libra Cl.	0.13
312	NGC 5576	14 21 03.68	+03 16 15.6	19.8	E3	7.83	3.55	1482	Virgo-Libra Cl.	0.14
313	NGC 5577	14 21 13.11	+03 26 08.8	19.9	SA(rs)bc:	9.75	3.39	1490	Virgo-Libra Cl.	0.18
314	UGC 9215	14 23 27.12	+01 43 34.7	18.6	SB(s)d	10.54	2.19	1389	Virgo-Libra Cl.	0.14
315	UGC 9242	14 25 21.02	+39 32 22.5	19.5	Sc	11.73	5.01	1440	Canes Ven. Spur	0.05
316	NGC 5638	14 29 40.39	+03 14 00.2	22.3	E1	8.25	2.69	1845	Virgo-Libra Cl.	0.14
317	IC 1022	14 30 01.85	+03 46 22.3	23.0	S?	11.70	1.10	1716	Virgo-Libra Cl.	0.15
318	NGC 5645	14 30 39.35	+07 16 30.3	18.3	SB(s)d	9.69	2.40	1370	Virgo-Libra Cl.	0.12
319	NGC 5669	14 32 43.88	+09 53 30.5	18.3	SAB(rs)cd	10.35	3.98	1368	Virgo-Libra Cl.	0.12
320	NGC 5668	14 33 24.34	+04 27 01.6	21.1	SA(s)d	11.71	3.31	1583	Virgo-Libra Cl.	0.16
321	NGC 5692	14 38 18.12	+03 24 37.2	20.8	S?	10.54	0.89	1581	Virgo-Libra Cl.	0.16
322	NGC 5701	14 39 11.06	+05 21 48.8	20.1	(R)SB(rs)0/a;LINER	8.14	4.27	1505	Virgo-Libra Cl.	0.16
323	IC 1048	14 42 57.88	+04 53 24.5	21.8	S	9.55	2.24	1640	Virgo-Libra Cl.	0.16
324	VCC 140	12 15 12.50	+14 25 58.8	17.0	S0	10.87	0.52	1159	Virgo N Cloud	0.16
325	NGC 4239	12 17 14.64	+16 31 55.2	17.0	E	9.91	1.8	940	Virgo Cl.	0.12
326	VCC 308	12 18 50.90	+07 51 43.2	23.0	dS0	10.87	1.45	1596	Virgo B Cl.	0.09
327	VCC 324	12 19 09.89	+03 51 21.6	17.0	E pec;HII	11.66	0.7	1526	Virgo S Cl.	0.07
328	VCC 358	12 19 35.69	+05 50 49.2	23.0	SB0(rs)	9.84	1.21	2532	Virgo B Cl.	0.07
329	VCC 366	12 19 45.31	+06 00 21.6	23.0	S0	10.95	1.17	2292	Virgo B Cl.	0.08
330	VCC 373	12 19 49.20	+06 00 54.0	23.0	S0	9.73	1.1	2074	Virgo B Cl.	0.09
331	VCC 389	12 20 03.29	+14 57 39.6	17.0	dS0	10.85	1.05	1364	Virgo A Cl.	0.14
332	VCC 407	12 20 18.79	+09 32 42.0	17.0	dSB0	11.43	1.18	2024	Virgo N Cloud	0.08
333	VCC 411	12 20 24.31	+05 34 22.8	23.0	S0?	10.39	1.02	929	Virgo B Cl.	0.07
334	VCC 462	12 21 16.39	+04 35 45.6	17.0	(R)SB(r)0	9.42	1.7	2258	Virgo S Cl.	0.08
335	VCC 482	12 21 34.10	+04 46 44.4	17.0	SA(r)0/a: sp	11.02	1.4	2157	Virgo S Cl.	0.07
336	VCC 486	12 21 37.01	+05 45 57.6	23.0	SB0/SBa(r)	10.55	2.00	2472	Virgo B Cl.	0.08
337	VCC 490	12 21 38.81	+15 44 42.0	17.0	SAB0/a?(rs)	11.04	1.14	1267	Virgo A Cl.	0.09
338	VCC 523	12 22 04.10	+12 47 13.2	17.0	SB0	10.25	1.50	1981	Virgo A Cl.	0.19
339	VCC 534	12 22 12.41	+07 08 38.4	23.0	SAB(r)0+	9.82	2.01	869	Virgo B Cl.	0.08
340	VCC 543	12 22 19.51	+14 45 39.6	17.0	dE5	11.15	1.37	985	Virgo A Cl.	0.13

Continued on next page...

Table A.1 - Continued

HRS+	Alt. Name	R.A. (h m s)	Dec. (° ' ")	D (Mpc)	Type	K_{Stot} (7)	D_{25} (")	V (km s $^{-1}$)	Member	A_B (11)
(1)	(2)	(3)	(4)	(5)	(6)	(7)	(8)	(9)	(10)	(11)
341	VCC 575	12 22 43.30	+08 11 52.8	23.0	E?	9.98	0.84	1231	Virgo B Cl.	0.10
342	VCC 634	12 23 19.99	+15 49 15.6	17.0	SA0	10.88	1.22	479	Virgo A Cl.	0.11
343	VCC 655	12 23 37.49	+17 32 27.6	17.0	BCD:HII	10.29	1.7	1142	Virgo A Cl.	0.14
344	VCC 657	12 23 39.00	+07 03 14.4	23.0	S0	8.92	1.3	751	Virgo B Cl.	0.08
345	VCC 672	12 23 53.50	+07 06 25.2	23.0	SAB(s)0	10.65	1.81	922	Virgo B Cl.	0.09
346	VCC 698	12 24 04.99	+11 13 04.8	17.0	SA0: sp	9.73	1.43	2070	Virgo A Cl.	0.10
347	VCC 745	12 24 46.99	+07 21 10.8	23.0	dE6	11.38	1.09	1276	Virgo B Cl.	0.10
348	VCC 778	12 25 12.31	+14 45 43.2	17.0	SA0	8.71	1.70	1375	Virgo A Cl.	0.15
349	VCC 784	12 25 14.69	+15 36 25.2	17.0	S0- pec	8.72	1.90	1069	Virgo A Cl.	0.16
350	VCC 781	12 25 15.19	+12 42 54.0	17.0	dS0	11.62	1.10	-188	Virgo A Cl.	0.16
351	VCC 828	12 25 41.71	+12 48 39.6	17.0	E5	9.05	1.59	472	Virgo A Cl.	0.14
352	CGCG 014-034	12 25 42.65	+00 34 19.2	17.0	SB(rs)0:HII:Sbrst	9.69	2.02	2140	Virgo Cl.	0.10
353	VCC 856	12 25 57.91	+10 03 14.4	23.0	dE	11.1	0.97	1025	Virgo B Cl.	0.10
354	VCC 874	12 26 07.10	+16 10 51.6	17.0	SA(rs)0/a:HII	9.34	1.82	1747	Virgo A Cl.	0.10
355	VCC 929	12 26 40.49	+08 26 09.6	17.0	S0/a	10.26	1.22	910	Virgo S Cl.	0.09
356	VCC 940	12 26 47.09	+12 27 14.4	17.0	dE1	11.8	0.97	1411	Virgo A Cl.	0.13
357	VCC 951	12 26 54.31	+11 39 50.4	17.0	dE	11.33	1.30	2066	Virgo A Cl.	0.10
358	VCC 966	12 27 02.50	+15 27 39.6	17.0	SB(s)0/a	8.53	2.54	1603	Virgo A Cl.	0.10
359	VCC 984	12 27 13.30	+12 44 06.0	17.0	SBO+: sp	8.92	2.39	1866	Virgo A Cl.	0.12
360	VCC 990	12 27 16.80	+16 01 26.4	17.0	dE4	11.15	0.90	1727	Virgo A Cl.	0.12
361	VCC 1010	12 27 27.31	+12 17 24.0	17.0	SA(r)0	10.3	1.70	934	Virgo A Cl.	0.12
362	VCC 1025	12 27 36.70	+08 09 14.4	17.0	E0/S0	8.9	1.4	1071	Virgo S Cl.	0.09
363	VCC 1036	12 27 41.21	+12 18 57.6	17.0	dE6/dS0	10.61	1.91	1124	Virgo A Cl.	0.11
364	VCC 1049	12 27 54.79	+08 05 27.6	17.0	S0	11.71	0.73	620	Virgo S Cl.	0.09
365	VCC 1073	12 28 08.59	+12 05 34.8	17.0	dE3	10.75	1.17	1899	Virgo A Cl.	0.11
366	VCC 1087	12 28 14.90	+11 47 24.0	17.0	dE3	10.89	1.35	675	Virgo A Cl.	0.11
367	VCC 1122	12 28 41.71	+12 54 57.6	17.0	dE7	11.71	1.30	476	Virgo A Cl.	0.09
368	VCC 1125	12 28 43.30	+11 45 18.0	17.0	S0	9.09	2.53	165	Virgo A Cl.	0.12
369	VCC 1146	12 28 57.50	+13 14 31.2	17.0	E0	9.33	1.70	635	Virgo A Cl.	0.10
370	VCC 1178	12 29 21.29	+08 09 25.2	17.0	E3	9.47	1.10	1243	Virgo S Cl.	0.09
371	VCC 1183	12 29 22.51	+11 26 02.4	17.0	dS0	10.9	1.00	1335	Virgo A Cl.	0.13
372	VCC 1188	12 29 26.30	+16 24 18.0	17.0	S0/a	10.31	1.30	1554	Virgo A Cl.	0.13
373	VCC 1192	12 29 30.19	+07 59 34.8	17.0	E2	10.98	0.62	1423	Virgo S Cl.	0.09
374	VCC 1242	12 29 53.50	+14 04 08.4	17.0	S0 pec:	8.69	2.11	1588	Virgo A Cl.	0.18
375	VCC 1250	12 29 59.09	+12 20 56.4	17.0	SA(r)0	9.47	1.67	1970	Virgo A Cl.	0.12
376	VCC 1254	12 30 05.11	+08 04 22.8	17.0	dE0	11.04	0.72	1278	Virgo A Cl.	0.09
377	VCC 1261	12 30 10.30	+10 46 44.4	17.0	dE5	10.42	1.41	1871	Virgo A Cl.	0.12
378	VCC 1283	12 30 18.41	+13 34 40.8	17.0	SBO	9.64	1.38	876	Virgo A Cl.	0.12
379	VCC 1297	12 30 31.80	+12 29 27.6	17.0	Compact E0	10.09	0.6	1555	Virgo A Cl.	0.09
380	VCC 1304	12 30 39.79	+15 07 48.0	17.0	dS0	11.82	1.2	-108	Virgo A Cl.	0.12
381	VCC 1303	12 30 40.61	+09 00 57.6	23.0	SB(s)0	9.28	1.74	875	Virgo B Cl.	0.08
382	VCC 1318	12 30 51.41	+08 21 36.0	17.0	SB(s)0/a pec	9.28	3.17	972	Virgo S Cl.	0.08
383	VCC 1321	12 30 52.20	+16 45 32.4	17.0	E	9.36	1.70	967	Virgo A Cl.	0.12
384	VCC 1327	12 30 57.70	+12 16 15.6	17.0	E2	9.04	1.00	150	Virgo A Cl.	0.10

Continued on next page...

Table A.1 – Continued

HRS+ (1)	Alt. Name (2)	R.A. (h m s) (3)	Dec. (° ' ") (4)	D (Mpc) (5)	Type (6)	K_{rot} (7)	D_{25} (") (8)	V (km s ⁻¹) (9)	Member (10)	A _B (11)
385	VCC 1368	12 31 32.50	+11 37 30.0	17.0	SAB(s)0	9.67	1.99	1045	Virgo A Cl.	0.17
386	VCC 1422	12 32 14.21	+10 15 03.6	17.0	E1	10.54	1.18	1288	Virgo A Cl.	0.14
387	VCC 1440	12 32 33.41	+15 24 54.0	17.0	E0	11.55	0.63	382	Virgo A Cl.	0.11
388	VCC 1437	12 32 33.50	+09 10 26.4	17.0	E	12.15	0.68	1155	Virgo S Cl.	0.09
389	VCC 1453	12 32 44.21	+14 11 45.6	17.0	SAB	11.24	1.07	1949	Virgo A Cl.	0.15
390	VCC 1475	12 33 04.90	+16 15 57.6	17.0	S0	9.83	1.30	951	Virgo A Cl.	0.13
391	VCC 1491	12 33 13.99	+12 51 28.8	17.0	DE	11.92	0.84	1903	Virgo A Cl.	0.13
392	VCC 1521	12 33 45.00	+10 59 45.6	17.0	S0/a	10.44	1.40	1212	Virgo A Cl.	0.14
393	VCC 1528	12 33 51.60	+13 19 19.2	17.0	DE1	11.25	0.89	1647	Virgo A Cl.	0.12
394	VCC 1545	12 34 11.50	+12 02 56.4	17.0	E4	11.94	0.84	2000	Virgo A Cl.	0.17
395	VCC 1552	12 34 15.79	+13 04 33.6	17.0	SB0+Sy:LINER	8.69	3.1	195	Virgo A Cl.	0.18
396	VCC 1608	12 35 20.21	+06 06 54.0	17.0	E3	10.56	1.00	2382	Virgo S Cl.	0.09
397	VCC 1624	12 35 36.60	+03 02 02.4	17.0	SB0/a?sp:III	10.05	2.0	1154	Virgo S Cl.	0.09
398	VCC 1627	12 35 37.20	+12 22 55.2	17.0	E0	11.66	0.50	236	Virgo A Cl.	0.17
399	VCC 1630	12 35 37.99	+12 15 50.4	17.0	E	8.78	1.8	1172	Virgo A Cl.	0.17
400	CGCG 014-083	12 38 05.21	+01 28 37.2	17.0	E	9.57	1.63	1818	Virgo Cl.	0.11
401	VCC 1763	12 38 35.40	+02 39 28.8	17.0	SA(r)0	10.19	1.1	901	Virgo S Cl.	0.09
402	VCC 1827	12 40 11.90	+08 23 02.4	17.0	SB0	9.97	1.47	1961	Virgo E Cl.	0.10
403	VCC 1833	12 40 19.61	+15 56 06.0	17.0	S0	11.26	0.83	1820	Virgo E Cl.	0.16
404	VCC 1834	12 40 22.99	+03 07 04.8	17.0	S0	9.64	1.2	852	Virgo S Cl.	0.11
405	CGCG 014-099	12 40 27.17	+01 11 45.6	17.0	SA0/a	9.76	1.78	1836	Virgo Cl.	0.07
406	VCC 1861	12 40 58.49	+11 11 02.4	17.0	de0	11.12	1.03	629	Virgo E Cl.	0.13
407	VCC 1871	12 41 15.70	+11 23 13.2	17.0	E3	10.59	0.76	588	Virgo E Cl.	0.13
408	VCC 1902	12 41 59.30	+12 56 34.8	17.0	S0	9.92	1.59	1141	Virgo E Cl.	0.12
409	VCC 1910	12 42 08.59	+11 45 14.4	17.0	DE1	10.66	0.9	206	Virgo E Cl.	0.13
410	VCC 1912	12 42 09.10	+12 35 49.2	17.0	ds0	11.13	1.6	-169	Virgo E Cl.	0.09
411	VCC 1913	12 42 10.70	+07 40 37.2	17.0	SB0+sp	10.97	2.2	1892	Virgo S Cl.	0.09
412	VCC 1947	12 42 56.30	+03 40 33.6	17.0	de2	10.74	0.81	974	Virgo S Cl.	0.11
413	VCC 1949	12 42 57.70	+12 17 13.2	17.0	ds0	10.74	1.62	1931	Virgo E Cl.	0.14
414	VCC 1955	12 43 07.61	+12 03 03.6	17.0	S0:III	11.0	1.29	2011	Virgo E Cl.	0.14
415	VCC 1999	12 44 29.40	+13 29 56.4	17.0	S0/a	9.31	1.76	480	Virgo E Cl.	0.11
416	VCC 2019	12 45 20.40	+13 41 34.8	17.0	E7	11.42	0.9	1895	Virgo E Cl.	0.09
417	VCC 2048	12 47 15.31	+10 12 10.8	17.0	ds0	10.86	1.83	1084	Virgo E Cl.	0.14
418	VCC 2066	12 48 15.10	+10 59 02.4	17.0	SB0 pec:III	8.88	3.2	1160	Virgo E Cl.	0.17
419	VCC 2087	12 51 06.79	+10 54 43.2	17.0	SB(s)0	9.03	1.67	928	Virgo E Cl.	0.09
420	CGCG 043-054	12 53 14.52	+04 27 50.4	17.0	S0/a?III	10.65	1.1	716	Virgo Cl.	0.17
421	CGCG 043-064	12 55 02.78	+08 03 57.6	17.0	SBa pec	8.99	1.7	2799	Virgo Cl.	0.14
422	CGCG 071-094	13 00 10.82	+12 28 58.8	17.0	SA(r)0	8.99	2.21	1377	Virgo Cl.	0.13
423	CGCG 089-092	12 34 34.73	+18 12 10.8	17.0	SB(s)asp	9.29	3.37	1397	Coma I Cl.	0.10
424	CGCG 089-094	12 34 49.44	+17 48 54.0	17.0	S0	11.64	1.3	1115	Coma I Cl.	0.10
425	CGCG 159-069	12 45 16.90	+27 07 26.4	17.0	SB(s)0/a pec:BCD	10.32	1.4	1069	Coma I Cl.	0.06
426	-	12 41 24.55	+12 10 30.0	16.5	S0	11.44	0.52	1159	Virgo E Cl.	0.16
427	CGCG 014-104	12 41 22.90	-03 03 28.2	20.8	SA0+	11.37	1.27	1458	Virgo Out.	0.13
428	CGCG 095-052	10 52 21.38	+17 56 06.0	21.8	ds0?	11.60	0.7	1526	Leo Cl.	0.16

Continued on next page...

Table A.1 – Continued

HRS+ (1)	Alt. Name (2)	R.A.(h m s) (3)	Dec.($^{\circ}$ '''') (4)	D (Mpc) (5)	Type (6)	K_{Stot} (7)	D_{25} (l) (8)	V (km s $^{-1}$) (9)	Member (10)	A_B (11)
429	IC 676	11 12 39.79	+09 03 20.9	20.7	(R)SB(r)0+;Sbrst	9.69	1.72	1453	Leo Cl.	0.10
430	IC 1024	14 31 27.19	+03 00 32.4	20.7	S0?	10.07	1.6	1455	Virgo-Libra Cl.	0.12
431	MCG -01-33-007	12 47 38.21	-05 52 01.2	19.1	dE0?	11.19	0.4	1383	Virgo Out.	0.12
432	MRK 1342	13 01 10.90	-05 33 21.6	23.6	S0	11.27	1.5	1213	Virgo Out.	0.14
433	NGC 3248	10 27 45.41	+22 50 49.2	21.7	S0	9.53	1.92	1523	Leo Cl.	0.09
434	NGC 3265	10 31 06.77	+28 47 45.6	18.8	E	10.43	0.96	1319	Leo Cl.	0.10
435	NGC 3400	10 50 45.48	+28 28 08.4	20.1	SB(s)a	10.15	1.37	1422	Leo Cl.	0.08
436	NGC 3418	10 51 23.93	+28 06 39.6	18.4	SAB(s)0/a	10.32	1.34	1268	Leo Cl.	0.07
437	NGC 3522	11 06 40.44	+20 05 06.0	17.4	E	10.37	1.2	1221	Leo Cl.	0.10
438	NGC 3524	11 06 32.09	+11 23 06.0	19.5	S0/a	9.61	1.81	1365	Leo Cl.	0.07
439	NGC 3630	11 20 16.97	+02 57 50.8	21.2	S0	8.84	4.6	1485	Leo Cl.	0.18
440	NGC 3757	11 37 02.83	+58 24 54.0	16.5	S0	9.62	1.1	1161	Ursa Major Cl.	0.05
441	NGC 3795B	11 38 08.40	+58 45 28.8	20.5	E?	10.20	0.98	1437	Ursa Major Cl.	0.06
442	NGC 3838	11 44 13.68	+57 56 52.8	18.9	SA0/a?	9.34	1.5	1320	Ursa Major Cl.	0.04
443	NGC 4813	12 56 36.12	-06 49 01.2	19.9	Sa;Sy2;LINER	9.87	1.2	1394	Virgo Out.	0.17
444	NGC 5379	13 55 34.30	+59 44 31.2	22.9	S0	10.31	1.88	1607	Canes Ven-Came. Cl.	0.07
445	NGC 5475	14 05 12.41	+55 44 27.6	24.5	Sa	9.40	1.57	1715	Canes Ven-Came. Cl.	0.05
446	NGC 5574	14 20 55.94	+03 14 16.8	23.7	SB0	9.53	1.6	1659	Virgo-Libra Cl.	0.13
447	NGC 5582	14 20 42.96	+39 41 34.8	19.5	E	8.93	2.8	1362	Canes Ven.	0.05
448	NGC 5636	14 29 39.00	+03 15 58.3	24.9	SAB(r)0+	11.28	1.26	1745	Virgo-Libra Cl.	0.14
449	UGC 5833	10 43 05.98	+20 25 19.2	18.9	S0	11.11	1.5	1327	Leo Cl.	0.12
450	UGC 6324	11 18 22.08	+18 44 16.8	15.2	S0	11.95	1.7	1068	Leo Cl.	0.09
451	UGC 6570	11 35 49.97	+35 20 06.0	22.9	S0/a;HII	10.72	1.22	1603	Ursa Maj. SS	0.09
452	UGC 6805	11 50 12.29	+42 04 26.4	16.5	S0	11.46	0.62	1158	Ursa Maj. SS	0.09
453	UGC 8986	14 04 15.84	+04 06 43.2	17.6	S0?	11.35	0.98	1232	Virgo-Libra Cl.	0.11
454	UGC 9519	14 46 21.07	+34 22 12.0	24.1	S0	10.23	0.8	1692	Canes Ven.	0.10

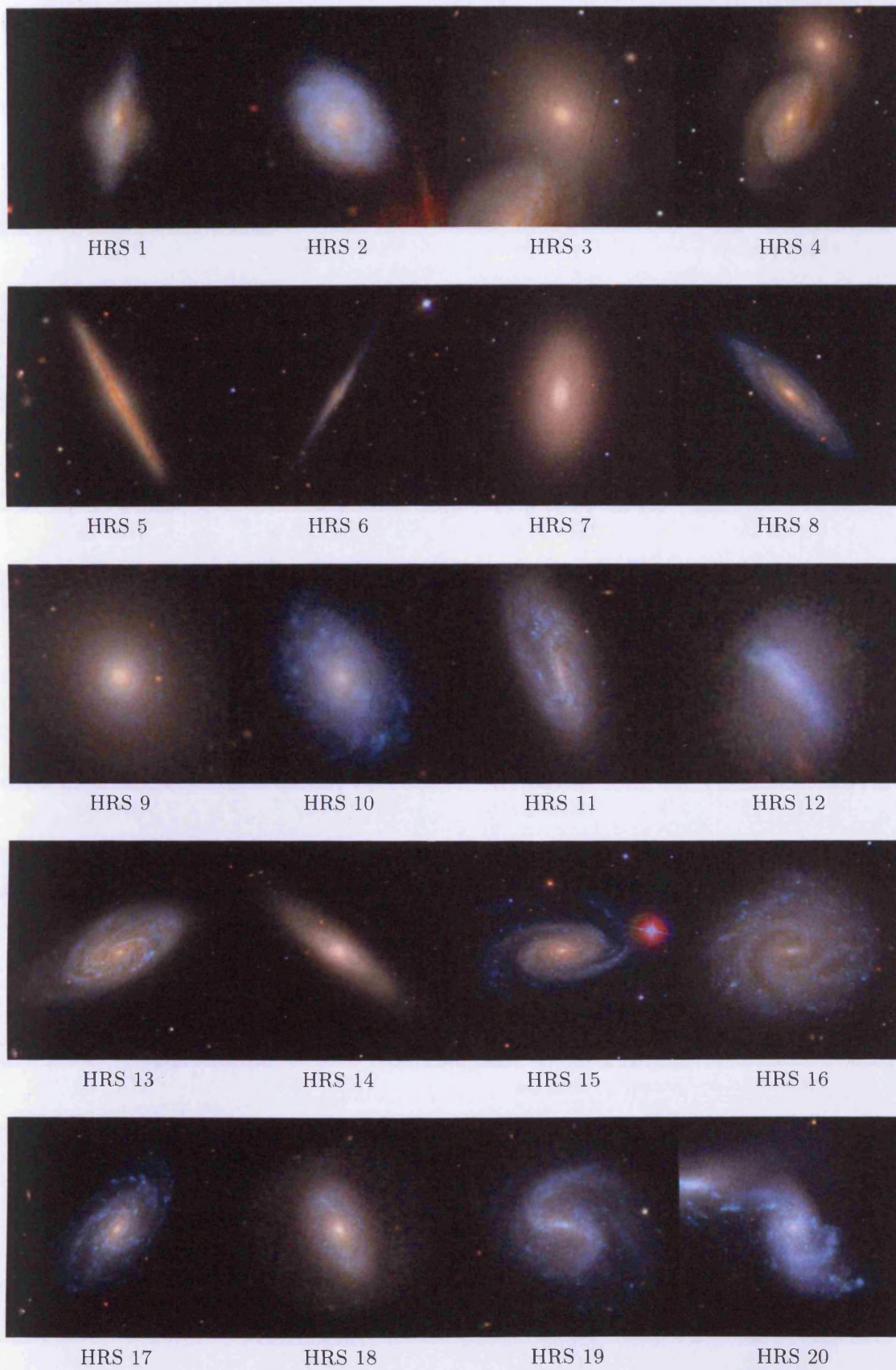


Figure A.1: SDSS composite images of all the HRS+ galaxies.

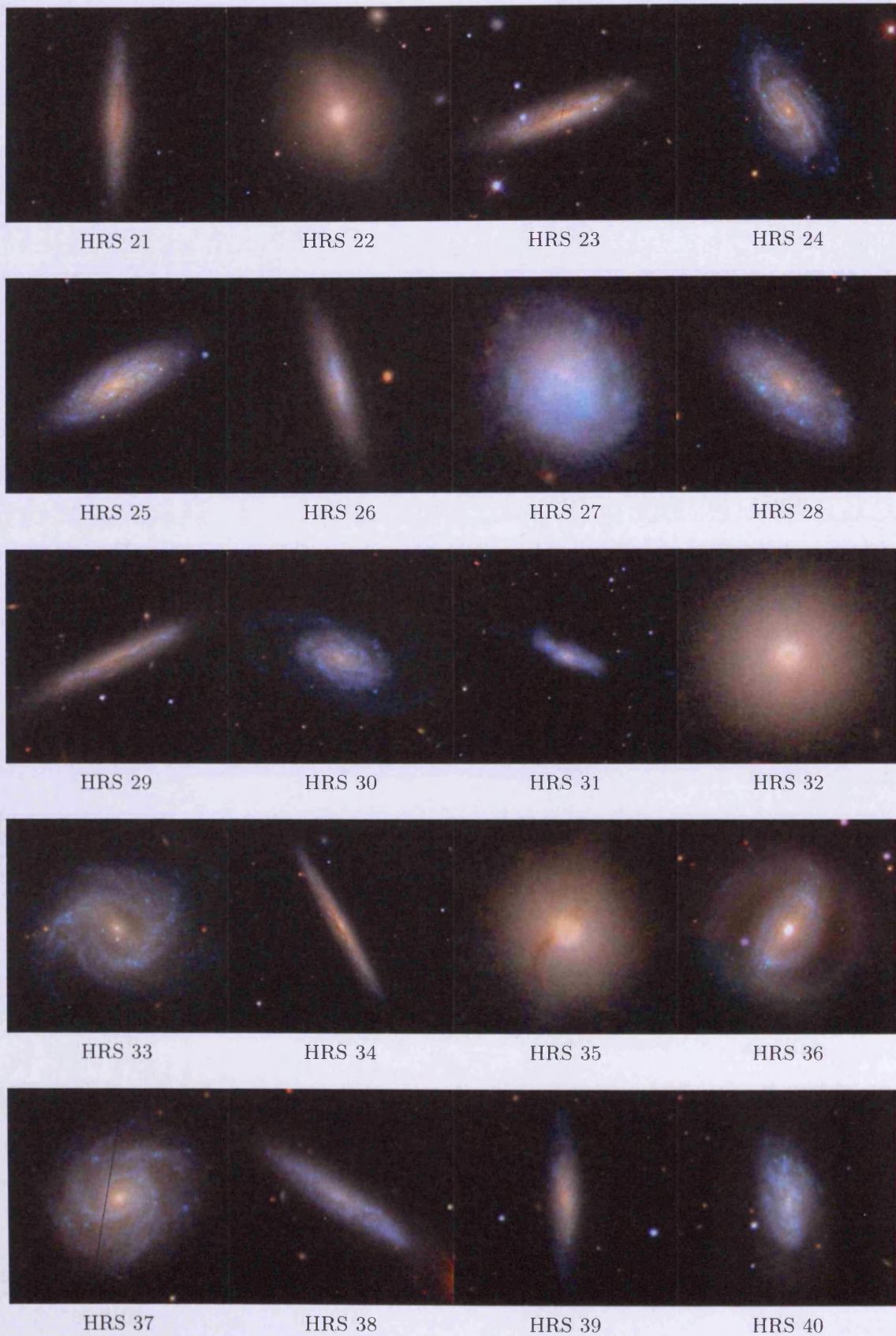


Figure A.1: Continued from previous page.

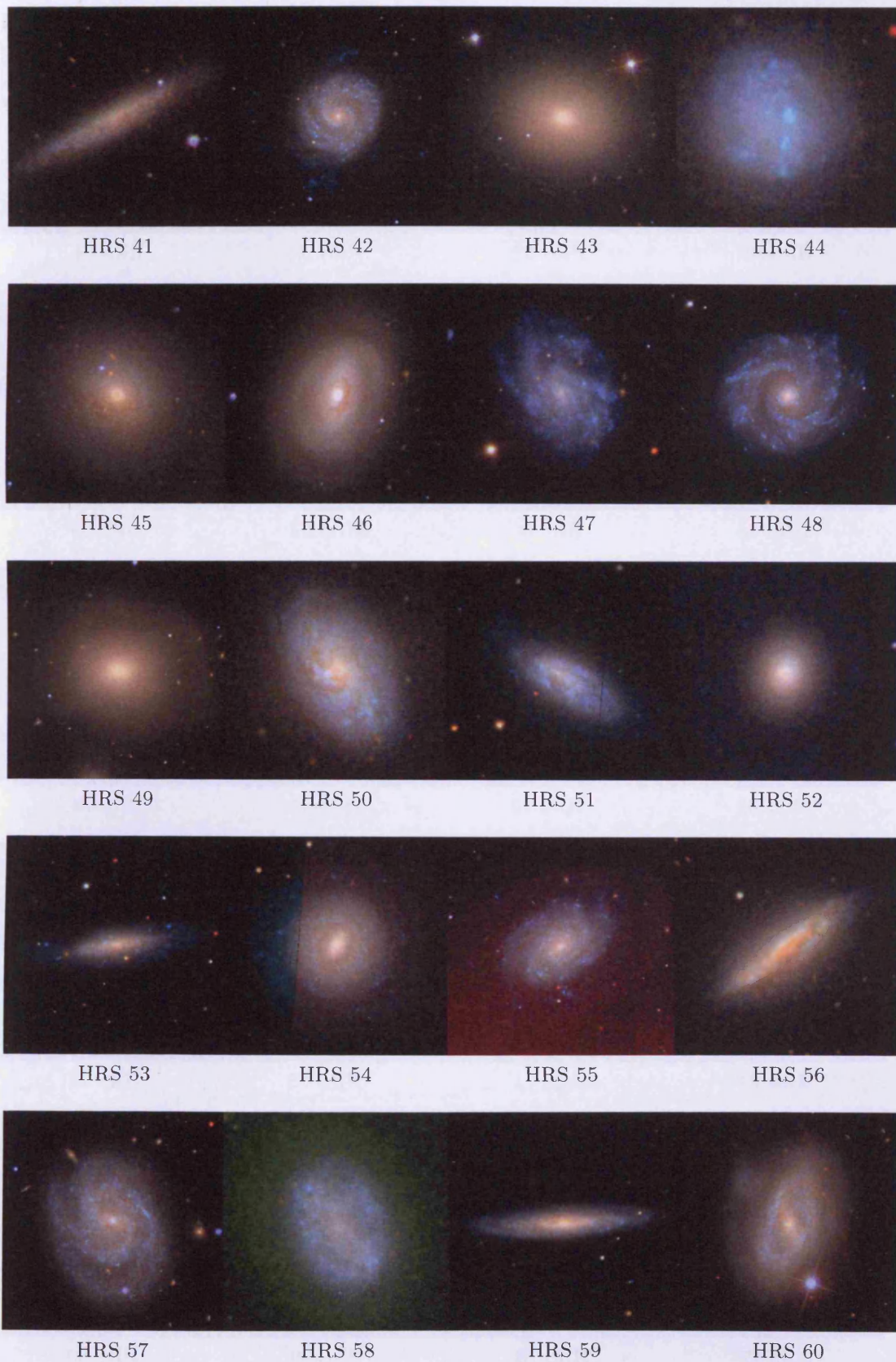


Figure A.1: Continued from previous page.

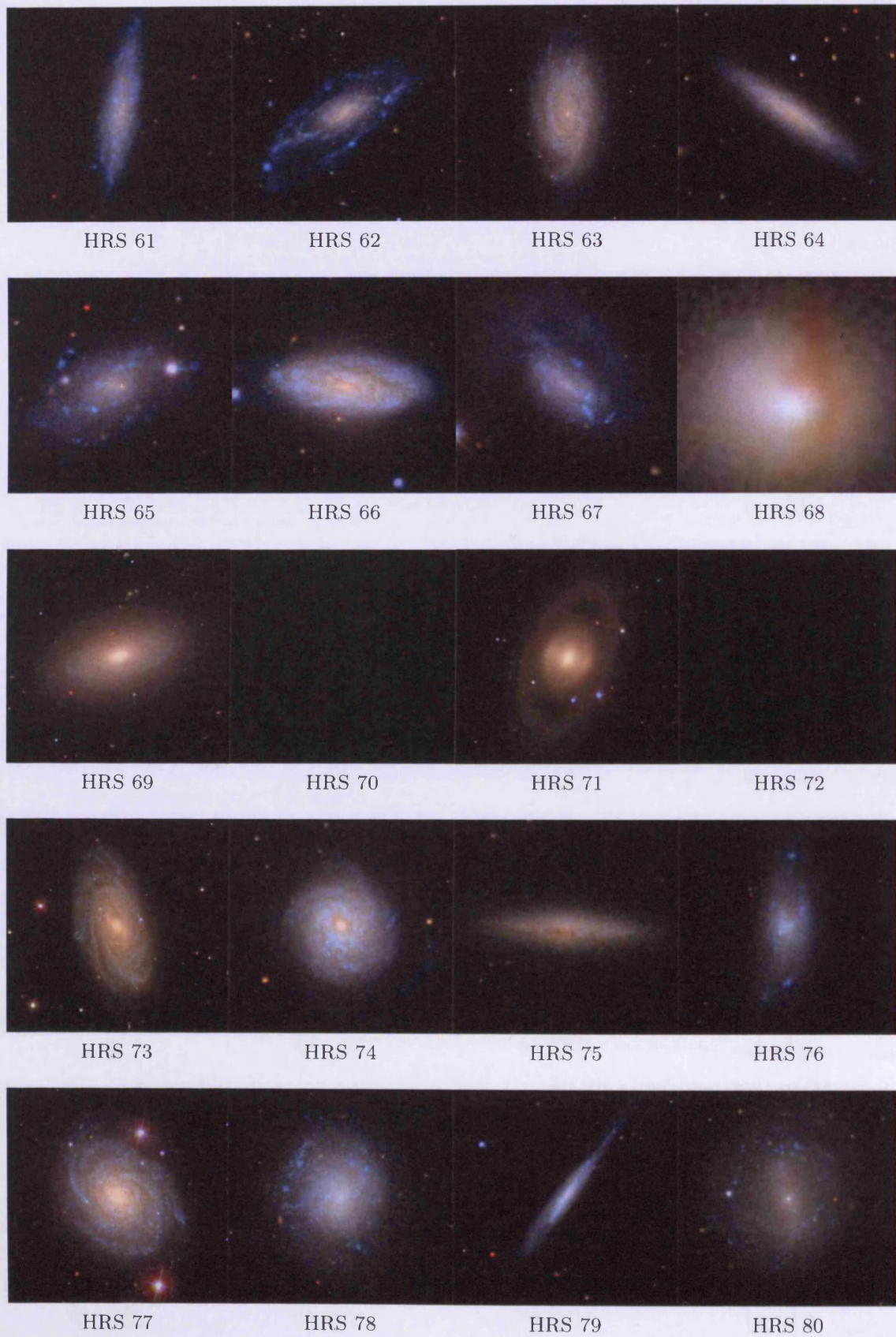
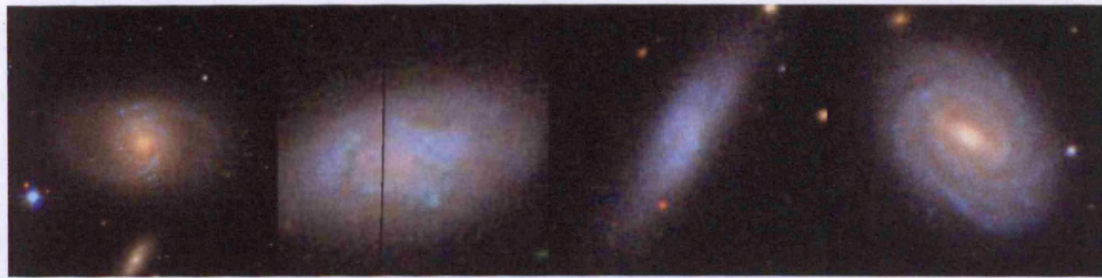


Figure A.1: Continued from previous page.



HRS 81

HRS 82

HRS 83

HRS 84



HRS 85

HRS 86

HRS 87

HRS 88



HRS 89

HRS 90

HRS 91

HRS 92



HRS 93

HRS 94

HRS 95

HRS 96



HRS 97

HRS 98

HRS 99

HRS 100

Figure A.1: Continued from previous page.



Figure A.1: Continued from previous page.



HRS 121

HRS 122

HRS 123

HRS 124



HRS 125

HRS 126

HRS 127

HRS 128



HRS 129

HRS 130

HRS 131

HRS 132



HRS 133

HRS 134

HRS 135

HRS 136



HRS 137

HRS 138

HRS 139

HRS 140

Figure A.1: Continued from previous page.

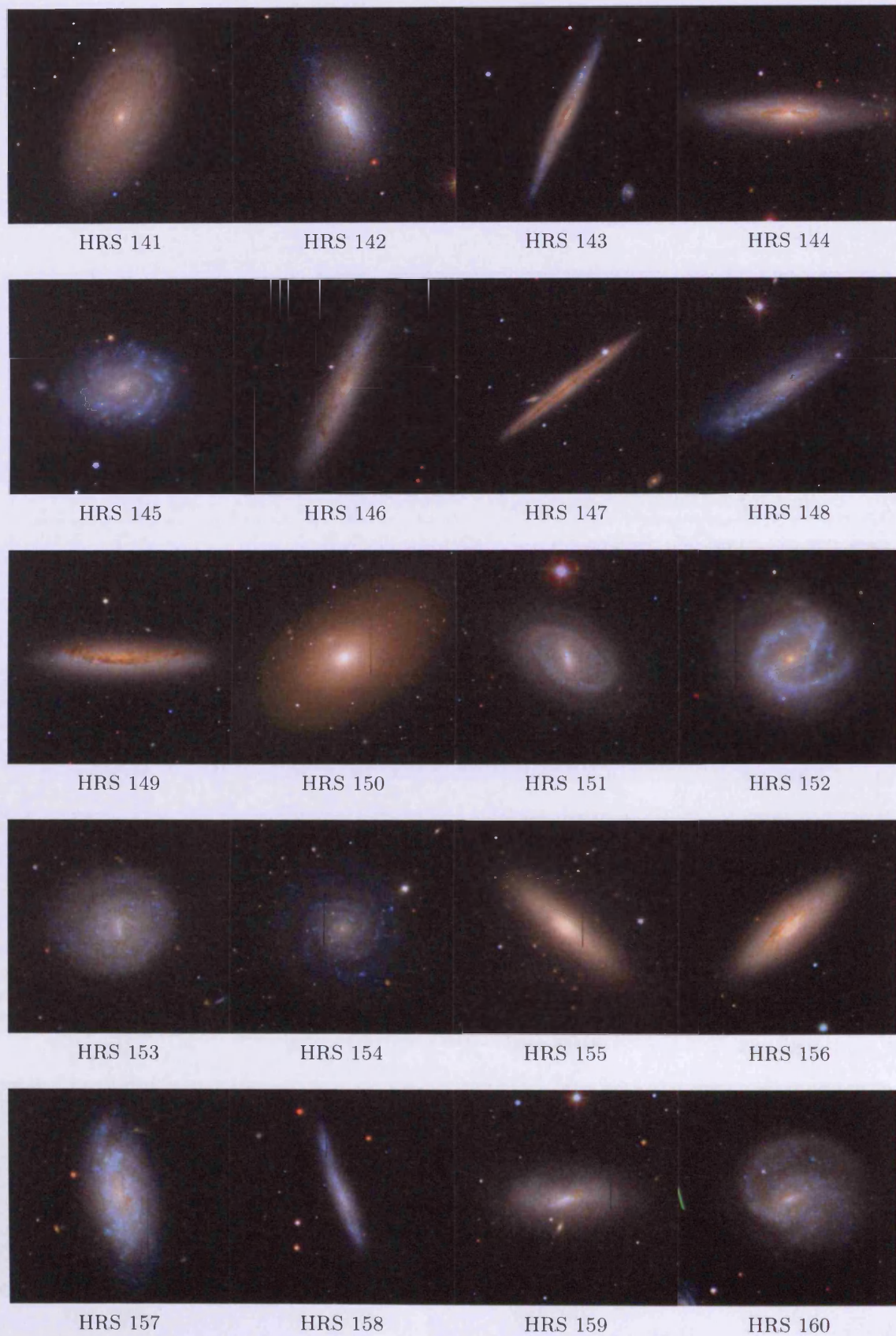


Figure A.1: Continued from previous page.



HRS 161

HRS 162

HRS 163

HRS 164



HRS 165

HRS 166

HRS 167

HRS 168



HRS 169

HRS 170

HRS 171

HRS 172



HRS 173

HRS 174

HRS 175

HRS 176



HRS 177

HRS 178

HRS 179

HRS 180

Figure A.1: Continued from previous page.

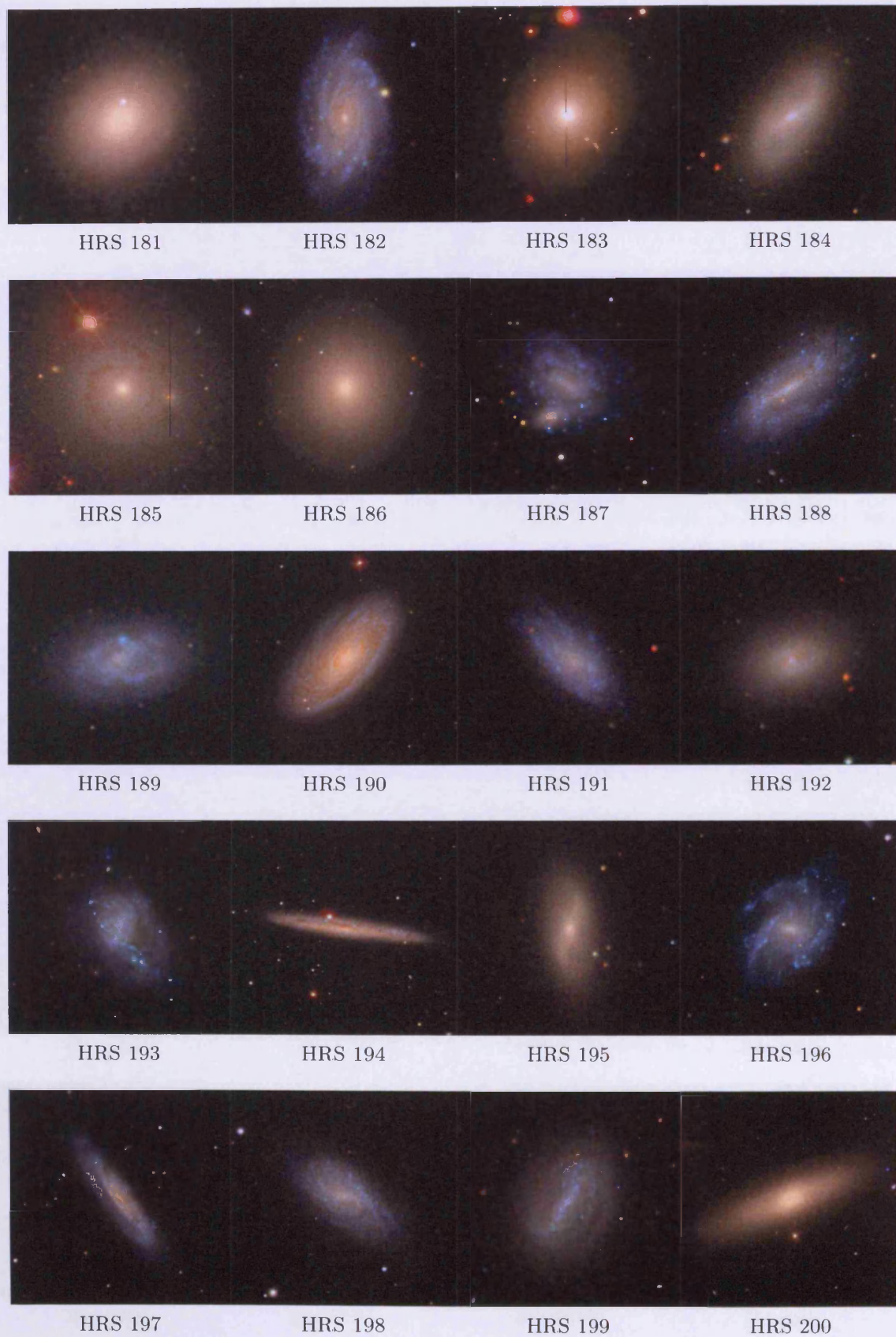


Figure A.1: Continued from previous page.

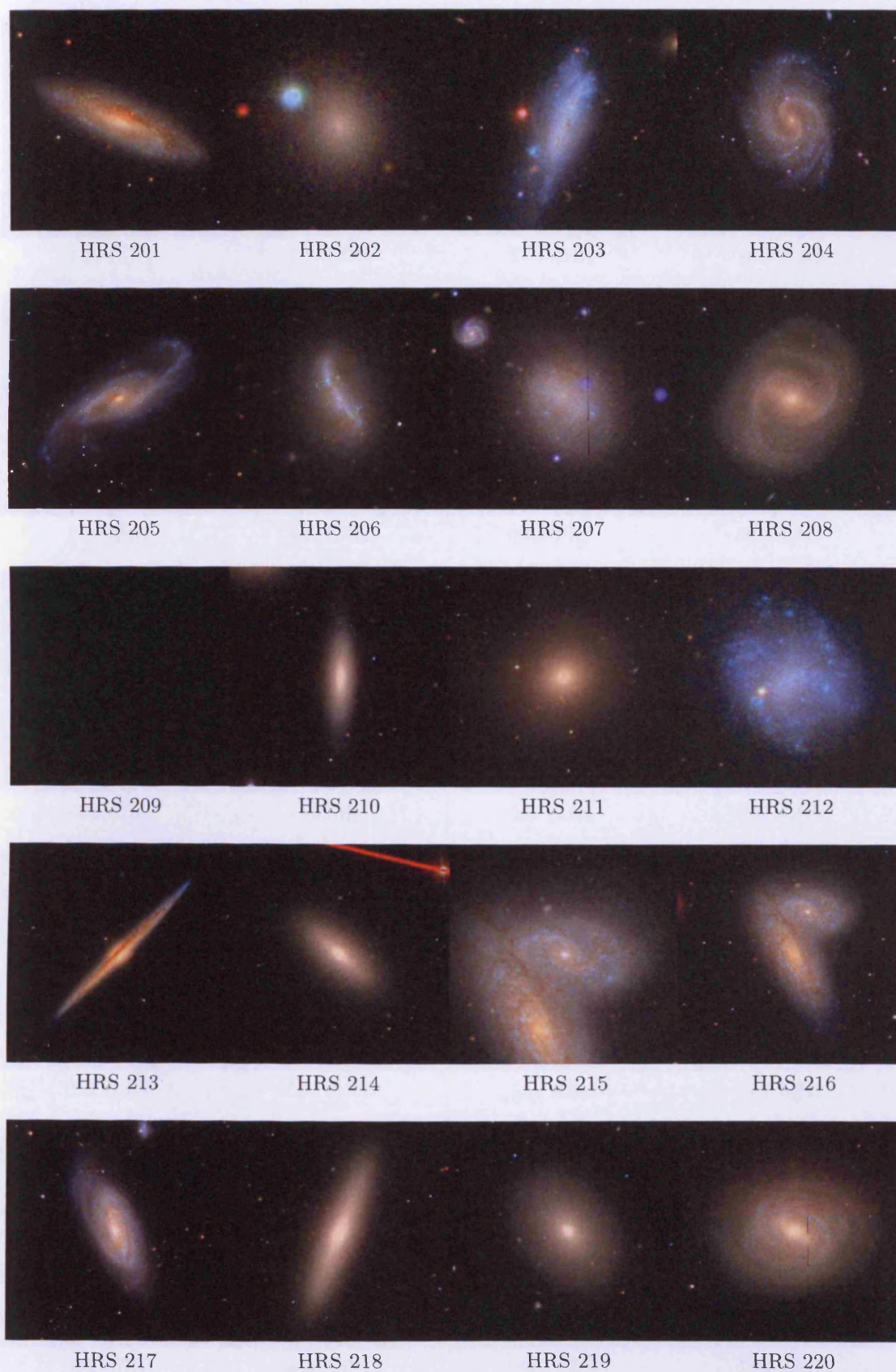


Figure A.1: Continued from previous page.

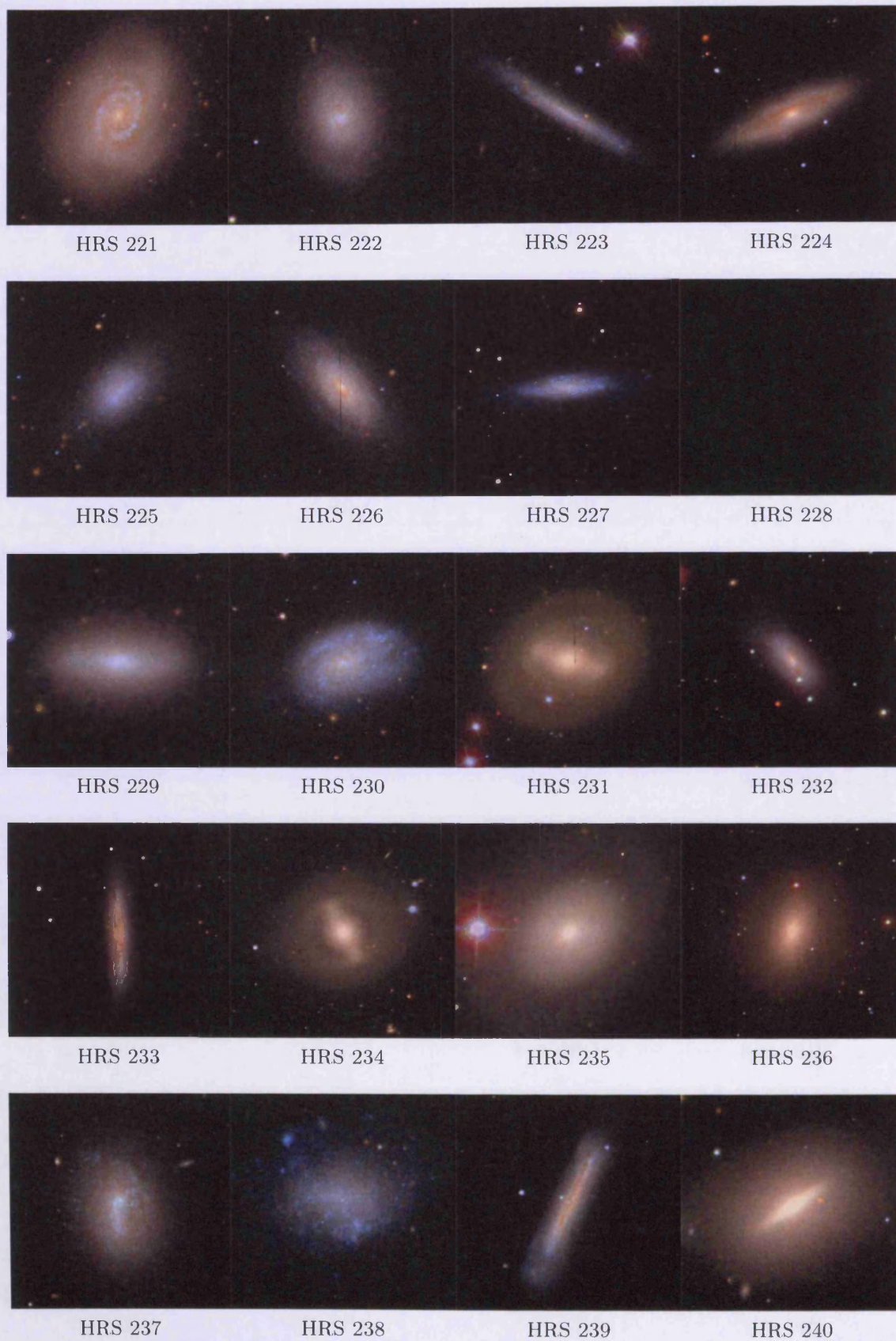


Figure A.1: Continued from previous page.

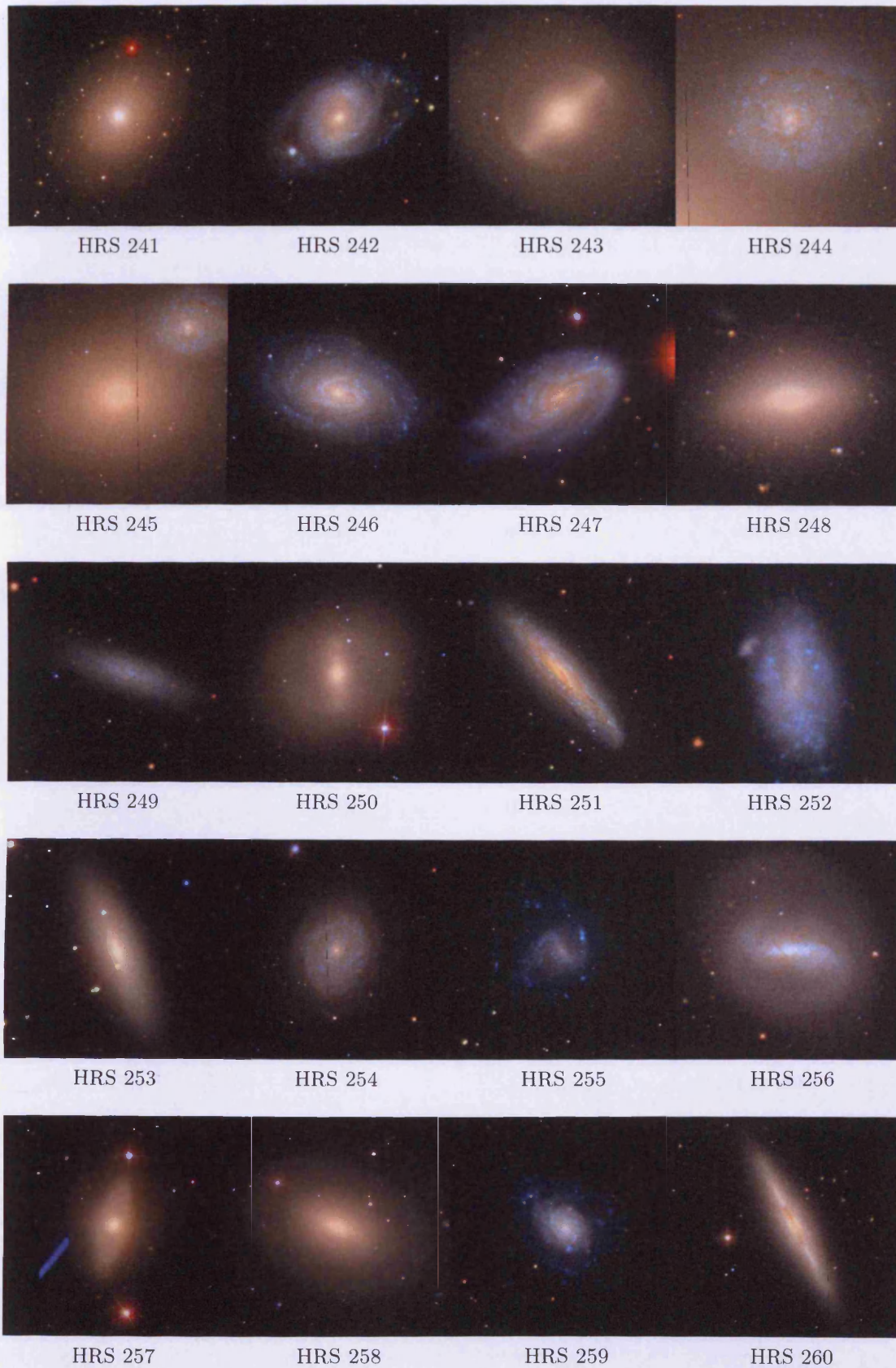


Figure A.1: Continued from previous page.



Figure A.1: Continued from previous page.



Figure A.1: Continued from previous page.



Figure A.1: Continued from previous page.

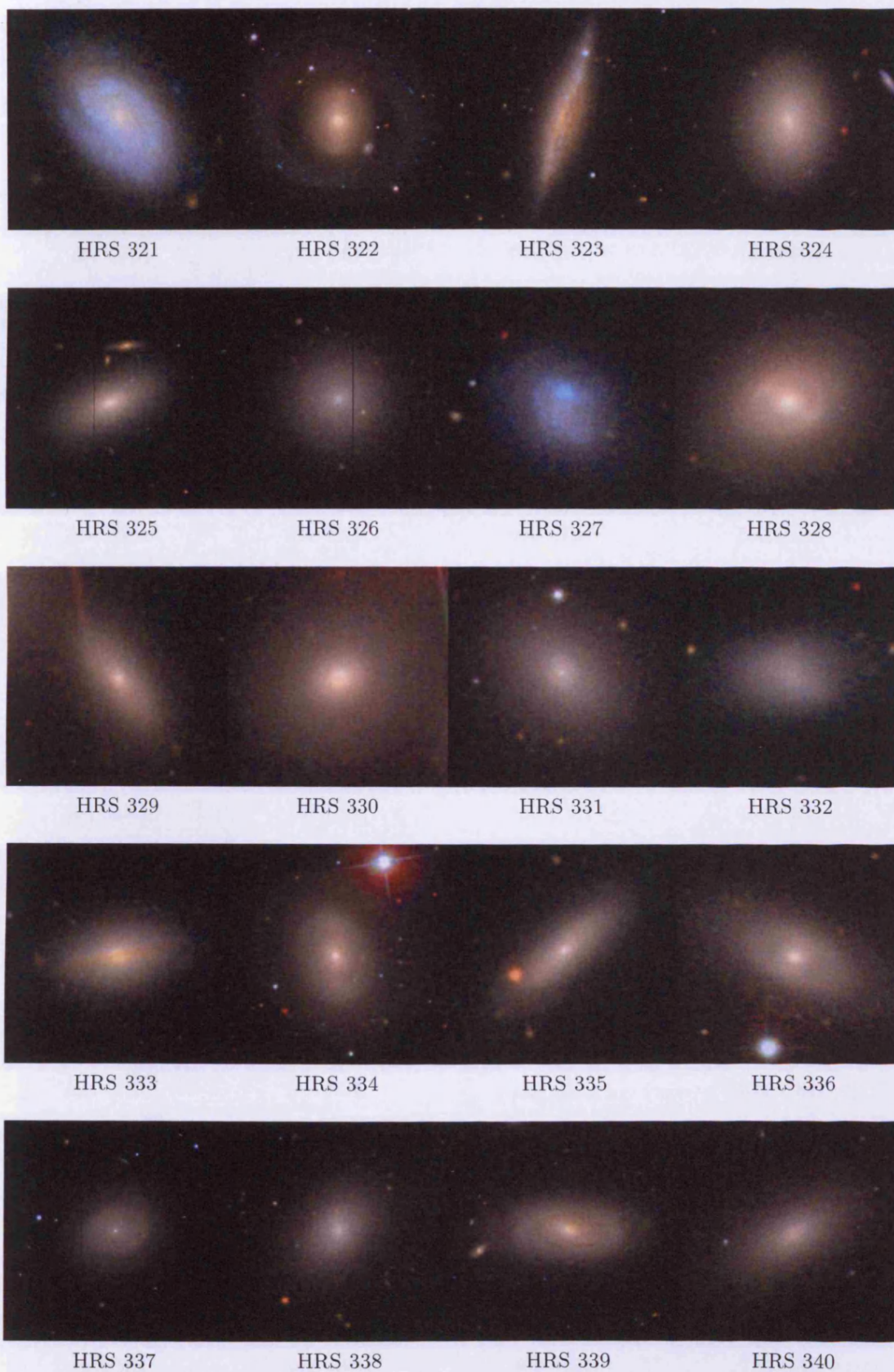


Figure A.1: Continued from previous page.

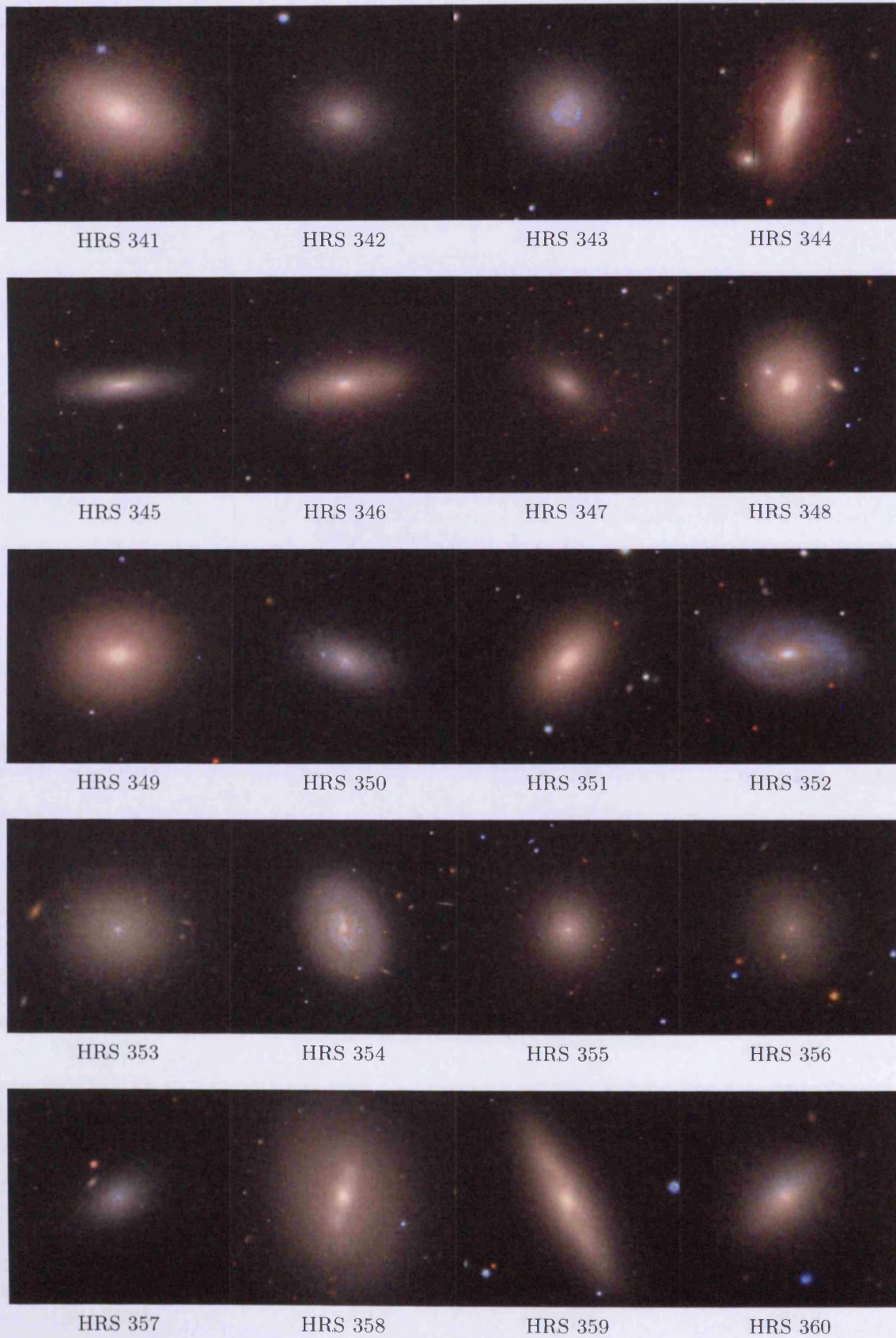


Figure A.1: Continued from previous page.

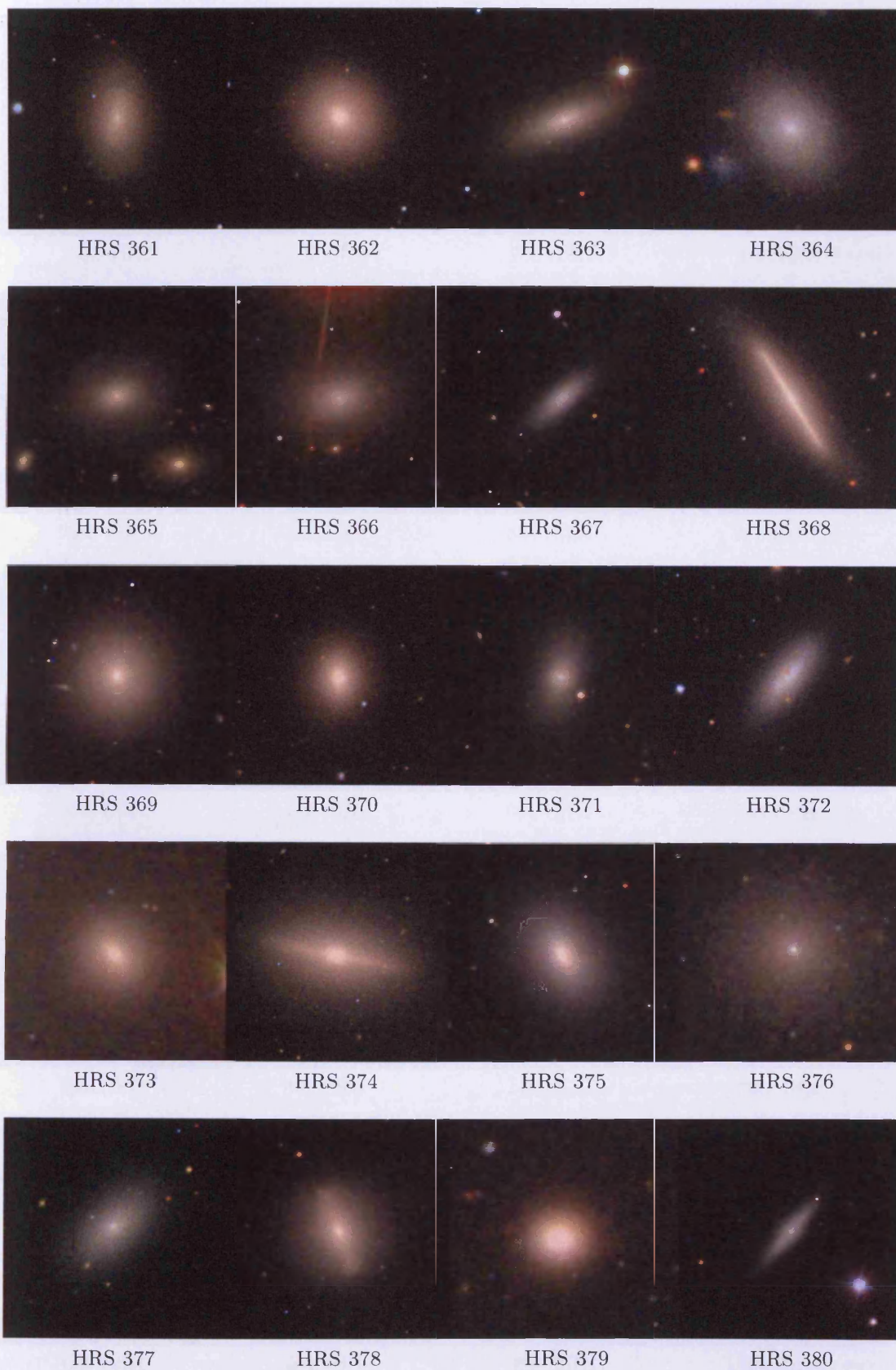


Figure A.1: Continued from previous page.

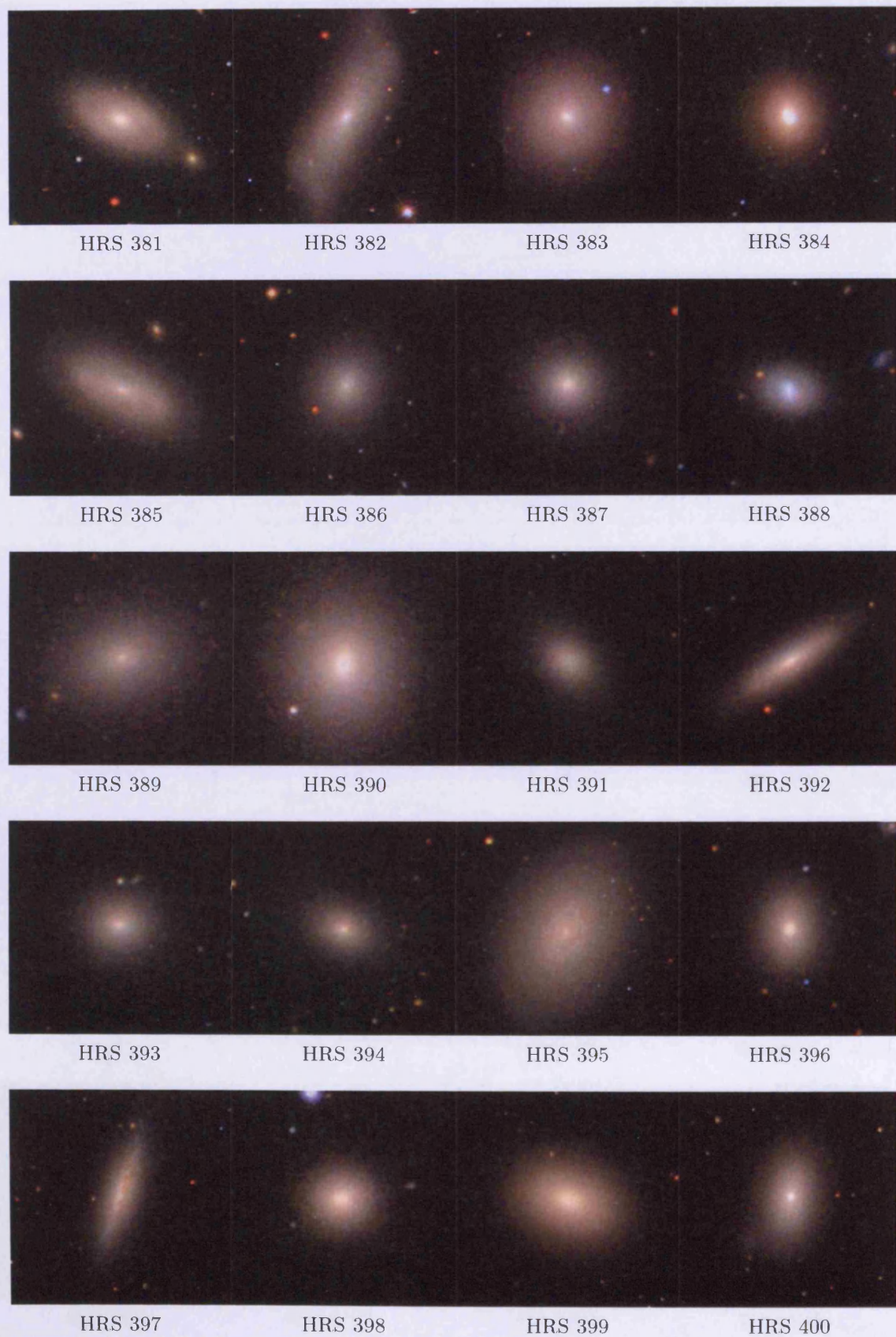


Figure A.1: Continued from previous page.

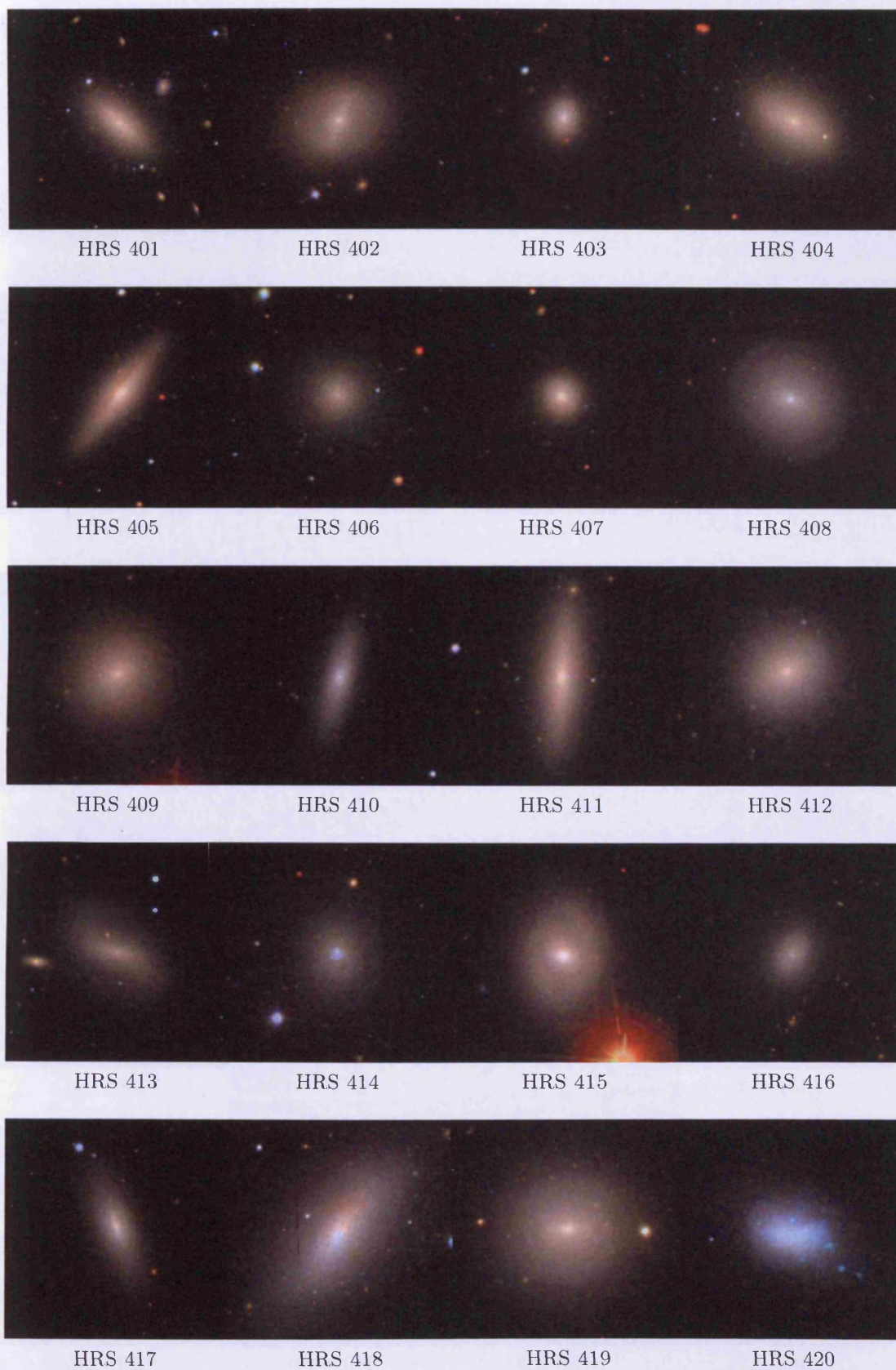


Figure A.1: Continued from previous page.



Figure A.1: Continued from previous page.

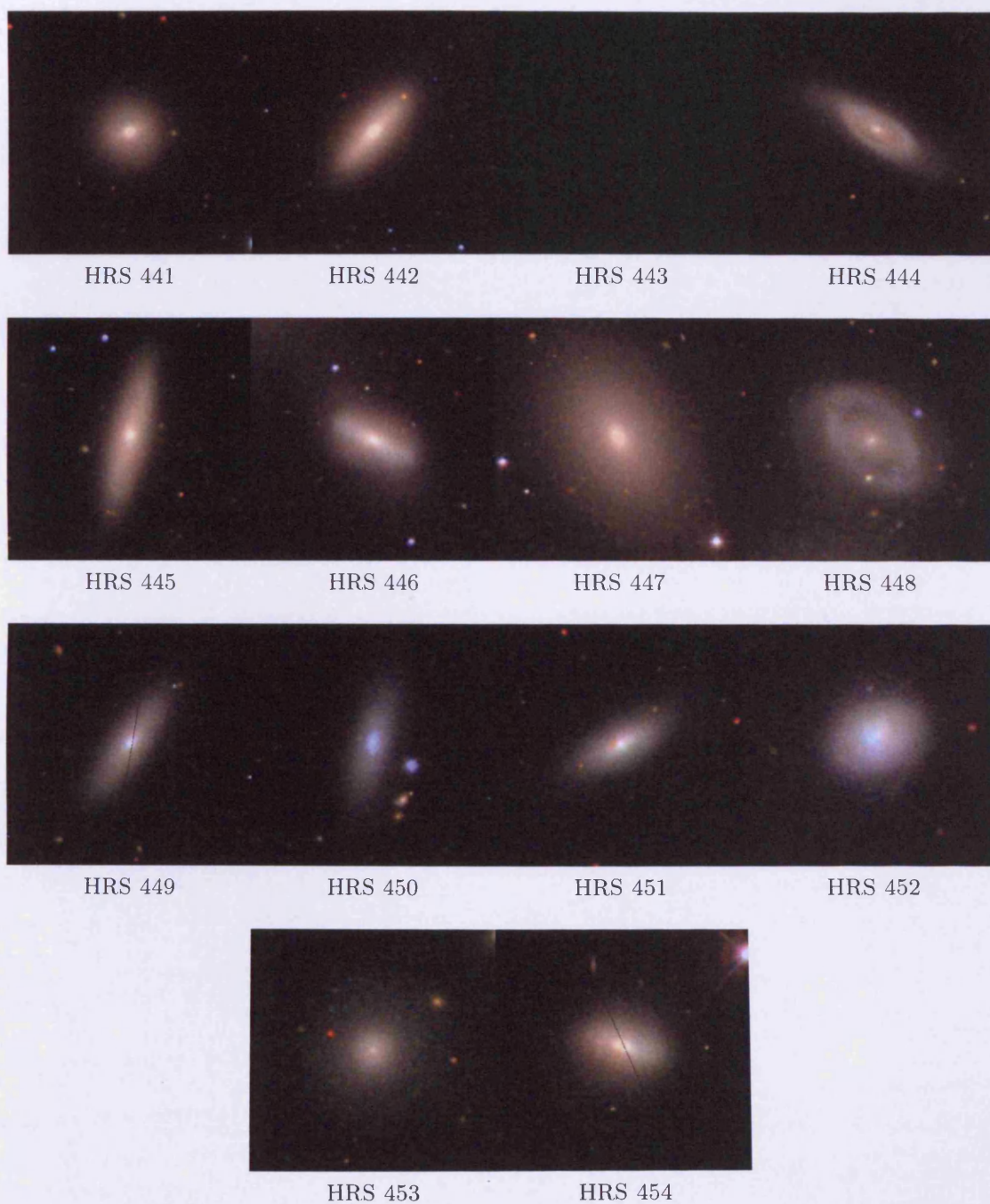


Figure A.1: Continued from previous page.

APPENDIX B: OPTICAL SPECTROSCOPY

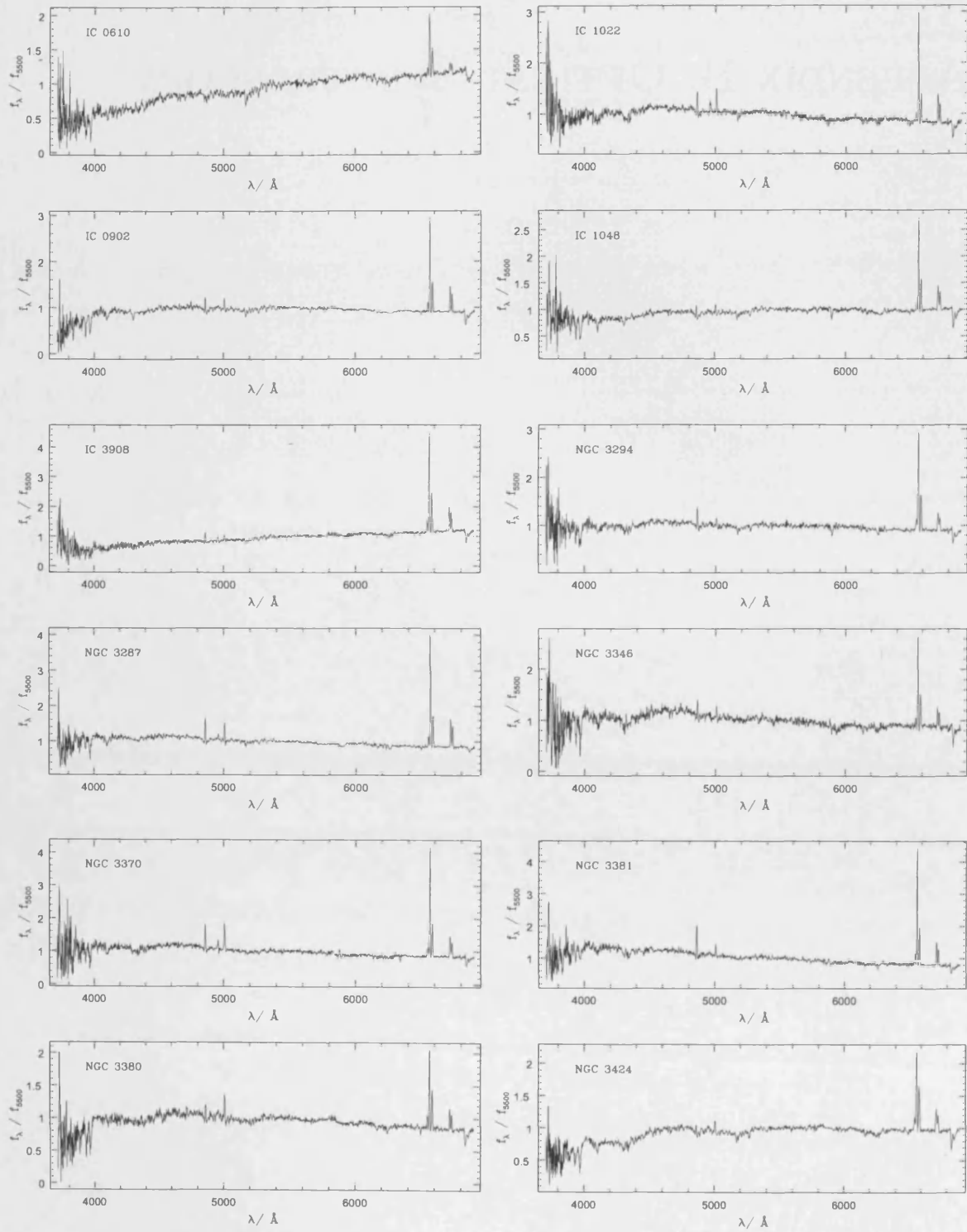


Figure B.1: The reduced and calibrated spectra of the 95 galaxies comprising the B08 observations.

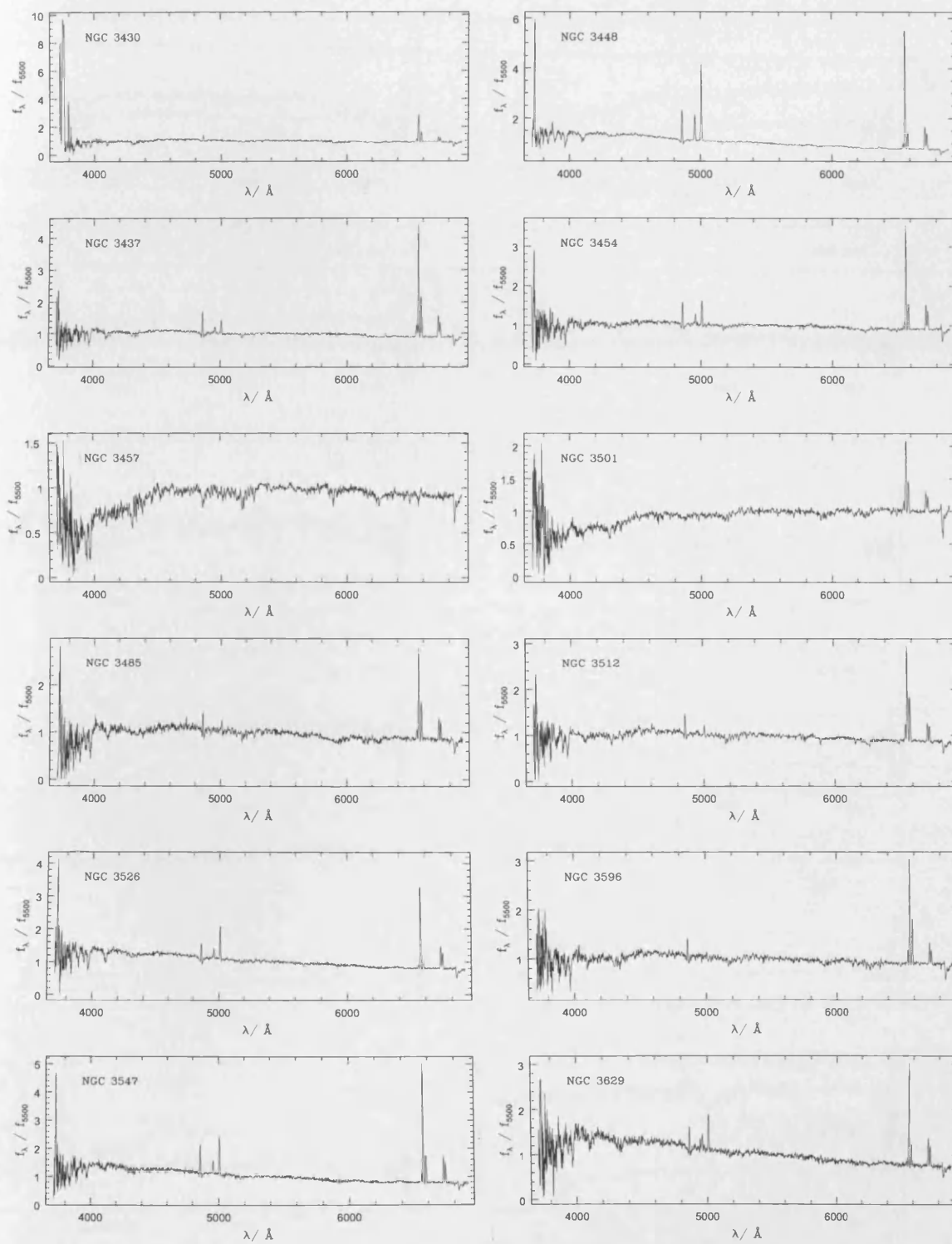


Figure B.1: Continued from previous page.

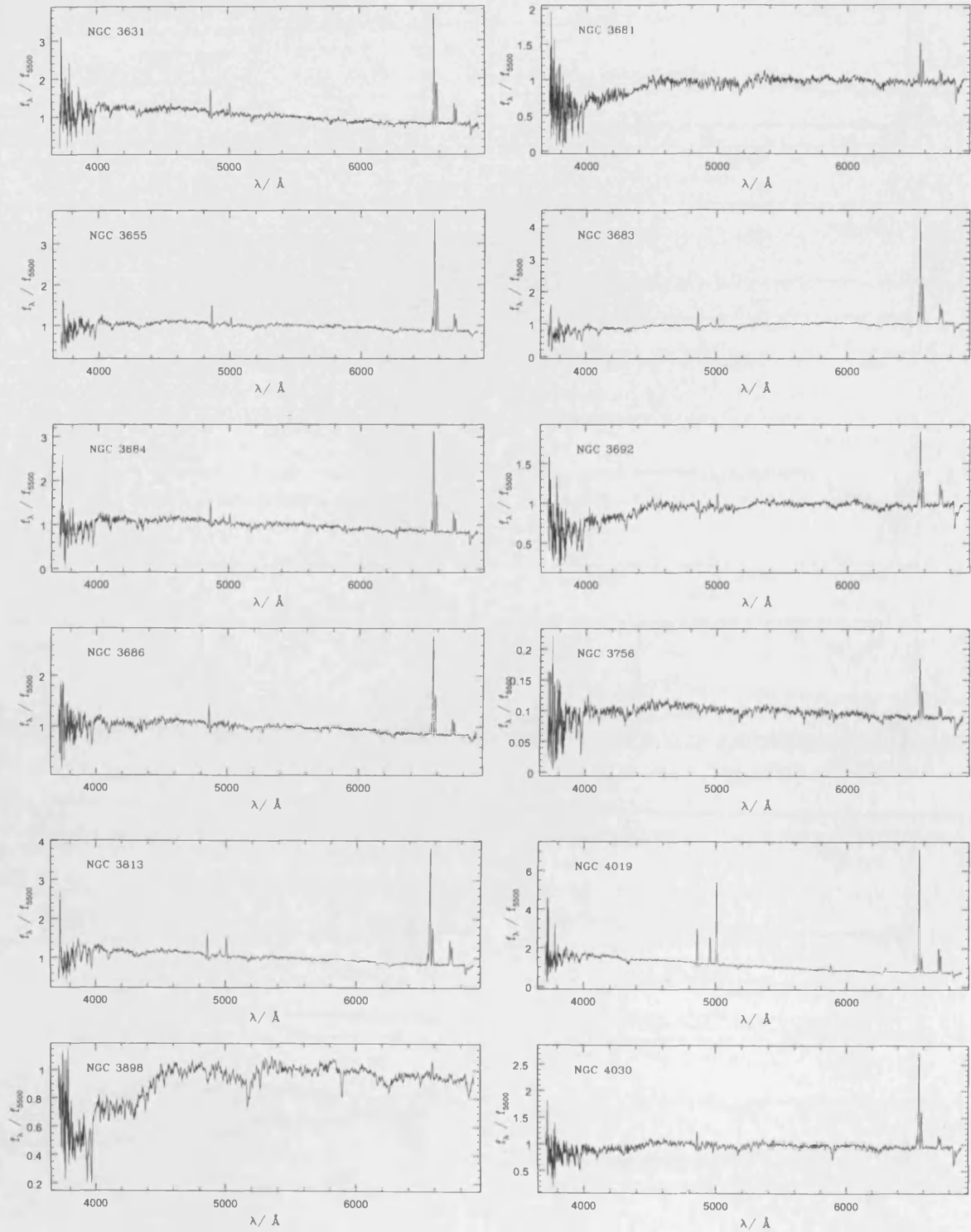


Figure B.1: Continued from previous page.

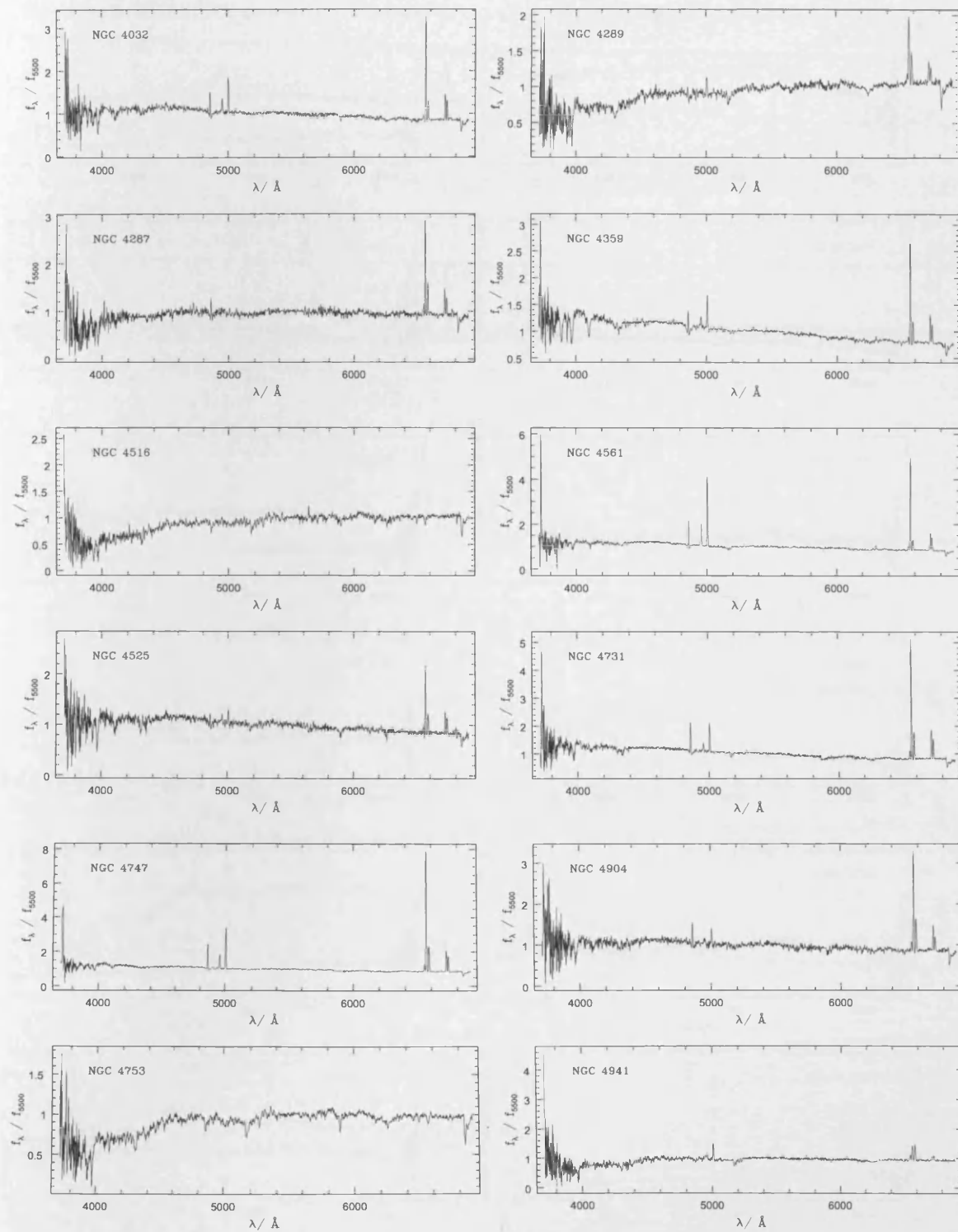


Figure B.1: Continued from previous page.

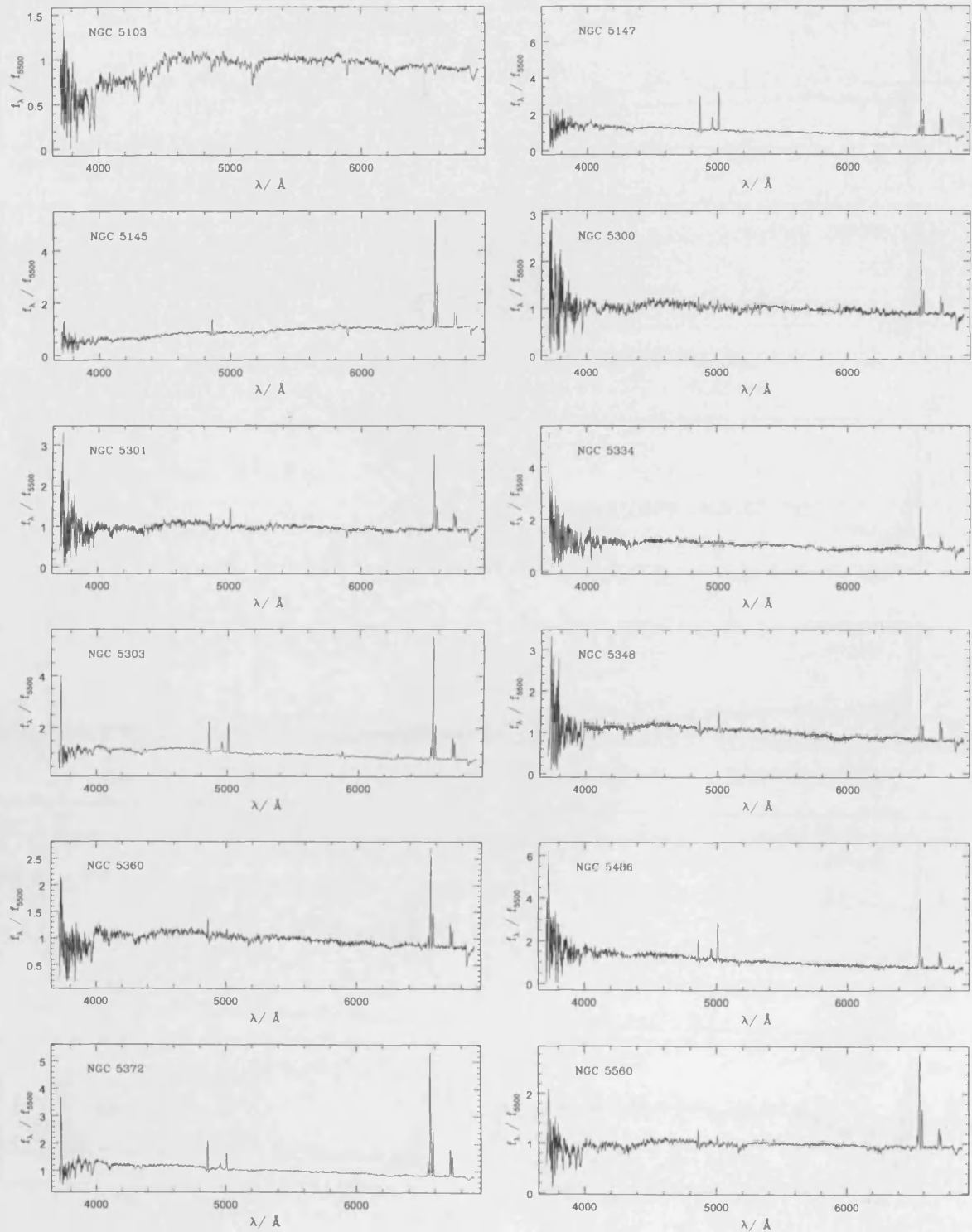


Figure B.1: Continued from previous page.

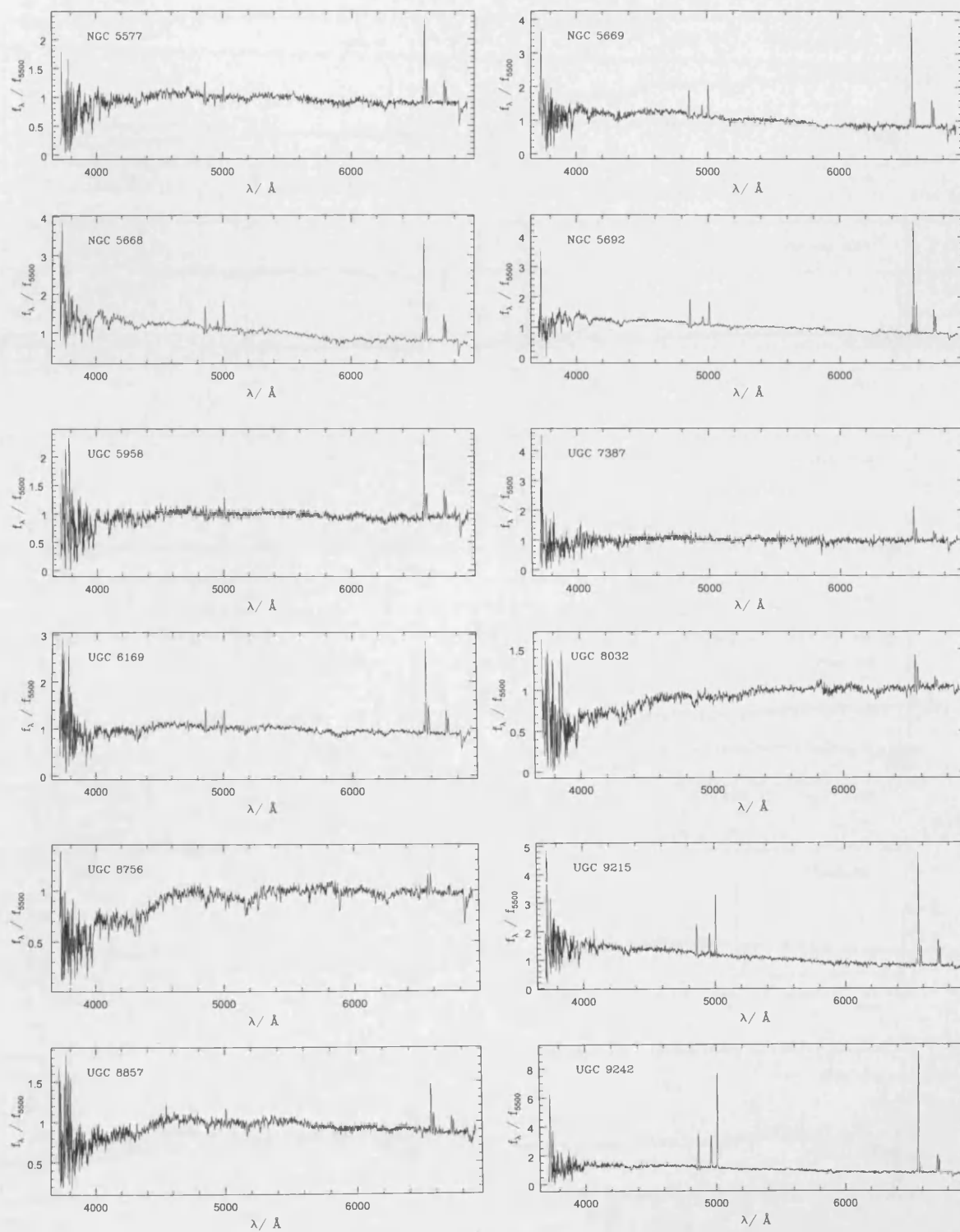


Figure B.1: Continued from previous page.

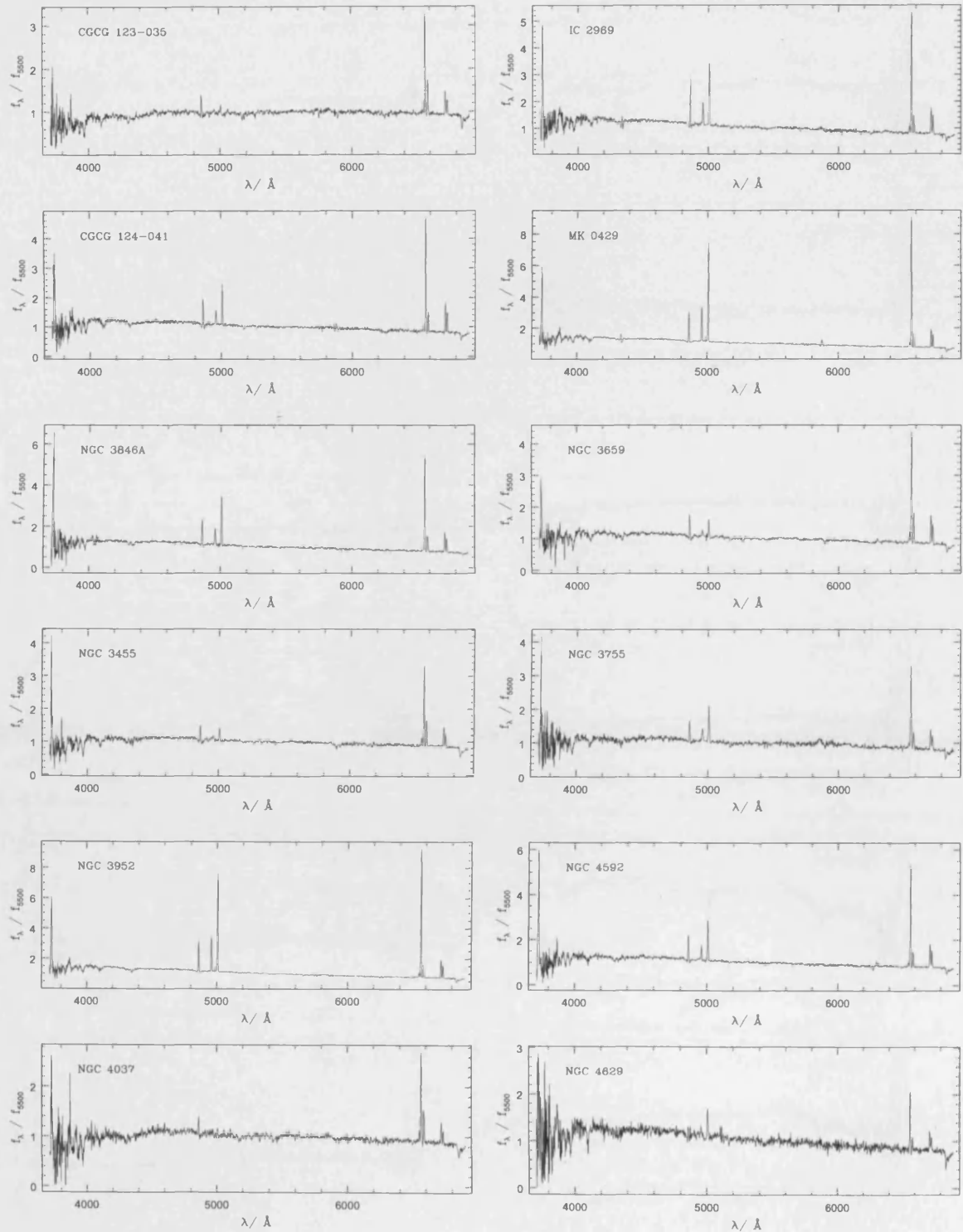


Figure B.1: Continued from previous page.

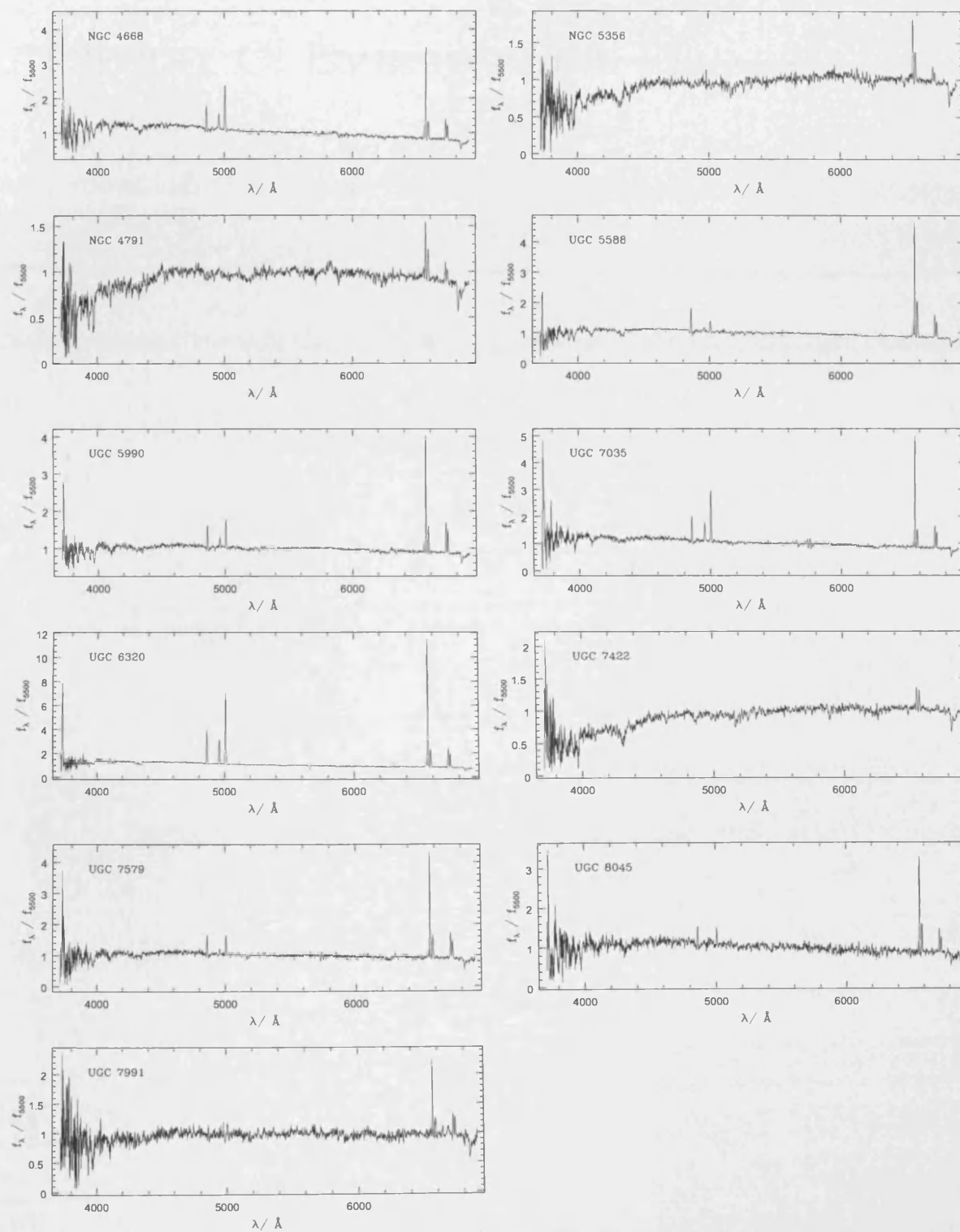


Figure B.1: Continued from previous page.

APPENDIX C: EMISSION LINE FLUXES

Table C.1: Measured C_1 values and corrected emission line intensities, normalised to the $H\alpha$ intensity, from spectra obtained from the B08 observations (see Chapter 4).

Name	R.A. (h m s)	Dec. ($^{\circ}$ ' '')	C_1	[OII] $\lambda 3727$	H δ $\lambda 4101$	H β $\lambda 4861$	[OIII] $\lambda 4958$	[OIII] $\lambda 5007$	[NII] $\lambda 6548$	H α $\lambda 6563$	[NII] $\lambda 6584$	[SII] $\lambda 6717$	[SII] $\lambda 6731$
CGCG 123-035	10 17 39.69	+22 48 36.1	0.94	0.95	-	0.35	-	0.12	0.12	1.00	0.33	0.20	0.13
CGCG 124-041	10 35 42.04	+26 07 33.0	0.31	1.47	-	0.35	0.15	0.43	0.07	1.00	0.18	0.24	0.18
IC 2969	11 52 30.1s	-03 52 15.0	0.26	1.34	-	0.35	0.22	0.62	0.06	1.00	0.15	0.20	0.14
CGCG 186-045	11 46 26.08	+34 51 07.0	0.41	1.20	-	0.35	0.35	1.01	0.05	1.00	0.11	0.13	0.10
NGC 3846A	11 44 14.82	+55 02 05.9	0.11	1.57	-	0.35	0.17	0.56	0.04	1.00	0.15	0.20	0.14
NGC 3455	10 54 31.09	+17 17 05.0	0.63	2.25	-	0.35	0.25	0.24	0.10	1.00	0.31	0.24	0.16
NGC 3659	11 23 45.53	+17 49 07.2	0.57	1.16	-	0.35	0.10	0.23	0.09	1.00	0.27	0.25	0.17
NGC 3755	11 36 33.36	+36 24 37.2	0.46	1.46	-	0.35	0.26	0.56	0.06	1.00	0.19	0.22	0.14
NGC 3952	11 53 40.55	-03 59 45.8	0.41	1.21	-	0.35	0.35	1.01	0.04	1.00	0.10	0.13	0.09
NGC 4037	12 01 23.66	+13 24 03.6	0.80	2.69	-	0.35	-	-	0.11	1.00	0.36	0.21	0.13
NGC 4592	12 39 18.73	-00 31 55.0	0.34	2.09	-	0.35	0.17	0.53	0.05	1.00	0.16	0.23	0.15
NGC 4629	12 42 32.67	-01 21 02.4	0.39	1.50	-	0.35	0.27	0.67	-	1.00	0.16	0.26	0.22
NGC 4668	12 45 31.98	-00 32 08.6	0.46	2.71	-	0.35	0.23	0.66	0.06	1.00	0.18	0.21	0.15
NGC 4791	12 54 43.96	+08 03 10.6	1.36	-	-	0.35	-	-	0.18	1.00	0.57	0.32	0.26
NGC 5356	13 54 58.45	+05 20 01.4	0	0.00	-	0.35	0.67	0.92	-	1.00	0.61	1.09	0.76
UGC 5588	10 20 57.20	+25 21 54.0	0.64	1.36	-	0.35	0.07	0.16	0.11	1.00	0.33	0.20	0.14
UGC 5990	10 52 38.34	+34 28 59.3	0.63	1.56	-	0.35	0.14	0.36	0.08	1.00	0.23	0.25	0.18
UGC 6320	11 18 17.25	+18 50 49.5	0.36	1.23	-	0.35	0.26	0.75	0.05	1.00	0.14	0.14	0.10
UGC 7035	12 03 40.14	+02 38 28.3	0.43	1.84	-	0.35	0.22	0.60	0.05	1.00	0.16	0.20	0.15
UGC 7422	12 22 01.30	+05 06 00.0	0	-	-	0.35	-	-	0.22	1.00	0.86	-	-
UGC 7579	12 27 55.40	+05 43 16.0	0.82	2.53	-	0.35	0.09	0.34	0.09	1.00	0.22	0.24	0.16
UGC 7991	12 50 38.95	+01 27 52.2	1.12	-	-	0.35	-	-	-	1.00	0.23	0.27	0.21
UGC 8045	12 55 23.50	+07 54 35.0	0.60	2.08	-	0.35	-	0.21	0.10	1.00	0.30	0.22	0.12
IC 610	10 26 28.44	+20 13 39.8	0	0.00	-	0.35	0.67	0.92	0.11	1.00	0.67	0.72	0.60
IC 902	13 36 01.21	+49 57 39.0	0.94	2.19	-	0.35	-	0.19	0.09	1.00	0.33	0.26	0.19
IC 1022	14 30 01.84	+03 46 22.3	0.45	-	-	0.35	0.17	0.30	0.08	1.00	0.28	0.26	0.18
IC 1048	14 42 58.01	+04 53 22.5	1.42	-	-	0.35	-	0.18	0.10	1.00	0.35	0.24	0.18
IC 3908	12 56 40.28	-07 33 27.1	1.62	-	-	0.35	0.15	0.18	0.12	1.00	0.39	0.22	0.17
NGC 3287	10 34 47.30	+21 38 52.0	0.58	1.13	-	0.35	0.09	0.20	0.09	1.00	0.29	0.24	0.18
NGC 3294	10 36 16.24	+37 19 28.8	1.27	-	-	0.35	-	0.17	0.10	1.00	0.36	0.17	0.12
NGC 3346	10 43 38.91	+14 52 18.6	1.34	-	-	0.35	-	0.25	0.09	1.00	0.37	0.20	0.17
NGC 3370	10 47 04.05	+17 16 25.0	0.33	1.14	-	0.35	0.09	0.28	0.09	1.00	0.29	0.18	0.14
NGC 3380	10 48 12.18	+28 36 06.4	0.72	3.73	-	0.35	0.36	0.46	0.16	1.00	0.50	0.26	0.20
NGC 3381	10 48 24.81	+34 42 41.0	0.30	0.85	-	0.35	0.05	0.12	0.10	1.00	0.33	0.20	0.13
NGC 3424	10 51 46.33	+32 54 02.7	1.53	3.25	-	0.35	-	0.37	0.15	1.00	0.51	0.25	0.18
NGC 3437	10 52 35.70	+22 56 04.0	0.72	0.75	-	0.35	0.10	0.20	0.11	1.00	0.35	0.19	0.14
NGC 3448	10 54 39.00	+54 18 19.0	0.29	1.25	0.31	0.35	0.25	0.73	0.04	1.00	0.14	0.19	0.13
NGC 3454	10 54 29.40	+17 20 38.0	0.19	0.80	-	0.35	0.09	0.25	0.07	1.00	0.25	0.23	0.19
NGC 3485	11 00 02.40	+14 50 29.0	0.40	2.23	-	0.35	-	0.14	0.12	1.00	0.41	0.21	0.17
NGC 3501	11 02 47.26	+17 59 21.6	0	0.00	-	0.35	0.65	0.89	0.11	1.00	0.53	0.96	0.64
NGC 3512	11 04 02.90	+28 02 12.0	0.43	1.34	-	0.35	-	0.13	0.16	1.00	0.49	0.20	0.16

Continued on next page...

Table C.1 - Continued

Name	R.A. (h m s)	Dec. ($^{\circ}$ '")	C_1	[OII] $\lambda 3727$	H δ $\lambda 4101$	H β $\lambda 4861$	[OIII] $\lambda 4958$	[OIII] $\lambda 5007$	[NII] $\lambda 6548$	H α $\lambda 6563$	[NII] $\lambda 6584$	[SII] $\lambda 6717$	[SII] $\lambda 6731$
NGC 3526	11 06 56.80	+07 10 28.0	0.54	1.85	-	0.35	0.21	0.56	0.05	1.00	0.17	0.25	0.19
NGC 3547	11 09 55.94	+10 43 15.0	0.24	1.08	-	0.35	0.13	0.36	0.07	1.00	0.25	0.22	0.17
NGC 3596	11 15 06.20	+14 47 13.2	0.52	-	-	0.35	-	-	0.12	1.00	0.41	0.19	0.13
NGC 3629	11 20 31.80	+26 57 48.1	0.45	1.94	-	0.35	0.18	0.46	0.06	1.00	0.23	0.26	0.18
NGC 3631	11 21 02.87	+53 10 10.4	0.56	1.35	-	0.35	-	0.14	0.12	1.00	0.37	0.18	0.13
NGC 3655	11 22 54.61	+16 35 24.1	0.84	0.97	-	0.35	0.08	0.10	0.11	1.00	0.37	0.14	0.10
NGC 3683	11 27 31.84	+56 52 37.4	0.93	0.88	-	0.35	0.14	0.13	0.13	1.00	0.39	0.18	0.13
NGC 3684	11 27 11.19	+17 01 48.6	0.68	0.92	-	0.35	0.10	0.13	0.11	1.00	0.39	0.18	0.14
NGC 3686	11 27 43.97	+17 13 27.0	0.45	-	-	0.35	-	-	0.11	1.00	0.40	0.17	0.12
NGC 3692	11 28 24.01	+09 24 27.4	0.86	-	-	0.35	-	0.25	0.15	1.00	0.46	0.27	0.20
NGC 3756	11 36 48.01	+54 17 36.8	0	0.00	-	0.35	0.76	1.12	0.12	1.00	0.67	0.98	0.84
NGC 3813	11 41 18.65	+36 32 48.5	0.78	1.60	-	0.35	0.13	0.24	0.09	1.00	0.31	0.21	0.15
NGC 3898	11 49 15.10	+56 05 05.0	0	0.00	-	0.35	0.80	1.21	2.70	1.00	5.49	-	-
NGC 4019	12 01 10.54	+14 06 13.5	0.15	0.33	-	0.35	0.24	0.72	0.04	1.00	0.13	0.18	0.14
NGC 4030	12 00 23.62	-01 06 00.3	1.02	-	-	0.35	-	-	0.11	1.00	0.37	0.12	0.09
NGC 4032	12 00 32.90	+20 04 28.0	0.44	0.47	-	0.35	0.19	0.46	0.06	1.00	0.20	0.25	0.18
NGC 4287	12 20 48.48	+05 38 23.4	0.90	-	-	0.35	-	-	0.13	1.00	0.36	0.25	0.18
NGC 4289	12 21 02.30	+03 43 20.0	0	0.00	-	0.35	0.66	0.00	0.10	1.00	0.60	1.07	0.79
NGC 4359	12 24 11.40	+31 31 18.0	0.78	2.46	-	0.35	0.21	0.53	0.06	1.00	0.22	0.26	0.19
NGC 4525	12 33 51.13	+30 16 38.9	0.47	-	-	0.35	0.17	0.29	0.08	1.00	0.27	0.30	0.25
NGC 4561	12 36 08.30	+19 19 20.0	0.06	0.94	-	0.35	0.27	0.77	0.05	1.00	0.24	0.20	0.15
NGC 4731	12 51 00.86	-06 23 28.4	0.39	1.34	-	0.35	0.09	0.29	0.07	1.00	0.21	0.23	0.16
NGC 4747	12 51 45.95	+25 46 37.4	0.64	1.03	-	0.35	0.18	0.52	0.07	1.00	0.21	0.16	0.12
NGC 4753	12 52 22.00	-01 11 59.0	0	0.13	-	0.35	0.37	0.38	1.00	1.00	0.00	1.14	1.14
NGC 4904	13 00 58.65	-00 01 39.4	0.60	-	-	0.35	0.13	0.22	0.12	1.00	0.33	0.23	0.16
NGC 4941	13 04 12.88	-05 33 06.7	0	0.00	-	0.35	0.00	0.00	0.40	1.00	1.63	0.96	1.20
NGC 5145	13 25 13.91	+43 16 02.1	1.19	-	-	0.35	0.07	0.03	0.12	1.00	0.40	0.13	0.10
NGC 5147	13 26 19.73	+02 06 03.0	0.17	-	-	0.35	0.12	0.35	0.08	1.00	0.22	0.20	0.14
NGC 5300	13 48 16.03	+03 57 03.1	0.58	-	-	0.35	0.21	0.36	0.09	1.00	0.35	0.25	0.20
NGC 5301	13 46 24.67	+46 06 25.4	0.92	3.47	-	0.35	0.16	0.36	0.06	1.00	0.29	0.22	0.16
NGC 5303	13 47 44.99	+38 18 16.6	0.44	1.22	-	0.35	0.12	0.30	0.09	1.00	0.28	0.17	0.12
NGC 5334	13 52 54.45	-01 06 52.6	0.54	-	-	0.35	-	0.30	0.06	1.00	0.36	0.28	0.20
NGC 5348	13 54 11.30	+05 13 39.0	0.73	3.47	-	0.35	0.04	0.42	0.08	1.00	0.21	0.25	0.17
NGC 5360	13 55 38.75	+04 59 06.2	0.73	-	-	0.35	0.08	0.17	0.10	1.00	0.36	0.20	0.15
NGC 5372	13 54 45.99	+58 40 00.7	0.48	0.98	-	0.35	0.15	0.54	0.03	1.00	0.15	0.23	0.15
NGC 5486	14 07 24.96	+55 06 11.0	0	1.46	-	0.35	-	0.14	0.13	1.00	0.40	0.19	0.15
NGC 5560	14 20 04.40	+03 59 33.0	0.77	1.55	-	0.35	-	0.20	0.09	1.00	0.28	0.25	0.20
NGC 5577	14 21 13.20	+03 26 10.0	0.71	-	-	0.35	0.06	0.32	0.07	1.00	0.24	0.25	0.17
NGC 5668	14 33 24.33	+04 27 01.7	0.22	0.75	-	0.35	0.06	0.20	0.09	1.00	0.24	0.24	0.18
NGC 5669	14 32 44.00	+09 53 31.0	0.51	1.58	-	0.35	0.13	0.43	0.03	1.00	0.24	0.24	0.18
NGC 5692	14 38 18.11	+03 24 37.1	0.32	0.98	-	0.35	0.12	0.26	0.09	1.00	0.28	0.21	0.16
UGC 5958	10 51 15.88	+27 50 55.6	1.16	-	-	0.35	0.15	0.28	0.06	1.00	0.29	0.26	0.22
UGC 6169	11 07 03.35	+12 03 36.1	0.70	-	-	0.35	0.15	0.28	0.09	1.00	0.28	0.24	0.17
UGC 7387	12 20 17.34	+04 12 06.0	0	0.00	-	0.35	0.66	0.90	0.13	1.00	0.54	1.03	0.77

Continued on next page...

Table C.1 - Continued

Name	R.A.(h m s)	Dec.($^{\circ}$ ''')	C_1	[OII] $\lambda 3727$	H δ $\lambda 4101$	H β $\lambda 4861$	[OIII] $\lambda 4958$	[OIII] $\lambda 5007$	[NII] $\lambda 6548$	H α $\lambda 6563$	[NII] $\lambda 6584$	[SII] $\lambda 6717$	[SII] $\lambda 6731$
UGC 8032	12 54 44.19	+13 14 14.1	0	0.00	-	0.35	0.70	0.99	-	1.00	0.97	1.27	1.27
UGC 8756	13 50 35.88	+42 32 29.5	0	0.00	-	0.35	0.74	1.09	0.30	1.00	1.79	3.07	2.39
UGC 8857	13 56 26.61	+04 23 48.0	1.04	-	-	0.35	-	0.58	-	1.00	0.31	0.34	0.26
UGC 9215	14 23 27.11	+01 43 34.6	0.25	1.64	-	0.35	0.20	0.64	0.06	1.00	0.19	0.23	0.16
UGC 9242	14 25 21.02	+39 32 22.4	0.08	0.94	-	0.35	0.27	0.83	-	1.00	0.10	0.16	0.11

APPENDIX D: RADIAL PROFILES

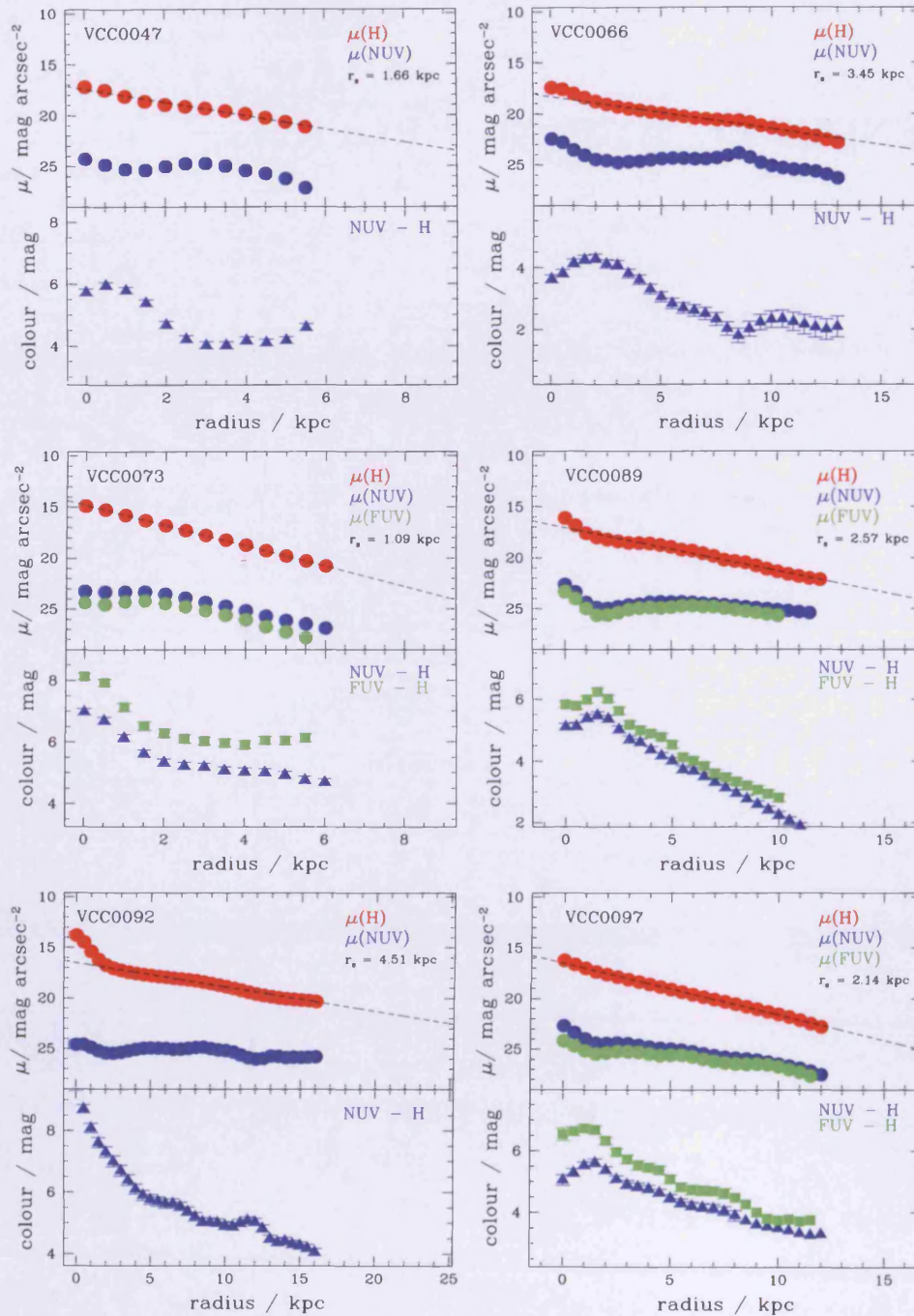


Figure D.1: Each diagram shows the surface photometry for a galaxy. *Upper panels:* The surface brightness profiles obtained using NUV, FUV and H band photometry (filled circles). The disk scale length r_s is based on the least squares fit to the profile (black dashed line). *Lower panels:* The radial UV-H colour profiles based on the observed surface brightness profiles.

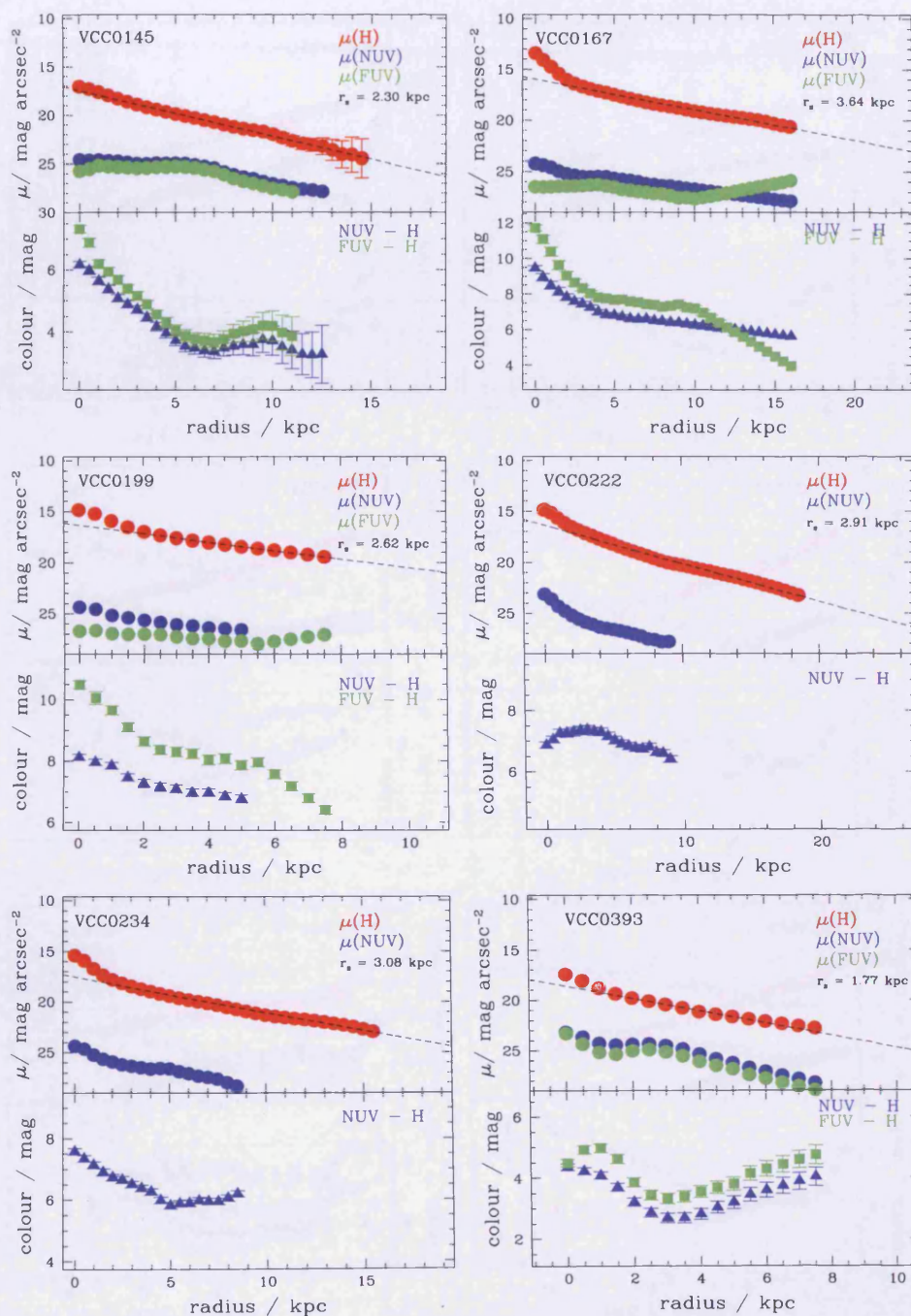


Figure D.1: Continued from previous page.

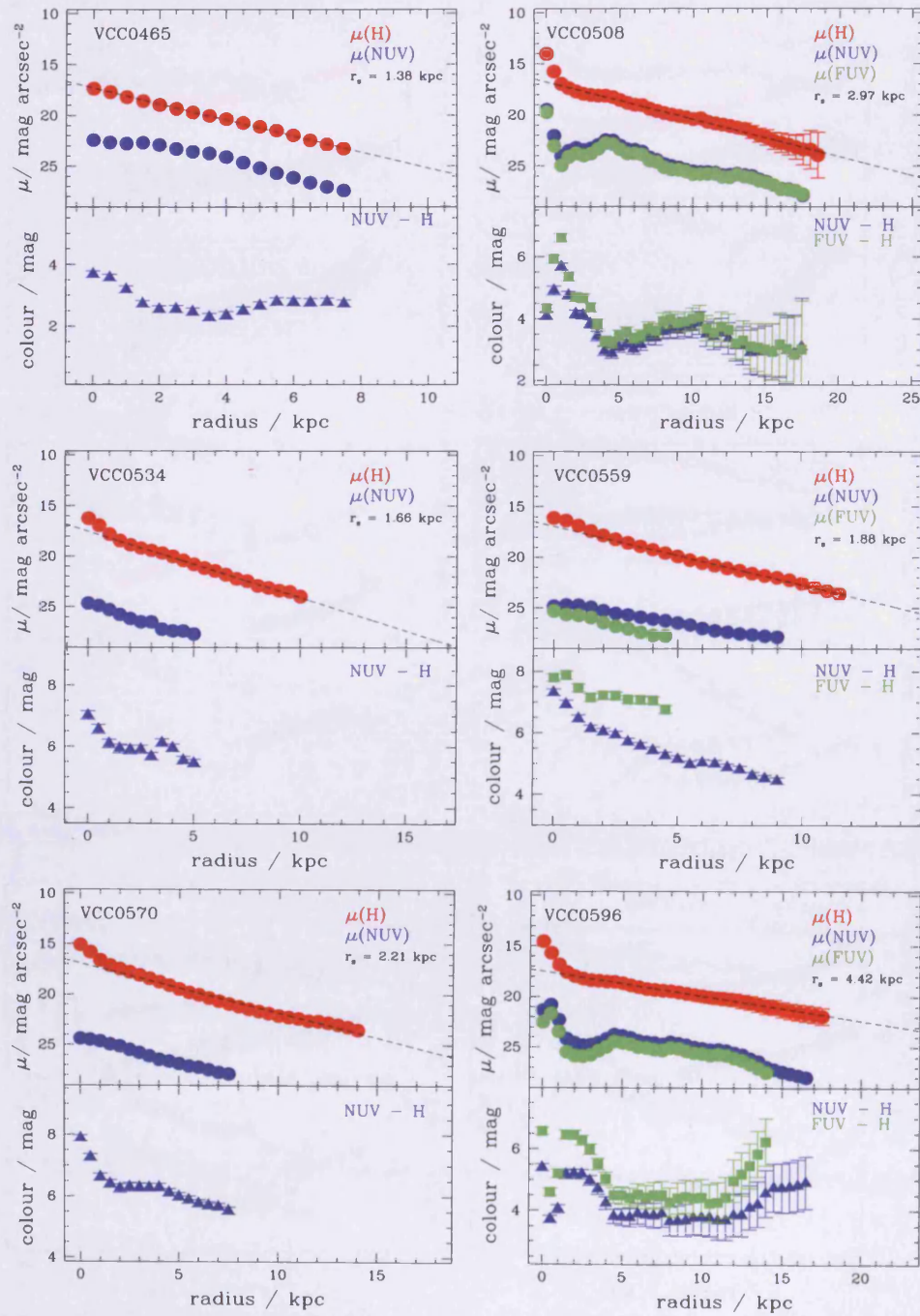


Figure D.1: Continued from previous page.

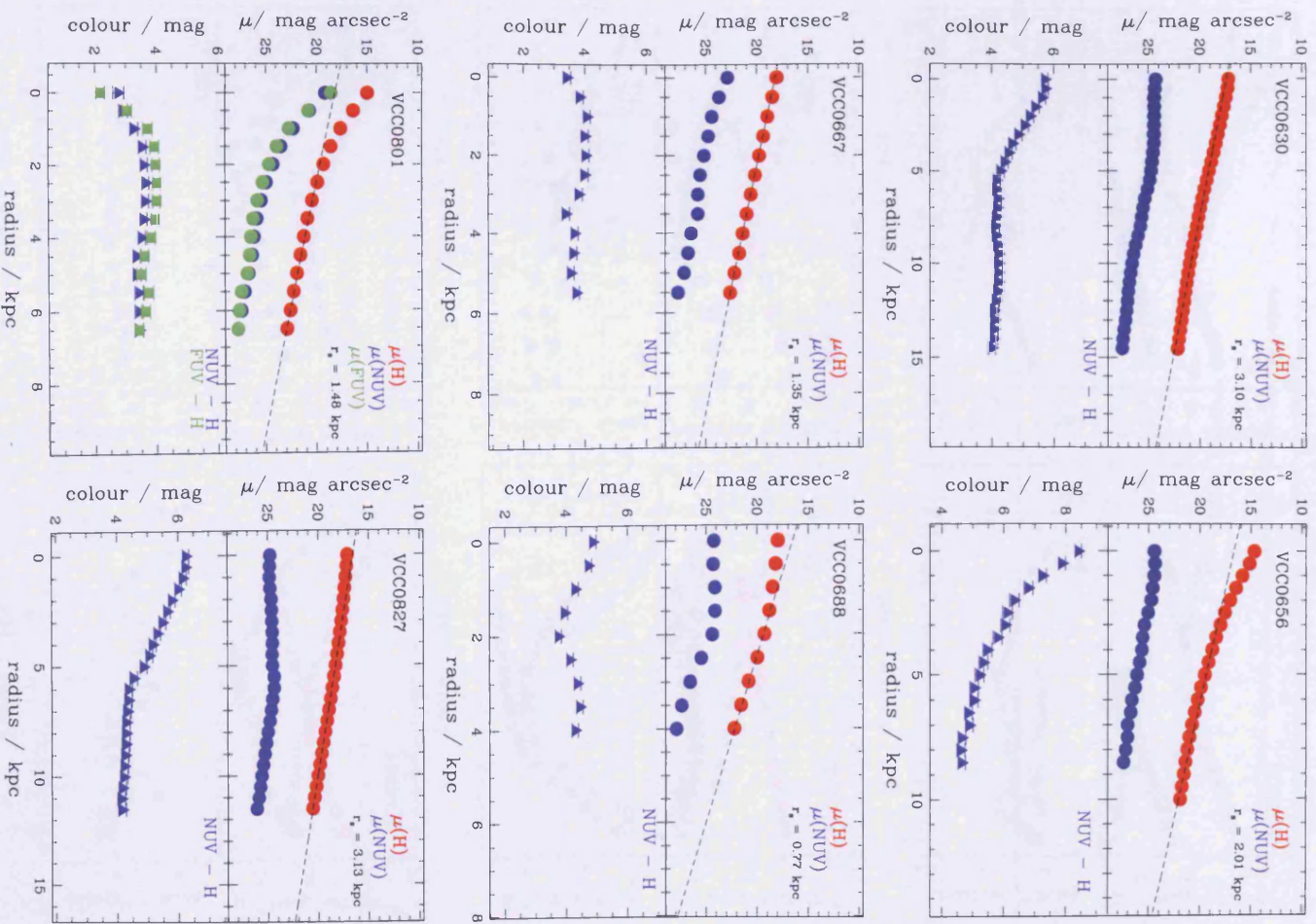


Figure D.1: Continued from previous page.

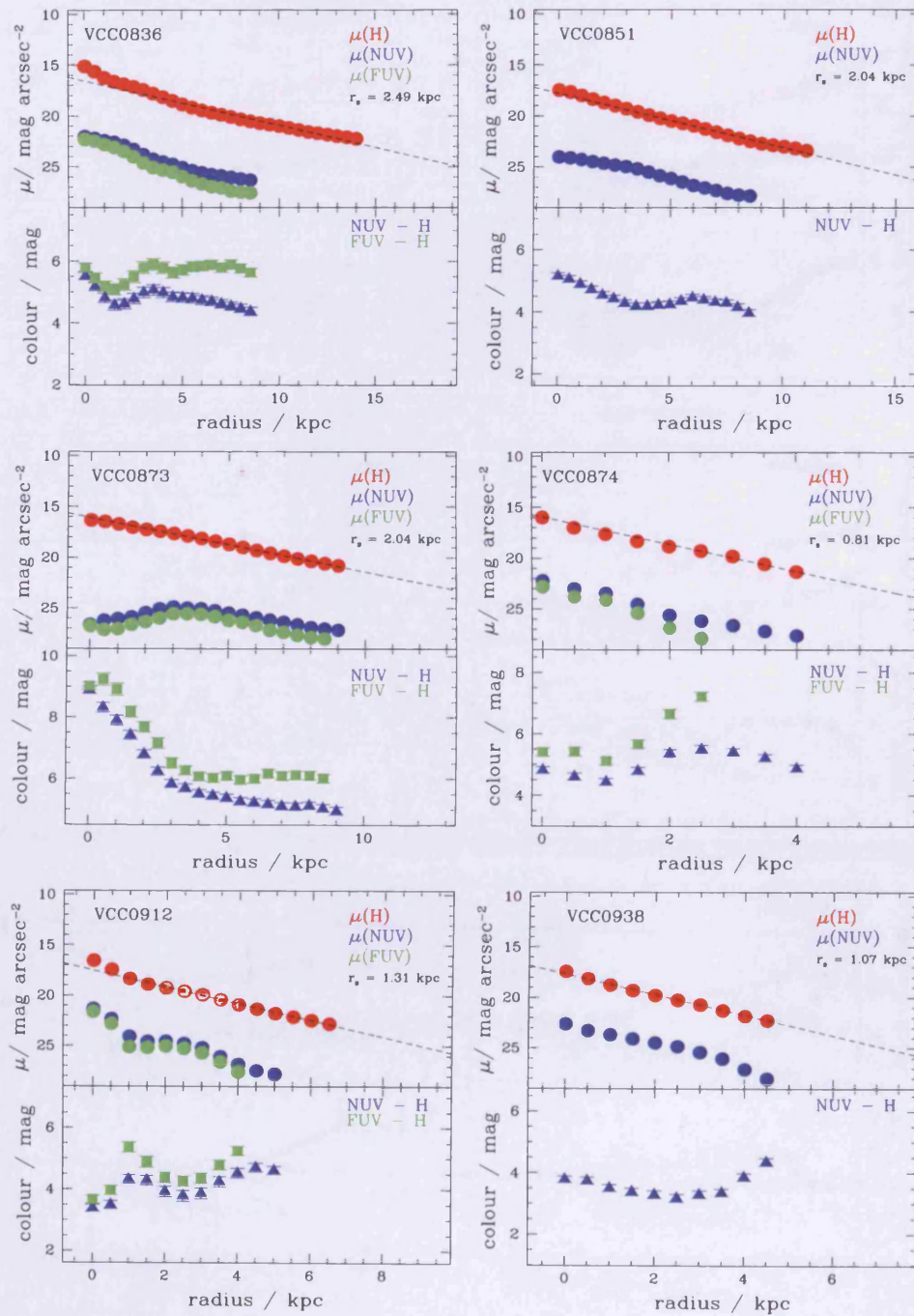


Figure D.1: Continued from previous page.

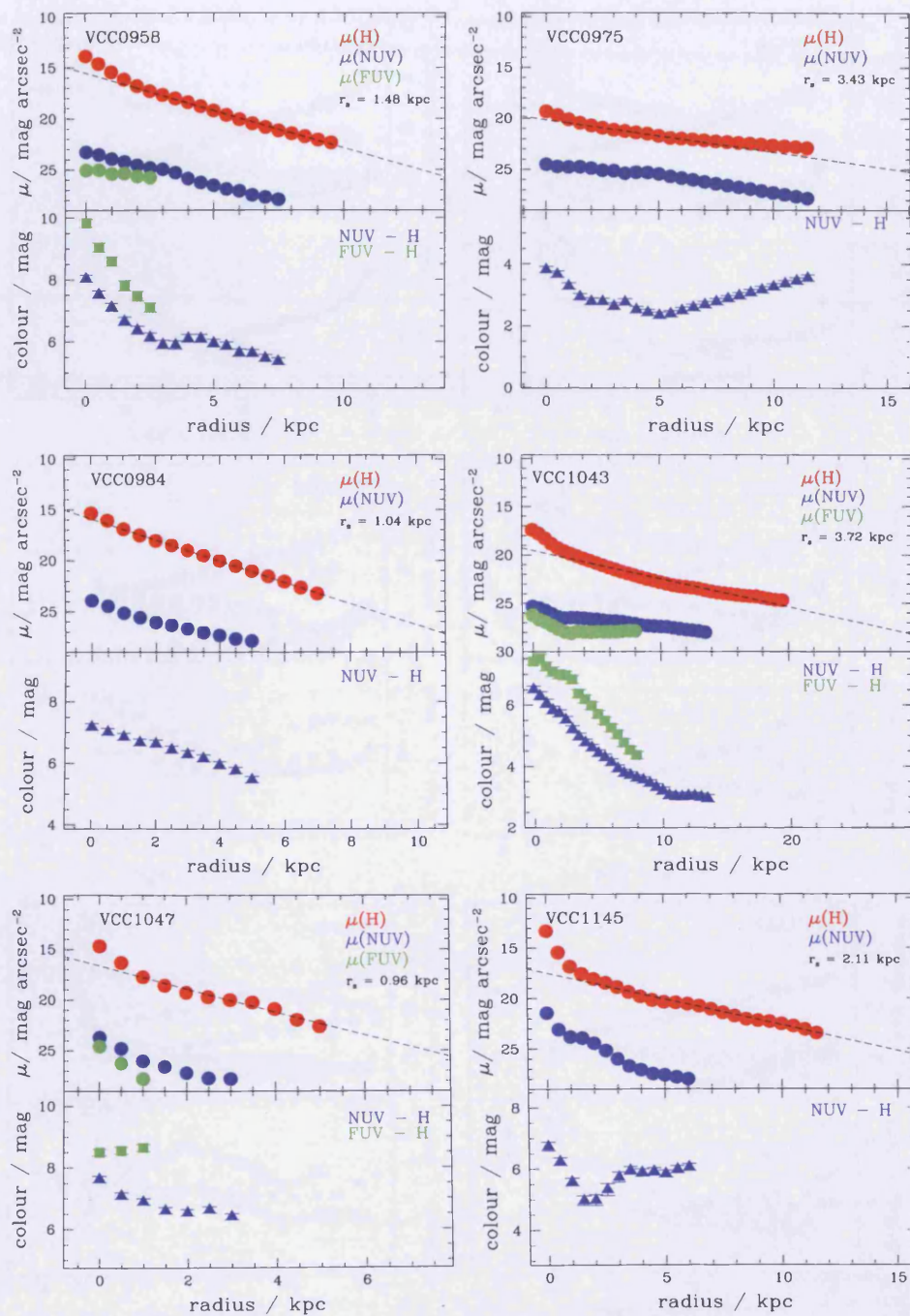


Figure D.1: Continued from previous page.

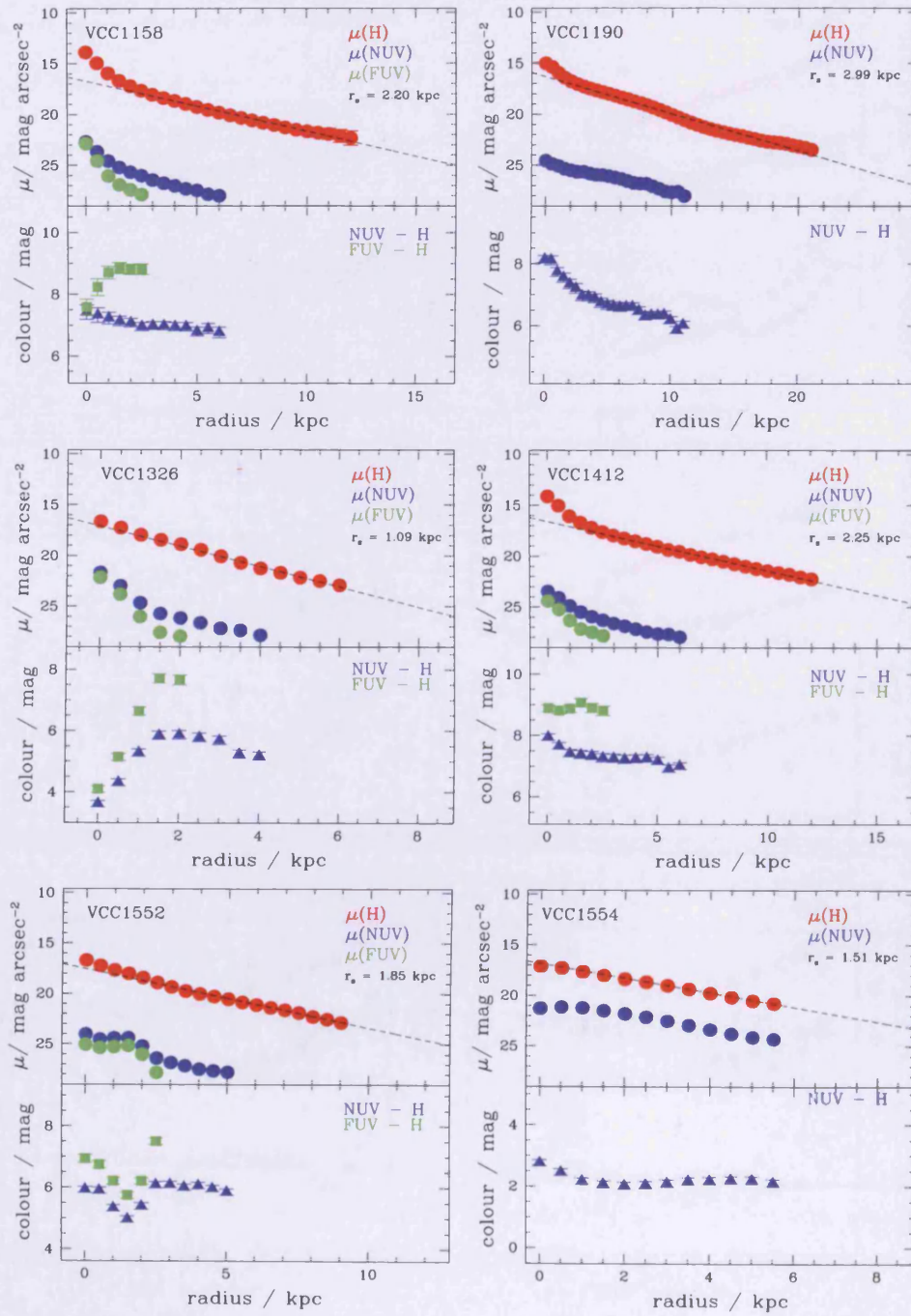


Figure D.1: Continued from previous page.

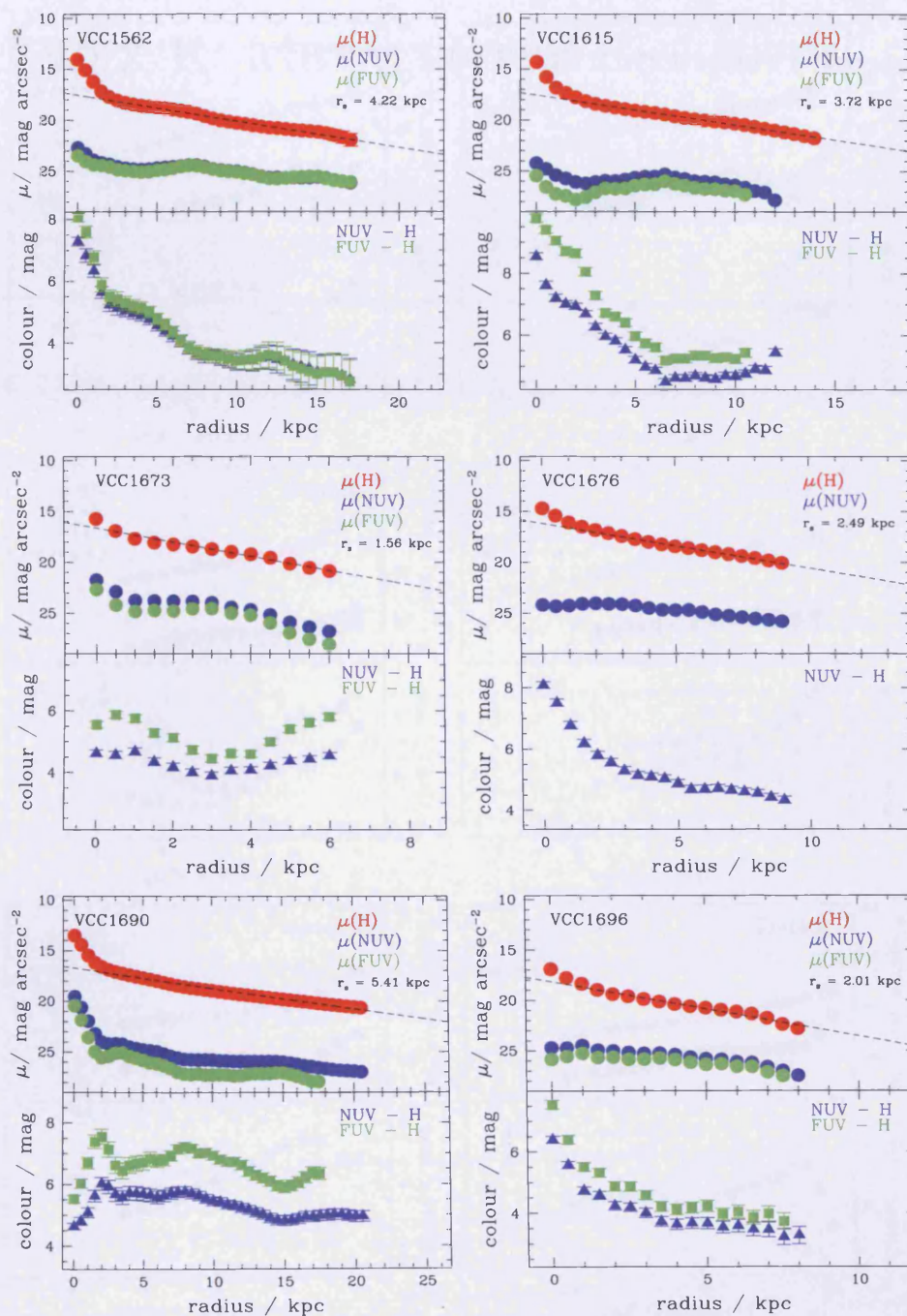


Figure D.1: Continued from previous page.

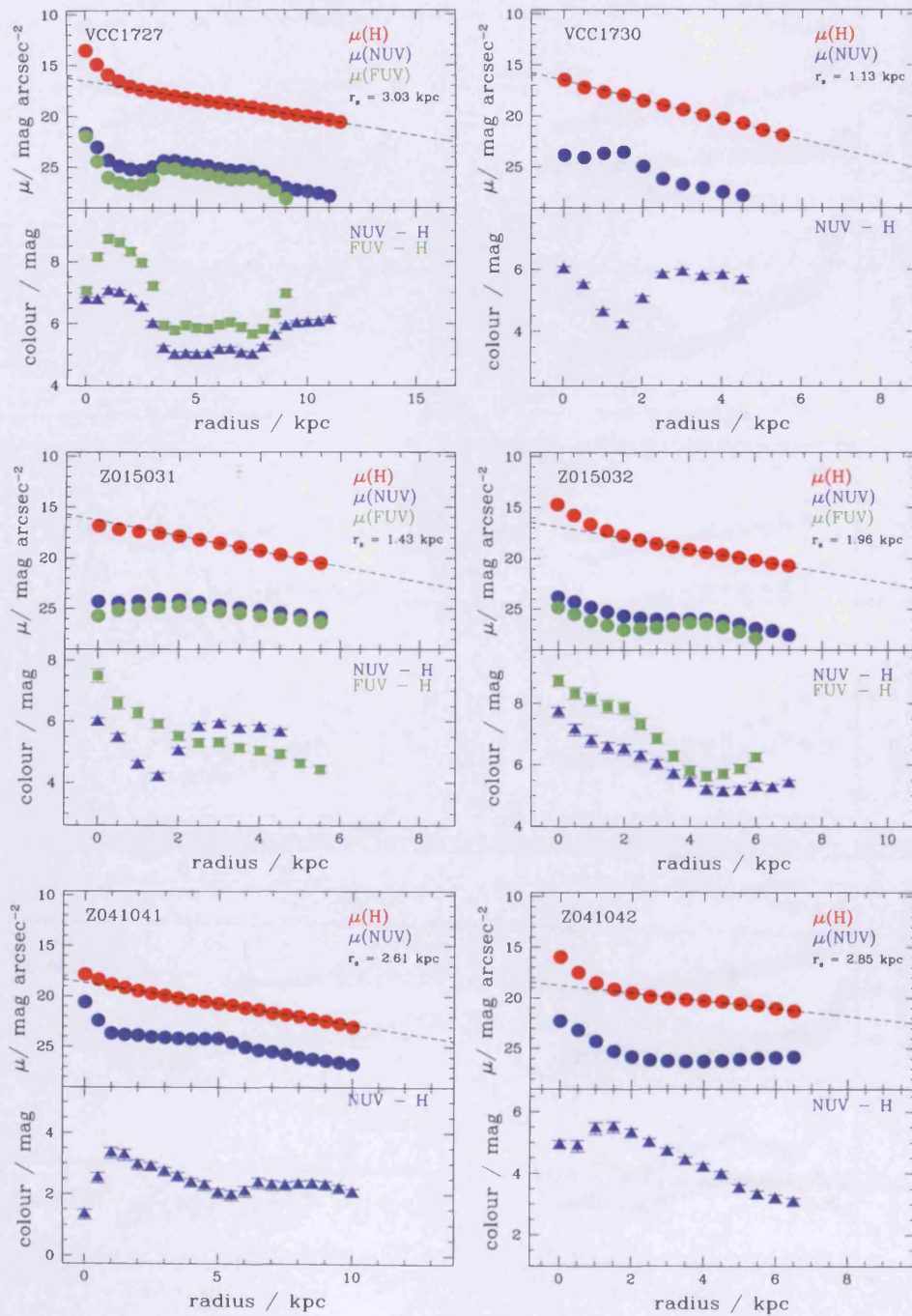


Figure D.1: Continued from previous page.

APPENDIX E: METALLICITY ESTIMATES

E.1 MEASURED OXYGEN ABUNDANCES

Table E.1: Oxygen abundances in units of $12 + \log(\text{O}/\text{H})$ based on different line ratio calibration methods (see Section 8.5).

Galaxy	R.A.(h m s)	Dec.($^{\circ}$ ' ")	C1	OII	M91	Z94	D02	O3N2	N2	P05
CGCG 522-038	01 52 45.75	+36 37 07.9	0.75	<	-	-	8.86	-	8.80	-
CGCG 522-041	01 52 53.79	+36 03 12.1	0.65	<	-	-	8.76	8.70	8.64	-
CGCG 522-058	01 54 53.93	+36 55 05.2	0.72	<	-	-	8.93	8.82	-	-
CGCG 522-060	01 54 57.88	+35 25 11.5	0.58	<	-	-	8.83	-	8.75	-
CGCG 522-062	01 55 01.80	+06 55 12.7	0.34	<	-	-	8.79	8.85	8.68	-
CGCG 522-065	01 55 14.06	+35 27 27.1	9.99	<	-	-	-	-	-	-
CGCG 522-072	01 56 21.39	+35 34 21.5	0.88	<	-	-	8.71	8.66	8.57	-
CGCG 522-079	01 56 40.05	+35 35 29.7	0.76	<	-	-	8.80	-	8.70	-
CGCG 119-016	08 14 14.07	+21 21 18.3	0.00	<	-	-	8.94	-	-	-
CGCG 119-024	08 16 33.89	+21 24 34.8	9.99	<	-	-	-	-	-	-
CGCG 119-027	08 16 57.57	+20 30 44.3	>1.40	.	-	-	8.82	-	8.72	-
CGCG 119-028	08 17 25.46	+21 09 48.6	0.58	<	-	-	8.27	8.20	8.21	-
CGCG 119-029	08 17 25.84	+21 41 07.6	0.62	.	-	-	8.82	8.73	8.72	-
CGCG 119-031	08 17 34.96	+20 54 10.0	9.99	<	-	-	-	-	-	-
CGCG 119-034	08 17 52.37	+21 06 37.0	0.67	.	-	-	8.83	8.76	8.75	-
CGCG 119-035	08 17 56.85	+22 26 09.8	0.40	<	-	-	8.57	8.38	8.42	-
CGCG 119-040	08 18 25.78	+20 47 15.0	>0.13	.	-	-	9.03	-	-	-
CGCG 119-041	08 18 29.45	+20 45 40.8	1.15	<	-	-	8.88	8.96	8.82	-
CGCG 119-043	08 18 49.13	+21 13 05.6	0.90	<	-	-	8.72	8.62	8.59	-
CGCG 119-044	08 18 50.23	+22 06 56.5	1.07	<	-	-	8.35	8.23	8.25	-
CGCG 119-046	08 19 01.88	+21 11 07.8	0.72	.	-	-	8.82	8.63	8.74	-
CGCG 119-047	08 19 05.05	+21 47 27.6	0.56	<	-	-	8.78	8.70	8.67	-
CGCG 119-048	08 19 10.65	+21 26 07.3	9.99	<	-	-	-	-	-	-
CGCG 119-050	08 19 12.83	+20 30 37.1	0.00	.	-	-	-	-	-	-
CGCG 119-051	08 19 13.00	+20 45 25.1	0.10	<	-	-	8.63	8.49	8.48	-
CGCG 119-053	08 19 19.82	+21 03 31.7	0.04	<	-	-	8.76	8.73	8.64	-
CGCG 119-054	08 19 32.08	+21 23 38.0	1.41	<	-	-	8.84	8.75	8.76	-
CGCG 119-056	08 19 41.39	+22 02 30.5	0.97	<	-	-	8.44	8.32	8.31	-
CGCG 119-057	08 19 48.27	+22 01 53.1	0.00	.	-	-	8.95	-	-	-
CGCG 119-059	08 19 58.89	+21 03 58.4	0.00	.	-	-	8.60	-	8.45	-
CGCG 119-061	08 20 10.78	+21 04 06.7	>1.06	<	-	-	-	-	-	-
CGCG 119-063	08 20 23.54	+21 07 53.9	9.99	<	-	-	-	-	-	-
CGCG 119-065	08 20 35.65	+21 04 04.2	9.99	.	-	-	-	-	-	-
CGCG 119-066	08 20 51.60	+22 39 23.3	0.81	.	8.43	8.50	8.63	8.57	8.48	7.75
CGCG 119-067	08 21 21.08	+20 52 02.5	9.99	.	-	-	-	-	-	-
CGCG 119-068	08 21 21.93	+20 54 39.4	0.51	.	8.92	9.07	8.80	8.66	8.70	8.57
CGCG 119-071	08 22 01.46	+21 20 32.1	>1.43	<	-	-	8.89	-	8.85	-
CGCG 119-074	08 22 43.46	+22 33 11.6	9.99	<	-	-	-	-	-	-
CGCG 119-078	08 23 11.37	+22 39 54.8	9.99	.	-	-	-	-	-	-
CGCG 119-081	08 23 41.35	+21 26 05.1	9.99	.	-	-	-	-	-	-
CGCG 119-082	08 23 55.24	+20 58 31.3	9.99	.	-	-	-	-	-	-
CGCG 119-083	08 24 01.59	+21 01 38.9	>1.64	.	-	-	8.93	-	-	-
CGCG 119-085	08 24 20.23	+20 31 57.8	0.00	<	-	-	8.94	-	-	-
CGCG 119-091	08 25 12.06	+20 20 04.7	9.99	<	-	-	-	-	-	-
CGCG 119-109	08 27 41.93	+21 28 46.9	>1.84	.	-	-	8.89	-	8.85	-
CGCG 123-035	10 17 39.69	+22 48 36.1	0.94	.	-	-	8.76	8.72	8.64	-
UGC 5588	10 20 57.20	+25 21 54.0	0.64	.	8.70	8.83	8.76	8.68	8.64	8.03
IC 610	10 26 28.44	+20 13 39.8	9.99	.	-	-	8.99	-	-	-
NGC 3287	10 34 47.30	+21 38 52.0	0.58	.	8.77	8.89	8.72	8.63	8.59	8.18
CGCG 124-041	10 35 42.04	+26 07 33.0	0.31	.	8.61	8.68	8.57	8.46	8.42	8.08
NGC 3294	10 36 16.24	+37 19 28.8	1.27	.	-	-	8.79	8.68	8.68	-
NGC 3346	10 43 38.91	+14 52 18.6	1.34	.	-	-	8.80	8.63	8.70	-
NGC 3370	10 47 04.05	+17 16 25.0	0.33	.	8.75	8.86	8.72	8.58	8.59	8.20
NGC 3380	10 48 12.18	+28 36 06.4	0.72	.	7.89	7.84	8.90	8.59	8.86	7.17
NGC 3381	10 48 24.81	+34 42 41.0	0.30	.	8.87	9.03	8.76	8.72	8.64	8.27
UGC 5958	10 51 15.88	+27 50 55.6	1.16	.	-	-	8.72	8.58	8.59	-
NGC 3424	10 51 46.33	+32 54 02.7	1.53	.	-	-	8.90	8.62	-	-
NGC 3437	10 52 35.70	+22 56 04.0	0.72	.	8.88	9.02	8.78	8.66	8.67	8.41
UGC 5990	10 52 38.34	+34 28 59.3	0.63	.	8.60	8.67	8.65	8.52	8.50	8.02
NGC 3454	10 54 29.40	+17 20 38.0	0.19	.	8.85	8.99	8.68	8.58	8.53	8.39
NGC 3455	10 54 31.09	+17 17 05.0	0.63	.	8.39	8.44	8.74	8.61	8.62	7.70
NGC 3448	10 54 39.00	+54 18 19.0	0.29	.	8.60	8.62	8.49	8.35	8.35	8.20
NGC 3485	11 00 02.40	+14 50 29.0	0.40	.	-	-	8.83	8.73	8.75	-
NGC 3501	11 02 47.26	+17 59 21.6	9.99	.	-	-	8.91	-	-	-
NGC 3512	11 04 02.90	+28 02 12.0	0.43	.	-	-	8.89	8.76	8.85	-

Continued on next page...

Table E.1 – Continued

Galaxy	R.A.(h m s)	Dec.($^{\circ}$ '")	C1	OII	M91	Z94	D02	O3N2	N2	P05
NGC 3526	11 06 56.80	+07 10 28.0	0.54	.	8.46	8.48	8.55	8.41	8.40	7.92
UGC 6169	11 07 03.35	+12 03 36.1	0.70	.	-	-	8.71	8.58	8.57	-
NGC 3547	11 09 55.94	+10 43 15.0	0.24	.	8.74	8.84	8.68	8.53	8.53	8.26
NGC 3596	11 15 06.20	+14 47 13.2	0.52	.	-	-	8.83	-	8.75	-
UGC 6320	11 18 17.25	+18 50 49.5	0.36	.	8.60	8.61	8.49	8.35	8.35	8.21
NGC 3629	11 20 31.80	+26 57 48.1	0.45	.	8.46	8.50	8.65	8.48	8.50	7.86
NGC 3631	11 21 02.87	+53 10 10.4	0.56	.	-	-	8.80	8.71	8.70	-
NGC 3655	11 22 54.61	+16 35 24.1	0.84	.	-	-	8.80	8.76	8.70	-
NGC 3659	11 23 45.53	+17 49 07.2	0.57	.	8.75	8.87	8.70	8.60	8.56	8.18
NGC 3684	11 27 11.19	+17 01 48.6	0.68	.	8.84	8.98	8.82	8.73	8.72	8.27
NGC 3683	11 27 31.84	+56 52 37.4	0.93	.	8.85	9.00	8.82	8.72	8.72	8.29
NGC 3686	11 27 43.97	+17 13 27.0	0.45	.	-	-	8.82	-	8.74	-
NGC 3692	11 28 24.01	+09 24 27.4	0.86	.	-	-	8.87	8.66	8.81	-
NGC 3755	11 36 33.36	+36 24 37.2	0.46	.	8.57	8.60	8.59	8.43	8.44	8.10
NGC 3756	11 36 48.01	+54 17 36.8	9.99	.	-	-	8.99	-	-	-
NGC 3813	11 41 18.65	+36 32 48.5	0.78	.	8.61	8.71	8.74	8.61	8.62	7.97
CGCG 097-064	11 42 14.53	+20 05 49.6	9.99	.	-	-	-	-	-	-
CGCG 097-062	11 42 14.64	+19 58 32.5	0.52	.	8.86	8.98	8.73	8.60	8.60	8.48
CGCG 097-063	11 42 15.51	+20 02 54.1	0.00	<	-	-	8.70	-	8.56	-
CGCG 097-068	11 42 24.47	+20 07 06.4	1.41	.	8.67	8.80	8.80	8.69	8.70	7.99
CGCG 097-073	11 42 56.43	+19 57 59.0	0.03	.	8.62	8.67	8.82	8.53	8.74	8.16
CGCG 097-079	11 43 13.35	+20 00 16.4	0.06	.	8.67	8.74	8.51	8.40	8.37	8.24
CGCG 097-087	11 43 48.90	+19 58 08.0	0.38	.	8.59	8.63	8.65	8.46	8.50	8.11
CGCG 097-091	11 43 59.04	+20 04 37.5	0.61	.	-	-	8.95	8.75	-	-
CGCG 097-088	11 43 59.54	+19 46 43.8	9.99	.	-	-	-	-	-	-
CGCG 097-097	11 44 00.80	+20 01 45.0	9.99	.	-	-	-	-	-	-
CGCG 097-093	11 44 01.85	+19 47 03.4	0.12	.	8.73	8.87	8.68	8.65	8.53	8.06
NGC 3846A	11 44 14.82	+55 02 05.9	0.11	.	8.55	8.59	8.51	8.40	8.37	8.05
CGCG 097-114	11 44 47.71	+19 46 23.1	0.77	.	8.83	8.98	8.65	8.67	8.50	8.21
CGCG 097-120	11 44 49.11	+19 47 41.9	1.92	.	-	-	8.96	-	-	-
CGCG 097-122	11 44 52.30	+19 27 16.9	0.96	<	-	-	8.84	8.64	8.76	-
CGCG 097-125	11 44 54.82	+19 46 35.2	0.88	.	7.90	7.82	8.74	8.47	8.62	7.23
CGCG 097-123	11 44 55.82	+19 29 37.6	9.99	.	-	-	-	-	-	-
CGCG 097-129	11 45 03.89	+19 58 22.9	>1.06	.	-	-	8.92	-	-	-
CGCG 097-138	11 45 44.77	+20 01 51.1	0.00	<	-	-	8.57	-	8.42	-
CGCG 127-049	11 45 48.83	+20 37 42.4	0.81	<	-	-	8.79	8.73	8.68	-
CGCG 186-045	11 46 26.08	+34 51 07.0	0.41	.	8.54	8.50	8.42	8.27	8.29	8.20
NGC 3898	11 49 15.10	+56 05 05.0	9.99	.	-	-	-	-	-	-
IC 2969	11 52 30.1s	-03 52 15.0	0.26	.	8.60	8.63	8.51	8.38	8.37	8.16
NGC 3952	11 53 40.55	-03 59 45.8	0.41	.	8.54	8.50	8.39	8.26	8.28	8.20
NGC 4030	12 00 23.62	-01 06 00.3	1.02	.	-	-	8.80	-	8.70	-
NGC 4032	12 00 32.90	+20 04 28.0	0.44	.	8.88	8.99	8.60	8.46	8.45	8.61
NGC 4019	12 01 10.54	+14 06 13.5	0.15	.	8.86	8.94	8.47	8.34	8.33	8.64
NGC 4037	12 01 23.66	+13 24 03.6	0.80	.	-	-	8.79	-	8.68	-
CGCG 013-046	12 02 41.91	+01 58 43.7	>1.26	.	-	-	8.94	-	-	-
UGC 7035	12 03 40.14	+02 38 28.3	0.43	.	8.46	8.47	8.53	8.40	8.39	7.93
CGCG 069-058	12 08 09.15	+10 22 45.1	9.99	.	-	-	-	-	-	-
VCC 1	12 08 20.02	+13 41 00.2	0.67	<	-	-	8.77	8.72	8.66	-
VCC 24	12 10 35.65	+11 45 38.5	0.62	<	-	-	8.47	8.31	8.33	-
VCC 25	12 10 37.33	+16 01 59.5	0.41	<	-	-	8.77	8.66	8.66	-
VCC 47	12 12 11.77	+13 14 47.8	>0.94	.	-	-	8.74	-	8.62	-
VCC 49	12 12 16.46	+13 12 23.9	9.99	.	-	-	-	-	-	-
VCC 58	12 12 32.21	+12 07 25.9	0.00	.	-	-	8.99	-	-	-
VCC 66	12 12 46.27	+10 51 56.0	0.52	<	-	-	8.60	8.45	8.45	-
VCC 73	12 13 02.99	+07 02 19.0	0.79	<	-	-	8.93	8.73	-	-
VCC 87	12 13 40.91	+15 27 13.2	0.08	<	-	-	8.44	8.39	8.31	-
VCC 89	12 13 47.34	+13 25 30.2	0.55	<	-	-	8.81	8.72	8.71	-
VCC 92	12 13 48.24	+14 54 01.2	0.89	<	-	-	8.93	8.77	-	-
VCC 97	12 13 53.65	+13 10 22.2	>1.10	.	-	-	8.78	-	8.67	-
VCC 119	12 14 37.43	+12 48 47.4	0.36	<	-	-	8.35	8.37	8.25	-
VCC 131	12 15 04.41	+14 01 44.5	0.35	<	-	-	8.77	8.68	8.66	-
VCC 134	12 15 05.24	+13 35 41.5	0.44	<	-	-	8.82	8.68	8.72	-
VCC 142	12 15 13.16	+13 11 05.6	0.16	.	8.75	8.87	8.72	8.62	8.59	8.15
VCC 145	12 15 16.77	+13 01 26.6	0.03	<	-	-	8.71	8.61	8.57	-
VCC 152	12 15 30.31	+09 35 08.6	1.14	<	-	-	8.75	8.68	8.63	-
VCC 157	12 15 39.28	+13 54 05.7	0.75	<	-	-	8.81	-	8.71	-
VCC 159	12 15 41.50	+08 17 07.7	>1.48	.	-	-	-	-	-	-
VCC 162	12 15 46.12	+10 41 53.7	0.00	.	-	-	8.31	-	8.23	-
VCC 167	12 15 54.22	+13 08 59.7	>1.40	<	-	-	8.97	-	-	-
VCC 187	12 16 22.77	+13 18 27.9	0.91	.	8.23	8.29	8.69	8.55	8.54	7.49
VCC 220	12 17 06.50	+07 37 23.1	9.99	.	-	-	-	-	-	-
VCC 221	12 17 08.62	+03 40 50.1	0.41	.	8.90	9.06	8.72	8.67	8.59	8.38

Continued on next page...

Table E.1 – Continued

Galaxy	R.A. (h m s)	Dec. (° ' '')	C1	OII	M91	Z94	D02	O3N2	N2	P05
VCC 226	12 17 11.34	+15 19 27.1	>1.89	.	-	-	8.77	-	8.66	-
VCC 228	12 17 16.45	+12 47 42.1	0.15	.	8.74	8.85	8.65	8.55	8.50	8.22
VCC 307	12 18 49.40	+14 24 59.6	0.59	<	-	-	8.78	8.78	8.67	-
VCC 318	12 19 03.40	+08 51 22.7	0.18	<	-	-	8.55	8.40	8.40	-
VCC 324	12 19 09.90	+03 51 20.0	0.39	.	8.59	8.54	8.27	8.19	8.21	8.31
VCC 334	12 19 14.10	+13 52 55.0	0.37	.	8.20	-	8.35	8.28	8.25	8.07
VCC 345	12 19 23.57	+05 49 32.8	9.99	.	-	-	-	-	-	-
VCC 355	12 19 30.70	+14 52 38.0	9.99	.	-	-	-	-	-	-
VCC 358	12 19 35.66	+05 50 47.9	9.99	.	-	-	-	-	-	-
VCC 369	12 19 45.59	+12 47 57.0	9.99	.	-	-	-	-	-	-
VCC 382	12 19 55.90	+05 20 34.0	0.00	.	-	-	-	-	-	-
VCC 386	12 20 03.70	+05 20 28.1	9.99	.	-	-	-	-	-	-
VCC 393	12 20 07.47	+07 41 28.1	>1.93	.	-	-	8.70	-	8.56	-
UGC 7387	12 20 17.34	+04 12 06.0	9.99	.	-	-	8.92	-	-	-
NGC 4287	12 20 48.48	+05 38 23.4	0.90	.	-	-	8.79	-	8.68	-
NGC 4289	12 21 02.30	+03 43 20.0	9.99	.	-	-	8.95	-	-	-
VCC 459	12 21 11.46	+17 38 18.5	0.21	.	8.51	-	8.42	8.27	8.29	8.67
VCC 460	12 21 12.68	+18 22 56.5	9.99	<	-	-	-	-	-	-
VCC 465	12 21 17.82	+11 30 31.5	0.02	.	8.78	8.87	8.53	8.44	8.39	8.40
VCC 483	12 21 32.67	+14 36 22.6	>1.46	<	-	-	8.81	-	8.71	-
VCC 491	12 21 40.20	+11 30 09.7	0.06	.	8.61	8.62	8.47	8.34	8.33	8.21
VCC 497	12 21 42.26	+14 35 51.7	9.99	.	-	-	-	-	-	-
VCC 508	12 21 54.84	+04 28 24.8	0.49	.	8.89	9.03	8.85	8.78	8.77	8.44
UGC 7422	12 22 01.30	+05 06 00.0	0.00	.	-	-	9.07	-	-	-
VCC 522	12 22 03.54	+12 44 27.8	9.99	.	-	-	-	-	-	-
VCC 523	12 22 04.23	+12 47 12.8	9.99	.	-	-	-	-	-	-
VCC 534	12 22 12.35	+07 08 38.9	9.99	.	-	-	-	-	-	-
VCC 538	12 22 14.94	+07 09 51.9	9.99	.	-	-	-	-	-	-
VCC 552	12 22 27.02	+04 34 00.0	0.03	.	8.54	8.52	8.42	8.29	8.29	8.16
VCC 559	12 22 31.29	+15 32 14.0	>2.40	<	-	-	8.87	-	8.81	-
VCC 562	12 22 36.00	+12 09 28.0	0.24	.	8.10	-	8.22	8.18	8.18	8.02
VCC 596	12 22 54.82	+15 49 20.2	>2.15	<	-	-	8.69	-	8.54	-
VCC 630	12 23 17.02	+11 22 07.3	>1.77	<	-	-	8.74	-	8.62	-
VCC 634	12 23 19.89	+15 49 10.3	9.99	.	-	-	-	-	-	-
VCC 636	12 23 21.08	+15 52 04.3	9.99	.	-	-	-	-	-	-
VCC 655	12 23 37.45	+17 32 28.5	0.75	.	-	-	8.72	8.80	8.59	-
VCC 656	12 23 38.81	+06 57 14.5	>2.04	<	-	-	8.91	-	-	-
VCC 664	12 23 44.36	+12 28 42.5	0.00	.	-	-	8.35	-	8.25	-
VCC 667	12 23 48.48	+07 11 11.5	0.43	.	-	-	8.57	-	8.42	-
VCC 685	12 23 57.82	+16 41 38.6	9.99	.	-	-	-	-	-	-
VCC 688	12 24 00.10	+07 47 05.6	1.89	.	-	-	8.42	-	8.29	-
VCC 692	12 24 01.37	+12 12 16.6	0.17	<	-	-	8.72	8.65	8.59	-
VCC 699	12 24 07.44	+06 36 26.7	0.00	.	-	-	8.63	-	8.48	-
NGC 4359	12 24 11.40	+31 31 18.0	0.78	.	8.28	8.29	8.63	8.46	8.48	7.65
VCC 713	12 24 14.10	+08 32 03.7	>0.84	.	-	-	8.99	-	-	-
VCC 731	12 24 27.84	+07 19 04.8	9.99	.	-	-	-	-	-	-
VCC 758	12 24 54.71	+07 26 38.0	9.99	.	-	-	-	-	-	-
VCC 759	12 24 55.08	+11 42 16.0	9.99	.	-	-	-	-	-	-
VCC 762	12 25 02.80	+07 30 23.1	9.99	.	-	-	-	-	-	-
VCC 781	12 25 14.73	+12 42 53.2	9.99	.	-	-	-	-	-	-
VCC 787	12 25 18.10	+05 44 27.2	0.00	.	-	-	8.63	-	8.48	-
VCC 794	12 25 22.04	+16 25 47.2	9.99	.	-	-	-	-	-	-
VCC 792	12 25 22.07	+10 01 01.2	>1.56	<	-	-	8.95	-	-	-
VCC 798	12 25 24.20	+18 11 23.3	9.99	.	-	-	-	-	-	-
VCC 801	12 25 25.43	+16 28 12.3	0.18	.	8.79	8.90	8.70	8.56	8.56	8.33
VCC 809	12 25 33.17	+12 15 36.3	0.69	<	-	-	8.65	8.53	8.50	-
VCC 828	12 25 41.69	+12 48 41.4	9.99	.	-	-	-	-	-	-
CGCG 014-034	12 25 42.64	+00 34 20.4	0.52	.	8.91	9.06	8.60	8.60	8.45	8.43
VCC 827	12 25 42.71	+07 12 55.4	0.38	.	8.44	8.45	8.60	8.42	8.45	7.92
VCC 836	12 25 46.60	+12 39 40.4	0.55	.	8.09	7.86	8.87	8.39	8.81	7.74
VCC 841	12 25 47.40	+14 57 12.0	0.61	.	8.71	8.77	8.44	8.37	8.31	8.31
VCC 849	12 25 50.59	+10 27 32.5	0.46	.	8.40	8.43	8.65	8.52	8.50	7.80
VCC 848	12 25 52.60	+05 48 36.0	0.00	.	-	-	8.53	-	8.39	-
VCC 851	12 25 54.16	+07 33 13.5	0.75	<	-	-	8.69	8.56	8.54	-
VCC 857	12 25 55.64	+18 12 49.5	9.99	.	-	-	-	-	-	-
VCC 865	12 25 59.19	+15 40 12.5	0.54	.	8.46	8.45	8.60	8.50	8.45	7.98
VCC 874	12 26 07.11	+16 10 51.6	1.80	<	-	-	8.85	-	8.77	-
VCC 873	12 26 07.32	+13 06 43.6	1.48	<	-	-	8.82	-	8.74	-
VCC 905	12 26 29.16	+08 52 16.8	0.25	.	7.93	7.91	8.75	8.60	8.63	7.21
VCC 912	12 26 32.16	+12 36 39.8	0.82	<	-	-	8.79	-	8.68	-
VCC 921	12 26 35.80	+03 57 56.8	0.51	.	-	-	8.86	8.76	8.80	-
VCC 938	12 26 46.67	+07 55 07.9	0.49	.	8.75	8.89	8.78	8.78	8.67	8.05

Continued on next page...

Table E.1 – Continued

Galaxy	R.A.(h m s)	Dec.($^{\circ}$ '")	C1	OII	M91	Z94	D02	O3N2	N2	P05
VCC 939	12 26 47.25	+08 53 03.9	0.29	.	8.40	8.45	8.71	8.65	8.57	7.72
VCC 945	12 26 51.06	+13 10 32.9	>1.17	.	-	-	-	-	-	-
VCC 950	12 26 51.38	+11 33 16.9	>0.79	.	-	-	8.60	-	8.45	-
VCC 951	12 26 54.36	+11 40 06.0	9.99	.	-	-	-	-	-	-
VCC 958	12 26 56.30	+15 02 48.0	>0.66	<	-	-	-	-	-	-
VCC 957	12 26 58.58	+02 29 42.0	0.37	.	8.81	8.94	8.70	8.60	8.56	8.31
VCC 973	12 27 08.70	+16 19 33.1	0.77	.	-	-	8.78	8.58	8.67	-
VCC 971	12 27 08.93	+05 52 48.1	0.27	.	8.39	-	8.42	8.32	8.29	8.29
VCC 975	12 27 11.04	+07 15 47.1	>0.31	.	-	-	8.47	-	8.33	-
VCC 980	12 27 11.26	+15 53 50.1	0.32	.	8.34	8.34	8.51	8.38	8.37	7.76
VCC 979	12 27 11.65	+09 25 15.1	0.43	.	-	-	9.04	-	-	-
VCC 984	12 27 13.30	+12 44 05.1	9.99	.	-	-	-	-	-	-
VCC 995	12 27 21.55	+10 51 55.2	0.55	.	8.68	-	8.17	8.13	8.15	9.16
VCC 1003	12 27 26.31	+11 06 29.2	9.99	<	-	-	-	-	-	-
VCC 1002	12 27 26.37	+06 15 44.2	0.92	.	-	-	8.87	-	8.81	-
VCC 1010	12 27 26.65	+12 17 27.2	9.99	.	-	-	-	-	-	-
VCC 1018	12 27 32.87	+06 13 54.3	0.00	.	-	-	8.92	-	-	-
VCC 1028	12 27 38.33	+14 27 24.3	9.99	.	-	-	-	-	-	-
VCC 1030	12 27 40.42	+13 04 44.3	9.99	.	-	-	-	-	-	-
VCC 1036	12 27 42.23	+12 18 54.4	9.99	.	-	-	-	-	-	-
VCC 1043	12 27 45.52	+13 00 31.4	>0.35	<	-	-	-	-	-	-
VCC 1047	12 27 53.52	+12 17 35.5	9.99	.	-	-	-	-	-	-
UGC 7579	12 27 55.40	+05 43 16.0	0.82	.	8.31	8.37	8.63	8.52	8.48	7.57
VCC 1062	12 28 03.66	+09 48 17.5	9.99	.	-	-	-	-	-	-
VCC 1068	12 28 06.23	+12 04 42.6	9.99	.	-	-	-	-	-	-
VCC 1073	12 28 08.53	+12 05 35.6	9.99	.	-	-	-	-	-	-
VCC 1086	12 28 16.00	+09 26 10.6	>1.10	<	-	-	9.05	-	-	-
VCC 1091	12 28 18.70	+08 43 46.7	0.25	.	8.51	8.49	8.42	8.30	8.29	8.10
VCC 1110	12 28 29.27	+17 05 06.8	9.99	<	-	-	-	-	-	-
VCC 1107	12 28 30.29	+07 19 30.8	9.99	.	-	-	-	-	-	-
VCC 1118	12 28 40.50	+09 15 32.9	0.63	.	-	-	8.77	8.80	8.66	-
VCC 1125	12 28 43.34	+11 45 20.9	9.99	.	-	-	-	-	-	-
VCC 1146	12 28 57.51	+13 14 31.0	9.99	.	-	-	-	-	-	-
VCC 1145	12 28 59.20	+03 34 16.0	>1.20	<	-	-	-	-	-	-
VCC 1154	12 29 00.00	+13 58 45.0	9.99	.	-	-	-	-	-	-
VCC 1158	12 29 03.01	+13 11 01.1	9.99	.	-	-	-	-	-	-
VCC 1189	12 29 28.83	+06 46 12.3	0.33	.	8.50	8.55	8.62	8.48	8.47	7.91
VCC 1192	12 29 30.35	+07 59 38.3	9.99	.	-	-	-	-	-	-
VCC 1193	12 29 30.59	+07 41 48.3	0.41	.	8.68	8.79	8.69	8.57	8.54	8.09
VCC 1196	12 29 31.25	+14 02 58.3	9.99	.	-	-	-	-	-	-
VCC 1200	12 29 34.53	+10 47 37.3	>0.49	.	-	-	-	-	-	-
VCC 1203	12 29 37.35	+07 56 01.4	9.99	.	-	-	-	-	-	-
VCC 1205	12 29 37.87	+07 49 24.4	0.33	.	8.71	8.83	8.70	8.63	8.56	8.09
VCC 1217	12 29 42.54	+11 24 04.4	9.99	.	-	-	-	-	-	-
VCC 1226	12 29 46.80	+08 00 00.0	9.99	.	-	-	-	-	-	-
VCC 1231	12 29 48.82	+13 25 45.5	9.99	.	-	-	-	-	-	-
VCC 1242	12 29 53.32	+14 04 05.5	9.99	.	-	-	-	-	-	-
VCC 1253	12 30 02.37	+13 38 10.6	9.99	.	-	-	-	-	-	-
VCC 1254	12 30 05.31	+08 04 28.6	9.99	.	-	-	-	-	-	-
VCC 1283	12 30 18.46	+13 34 40.7	9.99	.	-	-	-	-	-	-
VCC 1290	12 30 26.47	+04 14 52.8	0.00	.	-	-	8.69	-	8.54	-
VCC 1297	12 30 31.82	+12 29 25.9	9.99	.	-	-	-	-	-	-
VCC 1316	12 30 49.41	+12 23 28.0	9.99	.	-	-	-	-	-	-
VCC 1326	12 30 57.15	+11 28 59.1	>0.02	.	-	-	-	-	-	-
VCC 1327	12 30 57.72	+12 16 16.1	9.99	.	-	-	-	-	-	-
VCC 1330	12 30 59.58	+08 04 39.1	9.99	.	-	-	-	-	-	-
VCC 1348	12 31 15.70	+12 19 54.3	9.99	.	-	-	-	-	-	-
VCC 1356	12 31 22.92	+11 29 34.3	0.19	.	8.32	-	8.22	8.19	8.18	8.33
VCC 1368	12 31 32.79	+11 37 36.4	9.99	.	-	-	-	-	-	-
VCC 1379	12 31 39.62	+16 51 07.5	0.00	<	-	-	9.04	-	-	-
VCC 1393	12 31 54.69	+15 07 26.6	0.32	.	-	-	8.70	8.70	8.56	-
VCC 1401	12 31 58.91	+14 25 09.7	1.42	<	-	-	8.91	-	-	-
VCC 1410	12 32 03.22	+16 41 14.7	0.00	<	-	-	8.62	-	8.47	-
VCC 1411	12 32 04.83	+11 49 02.7	9.99	.	-	-	-	-	-	-
VCC 1412	12 32 06.13	+11 10 34.8	9.99	.	-	-	-	-	-	-
VCC 1419	12 32 10.46	+13 25 09.8	>1.68	<	-	-	8.82	-	8.72	-
VCC 1426	12 32 22.80	+11 53 38.9	9.99	.	-	-	-	-	-	-
VCC 1448	12 32 40.83	+12 46 13.1	9.99	.	-	-	-	-	-	-
VCC 1450	12 32 41.91	+14 02 56.1	0.00	<	-	-	8.68	-	8.53	-
CGCG 014-063	12 32 45.48	+00 06 43.1	0.52	.	8.59	8.62	8.70	8.55	8.56	8.18
VCC 1486	12 33 09.94	+11 20 49.4	0.94	.	-	-	8.44	8.45	8.31	-
VCC 1491	12 33 13.98	+12 51 27.4	9.99	.	-	-	-	-	-	-

Continued on next page...

Table E.1 - Continued

Galaxy	R.A. (h m s)	Dec. (° ' '')	C1	On	M91	Z94	D02	OSN2	N2	P05
VCC 1499	12 33 19.77	+12 51 11.5	9.99	.	-	-	-	-	-	-
VCC 1508	12 33 30.18	+08 39 16.6	0.46	.	8.51	8.56	8.65	8.49	8.50	7.96
VCC 1516	12 33 39.78	+09 10 30.7	1.19	.	-	-	8.82	8.67	8.72	-
VCC 1524	12 33 47.74	+15 10 01.8	0.00	.	-	-	8.51	-	8.37	-
NGC 4525	12 33 51.13	+30 16 38.9	0.47	.	-	-	8.70	8.57	8.56	-
VCC 1532	12 33 56.79	+15 21 16.9	0.52	.	-	-	8.74	8.74	8.62	-
VCC 1540	12 34 08.46	+02 39 11.0	1.43	<	-	-	8.90	-	8.86	-
VCC 1552	12 34 15.77	+13 04 29.1	>0.78	<	-	-	9.02	-	-	-
VCC 1554	12 34 19.31	+06 28 07.1	0.28	.	8.58	8.60	8.44	8.33	8.31	8.17
VCC 1569	12 34 31.68	+13 30 13.2	0.36	.	8.48	-	8.22	8.23	8.18	8.40
VCC 1575	12 34 39.28	+07 09 38.3	0.50	<	-	-	8.74	8.90	8.62	-
VCC 1581	12 34 44.93	+06 18 07.4	0.00	.	-	-	8.22	-	8.18	-
VCC 1588	12 34 50.48	+15 33 05.4	1.05	<	-	-	8.81	-	8.71	-
VCC 1593	12 34 55.87	+15 33 56.5	0.23	.	8.82	8.94	8.82	8.63	8.74	8.37
VCC 1615	12 35 26.33	+14 29 48.8	>1.59	<	-	-	9.05	-	-	-
VCC 1619	12 35 30.84	+12 13 16.9	9.99	<	-	-	9.09	-	-	-
VCC 1630	12 35 38.13	+12 15 55.9	9.99	.	-	-	-	-	-	-
VCC 1632	12 35 39.87	+12 33 25.0	9.99	.	-	-	-	-	-	-
NGC 4561	12 36 08.30	+19 19 20.0	0.06	.	8.68	8.70	8.44	8.32	8.31	8.35
VCC 1673	12 36 32.66	+11 15 28.6	9.99	<	-	-	8.78	-	8.67	-
VCC 1676	12 36 34.16	+11 14 19.6	1.18	<	-	-	8.80	8.86	8.70	-
VCC 1675	12 36 34.65	+08 03 17.6	0.00	<	-	-	8.59	-	8.44	-
VCC 1678	12 36 37.61	+06 37 16.6	0.24	.	8.51	8.52	8.42	8.31	8.29	8.05
VCC 1683	12 36 38.31	+10 56 29.6	9.99	.	-	-	-	-	-	-
VCC 1686	12 36 43.57	+13 15 31.7	0.74	.	8.74	-	8.60	8.44	8.45	8.84
VCC 1690	12 36 49.78	+13 09 45.7	>0.38	<	-	-	-	-	-	-
VCC 1699	12 37 02.24	+06 55 30.9	0.00	.	-	-	8.42	-	8.29	-
VCC 1725	12 37 41.51	+08 33 31.3	0.00	.	-	-	8.49	-	8.35	-
VCC 1727	12 37 43.48	+11 49 04.4	>0.14	<	-	-	-	-	-	-
VCC 1726	12 37 45.08	+07 06 22.4	0.00	<	-	-	-	-	-	-
VCC 1730	12 37 48.60	+05 22 06.4	>1.34	<	-	-	8.89	-	8.85	-
VCC 1757	12 38 17.79	+13 06 35.8	>1.16	<	-	-	8.90	-	-	-
NGC 4592	12 38 20.81	+07 53 28.8	0.62	.	8.43	-	8.31	8.33	8.23	8.31
VCC 1789	12 39 18.73	-00 31 55.0	0.34	.	8.40	8.43	8.53	8.41	8.39	7.80
VCC 1791	12 39 24.55	+07 57 52.5	0.49	.	8.30	8.21	-	-	-	7.87
VCC 1811	12 39 51.63	+15 17 53.9	0.50	<	-	-	8.74	8.62	8.62	-
VCC 1813	12 39 55.88	+10 10 34.9	9.99	.	-	-	-	-	-	-
VCC 1859	12 40 57.47	+11 54 41.7	>2.31	<	-	-	8.97	-	8.77	-
VCC 1868	12 41 12.26	+11 53 08.9	1.45	<	-	-	8.85	-	-	-
VCC 1869	12 41 13.52	+10 09 22.9	9.99	.	-	-	-	-	-	-
VCC 1903	12 42 02.46	+11 38 48.5	9.99	.	-	-	-	-	-	-
VCC 1918	12 42 18.10	+05 44 21.7	>1.11	.	-	-	-	-	-	-
CGCG 014-110	12 42 31.91	-00 04 57.0	>1.20	<	-	-	8.49	-	8.35	-
NGC 4629	12 42 32.67	-01 21 02.4	0.39	.	8.53	8.55	8.53	8.38	8.39	8.09
VCC 1929	12 42 37.12	+14 21 22.0	0.35	.	8.43	8.47	8.62	8.49	8.47	7.80
VCC 1932	12 42 40.83	+14 17 46.0	1.01	.	8.58	8.63	8.85	8.71	8.77	8.07
VCC 1938	12 42 47.66	+11 26 34.1	9.99	<	-	-	-	-	-	-
VCC 1943	12 42 52.35	+13 15 26.2	1.13	.	7.77	7.59	8.93	8.62	-	7.22
VCC 1970	12 43 29.11	+10 05 34.7	9.99	.	-	-	-	-	-	-
VCC 1972	12 43 32.28	+11 34 54.7	0.81	.	-	-	8.73	-	8.60	-
VCC 1978	12 43 39.58	+11 33 09.8	9.99	<	-	-	-	-	-	-
CGCG 100-004	12 43 42.47	+16 23 34.8	0.52	.	8.84	8.98	8.87	8.74	8.81	8.27
VCC 1987	12 43 56.71	+13 07 34.0	0.38	.	-	-	8.73	8.69	8.60	-
VCC 1992	12 44 10.02	+12 06 59.2	0.00	<	-	-	-	-	-	-
VCC 1999	12 44 29.38	+13 29 53.5	9.99	.	-	-	-	-	-	-
VCC 2000	12 44 32.31	+11 11 26.5	9.99	.	-	-	-	-	-	-
VCC 2006	12 44 45.93	+12 21 11.7	9.99	.	-	-	-	-	-	-
NGC 4668	12 45 31.98	-00 32 08.6	0.46	.	8.18	8.15	8.57	8.40	8.42	7.56
VCC 2033	12 46 04.76	+08 28 30.8	0.01	.	8.68	8.74	8.44	8.37	8.31	8.26
VCC 2037	12 46 15.30	+10 12 21.0	0.28	.	8.27	-	8.39	8.34	8.28	8.02
VCC 2058	12 47 45.39	+13 45 48.3	1.30	.	-	-	8.79	-	-	-
VCC 2066	12 48 15.05	+10 59 06.7	>2.32	<	-	-	8.99	-	8.68	-
VCC 45	12 48 22.83	-41 07 24.7	9.99	<	-	-	-	-	-	-
VCC 2070	12 48 22.96	+08 29 13.8	9.99	<	-	-	-	-	-	-
CGCG 043-034	12 49 11.87	+03 23 24.5	0.71	.	8.47	8.54	8.68	8.54	8.53	7.84
CCC 94	12 49 25.48	-41 25 46.5	9.99	.	-	-	-	-	-	-
CCC 95	12 49 26.19	-41 29 23.5	9.99	.	-	-	-	-	-	-
CCC 96	12 49 26.69	-41 27 47.8	9.99	.	-	-	-	-	-	-
CGCG 100-011	12 49 38.89	+15 09 55.0	9.99	<	-	-	-	-	-	-
CCC 119	12 49 51.58	-41 13 34.2	9.99	.	-	-	-	-	-	-
CCC 122	12 49 54.15	-41 16 46.4	9.99	.	-	-	-	-	-	-

Continued on next page....

E.1. MEASURED OXYGEN ABUNDANCES

Table E.1 – Continued

Galaxy	R.A.(h m s)	Dec.(^o ' '')	C1	CII	M91	Z94	D02	O3N2	N2	P05
UGC 7991	12 50 38.95	+01 27 52.2	1.12	.	8.69	8.79	8.65	8.50	8.50	8.10
NGC 4731	12 51 00.86	-06 23 28.4	0.39	.	8.69	8.79	8.66	8.55	8.51	8.10
VCC 2087	12 51 06.81	+10 54 44.3	9.99	.	-	-	-	-	-	-
NGC 4747	12 51 45.95	+25 46 37.4	0.64	.	8.72	8.79	8.62	8.45	8.47	8.31
CGCG 071-060	12 51 55.15	+12 05 00.1	0.78	<	-	-	8.77	8.57	8.66	-
COC 222	12 52 12.85	-41 20 20.7	1.25	.	-	-	8.82	-	8.72	-
COC 226	12 52 15.98	-41 23 26.4	9.99	.	-	-	-	-	-	-
VCC 2092	12 52 17.64	+11 18 48.4	9.99	.	-	-	-	-	-	-
NGC 4753	12 52 22.00	-01 11 59.0	0.00	.	-	-	-	-	-	-
VCC 2095	12 52 55.92	+11 13 50.1	9.99	.	-	-	-	-	-	-
NGC 4791	12 54 43.96	+08 03 10.6	1.36	.	-	-	8.94	-	-	-
UGC 8032	12 54 44.19	+13 14 14.1	9.99	.	-	-	-	-	-	-
UGC 8045	12 55 23.50	+07 54 35.0	0.60	.	-	-	8.73	8.63	8.60	-
CGCG 043-071	12 55 49.50	+04 18 14.0	0.49	.	8.67	8.77	8.84	8.65	8.76	8.09
CGCG 160-020	12 56 06.05	+27 40 39.9	0.00	.	-	-	8.62	-	8.47	-
CGCG 160-026	12 56 28.56	+27 17 29.2	0.37	.	-	-	8.72	8.68	8.59	-
IC 3908	12 56 40.28	-07 33 27.1	1.62	.	9.00	9.18	8.82	8.69	8.72	-
CGCG 160-055	12 58 05.55	+28 14 32.8	0.28	.	-	-	8.88	8.74	8.82	8.69
CGCG 160-058	12 58 09.48	+28 42 29.5	0.81	<	-	-	8.78	8.72	8.67	-
CGCG 160-064	12 58 35.33	+27 15 51.5	0.45	.	8.71	8.81	8.66	8.54	8.51	8.16
CGCG 160-067	12 58 37.17	+27 10 38.0	0.36	.	8.74	8.86	8.71	8.59	8.57	8.17
CGCG 160-212	12 58 56.12	+27 50 00.9	>0.06	.	-	-	-	-	-	-
CGCG 160-213	12 59 02.07	+28 06 55.6	0.56	<	-	-	8.80	8.74	8.70	-
CGCG 160-215	12 59 03.95	+28 07 24.5	9.99	.	-	-	-	-	-	-
CGCG 160-219	12 59 07.84	+27 51 16.5	9.99	.	-	-	-	-	-	-
CGCG 071-092	12 59 27.14	+14 10 15.8	9.99	.	8.70	8.77	8.51	8.40	8.37	8.29
CGCG 160-076	12 59 40.23	+28 37 51.2	0.34	.	8.70	8.74	8.51	8.40	8.37	8.29
CGCG 160-241	13 00 08.00	+27 58 35.0	9.99	.	-	-	-	-	-	-
CGCG 160-086	13 00 33.58	+27 38 14.2	0.57	.	8.63	8.74	8.70	8.61	8.56	7.98
CGCG 160-252	13 00 37.74	+28 03 28.2	0.95	.	8.90	9.05	8.85	8.70	8.79	8.43
CGCG 043-093	13 00 39.34	+02 30 02.2	0.24	.	8.86	9.00	8.90	8.74	-	8.36
CGCG 160-088	13 00 39.63	+29 01 11.1	1.57	.	-	-	8.90	-	-	-
CGCG 160-258	13 00 51.51	+28 02 33.5	9.99	<	-	-	-	-	-	-
CGCG 160-260	13 00 56.10	+27 47 27.5	0.81	.	-	-	8.85	-	8.77	-
NGC 4904	13 00 58.65	-00 01 39.4	0.60	.	-	-	8.76	8.64	8.64	-
CGCG 160-095	13 01 26.09	+27 53 08.1	>0.87	.	-	-	-	-	-	-
CGCG 160-097	13 01 31.69	+27 50 49.2	9.99	<	-	-	-	-	-	-
CGCG 160-103	13 01 53.62	+27 37 26.6	9.99	.	-	-	-	-	-	-
CGCG 160-106	13 02 07.89	+27 38 54.3	1.01	.	-	-	8.83	8.75	8.75	-
CGCG 160-108	13 02 12.74	+28 12 52.9	0.45	.	9.01	9.19	8.78	8.72	8.67	8.67
CGCG 160-110	13 02 21.41	+28 13 49.2	9.99	<	-	-	-	-	-	-
NGC 4941	13 04 12.88	-05 33 06.7	9.99	.	8.59	8.64	8.53	8.41	8.39	8.12
CGCG 160-128	13 04 22.57	+28 48 38.5	0.09	.	8.64	8.70	8.55	8.41	8.40	8.20
CGCG 160-127	13 04 26.46	+27 18 16.7	0.38	.	8.71	8.72	8.44	8.30	8.31	8.43
CGCG 160-139	13 06 37.92	+28 50 59.1	0.15	.	8.71	8.72	8.44	8.30	8.31	8.43
NGC 5145	13 26 13.91	+43 16 02.1	1.19	.	-	-	8.82	8.94	8.74	-
NGC 5147	13 26 19.73	+02 06 03.0	0.17	.	-	-	8.63	8.51	8.48	-
IC 902	13 36 01.21	+49 57 39.0	0.94	.	-	-	8.76	8.66	8.64	-
NGC 5301	13 46 24.67	+46 06 25.4	0.92	.	8.00	8.03	8.72	8.55	8.59	7.23
NGC 5303	13 47 44.99	+38 18 16.6	0.44	.	8.71	8.82	8.71	8.57	8.57	8.17
NGC 5300	13 48 16.03	+03 57 03.1	0.58	.	-	-	8.78	8.66	8.67	-
UGC 8756	13 50 35.88	+42 32 29.5	9.99	.	-	-	-	-	-	-
NGC 5334	13 52 54.45	-01 06 52.6	0.54	.	-	-	8.79	8.60	8.68	-
NGC 5348	13 54 11.30	+05 13 39.0	0.79	.	-	-	8.62	8.48	8.47	-
NGC 5372	13 54 45.99	+58 40 00.7	0.48	.	8.82	8.96	8.79	8.68	8.68	8.24
NGC 5356	13 54 58.45	+05 20 01.4	9.99	.	-	-	8.96	-	-	-
NGC 5360	13 55 38.75	+04 59 06.2	0.73	.	-	-	8.77	8.75	8.66	-
UGC 8857	13 56 26.61	+04 23 48.0	1.04	.	-	-	8.74	8.49	8.62	-
NGC 5486	14 07 24.96	+55 06 11.0	0.00	.	-	-	8.51	8.37	8.37	-
NGC 5560	14 20 04.40	+03 59 33.0	0.25	.	-	-	8.82	8.73	8.74	-
NGC 5577	14 21 13.20	+03 26 10.0	0.71	.	-	-	8.71	8.63	8.57	-
UGC 9215	14 23 27.11	+01 43 34.6	0.25	.	8.51	8.53	8.59	8.41	8.44	8.02
UGC 9242	14 25 21.02	+39 32 22.4	0.08	.	8.67	8.68	8.39	8.28	8.28	8.34
IC 1022	14 30 01.84	+03 46 22.3	0.45	.	-	-	8.71	8.57	8.57	-
NGC 5669	14 32 44.00	+09 53 31.0	0.51	.	8.58	8.65	8.66	8.50	8.51	8.02
NGC 5668	14 33 24.33	+04 27 01.7	0.22	.	8.86	8.99	8.66	8.54	8.51	8.43
NGC 5692	14 38 18.11	+03 24 37.1	0.32	.	8.79	8.91	8.71	8.59	8.57	8.29
IC 1048	14 42 58.01	+04 53 22.5	1.42	.	-	-	8.78	8.67	8.67	-

E.2 FINAL OXYGEN ABUNDANCES

Table E.2: Oxygen abundances derived from different calibrations and converted into the D02 base metallicity, then averaged to give the final metallicity measurement for each galaxy (see Section 8.6).

Name	R.A.(h m s)	Dec.($^{\circ}$ ''')	M91	Z94	D02	PP04 O3N2	PP04 N2	\bar{Z}	E(\bar{Z})	Methods
CGCG 522-038	01 52 45.75	+36 37 07.9	-	-	8.86	-	8.86	8.86	0.01	2
CGCG 522-041	01 52 53.79	+36 03 12.1	-	-	8.76	8.77	8.76	8.76	0.01	3
CGCG 522-058	01 54 53.93	+36 55 05.2	-	-	8.93	8.82	-	8.87	0.18	2
CGCG 522-060	01 54 57.88	+35 25 11.5	-	-	8.83	-	8.83	8.83	0.01	2
CGCG 522-062	01 55 01.80	+06 55 12.7	-	-	8.79	8.83	8.79	8.80	0.06	3
CGCG 522-065	01 55 14.06	+35 27 27.1	-	-	-	-	-	-	-	-
CGCG 522-072	01 56 21.39	+35 34 21.5	-	-	8.71	8.74	8.71	8.72	0.04	3
CGCG 522-079	01 56 40.05	+35 35 29.7	-	-	8.80	-	8.80	8.80	0.01	2
CGCG 119-016	08 14 14.07	+21 21 18.3	-	-	8.94	-	-	8.94	0.08	1
CGCG 119-024	08 16 33.89	+21 24 34.8	-	-	-	-	-	-	-	-
CGCG 119-027	08 16 57.57	+20 30 44.3	-	-	8.82	-	8.82	8.82	0.01	2
CGCG 119-028	08 17 25.46	+21 09 48.6	-	-	8.27	8.28	8.29	8.28	0.01	3
CGCG 119-029	08 17 25.84	+21 41 07.6	-	-	8.82	8.78	8.82	8.80	0.05	3
CGCG 119-031	08 17 34.96	+20 54 10.0	-	-	-	-	-	-	-	-
CGCG 119-034	08 17 52.37	+21 06 37.0	-	-	8.83	8.80	8.83	8.82	0.05	3
CGCG 119-035	08 17 56.85	+22 26 09.8	-	-	8.57	8.50	8.57	8.55	0.10	3
CGCG 119-040	08 18 25.78	+20 47 15.0	-	-	9.03	-	-	9.03	0.08	1
CGCG 119-041	08 18 29.45	+20 45 40.8	-	-	8.88	-	8.88	8.88	0.01	2
CGCG 119-043	08 18 49.13	+21 13 05.6	-	-	8.72	8.72	8.72	8.72	0.01	3
CGCG 119-044	08 18 50.23	+22 06 56.5	-	-	8.35	8.32	8.36	8.34	0.05	3
CGCG 119-046	08 19 01.88	+21 11 07.8	-	-	8.82	8.72	8.82	8.79	0.16	3
CGCG 119-047	08 19 05.05	+21 47 27.6	-	-	8.78	8.77	8.78	8.78	0.02	3
CGCG 119-048	08 19 10.65	+21 26 07.3	-	-	-	-	-	-	-	-
CGCG 119-050	08 19 12.83	+20 30 37.1	-	-	-	-	-	-	-	-
CGCG 119-051	08 19 13.00	+20 45 25.1	-	-	8.63	8.61	8.63	8.63	0.03	3
CGCG 119-053	08 19 19.82	+21 03 31.7	-	-	8.76	8.78	8.76	8.77	0.03	3
CGCG 119-054	08 19 32.08	+21 23 38.0	-	-	8.84	8.79	8.84	8.82	0.07	3
CGCG 119-056	08 19 41.39	+22 02 30.5	-	-	8.44	8.44	8.44	8.44	0.01	3
CGCG 119-057	08 19 48.27	+22 01 53.1	-	-	8.95	-	-	8.95	0.08	1
CGCG 119-059	08 19 58.89	+21 03 58.4	-	-	8.60	-	8.60	8.60	0.01	2
CGCG 119-061	08 20 10.78	+21 04 06.7	-	-	-	-	-	-	-	-
CGCG 119-063	08 20 23.54	+21 07 53.9	-	-	-	-	-	-	-	-
CGCG 119-065	08 20 35.65	+21 04 04.2	-	-	-	-	-	-	-	-
CGCG 119-066	08 20 51.60	+22 39 23.3	-	8.31	8.63	8.68	8.63	8.54	0.51	4
CGCG 119-067	08 21 21.08	+20 52 02.5	-	-	-	-	-	-	-	-
CGCG 119-068	08 21 21.93	+20 54 39.4	8.79	8.78	8.80	8.74	8.80	8.78	0.06	5
CGCG 119-071	08 22 01.46	+21 20 32.1	-	-	8.89	-	8.89	8.89	0.01	2
CGCG 119-074	08 22 43.46	+22 33 11.6	-	-	-	-	-	-	-	-
CGCG 119-078	08 23 11.37	+22 39 54.8	-	-	-	-	-	-	-	-
CGCG 119-081	08 23 41.35	+21 26 05.1	-	-	-	-	-	-	-	-
CGCG 119-082	08 23 55.24	+20 58 31.3	-	-	-	-	-	-	-	-
CGCG 119-083	08 24 01.59	+21 01 38.9	-	-	8.93	-	-	8.93	0.08	1
CGCG 119-085	08 24 20.23	+20 31 57.8	-	-	8.94	-	-	8.94	0.08	1
CGCG 119-091	08 25 12.06	+20 20 04.7	-	-	-	-	-	-	-	-
CGCG 119-109	08 27 41.93	+21 28 46.9	-	-	8.89	-	8.89	8.89	0.01	2
CGCG 123-035	10 17 39.69	+22 48 36.1	-	-	8.76	8.78	8.76	8.77	0.02	3
UGC 5588	10 20 57.20	+25 21 54.0	8.65	8.65	8.76	8.76	8.76	8.71	0.17	5
IC 610	10 26 28.44	+20 13 39.8	-	-	8.99	-	-	8.99	0.08	1
NGC 3287	10 34 47.30	+21 38 52.0	8.71	8.69	8.72	8.72	8.72	8.71	0.04	5
CGCG 124-041	10 35 42.04	+26 07 33.0	8.54	8.52	8.57	8.58	8.57	8.55	0.07	5
NGC 3294	10 36 16.24	+37 19 28.8	-	-	8.79	8.76	8.79	8.78	0.05	3
NGC 3346	10 43 38.91	+14 52 18.6	-	-	8.80	8.73	8.80	8.77	0.11	3
NGC 3370	10 47 04.05	+17 16 25.0	8.69	8.67	8.72	8.69	8.72	8.70	0.06	5
NGC 3380	10 48 12.18	+28 36 06.4	-	-	8.90	8.70	8.90	8.83	0.32	3
NGC 3381	10 48 24.81	+34 42 41.0	8.77	8.76	8.76	8.78	8.76	8.77	0.01	5
UGC 5958	10 51 15.88	+27 50 55.6	-	-	8.72	8.69	8.72	8.71	0.05	3
NGC 3424	10 51 46.33	+32 54 02.7	-	-	8.90	8.72	-	8.81	0.30	2
NGC 3437	10 52 35.70	+22 56 04.0	8.78	8.76	8.78	8.74	8.78	8.77	0.04	5
UGC 5990	10 52 38.34	+34 28 59.3	8.53	8.51	8.65	8.64	8.65	8.59	0.19	5
NGC 3454	10 54 29.40	+17 20 38.0	8.77	8.75	8.68	8.69	8.68	8.71	0.12	5
NGC 3455	10 54 31.09	+17 17 05.0	-	8.23	8.74	8.71	8.74	8.57	0.74	4
NGC 3448	10 54 39.00	+54 18 19.0	8.53	8.45	8.49	8.47	8.49	8.48	0.08	5
NGC 3485	11 00 02.40	+14 50 29.0	-	-	8.83	8.78	8.83	8.81	0.08	3
NGC 3501	11 02 47.26	+17 59 21.6	-	-	8.91	-	-	8.91	0.08	1

Continued on next page...

Table E.2 – Continued

Name	R.A.(h m s)	Dec.(° ' ")	M91	Z94	D02	PP04 O3N2	PP04 N2	\bar{Z}	E(\bar{Z})	Methods
NGC 3512	11 04 02.90	+28 02 12.0	-	-	8.89	8.80	8.89	8.86	0.14	3
NGC 3526	11 06 56.80	+07 10 28.0	-	8.29	8.55	8.54	8.55	8.46	0.38	4
UGC 6169	11 07 03.35	+12 03 36.1	-	-	8.71	8.69	8.71	8.70	0.03	3
NGC 3547	11 09 55.94	+10 43 15.0	8.69	8.66	8.68	8.65	8.68	8.67	0.04	5
NGC 3596	11 15 06.20	+14 47 13.2	-	-	8.83	-	8.83	8.83	0.01	2
UGC 6320	11 18 17.25	+18 50 49.5	8.53	8.45	8.49	8.46	8.49	8.48	0.09	5
NGC 3629	11 20 31.80	+26 57 48.1	-	8.31	8.65	8.61	8.65	8.53	0.48	4
NGC 3631	11 21 02.87	+53 10 10.4	-	-	8.80	8.77	8.80	8.79	0.04	3
NGC 3655	11 22 54.61	+16 35 24.1	-	-	8.80	8.80	8.80	8.80	0.01	3
NGC 3659	11 23 45.53	+17 49 07.2	8.69	8.68	8.70	8.70	8.70	8.69	0.03	5
NGC 3684	11 27 11.19	+17 01 48.6	8.76	8.74	8.82	8.78	8.82	8.78	0.09	5
NGC 3683	11 27 31.84	+56 52 37.4	8.77	8.75	8.82	8.78	8.82	8.78	0.08	5
NGC 3686	11 27 43.97	+17 13 27.0	-	-	8.82	-	8.82	8.82	0.01	2
NGC 3692	11 28 24.01	+09 24 27.4	-	-	8.87	8.75	8.87	8.83	0.19	3
NGC 3755	11 36 33.36	+36 24 37.2	8.49	8.43	8.59	8.55	8.59	8.52	0.20	5
NGC 3756	11 36 48.01	+54 17 36.8	-	-	8.99	-	-	8.99	0.08	1
NGC 3813	11 41 18.65	+36 32 48.5	8.54	8.54	8.74	8.71	8.74	8.65	0.30	5
CGCG 097-064	11 42 14.53	+20 05 49.6	-	-	-	-	-	-	-	-
CGCG 097-062	11 42 14.64	+19 58 32.5	8.77	8.74	8.73	8.71	8.73	8.74	0.06	5
CGCG 097-063	11 42 15.51	+20 02 54.1	-	-	8.70	-	8.70	8.70	0.01	2
CGCG 097-068	11 42 24.47	+20 07 06.4	8.62	8.62	8.80	8.76	8.80	8.71	0.26	5
CGCG 097-073	11 42 56.43	+19 57 59.0	8.56	8.51	8.82	8.65	8.82	8.66	0.42	5
CGCG 097-079	11 43 13.35	+20 00 16.4	8.62	8.57	8.51	8.53	8.51	8.55	0.13	5
CGCG 097-087	11 43 48.90	+19 58 08.0	8.52	8.47	8.65	8.58	8.65	8.56	0.23	5
CGCG 097-091	11 43 59.04	+20 04 37.5	-	-	8.95	8.79	-	8.87	0.27	2
CGCG 097-088	11 43 59.54	+19 46 43.8	-	-	-	-	-	-	-	-
CGCG 097-097	11 44 00.80	+20 01 45.0	-	-	-	-	-	-	-	-
CGCG 097-093	11 44 01.85	+19 47 03.4	8.68	8.68	8.68	8.74	8.68	8.69	0.07	5
NGC 3846A	11 44 14.82	+55 02 05.9	8.46	8.42	8.51	8.52	8.51	8.48	0.12	5
CGCG 097-114	11 44 47.71	+19 46 23.1	8.75	8.74	8.65	8.75	8.65	8.71	0.15	5
CGCG 097-120	11 44 49.11	+19 47 41.9	-	-	8.96	-	-	8.96	0.08	1
CGCG 097-122	11 44 52.30	+19 27 16.9	-	-	8.84	8.73	8.84	8.80	0.17	3
CGCG 097-125	11 44 54.82	+19 46 35.2	-	-	8.74	8.60	8.74	8.69	0.23	3
CGCG 097-123	11 44 55.82	+19 29 37.6	-	-	-	-	-	-	-	-
CGCG 097-129	11 45 03.89	+19 58 22.9	-	-	8.92	-	-	8.92	0.08	1
CGCG 097-138	11 45 44.77	+20 01 51.1	-	-	8.57	-	8.57	8.57	0.01	2
CGCG 127-049	11 45 48.83	+20 37 42.4	-	-	8.79	8.78	8.79	8.79	0.01	3
CGCG 186-045	11 46 26.08	+34 51 07.0	8.45	8.31	8.42	8.37	8.42	8.39	0.15	5
NGC 3898	11 49 15.10	+56 05 05.0	-	-	-	-	-	-	-	-
IC 2969	11 52 30.1s	-03 52 15.0	8.53	8.47	8.51	8.50	8.51	8.50	0.06	5
NGC 3952	11 53 40.55	-03 59 45.8	8.44	8.31	8.39	8.36	8.39	8.37	0.14	5
NGC 4030	12 00 23.62	-01 06 00.3	-	-	8.80	-	8.80	8.80	0.01	2
NGC 4032	12 00 32.90	+20 04 28.0	8.78	8.75	8.60	8.59	8.60	8.67	0.26	5
NGC 4019	12 01 10.54	+14 06 13.5	8.77	8.72	8.47	8.46	8.47	8.59	0.44	5
NGC 4037	12 01 23.66	+13 24 03.6	-	-	8.79	-	8.79	8.79	0.01	2
CGCG 013-046	12 02 41.91	+01 58 43.7	-	-	8.94	-	-	8.94	0.08	1
UGC 7035	12 03 40.14	+02 38 28.3	-	8.27	8.53	8.52	8.53	8.45	0.38	4
CGCG 069-058	12 08 09.15	+10 22 45.1	-	-	-	-	-	-	-	-
VCC 1	12 08 20.02	+13 41 00.2	-	-	8.77	8.78	8.77	8.78	0.01	3
VCC 24	12 10 35.65	+11 45 38.5	-	-	8.47	8.42	8.47	8.45	0.07	3
VCC 25	12 10 37.33	+16 01 59.5	-	-	8.77	8.74	8.77	8.76	0.04	3
VCC 47	12 12 11.77	+13 14 47.8	-	-	8.74	-	8.74	8.74	0.01	2
VCC 49	12 12 16.46	+13 12 23.9	-	-	-	-	-	-	-	-
VCC 58	12 12 32.21	+12 07 25.9	-	-	8.99	-	-	8.99	0.08	1
VCC 66	12 12 46.27	+10 51 56.0	-	-	8.60	8.58	8.60	8.59	0.04	3
VCC 73	12 13 02.99	+07 02 19.0	-	-	8.93	8.78	-	8.85	0.23	2
VCC 87	12 13 40.91	+15 27 13.2	-	-	8.44	8.51	8.44	8.47	0.10	3
VCC 89	12 13 47.34	+13 25 30.2	-	-	8.81	8.78	8.81	8.80	0.05	3
VCC 92	12 13 48.24	+14 54 01.2	-	-	8.93	8.80	-	8.86	0.21	2
VCC 97	12 13 53.65	+13 10 22.2	-	-	8.78	-	8.78	8.78	0.01	2
VCC 119	12 14 37.43	+12 48 47.4	-	-	8.35	8.49	8.36	8.40	0.22	3
VCC 131	12 15 04.41	+14 01 44.5	-	-	8.77	8.76	8.77	8.77	0.02	3
VCC 134	12 15 05.24	+13 35 41.5	-	-	8.82	8.75	8.82	8.79	0.09	3
VCC 142	12 15 13.16	+13 11 05.6	8.69	8.68	8.72	8.72	8.72	8.71	0.05	5
VCC 145	12 15 16.77	+13 01 26.6	-	-	8.71	8.71	8.71	8.71	0.01	3
VCC 152	12 15 30.31	+09 35 08.6	-	-	8.75	8.76	8.75	8.76	0.01	3
VCC 157	12 15 39.28	+13 54 05.7	-	-	8.81	-	8.81	8.81	0.01	2
VCC 159	12 15 41.50	+08 17 07.7	-	-	-	-	-	-	-	-
VCC 162	12 15 46.12	+10 41 53.7	-	-	8.31	-	8.32	8.32	0.01	2
VCC 167	12 15 54.22	+13 08 59.7	-	-	8.97	-	-	8.97	0.08	1
VCC 187	12 16 22.77	+13 18 27.9	-	-	8.69	8.66	8.69	8.68	0.04	3
VCC 220	12 17 06.50	+07 37 23.1	-	-	-	-	-	-	-	-

Continued on next page...

Table E.2 – Continued

Name	R.A. (h m s)	Dec. (° ′ ″)	M91	Z94	D02	PP04 O3N2	PP04 N2	Z	E(Z)	Methods
VCC 221	12 17 08.62	+03 40 50.1	8.79	8.78	8.72	8.75	8.72	8.75	0.08	5
VCC 226	12 17 11.34	+15 19 27.1	-	-	8.77	-	8.77	8.77	0.01	2
VCC 228	12 17 16.45	+12 47 42.1	8.69	8.67	8.65	8.66	8.65	8.66	0.04	5
VCC 307	12 18 49.40	+14 24 59.6	-	8.78	8.81	8.78	8.79	8.79	0.04	3
VCC 318	12 19 03.40	+08 51 22.7	-	-	8.55	8.52	8.55	8.54	0.04	3
VCC 324	12 19 09.90	+03 51 20.0	8.52	8.36	8.27	8.26	8.29	8.35	0.30	5
VCC 334	12 19 14.10	+13 52 55.0	8.27	-	8.35	8.39	8.36	8.34	0.14	4
VCC 345	12 19 23.57	+05 49 32.8	-	-	-	-	-	-	-	-
VCC 355	12 19 30.70	+14 52 38.0	-	-	-	-	-	-	-	-
VCC 358	12 19 35.66	+05 50 47.9	-	-	-	-	-	-	-	-
VCC 369	12 19 45.59	+12 47 57.0	-	-	-	-	-	-	-	-
VCC 382	12 19 55.90	+05 20 34.0	-	-	-	-	-	-	-	-
VCC 386	12 20 03.70	+05 20 28.1	-	-	-	-	-	-	-	-
VCC 393	12 20 07.47	+07 41 28.1	-	-	8.70	-	8.70	8.70	0.01	2
UGC 7387	12 20 17.34	+04 12 06.0	-	-	8.92	-	8.92	8.92	0.08	1
NGC 4287	12 20 48.48	+05 38 23.4	-	-	8.79	-	8.79	8.79	0.01	2
NGC 4289	12 21 02.30	+03 43 20.0	-	-	8.95	-	8.95	8.95	0.08	1
VCC 459	12 21 11.46	+17 38 18.5	-	-	8.42	8.37	8.42	8.40	0.07	3
VCC 460	12 21 12.68	+18 22 56.5	-	-	-	-	-	-	-	-
VCC 465	12 21 17.82	+11 30 31.5	8.72	8.68	8.53	8.56	8.53	8.61	0.24	5
VCC 483	12 21 32.67	+14 36 22.6	-	-	8.81	8.81	8.81	8.81	0.01	2
VCC 491	12 21 40.20	+11 30 09.7	8.54	8.46	8.47	8.46	8.47	8.48	0.09	5
VCC 497	12 21 42.26	+14 35 51.7	-	-	-	-	-	-	-	-
VCC 508	12 21 54.84	+04 28 24.8	8.78	8.77	8.85	8.81	8.85	8.81	0.10	5
UGC 7422	12 22 01.30	+05 06 00.0	-	-	9.07	-	9.07	9.07	0.08	1
VCC 522	12 22 03.54	+12 44 27.8	-	-	-	-	-	-	-	-
VCC 523	12 22 04.23	+12 47 12.8	-	-	-	-	-	-	-	-
VCC 534	12 22 12.35	+07 08 38.9	-	-	-	-	-	-	-	-
VCC 538	12 22 14.94	+07 09 51.9	-	-	-	-	-	-	-	-
VCC 552	12 22 27.02	+04 34 00.0	8.44	8.33	8.42	8.39	8.42	8.40	0.12	5
VCC 559	12 22 31.29	+15 32 14.0	-	-	8.87	-	8.87	8.87	0.01	2
VCC 562	12 22 36.00	+12 09 28.0	8.16	-	8.69	8.25	8.24	8.22	0.12	4
VCC 596	12 22 54.82	+15 49 20.2	-	-	8.69	-	8.69	8.69	0.01	2
VCC 630	12 23 17.02	+11 22 07.3	-	-	8.74	-	8.74	8.74	0.01	2
VCC 634	12 23 19.89	+15 49 10.3	-	-	-	-	-	-	-	-
VCC 636	12 23 21.08	+15 52 04.3	-	-	8.72	8.81	8.72	8.75	0.14	3
VCC 655	12 23 37.45	+17 32 28.5	-	-	8.91	-	8.91	8.91	0.08	1
VCC 656	12 23 38.81	+06 57 14.5	-	-	8.35	-	8.36	8.36	0.01	2
VCC 664	12 23 44.36	+12 28 42.5	-	-	8.57	-	8.57	8.57	0.01	2
VCC 667	12 23 48.48	+07 11 11.5	-	-	8.81	-	8.81	8.81	0.01	2
VCC 685	12 23 57.82	+16 41 38.6	-	-	8.42	-	8.42	8.42	0.01	2
VCC 688	12 24 00.10	+07 47 05.6	-	-	8.72	8.74	8.72	8.73	0.02	3
VCC 692	12 24 01.37	+12 12 16.6	-	-	8.63	8.63	8.63	8.63	0.01	2
VCC 699	12 24 07.44	+06 36 26.7	-	-	8.63	8.58	8.63	8.62	0.08	3
NGC 4359	12 24 11.40	+31 31 18.0	-	-	8.99	-	8.99	8.99	0.08	1
VCC 713	12 24 14.10	+08 32 03.7	-	-	8.81	-	8.81	8.81	0.01	2
VCC 731	12 24 27.84	+07 19 04.8	-	-	-	-	-	-	-	-
VCC 758	12 24 54.71	+07 26 38.0	-	-	-	-	-	-	-	-
VCC 759	12 24 55.08	+11 42 16.0	-	-	-	-	-	-	-	-
VCC 762	12 25 02.80	+07 30 23.1	-	-	-	-	-	-	-	-
VCC 761	12 25 14.73	+12 42 53.2	-	-	8.63	-	8.63	8.63	0.01	2
VCC 787	12 25 18.10	+05 44 27.2	-	-	-	-	-	-	-	-
VCC 794	12 25 22.04	+16 25 47.2	-	-	8.95	-	8.95	8.95	0.08	1
VCC 792	12 25 22.07	+10 01 01.2	-	-	8.70	-	8.70	8.70	0.05	5
VCC 798	12 25 24.20	+18 11 23.3	-	-	8.65	-	8.65	8.65	0.01	3
VCC 801	12 25 25.43	+16 28 12.3	8.72	8.70	8.70	8.67	8.70	8.70	0.05	5
VCC 809	12 25 33.17	+12 15 36.3	-	-	8.65	8.65	8.65	8.65	0.01	3
VCC 828	12 25 41.69	+12 48 41.4	-	-	-	-	-	-	-	-
CGCG 014-034	12 25 42.64	+00 34 20.4	8.79	8.78	8.60	8.70	8.60	8.70	0.25	5
VCC 827	12 25 42.71	+07 12 55.4	-	8.23	8.60	8.54	8.60	8.47	0.52	4
VCC 836	12 25 46.60	+12 39 40.4	-	-	8.87	8.52	8.87	8.75	0.56	5
VCC 841	12 25 47.40	+14 57 12.0	8.65	8.60	8.44	8.48	8.44	8.44	0.27	3
VCC 849	12 25 50.59	+10 27 32.5	-	8.22	8.65	8.64	8.65	8.51	0.63	4
VCC 848	12 25 52.60	+05 48 36.0	-	-	8.53	-	8.53	8.53	0.01	2
VCC 851	12 25 54.16	+07 33 13.5	-	-	8.69	8.68	8.69	8.68	0.02	3
VCC 857	12 25 55.64	+18 12 49.5	-	-	-	-	-	-	-	-
VCC 865	12 25 59.19	+15 40 12.5	-	8.24	8.60	8.62	8.60	8.49	0.54	4
VCC 874	12 26 07.11	+16 10 51.6	-	-	8.85	-	8.85	8.85	0.01	2
VCC 873	12 26 07.32	+13 06 43.6	-	-	8.82	-	8.82	8.82	0.01	2
VCC 905	12 26 29.16	+08 52 16.8	-	-	8.75	8.70	8.75	8.74	0.08	3
VCC 912	12 26 32.16	+12 36 39.8	-	-	8.79	-	8.79	8.79	0.01	2
VCC 921	12 26 35.80	+03 57 56.8	-	-	8.86	8.80	8.86	8.84	0.10	3

Continued on next page...

Table E.2 – Continued

Name	R.A. (h m s)	Dec. (° ' '')	M91	Z94	D02	PP04 O3N2	PP04 N2	\bar{Z}	$E(\bar{Z})$	Methods
VCC 938	12 26 46.67	+07 55 07.9	8.69	8.69	8.78	8.81	8.78	8.75	0.15	5
VCC 939	12 26 47.25	+08 53 03.9	8.24	8.24	8.71	8.74	8.71	8.57	0.71	4
VCC 945	12 26 51.06	+13 10 32.9	-	-	-	-	-	-	-	-
VCC 950	12 26 51.38	+11 33 16.9	-	-	8.60	-	8.60	8.60	0.01	2
VCC 951	12 26 54.36	+11 40 06.0	-	-	-	-	-	-	-	-
VCC 958	12 26 56.30	+15 02 48.0	-	-	-	-	-	-	-	-
VCC 957	12 26 58.58	+02 29 42.0	8.74	8.72	8.70	8.70	8.70	8.71	0.04	5
VCC 973	12 27 08.70	+16 19 33.1	-	-	8.78	8.69	8.78	8.75	0.14	3
VCC 971	12 27 08.93	+05 52 48.1	8.48	-	8.42	8.44	8.42	8.44	0.08	4
VCC 975	12 27 11.04	+07 15 47.1	-	-	8.47	-	8.47	8.47	0.01	2
VCC 980	12 27 11.26	+15 53 50.1	-	-	8.51	8.50	8.51	8.51	0.01	3
VCC 979	12 27 11.65	+09 25 15.1	-	-	9.04	-	-	9.04	0.08	1
VCC 984	12 27 13.30	+12 44 05.1	-	-	-	-	-	-	-	-
VCC 985	12 27 21.55	+10 51 55.2	-	-	8.17	8.18	8.19	8.18	0.02	3
VCC 1003	12 27 26.31	+11 06 29.2	-	-	-	-	-	-	-	-
VCC 1002	12 27 26.37	+06 15 44.2	-	-	8.87	-	8.87	8.87	0.01	2
VCC 1010	12 27 26.65	+12 17 27.2	-	-	-	-	-	-	-	-
VCC 1018	12 27 32.87	+06 13 54.3	-	-	8.92	-	-	8.92	0.08	1
VCC 1028	12 27 38.33	+14 27 24.3	-	-	-	-	-	-	-	-
VCC 1030	12 27 40.42	+13 04 44.3	-	-	-	-	-	-	-	-
VCC 1036	12 27 42.23	+12 18 54.4	-	-	-	-	-	-	-	-
VCC 1043	12 27 45.52	+13 00 31.4	-	-	-	-	-	-	-	-
VCC 1047	12 27 53.52	+12 17 35.5	-	-	-	-	-	-	-	-
UGC 7579	12 27 55.40	+05 43 16.0	-	-	8.63	8.64	8.63	8.64	0.01	3
VCC 1062	12 28 03.66	+09 48 17.5	-	-	-	-	-	-	-	-
VCC 1068	12 28 06.23	+12 04 42.6	-	-	-	-	-	-	-	-
VCC 1073	12 28 08.53	+12 05 35.6	-	-	-	-	-	-	-	-
VCC 1086	12 28 16.00	+09 26 10.6	-	-	9.05	-	-	9.05	0.08	1
VCC 1091	12 28 18.70	+08 43 46.7	8.40	8.30	8.42	8.41	8.42	8.38	0.15	5
VCC 1110	12 28 29.27	+17 05 06.8	-	-	-	-	-	-	-	-
VCC 1107	12 28 30.29	+07 19 30.8	-	-	8.77	8.81	8.77	8.79	0.06	3
VCC 1118	12 28 40.50	+09 15 32.9	-	-	-	-	-	-	-	-
VCC 1125	12 28 43.34	+11 45 20.9	-	-	-	-	-	-	-	-
VCC 1146	12 28 57.51	+13 14 31.0	-	-	-	-	-	-	-	-
VCC 1145	12 28 59.20	+03 34 16.0	-	-	-	-	-	-	-	-
VCC 1154	12 29 00.00	+13 58 45.0	-	-	-	-	-	-	-	-
VCC 1158	12 29 03.01	+13 11 01.1	-	-	-	-	-	-	-	-
VCC 1189	12 29 28.83	+06 46 12.3	8.38	8.37	8.62	8.60	8.62	8.51	0.37	5
VCC 1192	12 29 30.35	+07 59 38.3	-	-	-	-	-	-	-	-
VCC 1193	12 29 30.59	+07 41 48.3	8.63	8.62	8.69	8.68	8.69	8.66	0.10	5
VCC 1196	12 29 31.25	+14 02 58.3	-	-	-	-	-	-	-	-
VCC 1200	12 29 34.53	+10 47 37.3	-	-	-	-	-	-	-	-
VCC 1203	12 29 37.35	+07 56 01.4	-	-	-	-	-	-	-	-
VCC 1205	12 29 37.87	+07 49 24.4	8.66	8.65	8.70	8.72	8.70	8.68	0.09	5
VCC 1217	12 29 42.54	+11 24 04.4	-	-	-	-	-	-	-	-
VCC 1226	12 29 46.80	+08 00 00.0	-	-	-	-	-	-	-	-
VCC 1231	12 29 48.82	+13 25 45.5	-	-	-	-	-	-	-	-
VCC 1242	12 29 53.32	+14 04 05.5	-	-	-	-	-	-	-	-
VCC 1253	12 30 02.37	+13 38 10.6	-	-	-	-	-	-	-	-
VCC 1254	12 30 05.31	+08 04 28.6	-	-	-	-	-	-	-	-
VCC 1283	12 30 18.46	+13 34 40.7	-	-	-	-	-	-	-	-
VCC 1290	12 30 26.47	+04 14 52.8	-	-	8.69	-	8.69	8.69	0.01	2
VCC 1297	12 30 31.82	+12 29 25.9	-	-	-	-	-	-	-	-
VCC 1316	12 30 49.41	+12 23 28.0	-	-	-	-	-	-	-	-
VCC 1326	12 30 57.15	+11 28 59.1	-	-	-	-	-	-	-	-
VCC 1327	12 30 57.72	+12 16 16.1	-	-	-	-	-	-	-	-
VCC 1330	12 30 59.58	+08 04 39.1	-	-	-	-	-	-	-	-
VCC 1348	12 31 15.70	+12 19 54.3	-	-	-	-	-	-	-	-
VCC 1356	12 31 22.92	+11 29 34.3	8.41	-	8.22	8.27	8.24	8.29	0.25	4
VCC 1368	12 31 32.79	+11 37 36.4	-	-	-	-	-	-	-	-
VCC 1379	12 31 39.62	+16 51 07.5	-	-	9.04	-	-	9.04	0.08	1
VCC 1393	12 31 54.69	+15 07 26.6	-	-	8.70	8.77	8.70	8.72	0.11	3
VCC 1401	12 31 58.91	+14 25 09.7	-	-	8.91	-	-	8.91	0.08	1
VCC 1410	12 32 03.22	+16 41 14.7	-	-	8.62	-	-	8.62	0.01	2
VCC 1411	12 32 04.83	+11 49 02.7	-	-	-	-	-	-	-	-
VCC 1412	12 32 06.13	+11 10 34.8	-	-	-	-	-	-	-	-
VCC 1419	12 32 10.46	+13 25 09.8	-	-	8.82	-	8.82	8.82	0.01	2
VCC 1426	12 32 22.80	+11 53 38.9	-	-	-	-	-	-	-	-
VCC 1448	12 32 40.83	+12 46 13.1	-	-	-	-	-	-	-	-
VCC 1450	12 32 41.91	+14 02 56.1	-	-	8.68	-	-	8.68	0.01	2
CGCG 014-063	12 32 45.48	+00 06 43.1	8.52	8.45	8.70	8.66	8.70	8.59	0.33	5
VCC 1486	12 33 09.94	+11 20 49.4	-	-	8.44	8.58	8.44	8.49	0.21	3

Continued on next page...

Table E.2 – Continued

Name	R.A.(h m s)	Dec.($^{\circ}$ ' '')	M91	Z94	D02	PP04 O3N2	PP04 N2	\bar{Z}	$E(\bar{Z})$	Methods
VCC 1491	12 33 13.98	+12 51 27.4	-	-	-	-	-	-	-	-
VCC 1499	12 33 19.77	+12 51 11.5	-	-	-	-	-	-	-	-
VCC 1508	12 33 30.18	+08 39 16.6	8.40	8.38	8.65	8.61	8.65	8.52	0.39	5
VCC 1516	12 33 39.78	+09 10 30.7	-	-	8.82	8.75	8.82	8.79	0.11	3
VCC 1524	12 33 47.74	+15 10 01.8	-	-	8.51	-	8.51	8.51	0.01	2
NGC 4525	12 33 51.13	+30 16 38.9	-	-	8.70	8.68	8.70	8.69	0.03	3
VCC 1532	12 33 56.79	+15 21 16.9	-	-	8.74	8.79	8.74	8.76	0.06	3
VCC 1540	12 34 08.46	+02 39 11.0	-	-	8.90	-	8.90	8.90	0.01	2
VCC 1552	12 34 15.77	+13 04 29.1	-	-	9.02	-	-	9.02	0.08	1
VCC 1554	12 34 19.31	+06 28 07.1	8.51	8.43	8.44	8.45	8.44	8.45	0.08	5
VCC 1569	12 34 31.68	+13 30 13.2	-	-	8.22	8.32	8.24	8.26	0.15	3
VCC 1575	12 34 39.28	+07 09 38.3	-	-	8.74	-	8.74	8.74	0.01	2
VCC 1581	12 34 44.93	+06 18 07.4	-	-	8.22	-	8.24	8.23	0.02	2
VCC 1588	12 34 50.48	+15 33 05.4	-	-	8.81	-	8.81	8.81	0.01	2
VCC 1593	12 34 55.87	+15 33 56.5	8.74	8.72	8.82	8.72	8.82	8.76	0.14	5
VCC 1615	12 35 26.33	+14 29 48.8	-	-	9.05	-	-	9.05	0.08	1
VCC 1619	12 35 30.84	+12 13 16.9	-	-	9.09	-	-	9.09	0.08	1
VCC 1630	12 35 38.13	+12 15 55.9	-	-	-	-	-	-	-	-
VCC 1632	12 35 39.87	+12 33 25.0	-	-	-	-	-	-	-	-
NGC 4561	12 36 08.30	+19 19 20.0	8.62	8.54	8.44	8.43	8.44	8.50	0.23	5
VCC 1673	12 36 32.66	+11 15 28.6	-	-	8.78	-	8.78	8.78	0.01	2
VCC 1676	12 36 34.16	+11 14 19.6	-	-	8.80	8.83	8.80	8.81	0.05	3
VCC 1675	12 36 34.65	+08 03 17.6	-	-	8.59	-	8.59	8.59	0.01	2
VCC 1678	12 36 37.61	+06 37 16.6	8.40	8.33	8.42	8.42	8.42	8.39	0.11	5
VCC 1683	12 36 38.31	+10 56 29.6	-	-	-	-	-	-	-	-
VCC 1686	12 36 43.57	+13 15 31.7	-	-	8.60	8.57	8.60	8.59	0.06	3
VCC 1690	12 36 49.78	+13 09 45.7	-	-	-	-	-	-	-	-
VCC 1699	12 37 02.24	+06 55 30.9	-	-	8.42	-	8.42	8.42	0.01	2
VCC 1725	12 37 41.51	+08 33 31.3	-	-	8.49	-	8.49	8.49	0.01	2
VCC 1727	12 37 43.48	+11 49 04.4	-	-	-	-	-	-	-	-
VCC 1726	12 37 45.08	+07 06 22.4	-	-	-	-	-	-	-	-
VCC 1730	12 37 48.60	+05 22 06.4	-	-	8.89	-	8.89	8.89	0.01	2
VCC 1757	12 38 17.79	+13 06 35.8	-	-	8.90	-	-	8.90	0.08	1
VCC 1758	12 38 20.81	+07 53 28.8	-	-	8.31	8.44	8.32	8.36	0.19	3
NGC 4592	12 39 18.73	-00 31 55.0	-	8.21	8.53	8.54	8.53	8.43	0.48	4
VCC 1789	12 39 21.34	+04 56 19.5	-	-	-	-	-	-	-	-
VCC 1791	12 39 24.55	+07 57 52.5	-	-	-	-	-	-	-	-
VCC 1811	12 39 51.63	+15 17 53.9	-	-	8.74	8.72	8.74	8.73	0.04	3
VCC 1813	12 39 55.88	+10 10 34.9	-	-	-	-	-	-	-	-
VCC 1859	12 40 57.47	+11 54 41.7	-	-	8.97	-	-	8.97	0.08	1
VCC 1868	12 41 12.26	+11 53 08.9	-	-	8.85	-	8.85	8.85	0.01	2
VCC 1869	12 41 13.52	+10 09 22.9	-	-	-	-	-	-	-	-
VCC 1903	12 42 02.46	+11 38 48.5	-	-	-	-	-	-	-	-
VCC 1918	12 42 18.10	+05 44 21.7	-	-	-	-	-	-	-	-
CGCG 014-110	12 42 31.91	-00 04 57.0	-	-	8.49	-	8.49	8.49	0.01	2
NGC 4629	12 42 32.67	-01 21 02.4	8.44	8.37	8.53	8.50	8.53	8.47	0.21	5
VCC 1929	12 42 37.12	+14 21 22.0	-	8.27	8.62	8.61	8.62	8.51	0.51	4
VCC 1932	12 42 40.83	+14 17 46.0	8.50	8.46	8.85	8.77	8.85	8.66	0.54	5
VCC 1938	12 42 47.66	+11 26 34.1	-	-	-	-	-	-	-	-
VCC 1943	12 42 52.35	+13 15 26.2	-	-	8.93	8.72	-	8.82	0.35	2
VCC 1970	12 43 29.11	+10 05 34.7	-	-	-	-	-	-	-	-
VCC 1972	12 43 32.28	+11 34 54.7	-	-	8.73	-	8.73	8.73	0.01	2
VCC 1978	12 43 39.58	+11 33 09.8	-	-	-	-	-	-	-	-
CGCG 100-004	12 43 42.47	+16 23 34.8	8.76	8.74	8.87	8.79	8.87	8.80	0.16	5
VCC 1987	12 43 56.71	+13 07 34.0	-	-	8.73	8.76	8.73	8.74	0.04	3
VCC 1992	12 44 10.02	+12 06 59.2	-	-	-	-	-	-	-	-
VCC 1999	12 44 29.38	+13 29 53.5	-	-	-	-	-	-	-	-
VCC 2000	12 44 32.31	+11 11 26.5	-	-	-	-	-	-	-	-
VCC 2006	12 44 45.93	+12 21 11.7	-	-	-	-	-	-	-	-
NGC 4668	12 45 31.98	-00 32 08.6	-	-	8.57	8.52	8.57	8.55	0.08	3
VCC 2033	12 46 04.76	+08 28 30.8	8.63	8.58	8.44	8.49	8.44	8.52	0.23	5
VCC 2037	12 46 15.30	+10 12 21.0	8.34	-	8.39	8.45	8.39	8.39	0.13	4
VCC 2058	12 47 45.39	+13 45 48.3	-	-	8.79	-	8.79	8.79	0.01	2
VCC 2066	12 48 15.05	+10 59 06.7	-	-	8.99	-	-	8.99	0.08	1
CCC 45	12 48 22.83	-41 07 24.7	-	-	-	-	-	-	-	-
VCC 2070	12 48 22.96	+08 29 13.8	-	-	-	-	-	-	-	-
CGCG 043-034	12 49 11.87	+03 23 24.5	-	8.35	8.68	8.66	8.68	8.57	0.46	4
CCC 94	12 49 25.48	-41 25 46.5	-	-	-	-	-	-	-	-
CCC 95	12 49 26.19	-41 29 23.5	-	-	-	-	-	-	-	-
CCC 96	12 49 26.69	-41 27 47.8	-	-	-	-	-	-	-	-
CGCG 100-011	12 49 38.89	+15 09 55.0	-	-	-	-	-	-	-	-
CCC 119	12 49 51.58	-41 13 34.2	-	-	-	-	-	-	-	-

Continued on next page...

E.2. FINAL OXYGEN ABUNDANCES

279

Table E.2 - Continued

Name	R.A.(h m s)	Dec.($^{\circ}$ '")	M91	Z94	D02	PP04 O3N2	PP04 N2	Z	E(Z)	Methods
CGCG 122	12 49 54.15	-41 16 46.4	-	-	-	-	-	-	-	-
UGC 7991	12 50 38.95	+01 27 52.2	-	-	8.65	-	-	8.65	0.01	2
NGC 4731	12 51 00.86	-06 23 28.4	8.63	8.62	8.66	8.67	8.66	8.65	0.06	5
VCG 2087	12 51 06.81	+10 54 44.3	-	-	-	-	-	-	-	-
NGC 4747	12 51 45.95	+25 46 37.4	8.66	8.62	8.62	8.58	8.62	8.62	0.08	5
CGCG 071-060	12 51 55.15	+12 05 00.1	-	-	8.77	8.68	8.77	8.74	0.14	3
CGC 222	12 52 12.85	-41 20 20.7	-	-	8.82	-	8.82	8.82	0.01	2
CGC 226	12 52 15.98	-41 23 26.4	-	-	-	-	-	-	-	-
VCG 2092	12 52 17.64	+11 18 48.4	-	-	-	-	-	-	-	-
NGC 4753	12 52 22.00	-01 11 59.0	-	-	-	-	-	-	-	-
VCG 2095	12 52 55.92	+11 13 50.1	-	-	-	-	-	-	-	-
NGC 4791	12 54 43.96	+08 03 10.6	-	-	8.94	-	-	8.94	0.08	1
UGC 8032	12 54 44.19	+13 14 14.1	-	-	-	-	-	-	-	-
UGC 8045	12 55 23.50	+07 54 35.0	-	-	8.73	8.72	8.73	8.73	0.01	3
CGCG 043-071	12 55 49.50	+04 18 14.0	8.62	8.60	8.84	8.74	8.84	8.72	0.32	5
CGCG 160-020	12 56 06.05	+27 40 39.9	-	-	8.62	-	8.62	8.62	0.01	2
CGCG 160-026	12 56 28.56	+27 17 29.2	-	-	8.72	8.76	8.72	8.73	0.05	3
IC 3908	12 56 40.28	-07 33 27.1	-	-	8.82	8.76	8.82	8.80	0.09	3
CGCG 160-055	12 58 05.55	+28 14 32.8	8.81	8.81	8.88	8.79	8.88	8.83	0.11	5
CGCG 160-058	12 58 09.48	+28 42 29.5	-	-	8.78	8.78	8.78	8.78	0.01	3
CGCG 160-064	12 58 35.33	+27 15 51.5	8.65	8.63	8.66	8.66	8.66	8.65	0.03	5
CGCG 160-067	12 58 37.17	+27 10 36.0	8.69	8.67	8.71	8.69	8.71	8.69	0.05	5
CGCG 160-212	12 58 56.12	+27 50 00.9	-	-	-	-	-	-	-	-
CGCG 160-213	12 59 02.07	+28 06 55.6	-	-	8.80	8.79	8.80	8.79	0.02	3
CGCG 160-215	12 59 03.95	+28 07 24.5	-	-	-	-	-	-	-	-
CGCG 160-219	12 59 07.84	+27 51 16.5	-	-	-	-	-	-	-	-
CGCG 071-092	12 59 27.14	+14 10 15.8	-	-	-	-	-	-	-	-
CGCG 160-076	12 59 40.23	+28 37 51.2	8.65	8.60	8.51	8.52	8.51	8.57	0.17	5
CGCG 160-241	13 00 08.00	+27 58 35.0	-	-	-	-	-	-	-	-
CGCG 160-086	13 00 33.58	+27 38 14.2	8.57	8.57	8.70	8.71	8.70	8.64	0.21	-
CGCG 160-252	13 00 37.74	+28 03 28.2	8.79	8.78	8.85	8.77	8.85	8.80	0.11	5
CGCG 043-093	13 00 39.34	+02 30 02.2	8.77	8.75	8.90	8.79	-	8.80	0.17	4
CGCG 160-088	13 00 39.63	+29 01 11.1	-	-	8.90	-	-	8.90	0.08	1
CGCG 160-258	13 00 51.51	+28 02 33.5	-	-	-	-	-	-	-	-
CGCG 160-260	13 00 56.10	+27 47 27.5	-	-	8.85	-	8.85	8.85	0.01	2
NGC 4904	13 00 58.65	-00 01 39.4	-	-	8.76	8.73	8.76	8.75	0.05	3
CGCG 160-095	13 01 26.09	+27 53 08.1	-	-	-	-	-	-	-	-
CGCG 160-097	13 01 31.69	+27 50 49.2	-	-	-	-	-	-	-	-
CGCG 160-103	13 01 53.62	+27 37 26.6	-	-	-	-	-	-	-	-
CGCG 160-106	13 02 07.89	+27 38 54.3	-	-	8.83	8.79	8.83	8.82	0.06	3
CGCG 160-110	13 02 12.74	+28 12 52.9	8.81	8.81	8.78	8.78	8.78	8.79	0.04	5
CGCG 160-110	13 02 21.41	+28 13 49.2	-	-	-	-	-	-	-	-
NGC 4941	13 04 12.88	-05 33 06.7	-	-	-	-	-	-	-	-
CGCG 160-128	13 04 22.57	+28 48 38.5	8.52	8.47	8.53	8.53	8.53	8.51	0.07	5
CGCG 160-127	13 04 26.46	+27 18 16.7	8.59	8.54	8.55	8.54	8.55	8.55	0.05	5
CGCG 160-139	13 06 37.92	+28 50 59.1	8.65	8.66	8.44	8.41	8.44	8.51	0.28	5
NGC 5145	13 25 13.91	+43 16 02.1	-	-	8.82	-	8.82	8.82	0.01	2
NGC 5147	13 26 19.73	+02 06 03.0	-	-	8.63	8.63	8.63	8.63	0.01	3
IC 902	13 36 01.21	+49 57 39.0	-	-	8.76	8.74	8.76	8.76	0.03	3
NGC 5301	13 46 24.67	+46 06 25.4	-	-	8.72	8.66	8.72	8.70	0.09	5
NGC 5303	13 47 44.99	+38 18 16.6	8.66	8.64	8.71	8.68	8.71	8.68	0.09	5
NGC 5300	13 48 16.03	+03 57 03.1	-	-	8.78	8.75	8.78	8.77	0.05	3
UGC 8756	13 50 35.88	+42 32 29.5	-	-	-	-	-	-	-	-
NGC 5334	13 52 54.45	-01 06 52.6	-	-	8.79	8.71	8.79	8.76	0.13	3
NGC 5348	13 54 11.30	+05 13 39.0	-	-	8.62	8.61	8.62	8.61	0.02	3
NGC 5372	13 54 45.99	+58 40 00.7	8.74	8.73	8.79	8.76	8.79	8.76	0.07	5
NGC 5356	13 54 58.45	+05 20 01.4	-	-	8.96	-	-	-	0.08	1
NGC 5360	13 55 38.75	+04 59 06.2	-	-	8.77	8.79	8.77	8.78	0.03	3
UGC 8857	13 56 26.61	+04 23 48.0	-	-	8.74	8.61	8.74	8.70	0.20	3
NGC 5486	14 07 24.96	+55 06 11.0	-	-	8.51	-	8.51	8.51	0.01	2
NGC 5560	14 20 04.40	+03 59 33.0	-	-	8.82	8.78	8.82	8.82	0.01	3
NGC 5577	14 21 13.20	+03 26 10.0	-	-	8.71	8.72	8.71	8.71	0.07	3
UGC 9215	14 23 27.11	+01 43 34.6	8.40	8.35	8.59	8.53	8.59	8.48	0.32	5
UGC 9242	14 25 21.02	+39 32 22.4	8.61	8.52	8.39	8.39	8.39	8.47	0.28	5
IC 1022	14 30 01.84	+03 46 22.3	-	-	8.71	8.68	8.71	8.70	0.05	5
NGC 5669	14 32 44.00	+09 53 31.0	8.50	8.48	8.66	8.62	8.66	8.66	0.24	5
NGC 5668	14 33 24.33	+04 27 01.7	8.77	8.75	8.66	8.65	8.66	8.70	0.15	5
NGC 5692	14 38 18.11	+03 24 37.1	8.73	8.71	8.71	8.69	8.71	8.71	0.03	5
IC 1048	14 42 58.01	+04 53 22.5	-	-	8.78	8.75	8.78	8.77	0.05	3

Table E.3: Oxygen abundances derived from different calibrations and converted into the PP04 O3N2 base metallicity, then averaged to give the final metallicity measurement for each galaxy (see Section 8.6).

Name	R.A.(h m s)	Dec.($^{\circ}$ ' '')	M91	Z94	D02	PP04 O3N2	PP04 N2	\bar{Z}	E(\bar{Z})	Methods
CGCG 522-038	01 52 45.75	+36 37 07.9	-	-	8.82	-	-	8.82	0.09	1
CGCG 522-041	01 52 53.79	+36 03 12.1	-	-	8.69	8.70	8.71	8.70	0.02	3
CGCG 522-058	01 54 53.93	+36 55 05.2	-	-	-	8.82	-	8.82	0.10	1
CGCG 522-060	01 54 57.88	+35 25 11.5	-	-	8.78	-	8.83	8.80	0.07	2
CGCG 522-062	01 55 01.80	+06 55 12.7	-	-	8.73	8.85	8.75	8.78	0.17	3
CGCG 522-065	01 55 14.06	+35 27 27.1	-	-	-	-	-	-	-	-
CGCG 522-072	01 56 21.39	+35 34 21.5	-	-	8.63	8.66	8.63	8.64	0.04	3
CGCG 522-079	01 56 40.05	+35 35 29.7	-	-	8.74	-	8.77	8.75	0.05	2
CGCG 119-016	08 14 14.07	+21 21 18.3	-	-	-	-	-	-	-	-
CGCG 119-024	08 16 33.89	+21 24 34.8	-	-	-	-	-	-	-	-
CGCG 119-027	08 16 57.57	+20 30 44.3	-	-	8.76	-	8.80	8.78	0.06	2
CGCG 119-028	08 17 25.46	+21 09 48.6	-	-	8.19	8.20	8.20	8.20	0.02	3
CGCG 119-029	08 17 25.84	+21 41 07.6	-	-	8.76	8.73	8.80	8.76	0.08	3
CGCG 119-031	08 17 34.96	+20 54 10.0	-	-	-	-	-	-	-	-
CGCG 119-034	08 17 52.37	+21 06 37.0	-	-	8.78	8.76	8.83	8.79	0.08	3
CGCG 119-035	08 17 56.85	+22 26 09.8	-	-	8.46	8.38	8.45	8.43	0.11	3
CGCG 119-040	08 18 25.78	+20 47 15.0	-	-	-	-	-	-	-	-
CGCG 119-041	08 18 29.45	+20 45 40.8	-	-	8.84	8.96	-	8.90	0.19	2
CGCG 119-043	08 18 49.13	+21 13 05.6	-	-	8.64	8.62	8.65	8.63	0.03	3
CGCG 119-044	08 18 50.23	+22 06 56.5	-	-	8.25	8.23	8.26	8.25	0.03	3
CGCG 119-046	08 19 01.88	+21 11 07.8	-	-	8.77	8.63	8.81	8.74	0.25	3
CGCG 119-047	08 19 05.05	+21 47 27.6	-	-	8.71	8.70	8.74	8.72	0.05	3
CGCG 119-048	08 19 10.65	+21 26 07.3	-	-	-	-	-	-	-	-
CGCG 119-050	08 19 12.83	+20 30 37.1	-	-	-	-	-	-	-	-
CGCG 119-051	08 19 13.00	+20 45 25.1	-	-	8.54	8.49	8.53	8.52	0.06	3
CGCG 119-053	08 19 19.82	+21 03 31.7	-	-	8.69	8.73	8.71	8.71	0.05	3
CGCG 119-054	08 19 32.08	+21 23 38.0	-	-	8.79	8.75	8.84	8.79	0.11	3
CGCG 119-056	08 19 41.39	+22 02 30.5	-	-	8.34	8.32	8.33	8.33	0.01	3
CGCG 119-057	08 19 48.27	+22 01 53.1	-	-	-	-	-	-	-	-
CGCG 119-059	08 19 58.89	+21 03 58.4	-	-	8.50	-	8.49	8.50	0.01	2
CGCG 119-061	08 20 10.78	+21 04 06.7	-	-	-	-	-	-	-	-
CGCG 119-063	08 20 23.54	+21 07 53.9	-	-	-	-	-	-	-	-
CGCG 119-065	08 20 35.65	+21 04 04.2	-	-	-	-	-	-	-	-
CGCG 119-066	08 20 51.60	+22 39 23.3	-	8.22	8.54	8.57	8.53	8.45	0.46	4
CGCG 119-067	08 21 21.08	+20 52 02.5	-	-	-	-	-	-	-	-
CGCG 119-068	08 21 21.93	+20 54 39.4	8.75	8.73	8.74	8.66	8.77	8.73	0.11	5
CGCG 119-071	08 22 01.46	+21 20 32.1	-	-	8.86	-	-	8.86	0.09	1
CGCG 119-074	08 22 43.46	+22 33 11.6	-	-	-	-	-	-	-	-
CGCG 119-078	08 23 11.37	+22 39 54.8	-	-	-	-	-	-	-	-
CGCG 119-081	08 23 41.35	+21 26 05.1	-	-	-	-	-	-	-	-
CGCG 119-082	08 23 55.24	+20 58 31.3	-	-	-	-	-	-	-	-
CGCG 119-083	08 24 01.59	+21 01 38.9	-	-	-	-	-	-	-	-
CGCG 119-085	08 24 20.23	+20 31 57.8	-	-	-	-	-	-	-	-
CGCG 119-091	08 25 12.06	+20 20 04.7	-	-	-	-	-	-	-	-
CGCG 119-109	08 27 41.93	+21 28 46.9	-	-	8.86	-	-	8.86	0.09	1
CGCG 123-035	10 17 39.69	+22 48 36.1	-	-	8.69	8.72	8.71	8.71	0.03	3
UGC 5588	10 20 57.20	+25 21 54.0	8.54	8.54	8.69	8.68	8.71	8.63	0.23	5
IC 610	10 26 28.44	+20 13 39.8	-	-	-	-	-	-	-	-
NGC 3287	10 34 47.30	+21 38 52.0	8.61	8.59	8.64	8.63	8.65	8.62	0.06	5
CGCG 124-041	10 35 42.04	+26 07 33.0	8.42	8.39	8.46	8.46	8.45	8.44	0.08	5
NGC 3294	10 36 16.24	+37 19 28.8	-	-	8.73	8.68	8.75	8.72	0.09	3
NGC 3346	10 43 38.91	+14 52 18.6	-	-	8.74	8.63	8.77	8.71	0.18	3
NGC 3370	10 47 04.05	+17 16 25.0	8.59	8.56	8.64	8.58	8.65	8.60	0.10	5
NGC 3380	10 48 12.18	+28 36 06.4	-	-	-	8.59	-	8.59	0.10	1
NGC 3381	10 48 24.81	+34 42 41.0	8.71	8.70	8.69	8.72	8.71	8.71	0.03	5
UGC 5958	10 51 15.88	+27 50 55.6	-	-	8.64	8.58	8.65	8.62	0.08	3
NGC 3424	10 51 46.33	+32 54 02.7	-	-	-	8.62	-	8.62	0.10	1
NGC 3437	10 52 35.70	+22 56 04.0	8.71	8.69	8.71	8.66	8.74	8.70	0.08	5
UGC 5990	10 52 38.34	+34 28 59.3	8.41	8.39	8.55	8.52	8.54	8.48	0.21	5
NGC 3454	10 54 29.40	+17 20 38.0	8.69	8.67	8.58	8.58	8.58	8.62	0.15	5
NGC 3455	10 54 31.09	+17 17 05.0	-	8.16	8.66	8.61	8.68	8.51	0.68	4
NGC 3448	10 54 39.00	+54 18 19.0	8.41	8.33	8.38	8.35	8.37	8.37	0.08	5
NGC 3485	11 00 02.40	+14 50 29.0	-	-	8.78	8.73	8.83	8.78	0.12	3
NGC 3501	11 02 47.26	+17 59 21.6	-	-	-	-	-	-	-	-
NGC 3512	11 04 02.90	+28 02 12.0	-	-	8.86	8.76	-	8.81	0.14	2
NGC 3526	11 06 56.80	+07 10 28.0	-	8.20	8.45	8.41	8.43	8.36	0.31	4
UGC 6169	11 07 03.35	+12 03 36.1	-	-	8.63	8.58	8.63	8.61	0.07	3

Continued on next page...

E.2. FINAL OXYGEN ABUNDANCES

281

Table E-3 - Continued

Name	R.A.(h m s)	Dec.(° ' ")	M91	Z94	D02	PP04 O3N2	PP04 N2	Z	E(Z)	Methods
NGC 3547	11 09 55.94	+10 43 15.0	8.58	8.54	8.58	8.53	8.58	8.56	0.06	5
NGC 3596	11 15 06.20	+14 47 13.2	-	-	8.78	-	8.83	8.80	0.07	2
U/GC 6320	11 18 17.25	+18 50 49.5	8.41	8.33	8.38	8.35	8.37	8.37	0.08	5
NGC 3629	11 20 31.80	+26 57 48.1	-	8.22	8.55	8.48	8.54	8.44	0.43	4
NGC 3631	11 21 02.87	+53 10 10.4	-	-	8.74	8.71	8.77	8.74	0.07	3
NGC 3655	11 22 54.61	+16 35 24.1	-	-	8.74	8.76	8.77	8.76	0.04	3
NGC 3659	11 23 45.53	+17 49 07.2	8.59	8.57	8.61	8.60	8.61	8.60	0.05	5
NGC 3684	11 27 11.19	+17 01 48.6	8.68	8.66	8.76	8.73	8.80	8.72	0.15	5
NGC 3688	11 27 31.84	+56 52 37.4	8.69	8.68	8.76	8.72	8.80	8.73	0.13	5
NGC 3686	11 27 43.97	+17 13 27.0	-	-	8.77	-	8.81	8.79	0.06	2
NGC 3692	11 28 24.01	+09 24 27.4	-	-	8.83	8.66	-	8.75	0.26	2
NGC 3755	11 36 33.36	+36 24 37.2	8.37	8.32	8.48	8.43	8.47	8.41	0.19	5
NGC 3756	11 36 48.01	+54 17 36.8	-	-	-	-	-	-	-	5
NGC 3813	11 41 18.65	+36 32 48.5	8.42	8.42	8.66	8.61	8.68	8.55	0.35	5
CGCG 097-064	11 42 14.53	+20 05 49.6	-	-	-	-	-	-	-	-
CGCG 097-062	11 42 14.64	+19 58 32.5	8.70	8.66	8.65	8.60	8.66	8.66	0.09	5
CGCG 097-063	11 42 15.51	+20 02 54.1	-	-	8.61	-	8.61	8.61	0.01	2
CGCG 097-068	11 42 24.47	+20 07 06.4	8.50	8.50	8.74	8.69	8.77	8.63	0.35	5
CGCG 097-073	11 42 56.43	+19 57 59.0	8.44	8.38	8.77	8.53	8.81	8.57	0.53	5
CGCG 097-079	11 43 13.35	+20 00 16.4	8.50	8.45	8.40	8.40	8.39	8.43	0.12	5
CGCG 097-087	11 43 48.90	+19 58 08.0	8.40	8.35	8.55	8.46	8.54	8.45	0.24	5
CGCG 097-091	11 43 59.04	+20 04 37.5	-	-	-	8.75	-	8.75	0.10	1
CGCG 097-088	11 43 59.54	+19 46 43.8	-	-	-	-	-	-	-	-
CGCG 097-097	11 44 00.80	+20 01 45.0	-	-	-	-	-	-	-	-
CGCG 097-093	11 44 01.85	+19 47 03.4	8.57	8.57	8.58	8.65	8.58	8.59	0.09	5
NGC 3846A	11 44 14.82	+55 02 05.9	8.35	8.31	8.40	8.40	8.39	8.37	0.11	5
CGCG 097-114	11 44 47.71	+19 46 23.1	8.67	8.66	8.55	8.67	8.54	8.62	0.17	5
CGCG 097-120	11 44 49.11	+19 47 41.9	-	-	8.79	8.64	8.84	8.76	0.27	3
CGCG 097-122	11 44 52.30	+19 27 16.9	-	-	-	-	8.68	8.61	0.29	3
CGCG 097-125	11 44 54.82	+19 46 35.2	-	-	8.66	8.47	-	-	-	-
CGCG 097-123	11 44 55.82	+19 29 37.6	-	-	-	-	-	-	-	-
CGCG 097-129	11 45 03.89	+19 58 22.9	-	-	-	-	-	-	-	-
CGCG 097-138	11 45 44.77	+20 01 51.1	-	-	8.46	-	8.45	8.46	0.01	2
CGCG 127-049	11 45 48.83	+20 37 42.4	-	-	8.73	8.73	8.75	8.74	0.03	3
CGCG 186-045	11 46 26.08	+34 51 07.0	8.33	8.22	8.31	8.27	8.31	8.29	0.11	5
NGC 3898	11 49 15.10	+56 05 05.0	-	-	-	-	-	-	-	-
IC 2969	11 52 30.15	-03 52 15.0	8.41	8.35	8.40	8.38	8.39	8.39	0.06	5
NGC 3952	11 53 40.55	-03 59 45.8	8.33	8.22	8.28	8.26	8.28	8.27	0.11	5
NGC 4030	12 00 23.62	-01 06 00.3	-	-	8.74	-	8.77	8.75	0.05	2
NGC 4032	12 00 32.90	+20 04 28.0	8.72	8.67	8.50	8.46	8.49	8.58	0.32	5
NGC 4019	12 01 10.54	+14 06 13.5	8.70	8.63	8.36	8.34	8.35	8.49	0.47	5
NGC 4037	12 01 23.66	+13 24 03.6	-	-	8.73	-	8.75	8.74	0.04	2
CGCG 013-046	12 02 41.91	+01 58 48.3	-	-	-	-	-	-	-	-
U/GC 7035	12 03 40.14	+02 38 28.3	-	8.19	8.43	8.40	8.41	8.35	0.31	4
CGCG 069-058	12 08 09.15	+10 22 45.1	-	-	-	-	-	-	-	-
VCC 1	12 08 20.02	+13 41 00.2	-	-	8.70	8.72	8.72	8.72	0.03	3
VCC 24	12 10 35.65	+11 45 38.5	-	-	8.36	8.31	8.35	8.34	0.06	3
VCC 25	12 10 37.33	+16 01 59.5	-	-	8.70	8.66	8.72	8.70	0.08	3
VCC 47	12 12 11.77	+13 14 47.8	-	-	8.66	-	8.68	8.67	0.02	2
VCC 49	12 12 16.46	+13 12 23.9	-	-	-	-	-	-	-	-
VCC 58	12 12 32.21	+12 07 25.9	-	-	-	-	-	-	-	-
VCC 66	12 12 46.27	+10 51 56.0	-	-	8.50	8.45	8.49	8.48	0.06	3
VCC 73	12 13 02.99	+07 02 19.0	-	-	8.73	8.73	8.73	8.73	0.10	1
VCC 87	12 13 40.91	+15 27 13.2	-	-	8.34	8.39	8.33	8.35	0.08	3
VCC 89	12 13 47.34	+13 25 30.2	-	-	8.75	8.72	8.78	8.75	0.08	3
VCC 92	12 13 48.24	+14 54 01.2	-	-	8.77	8.77	-	8.77	0.10	1
VCC 97	12 13 53.65	+13 10 22.2	-	-	8.71	-	8.74	8.73	0.14	2
VCC 119	12 14 37.43	+12 48 47.4	-	-	8.25	8.37	8.26	8.29	0.17	3
VCC 131	12 15 04.41	+14 01 44.5	-	-	8.70	8.68	8.72	8.70	0.05	3
VCC 134	12 15 05.24	+13 35 41.5	-	-	8.76	8.68	8.80	8.75	0.15	5
VCC 142	12 15 13.16	+13 11 05.6	8.59	8.57	8.64	8.62	8.65	8.61	0.09	5
VCC 145	12 15 16.77	+13 01 26.6	-	-	8.63	8.61	8.63	8.62	0.03	3
VCC 152	12 15 30.31	+09 35 08.6	-	-	8.68	8.68	8.69	8.69	0.02	3
VCC 157	12 15 39.28	+13 54 05.7	-	-	8.75	-	8.78	8.77	0.05	2
VCC 159	12 15 41.50	+08 17 07.7	-	-	-	-	-	-	-	-
VCC 162	12 15 46.12	+10 41 53.7	-	-	8.22	-	8.23	8.23	0.01	2
VCC 167	12 15 54.22	+13 08 59.7	-	-	-	-	-	-	-	-
VCC 187	12 16 22.77	+13 18 27.9	-	-	8.60	8.55	8.60	8.58	0.07	3
VCC 220	12 17 06.50	+07 37 23.1	-	-	-	-	-	-	-	-
VCC 221	12 17 08.62	+03 40 50.1	8.74	8.72	8.64	8.67	8.65	8.69	0.12	5
VCC 226	12 17 11.34	+15 19 27.1	-	-	8.70	-	8.72	8.71	0.03	2
VCC 228	12 17 16.45	+12 47 42.1	8.58	8.55	8.55	8.55	8.54	8.56	0.04	5

Continued on next page...

Table E.3 – Continued

Name	R.A. (h m s)	Dec. (° ′ ″)	M91	Z94	D02	PP04 O3N2	PP04 N2	\bar{Z}	$E(\bar{Z})$	Methods
VCC 307	12 18 49.40	+14 24 59.6	-	-	8.71	8.78	8.74	8.75	0.09	3
VCC 318	12 19 03.40	+08 51 22.7	-	-	8.45	8.40	8.43	8.43	0.06	3
VCC 324	12 19 09.90	+03 51 20.0	8.40	8.26	8.19	8.19	8.20	8.25	0.24	5
VCC 334	12 19 14.10	+13 52 55.0	8.21	-	8.25	8.28	8.26	8.25	0.08	4
VCC 345	12 19 23.57	+05 49 32.8	-	-	-	-	-	-	-	-
VCC 355	12 19 30.70	+14 52 38.0	-	-	-	-	-	-	-	-
VCC 358	12 19 35.66	+05 50 47.9	-	-	-	-	-	-	-	-
VCC 369	12 19 45.59	+12 47 57.0	-	-	-	-	-	-	-	-
VCC 382	12 19 55.90	+05 20 34.0	-	-	-	-	-	-	-	-
VCC 386	12 20 03.70	+05 20 28.1	-	-	-	-	-	-	-	-
VCC 393	12 20 07.47	+07 41 28.1	-	-	8.61	-	8.61	8.61	0.01	2
UGC 7387	12 20 17.34	+04 12 06.0	-	-	-	-	-	-	-	-
NGC 4287	12 20 48.48	+05 38 23.4	-	-	8.73	-	8.75	8.74	0.04	2
NGC 4289	12 21 02.30	+03 43 20.0	-	-	-	-	-	-	-	-
VCC 459	12 21 11.46	+17 38 18.5	-	-	8.31	8.27	8.31	8.29	0.05	3
VCC 460	12 21 12.68	+18 22 56.5	-	-	-	-	-	-	-	-
VCC 465	12 21 17.82	+11 30 31.5	8.62	8.57	8.43	8.44	8.41	8.50	0.26	5
VCC 483	12 21 32.67	+14 36 22.6	-	-	8.75	-	8.78	8.77	0.05	2
VCC 491	12 21 40.20	+11 30 09.7	8.42	8.34	8.36	8.34	8.35	8.36	0.08	5
VCC 497	12 21 42.26	+14 35 51.7	-	-	-	-	-	-	-	-
VCC 508	12 21 54.84	+04 28 24.8	8.73	8.70	8.80	8.78	8.85	8.77	0.16	5
UGC 7422	12 22 01.30	+05 06 00.0	-	-	-	-	-	-	-	-
VCC 522	12 22 03.54	+12 44 27.8	-	-	-	-	-	-	-	-
VCC 523	12 22 04.23	+12 47 12.8	-	-	-	-	-	-	-	-
VCC 534	12 22 12.35	+07 08 38.9	-	-	-	-	-	-	-	-
VCC 538	12 22 14.94	+07 09 51.9	-	-	-	-	-	-	-	-
VCC 552	12 22 27.02	+04 34 00.0	8.32	8.24	8.31	8.29	8.31	8.29	0.09	5
VCC 559	12 22 31.29	+15 32 14.0	-	-	8.83	-	-	8.83	0.09	1
VCC 562	12 22 36.00	+12 09 28.0	8.13	-	8.15	8.18	8.17	8.16	0.05	4
VCC 596	12 22 54.82	+15 49 20.2	-	-	8.60	-	8.60	8.60	0.01	2
VCC 630	12 23 17.02	+11 22 07.3	-	-	8.66	-	8.68	8.67	0.02	2
VCC 634	12 23 19.89	+15 49 10.3	-	-	-	-	-	-	-	-
VCC 636	12 23 21.08	+15 52 04.3	-	-	-	-	-	-	-	-
VCC 655	12 23 37.45	+17 32 28.5	-	-	8.64	8.80	8.65	8.69	0.23	3
VCC 656	12 23 38.81	+06 57 14.5	-	-	-	-	-	-	-	-
VCC 664	12 23 44.36	+12 28 42.5	-	-	8.25	-	8.26	8.26	0.01	2
VCC 667	12 23 48.48	+07 11 11.5	-	-	8.46	-	8.45	8.46	0.01	2
VCC 685	12 23 57.82	+16 41 38.6	-	-	-	-	-	-	-	-
VCC 688	12 24 00.10	+07 47 05.6	-	-	8.31	-	8.31	8.31	0.01	2
VCC 692	12 24 01.37	+12 12 16.6	-	-	8.64	8.65	8.65	8.65	0.01	3
VCC 699	12 24 07.44	+06 36 26.7	-	-	8.54	-	8.53	8.53	0.01	2
NGC 4359	12 24 11.40	+31 31 18.0	-	-	8.54	8.46	8.53	8.51	0.11	3
VCC 713	12 24 14.10	+08 32 03.7	-	-	-	-	-	-	-	-
VCC 731	12 24 27.84	+07 19 04.8	-	-	-	-	-	-	-	-
VCC 758	12 24 54.71	+07 26 38.0	-	-	-	-	-	-	-	-
VCC 759	12 24 55.08	+11 42 16.0	-	-	-	-	-	-	-	-
VCC 762	12 25 02.80	+07 30 23.1	-	-	-	-	-	-	-	-
VCC 781	12 25 14.73	+12 42 53.2	-	-	-	-	-	-	-	-
VCC 787	12 25 18.10	+05 44 27.2	-	-	8.54	-	8.53	8.53	0.01	2
VCC 794	12 25 22.04	+16 25 47.2	-	-	-	-	-	-	-	-
VCC 792	12 25 22.07	+10 01 01.2	-	-	-	-	-	-	-	-
VCC 798	12 25 24.20	+18 11 23.3	-	-	-	-	-	-	-	-
VCC 801	12 25 25.43	+16 28 12.3	8.63	8.59	8.61	8.56	8.61	8.60	0.07	5
VCC 809	12 25 33.17	+12 15 36.3	-	-	8.55	8.53	8.54	8.54	0.02	3
VCC 828	12 25 41.69	+12 48 41.4	-	-	-	-	-	-	-	-
CGCG 014-034	12 25 42.64	+00 34 20.4	8.74	8.72	8.50	8.60	8.49	8.62	0.32	5
VCC 827	12 25 42.71	+07 12 55.4	-	8.17	8.50	8.42	8.49	8.38	0.43	4
VCC 836	12 25 46.60	+12 39 40.4	-	-	8.83	8.39	-	8.61	0.69	2
VCC 841	12 25 47.40	+14 57 12.0	8.54	8.48	8.34	8.37	8.33	8.42	0.26	5
VCC 849	12 25 50.59	+10 27 32.5	-	8.15	8.55	8.52	8.54	8.42	0.54	4
VCC 848	12 25 52.60	+05 48 36.0	-	-	8.43	-	8.41	8.42	0.01	2
VCC 851	12 25 54.16	+07 33 13.5	-	-	8.60	8.56	8.60	8.59	0.04	3
VCC 857	12 25 55.64	+18 12 49.5	-	-	-	-	-	-	-	-
VCC 865	12 25 59.19	+15 40 12.5	-	8.17	8.50	8.50	8.49	8.40	0.45	4
VCC 874	12 26 07.11	+16 10 51.6	-	-	8.80	-	8.85	8.83	0.08	2
VCC 873	12 26 07.32	+13 06 43.6	-	-	8.77	-	8.81	8.79	0.06	2
VCC 905	12 26 29.16	+08 52 16.8	-	-	8.68	8.60	8.69	8.66	0.13	3
VCC 912	12 26 32.16	+12 36 39.8	-	-	8.73	-	8.75	8.74	0.04	2
VCC 921	12 26 35.80	+03 57 56.8	-	-	8.82	8.76	-	8.79	0.09	2
VCC 938	12 26 46.67	+07 55 07.9	8.59	8.59	8.71	8.78	8.74	8.68	0.24	5
VCC 939	12 26 47.25	+08 53 03.9	-	8.17	8.63	8.65	8.63	8.50	0.65	4
VCC 945	12 26 51.06	+13 10 32.9	-	-	-	-	-	-	-	-

Continued on next page...

Table E.3 - Continued

Name	R.A.(h m s)	Dec.($^{\circ}$ '")	M91	Z94	D02	PP04 O3N2	PP04 N2	\bar{Z}	$E(\bar{Z})$	Methods
VCC 950	12 26 51.38	+11 33 16.9	-	-	8.50	-	8.49	8.50	0.01	2
VCC 951	12 26 54.36	+11 40 06.0	-	-	-	-	-	-	-	-
VCC 958	12 26 56.30	+15 02 48.0	-	-	-	-	-	-	-	-
VCC 957	12 26 58.58	+02 29 42.0	8.65	8.63	8.61	8.60	8.61	8.62	0.05	5
VCC 973	12 27 08.70	+16 19 33.1	-	-	8.71	8.58	8.74	8.68	0.21	3
VCC 971	12 27 08.93	+05 52 48.1	8.35	-	8.31	8.32	8.31	8.32	0.05	4
VCC 975	12 27 11.04	+07 15 47.1	-	-	8.36	-	8.35	8.35	0.01	2
VCC 980	12 27 11.26	+15 53 50.1	-	-	8.40	8.38	8.39	8.39	0.03	3
VCC 979	12 27 11.65	+09 25 15.1	-	-	-	-	-	-	-	-
VCC 984	12 27 13.30	+12 44 05.1	-	-	-	-	-	-	-	-
VCC 995	12 27 21.55	+10 51 55.2	-	-	8.11	8.13	8.13	8.13	0.02	3
VCC 1003	12 27 26.31	+11 06 29.2	-	-	-	-	-	-	-	-
VCC 1002	12 27 26.37	+06 15 44.2	-	-	8.83	-	-	8.83	0.09	1
VCC 1010	12 27 26.65	+12 17 27.2	-	-	-	-	-	-	-	-
VCC 1018	12 27 32.87	+06 13 54.3	-	-	-	-	-	-	-	-
VCC 1028	12 27 38.33	+14 27 24.3	-	-	-	-	-	-	-	-
VCC 1030	12 27 40.42	+13 04 44.3	-	-	-	-	-	-	-	-
VCC 1036	12 27 42.23	+12 18 54.4	-	-	-	-	-	-	-	-
VCC 1043	12 27 45.52	+13 00 31.4	-	-	-	-	-	-	-	-
VCC 1047	12 27 53.52	+12 17 35.5	-	-	-	-	-	-	-	-
UGC 7579	12 27 55.40	+05 43 16.0	-	-	8.54	8.52	8.53	8.53	0.02	3
VCC 1062	12 28 03.66	+09 48 17.5	-	-	-	-	-	-	-	-
VCC 1068	12 28 06.23	+12 04 42.6	-	-	-	-	-	-	-	-
VCC 1073	12 28 08.53	+12 05 35.6	-	-	-	-	-	-	-	-
VCC 1086	12 28 16.00	+09 26 10.6	-	-	-	-	-	-	-	-
VCC 1091	12 28 18.70	+08 43 46.7	8.28	8.21	8.31	8.30	8.31	8.28	0.11	5
VCC 1110	12 28 29.27	+17 05 06.8	-	-	-	-	-	-	-	-
VCC 1107	12 28 30.29	+07 19 30.8	-	-	-	-	-	-	-	-
VCC 1118	12 28 40.50	+09 15 32.9	-	-	8.70	8.80	8.72	8.74	0.13	3
VCC 1125	12 28 43.34	+11 45 20.9	-	-	-	-	-	-	-	-
VCC 1146	12 28 57.51	+13 14 31.0	-	-	-	-	-	-	-	-
VCC 1145	12 28 59.20	+03 34 16.0	-	-	-	-	-	-	-	-
VCC 1154	12 29 00.00	+13 58 45.0	-	-	-	-	-	-	-	-
VCC 1158	12 29 03.01	+13 11 01.1	-	-	-	-	-	-	-	-
VCC 1189	12 29 28.83	+06 46 12.3	8.27	8.27	8.52	8.48	8.51	8.40	0.35	5
VCC 1192	12 29 30.35	+07 59 38.3	-	-	-	-	-	-	-	-
VCC 1193	12 29 30.59	+07 41 48.3	8.51	8.50	8.60	8.57	8.60	8.55	0.13	5
VCC 1196	12 29 31.25	+14 02 58.3	-	-	-	-	-	-	-	-
VCC 1200	12 29 34.53	+10 47 37.3	-	-	-	-	-	-	-	-
VCC 1203	12 29 37.35	+07 56 01.4	-	-	-	-	-	-	-	-
VCC 1205	12 29 37.87	+07 49 24.4	8.55	8.53	8.61	8.63	8.61	8.58	0.12	5
VCC 1217	12 29 42.54	+11 24 04.4	-	-	-	-	-	-	-	-
VCC 1226	12 29 46.80	+08 00 00.0	-	-	-	-	-	-	-	-
VCC 1231	12 29 48.82	+13 25 45.5	-	-	-	-	-	-	-	-
VCC 1242	12 29 53.32	+14 04 05.5	-	-	-	-	-	-	-	-
VCC 1253	12 30 02.37	+13 38 10.6	-	-	-	-	-	-	-	-
VCC 1254	12 30 05.31	+08 04 28.6	-	-	-	-	-	-	-	-
VCC 1283	12 30 18.46	+13 34 40.7	-	-	-	-	-	-	-	-
VCC 1290	12 30 26.47	+04 14 52.8	-	-	8.60	-	8.60	8.60	0.01	2
VCC 1297	12 30 31.82	+12 29 25.9	-	-	-	-	-	-	-	-
VCC 1316	12 30 49.41	+12 23 28.0	-	-	-	-	-	-	-	-
VCC 1326	12 30 57.15	+11 28 59.1	-	-	-	-	-	-	-	-
VCC 1327	12 30 57.72	+12 16 16.1	-	-	-	-	-	-	-	-
VCC 1340	12 30 59.58	+08 04 39.1	-	-	-	-	-	-	-	-
VCC 1348	12 31 15.70	+12 19 54.3	-	-	-	-	-	-	-	-
VCC 1356	12 31 22.92	+11 29 34.3	8.30	-	8.15	8.19	8.17	8.21	0.18	4
VCC 1368	12 31 32.79	+11 37 36.4	-	-	-	-	-	-	-	-
VCC 1379	12 31 39.62	+16 51 07.5	-	-	-	-	-	-	-	-
VCC 1393	12 31 54.69	+15 07 26.6	-	-	8.61	8.70	8.61	8.64	0.13	3
VCC 1401	12 31 58.91	+14 25 09.7	-	-	-	-	-	-	-	-
VCC 1410	12 32 03.22	+16 41 14.7	-	-	8.52	-	8.51	8.51	0.01	2
VCC 1411	12 32 04.83	+11 49 02.7	-	-	-	-	-	-	-	-
VCC 1412	12 32 06.13	+11 10 34.8	-	-	-	-	-	-	-	-
VCC 1419	12 32 10.46	+13 25 09.8	-	-	8.76	-	8.80	8.78	0.06	2
VCC 1426	12 32 22.80	+11 53 38.9	-	-	-	-	-	-	-	-
VCC 1448	12 32 40.83	+12 46 13.1	-	-	-	-	-	-	-	-
VCC 1450	12 32 41.91	+14 02 56.1	-	-	8.58	-	8.58	8.58	0.01	2
CGCG 014-063	12 32 45.48	+00 06 43.1	8.40	8.33	8.61	8.55	8.61	8.49	0.35	5
VCC 1486	12 33 09.94	+11 20 49.4	-	-	8.34	8.45	8.33	8.37	0.18	3
VCC 1491	12 33 13.98	+12 51 27.4	-	-	-	-	-	-	-	-
VCC 1499	12 33 19.77	+12 51 11.5	-	-	-	-	-	-	-	-
VCC 1508	12 33 30.18	+08 39 16.6	8.29	8.27	8.55	8.49	8.54	8.42	0.38	5

Continued on next page...

Table E.3 – Continued

Name	R.A.(h m s)	Dec.($^{\circ}$ '")	M91	Z94	D02	PP04 O3N2	PP04 N2	Z	E(Z)	Methods
VCC 1516	12 33 39.78	+09 10 30.7	-	-	8.76	8.67	8.80	8.74	0.17	3
VCC 1524	12 33 47.74	+15 10 01.8	-	-	8.40	-	8.39	8.40	0.01	2
NGC 4525	12 33 51.13	+30 16 38.9	-	-	8.61	8.57	8.61	8.60	0.06	3
VCC 1532	12 33 56.79	+15 21 16.9	-	-	8.66	8.74	8.68	8.69	0.09	3
VCC 1540	12 34 08.46	+02 39 11.0	-	-	-	-	-	-	-	-
VCC 1552	12 34 15.77	+13 04 29.1	-	-	-	-	-	-	-	-
VCC 1554	12 34 19.31	+06 28 07.1	8.39	8.32	8.34	8.33	8.33	8.34	0.07	5
VCC 1569	12 34 31.68	+13 30 13.2	-	-	8.15	8.23	8.17	8.19	0.11	3
VCC 1575	12 34 39.28	+07 09 38.3	-	-	8.66	8.90	8.68	8.75	0.34	3
VCC 1581	12 34 44.93	+06 18 07.4	-	-	8.15	-	8.17	8.16	0.02	2
VCC 1588	12 34 50.48	+15 33 05.4	-	-	8.75	-	8.78	8.77	0.05	2
VCC 1593	12 34 55.87	+15 33 56.5	8.66	8.63	8.77	8.63	8.81	8.69	0.23	5
VCC 1615	12 35 26.33	+14 29 48.8	-	-	-	-	-	-	-	-
VCC 1619	12 35 30.84	+12 13 16.9	-	-	-	-	-	-	-	-
VCC 1630	12 35 38.13	+12 15 55.9	-	-	-	-	-	-	-	-
VCC 1632	12 35 39.87	+12 33 25.0	-	-	-	-	-	-	-	-
NGC 4561	12 36 08.30	+19 19 20.0	8.51	8.42	8.34	8.32	8.33	8.39	0.22	5
VCC 1673	12 36 32.66	+11 15 28.6	-	-	8.71	-	8.74	8.73	0.04	2
VCC 1676	12 36 34.16	+11 14 19.6	-	-	8.74	8.86	8.77	8.79	0.16	3
VCC 1675	12 36 34.65	+08 03 17.6	-	-	8.48	-	8.47	8.48	0.01	2
VCC 1678	12 36 37.61	+06 37 16.6	8.28	8.24	8.31	8.31	8.31	8.29	0.08	5
VCC 1683	12 36 38.31	+10 56 29.6	-	-	-	-	-	-	-	-
VCC 1686	12 36 43.57	+13 15 31.7	-	-	8.50	8.44	8.49	8.48	0.08	3
VCC 1690	12 36 49.78	+13 09 45.7	-	-	-	-	-	-	-	-
VCC 1699	12 37 02.24	+06 55 30.9	-	-	8.31	-	8.31	8.31	0.01	2
VCC 1725	12 37 41.51	+08 33 31.3	-	-	8.38	-	8.37	8.38	0.01	2
VCC 1727	12 37 43.48	+11 49 04.4	-	-	-	-	-	-	-	-
VCC 1726	12 37 45.08	+07 06 22.4	-	-	-	-	-	-	-	-
VCC 1730	12 37 48.60	+05 22 06.4	-	-	8.86	-	-	8.86	0.09	1
VCC 1757	12 38 17.79	+13 06 35.8	-	-	-	-	-	-	-	-
VCC 1758	12 38 20.81	+07 53 28.8	-	-	8.22	8.33	8.23	8.26	0.15	3
NGC 4592	12 39 18.73	-00 31 55.0	-	8.14	8.43	8.41	8.41	8.34	0.38	4
VCC 1789	12 39 21.34	+04 56 19.5	-	-	-	-	-	-	-	-
VCC 1791	12 39 24.55	+07 57 52.5	-	-	-	-	-	-	-	-
VCC 1811	12 39 51.63	+15 17 53.9	-	-	8.66	8.62	8.68	8.65	0.07	3
VCC 1813	12 39 55.88	+10 10 34.9	-	-	-	-	-	-	-	-
VCC 1859	12 40 57.47	+11 54 41.7	-	-	-	-	-	-	-	-
VCC 1868	12 41 12.26	+11 53 08.9	-	-	8.80	-	8.85	8.83	0.08	2
VCC 1869	12 41 13.52	+10 09 22.9	-	-	-	-	-	-	-	-
VCC 1903	12 42 02.46	+11 38 48.5	-	-	-	-	-	-	-	-
VCC 1918	12 42 18.10	+05 44 21.7	-	-	-	-	-	-	-	-
CGCG 014-110	12 42 31.91	-00 04 57.0	-	-	8.38	-	8.37	8.38	0.01	2
NGC 4629	12 42 32.67	-01 21 02.0	8.32	8.26	8.43	8.38	8.41	8.36	0.18	5
VCC 1929	12 42 37.12	+14 21 22.4	-	8.19	8.52	8.49	8.51	8.41	0.43	4
VCC 1932	12 42 40.83	+14 17 46.0	8.38	8.34	8.80	8.71	8.85	8.60	0.66	5
VCC 1938	12 42 47.66	+11 26 34.1	-	-	-	8.62	-	-	-	-
VCC 1943	12 42 52.35	+13 15 26.2	-	-	-	-	-	8.62	0.10	1
VCC 1970	12 43 29.11	+10 05 34.7	-	-	-	-	8.66	8.66	0.01	2
VCC 1972	12 43 32.28	+11 34 54.7	-	-	8.65	-	-	8.66	0.01	2
VCC 1978	12 43 39.58	+11 33 09.8	-	-	-	-	-	-	-	-
CGCG 100-004	12 43 42.47	+16 23 34.8	8.68	8.66	8.83	8.74	8.74	8.72	0.19	4
VCC 1987	12 43 56.71	+13 07 34.0	-	-	8.65	8.69	8.66	8.67	0.04	3
VCC 1992	12 44 10.02	+12 06 59.2	-	-	-	-	-	-	-	-
VCC 1999	12 44 29.38	+13 29 53.5	-	-	-	-	-	-	-	-
VCC 2000	12 44 32.31	+11 11 26.5	-	-	-	-	-	-	-	-
VCC 2006	12 44 45.93	+12 21 11.7	-	-	-	-	-	-	-	-
NGC 4668	12 45 31.98	-00 32 08.6	-	-	8.46	8.40	8.45	8.44	0.09	3
VCC 2033	12 46 04.76	+08 28 30.8	8.51	8.45	8.34	8.37	8.33	8.40	0.22	5
VCC 2037	12 46 15.30	+10 12 21.0	8.26	-	8.28	8.34	8.28	8.29	0.09	4
VCC 2058	12 47 45.39	+13 45 48.3	-	-	8.73	-	8.75	8.74	0.04	2
VCC 2066	12 48 15.05	+10 59 06.7	-	-	-	-	-	-	-	-
CGC 45	12 48 22.83	-41 07 24.7	-	-	-	-	-	-	-	-
VCC 2070	12 48 22.96	+08 29 13.8	-	-	-	-	-	-	-	-
CGCG 043-034	12 49 11.87	+03 23 24.5	-	8.25	8.58	8.54	8.58	8.48	0.44	4
CGC 94	12 49 25.48	-41 25 46.5	-	-	-	-	-	-	-	-
CGC 95	12 49 26.19	-41 29 23.5	-	-	-	-	-	-	-	-
CGC 96	12 49 26.69	-41 27 47.8	-	-	-	-	-	-	-	-
CGCG 100-011	12 49 38.89	+15 09 55.0	-	-	-	-	-	-	-	-
CGC 119	12 49 51.58	-41 13 34.2	-	-	-	-	-	-	-	-
CGC 122	12 49 54.15	-41 16 46.4	-	-	-	-	-	-	-	-
UGC 7991	12 50 38.95	+01 27 52.2	-	-	8.55	-	8.54	8.55	0.01	2
NGC 4731	12 51 00.86	-06 23 28.4	8.52	8.50	8.57	8.55	8.56	8.54	0.08	5

Continued on next page...

Table E.3 – Continued

Name	R.A. (h. m. s)	Dec. ($^{\circ}$ ' '')	M91	Z94	D02	PP04 O3N2	PP04 N2	Z	E(Z)	Methods
VCC 2087	12 51 06.81	+10 54 44.3	-	-	-	-	-	-	-	-
NGC 4747	12 51 46.95	+25 46 37.4	8.55	8.50	8.52	8.45	8.51	8.51	0.09	5
CGCG 071-060	12 51 55.15	+12 05 00.1	-	-	8.70	8.57	8.72	8.67	0.21	3
CCC 222	12 52 12.85	-41 20 20.7	-	-	8.76	-	8.80	8.78	0.06	2
CCC 226	12 52 15.98	-41 23 26.4	-	-	-	-	-	-	-	-
VCC 2092	12 52 17.64	+11 18 48.4	-	-	-	-	-	-	-	-
NGC 4753	12 52 22.00	-01 11 59.0	-	-	-	-	-	-	-	-
VCC 2095	12 52 56.92	+11 13 50.1	-	-	-	-	-	-	-	-
NGC 4791	12 54 43.96	+08 03 10.6	-	-	-	-	-	-	-	-
UGC 8032	12 54 44.19	+13 14 14.1	-	-	-	-	-	-	-	-
UGC 8045	12 55 23.50	+07 54 35.0	-	-	8.65	8.63	8.66	8.65	0.04	3
CGCG 043-071	12 55 49.50	+04 18 14.0	8.50	8.48	8.79	8.65	8.84	8.64	0.44	5
CGCG 160-020	12 56 06.05	+27 40 39.9	-	-	8.52	-	8.51	8.51	0.01	2
CGCG 160-026	12 56 28.56	+27 17 29.2	-	-	8.64	8.68	8.65	8.66	0.05	3
IC 3908	12 56 40.28	-07 33 27.1	-	-	8.76	8.69	8.80	8.75	0.14	3
CGCG 160-055	12 58 05.55	+28 14 32.8	8.81	8.81	8.84	8.74	-	8.80	0.10	4
CGCG 160-058	12 58 09.48	+28 42 29.5	-	-	8.71	8.72	8.74	8.72	0.03	3
CGCG 160-064	12 58 35.33	+27 15 51.5	8.54	8.51	8.57	8.54	8.56	8.54	0.05	5
CGCG 160-067	12 58 37.17	+27 10 36.0	8.58	8.56	8.63	8.59	8.63	8.59	0.08	5
CGCG 160-212	12 58 56.12	+27 50 00.9	-	-	-	-	-	-	-	-
CGCG 160-213	12 59 02.07	+28 06 55.6	-	-	8.74	8.74	8.77	8.75	0.04	3
CGCG 160-215	12 59 03.95	+28 07 24.5	-	-	-	-	-	-	-	-
CGCG 160-219	12 59 07.84	+27 51 16.5	-	-	-	-	-	-	-	-
CGCG 071-092	12 59 27.14	+14 10 15.8	-	-	-	-	-	-	-	-
CGCG 160-076	12 59 40.23	+28 37 51.2	8.54	8.48	8.40	8.40	8.39	8.45	0.17	5
CGCG 160-241	13 00 08.00	+27 58 35.0	-	-	-	-	-	-	-	-
CGCG 160-086	13 00 33.58	+27 38 14.2	8.45	8.45	8.61	8.61	8.61	8.54	0.24	5
CGCG 160-252	13 00 37.74	+28 03 28.2	8.74	8.72	8.81	8.70	8.87	8.76	0.18	5
CGCG 043-093	13 00 39.34	+02 30 02.2	8.70	8.68	-	8.74	-	8.70	0.07	3
CGCG 160-088	13 00 39.63	+29 01 11.1	-	-	-	-	-	-	-	-
CGCG 160-258	13 00 51.51	+28 02 33.5	-	-	-	-	-	-	-	-
CGCG 160-260	13 00 56.10	+27 47 27.5	-	-	8.80	-	8.85	8.83	0.08	2
NGC 4904	13 01 26.09	-00 01 39.4	-	-	8.69	8.64	8.71	8.68	0.09	3
CGCG 160-095	13 01 26.09	+27 53 08.1	-	-	-	-	-	-	-	-
CGCG 160-097	13 01 31.69	+27 50 49.2	-	-	-	-	-	-	-	-
CGCG 160-103	13 01 53.62	+27 37 26.6	-	-	-	-	-	-	-	-
CGCG 160-106	13 02 07.89	+27 38 54.3	-	-	8.78	8.75	8.83	8.79	0.10	3
CGCG 160-108	13 02 12.74	+28 12 52.9	8.82	8.82	8.71	8.72	8.74	8.76	0.14	5
CGCG 160-110	13 02 21.41	+28 13 49.2	-	-	-	-	-	-	-	-
NGC 4941	13 04 12.88	-05 33 06.7	-	-	-	-	-	-	-	-
CGCG 160-128	13 04 22.57	+28 48 38.5	8.40	8.35	8.43	8.41	8.41	8.40	0.07	5
CGCG 160-127	13 04 26.46	+27 18 16.7	8.47	8.41	8.45	8.41	8.43	8.43	0.06	5
CGCG 160-139	13 06 37.92	+28 50 59.1	8.54	8.43	8.34	8.30	8.33	8.39	0.27	5
NGC 5145	13 25 13.91	+43 16 02.1	-	-	8.77	8.94	8.81	8.84	0.22	3
NGC 5147	13 26 19.73	+02 06 03.0	-	-	8.54	8.51	8.53	8.53	0.02	3
IC 902	13 36 01.21	+49 57 39.0	-	-	8.69	8.66	8.71	8.68	0.07	3
NGC 5301	13 46 24.67	+46 06 25.4	-	-	8.64	8.55	8.65	8.61	0.14	3
NGC 5303	13 47 44.99	+38 18 16.6	8.55	8.52	8.63	8.57	8.63	8.58	0.12	5
NGC 5300	13 48 16.03	+03 57 03.1	-	-	8.71	8.66	8.74	8.71	0.09	3
UGC 8756	13 50 35.88	+42 32 29.5	-	-	-	-	-	-	-	-
NGC 5334	13 52 54.45	-01 06 52.6	-	-	8.73	8.60	8.75	8.69	0.20	3
NGC 5348	13 54 11.30	+05 13 39.0	-	-	8.52	8.48	8.51	8.50	0.04	3
NGC 5372	13 54 45.99	+58 40 00.7	8.66	8.64	8.73	8.68	8.75	8.69	0.12	5
NGC 5356	13 54 58.45	+05 20 01.4	-	-	-	-	-	-	-	-
NGC 5360	13 55 38.75	+04 59 06.2	-	-	8.70	8.75	8.72	8.73	0.06	3
UGC 8857	13 56 26.61	+04 23 48.0	-	-	8.66	8.49	8.68	8.61	0.27	3
NGC 5486	14 07 24.96	+55 06 11.0	-	-	8.40	-	8.39	8.40	0.01	2
NGC 5560	14 20 04.40	+03 59 33.0	-	-	8.77	8.73	8.81	8.77	0.11	3
NGC 5577	14 21 13.20	+03 26 10.0	-	-	8.63	8.63	8.63	8.63	0.01	3
UGC 9215	14 23 27.11	+01 43 34.6	8.29	8.25	8.48	8.41	8.47	8.37	0.29	5
UGC 9242	14 25 21.02	+39 32 22.4	8.49	8.40	8.28	8.28	8.28	8.35	0.26	5
IC 1022	14 30 01.84	+03 46 22.3	-	-	8.63	8.57	8.63	8.61	0.08	3
NGC 5669	14 32 44.00	+09 53 31.0	8.38	8.36	8.57	8.50	8.56	8.47	0.26	5
NGC 5668	14 33 24.33	+04 27 01.7	8.70	8.67	8.57	8.54	8.56	8.61	0.19	5
NGC 5692	14 38 18.11	+03 24 37.1	8.64	8.61	8.63	8.59	8.63	8.62	0.05	5
IC 1048	14 42 58.01	+04 53 22.5	-	-	8.71	8.67	8.74	8.71	0.08	3

BIBLIOGRAPHY

- Abazajian K. N., Adelman-McCarthy J. K., Agüeros M. A., Allam S. S., Allende Prieto C., An D., Anderson K. S. J., Anderson S. F., et al. 2009, *ApJS*, 182, 543
- Alloin D., Collin-Souffrin S., Joly M., Vigroux L., 1979, *A&A*, 78, 200
- Anderson S. F., Voges W., Margon B., Trümper J., Agüeros M. A., Boller T., Collinge M. J., Homer L., et al. 2003, *AJ*, 126, 2209
- Arnouts S., Walcher C. J., Le Fèvre O., Zamorani G., Ilbert O., Le Brun V., Pozzetti L., Bardelli S., et al. 2007, *A&A*, 476, 137
- Athanassoula E., Bosma A., Creze M., Schwarz M. P., 1982, *A&A*, 107, 101
- Baes M., Buyle P., Hau G. K. T., Dejonghe H., 2003, *MNRAS*, 341, L44
- Baldry I. K., Glazebrook K., Brinkmann J., Ivezić Ž., Lupton R. H., Nichol R. C., Szalay A. S., 2004, *ApJ*, 600, 681
- Baldwin J. A., Phillips M. M., Terlevich R., 1981, *PASP*, 93, 5
- Barth A. J., Ho L. C., Rutledge R. E., Sargent W. L. W., 2004, *ApJ*, 607, 90
- Baugh C. M., 2006, *Reports on Progress in Physics*, 69, 3101
- Baugh C. M., Cole S., Frenk C. S., 1996, *MNRAS*, 283, 1361
- Baugh C. M., Cole S., Frenk C. S., Lacey C. G., 1998, *ApJ*, 498, 504
- Bekki K., Couch W. J., 2003, *ApJL*, 596, L13
- Bekki K., Couch W. J., Shioya Y., 2002, *ApJ*, 577, 651
- Bell E. F., de Jong R. S., 2001, *ApJ*, 550, 212
- Bell E. F., McIntosh D. H., Katz N., Weinberg M. D., 2003, *ApJS*, 149, 289

- Bell E. F., Zheng X. Z., Papovich C., Borch A., Wolf C., Meisenheimer K., 2007, *ApJ*, 663, 834
- Benson A. J., Lacey C. G., Baugh C. M., Cole S., Frenk C. S., 2002, *MNRAS*, 333, 156
- Bertola F., Buson L. M., Zeilinger W. W., 1988, *Nature*, 335, 705
- Bertola F., Capaccioli M., Oke J. B., 1982, *ApJ*, 254, 494
- Bertola F., Corsini E. M., Vega Beltrán J. C., Pizzella A., Sarzi M., Cappellari M., Funes J. G., 1999, *ApJL*, 519, L127
- Bettoni D., Galletta G., Sage L. J., 1993, *A&A*, 280, 121
- Binggeli B., Cameron L. M., 1991, *A&A*, 252, 27
- Binggeli B., Sandage A., Tammann G. A., 1985, *AJ*, 90, 1681
- Birnbom Y., Dekel A., Neistein E., 2007, *MNRAS*, 380, 339
- Blumenthal G. R., Faber S. M., Primack J. R., Rees M. J., 1984, *Nature*, 311, 517
- Böhringer H., Briel U. G., Schwarz R. A., Voges W., Hartner G., Trümper J., 1994, *Nature*, 368, 828
- Booth C. M., Schaye J., 2010, *MNRAS*, 405, L1
- Boselli A., Boissier S., Cortese L., Buat V., Hughes T. M., Gavazzi G., 2009, *ApJ*, 706, 1527
- Boselli A., Boissier S., Cortese L., Gavazzi G., 2008, *ApJ*, 674, 742
- Boselli A., Boissier S., Cortese L., Gil de Paz A., Buat V., Iglesias-Paramo J., Madore B. F., Barlow T., et al. 2005, *ApJL*, 623, L13
- Boselli A., Boissier S., Cortese L., Gil de Paz A., Seibert M., Madore B. F., Buat V., Martin D. C., 2006, *ApJ*, 651, 811
- Boselli A., Cortese L., Deharveng J. M., Gavazzi G., Yi K. S., Gil de Paz A., Seibert M., Boissier S., Donas J., Lee Y., Madore B. F., Martin D. C., Rich R. M., Sohn Y., 2005, *ApJL*, 629, L29
- Boselli A., Eales S., Cortese L., Bendo G., Chanical P., Buat V., Davies J., Auld R., et al. 2010, *PASP*, 122, 261

- Boselli A., Gavazzi G., 2006, *PASP*, 118, 517
- Boselli A., Gavazzi G., Donas J., Scodreggio M., 2001, *AJ*, 121, 753
- Boselli A., Gavazzi G., Franzetti P., Pierini D., Scodreggio M., 2000, *A&AS*, 142, 73
- Boselli A., Lequeux J., Gavazzi G., 2002, *A&A*, 384, 33
- Boselli A., Sauvage M., Lequeux J., Donati A., Gavazzi G., 2003, *A&A*, 406, 867
- Boselli A., Tuffs R. J., Gavazzi G., Hippelein H., Pierini D., 1997, *A&AS*, 121, 507
- Bower R. G., Benson A. J., Malbon R., Helly J. C., Frenk C. S., Baugh C. M., Cole S., Lacey C. G., 2006, *MNRAS*, 370, 645
- Bravo-Alfaro H., Cayatte V., van Gorkom J. H., Balkowski C., 2000, *AJ*, 119, 580
- Bresolin F., 2006, *ArXiv astro-ph/0608410*
- Bresolin F., 2007, *ApJ*, 656, 186
- Bridle A. H., Hough D. H., Lonsdale C. J., Burns J. O., Laing R. A., 1994, *AJ*, 108, 766
- Brown W. R., Geller M. J., Kenyon S. J., Kurtz M. J., 2006, *ApJ*, 647, 303
- Bruzual G., Charlot S., 2003, *MNRAS*, 344, 1000
- Buat V., 1992, *A&A*, 264, 444
- Buat V., Xu C., 1996, *A&A*, 306, 61
- Bullock J. S., Dekel A., Kolatt T. S., Kravtsov A. V., Klypin A. A., Porciani C., Primack J. R., 2001, *ApJ*, 555, 240
- Burstein D., Bertola F., Buson L. M., Faber S. M., Lauer T. R., 1988, *ApJ*, 328, 440
- Buta R., 1995, *ApJS*, 96, 39
- Byrd G., Valtonen M., 1990, *ApJ*, 350, 89
- Calura F., Pipino A., Chiappini C., Matteucci F., Maiolino R., 2009, *A&A*, 504, 373
- Carroll S. M., 2004, in R. E. Allen, D. V. Nanopoulos, & C. N. Pope ed., *The New Cosmology: Conference on Strings and Cosmology Vol. 743 of American Institute of Physics Conference Series, Why is the Universe Accelerating?*. pp 16–32

- Cayatte V., Kotanyi C., Balkowski C., van Gorkom J. H., 1994, *AJ*, 107, 1003
- Cayatte V., van Gorkom J. H., Balkowski C., Kotanyi C., 1990, *AJ*, 100, 604
- Code A. D., 1969, *PASP*, 81, 475
- Cole S., Lacey C., 1996, *MNRAS*, 281, 716
- Cole S., Norberg P., Baugh C. M., Frenk C. S., Bland-Hawthorn J., Bridges T., Cannon R., Colless M., et al. 2001, *MNRAS*, 326, 255
- Colless M., Dalton G., Maddox S., Sutherland W., Norberg P., Cole S., Bland-Hawthorn J., Bridges T., et al. 2001, *MNRAS*, 328, 1039
- Cortese L., Boselli A., Buat V., Gavazzi G., Boissier S., Gil de Paz A., Seibert M., Madore B. F., Martin D. C., 2006, *ApJ*, 637, 242
- Cortese L., Boselli A., Franzetti P., Decarli R., Gavazzi G., Boissier S., Buat V., 2008, *MNRAS*, 386, 1157
- Cortese L., Boselli A., Gavazzi G., Iglesias-Paramo J., Madore B. F., Barlow T., Bianchi L., Byun Y., et al. 2005, *ApJL*, 623, L17
- Cortese L., Davies J. I., Pohlen M., et al. 2010, *A&A*, 518, L49+
- Cortese L., Gavazzi G., Boselli A., Franzetti P., Kennicutt R. C., O'Neil K., Sakai S., 2006, *A&A*, 453, 847
- Cortese L., Hughes T. M., 2009, *MNRAS*, 400, 1225
- Cowie L. L., Songaila A., 1977, *Nature*, 266, 501
- Croton D. J., Springel V., White S. D. M., De Lucia G., Frenk C. S., Gao L., Jenkins A., Kauffmann G., Navarro J. F., Yoshida N., 2006, *MNRAS*, 365, 11
- Crowl H. H., Kenney J. D. P., 2008, *AJ*, 136, 1623
- Cutri R. M., Nelson B. O., Francis P. J., Smith P. S., 2002, in R. F. Green, E. Y. Khachikian, & D. B. Sanders ed., *IAU Colloq. 184: AGN Surveys Vol. 284 of Astronomical Society of the Pacific Conference Series, The 2MASS Red AGN Survey*. pp 127–+
- Dalcanton J. J., 2007, *ApJ*, 658, 941

- Dalla Vecchia C., Bower R. G., Theuns T., Balogh M. L., Mazzotta P., Frenk C. S., 2004, MNRAS, 355, 995
- Davé R., Oppenheimer B. D., 2007, MNRAS, 374, 427
- Davis M., Efstathiou G., Frenk C. S., White S. D. M., 1985, ApJ, 292, 371
- de Blok W. J. G., McGaugh S. S., 1998, ApJ, 508, 132
- De Lucia G., Kauffmann G., White S. D. M., 2004, MNRAS, 349, 1101
- de Rossi M. E., Tissera P. B., Scannapieco C., 2007, MNRAS, 374, 323
- Decarli R., Gavazzi G., Arosio I., Cortese L., Boselli A., Bonfanti C., Colpi M., 2007, MNRAS, 381, 136
- Denicoló G., Terlevich R., Terlevich E., 2002, MNRAS, 330, 69
- Desai V., Dalcanton J. J., Aragón-Salamanca A., Jablonka P., Poggianti B., Gogarten S. M., Simard L., Milvang-Jensen B., Rudnick G., Zaritsky D., Clowe D., Halliday C., Pelló R., Saglia R., White S., 2007, ApJ, 660, 1151
- Díaz A. I., Pérez-Montero E., 2000, MNRAS, 312, 130
- Dopita M. A., Evans I. N., 1986, ApJ, 307, 431
- Dors Jr. O. L., Copetti M. V. F., 2006, A&A, 452, 473
- Draine B. T., Dale D. A., Bendo G., Gordon K. D., Smith J. D. T., Armus L., Engelbracht C. W., Helou G., et al. 2007, ApJ, 663, 866
- Dressler A., 1980, ApJ, 236, 351
- Dressler A., Oemler Jr. A., Couch W. J., Smail I., Ellis R. S., Barger A., Butcher H., Poggianti B. M., Sharples R. M., 1997, ApJ, 490, 577
- Dreyer J. L. E., 1888, Mem. RAS, 49, 1
- Dreyer J. L. E., 1908, Mem. RAS, 59, 105
- Drory N., Fisher D. B., 2007, ApJ, 664, 640
- Drory N., Salvato M., Gabasch A., Bender R., Hopp U., Feulner G., Pannella M., 2005, ApJL, 619, L131
- Edmunds M. G., 1990, MNRAS, 246, 678

- Edmunds M. G., 2001, MNRAS, 328, 223
- Edmunds M. G., Pagel B. E. J., 1984, MNRAS, 211, 507
- Ellison S. L., Simard L., Cowan N. B., Baldry I. K., Patton D. R., McConnachie A. W., 2009, MNRAS, 396, 1257
- Elmegreen B. G., Bournaud F., Elmegreen D. M., 2008, ApJ, 688, 67
- Erb D. K., 2008, ApJ, 674, 151
- Erb D. K., Shapley A. E., Pettini M., Steidel C. C., Reddy N. A., Adelberger K. L., 2006, ApJ, 644, 813
- Faber S. M., Willmer C. N. A., Wolf C., Koo D. C., Weiner B. J., Newman J. A., Im M., Coil A. L., Conroy C., 2007, ApJ, 665, 265
- Ferland G. J., Korista K. T., Verner D. A., Ferguson J. W., Kingdon J. B., Verner E. M., 1998, PASP, 110, 761
- Ferrarese L., Ford H., 2005, Space Sci. Rev., 116, 523
- Ferrarese L., Merritt D., 2000, ApJL, 539, L9
- Fine S., Croom S. M., Miller L., Babic A., Moore D., Brewer B., Sharp R. G., Boyle B. J., Shanks T., Smith R. J., Outram P. J., Loaring N. S., 2006, MNRAS, 373, 613
- Fioc M., Rocca-Volmerange B., 1997, A&A, 326, 950
- Forman W., Jones C., Churazov E., Markevitch M., Nulsen P., Vikhlinin A., Begelman M., Böhringer H., Eilek J., Heinz S., Kraft R., Owen F., Pahre M., 2007, ApJ, 665, 1057
- Frayser D. T., Brown R. L., 1997, ApJS, 113, 221
- Freeman K. C., 1970, ApJ, 160, 811
- Fujita Y., 2004, PASJ, 56, 29
- Fumagalli M., Krumholz M. R., Prochaska J. X., Gavazzi G., Boselli A., 2009, ApJ, 697, 1811
- Garnett D. R., 2002, ApJ, 581, 1019

- Garnett D. R., Shields G. A., Skillman E. D., Sagan S. P., Dufour R. J., 1997, *ApJ*, 489, 63
- Gavazzi G., 1989, *ApJ*, 346, 59
- Gavazzi G., Bonfanti C., Sanvito G., Boselli A., Scodreggio M., 2002, *ApJ*, 576, 135
- Gavazzi G., Boselli A., Donati A., Franzetti P., Scodreggio M., 2003a, *A&A*, 400, 451
- Gavazzi G., Boselli A., Donati A., Franzetti P., Scodreggio M., 2003b, *A&A*, 400, 451
- Gavazzi G., Boselli A., Scodreggio M., Pierini D., Belsole E., 1999, *MNRAS*, 304, 595
- Gavazzi G., Franzetti P., Scodreggio M., Boselli A., Pierini D., Baffa C., Lisi F., Hunt L. K., 2000, *A&AS*, 142, 65
- Gavazzi G., Zaccardo A., Sanvito G., Boselli A., Bonfanti C., 2004, *A&A*, 417, 499
- Geller M. J., Huchra J. P., 1989, *Science*, 246, 897
- Georgakakis A., Nandra K., Yan R., Willner S. P., Lotz J. M., Pierce C. M., Cooper M. C., Laird E. S., Koo D. C., Barmby P., Newman J. A., Primack J. R., Coil A. L., 2008, *MNRAS*, 385, 2049
- Ghigna S., Moore B., Governato F., Lake G., Quinn T., Stadel J., 1998, *MNRAS*, 300, 146
- Gil de Paz A., Boissier S., Madore B. F., Seibert M., Joe Y. H., Boselli A., Wyder T. K., et al. 2007, *ApJS*, 173, 185
- Girardi M., Giuricin G., Mardirossian F., Mezzetti M., Boschini W., 1998, *ApJ*, 505, 74
- Glazebrook K., Blake C., Couch W., Forbes D., Drinkwater M., Jurek R., Pimbblet K., Madore B., Martin C., Small T., Forster K., Colless M., Sharp R., Croom S., Woods D., Pracy M., Gilbank D., Yee H., Gladders M., 2007, in N. Metcalfe & T. Shanks ed., *Cosmic Frontiers Vol. 379 of Astronomical Society of the Pacific Conference Series, The WiggleZ Project: AAOmega and Dark Energy*. pp 72–+
- Gordon K. D., Clayton G. C., Witt A. N., Misselt K. A., 2000, *ApJ*, 533, 236
- Griffin M. J., Abergel A., Abreu A., Ade P. A. R., André P., Augeres J., Babbedge T., Bae Y., et al. 2010, *A&A*, 518, L3+

- Gunn J. E., Gott J. R. I., 1972, *ApJ*, 176, 1
- Haines C. P., Gargiulo A., Merluzzi P., 2008, *MNRAS*, 385, 1201
- Hau G. K. T., Bower R. G., Kilborn V., Forbes D. A., Balogh M. L., Oosterloo T., 2008, *MNRAS*, 385, 1965
- Haynes M. P., Giovanelli R., 1984, *AJ*, 89, 758
- Haynes M. P., Jore K. P., Barrett E. A., Broeils A. H., Murray B. M., 2000, *AJ*, 120, 703
- Heckman T. M., Kauffmann G., Brinchmann J., Charlot S., Tremonti C., White S. D. M., 2004, *ApJ*, 613, 109
- Henry R. B. C., Pagel B. E. J., Chincarini G. L., 1994, *MNRAS*, 266, 421
- Henry R. B. C., Pagel B. E. J., Lassetter D. F., Chincarini G. L., 1992, *MNRAS*, 258, 321
- Hernán-Caballero A., Pérez-Fournon I., Hatziminaoglou E., Afonso-Luis A., Rowan-Robinson M., Rigopoulou D., Farrah D., Lonsdale C. J., et al. 2009, *MNRAS*, 395, 1695
- Herschel J. F. W., 1864, *Royal Society of London Philosophical Transactions Series I*, 154, 1
- Hirashita H., 1999, *ApJL*, 510, L99
- Ho L. C., Filippenko A. V., Sargent W. L. W., 1997, *ApJS*, 112, 315
- Holmberg E., 1958, *Meddelanden fran Lunds Astronomiska Observatorium Serie II*, 136, 1
- Hopkins P. F., Cox T. J., Younger J. D., Hernquist L., 2009, *ApJ*, 691, 1168
- Horst H., Smette A., Gandhi P., Duschl W. J., 2006, *A&A*, 457, L17
- Howell J. H., 2006, *AJ*, 131, 2469
- Huang J., Glazebrook K., Cowie L. L., Tinney C., 2003, *ApJ*, 584, 203
- Hubble E. P., 1925, *Popular Astronomy*, 33, 252
- Hughes T. M., Cortese L., 2009, *MNRAS*, 396, L41

- Hummel E., van der Hulst J. M., Kennicutt R. C., Keel W. C., 1990, *A&A*, 236, 333
- Hunt L. K., Thuan T. X., Izotov Y. I., Sauvage M., 2010, *ApJ*, 712, 164
- Hunter S. D., Bertsch D. L., Catelli J. R., Dame T. M., Digel S. W., Dingus B. L., Esposito J. A., Fichtel C. E., et al. 1997, *ApJ*, 481, 205
- Iglesias-Páramo J., Buat V., Takeuchi T. T., Xu K., Boissier S., Boselli A., Burgarella D., Madore B. F., et al. 2006, *ApJS*, 164, 38
- Inoue A. K., 2001, *AJ*, 122, 1788
- Inoue A. K., 2003, *PASJ*, 55, 901
- Issa M. R., MacLaren I., Wolfendale A. W., 1990, *A&A*, 236, 237
- Jansen R. A., Kannappan S. J., 2001, *APSS*, 276, 1151
- Jarosik N., Bennett C. L., Dunkley J., Gold B., Greason M. R., Halpern M., Hill R. S., Hinshaw G., et al. 2010, *ArXiv astro-ph/10014744*
- Jarrett T. H., Chester T., Cutri R., Schneider S. E., Huchra J. P., 2003, *AJ*, 125, 525
- Jester S., 2005, *ApJ*, 625, 667
- Kannappan S. J., 2004, *ApJL*, 611, L89
- Kapferer W., Sluka C., Schindler S., Ferrari C., Ziegler B., 2009, *A&A*, 499, 87
- Kauffmann G., 1996, *MNRAS*, 281, 475
- Kauffmann G., Heckman T. M., Tremonti C., Brinchmann J., Charlot S., White S. D. M., Ridgway S. E., Brinkmann J., Fukugita M., Hall P. B., Ivezić Ž., Richards G. T., Schneider D. P., 2003, *MNRAS*, 346, 1055
- Kauffmann G., White S. D. M., Guiderdoni B., 1993, *MNRAS*, 264, 201
- Kauffmann G., White S. D. M., Heckman T. M., Ménard B., Brinchmann J., Charlot S., Tremonti C., Brinkmann J., 2004, *MNRAS*, 353, 713
- Kaviraj S., Schawinski K., Devriendt J. E. G., Ferreras I., Khochfar S., Yoon S., Yi S. K., Deharveng J., et al. 2007, *ApJS*, 173, 619
- Keel W. C., Kennicutt Jr. R. C., Hummel E., van der Hulst J. M., 1985, *AJ*, 90, 708
- Keeton C. R., 2001, *ApJ*, 561, 46

- Kenney J. D. P., Tal T., Crowl H. H., Feldmeier J., Jacoby G. H., 2008, *ApJL*, 687, L69
- Kennicutt Jr. R. C., 1983, *AJ*, 88, 483
- Kennicutt Jr. R. C., 1992, *ApJ*, 388, 310
- Kennicutt Jr. R. C., 1998, *ARA&A*, 36, 189
- Kennicutt Jr. R. C., Armus L., Bendo G., Calzetti D., Dale D. A., Draine B. T., Engelbracht C. W., Gordon K. D., et al. 2003, *PASP*, 115, 928
- Kennicutt Jr. R. C., Roettiger K. A., Keel W. C., van der Hulst J. M., Hummel E., 1987, *AJ*, 93, 1011
- Kennicutt Jr. R. C., Tamblyn P., Congdon C. E., 1994, *ApJ*, 435, 22
- Kewley L. J., Dopita M. A., 2002, *ApJS*, 142, 35
- Kewley L. J., Dopita M. A., Sutherland R. S., Heisler C. A., Trevena J., 2001, *ApJ*, 556, 121
- Kewley L. J., Ellison S. L., 2008, *ApJ*, 681, 1183
- Kobulnicky H. A., Kennicutt Jr. R. C., Pizagno J. L., 1999, *ApJ*, 514, 544
- Kobulnicky H. A., Kewley L. J., 2004, *ApJ*, 617, 240
- Kobulnicky H. A., Zaritsky D., 1999, *ApJ*, 511, 118
- Kochanek C. S., 1995, *ApJ*, 445, 559
- Kodama T., Yamada T., Akiyama M., Aoki K., Doi M., Furusawa H., Fuse T., Imanishi M., et al. 2004, *MNRAS*, 350, 1005
- Kong X., Cheng F. Z., 2002, *A&A*, 389, 845
- Koopmann R. A., Haynes M. P., Catinella B., 2006, *AJ*, 131, 716
- Koopmans L. V. E., Treu T., 2003, *ApJ*, 583, 606
- Köppen J., Weidner C., Kroupa P., 2007, *MNRAS*, 375, 673
- Kormendy J., Kennicutt Jr. R. C., 2004, *ARA&A*, 42, 603

- Kronberger T., Kapferer W., Ferrari C., Unterguggenberger S., Schindler S., 2008, *A&A*, 481, 337
- Kroupa P., Tout C. A., Gilmore G., 1993, *MNRAS*, 262, 545
- Krumholz M. R., McKee C. F., Tumlinson J., 2009, *ApJ*, 693, 216
- Krumm N., van Driel W., van Woerden H., 1985, *A&A*, 144, 202
- Lamareille F., Mouhcine M., Contini T., Lewis I., Maddox S., 2004, *MNRAS*, 350, 396
- Lamastra A., Bianchi S., Matt G., Perola G. C., Barcons X., Carrera F. J., 2009, *A&A*, 504, 73
- Larson R. B., Tinsley B. M., Caldwell C. N., 1980, *ApJ*, 237, 692
- Laurent O., Mirabel I. F., Charmandaris V., Gallais P., Madden S. C., Sauvage M., Vigroux L., Cesarsky C., 2000, *A&A*, 359, 887
- Lee S., Irwin J. A., 1997, *ApJ*, 490, 247
- Leitherer C., Schaerer D., Goldader J. D., González Delgado R. M., Robert C., Kune D. F., de Mello D. F., Devost D., Heckman T. M., 1999, *ApJS*, 123, 3
- Lemaitre G., Kohler D., Lacroix D., Meunier J. P., Vin A., 1990, *A&A*, 228, 546
- Lequeux J., Peimbert M., Rayo J. F., Serrano A., Torres-Peimbert S., 1979, *A&A*, 80, 155
- Liang Y. C., Yin S. Y., Hammer F., Deng L. C., Flores H., Zhang B., 2006, *ApJ*, 652, 257
- Lilly S. J., Le Fevre O., Hammer F., Crampton D., 1996, *ApJL*, 460, L1+
- Lintott C. J., Schawinski K., Slosar A., Land K., Bamford S., Thomas D., Raddick M. J., Nichol R. C., Szalay A., Andreescu D., Murray P., Vandenberg J., 2008, *MNRAS*, 389, 1179
- Liu X., 2002, in W. J. Henney, J. Franco, & M. Martos ed., *Revista Mexicana de Astronomia y Astrofisica Conference Series Vol. 12 of Revista Mexicana de Astronomia y Astrofisica Conference Series, Optical Recombination Lines and Temperature Fluctuations*. pp 70–76

- Lynden-Bell D., 1969, *Nature*, 223, 690
- Macciò A. V., Moore B., Stadel J., 2006, *ApJL*, 636, L25
- Madau P., Ferguson H. C., Dickinson M. E., Giavalisco M., Steidel C. C., Fruchter A., 1996, *MNRAS*, 283, 1388
- Magorrian J., Tremaine S., Richstone D., Bender R., Bower G., Dressler A., Faber S. M., Gebhardt K., Green R., Grillmair C., Kormendy J., Lauer T., 1998, *AJ*, 115, 2285
- Mannucci F., Cresci G., Maiolino R., Marconi A., Gnerucci A., 2010, *ArXiv astro-ph/10050006*
- Maraston C., 2005, *MNRAS*, 362, 799
- Marconi A., Hunt L. K., 2003, *ApJL*, 589, L21
- Marconi A., Risaliti G., Gilli R., Hunt L. K., Maiolino R., Salvati M., 2004, *MNRAS*, 351, 169
- Martig M., Bournaud F., Teyssier R., Dekel A., 2009, *ApJ*, 707, 250
- Martin D. C., Fanson J., Schiminovich D., Morrissey P., Friedman P. G., Barlow T. A., Conrow T., Grange R., et al. 2005, *ApJL*, 619, L1
- Martin D. C., Wyder T. K., Schiminovich D., Barlow T. A., Forster K., Friedman P. G., Morrissey P., Neff S. G., et al. 2007, *ApJS*, 173, 342
- Martín-Hernández N. L., Peeters E., Morisset C., Tielens A. G. G. M., Cox P., Roelfsema P. R., Baluteau J., Schaerer D., Mathis J. S., Damour F., Churchwell E., Kessler M. F., 2002, *A&A*, 381, 606
- Masters K. L., Mosleh M., Romer A. K., Nichol R. C., Bamford S. P., Schawinski K., Lintott C. J., Andreescu D., Campbell H. C., Crowcroft B., Doyle I., Edmondson E. M., Murray P., Raddick M. J., Slosar A., Szalay A. S., Vandenberg J., 2010, *MNRAS*, 405, 783
- Matteucci F., 1994, *A&A*, 288, 57
- McCall M. L., Rybski P. M., Shields G. A., 1985, *ApJS*, 57, 1
- McGaugh S. S., 1991, *ApJ*, 380, 140

- McNamara B. R., Nulsen P. E. J., 2007, *ARA&A*, 45, 117
- Mehlert D., Noll S., Appenzeller I., Saglia R. P., Bender R., Böhm A., Drory N., Fricke K., Gabasch A., Heidt J., Hopp U., Jäger K., Möllenhoff C., Seitz S., Stahl O., Ziegler B., 2002, *A&A*, 393, 809
- Meléndez M., Kraemer S. B., Armentrout B. K., Deo R. P., Crenshaw D. M., Schmitt H. R., Mushotzky R. F., Tueller J., Markwardt C. B., Winter L., 2008, *ApJ*, 682, 94
- Merritt D., 1984, *ApJ*, 276, 26
- Merritt D., Ferrarese L., 2001, in J. H. Knapen, J. E. Beckman, I. Shlosman, & T. J. Mahoney ed., *The Central Kiloparsec of Starbursts and AGN: The La Palma Connection* Vol. 249 of *Astronomical Society of the Pacific Conference Series*, Relationship of Black Holes to Bulges. pp 335–+
- Messier C., 1781, *Connaissance des Temps* for 1784
- Meurer G. R., Heckman T. M., Calzetti D., 1999, *ApJ*, 521, 64
- Meurer G. R., Heckman T. M., Leitherer C., Kinney A., Robert C., Garnett D. R., 1995, *AJ*, 110, 2665
- Miller C. J., Nichol R. C., Gómez P. L., Hopkins A. M., Bernardi M., 2003, *ApJ*, 597, 142
- Miller R. H., 1986, *A&A*, 167, 41
- Mo H. J., Mao S., White S. D. M., 1998, *MNRAS*, 295, 319
- Moore B., Katz N., Lake G., Dressler A., Oemler A., 1996, *Nature*, 379, 613
- Moore B., Lake G., Katz N., 1998, *ApJ*, 495, 139
- Moore B., Lake G., Quinn T., Stadel J., 1999, *MNRAS*, 304, 465
- Morrissey P., Conrow T., Barlow T. A., Small T., Seibert M., Wyder T. K., Budavári T., Arnouts S., et al. 2007, *ApJS*, 173, 682
- Morrissey P., Schiminovich D., Barlow T. A., Martin D. C., Blakkolb B., Conrow T., Cooke B., Erickson K., et al. 2005, *ApJL*, 619, L7
- Mouhcine M., Baldry I. K., Bamford S. P., 2007, *MNRAS*, 382, 801

- Mouhcine M., Bamford S. P., Aragón-Salamanca A., Nakamura O., Milvang-Jensen B., 2006, MNRAS, 369, 891
- Mouhcine M., Gibson B. K., Renda A., Kawata D., 2008, A&A, 486, 711
- Moustakas J., Kennicutt Jr. R. C., 2006, ApJS, 164, 81
- Moustakas J., Kennicutt Jr. R. C., Tremonti C. A., Dale D. A., Smith J., Calzetti D., 2010, ApJS, 190, 233
- Mundell C. G., 2002, Royal Society of London Philosophical Transactions Series A, 360, 2725
- Mundell C. G., Wilson A. S., Ulvestad J. S., Roy A. L., 2001, in R. T. Schilizzi ed., Galaxies and their Constituents at the Highest Angular Resolutions Vol. 205 of IAU Symposium, The nature of flat-spectrum nuclear radio emission in Seyfert galaxies. pp 72–+
- Nagar N. M., Falcke H., Wilson A. S., Ulvestad J. S., 2002, A&A, 392, 53
- Nandra K., Georgakakis A., Willmer C. N. A., Cooper M. C., Croton D. J., Davis M., Faber S. M., Koo D. C., Laird E. S., Newman J. A., 2007, ApJL, 660, L11
- Narayan R., Yi I., 1994, ApJL, 428, L13
- Narayan R., Yi I., 1995, ApJ, 444, 231
- Navarro J. F., Frenk C. S., White S. D. M., 1996, ApJ, 462, 563
- Netzer H., Mainieri V., Rosati P., Trakhtenbrot B., 2006, A&A, 453, 525
- Nilson P., 1973, Uppsala general catalogue of galaxies
- Noguchi M., 1999, ApJ, 514, 77
- Nulsen P. E. J., 1982, MNRAS, 198, 1007
- O'Connell R. W., 1999, ARA&A, 37, 603
- Okamoto T., Habe A., 1999, ApJ, 516, 591
- Okamoto T., Nemmen R. S., Bower R. G., 2008, MNRAS, 385, 161
- Osterbrock D. E., 1989, Astrophysics of gaseous nebulae and active galactic nuclei
- Pagel B. E. J., 1997, Nucleosynthesis and Chemical Evolution of Galaxies

- Pagel B. E. J., Edmunds M. G., Blackwell D. E., Chun M. S., Smith G., 1979, MNRAS, 189, 95
- Pagel B. E. J., Edmunds M. G., Smith G., 1980, MNRAS, 193, 219
- Pagel B. E. J., Patchett B. E., 1975, MNRAS, 172, 13
- Panuzzo P., Bressan A., Granato G. L., Silva L., Danese L., 2003, A&A, 409, 99
- Patil M. K., Pandey S. K., Kembhavi A., Sahu D. K., 2009, ArXiv astro-ph/09011747
- Peebles P. J. E., 1969, ApJ, 155, 393
- Peebles P. J. E., 1982, ApJL, 263, L1
- Peimbert A., Peimbert M., 2005, in S. Torres-Peimbert & G. MacAlpine ed., Revista Mexicana de Astronomia y Astrofisica Conference Series Vol. 23 of Revista Mexicana de Astronomia y Astrofisica Conference Series, Oxygen Recombination Line Abundances in Gaseous Nebulae. pp 9–14
- Peimbert M., Peimbert A., Esteban C., García-Rojas J., Bresolin F., Carigi L., Ruiz M. T., López-Sánchez A. R., 2007, in R. Guzmán ed., Revista Mexicana de Astronomia y Astrofisica Conference Series Vol. 29 of Revista Mexicana de Astronomia y Astrofisica Conference Series, The Calibration of the O/H Abundance Indicators for Extragalactic H II Regions based on O II Recombination Lines. pp 72–79
- Pettini M., Pagel B. E. J., 2004, MNRAS, 348, L59
- Pilbratt G. L., Riedinger J. R., Passvogel T., Crone G., Doyle D., Gageur U., Heras A. M., Jewell C., et al. 2010, A&A, 518, L1+
- Pilyugin L. S., 2001, A&A, 374, 412
- Pilyugin L. S., Thuan T. X., 2005, ApJ, 631, 231
- Pilyugin L. S., Thuan T. X., Vílchez J. M., 2007, MNRAS, 376, 353
- Pilyugin L. S., Vílchez J. M., Contini T., 2004, A&A, 425, 849
- Postman M., Franx M., Cross N. J. G., Holden B., Ford H. C., Illingworth G. D., Goto T., Demarco R., et al. 2005, ApJ, 623, 721
- Postman M., Geller M. J., 1984, ApJ, 281, 95
- Quataert E., 2003, Astronomische Nachrichten Supplement, 324, 435

- Quilis V., Moore B., Bower R., 2000, *Science*, 288, 1617
- Raimann D., Storchi-Bergmann T., Bica E., Melnick J., Schmitt H., 2000, *MNRAS*, 316, 559
- Roberts M. S., 1963, *ARA&A*, 1, 149
- Roberts M. S., Haynes M. P., 1994, *ARA&A*, 32, 115
- Roediger E., 2009, *Astronomische Nachrichten*, 330, 888
- Rubin R. H., Simpson J. P., Colgan S. W. J., Dufour R. J., Brunner G., McNabb I. A., Pauldrach A. W. A., Erickson E. F., Haas M. R., Citron R. I., 2008, *MNRAS*, 387, 45
- Rubin V. C., Ford Jr. W. K., Whitmore B. C., 1984, *ApJL*, 281, L21
- Rubin V. C., Ford W. K. J., Thonnard N., 1980, *ApJ*, 238, 471
- Rudolph A. L., Fich M., Bell G. R., Norsen T., Simpson J. P., Haas M. R., Erickson E. F., 2006, *ApJS*, 162, 346
- Salpeter E. E., 1955, *ApJ*, 121, 161
- Salpeter E. E., Hoffman G. L., 1996, *ApJ*, 465, 595
- Sandage A., Binggeli B., 1984, *AJ*, 89, 919
- Satyapal S., Dudik R. P., O'Halloran B., Gliozzi M., 2005, *ApJ*, 633, 86
- Savaglio S., Glazebrook K., Abraham R. G., Crampton D., Chen H., McCarthy P. J. P., Jørgensen I., Roth K. C., Hook I. M., Marzke R. O., Murowinski R. G., Carlberg R. G., 2004, *ApJ*, 602, 51
- Schawinski K., Thomas D., Sarzi M., Maraston C., Kaviraj S., Joo S.-J., Yi S. K., Silk J., 2007, *MNRAS*, 382, 1415
- Schechter P., 1976, *ApJ*, 203, 297
- Schiminovich D., Wyder T. K., Martin D. C., Johnson B. D., Salim S., Seibert M., Treyer M. A., Budavári T., et al. 2007, *ApJS*, 173, 315
- Schlegel D. J., Finkbeiner D. P., Davis M., 1998, *ApJ*, 500, 525
- Schmidt M., 1959, *ApJ*, 129, 243

- Schmidt M., 1963, *ApJ*, 137, 758
- Schödel R., Ott T., Genzel R., Eckart A., Mouawad N., Alexander T., 2003, *ApJ*, 596, 1015
- Searle L., Sargent W. L. W., 1972, *ApJ*, 173, 25
- Sersic J. L., 1968, *Atlas de galaxias australes*
- Seyfert C. K., 1943, *ApJ*, 97, 28
- Shakura N. I., Sunyaev R. A., 1973, *A&A*, 24, 337
- Shankar F., Lapi A., Salucci P., De Zotti G., Danese L., 2006, *ApJ*, 643, 14
- Shields G. A., Skillman E. D., Kennicutt Jr. R. C., 1991, *ApJ*, 371, 82
- Sijacki D., Springel V., 2006, *MNRAS*, 366, 397
- Skillman E. D., Kennicutt R. C., Hodge P. W., 1989, *ApJ*, 347, 875
- Skillman E. D., Kennicutt Jr. R. C., Shields G. A., Zaritsky D., 1996, *ApJ*, 462, 147
- Skrutskie M. F., Cutri R. M., Stiening R., Weinberg M. D., Schneider S., Carpenter J. M., Beichman C., Capps R., et al. 2006, *AJ*, 131, 1163
- Smoot G. F., Bennett C. L., Kogut A., Wright E. L., Aymon J., Boggess N. W., Cheng E. S., de Amici G., et al. 1992, *ApJL*, 396, L1
- Solanes J. M., Giovanelli R., Haynes M. P., 1996, *ApJ*, 461, 609
- Somerville R. S., Hopkins P. F., Cox T. J., Robertson B. E., Hernquist L., 2008, *MNRAS*, 391, 481
- Somerville R. S., Primack J. R., 1999, *MNRAS*, 310, 1087
- Spitoni E., Calura F., Matteucci F., Recchi S., 2010, *A&A*, 514, A73+
- Springob C. M., Haynes M. P., Giovanelli R., Kent B. R., 2005, *ApJS*, 160, 149
- Stasińska G., 2002, *ArXiv astro-ph/0207500*
- Stasińska G., 2005, *A&A*, 434, 507
- Stasińska G., 2010, in G. Bruzual & S. Charlot ed., *IAU Symposium Vol. 262 of IAU Symposium, Nebular abundances in galaxies: Beware of biases*. pp 93–96

- Stasińska G., Asari N. V., Fernandes R. C., Gomes J. M., Schlickmann M., Mateus A., Schoenell W., Sodr e Jr. L., 2008, MNRAS, 391, L29
- Stasińska G., Cid Fernandes R., Mateus A., Sodr e L., Asari N. V., 2006, MNRAS, 371, 972
- Storchi-Bergmann T., Calzetti D., Kinney A. L., 1994, ApJ, 429, 572
- Sutherland R. S., Dopita M. A., 1993, ApJS, 88, 253
- Tecce T. E., Cora S. A., Tissera P. B., Abadi M. G., Lagos C. d. P., 2010, ArXiv astro-ph/10065446
- Tonnesen S., Bryan G. L., 2009, ApJ, 694, 789
- Tremonti C. A., Heckman T. M., Kauffmann G., Brinchmann J., Charlot S., White S. D. M., Seibert M., Peng E. W., Schlegel D. J., Uomoto A., Fukugita M., Brinkmann J., 2004, ApJ, 613, 898
- Tsamis Y. G., Barlow M. J., Liu X., Danziger I. J., Storey P. J., 2003, MNRAS, 338, 687
- Tully R. B., Mould J. R., Aaronson M., 1982, ApJ, 257, 527
- van den Bergh S., 2007, AJ, 134, 1508
- van Driel W., Balkowski C., van Woerden H., 1989, A&A, 218, 49
- van Driel W., van Woerden H., 1991, A&A, 243, 71
- van Driel W., van Woerden H., Schwarz U. J., Gallagher III J. S., 1988, A&A, 191, 201
- Veilleux S., Osterbrock D. E., 1987, ApJS, 63, 295
- Vila-Costas M. B., Edmunds M. G., 1992, MNRAS, 259, 121
- Vilchez J. M., 1995, AJ, 110, 1090
- Vollmer B., 2009, A&A, 502, 427
- Vollmer B., Braine J., Combes F., Sofue Y., 2005, A&A, 441, 473
- Vollmer B., Cayatte V., Balkowski C., Duschl W. J., 2001, ApJ, 561, 708
- Vollmer B., Huchtmeier W., van Driel W., 2005, A&A, 439, 921

- Volonteri M., 2010, *A&A Rev.*, 18, 279
- Wang J., Fabbiano G., Risaliti G., Elvis M., Mundell C. G., Dumas G., Schinnerer E., Zezas A., 2010, *ApJL*, 719, L208
- Warmels R. H., 1988, *A&AS*, 72, 427
- Westoby P. B., Mundell C. G., Baldry I. K., 2007, *MNRAS*, 382, 1541
- Whitford A. E., 1958, *AJ*, 63, 201
- Whitmore B. C., Gilmore D. M., Jones C., 1993, *ApJ*, 407, 489
- Wilson A. S., Ulvestad J. S., 1982, *ApJ*, 263, 576
- Wu Q., 2009, *ApJL*, 701, L95
- Wu Q., Cao X., 2006, *PASP*, 118, 1098
- Wyder T. K., Martin D. C., Schiminovich D., Seibert M., Budavári T., Treyer M. A., Barlow T. A., Forster K., et al. 2007, *ApJS*, 173, 293
- Xu C., Buat V., 1995, *A&A*, 293, L65
- Yi S. K., Yoon S., Kaviraj S., Deharveng J., Rich R. M., Salim S., Boselli A., Lee Y., et al. 2005, *ApJL*, 619, L111
- Yin S. Y., Liang Y. C., Zhang B., 2007, in L. C. Ho & J.-W. Wang ed., *The Central Engine of Active Galactic Nuclei Vol. 373 of Astronomical Society of the Pacific Conference Series, A Study on the Revised R23-P Method for Metallicity Estimates Based on 20,000 SDSS Galaxies*. pp 686–+
- York D. G., Adelman J., Anderson Jr. J. E., Anderson S. F., Annis J., Bahcall N. A., Bakken J. A., Barkhouser R., et al. 2000, *AJ*, 120, 1579
- Young J. S., Scoville N. Z., 1991, *ARA&A*, 29, 581
- Zaritsky D., Kennicutt Jr. R. C., Huchra J. P., 1994, *ApJ*, 420, 87
- Zhang W., Li C., Kauffmann G., Zou H., Catinella B., Shen S., Guo Q., Chang R., 2009, *MNRAS*, 397, 1243
- Zwicky F., Herzog E., Wild P., 1961, *Catalogue of galaxies and of clusters of galaxies*, Vol. I

